Novel Switching Pt(II) Pincer Complexes.

Stubbs, Clare

Award date:
2020

Awarding institution:
University of Bath

Novel Switching Pt(II) Pincer Complexes

Clare Louise Stubbs

A thesis submitted for the degree of Doctor of Philosophy

Department of Chemistry

University of Bath

August 2019

Table of Contents

Table of Figures

Table of Tables

Table of Equations

Table of Schemes

Abbreviations

Abbreviation	**Definition**
AgCN	Silver cyanide
AgCl	Silver chloride
Azo	(*E*)-2,2'-(5-(phenyldiazenyl)-1,3-phenylene)dipyridine
Å	Angstrom
BF_4^-	Tetrafluoroborate
BPh_4^-	Tetraphenylborate
C^N^N	Pincer based on the 6-phenyl-2,2'-bipyridine fragment
C^N^C	Pincer based on the 2,6-diphenylpyridine fragment
cm^{-1}	Wavenumber
$CDCl_3$	Deuterated Chloroform
DCM	Dichloromethane
DMF	Dimethylformamide
DFT	Density Functional theory
D_6-DMSO	Deuterated dimethyl sulfoxide
ES	Excited state
GS	Ground State
HOMO	Highest Occupied Molecular Orbital
h	Hours
hkl	Miller Index notation
ILCT	Intra Ligand charge transfer
IR	Infra-red
K	Kelvin
KCN	Potassium cyanide
L	Ligand
LUMO	Lowest Occupied Molecular Orbital
M-L	Metal to Ligand
Min	Minute
MeOH	Methanol
MePh	(p-tolyl) group
MeCN	Acetonitrile
MHz	Mega Hertz
MLCT	Metal to Ligand charge transfer
MMLCT	Metal- Metal to Ligand charge transfer
mmol	Millimole
mg	Milligram
N^N^N	Pincer based on the terpyridine fragment
N^C^N	Pincer based on the 1,3-di(pyridin-2-yl)benzene fragment
N^C^C	Pincer based on the 2-([1,1'-biphenyl]-3-yl)pyridine fragment
NR_2	Amine, where R=H or extended carbon chain.
NMR	Nuclear Magnetic Resonance
nm	Nanometre
OLED	Organic Light Emitting Diode
OTf^-	Triflate
OTs^-	Tosyl
PF_6^-	Hexafluorophosphate
Ph	Phenyl group
Ph terpy	4'-phenyl-2,2':6',2''-terpyridine

ppm	Part per million
s	Seconds
Stilbene	(*E*)-2,2'-(5-styryl-1,3-phenylene)dipyridine
Terpy	Pincer based on the terpyridine ligand
Tolyl Terpy	4'-(p-tolyl)-2,2':6',2''-terpyridine
UV-Vis	UV-Visible
VOCs	Volatile Organic Compounds
vs	Against or as opposed to
λ_{max}	Wavelength of maximum Absorption or emission
°	Degrees
°C	Degrees Celsius
2θ	Scattering angle
α,β,γ	Unit cell parameters- angles
a, b, c	Unit cell parameters- lengths

Acknowledgments

I would like to thank my supervisor Paul Raithby for all of his support and advice throughout my PhD. In addition to the metastable materials group in particular Dr Lauren Hatcher and Dr Jonathan Skelton, whose support with Single Crystal X-Ray diffraction and computational studies respectively made this research possible.

This research built on the work conducted by Dr Mat Bryant and I would like to thank him for his advice and guidance and ideas from which I was able to start my research.

Thanks also to Dr Simon Teat as a number of the solid state structures would not have been obtained without access to the small crystal beamline at the ALS.

I would also like to thank the University of Bath for providing me with the funding to carry out this research.

Finally I would like to thank my family for all of their support and encouragement during my PhD, in particular during the stage of writing up.

Abstract

The research presented in this thesis is concerned with the design, synthesis and structural analysis of new platinum (II) pincer complexes with a view to developing new solid state and solution state molecular switches.

Chapter 1 consists of a literature review that starts by introducing platinum and its numerous uses across a variety of fields. This review also considers the photophysics of platinum and considers the background theory for the observed spectral properties of Pt(II) complexes. The end of this chapter investigates the history and current research of Pt(II) complexes that are relevant to the research presented in this thesis. **Chapter 2** is a description of the instrumental methods frequently used in this thesis. These include a description of single crystal X-Ray crystallography, solution state UV-Vis and emission spectroscopy, reflectance spectroscopy and NMR spectroscopy. **Chapter 3** lays out the general research aim of this thesis, in addition to more detailed aims for each of the chapters.

Chapter 4 is the first of the results chapters. It consists of a systematic study of a group of Pt(II) terpyridine complexes. The start of this chapter reviews the key literature in the area that inspired the research in this chapter. This study was designed to investigate the effects of ligand substitution and counter-ion sterics in a systematic way to assist in the development of a design methodology for *'smart'* materials. This investigation focussed on the structural analysis of thirteen complexes, two of which had been previously published in the literature. **Chapter 5** shifted the focus from the use of terpyridine based ligands to N^C^N ligands. The central phenyl ring in this ligand increases the emissive properties of the Pt complexes. This chapter built on previous work within the Raithby group, utilising the same N^C^N pincer that had led to the discovery of a vapochromic complex. In this chapter, the ligand in the 4th position of the Pt co-ordination sphere was altered with ligands of various configurations and the spectral properties of the complexes were analysed using the techniques described in chapter 2. As a result a number of complexes were synthesised that displayed solvato and vapochromic capabilities and have potential uses in the field of chemical sensing. **Chapter 6** focussed on developing complexes for a specific purpose. In this instance photo-switching. The functional groups azobenzene and stilbene were used to establish a benchmark for future materials. These functional groups were substituted onto two different areas of the Pt complex, on the pincer and via an acetylide on the 4th co-ordination site of the Pt centre. Computational techniques were utilised to predict the orbital arrangements and solution state spectra of the complex and therefore whether they would undergo a *cis/trans* isomerisation. Once each of the complexes had been analysed it was found that the computational predictions were correct and with further development would be an invaluable tool in predicting the behaviour of these complexes. **Chapter 7** built on the research conducted in chapter 6 and used computational methods to predict whether a complex would be sensitive to changes in pH. In this instance the two different substitution patterns showed sensitivity to changes in pH, however the behaviour for each complex was unique. Three pH sensitive complexes were discovered as part of the research in this chapter and show promise as solution and solid-state sensors.

The conclusions and potential future research is detailed in **Chapter 8. Chapter 9** details the synthesis of each of the complexes discussed in this thesis.

CHAPTER 1

Literature Review

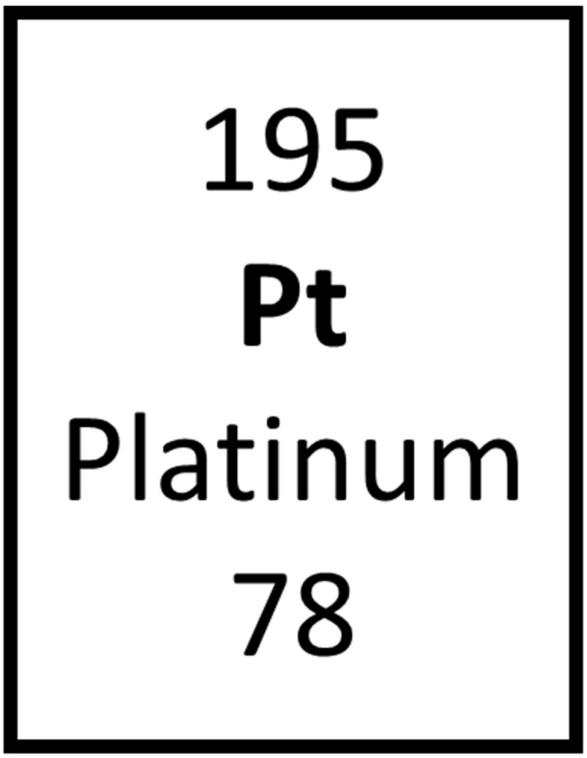

1.1.0 Introduction

Platinum is a heavy, third row transition metal with a range of diverse uses including but not limited to:

1. Heterogeneous and Homogenous catalysis,
2. Anti-cancer drugs,
3. Optoelectronics industry due to their long-lived triplet states.
4. Chemical Sensing

The automotive industry has been using precious metals such as Pt for catalytic convertors to control vehicle emissions. They have been successful in minimising the air pollution in cities and research is ongoing to develop more effective Pt-based catalysts for this industry.[1] In addition to this example of heterogeneous catalysis Pt has been used in homogenous catalysis to activate and functionalise C-H bonds. Shilov, 1972 reported one of the first catalytic cycles to use Pt salts.[2] The product of this cycle was an oxidised alkane. Recent studies on this system by the Khan group revealed that in this system the C-H bond is cleaved resulting in a transient 5 coordinate Pt-H species that has retained its Pt(II) oxidation state.[3] While this system shows promise for C-H activation, there are a number of associated problems such as a slow reaction rate, unstable catalysts, the use of Pt(IV) as an oxidant and the low conversion of alkane to methanol. These disadvantages are being addressed by the systematic change of the ligands coordinated to the Pt centre.

Further research in the area of platinum catalysis has focussed on the use of platinum nanoparticles, due to the increased surface area, which increases catalytic activity.[4-6] There is one paper in the literature of particular interest due to its use of a terpyridine based platinum complex in the process of photo-catalysis. This compound was used as a chromophore in conjunction with a cobalt-based complex in a homogeneous system. The result was the splitting of water to generate hydrogen with light.[7] It is clear to see from the breadth of literature that platinum catalysis continues to be an active area of research.

Another role of platinum compounds is in the treatment of cancer. One of the most famous examples is *cis*-platin.[8] It was approved for use in the UK in 1979. Since this discovery, there are many more platinum complexes on the market, with research aiming to develop complexes that target cancer more effectively. An excellent review published in 2016, [9] discussed the drawbacks of the current drugs and the areas where research is currently developing, including multi-platinum containing complexes as well as the use of platinum(IV). Although the mechanism behind how these Pt anti-cancer drugs work is still unclear it is thought that the drug crosslinks with the DNA, disrupting the growth of the cancerous tumour.

A further key feature of Pt complexes is the formation of electronic triplet states, these can be readily manipulated to create complexes that are of interest to the optoelectronics and chemical sensing industry. One of the earliest molecular wire examples known is the Magnus green salt.[10] This highly coloured compound promoted interest in the field of Pt chemistry. The metal-metal interactions that form in planar Pt(II) complexes facilitate interesting spectroscopic features that can be tuned.

One area of interest is the development of metallopolymers that aim to combine the chemical, electronic, magnetic, optical and redox properties of a metal centre with the ease of processibility and low cost of polymers.[11] There are two main types of platinum metallopolymers documented in the literature, linear polymers based on ethynylenic polymers and polymers based on cycloplatinated moieties. One study that focussed on the development of linear polymers, used a simple method of increasing the π conjugation in the bridging ligand. They found that this improved the optical properties of the polymer.[12]

In contrast a paper published by Khan *et al.* focussed on varying the spacer unit R, in the following chemical formula: $[\text{-Pt}(PBu_3^n)_2\text{- C}\equiv\text{C –R- C}\equiv\text{C -}]_n$. Platinum was used to induce strong spin orbit coupling so that the lifetime of the triplet state could be effectively measured. This study found that the triplet state emission time was independent of the R group and they observed that the triplet state emission reduced in accordance with the energy gap law used for organic polymers.[13] The synthetic flexibility and compatibility with different conjugated spacers together allow fine control over the photophysical properties.

There has been a number of comprehensive reviews published in recent years that detail the developments in this research area in more depth.[11, 14, 15] For example the incorporation of main group segments into the polymers such as ethers or sulphide groups. As a results of this extensive research a number of materials have been developed that could be used as next generation inorganic semiconductors in photovoltaics.

The typical states from which Pt complexes emit are ^{3}LC (ligand centred) and ^{3}MLCT (metal-ligand charge transfer).[16] It is the planarity and the lack of axial ligands that contribute to the enhanced optical properties observed with Pt complexes. Platinum-based complexes also have unique luminescent properties that are attributed to metallophilic bonds;[16-18] these have been extensively studied in recent years. One example was published by Eisenburg *et al.;* they reported a series of highly luminescent platinum complexes, that used a polypyridine ligand.[19] They found that the complex was luminescent in both solution and the solid state but this solution state emission was readily quenched by oxygen. They attributed the luminescent properties to the square planar nature of the Pt centre.

Research conducted at a similar time by Hoffmann *et al.* discovered that by substituting the polypyridine rings enhanced solubility of the Pt complexes could be achieved, leading to solvatochromic abilities.[20] The complexes also exhibited high emission quantum yields in the solution and in the solid state. Interestingly they found that the ancillary ligand does not influence the triplet state, this is in agreement with the findings of Khan, 2015.[3, 20]

It is clear from the breadth of the research literature in the area that the pincer ligand and its substituents are more important for manipulating the luminescent properties than the ligand found in the 4th co-ordination sphere of the platinum. This will be discussed in further detail later in this literature review.

1.2.0 Photophysics

1.2.1 Interaction with light.

For absorption of a photon from incident light to occur the energy of the photon has to match the energy between the ground state (GS) and excited state (ES) orbitals of a complex, this process promotes an electron to the ES orbital. This is illustrated in Figure 1.1 by the purple or blue solid arrow. Since the complex can only absorb photons of a specific wavelength, the knowledge gained from this can be used to provide information on the electronic structure of the complex. In addition, this process, if it occurs in the visible region of the electromagnetic spectrum, can give us an indication of the colour of a complex. Generally, if one wavelength of light is absorbed by a molecule then it is the complementary colour that is observed, *e.g.* orange light absorbed, colour blue is observed. In some cases the colour that a complex may exhibit can be more complex, for example if all but one wavelength is absorbed, then it is the reflected wavelength that is the observed colour.

When an electron is promoted to a higher energy level following the absorption of a photon of light, the subsequent electronic decay back to the GS can occur by either a radiative or non-radiative process. In most cases a non-radiative pathway occurs in which the excitation energy decays into thermal motion. In Figure 1.1 the processes labelled as internal conversion and intersystem crossing are alternative radiationless decay pathways, but this is a slow mechanism for the electron to return to its ground state, which allows the radiative processes to compete.

The radiative decay processes are more unusual but lead to a complex exhibiting luminescent behaviour. There are two types of luminescent behaviour; fluorescence (green transition in Figure 1.1) and phosphorescence (red transition in Figure 1.1).[21] These mechanisms can be shown schematically in a Jablonski diagram (Figure 1.1) and are explained in greater detail in Section 1.2.3.

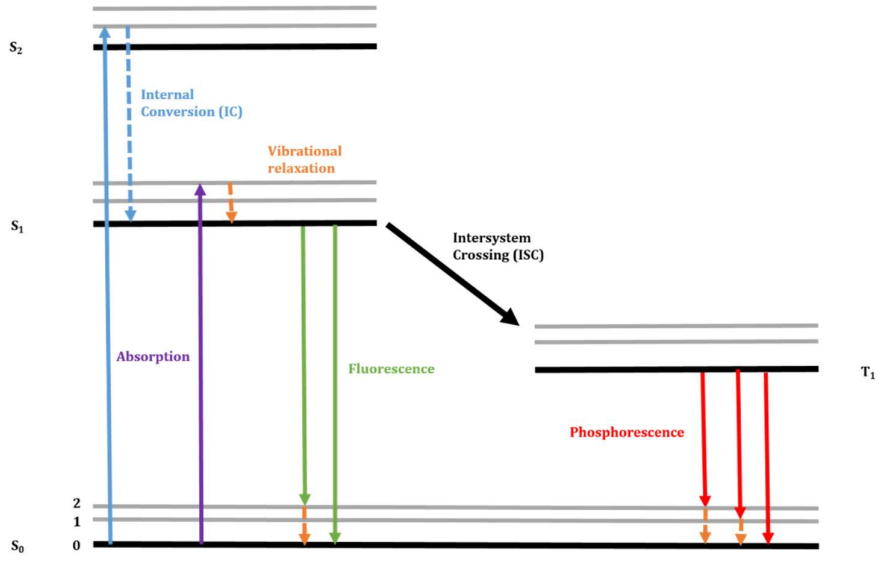

Figure 1.1: *Jablonski diagram, depicting the mechanisms behind non-radiative and radiative decay processes.*

1.2.2 Franck-Condon Principle.

The light emitted *via* radiative pathways is generally of lower frequency than the incident light, the separation between the two maxima is called a Stokes shift. This vibrational structure in the electronic spectra can be explained by the Franck-Condon principle. The principle states that:

'Because nuclei are so much more massive than the electron, an electronic transition takes place much faster than the nuclei can respond.'[22]

In an electronic transition, electron density is lost from one region of a molecule and builds up in others. The nuclei will then experience a new force field, which causes them to vibrate. To predict the final vibrational state, the vertical transition needs to be found. This is achieved by drawing a line from the minimum of the electronic ground state to the point at which this line intersects the electronic excited state. This is shown schematically in Figure 1.2. The vertical transition in Figure 1.2 results in electronic decay always occurring from the vibrational ground state of the electronic excited state, as the process of internal conversion (Figure 1.1) occurs much faster within the excited state than a radiative decay.[23]

Fluorescent and phosphorescent emission will also follow the Franck-Condon Principle, whereby the Stokes shift is caused by the process of internal conversion before the radiative decay. The size of the Stokes shift is related to structural change in the excited state, the larger the change the larger the Stokes shift.

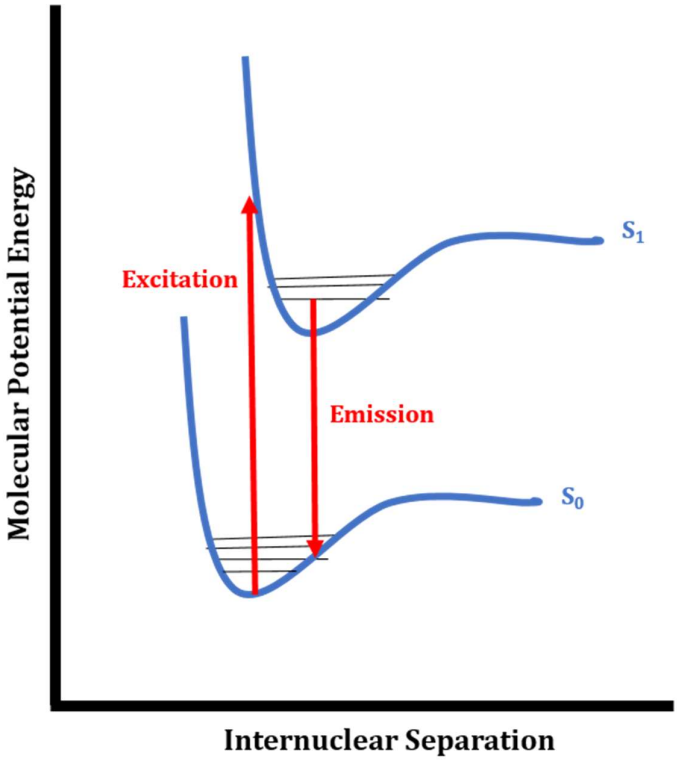

Figure 1.2: *Morse potential demonstrating the vertical transition defined by the Franck-Condon Principle.*

1.2.3 Fluorescence and Phosphorescence.

Fluorescence occurs when a photon is emitted from an excited singlet state, bringing the excited electron back down to the ground singlet state. It has a lifetime in the range 10^{-9} to 10^{-7} s. Shown in Figure 1.1 the downward electron transition is vertical, which is in agreement with the Franck-Condon principle. Fluorescence can be readily quenched in solution by the presence of solvents with widely spaced vibration levels, such as water, this is because they are able to accept large amounts of electronic energy.[24]

Phosphorescence occurs when the electron decays to the singlet ground state from an excited triplet state (Figure 1.1), the electron moves from a singlet to triplet state *via* a process known as intersystem crossing. For this process to occur the electron is unpaired as shown from Figure 1.3. The formation of the triplet state can be made more likely if a heavy element, such as platinum, is present because of the contribution from the spin orbit coupling increases.

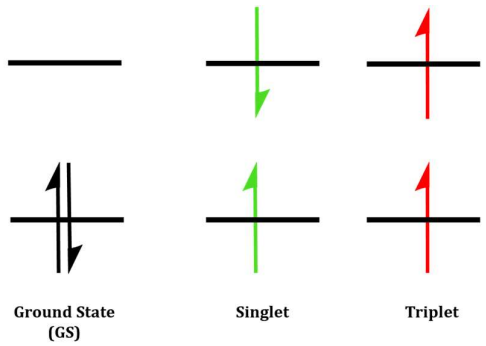

Figure 1.3: *Representation of the spin states in a singlet ground state, singlet excited state and triplet excited state.*

The subsequent emission of a photon from the triplet state is also forbidden because the spin of the electron would have to revert to form the singlet ground state. Fortunately, the spin-orbit coupling, which promotes the intersystem crossing, breaks the selection rule allowing emission to occur. Spin orbit coupling promotes this forbidden transition because the magnetic interaction between the spin and orbital motion of the electrons which shifts the atomic energy levels.

Typically, the emission is weak and continues for a longer period of time, in the range of 10^{-3} and 10^{2} s. Even with the presence of a heavy metal atom the process of phosphorescence due to spin flipping (intersystem crossing) is unlikely to occur due to the competition of fluorescent emission, however if the triplet excited state is of lower energy than the singlet then the process will become favourable (Figure 1.4).

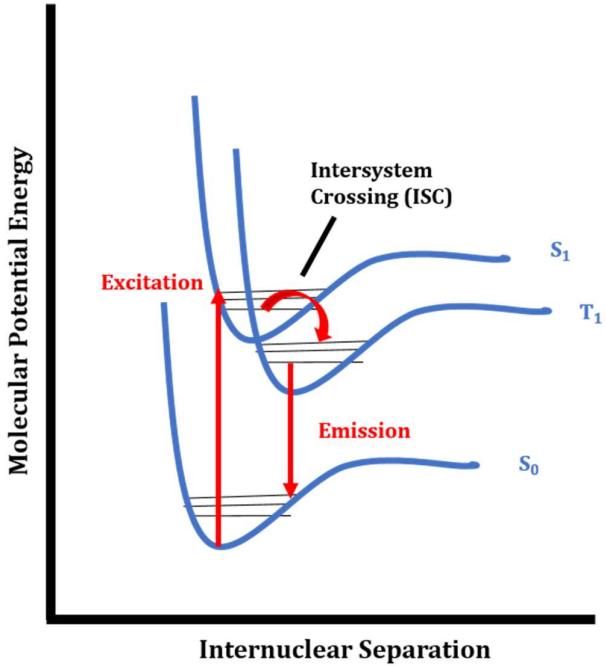

Figure 1.4: *Morse potentials depicting the transition required for fluorescent and phosphorescent transitions.*

The emission of fluorescence occurs at a lower frequency by comparison to absorbance, due to the time between its emission and the loss of some of the vibrational energy to the surroundings. Phosphorescence will occur at a lower frequency again due to the lower energy of the triplet state (Figure 1.4). This phenomenon can be explained by the Franck–Condon Principle. (Section 1.2.2)

1.2.4 Advantages of Luminescence

Luminescence of transition metal complexes has applications in the optoelectronics field and can be used in devices such as OLEDs and photovoltaics.[25] Currently in OLED devices efficiency can only reach approximately 25%,[26] this is because the organic fluorophores can only utilise transition between singlet states. If transition metal complexes were introduced this could theoretically be increased to 100% due to the inclusion of phosphorescent emission, allowed by the high spin orbit coupling of heavy atoms in the complexes. This is illustrated in Figure 1.3, section 1.2.3. The partial mixing between singlet and triplet states in these transition metal complexes encourage fast intersystem crossing and subsequent phosphorescence from a triplet state.[27]

The potential application of these complexes in the optoelectronic industry as new generation OLEDs has led to huge interest in the area. Transition metals of interest include Ru, Os, Ir, Re, Cu and Pt.[28] Platinum shows the best potential due to its higher triplet quantum yield and tuneable emission colour.[29] It is for these reasons that platinum has formed the basis of the research explored in this report.

1.3.0 Square Planar Platinum.

With research moving toward the use of cheaper and more sustainable metals found in the 3d row of the periodic table, the use of platinum, one of the more expensive transition metals,[30] needs to be justified. Platinum is a 5d transition metal, with a predominant oxidation state of 2+, giving rise to a d electron count of d^8. This is important as it affords an energetically favourable orbital stacking pattern that leads to a square planar geometry that will allow the molecules to stack in the solid state through Pt…Pt interactions, a key fact that will be discussed in detail throughout this report. In addition to the square planarity of its complexes, platinum(II) has a high spin orbit coupling constant, which facilitates intersystem crossing from singlet to triplet states and promotes luminescence.

1.3.1 Square Planar geometry

The generalised structure of square planar geometry is shown in Figure 1.5. This configuration is favoured by metals with 8 d electrons and a crystal field strong enough that a low spin state is favoured.[31]

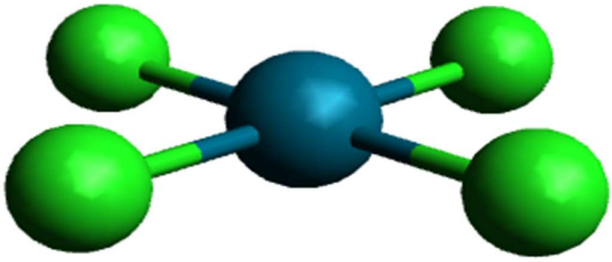

Figure 1.5: *Generalised structure of a square planar complex, [ML4]x*

Similarities can be drawn between square planar geometry and octahedral geometry, with the square planar geometry forming upon removal of ligands in the z direction. Figure 1.6 uses simple crystal field theory[31] to provide a schematic representation of the d-orbital splitting in square planar complexes.

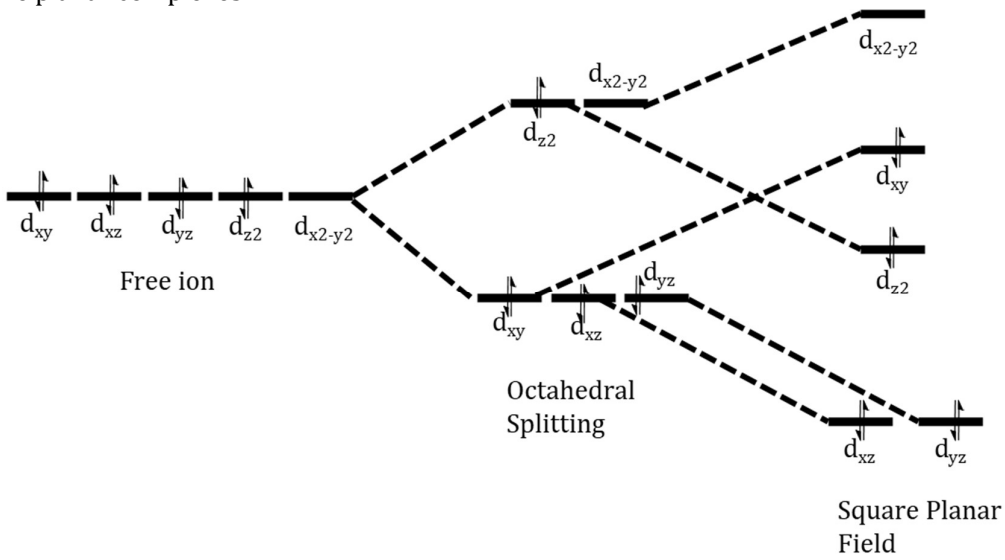

Figure 1.6: *Splitting diagram from free ion to octahedral geometry to square planar geometry for a d^8 ion.*

Figure 1.6 shows a decrease in repulsion experienced by the orbitals in the z direction and a subsequent increase in repulsion seen by the orbitals in the x,y plane, which is caused by the contraction of ligands occupying the equatorial positions. This means the d_{x2-y2} orbital is now the antibonding orbital and there is an overall stabilisation of the molecule when compared to octahedral geometry, provided the pairing energy of the electrons is low enough.

To favour the low spin state of d^8 metals, a large ligand field splitting is required. This is normally associated with the 4d and 5d transition metals, such as Rh(I), Ir(I), Pd(II), Pt(II) and Au(III). For 3d transition metals such as nickel complexes a strong field ligand such as cyanide is needed to force the switch from tetrahedral geometry to square planar.

1.3.2 The d_{x2-y2} antibonding orbital.

The d_{x2-y2} orbital in the square planar geometry is the antibonding orbital (Figure 1.6). If this orbital becomes populated following a photo-induced electronic transition (Section 1.2.1), a distortion occurs and the M-L bond length increases. This distortion is unfavourable for luminescence because it favours a non-radiative decay pathway. Non-radiative processes such as internal conversion are now thermally accessible for a complex and, as a result, they are only weakly luminescent in solution (for example in salts of the anion $[PtCl_4]^{2-}$).[18] Figure 1.7 illustrates this point with the use of potential energy surface diagrams. The distortion experienced upon population of the d_{x2-y2} orbital causes a displacement for the excited state surface. The isoenergetic crossing point (where both curves meet) is now thermally accessible to non-radiative decay mechanisms, shown by the red arrows on Figure 1.7.

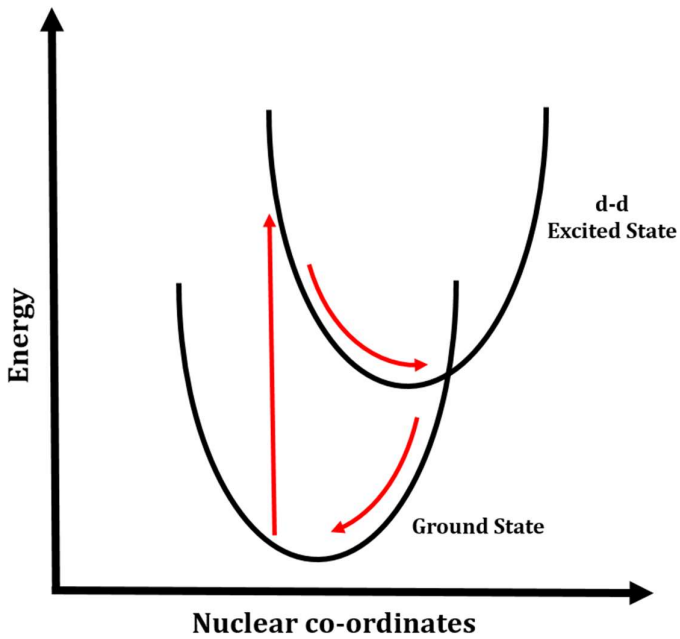

Figure 1.7: *Potential energy surfaces showing the difference between the ground state of a square planar complex and the excited state when the dx2-y2 orbital has been occupied.*[18]

1.4.0. Choice of ligand

1.4.1 Manipulation of the d_{x2-y2} orbital

As discussed in section 1.3.2 if the d_{x2-y2} orbital becomes occupied upon absorption of light, then it has a negative effect on luminescence. Ligand choice is the most effective way of manipulating the relative d_{x2-y2} orbital energy. There are two methods detailed in the literature, which have been successfully used to manipulate this orbital;

1. By lowering the emissive state away from the d_{x2-y2} orbital.
2. By raising the energy of the d_{x2-y2} orbital.

The first method can be achieved by the use of porphyrin ligands. Porphyrins are strong field ligands that cause a large energy gap between the d_{x2-y2} orbital and the rest of the d-orbitals. The porphyrin based π-π* state is of lower energy than the d_{x2-y2} orbital, therefore this avoids population of the d_{x2-y2} orbital during excitation. The emission observed in these complexes is generally low in energy and in the red region of the spectrum.[32] Recent research into these types of complex have yielded interesting results, with complexes emitting in the near IR region of the spectrum, with potential uses in the optoelectronics industry.[33, 34] A paper published by Schanze *et al.* investigated the substitution effects on the porphyrin ring. They found that increased π conjugation leads to enhanced light absorption and near IR emission. This study focussed on the use of naphthalene and anthracene derivatives and the wavelength of the emission varied dependant on the associated function group. Extensive studies of the complexes also showed that the decay from the triplet states is constant across the series.[34] An associated paper researched the applications of these Pt porphyrin complexes, as part of this research the group developed a set of OLEDs. They found that the solution state spectroscopy of the complexes did not fully correlate to the observed optical properties of the OLEDs. This was attributed to the various matrixes that were used in the development of the devices.[35] Manipulating the d_{x2-y2} orbital in this manner is restrictive because only the red region of the spectrum can be accessed.

The alternative method of raising the energy of d_{x2-y2} orbital has the potential to make use of the entire visible spectrum. The second method requires the inclusion of a strong field ligand into the Pt(II) co-ordination sphere that raises the energy of the d_{x2-y2} orbital, ligands that are commonly used are polypyridyl ligands. This is the approach taken in this research project and will be discussed further in the following sections.

1.4.2 Strong field ligands: Pincer Ligands

Figure 1.8 shows the generic structure of the strong field ligand used in this research, it is known as a "pincer" ligand. As with the porphyrins it is the strong field nature of the pincer ligand that stabilises the square planar arrangement, this decreases the chance of population of the d_{x2-y2} orbital and any subsequent detrimental effect on luminescence. However the pincer ligand differs to the porphyrin ligand as it raises the level of the d_{x2-y2} orbital, when at least one of the X in Figure 1.8 is a carbon forming a strong Pt-C σ bond;[36] this will be discussed in detail in the subsequent sections.

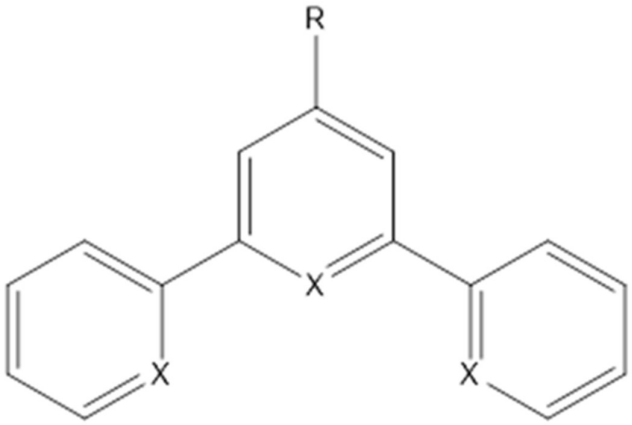

Figure 1.8: *Generalised structure of a pincer ligand, where X= C or N, R=H or functional group.*

These ligands are tridentate and form an excellent basis for luminescent platinum complexes. The positions labelled 'X' in Figure 1.8, can be either carbon or nitrogen atoms.

When all three 'X' positions are filled by nitrogen donor atoms the result is a terpyridine ligand, N^N^N. If the pincer ligand contains a carbon donor atom, a carbon-metal bond is formed to the Pt centre and a "cyclometallated complex" is formed.

1.4.3 Cyclometallation

A cyclometalling ligand is defined as a ligand that upon binding to the metal centre forms a ring, one bond of which is a carbon-metal (C-M) bond. This is advantageous in this research because pincer ligands with at a cyclometallation point provide strong σ- donation to the metal centre and good π-acceptors via the heterocycles; in this case the pyridyl groups.

When the Pt centre is bound in this way it experiences a strong ligand field environment and a large d-orbital splitting which can be directly attributed to the strong σ donation though the C-M bond. This effect results in pushing the d_{x2-y2} orbital to higher energy, as described in Section 1.4.1. These complexes usually have more pronounced spectral qualities when compared to terpyridine based complexes (Section 1.4.4) as the luminescence is not quenched.

Cyclometallating ligands can take on a series of symmetric and asymmetric variations. Asymmetric configurations include: C^N^N, N^C^C and C^C^N. There are several examples of highly luminescent platinum complexes with asymmetric pincer ligands in the literature.[37, 38] Possible symmetric configurations include: C^N^C and N^C^N, where there are a significant number of examples of highly luminescent platinum complexes in the literature.[39-41]

1.4.4 Terpyridines

The first terpyridyl platinum complex was synthesised in 1934 by Morgan and Burstall, the structure is shown in Figure 1.9.[42]

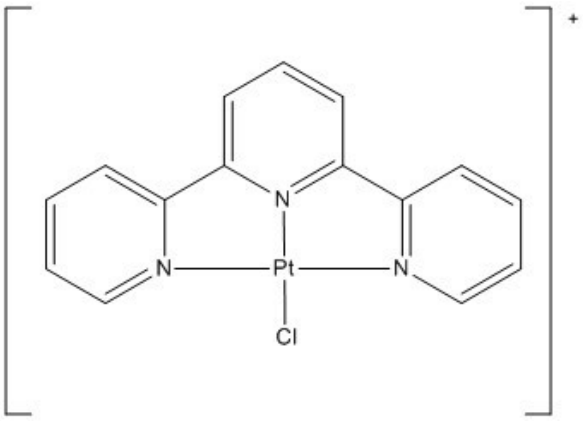

Figure 1.9: *Structure of complex synthesised by Morgan and Burstall in 1934.*

It was not until the 1999 that the luminescence of these complexes was discovered, with McMillin and co-workers conducting the initial research into these complexes.[43] It is important to note that with a Cl^- anion in the fourth coordination site these complexes require a counter-ion to balance the 2+ charge on the platinum. These counter-ions can take many shapes and forms, with luminescent behaviour noted for many different types of counter-ion.[44, 45] These complexes have varied behaviour and the inclusion of counter-ions may disrupt the solid-state stacking in certain instances, but no systematic study of the effect of the counter-ion on the stacking motifs has yet been carried out. This makes the terpyridine ligand of interest in further research, particularly when comparing its spectral properties with those of cyclometallating ligands.

1.4.5 N^C^N pincer

The first N^C^N platinum pincer complex was synthesised much later than the analogous terpyridine complex. It was synthesised in 1999 by Cardenas *et al*. structure shown in Figure 1.10.[46]

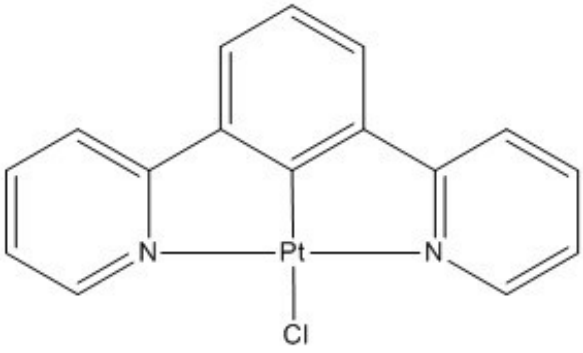

Figure 1.10: *Structure of the first N^C^N Pt complex, synthesised by Cardenas et al.*

The substitution of the central pyridine ring for a arene ring leads to substantial changes in luminescence, with reports indicating they outperform analogous cyclometallating ligands such as N^N^C,[47] having the cyclometallated Pt-C bond trans to the Cl^- ligand in the fourth coordination site.

Functionalisation of the pincer has led to the tuning of emission properties from these complexes. Particular interest has been focussed on the functionalisation of the 4-position of the central arene ring. The functionalisation of this position can lead to drastic changes in emission properties. Currently a variety of complexes have been reported, with emission frequencies spanning the entire visible spectrum.[47-50] Examples of complexes, which emit in the red and the blue region of the spectrum are given in Figure 1.11.

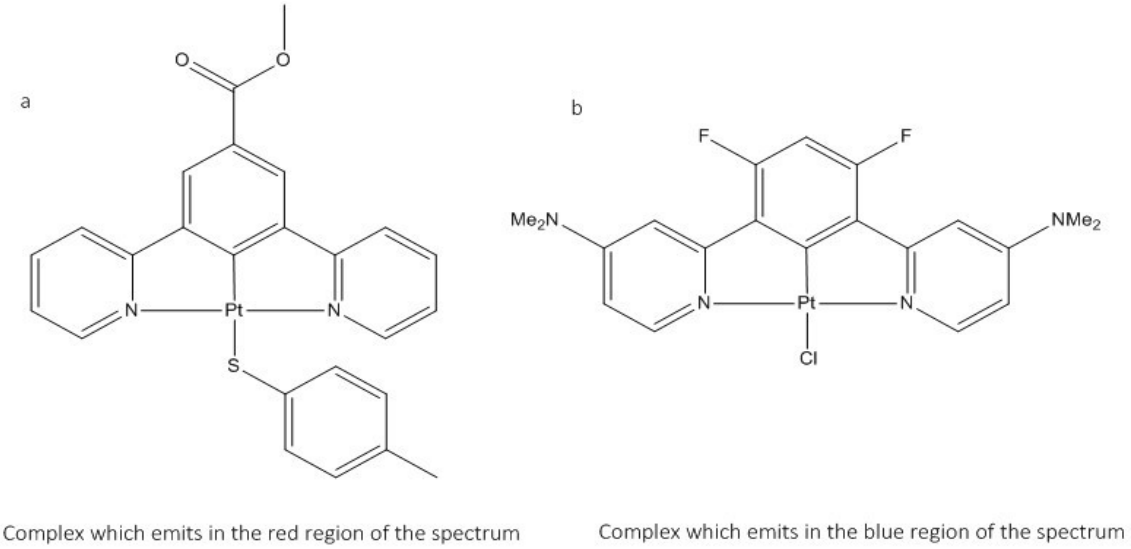

Complex which emits in the red region of the spectrum

Complex which emits in the blue region of the spectrum

Figure 1.11: *a. Structure of complex known to emit in the red region of the spectrum.[51] b. Structure of complex known to emit in the blue region of the spectrum.[52]*

It was originally reported by Williams *et al.* that the electronic transitions for the N^C^N complexes are $^3\pi$-π^* in character. This suggests that the HOMO of the molecule is based entirely on the pincer ligand.[47] This reported result is different to that suggested for the N^N^C ligands whereby the transition is MLCT in character and therefore is predominantly metal based. The reasoning for the change in interaction type has been put down to the change in chelation of the ligand to the metal centre when moving from an N^N^C to the N^C^N ligand. A subsequent detailed DFT study by Sotoyama *et al.* showed there is d→π character in the transition, which accounts for the observed good triplet conversion in the emission spectroscopy.[53] This paper compared the experimental spectroscopic information with that calculated using computation techniques (Gaussian 98 package with B3LYP functionals in a density functional theory calculations), good agreement between the methods were obtained. This study proved the 4 HOMOs of the complexes are characterised by mixing of the Pt orbitals with ligand orbitals of the correct symmetry, unlike the theory reported by Williams *et al.* Figure 1.12 shows that b_1 and a_2 are mixtures of Pt d-orbitals with the π-orbitals of the pincer and chloride ligand, whereas b_2 and a_1 are predominantly σ in character. Conversely the LUMO is found to be predominantly ligand-based.

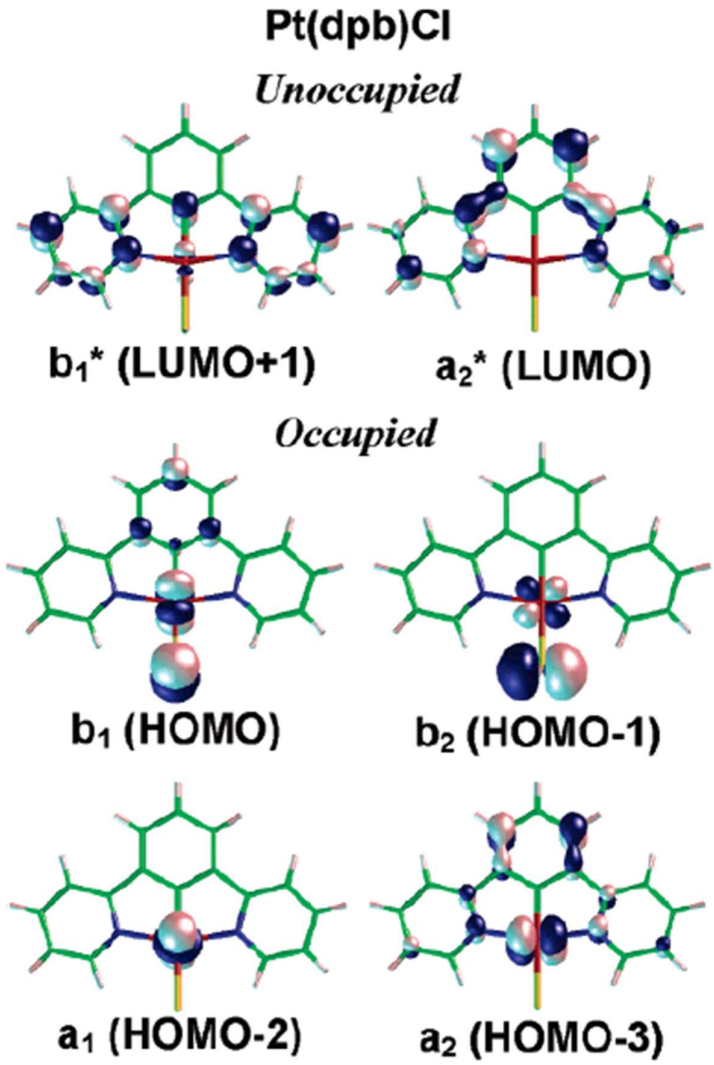

Figure 1.12: *Frontier orbitals of the complex Pt(dpb)Cl.*[53]

1.5.0 Introducing a switch.

Introducing a 'switch' into platinum pincer complexes, so that there is a measurable change in physical properties can be achieved by two different methods, both of which rely on the material being in the solid state. The methods of interest are:

1. Directly changing the π-ligand influence on the metal,
2. Manipulating dz^2 interactions between the metal centres.

It is important to understand what influence each of these methods has on the properties of a complex, in order for the rational design of new complexes with optimised properties that can be targeted at specific applications.

1.5.1 Method 1: Changing the π-influence on the metal.

To understand how the π-influence of a ligand may affect the metal, the basic configuration of the orbitals must be first considered.

The square planar splitting diagram given in Figure 1.6 shows only σ interactions, but here we instead consider what would happen if there was an interaction between the metal centre and a π-acceptor ligand, which would be high in the spectrochemical series. It is most likely a π-interaction between high-energy vacant orbitals of the ligand and metal d-orbitals would occur. This would in turn split into an occupied π-orbital with low energy and an unoccupied π* with high energy (Figure 1.13).[31] If instead the metal interacted with a π donor ligand that is low in the spectrochemical series, the combination would be between occupied metal and ligand d-orbitals of the correct symmetry, creating a HOMO with π* character (Figure 1.13).

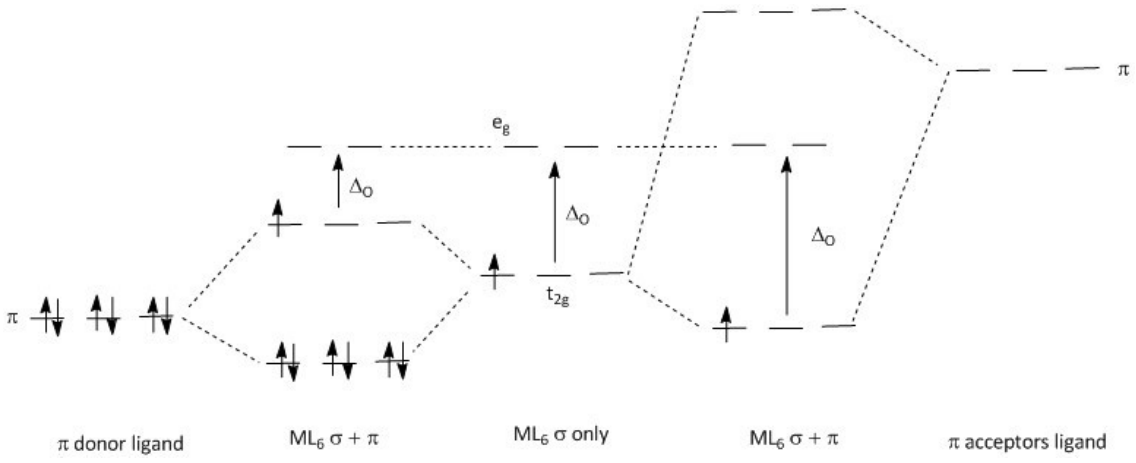

Figure 1.13*: MO diagram showing how the ligand and metal orbitals interact in an octahedral complex.*[31]

Figure 1.14 shows diagrammatically how metal and ligand orbitals interact. It can be seen from this schematic that d_{xy} and d_{z2} have the incorrect symmetry to interact with the planar ligand, therefore no π-interaction is observed between them. [54] In addition Figure 1.14 shows how the d_{xz} orbital possesses the correct symmetry to interact with the ligand occupying the 4th co-ordination site. Provided the ligand, L, has orbitals of the correct symmetry then, the d_{xy} is also

able to interact because this orbital is dependent on the identity of the ligand. The energy of the orbital is likely to be affected by the π donor/ acceptor strength of the ligand, L.

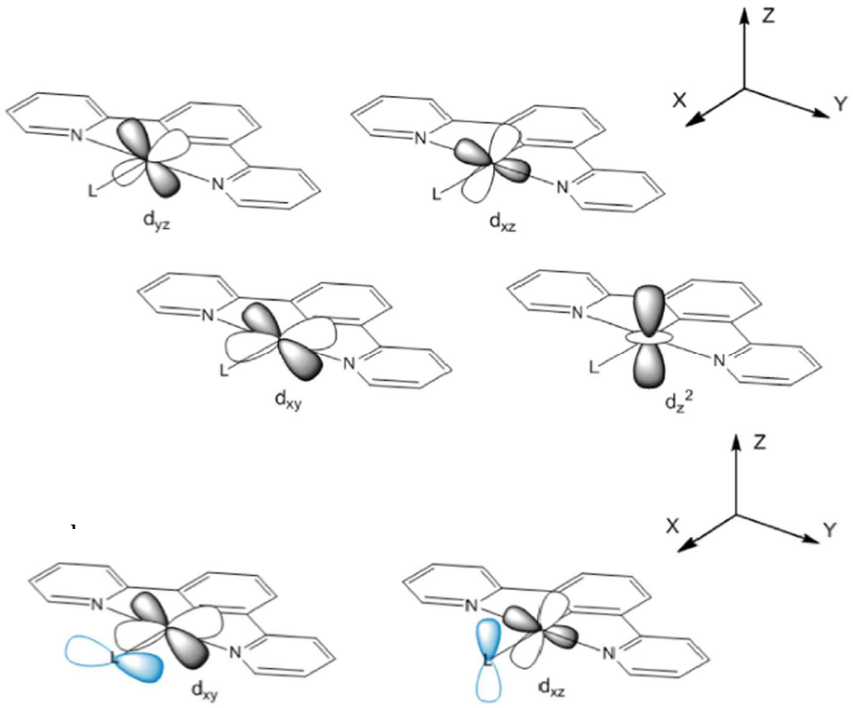

Figure 1.14*: Orbital schematic showing a. interaction of pincer ligand with metal centre, b. interaction of ligand, L with metal centre.*[55]

By using this methodology, the energy of platinum HOMO can be intentionally manipulated because it is sensitive to the ligand occupying the 4th co-ordination site. If a ligand was used which could overlap both the d_{xy} and d_{xz} (Figure 1.14(b)), a good communication channel to the platinum centre would be built, which could then be used as a reporting mechanism for any changes in π-donating/ accepting strength.

A suitable ligand for this strategy would be an acetylide because the C≡C triple bond extends the aromaticity of the complex.[56-60] If a functional group with switchable properties was then attached to the acetylide, such as ferrocene or azobenzene, when these groups reacted to stimuli; the effect would be transmitted to the metal centre and the complex would undergo a change.

1.5.2 Method 2: Manipulating d_{z^2} Interactions.

The square planar geometry of these systems means that with sterically unhindered ligands such as the pincer ligands discussed in Section 1.4.2, entirely planar complexes can be synthesised. This allows for Pt…Pt interactions to occur between neighbouring Pt pincer molecules in the solid state (Figure 1.15). These intermolecular interactions can only occur upon aggregation of molecules in the solid state or in some instances in concentrated solutions.[61] This phenomenon would not be observed with the respective octahedral complexes because the co-ordination sphere is essentially spherical and does not allow the metal centres to get in close proximity to each other.

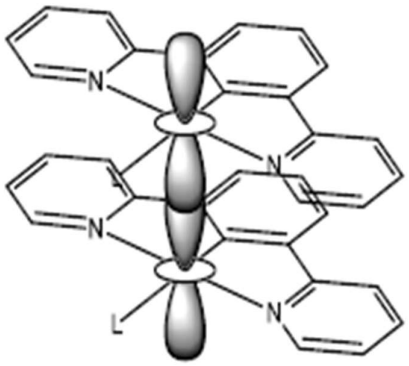

Figure 1.15*: dz² interactions in platinum complexes when complexes stack.*

The planarity of the system allows the d_z^2 orbital to sit perpendicular to the plane of the molecule with a separation in the range of 3.0- 3.5 Å between the metal centres, this will allow these orbitals to interact and form bonding/ antibonding dσ and dσ* molecular orbitals (Figure 1.16).

For effective d_z^2 overlap the complexes need to be neutral, this ensure there is no disruption to the stacking in the solid state.[18] N^C^N ligands will be used extensively in this research, this means that the ligand in the 4th co-ordination sphere needs to be monoanionic, for example: chloride, cyanide or acetylides.

These types of interactions have an effect on optical spectroscopy and excited state energies. When the interaction is present the HOMO is raised in energy and the transition is now dσ*-π* in character as opposed to π-π* (Figure 1.16), the transitions are now shifted to lower energy. No formal bond between the platinum occurs as the dσ and dσ* remain fully occupied.

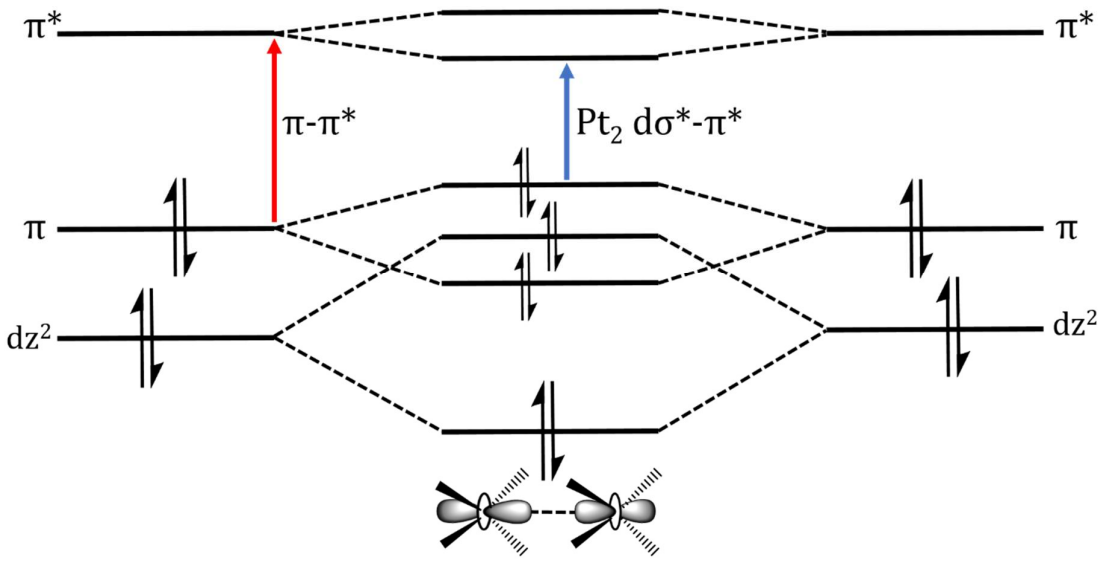

Figure 1.16: *Frontier MO diagram showing the orbital mixing when dz² orbitals interact.*

These d_z^2 interactions tend to be observed only in the solid state as the molecules in the solution state will be surrounded by a solvent shell and therefore these interactions will not be accessible. Conversely, ligands that have extended π-systems such as pincer ligands can display π-stacking interactions. The π-stacking interactions have a similar effect on optical spectroscopy as the d_z^2 interactions but tend to be much weaker. These interactions can also be observed in the solution state by conducting a concentration dependant emission spectroscopy experiment.

These d_z^2 interactions provide a way to tune the electronic properties of these complexes. If the Pt…Pt distance in the solid state can be altered, then a colour change could be observed due to the sensitivity of the d_z^2 interactions. For example, shorter platinum distances lead to greater overlap of the d_z^2 orbitals. This greater overlap will raise the HOMO and decrease the distance between the HOMO and LUMO in this interaction, see Figure 1.16. The decrease in energy means that a red shift will be observed the opposite will be seen for longer platinum distances. If the distance between the platinum atoms in the stacks can be altered or disrupted by an external influence (e.g. applying pressure or a vacuum or by introducing guest molecules such as volatile organic compounds (VOCs)) then a reversible colour change would be observed.

1.5.3 Tuning the *'switch'*

It can be difficult to intentionally tune '*switching'* properties due to several factors, each of which can affect the performance of these complexes. These include the following:

1. presence of void space in the solid-state structure,
2. counter-ion size and shape,
3. polymorphism,
4. solvates.

The location of the individual solvent molecules in the crystal lattice is particularly important for *'switching'* behaviour. For example, solvent molecules located in discrete pockets of space between the complex molecules, with no route to travel through the structure, can lead to difficulty in movement of VOCs in and out of the material, the colour or luminescent response will therefore be slow. Conversely, if the solvent is arranged in channels it is easier for it to move in and out of the structure therefore a faster response time will be observed.

Changing the counter-ion can have an effect on the spectral properties that a complex exhibits. There are several individual examples of complexes with the same terpyridine ligand structure but different counter-ions and the spectral properties for the two complexes differ, examples will be given throughout this literature review.

Polymorphism is the ability of a solid material to exist in two or more different crystalline forms. It is not unusual for polymorphs to display different *'switching'* behaviour to each other or none at all. Similar observations have been noted for solvates of a complex due to differing stacking arrangements; this will be discussed in more depth on the results section of this report.

1.5.4 Types of *'switch'*

1. **Counter-ion exchange.**

As mentioned in Section 1.4.4, the size and the shape of the counter ion in terpyridine complexes and in cationic or anionic cyclometallated complexes are important. This is because if the counter-ion is too large then this could disrupt any potential platinum stacking. As well as disruption of stacking, larger anions tend to pack in a more efficient manner and no void space is observed. This means no solvent will be included in the structure, which would limit any type of vapochromic behaviour. This is why the majority of the literature focusses on the use of small anions.

A paper published by Connick *et al.* in 2010 illustrates this point.[62] The complex was 2,2′:6′,2″-terpyridine platinum chloride hexafluorophosphate. Upon exposing this material to the perchlorate ion, the complex turned bright red and strong luminescence was observed (Figure 1.17).[62]

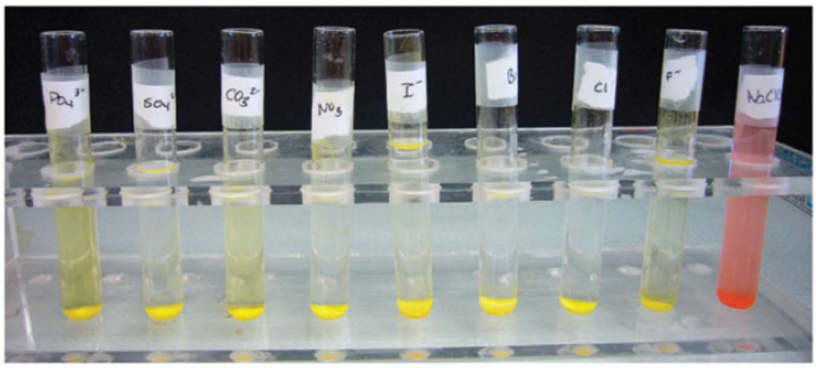

Figure 1.17*: Colours of 2,2′:6′,2″-Terpyridine platinum chloride when exposed to various counter-ions.*[62]

It can be clearly seen from Figure 1.17 that this complex is selective to the perchlorate anion, as this is the only one that induced a colour change. The colour change takes on average a few minutes in the powder form, with this time increasing to a few hours for crystalline samples. The change itself is reversible but the reverse change requires the sample to be exposed to the hexafluorophosphate anion for 24 h. It is thought that the mechanism behind this change is a simple counter-ion exchange reaction. Both the yellow form and the red form have been studied using crystallography. Unsurprisingly, in the red form the complexes form near linear chains with short Pt…Pt distances, giving rise to a metal-metal interaction. In addition, the perchlorate anion and the water in the structure form an extensive hydrogen-bonding network. Further studies of the red form show that the complex dehydrates at 100 °C and this process is accompanied by a second colour change of red to yellow. Unfortunately crystallinity is lost in this process and therefore no crystal structure was determined for the dehydrated form.[63]

2. **Vapochromism**

A vapochromic substance is defined as *'one which changes colour under exposure to certain vapours'.*[64]

If a complex displays vapochromic behaviour then analyte detection can be determined by eye. Analytes might include: volatile organic compounds (VOCs), water impurities, anions that may be precursors to explosives *etc*. There is a separate but similar phenomenon known as vapoluminescence, which is the change in luminescence properties when the complex is exposed to vapour.[65, 66]

Vapochromic behaviour has been observed in a variety of Pt(II)-pincer complexes, with bidentate and tridentate ligands.

One of the first terpyridine complexes to exhibit vapochromic behaviour is shown in Figure 1.18.

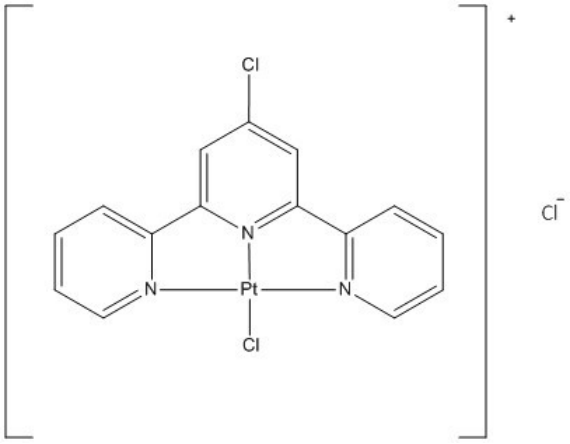

Figure 1.18: *Structure of terpyridine based vapochromic complex.*

This complex is highly selective and only responds to methanol vapour, [67] going from red to yellow upon contact with methanol. In the absence of single crystal data it can be inferred from the red to yellow colour change as well as the blue shift in emission spectrum that the Pt…Pt stacks have been lengthened or the stacking has been disrupted to the point where the platinum atoms are no longer aligned.

A second example of a terpyridine complex, which displays vapochromic behaviour is shown in Figure 1.19.

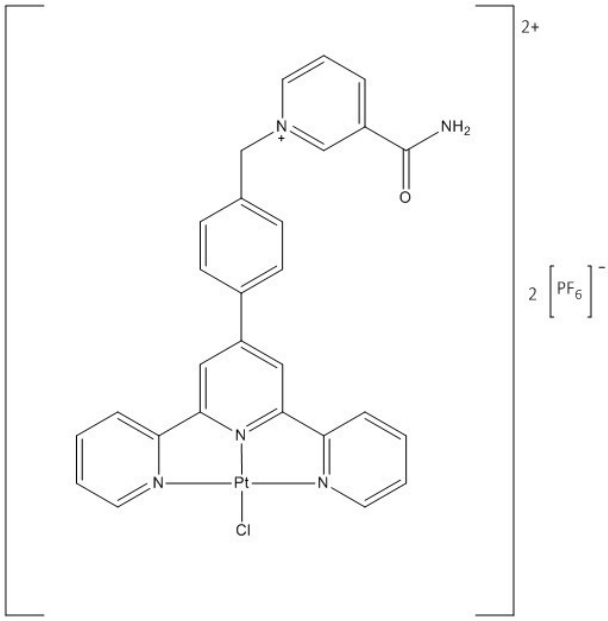

Figure 1.19: *Nicotinamide terpyridine complex, which exhibits vapochromic behaviour.*

This complex changes from red to orange upon exposure to methanol and has also been studied crystallographically.[68] The structures of both coloured complexes are very similar it is not until the crystal packing is analysed that differences are seen. As expected, the void space within the structure has been filled with methanol and the Pt…Pt distances for the orange form are longer. This colour change has been observed in the single crystal, which is unusual as the crystals for these types of complexes tend to degrade on loss and gain of solvent.

There are further examples of terpyridine complexes that exhibit vapochromic behaviour, but when searching for examples based on the N^C^N ligand discussed in Section 1.4.5 the literature mainly focuses on luminescence changes, with few examples of vapochromic behaviour. There is however one example, which has amide groups attached to the pincer (Figure 1.20) where vapochromism occurs.[69]

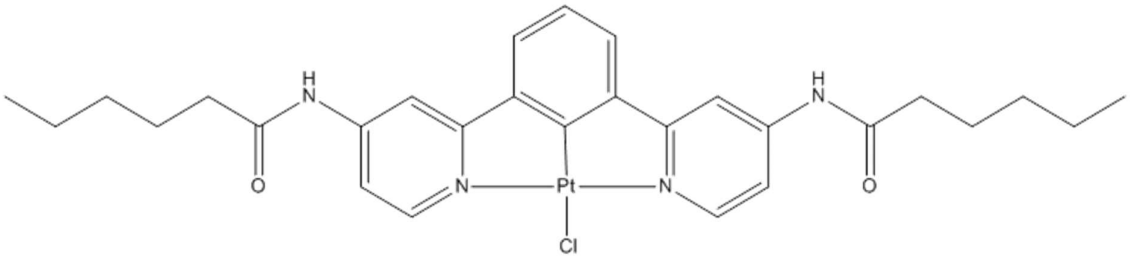

Figure 1.20*: Amide N^C^N complex, which displays vapoluminescent behaviour.*

This complex was synthesised by Choi *et al.* in 2012 and was found to have interesting vapoluminescent behaviour in the presence of methanol, going from green to yellow on exposure to the solvent (Figure 1.21). [69] A crystallographic study of this complex showed that the DMF solvate, which is green had long Pt…Pt distances whereas the yellow methanol solvate exhibited shorter Pt…Pt distances, which fell within the range for M-M interactions as explained in section

1.5.1. The change of solvate also changed the manner of the hydrogen-bonding network which assisted the change in Pt…Pt distance.

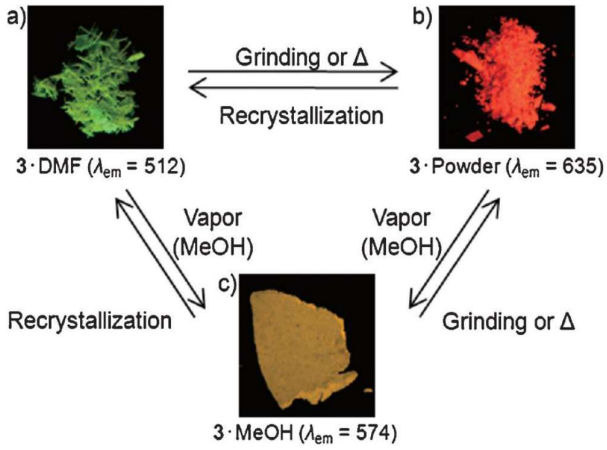

Figure 1.21*: Amide N^C^N complex, diagram showing the change in luminescence upon expose to vapour or mechanical grinding.*[69]

As seen in Figure 1.21, this complex does not just show changes in luminescence on exposure to vapours, but also when the sample is manipulated by light mechanical grinding its green luminescence converts to orange luminescence with an emission peak at 635 nm. This phenomenon is known as mechanochromism.

3. Mechanochromism

Mechanochromism occurs when luminescent materials change the colour of their emission when pressure or other mechanical force is applied.[70] Materials that exhibit this behaviour can be used for a variety of applications including mechanosensors, security papers used in passport production and in optoelectronics.

Pt(5dpb)Cl was one of the first platinum complexes (Figure 1.22) discovered in which a change in luminescence upon grinding was observed. There had been reports of gold and zinc-based complexes in the literature that display mechanochromism, these are covered in a good review on the area by Sagara and Kato.[71] In this particular example the luminescence of the complex changes from yellow to orange upon grinding, but the actual solid sample retains its yellow colour. Spectroscopic and diffraction studies concluded that the change is caused by a dynamic process in the photo-excited state.[72]

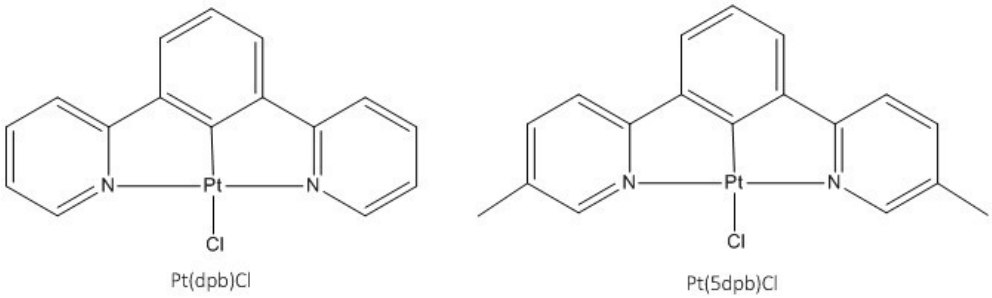

Figure 1.22*: Complexes synthesised by Abe et al., which display mechanochromic behaviour.*

In addition to this complex, the author of this paper investigated a second complex, labelled Pt(dpb)Cl in Figure 1.22. In this example both a colour and luminescence change were observed, with the complex turning orange and the luminescence bright red. Upon studying its properties, it became clear that this complex operates by a different mechanism. Although this complex had been previously synthesised,[73] these properties had not been studied. The powder diffraction study suggested that upon grinding the sample loses crystallinity and becomes amorphous. It is the dimer or aggregate obtained, which is responsible for the red luminescence.

One final example of mechanochromism occurs in a system similar to the one depicted in Figure 1.19, except that the counter-ion had been exchanged for $^{-}$OTf, by an exchange reaction in water and methanol. This particular complex was one of the first examples of a terpyridine complex displaying this behaviour. In this example a reversible colour change is seen from yellow to orange (Figure 1.23), in addition to a luminescence change of orange to red. [74]

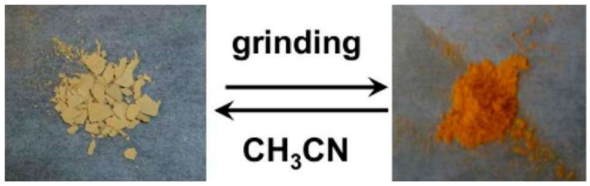

Figure 1.23*: Complex synthesised by Han et al., showing changes in colour upon grinding and recrystallization.*[74]

Crystallographic studies of this complex suggest that the red luminescence of the ground state is caused by shorter Pt…Pt distance, creating M-M interactions. The red shift in colour is in agreement with overlap between the adjacent dz^2 orbitals occurring.

4. Solvatochromism

Solvatochromism is the ability of a complex to change colour dependant on the polarity of the solvent. There are not many examples of this in the literature for terpyridine or N^C^N pincer complexes, but one complex synthesised by Yam *et al.* utilised a terpyridine ligand and an unusual acetylide ligand in the 4th co-ordination site (Figure 1.24) to great effect.

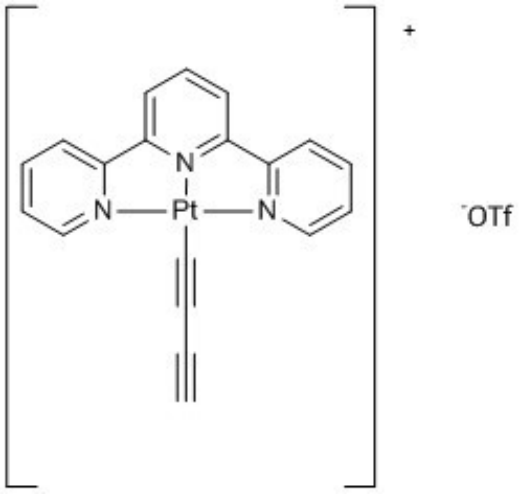

Figure 1.24*: Complex synthesised by Yam et al., 2002.*

The complex was found to exist in two distinct forms, one dark green in colour and the other red, both had been analysed crystallographically. The green form has an extended linear chain of molecules whereas the red form sees the linear chain interrupted and a zig-zag packing motif forms.[61] It was not until solution state UV-Vis of the complex was carried out that the solvatochromic behaviour of this complex was discovered. It was found that when the complex was dissolved in acetonitrile it yielded a yellow solution, upon addition of diethyl ether the complex turned from yellow green to blue (Figure 1.25). These complexes were stable to aggregation for 2 h at room temperature.

Figure 1.25*: Change in colour on the addition of diethyl ether to a terpyridine complex.* [61]

1.6.0 Sensing Applications

Several reviews have been written on the potential sensing capabilities of luminescent platinum (II) complexes.[75-78] The majority of complexes to date have focussed on the manipulation of d_z^2 interactions to initiate colour change in the solid state (Section 1.5.3). Utilisation of this method will lead to the design of sensors that respond to a variety of stimuli such as VOCs, pressure, light and change of anion.[53, 60, 69, 78] Several examples of this type of complex are given in Sections 1.5.4 through to 1.5.6.

While materials continue to be developed with sensing properties, there have been few examples where these materials have been incorporated into devices. One method would be to encapsulate the material into a medium such as a polymer, which can then be coated onto a surface. There is a good example in a paper by Rowan *et al.* in 2012, in which a vapochromic terpyridine-based complex was encapsulated into a polymethacrelate polymer.[79] The complex converts from yellow to red upon exposure to acetonitrile vapour. However, the films of the complex took several minutes to respond to acetonitrile vapour but did eventually complete the correct colour change. The colour change was reversible, but it took several days for the film to regain its yellow colour, unless heated to 100 °C. The slow conversion rate of red to yellow the complex exhibits when encased in polymer has been attributed to the polymer properties. With complexes that show vapochromic capabilities it is important that the polymer itself is porous to allow the diffusion of solvent quickly and efficiently. This study showed that while these complexes can be incorporated into thin films, more research is required into the type of medium used to encapsulate these complexes. Ideally, the medium would not inhibit the operation of the material while at the same time protecting it. Once the material has been incorporated into a suitable matrix, it can be utilised in a number of sensing applications. One paper published by Sangan *et al.* has used a vapochromic material to monitor the mixing of fluid streams in a gas turbine.[80] This is the first reported use of vapochromic materials for this application and it demonstrates the importance of developing *'smart'* materials.

CHAPTER 2

Methods

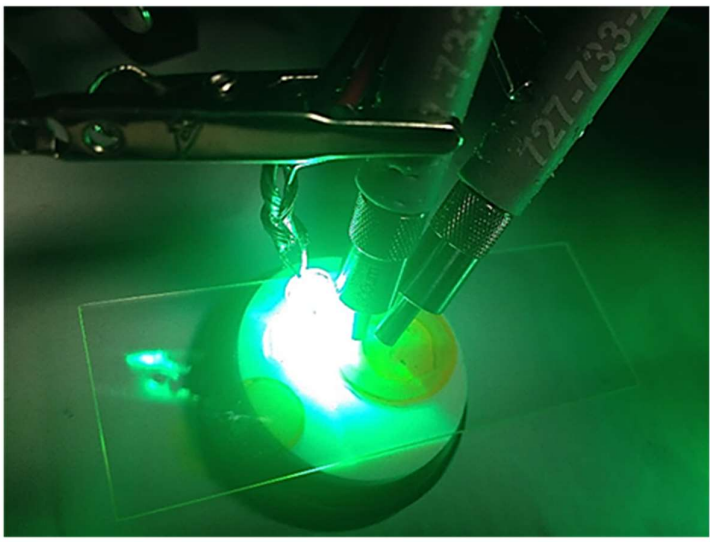

2.1.0 X- Ray Crystallography.

2.1.1 Bragg's Law and Miller indices

Diffraction occurs from the plane of a crystal because the distance between those planes, d_{hkl} (Figure 2.1) is the same order of magnitude as the wavelength of an X-ray. This allows the use of X-rays to investigate the structure of molecular solids. X-Ray crystallography can therefore be used to monitor the change in structure of a crystalline solid and provides vital information on the change in solid-state structure when a complex has undergone a *'switch'*.

Bragg's Law defines the conditions needed to observe diffraction from a given set of Miller planes.; *hkl*. Bragg's Law is depicted in Figure 2.1 and Equation 2.1

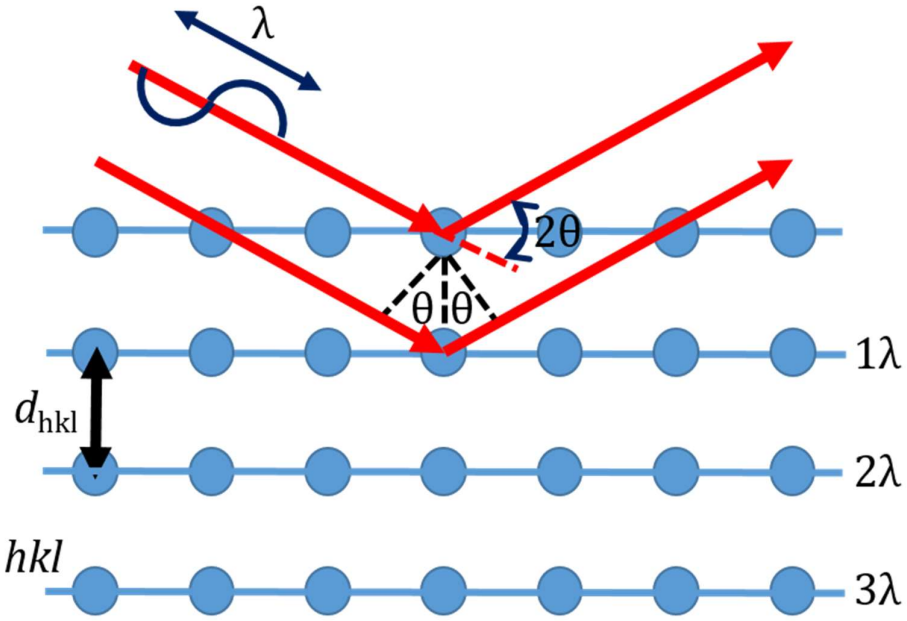

Figure 2.1*: Schematic representation of Bragg's Law, each of the parallel sets of blue dots represents a Miller plane in the crystal.*

$$n\lambda = 2dsin\theta$$

Equation 2.1*: Bragg's Law*

Each plane in a crystal is given a label, this is known as the Miller index (*hkl*). Miller indices define the orientation or plane of a crystal as it intersects the crystallographic axis.

When *n* in Bragg's Law is equal to an integer e.g. 1, 2, 3 then the waves are travelling in phase and constructive interference will be observed. When the waves interfere constructively, the resulting combined wave will have a larger amplitude, the result is a bright spot on the diffraction pattern. When n is not equal to an integer the waves are travelling out of phase and destructive interference occurs. With destructive interference, the two waves are out of phase and when

combined the amplitude decreases, if the waves are completely out of phase this falls to zero. This means that no spots will be observed on the diffraction pattern.

2.1.2 The Diffraction Pattern and Reciprocal Space.

The diffraction pattern is made up of a series of reflections (or diffraction "spots"), each corresponding to an X-ray beam that has been diffracted from a plane in the real crystal. Thus, reflections in the diffraction pattern are labelled according to the *hkl* value of the plane they are diffracted from. While the crystal structure itself is defined in "real space", the diffraction pattern is defined in "reciprocal space". Reciprocal space is $1/d$, where d is the spacing between the Miller planes. This reciprocal relationship can be understood by considering a rearrangement of Bragg's law, showing that sin θ is proportional to $1/d$.
One practical consequence of this reciprocal relationship is that on the diffraction image large unit cells have compressed diffraction patterns, while small unit cells result in well-spaced reflections in the diffraction pattern.

2.1.3 Atomic Scattering Factors and the Structure Factor.

The atomic scattering factor is a measure of the variation in intensity of the diffracted X-ray beam with scattering angle. The scattering factor depends on the number of electrons in an atom and the Bragg angle. At high angle the scattering factor falls off more rapidly, as shown in Figure 2.2.

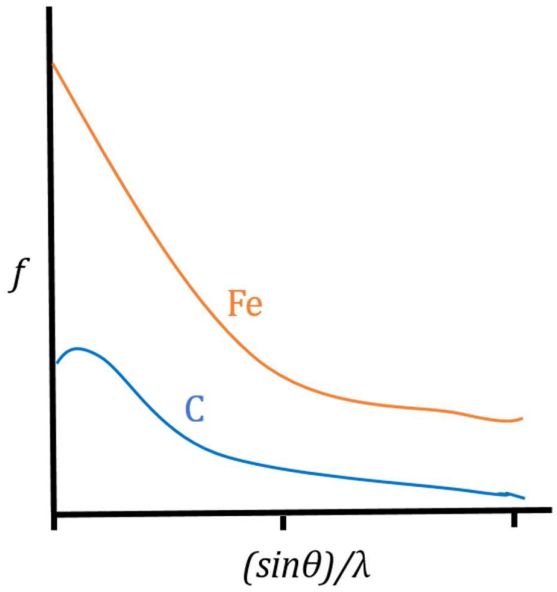

Figure 2.2*: Scattering factor of C and Fe as a function of, f, the unit of electrons against the Bragg angle.*

While the atomic scattering factor describes how an X-ray is diffracted from an individual atom of a given element, the diffraction from the whole crystal structure is described in terms of structure factors. A structure factor is calculated by summation over all atoms in the unit cell with an atomic scattering factor, as shown in Equation 2.2. This summation is carried out for each diffracted wave.

$$F_{hkl} = \Sigma f_j \cos 2\pi(hx_j + ky_j + lz_j) + i\Sigma f_j \sin 2\pi(hx_j + ky_j + lz_j)$$

Equation 2.2: *The structure factor, each sum is constrained to the limits, j= n to j=1.*

Here, *hkl*, defines the Miller plane that the X-ray is diffracted from, *x, y, z* is the position of the atoms in the unit cell and f_j is the atomic scattering factor of an atom. Each structure factor is proportional to the intensity of the diffraction from each *hkl* plane in the crystal. The intensity can be obtained directly from the experiment. The relationship is depicted in Equation 2.3.

$$I_{hkl} = (F_{hkl})^2$$

Equation 2.3: *Relationship between intensity and the structure factor.*

The structure factor is important in crystallography as it is used to produce an electron density map, which allows assignment of atoms in the structure. For this electron density map to be constructed each structure factor needs to be calculated including the phase. Unlike the intensity, the phase cannot be determined directly from the experiment. This is known as the Phase Problem and will be discussed in more detail in Section 2.1.9.

2.1.4 Unit Cell.

The unit cell is the smallest repeat unit of highest symmetry that, when translated in all three dimensions, describes the entire crystal structure.[81] The unit cell is described by a parallelepiped, with vectors *a, b, c,* which correspond to the lengths of the cell, with the angles *α,β,γ*. This is shown schematically in Figure 2.3.

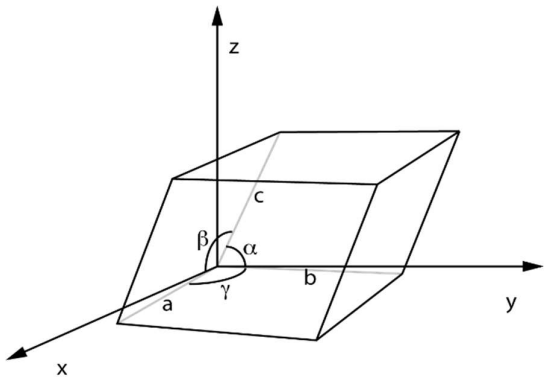

Figure 2.3: *Schematic representation of a Unit cell.*[82]

There are seven different crystal systems, which can be defined by these parameters. These are detailed in Table 2.1.

Table 2.1: *Parameters of the crystal systems.*

Crystal system.	**Unit cell Parameters**	
	a,b,c	***α,β,γ***
Cubic	*a=b=c*	*α=β=γ=90 °*
Hexagonal	*a=b≠c*	*α=β=90 ° γ=120 °*
Trigonal (Rhombohedral)	*a=b≠c (a=b=c)*	*α=β=90° γ=120° (α=β=γ≠90°)*
Tetragonal	*a=b≠c*	*α=β=γ=90 °*
Orthorhombic	*a≠b≠c*	*α=β=γ=90 °*
Monoclinic	*a≠b≠c*	*α=γ=90 ° β≠90 °*
Triclinic	*a≠b≠c*	*α≠β≠γ≠90 °*

The unit cells in Table 2.1 have been places in order of decreasing symmetry. There are four lattice types given the labels; primitive (P), body centred (I), face centred (F) and centred (C (or A or B)) (Figure 2.4). There is one lattice point for a P type lattice, 2 for an I type, four for F type and two for the C type lattice. When these lattice types are combined with the crystal systems, 14 distinct Bravais lattices are formed. The crystal structure will belong to any of these 14 lattices (Table 2.2).

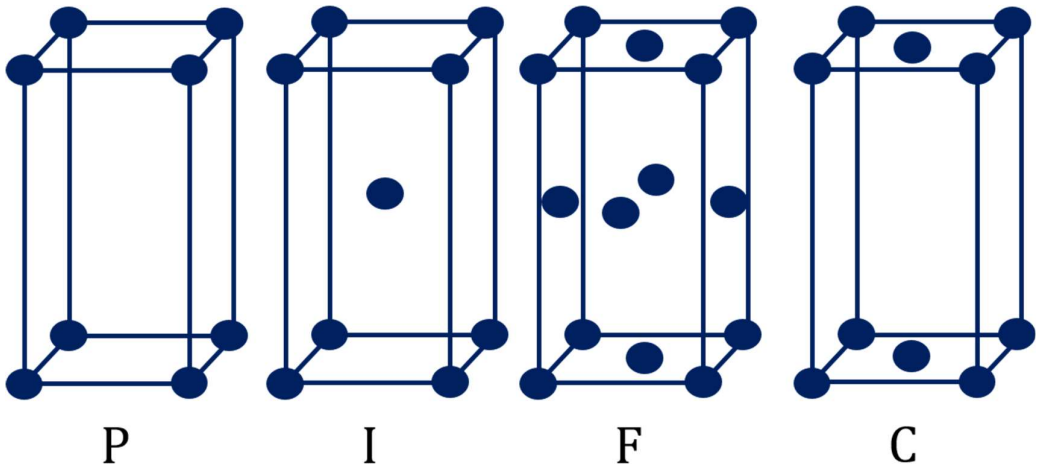

Figure 2.4: *The four Lattice types.*

Table 2.2: *The 14 Bravais Lattices.*

Crystal Type	**Lattice Type**
Cubic	P, I, F
Hexagonal	P
Trigonal	P (R)[1]
Tetragonal	P, I
Orthorhombic	P, I, F, C
Monoclinic	P, C
Triclinic	P

[1]*Where R is Rhombohedral axes.*

2.1.5 Symmetry Elements, systematic Absences and Space Groups.

There are a possible six different crystallographic symmetry elements, which are defined as a physically identifiable point, line or plane in a molecule to which a symmetry operation is applied. The symmetry operation must leave the molecule with an identical appearance. The six symmetry elements can be split into two groups; translational and non- translational.

Non- translational symmetry elements are:

1. Rotations: It is important to note for rotational symmetry in a single crystal environment only 2, 3, 4 and 6 exist and are defined to occur in an anticlockwise manner.
2. Mirror symmetry: If an object has mirror symmetry then the object will remain unchanged by reflection about that plane.
3. Inversion: An inversion centre is when the object becomes inverted through a central point, the centre of symmetry.
4. Rotary Inversion: If an object undergoes a rotation about an axis, followed by an inversion.

Translational symmetry elements involve periodic translations of an object in space. The two symmetry elements that fall into this group are called:

1. Glide planes
2. Screw axes

In glide planes, the objects are related to each other by the following transformations, first the object is translated by half the unit cell length followed by reflection in a mirror plane parallel to the translation direction. Glide planes can occur along the *a, b, c, n* and *d* axes. (Glide planes are defined as being perpendicular to an axis, *e.g*. in space group *Pbca*, the *b* glide is perpendicular to *a*, the *c* glide is perpendicular to *b* and the *a* glide is perpendicular to *c*).

In a screw axis, the object is rotated around an axis by 360°/n, followed by a translation by 1/n in unit cell length. The rotation occurs in an anticlockwise direction, Figure 2.5 shows this schematically for a 3_2 screw axis.

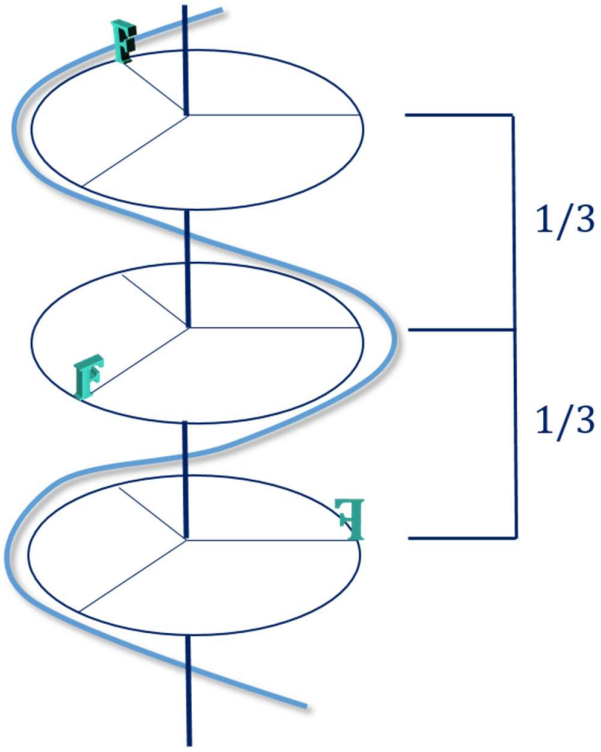

Figure 2.5*: 3_2 screw axis.*

The combination of the 14 Bravais Lattice types with all of the possible crystallographic symmetry operations, plus the restrictions imposed by the requirements of a crystal to have translational symmetry, give rise to 230 crystallographic 'Space Groups'. Information about a space group is obtained from the following sources:

- Unit cell shape and symmetry, and whether the lattice is centred or not
- Systematic absences
- Statistical distribution of intensities.

The first point has already been discussed in section 2.1.4. The information regarding the unit cell shape and centring is not enough information on its own to determine which of the 230 space group fits the data. Additional detail can be provided by the absences in the collected data. There are two types of absences; general and systematic. General absences are caused by the centring of the lattice and will therefore not be observed for primitive lattices. Table 2.3 gives an overview of the general absences expected for a given lattice type. As shown in the table a unique pattern of general absences is observed for each lattice type.

Table 2.3: *General absences.*

Lattice type	Conditions for general absences
P	None
A	$k + l = 2n + 1$ (i.e., the sum of k and l is odd)
B	$h + l = 2n + 1$ (i.e., the sum of h and l is odd)
C	$h + k = 2n + 1$ (i.e., the sum of h and k is odd)
F	Reflections must have either all even or all odd indices to be observed: Mixed odd and even indices are not allowed
I	$h + k + l = 2n + 1$ (i.e., the sum of the indices is odd)

Systematic absences are caused by the presence of translational symmetry elements in the crystal. This is because of destructive interference of the diffracted radiation as a result of the symmetry arrangements in the crystal. The conditions that are required for these absences to occur are given in Table 2.4.

Table 2.4: *Systematic absences.*

Symmetry element		**Conditions for systematic absences**
Screw axis along *a*	2_1, 4_2 4_1, 4_3	*(h, 0, 0) h = 2n + 1* *(h, 0, 0) h = 4n + 1*
Screw axis along *b*	2_1, 4_2 4_1, 4_3	*(0, k, 0) k = 2n + 1* *(0, k, 0) k = 4n + 1*
Screw axis along *c*	2_1, 4_2, 6_3 3_1, 3_2, 6_2, 6_4 4_1, 4_3 6_1, 6_5	*(0, 0, l) l = 2n + 1* *(0, 0, l) l = 3n + 1* *(0, 0, l) l = 4n + 1* *(0, 0, l) l = 6n + 1*
b glide perpendicular *a*		*(0, k, l) k = 2n + 1*
c glide perpendicular *a*		*(0, k, l) l = 2n + 1*
a glide perpendicular *b*		*(h, 0, l) h = 2n + 1*
c glide perpendicular *b*		*(h, 0, l) l = 2n + 1*
a glide perpendicular *c*		*(h, k, 0) h = 2n + 1*
b glide perpendicular *c*		*(h, k, 0) k = 2n + 1*

2.1.6 Standard X-ray crystallography experiment.

The standard crystallographic experiment can be split into two sections, the first involves crystal choice and collecting suitable data, as shown in Figure 2.6.

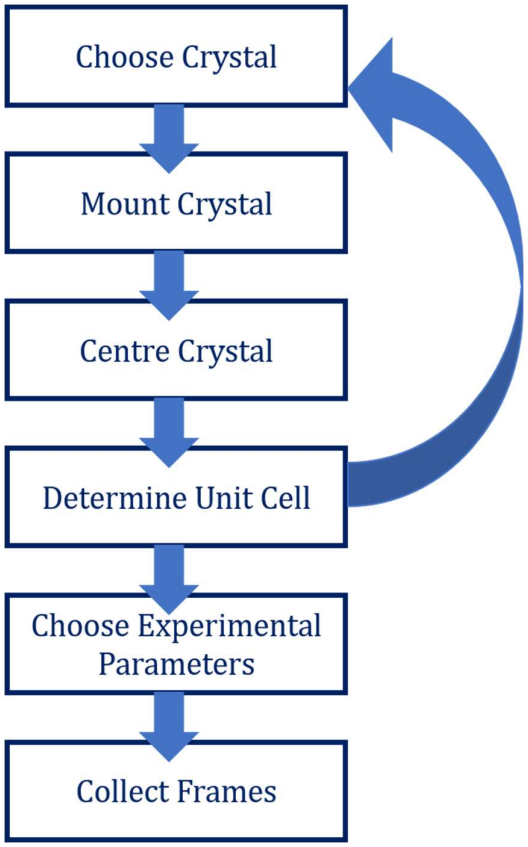

Figure 2.6: *Flow chart detailing the steps required for collection of single crystal data.*

The second stage is processing and solving the data to refine the crystal structure suitable for publication. The stages involved in this process are shown in Figure 2.7.

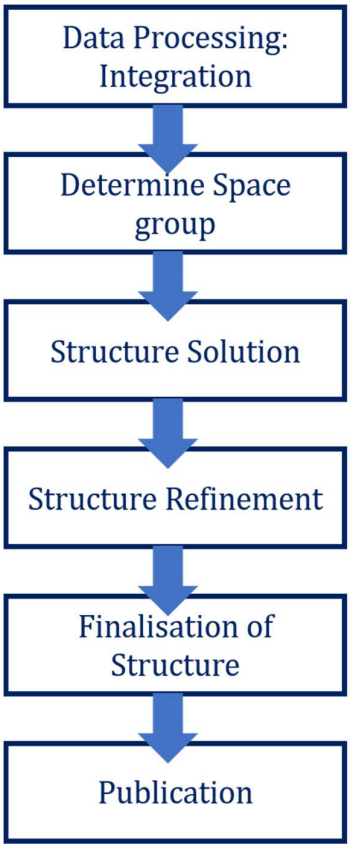

Figure 2.7*: Flow chart detailing the steps required for processing and solving single crystal data.*

2.1.7 Data collection.

The diffractometer.

The first step in the data collection process, shown in Figure 2.6, is to choose a suitable crystal. The size of crystal used will vary, but typically most in-house diffractometers will require a crystal 0.3 mm × 0.3 mm × 0.3 mm in size. In addition, the majority of single crystals will reflect polarised light uniformly across a crystal face and should have sharp edges.

Once a suitable single crystal has been chosen, it is mounted onto a goniometer. The goniometer is a xyz sample stage whose translations are adjusted to position the crystal at the centre of the beam and the diffractometer circles. The standard in-house machines have a four-circle goniometer with 'kappa' geometry. As shown in Figure 2.8.

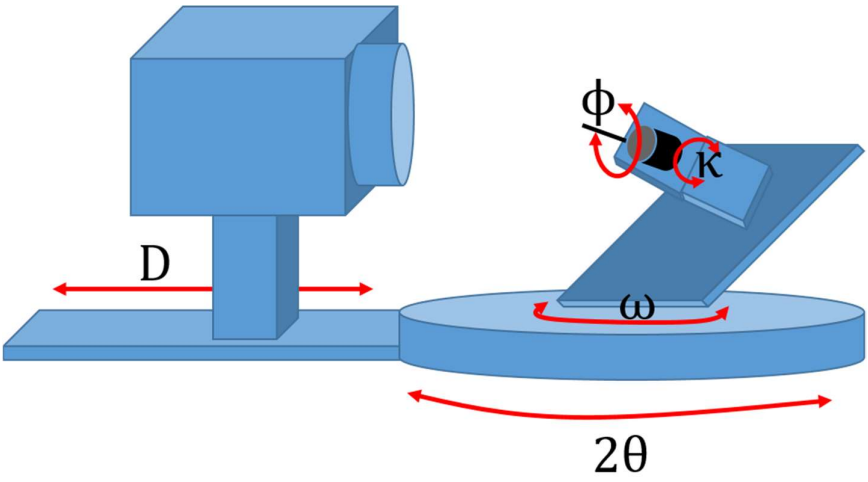

Figure 2.8*: Schematic showing the diffractometer circles.*

Shown in black in Figure 2.8. There are three circles shown in Figure 2.8 that can rotate the goniometer and one circle that rotates the detector. The circles are described below:

- 2θ: Moves the Detector.
- Φ: Rotates the goniometer about the long axis down the centre of the head, this rotation is unrestricted and a full 360 ˚ rotation can be achieved.
- ω: Rotates the χ circle. In this type of diffractometer, the value of χ is fixed to avoid movement restriction of the diffractometer.
- κ: Movement of κ allows for more orientations of the crystal to be studied, while avoiding a χ circle.

Choosing a suitable wavelength.

The majority of in-house diffractometers have one of two types of radiation to choose from (and sometimes both), Cu-K_α and Mo-K_α. There are advantages to both types of wavelength so the wavelength chosen will depend on the crystal.

Cu-K_α offers more intense diffraction in comparison to Mo-K_α, so if the diffraction is weak this may be a more suitable option. However, Mo-K_α radiation is absorbed less strongly, particularly by crystals that contain heavy metal elements, and is generally used for inorganic materials. On the other hand, the diffraction pattern is more spread out in reciprocal space using Cu-K_α radiation because of the longer wavelength, which is advantageous for unit cells with a long axis because spot overlap is avoided but it will take much longer to collect. Finally, Cu-K_α can provide an absolute structure for chiral molecules because the anomalous scattering is significant for this radiation but the crystal has to diffract to a high angle to get the appropriate amount of data.

In comparison MoK_α has a much lower X-ray absorption and this wavelength is suited to particular crystal morphologies such as needles. The compact diffraction patterns allows for a much faster collection and there will be more diffraction spots on the frames, which is advantageous for molecules with smaller unit cells.

Choosing a suitable temperature.

In addition to choosing the correct wavelength of radiation, the temperature at which the data is collected can be altered. Usually most crystal structures are collected at low temperature, the most typical temperature is 150 K. Collecting at low temperature reduces the atomic vibration in the crystal, this in turn sharpens the electron density and reduces the atomic displacement parameters.[83] Low temperatures also allows us to collect more data at higher diffraction angles due to less destructive interference caused by the decrease in atomic vibration. In addition to improving the quality of collected data the low temperature also helps to reduce crystal decay during the collection.[83] Crystal decay can be attributed to several different factors an example would be desolvation of the crystal. Desolvation can occur if there are solvent molecules present in the voids of the crystal. When the crystal is still in the crystallisation mother liquor, it will not lose this solvent, but when removed the crystal will start to lose the solvent. When this occurs, the crystal may lose its crystallinity, leading to an amorphous material and rings on the diffraction pattern or the diffraction may significantly drop off at high angle upon desolvation. The low temperature helps to trap the solvent within the crystal voids and reduces crystal decay.

2.1.8 Data Processing: Indexing and Integration

The first stage in processing data is to index the diffraction pattern to determine the unit cell, once this has been ascertained the images can be integrated (Figure 2.7). For the newer diffractometer software systems, this is completed during the data collection, but in some instances re-integrating the data may be required. The basic principle of integration is to locate the Bragg reflections on the frames and to determine the intensities of the reflections and generate a peak profile. A typical peak profile is shown in Figure 2.9.

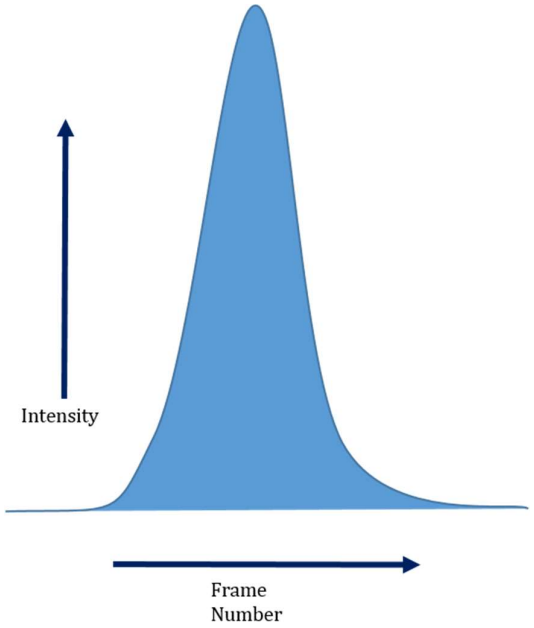

Figure 2.9*: Peak Profile*

2.1.9 Data Processing: Structure Solution

The next stage of data processing is solving the structure. Section 2.1.2 detailed how the diffraction experiment provides us with the intensities of the peaks but not the phases, these are

lost during the Fourier transform. To obtain an electron density map from which the structure can be solved the phases of the reflections need to be determined. This is known as the phase problem and is one of the most important issues in crystallography. There are two methods by which the phase problem can be solved, they are: Patterson methods [84] or Direct methods.[85]

The Patterson method produces a map that has similarities to an electron density map. It is used for structures, which contain heavy elements, as the peaks for smaller atoms are prone to overlap. The peaks do not relate to the position of the atoms, instead they are the vectors between the atoms. The peaks are therefore proportional to the product of the atomic number of the atoms involved.

The Patterson method uses the co-ordinates of one heavy atom, to determine the location of the other heavy atoms of the same type in the unit cell. The F_{hkl} values and their phases for all Miller planes can now be calculated.

Direct methods and dual space methods are the most commonly used methods when solving a crystal structure and follow an iterative process. The details of which are currently beyond the scope of this report.

2.1.10 Data Processing: Structure Refinement

The most common method of structure refinement is Least Squares refinement. As with the common structure solving algorithms, refinements are an iterative process. The details of how this process works are beyond the scope of this report.

When refinement is complete the R factor (Equation 2.4) should have a value of below 5% for publication. This relates to the agreement of the structure factors generated from the model with those generated from the experimental data.

$$\text{wR2} = \frac{\sum |Fobs - Fcalc|}{\sum |Fobs|}$$

Equation 2.4*: Calculation of the R factor.*

R factors are only one way to assess the quality/ reliability of a structure, an important statistic is the estimated standard deviation (ESD) on the atom positions and bond parameters. The ESD provides the uncertainty for a measurement.[86] Finally the structure can be compared to similar structures in the literature using the CCDC suite of programs such as Conquest and Mercury.[87, 88]

2.2.0 Optical Spectroscopy.

While X-ray crystallography is a useful technique, it does not probe the interesting optical properties of these complexes as described in Section 1.0.0. To do this optical spectroscopic techniques will be employed. The three main techniques used in this research are UV-Vis absorption, emission and reflectance spectroscopy. These will be discussed in more detail in the following sections.

2.2.1 UV-Vis absorption spectroscopy.

Most of the discussion so far concerning platinum pincers complexes has centred on two properties, their colour and luminescence. It is important to understand why a complex exhibits certain colours, so it can be manipulated in a systematic way. UV-Vis spectroscopy allows us to measure the wavelengths of light absorbed by a complex.

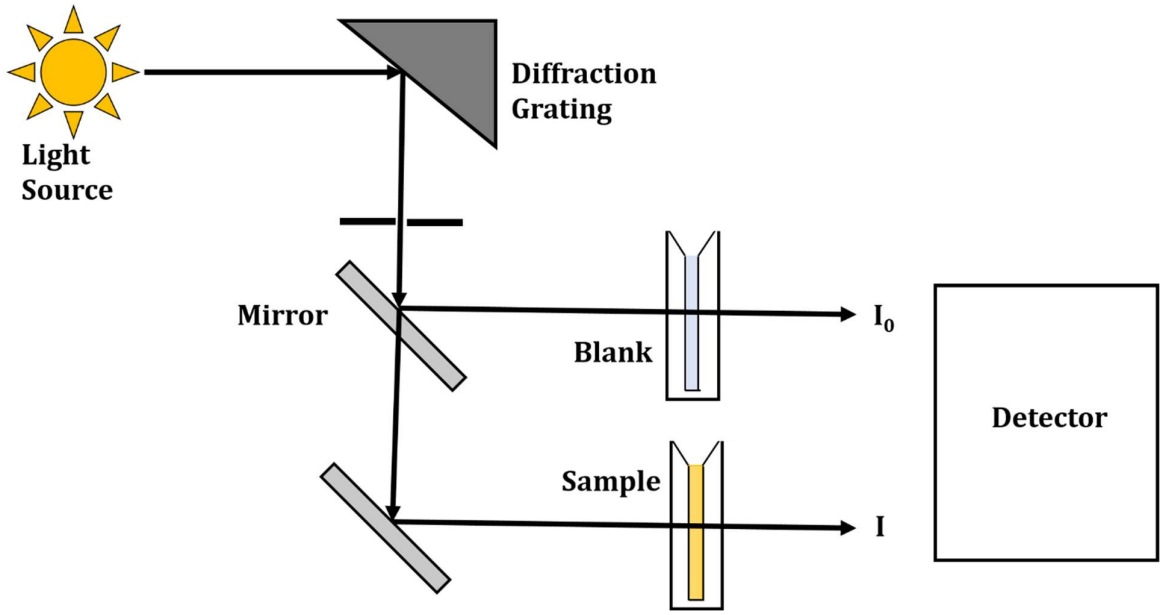

Figure 2.10*: Schematic of a standard UV-Vis solution state experiment.*

Figure 2.10 is a schematic of a typical UV-Vis spectrometer used to measure the spectrum in the solution state. The light emitted from the light source is split into its component wavelengths, with the filter selecting one of these wavelengths at a time. The selected wavelength is then split into two equal intensity beams, one that passes through the sample and the second through the reference. The reference cuvette contains only solvent, which matches the solvent used to dissolve the sample, the reference cuvette should not absorb light of any wavelength. Once any remaining light has hit the detectors the intensities of the separate beams are compared in the wavelength range being studied. The spectrometer will then scan the sample over a defined wavelength, generally 200-700 nm, in the manner described above.

The data is then presented in a graphical format, with wavelength on the x- axis and absorption ($A=\log(I_0/I)$) or transmittance ($T=I/I_0$) on the y-axis. When the complex does not absorb light $I=I_0$ and A=0 or T=1, if the light absorbed by the sample is less than the reference, then a peak at the corresponding wavelength will be observed on the graph.

2.2.2 Photoluminescent Emission spectroscopy.

Emission spectroscopy is a complementary technique to absorption spectroscopy. While absorption spectroscopy measures the colour of the complex, emission spectroscopy measures the luminescence. This is important information particularly if these complexes are going to be considered as future materials for OLEDs *etc*. Figure 2.11 shows the basic set up of a fluorescence spectrometer. The detector is located at 90 ° to the incident beam to stop any incident radiation hitting it.

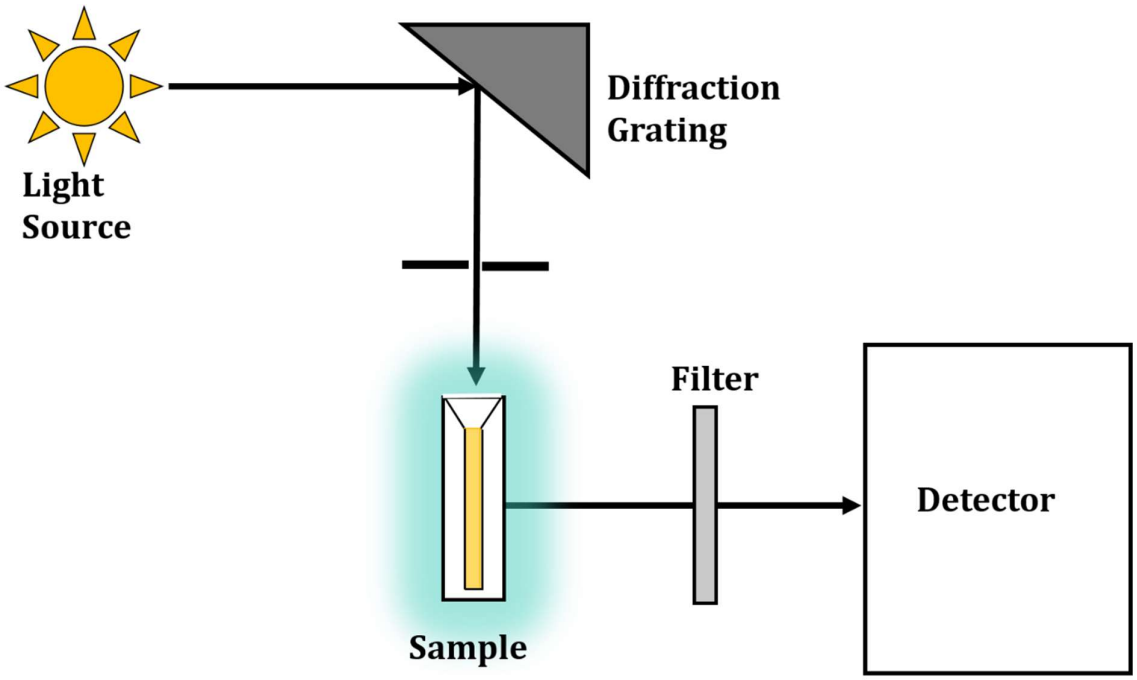

Figure 2.11*: Schematic of a standard fluorescence solution state experiment.*

As in absorption spectroscopy, the incident light is split into individual wavelengths, with one being selected by the diffraction grating, which irradiates the sample. It is here that the similarities end, because with emission spectroscopy one wavelength is used for the whole of the experiment. This excitation wavelength is determined from analysis of the absorption spectrum and corresponds to the peak maximum in the absorption spectrum. Once the sample has been irradiated it will emit in all directions, it is this light that is measured by the detector. A plot of intensity *vs* emission wavelength is then generated.

2.2.3 Reflectance spectroscopy.

While the previous two techniques described in Section 2.2.1 and 2.2.2 provide details on how materials behave in solution, reflectance spectroscopy will probe the materials in the solid state. There are two types of reflection specular and diffuse. Specular reflection occurs when the incident light is reflected in the same direction, whereas in diffuse reflection the incident light is reflected in all directions, the difference is illustrated in Figure 2.12.

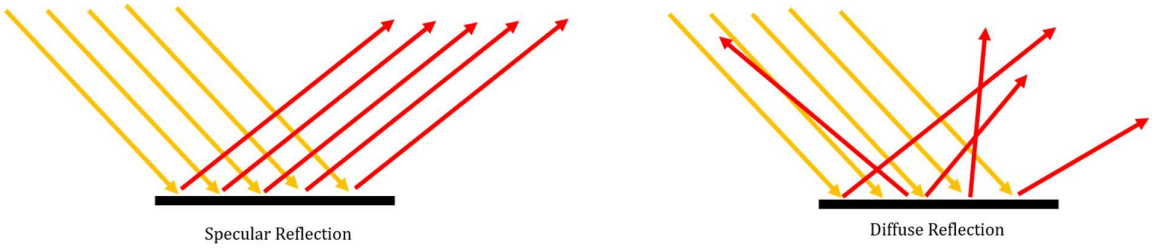

Figure 2.12: *Diffuse vs specular reflection. (Incident light shown in red)*

For the studies in this thesis, diffuse reflectance will be observed due to the rough and matte surface of the materials being measured. The set-up for measuring the diffuse reflectance is shown in Figure 2.13.

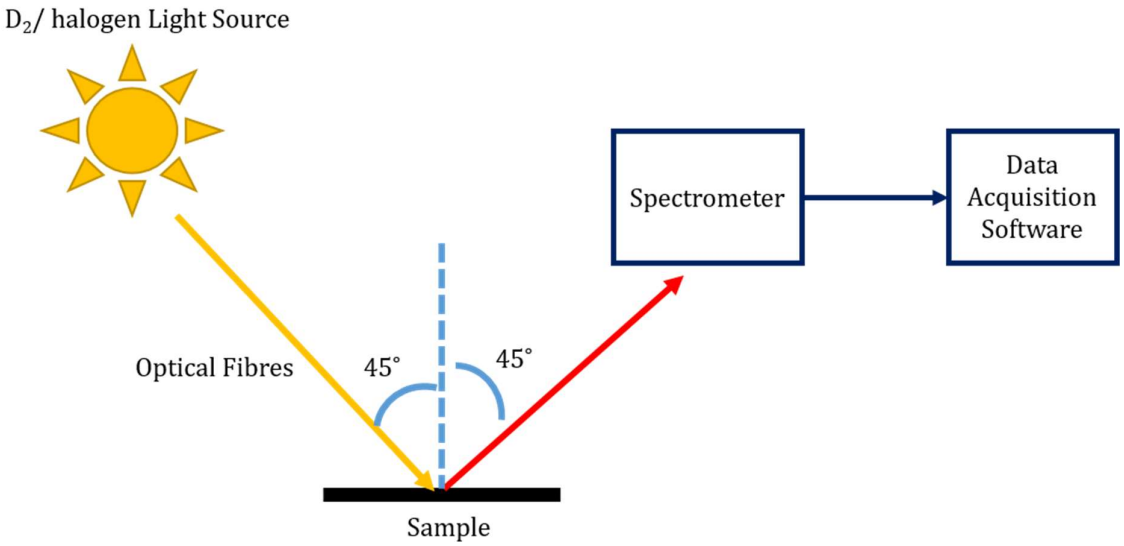

Figure 2.13: *Schematic of a Diffuse Reflectance set-up for solid-state measurements.*

The Diffuse Reflectance measurement will provide an accurate measure of the colour of the complex being studied, the colour is measured relative to a reflectance standard, not shown in Figure 2.13. the sample is illuminated with a UV-Visible light source and when it hits the sample diffuse reflection occurs, there are some wavelengths that are absorbed in this process and it is the information regarding the missing wavelengths that provides us with a colour measurement.

The advantages of using diffuse reflectance for this type of measurement include:

- Non-destructive,
- Quantitative,
- Local- surface measurement.

2.3.0 Nuclear magnetic resonance (NMR) Spectroscopy

NMR spectroscopy is a vital tool for determining the structure of the compound synthesised. In this research project ^{1}H NMR and heteronuclear NMR spectroscopy has been used to provide evidence of the final structure of the products.

2.3.1 Introduction to NMR Spectroscopy

Most elements have a naturally occurring magnetic isotope, for example, ^{1}H has a spin of ½ and a natural abundance of 99.9885%. When this magnetic nucleus is placed in a magnetic field the nuclear magnetic dipole will precess (Figure 2.14), this precession occur at the Larmor frequency[89], υ (Equation 2.5).

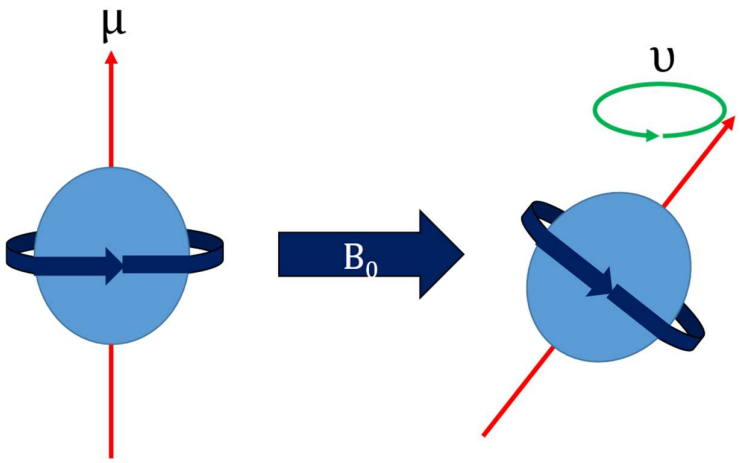

Figure 2.14*: Precession of a magnetic nuclei in an applied magnetic field (B_0), at the Larmor frequency (υ).*

$$\upsilon = \frac{\gamma B(0)}{2\pi}$$

Equation 2.5*: Larmor frequency (υ).*

In the equation depicted in Equation 2.5, the Larmor frequency is equivalent to the chemical shift of the nucleus and γ is the gyromagnetic ratio.

In the magnetic field the nucleus will have a number of energy states, which can be calculated using Equation 2.6:

$$No^{\circ}\ of\ energy\ states = 2I+1$$

Equation 2.6*: Calculating number of energy states for a magnetic nucleus.*

Taking the ^{1}H nucleus as an example. It has a chemical shift of ½, this means the nucleus has two energy states. This is depicted in Figure 2.15.

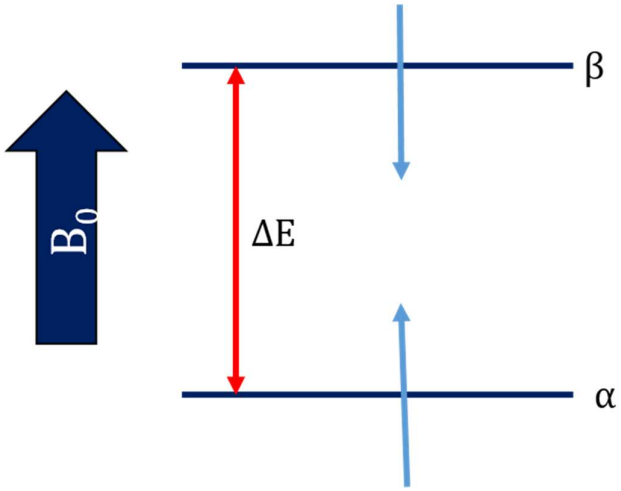

Figure 2.15: *Energy states for a ^{1}H Nucleus.*

The spins can point in the same direction or in opposite directions in the different energy levels. In the α state the nucleus is spin up, in the same direction as the applied magnetic field, B_0. This is the lower energy state. When the nucleus is spin down, as shown in the β state, it is positioned against the magnetic field and is therefore of higher energy.

ΔE is highly dependent on the strength of the interaction between the nucleus and the field, it is measured by applying electromagnetic radiation of frequency, υ. This causes the nuclei to flip from the lower α state to the higher β state. This only occurs if the following mathematical relation is met:[90]

$$\Delta E = h\upsilon$$

Equation 2.7: *Planck-Einstein Relation*

The equation represented in Equation 2.7 can be written in an alternative form:

$$\Delta E = h\frac{\gamma B(0)}{2\pi}$$

Equation 2.8: *Planck-Einstein Relation in an alternative format to show the relation between ΔE and the Larmor frequency.*

The relationship between the difference in energy levels and the Larmor frequency shows that this technique is sensitive to the chemical environment of the nucleus. This can give us vital information on the chemical shift of a complex, from which the structure can be derived.

2.3.2 NMR Spectrometer

To conduct an NMR experiment the following conditions need to be met:

1. Strong, static magnetic field,
2. Source of radiofrequency radiation,
3. Method for detecting the NMR signal.

Figure 2.16, is a schematic of an NMR spectrometer and shows how these conditions can be met.

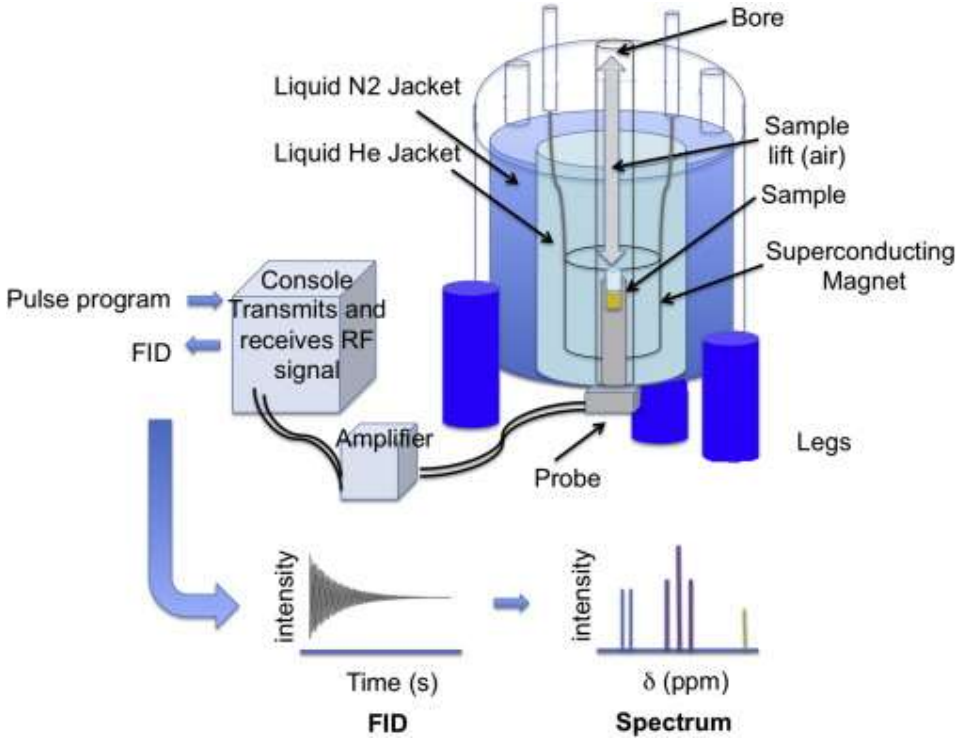

Figure 2.16: *Schematic of an NMR spectrometer.*[91]

The strong magnetic current is supplied by a superconducting magnet, this is kept cool by a jacket of liquid He and liquid N_2. The console, depicted in Figure 2.16 provides the source of radiofrequency radiation, which is then subsequently amplified before it is applied to the sample via the probe. Finally, the console receives the NMR signal, which is then computed into the spectrum.

2.3.3 Chemical shift

The chemical shift is defined as:

> *"The difference in resonance frequencies between the nucleus of interest (υ) and a reference nucleus (υ_{ref}) by means of a dimensionless parameter, δ."* [92]

It is represented by Equation 2.9.

$$\delta = 10^6 \frac{(\upsilon - \upsilon(ref))}{\upsilon(ref)}$$

Equation 2.9: *Formula for calculating chemical shift.*

Chemical shift, δ, has the units of parts per million (ppm), due to the scale of 10^6 in Equation 2.9. The value of υ_{ref} will vary dependent on the nuclei being studied, but for ^{1}H NMR υ_{ref} is usually measured relative to the methyl proton signal for trimethylsilane. This is because it is an inert compound that is soluble in a variety of solvents and has a strong single resonance typically found at low frequency.

The value of the chemical shift provides an insight into how shielded the nucleus being studied is. When the signal is upfield or at a high frequency, the nucleus is said to be deshielded and when the peak is downfield or at low frequency the nucleus is said to be shielded. Figure 2.17 shows typical proton chemical shifts.

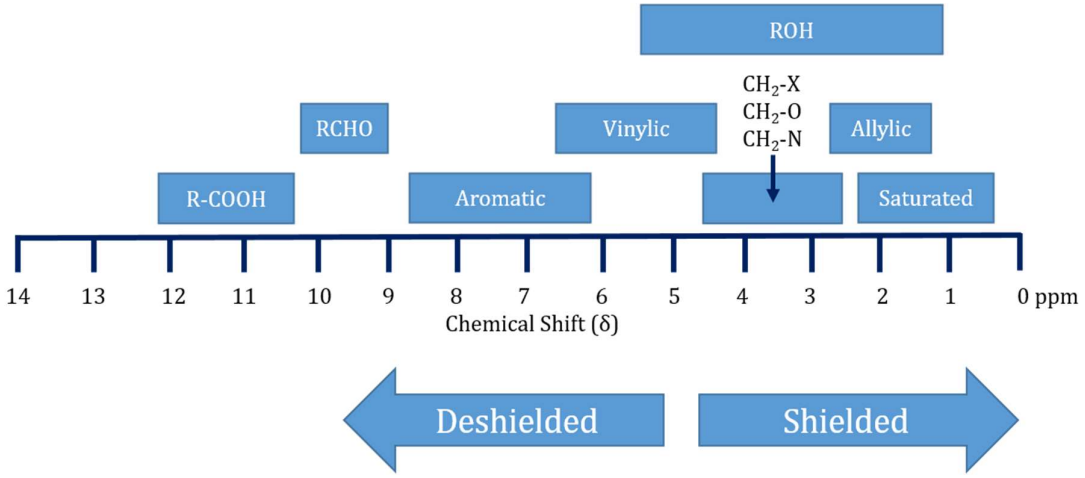

Figure 2.17*: Typical proton chemical shifts.*

It can be deduced from that there is a series of factors that affect how shielded or deshielded a nucleus is. These factors will now be discussed in more detail.

- Inductive effects: this is caused by the presence of electron-withdrawing groups (EWG) in the molecule. The EWG deshield the nucleus and will therefore move the chemical shift to a higher frequency. For example, exchanging the hydrogens in methane with chlorine has the following pattern of chemical shifts; CH_4, 0.23 ppm; CH_3Cl, 3.06 ppm; CH_2Cl_2, 5.5 ppm; $CHCl_3$, 7.26 ppm.
- Anisotropy: Commonly seen with molecules with π-bonds such as aromatics. This effect deshields the nucleus. Anisotropy is also seen in σ bonds, an example would be a rigid 6-membered ring, where the chemical shift of the axial and equatorial protons differ.
- Hydrogen bonds: When an intramolecular hydrogen bond can form in a molecule the hydrogen-bonded proton is heavily deshielded.

Additional factors that can affect chemical shift include: resonance, Van der Waals forces, isotope effects, temperature and solvent.

2.3.4 Equivalence

Nuclei can be chemical shift and magnetically equivalent or just chemical shift equivalent. When two protons have the same chemical shift, they are chemical shift equivalent. This occurs if the protons are interchangeable by a symmetry operation or by a rapid process. Possible symmetry operation include: rotational symmetry, the protons in this instance are homotopic and by a plane of symmetry or inversion, in this instance the protons are classified as enantiotopic. If the protons are not interchangeable by a symmetry operation they are called diastereotopic and will have different chemical shifts, an example would be protons on a carbon neighbouring a chiral centre.

Magnetic equivalence applies only to nuclei that are chemical shift equivalent. Two nuclei are magnetically equivalent if they are coupled equally to other nuclei in the spin system.

2.3.5 Coupling in ^{1}H NMR spectra

Spin-spin coupling arises from the pairing of nuclear spins with electronic spins and this magnetic interaction can provide vital information regarding the structure of the complexes. They are also known as*, scalar couplings or J-couplings.* These couplings are denoted by the coupling constant, J, shown in Figure 2.18.

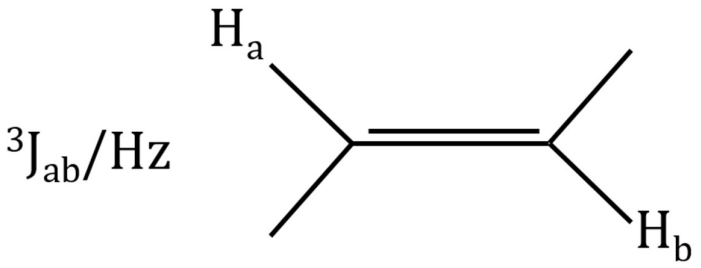

Figure 2.18*: J-couplings*

The "3" represents the number of bonds the coupling occurs through and ab denotes the nuclei involved in the coupling. The magnitude of the coupling constant is independent of field strength but it is affected by a series of factors described below.

- The geometrical relationship between the coupled nuclei. For example, the J coupling for an alkene can provide diagnostic evidence of a *cis* or *trans* bond. The J coupling for a *trans* bond analogous to the structure shown in Figure 2.18, would be stronger. This occurs due to better orbital overlap when compared to the *cis* form.
- The number of intervening bonds between the coupled nuclei. The example shown in Figure 2.18, has three intervening bonds, it is therefore a vicinal coupling and is weaker than a germinal coupling, which would have a value of 2. Long rang couplings with a value larger than 4 generally gives rise to weak couplings.
- Angle strain. In cyclic systems J values can differ dependant on the number of atoms in the ring.
- Heteroatoms: heteroatoms can act as insulators, in which no coupling is seen between the protons. However, they can also couple to the protons themselves if they have a naturally occurring magnetic isotope. Usually proton exchange would have to be slow for coupling to occur or a broad peak in the spectrum would be observed.

2.3.6 Splitting/multiplet patterns in ^{1}H NMR Spectra

When nuclei couple it can cause the peak to split, the pattern that is observed is known as a splitting pattern or multiplet pattern. These patterns are either first or second order.

In first order splitting patterns the number and intensity of peaks is governed by Pascal's triangle, where the multiplicity is found using Equation 2.10. Where n is the number of chemically equivalent protons and I is the spin of the nuclei.

$$Multiplicity = 2nI + 1$$

Equation 2.10: *Formula for calculating multiplicity of a first-order splitting pattern.*

For example if the fragment CH_3CH_2 is considered, when a proton on the CH_2 group couple to the CH_3 group, because there are 3 chemically equivalent nuclei the CH_2 group will be split into a quartet, with intensities 1:3:3:1. Equally, for the CH_3 group it will couple to the CH_2 group, which has 2 equivalent protons, the peak for the methyl group will appear as a triplet with intensities, 1:2:1.

The example used above is for a system with equivalent ½ spins, when there is coupling to two inequivalent spin ½ nuclei more complex splitting patterns are observed. Taking the molecule shown in Figure 2.19 as an example,

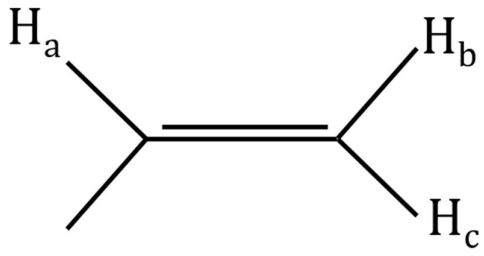

Figure 2.19: *Generic molecule.*

The 3 protons on the molecule shown in Figure 2.19 are not chemical shift equivalent. Taking the hydrogen labelled as H_b as an example, it will couple to H_a producing a doublet and then to H_c which will split each line of the doublet into a doublet. This pattern is referred to as a doublet of doublets and will have the following intensities, 1:1:1:1.

Equation 2.8 can also be used to predict the coupling of nuclei with spins greater than a half. However, nuclei with a spin greater than a ½ have an electric dipole moment in addition to the magnetic dipole moment. This additional dipole moment can interact with the local field gradients and for molecules in solution, this can sometimes give rise to broad and undefined NMR peaks.

When nuclei with a spin greater than a half do couple with a proton, the same method of predicting their coupling can be used as shown for the example in Figure 2.19.

2.3.7 ^{13}C NMR Spectroscopy

In comparison to ^{1}H nuclei, ^{13}C nuclei are only 1% naturally abundant, so observed coupling between carbons is rare, this low natural abundance also means that the spectra are noisy. The coupling constants for ^{13}C-^{1}H are large and can increase the noise in the spectrum. In order to avoid this ^{13}C NMR spectra are routinely decoupled, which removes the spin-spin coupling between these elements. Key points for analysing and understanding ^{13}C spectra are:

- Chemical shift equivalence applies.
- Magnetic equivalence will not apply unless the sample is ^{13}C enriched.

- ^{13}C chemical shifts are approximately 10X the equivalent ^{1}H shift shown in Figure 2.17.

2.3.8 2D NMR Spectroscopy

2D NMR is used for assigning peaks that are difficult to assign in a 1D NMR and for identifying protons that are close in space. The three main techniques are:

- COSY: Correlation Spectroscopy, it shows all of the coupling between protons in a spin system in two dimensions.
- NOSEY: Nuclear Overhauser Enhancement Spectroscopy, a NOESY spectrum will provide information on protons that are close in space and not coupled through bonds.
- HMQC: Heteronuclear Multiple Quantum Coherance, these spectra show directly coupled ^{1}H and ^{13}C nuclei. This helps to assign ^{13}C NMR.

CHAPTER 3

Aims

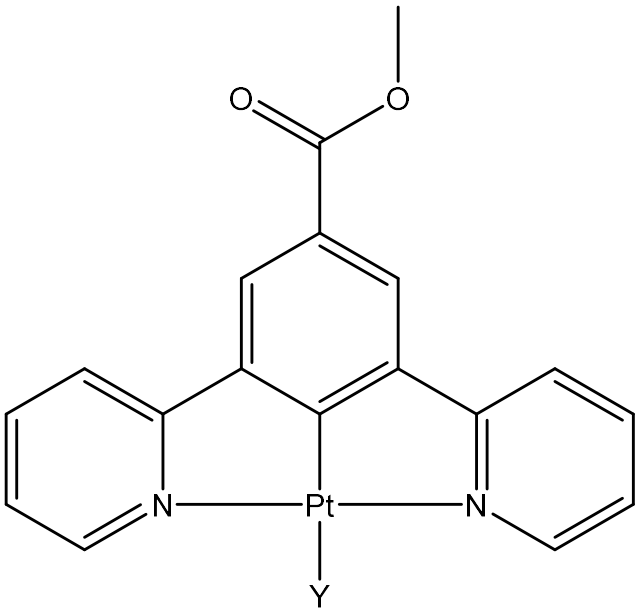

General Aim

Following on from recent work[93] within the Raithby group on the development of sensor molecules based on platinum(II) pincer complexes the aims of this thesis are to explore the factors that enhance the senor/switching properties of these complexes in a systematic way. The Pt(II) square planar geometry will remain constant throughout these studies since, for solid-state materials, the Pt…Pt stacking interaction seems to be a key component of the successful switching processes. Two general types of pincer ligand will be considered, the tridentate, tri-nitrogen donor terpyridyl ligand and the tridentate cyclometallated N^C^N pincer ligand. Both these ligands will be derivatised. The nature of the ligand occupying the fourth coordination site on Pt centre will also be altered systematically.

The specifically designed objectives of the study that will be covered in detail in the remainder of the thesis are outlined in the rest of this short chapter.

Aim of Chapter 4: Terpyridine Complexes.

The general formula of complexes to be studied in this section are [Pt(RTerpy)Cl][X], where the R group is a substituent on the 4'postion of the central pyridine ring and X^- is the counter-ion. The broad aim of this first section is to systematically investigate the effect of increasing the size of two components in the system (R and X^-) and whether this has an effect on the stacking and spectral properties of the complexes. The first component to be studied will be the counter-ion size. The counter-ions to be used in this study are; BF_4^-, PF_6^-, BPh_4^- and OTs^- and are shown in Figure 3.1.

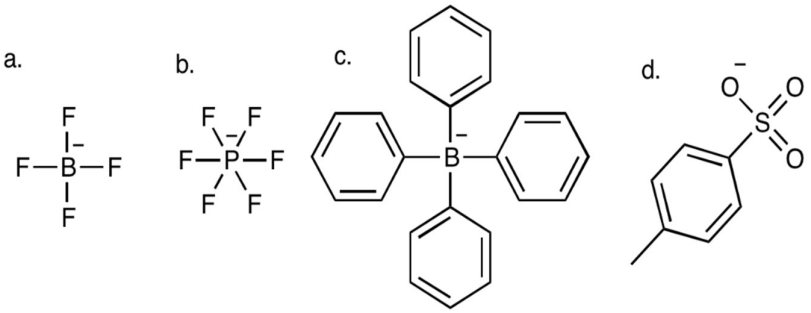

Figure 3.1*: The four counter-ions under investigation, a. Tetrafluoroborate, b. Hexafluorophosphate, c. Tetraphenylborate and d. Tosylate.*

The counter-ions have been chosen for the following reasons:

1. From a-c a steady increase in size and steric bulk is observed,
2. The anion depicted in Figure 3.1d has planar and tetrahedral component to its geometry as opposed to the tetrahedral and octahedral geometries observed for counter-ions a-c.

The second component to be studied will be the steric bulk of the substituent on the 4' position of the central pyridine ligand. Simple substituents have been chosen for this initial investigation and are shown in Figure 3.2.

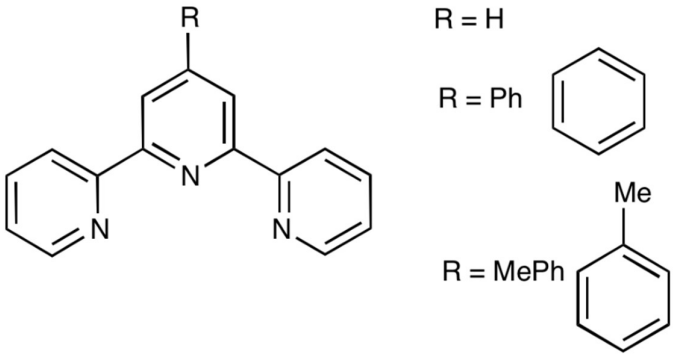

Figure 3.2*: The three terpyridine ligands under investigation, where R=H, Ph, MePh.*

After the thorough investigation of the chloride complexes, the ligand in the 4th co-ordination site will be altered. The ligand (L) will be exchanged for the cyanide group, which is a strong field ligand and positioned higher in the spectrochemical series than chloride. By exchanging to the cyanide ligand, the luminescent properties as well as the colour would be expected to change. To enable fair and clear comparison only the BF_4^- salts of these complexes will be studied.

Aim of Chapter 5: Ligand Manipulation

Previous work in the Raithby group led to the discovery of a rapid response vapochromic material.[93] The aim of this chapter is to build on this discovery and investigate the effect of the ligand in the 4th co-ordination site of the Pt centre. The generic structure of the complexes studied in this chapter is shown in Figure 3.3.

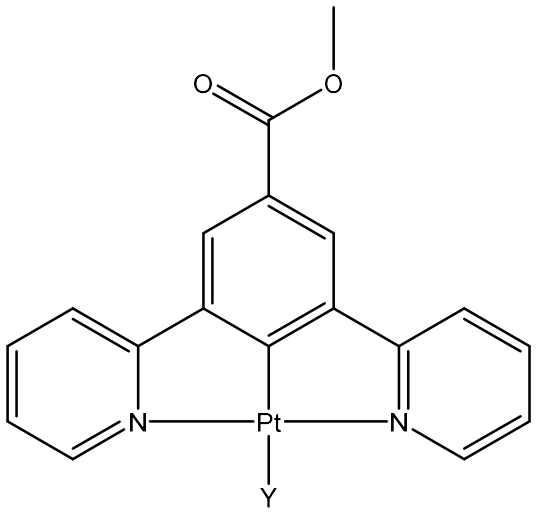

Figure 3.3*: Generic structure of the complexes synthesised in this chapter.*

In contrast to the complexes synthesised in chapter 4, the pincer ligand is of the cyclometallated N^C^N type which is used to improve the emission intensity of the complexes in the solid and solution state.[47] A variety of ligands will be used in this research to investigate the different spectral effects that are caused by the different ligands.

Aim of Chapter 6: Photo-switching N^C^N complexes.

The aim of this chapter is to develop a series of complexes that 'switch' on exposure to light. The two methods discussed in Section 1.5.0 will be used to achieve this. Figure 3.4 shows the generalised structures of the complexes to be synthesised, where the X can stand for either a nitrogen or carbon atom making the functional groups azobenzenes or stilbenes, respectively. These particular functional groups have been chosen because their photo-switching behaviour is well documented in the literature.

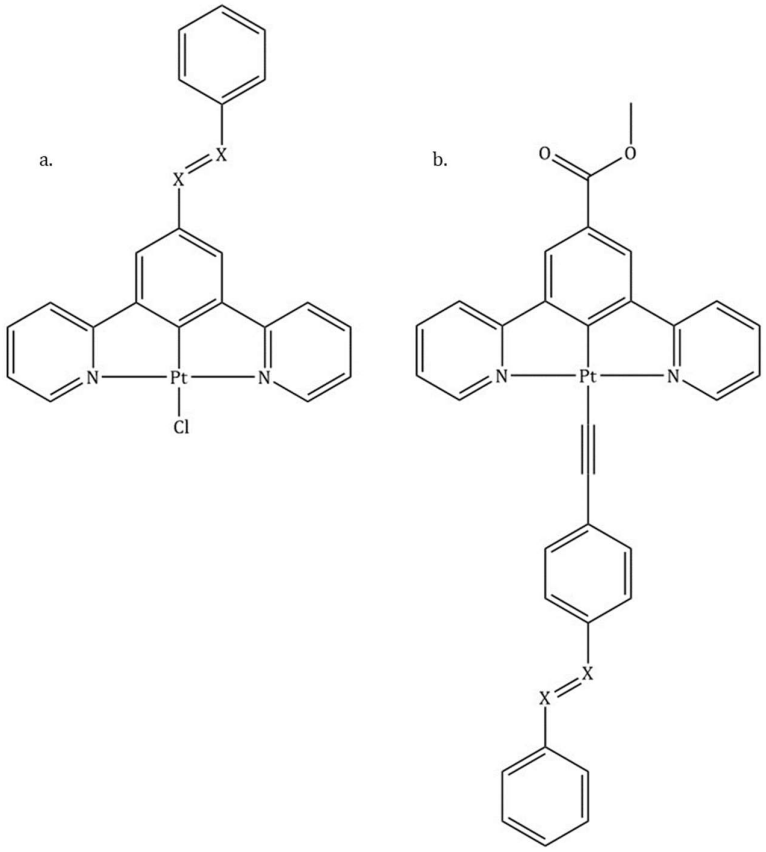

Figure 3.4: *Platinum complexes under investigation, where X= C or N*

In the case of complex a in Figure 3.4, method 2 will be used where the dz^2 orbital interactions will be manipulated, whereas for complex b, Figure 3.4, method 1 will be used where the acetylide ligand will be used as a communication channel to the metal centre.

Aim of Chapter 7: pH Sensitive Complexes

The aim of this chapter is to develop a series of complexes that are responsive to pH. The same methodology will used as described in chapter 6. A N^C^N pincer ligand will be functionalised with an amine group in addition to an acetylide group itself being functionalised with an amine group. The structures of the complexes synthesised in this chapter are provided in figure 3.5.

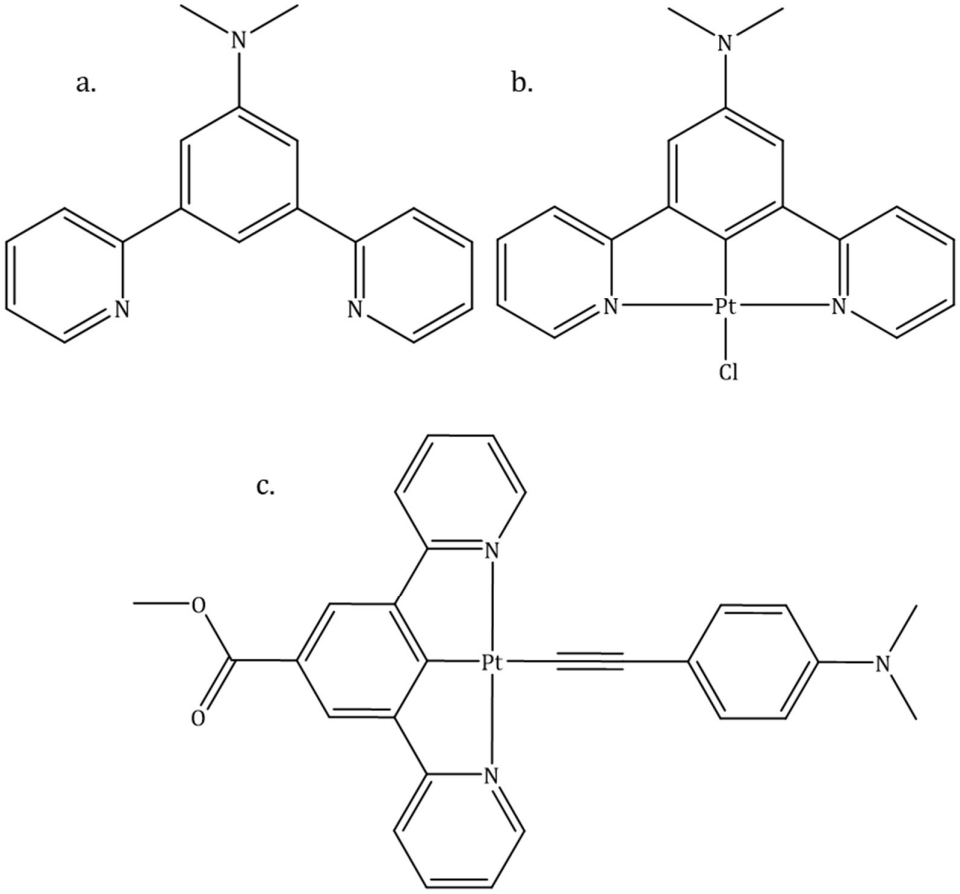

Figure 3.5*: Platinum complexes under investigation.*

CHAPTER 4

Terpyridine Complexes

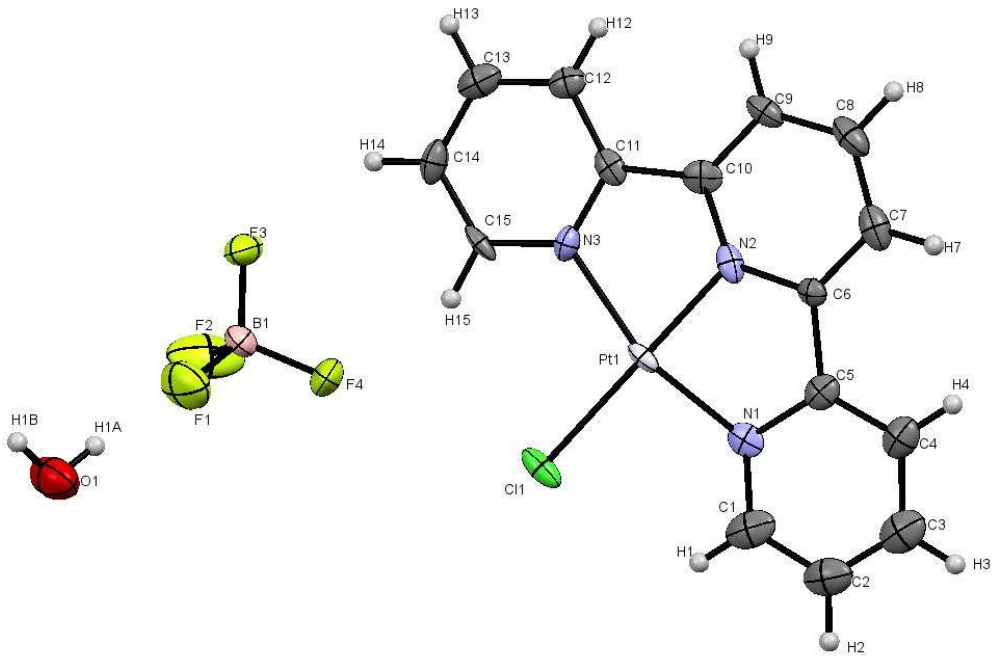

4.1.0 Introduction

Pt(II) complexes are known for their interesting spectral properties. The origin of these spectral properties have been discussed in detail in Section 1.2.0 However, if the spectral property could be tuned to exhibit a *'switch'* then these complexes could be used for a variety of sensing applications such as vapour[68], chemical[64], ion[94], DNA[95] sensing. This *'switch'* is incorporated into the complex by the manipulation of the dz^2 orbital interactions that form between the Pt centres in adjacent molecules. These strong intermolecular interactions are discussed in detail in Section 1.5.0.

4.1.1 'Smart' Materials and Applications

The tendency of Pt^{2+} complexes to aggregate is because of their square planar geometry;[61, 96] this allows metal-metal and ligand-ligand interactions to occur. The manipulation of these interactions leads to the formation of a *'switch'.*

One example of a *'smart'* material was developed by Connick *et al.* in 2004. Two different salts of the complex shown in Figure 4.1 were synthesised and subsequently investigated for a vapochromic response.[97]

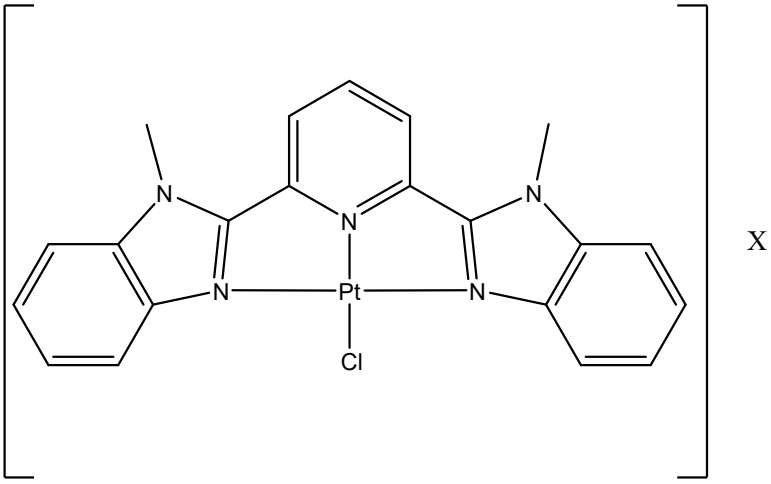

Figure 4.1*: Vapochromic complex synthesised by Connick et al, where X= Cl/ PF_6.*[97]

Connick found that the chloride salt of the material responded to methanol vapour and the solid switched from yellow to red. The PF_6 salt was vapochromic to acetonitrile vapour and turned from orange to deep red. The authors predicted that the change in colour occurred due to the change in distance between adjacent Pt centres. However it was not until 2007 that crystallographic evidence was provided to show that a change in the intermolecular Pt distance was the reason why the complex changed colour.[98]

In 2008, Castellano completed a systematic study of 18 Pt Terpy Chloride species, in which the substitution pattern of the tridentate ligand and the identity of the counter-ion was varied.[99] The structures of these complexes are shown in Figure 4.2.

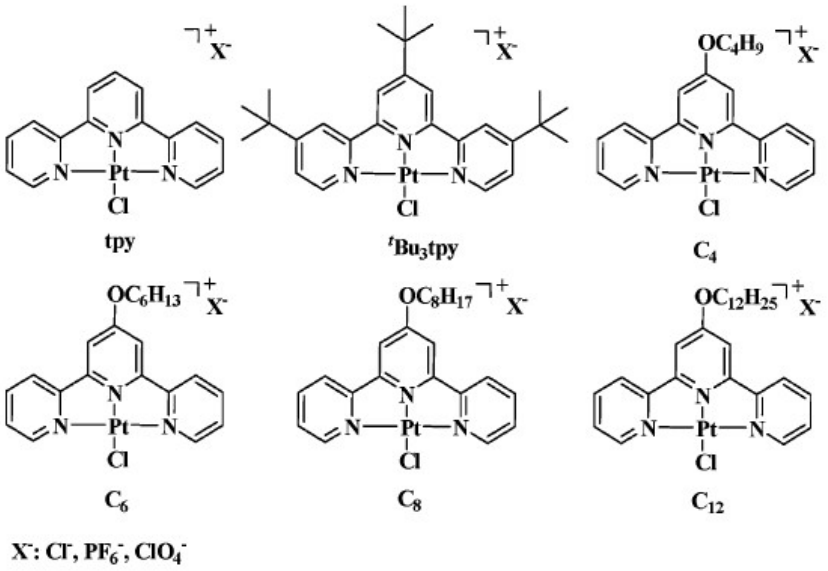

Figure 4.2: Chemical structures of the Pt(II) complexes used in the study by Castellano. Diagram has been taken directly from the literature.[99]

Each of the 18 complexes was arranged into a microarray and exposed to a series of vapours for 120 minutes to ensure equilibrium was achieved and the optical properties were then recorded. The results of these studies are provided in Figure 4.3.

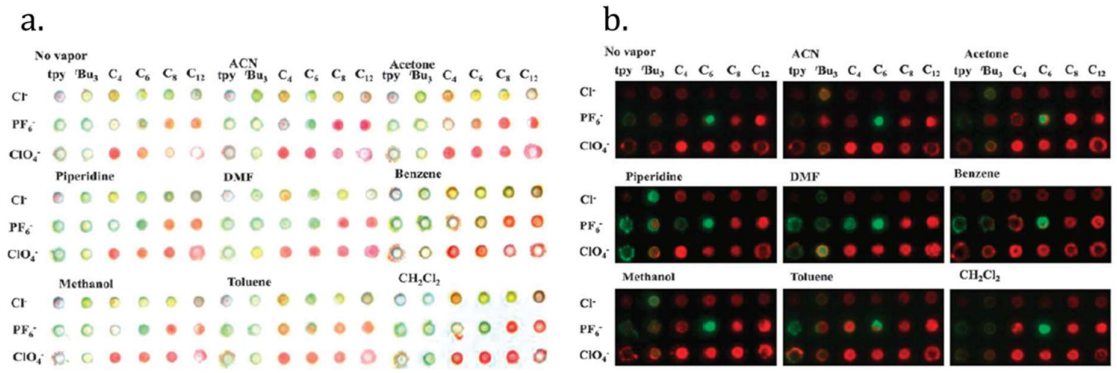

Figure 4.3: a. Vapochromic colorimetric response of the Pt(II) complexes when exposed to different VOC's. b. Vapoluminescent response of the Pt(II) complexes toward different VOC's, the arrays were excited using 365 nm light. Diagram has been taken from the literature.[99]

The results presented in Figure 4.3a show that the complexes functionalised with the C_8 and C_{12} groups and PF_6^- and ClO_4^- counter-ions have distinct vapochromic responses to ACN, acetone and CH_2Cl_2. In each case, the complexes turned a deep red colour on exposure to this solvent. More subtle changes were observed when the complexes were exposed to other solvents.

Figure 4.3b illustrates the vapoluminescent response of these complexes to the same series of VOC's. The first point of interest is the lack of emissive properties of the complexes with the Cl^- counter-ion. Further investigation of the results shows that the strongest responses are observed with ACN, piperidine and DMF, which the authors attributed to the presence of lone pairs of

electrons on the solvent. In addition aromatic solvents such as benzene and toluene caused a change in the colour of the observed emission, with green/ yellow emission being observed for some of the PF_6 salts. The authors surmised that this change in emission was caused by the lengthening of metal-metal σ interactions.

The authors concluded that the results of this research would allow the construction of microarrays that could respond to different analytes, including responses to aromatic solvents.

The complex shown in Figure 4.4 was synthesised by *Field et al* in 2012 and was found to have interesting spectral properties in response to different vapours.

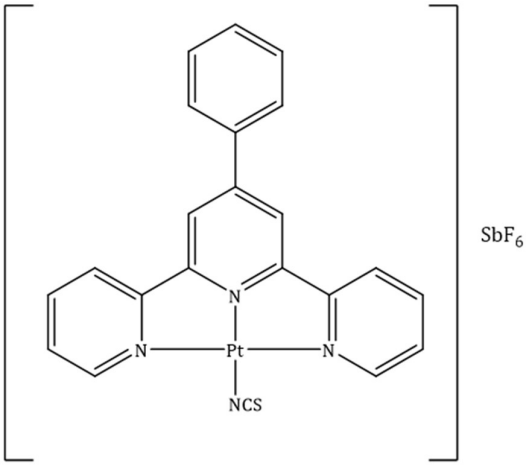

Figure 4.4*: Pt Terpyridine based complex.*

In the solid state the whole complex was essentially planar, which the authors thought to be unusual because the phenyl substituent on the central ring of the terpyridine would be expected to twist out of the plane of the molecule in order to reduce intramolecular interactions, and thus exhibit a non-planar aspect to the complex. The fully planar nature of the complex is perhaps even more surprising since the complex, having an overall positive charge, has a charge balancing $[SbF_6]^-$ anion present in the crystal lattice which will disrupt the crystal packing and, through the steric bulk of the anion, reduce likelihood of there being short Pt…Pt intermolecular interactions. Overall, the presence or absence of counter-ions and the geometry of the tridentate ligand both contribute to the packing and what the Pt…Pt distance in the crystal is.

In the crystalline complex the Pt…Pt distance is to long for intermolecular dz^2 interactions to occur, the planarity of the substituted tridentate ligand allow for significant π overlap to occur in the solid-state structure of this compound. This π interaction stabilises the complex and a porous material can be obtained which allowed for the reversible sorption of small molecules such as: acetonitrile, methanol and acetone. When the vapours moved in and out of the crystalline channels, no change in colour was observed however the process could be studied using solid state emission spectroscopy as the ^{3}MLCT bands increased in intensity upon the absorption of the organic vapours.[100]

A final example of a functionalised Pt terpyridine complex, was synthesised by *Maron et al* in 2016. In this paper, the authors studied how the spectral properties of the complexes changed

between the solution and solid state. A series of complexes were studied, the general formula is shown in Figure 4.5.

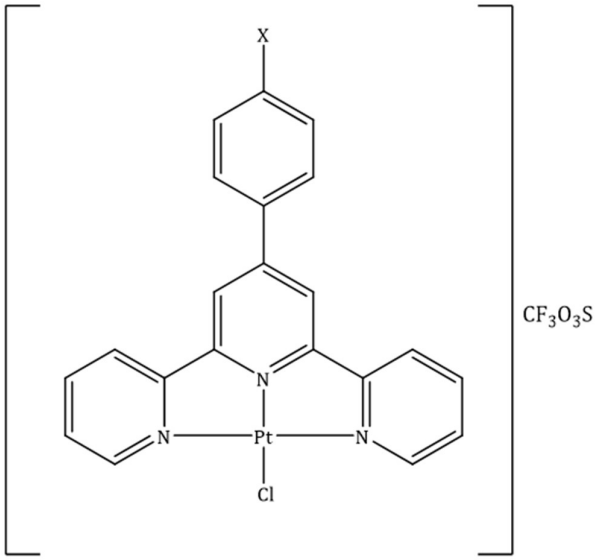

Figure 4.5*: Pt Terpyridine based complex, where X= Cl or Br*

The authors noted that the complexes were emissive in both solution and in the solid state, but a bathochromic shift occurred when moving from solution to solid state, due to the presence of Pt…Pt interactions.[101] It is important to note that the substituent on the terpyridine ligand and its π donation or accepting capabilities, defines the profile of the observed emission.

An alternative way to induce spectral changes in these complexes is *via* direct manipulation of terpyridine substituent and the introduction of an active functional group that can interact directly with ions or VOCs for which the complex acts as a sensor. There are several examples in the literature of ligand functionalisation being used for host-guest and ion binding applications.[76, 77, 94, 95, 102-104]

An example is described in a paper by *Yam* in 2009. In this work a series of complexes that had been functionalised with a crown ether moiety were studied. This work focussed on single molecular species as well as dimeric species that had been bridged using a sulphur-containing ligand. Figure 4.6 shows the structure of the single molecular species.

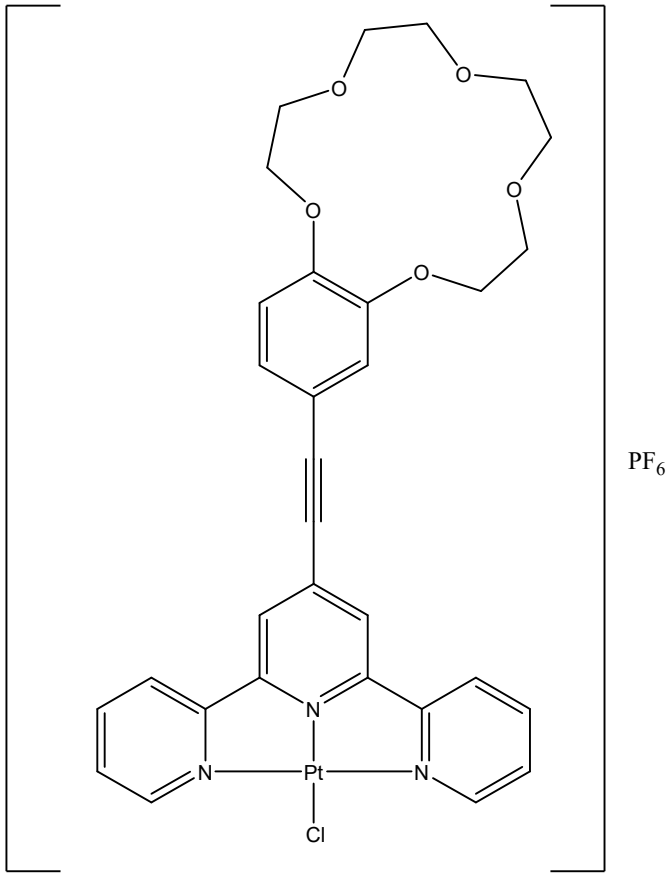

Figure 4.6*: Ion binding complex, synthesised by Yam et al.*

Crystal structure analysis of one of the single molecular species functionalised with a benzo-15-crown-5 ether found that due to the large bulky nature of the substituent no intermolecular Pt…Pt or π-π interactions could occur in the solid state. However, a solution state spectroscopy study of the complex found that the UV-Vis absorption profile changed when the complex was exposed to a potassium salt. This was an unexpected result since the K^+ ion is too large to fit inside the benzo-15-crown-5-ether. It was therefore suggested that the ion had been complexed between two crown ether molecules, allowing for intermolecular interactions to occur between the two molecules and a ion binding '*switch*' to be created.[105]

4.1.2 Pt…Pt Distance and Sterics

As discussed in Chapter 3, one of the primary aims of the research presented in this chapter is to investigate the role of the counter-ion and ligand substituents on the tridentate ligand in Pt…Pt stacking. The associated sterics could disrupt the stacking in the solid state and therefore the potential for Pt…Pt and π-π interactions as indicated for the complex in Figure 4.4. Field *et al*, in 2011, in earlier work investigated the effect of a tolyl group on the 4' position of the phenyl ring and how this affected the solid state structure of the complexes.[106] The authors discovered that the methyl group twists out of the plane of the pincer and there is a slight dihedral angle between the planes of 9.3 °. The distance between the molecules is below the 3.8 Å upper limit for π-π interactions, affording this stabilizing interaction. This would not occur if the methyl group was not approximately co-planar with the ligand. In addition, there is a staircase packing arrangement

observed within the crystal structure of the complex, which means that there are two Pt positions in the crystallographic unit cell that are related by symmetry.

In the given literature example[106] while the Pt…Pt separation is reported there was no attempt to define another key packing feature, that is how much the Pt centres were off-set from each other. This important parameter will affect the nature of the Pt…Pt interaction and thus the spectral properties of the complexes. The Pt offset can be calculated using Pythagoras' theorem as follows:

$$a^2 + b^2 = c^2$$

Equation 4.1*: Pythagoras' theorem.*

This equation can be used to calculate the unknown length in a right-angled triangle. Figure 4.7 illustrates how this formula is applied.

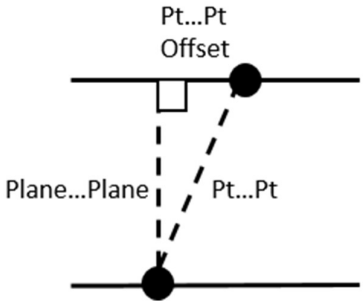

Figure 4.7*: Schematic diagram of how the Pt…Pt offset was calculated.*

Using the program *Mercury*[87] both the Pt…Pt distance, which is equal to *c* in Equation 4.1, and the Plane…Plane distance, represented by *b* in Equation 4.1, can be obtained. From this, the Pt…Pt offset can be calculated. The Pt-Pt-Pt angle can also be used as a measure of how linear the stacks in these complexes are, these will be expressed in degrees and the further away from 180° the less linear are the Pt…Pt interactions in the stacks.

4.1.3 Ligand Field Strength

The majority of the materials described previously use chloride as the ligand in the 4th co-ordination site of the square planar Pt(II) complex, however changing the identity of the ligand and its π donating or accepting properties can change the spectral properties of the complexes.

Hight et al, 2013, investigated the effects of using amine moieties to improve the emission frequencies in the solution state.[45] They incorporated the ligands on both the terpyridine ligand and in the 4th co-ordination site on the Pt and found that an increase in emission intensity was observed upon by increasing the π donating ability of the amine group. However, the greatest improvement of emission intensity was observed when a cyanide ligand replaced the chloride ligand in the 4th co-ordination site, Figure 4.8.

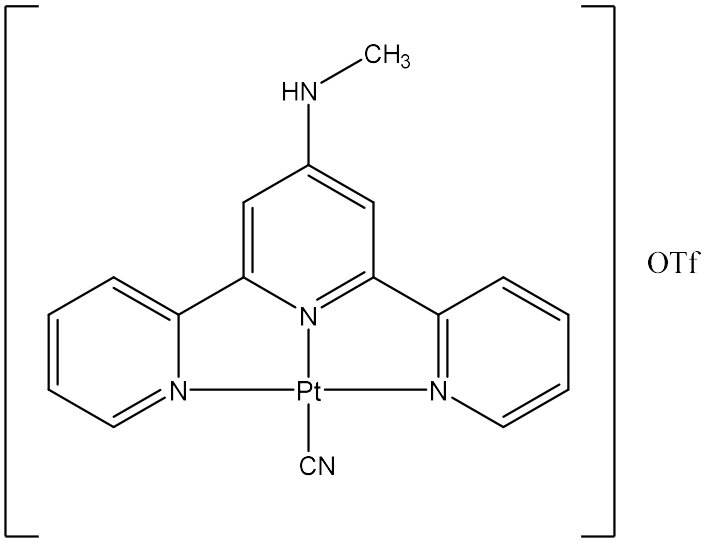

Figure 4.8*: Pt Terpyridine complex synthesised by Hight et al.*

The cyanide ligand is strong π acceptor ligand. This π accepting behaviour is seen alongside its ability to form strong M-L σ bonds; this effect is known as back-bonding.[107] It is thought that this effect would help to stabilise the π* hybrid orbital, which is formed upon interaction of the conjugated aromatic system with the ligand. This stabilisation would blue shift the lowest energy transition, in turn decreasing the energy gap between the frontier orbital and the dz^2 orbital. The interaction between the dz^2 orbital and the frontier orbital has an effect on the optical properties of the complex, potentially allowing tuning of these properties. It is not just the strong π accepting nature of the cyanide ligand that makes it an attractive choice for further investigation. The spectrochemical series classifies this ligand as, strong field. This raises the energy of the dx^2-y^2 orbital thus depopulating it, so that it has a less detrimental effect on the luminescence (Section 1.4.1).

The final reason why this ligand was chosen is its size. It is small, and negatively charged. This means that the same configuration of complex and counter-ion can be retained. Its small size means that it will not cause any steric hindrance and therefore not compete with any groups on the back of the pincer.

4.2.0 Synthetic Strategy.

In this section the synthetic strategy for the synthesis of the precursor tridentate ligands and of the Pt(II) complexes will be described along with their spectroscopic and crystallographic characterisation and the details of their luminescent properties. Where the precursors or complexes have been prepared previously the appropriate literature references will be cited.

4.2.1 Ligand Synthesis.

2,2':6',2''-Terpyridine and 4'-(p-tolyl)-2,2':6',2''-Terpyridine were purchased from Sigma Aldrich and used as supplied. The 4'-phenyl-2,2':6',2''-Terpyridine ligand was synthesised in house. A procedure called the Kröhkne synthesis was used and is detailed in Scheme 4.1.[108]

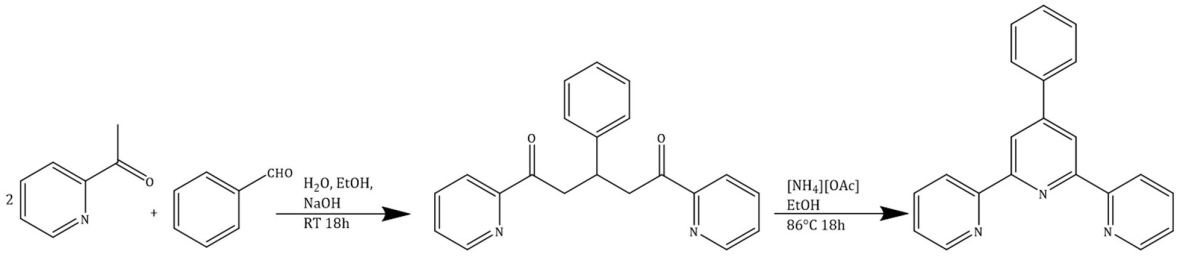

Scheme 4.1*: 4'-phenyl-2,2':6',2''-Terpyridine ligand synthesis*

Single crystals of the phenyl-terpyridine ligand were grown from slow evaporation of THF, the structure was consistent with that already reported in the literature.[108]

4.2.2 Complex Synthesis.

The metalation step for each of the pincer ligands is identical and is detailed in Scheme 4.2 and 4.3 for the BF_4^- and tosylate counter ions, respectively. This procedure has been adapted from the literature.[43]

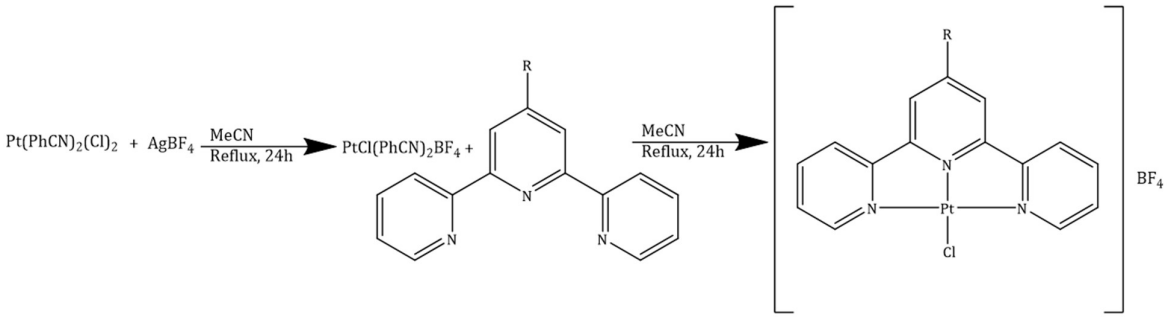

Scheme 4.2*: Platinum complex synthesis, counter-ion BF_4*

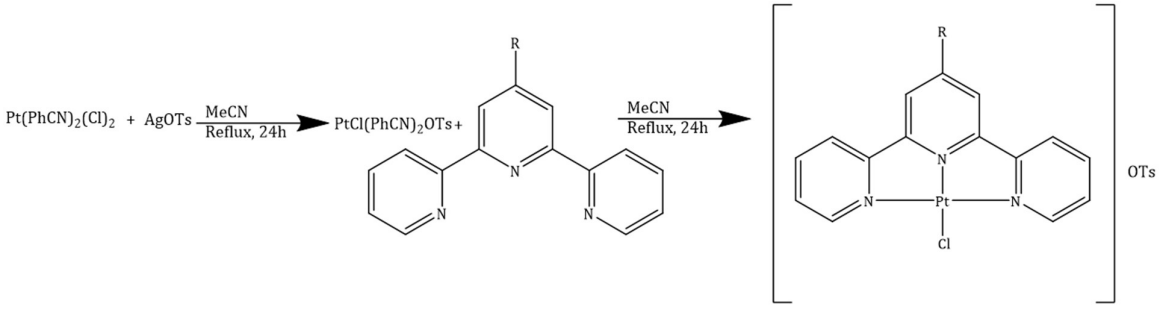

Scheme 4.3*: Platinum complex synthesis, counter-ion OTs*

4.2.3 Counter-Ion Exchange.

The first premise for this reaction to occur successfully is that the counter-ion being exchanged needs to be smaller than the new counter-ion, hence why the BF_4^- salts are the starting material. To exchange the counter-ion, the BF_4^- salt is fully dissolved in a mixture of water and acetonitrile before the sodium salt of the new counter-ion is added in a stoichiometric amount. The new complex then precipitates out of solution and is isolated by filtration. This process is shown in Scheme 4.4.

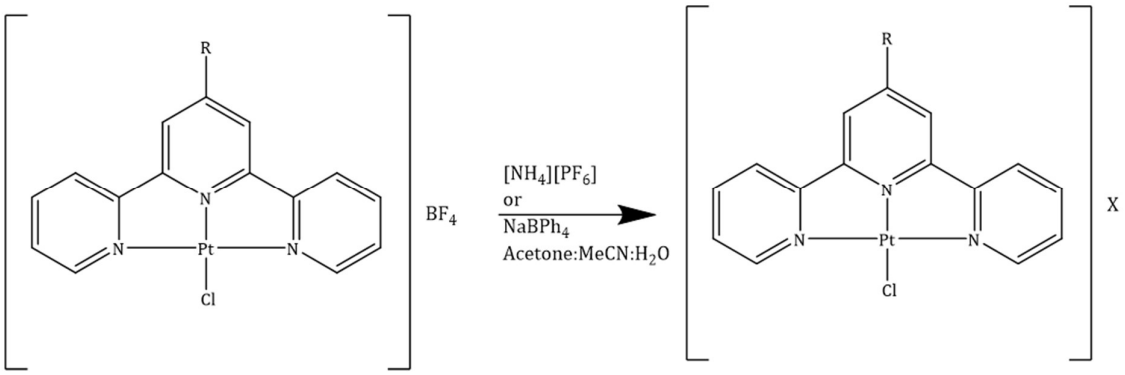

Scheme 4.4*: Counter-ion exchange reaction for the PF_6^- and BPh_4^- salts.*

4.3.0 2,2':6',2''-Terpyridine Platinum Chloride Tetrafluoroborate. (1) Acetonitrile Solvate

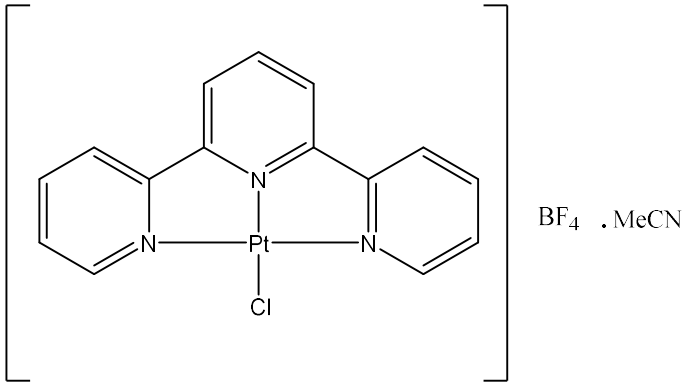

Complex **1** was isolated as a bright red solid**,** and characterised with IR spectroscopy; a peak at 1030 cm^{-1} confirmed the presence of the BF_4^- counter-ion. ^1H NMR spectroscopy and single crystal X-ray diffraction confirmed the structure of the complex. The complex has been reported previously but the analysis was carried out for completeness to allow a direct comparison with the new complexes prepared and reported in this chapter.[43]

4.3.1 Solution State Spectroscopy

Solution state UV-Vis absorption and emission spectroscopy was carried out for this complex. Figure 4.9 shows the measured spectra.

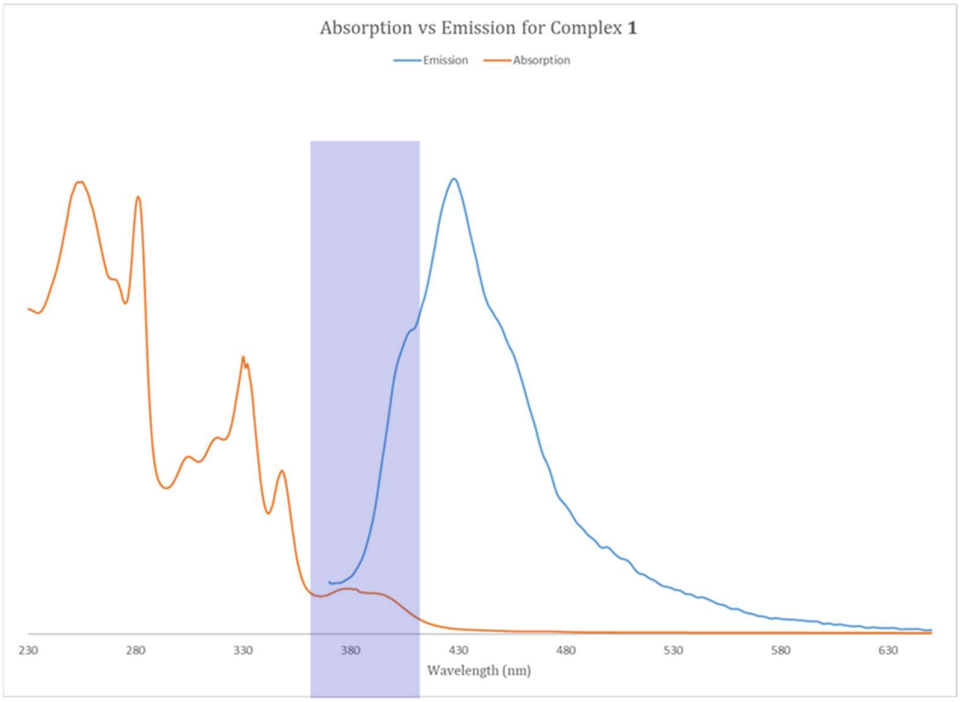

Figure 4.9*: Absorption spectrum of complex **1**, orange line. Emission spectra for complex **1**, blue line, λ_{ex}=340 nm. Solution concentration 1×10^{-4} M in acetonitrile.*

The absorption spectrum was measured in an acetonitrile solution, once the complex had been dissolved into acetonitrile a yellow solution formed. This is to be expected in the solution state because any stacking in the solid state would be disrupted and therefore a loss of the bright red colour occurs. The assignment of the spectra is as follows, the pair of maxima located between 300-350 nm can be assigned to π-π* transitions of the co-ordinated terpyridine ligand. The bands located at a higher wavelength than 350 nm, highlighted on Figure 4.9, can be assigned as a metal to ligand charge transfer (MLCT) band, which is in agreement with data presented in the literature.[109] McMillin *et al* assigned this band as a MLCT because they are too intense to be forbidden d-d transitions but too low in energy to be π-π* transitions.

The emission and UV-Vis spectra should have similar profiles with the emission resident at higher wavelengths, a result of the Franck-Condon principle as explained in Section 1.2.2. The emission profile for complex **1** does not have the same fine structure as the absorption spectra, shown in Figure 4.7.The main maximum peak can be seen in the emission, the Stokes shift (Section 1.2.2) between the maxima in the absorption spectrum is 174 nm and this high number is suggestive that the process of phosphorescence is occurring for this complex.

The emission spectra were recorded in a degassed solution, to avoid any detrimental effects on the luminescence caused by the presence of water or air, regardless, the emission of this complex in the solution state is still very weak. This is illustrated by Figure 4.10, which compares the difference in luminescence of this complex in the solution and solid state.

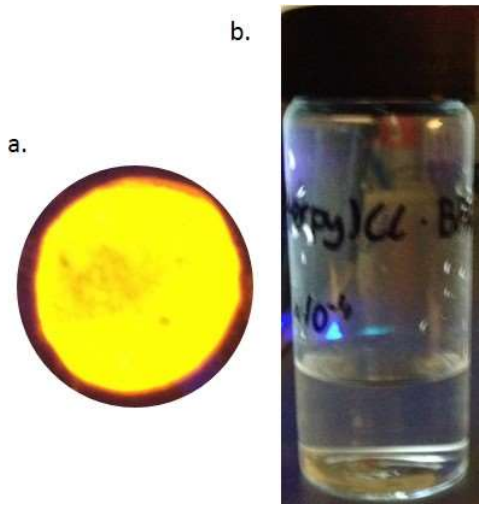

Figure 4.10*: Luminescence of complex **1** under UV lamp, Wavelength: 364 nm. a. Complex **1** in the solid state. b. Complex **1** in a 1×10^{-4} M degassed acetonitrile solution.*

The bright yellow luminescence observed in the solid state is replaced by weak green luminescence in the solution state. The red shift in emission seen from solution to solid state could be caused by the close Pt…Pt interactions observed in the solid state, as explained in Section 4.3.1. The luminescent properties of these complexes are important due to potential applications in the OLED industry (Section 1.6.0.).

4.3.2 Vapo/Solvachromic Behaviour

Complex **1** is the acetonitrile solvate of this complex and was found not to have any Vapo/Solvachromic properties when exposed to a variety of stimuli. The common laboratory solvents were tested such as chlorinated solvents, acetone, water and alcohols and no vapochromic response was observed. In addition, the complex was crushed under UV-light to test whether a change in emission would be observed with the application of pressure but no mechanochromic response was observed.

4.3.3 Crystal Structure Analysis

Crystal Structure.

Bright red-orange crystals of the complex were grown from the slow evaporation of acetonitrile solution. The complex salt crystallised in the monoclinic space group $P2_1/c$, with one molecule of acetonitrile per complex. Structure and data is consistent with previous reports in the literature.

Crystal Packing: Stacking and Pt Offset.

The strong luminescence that this complex displays in the solid state is suggestive of stacking in the solid state. Investigation of the packing of the unit cell, showed clear stacks formed through intermolecular Pt…Pt interactions, Figure 4.11.

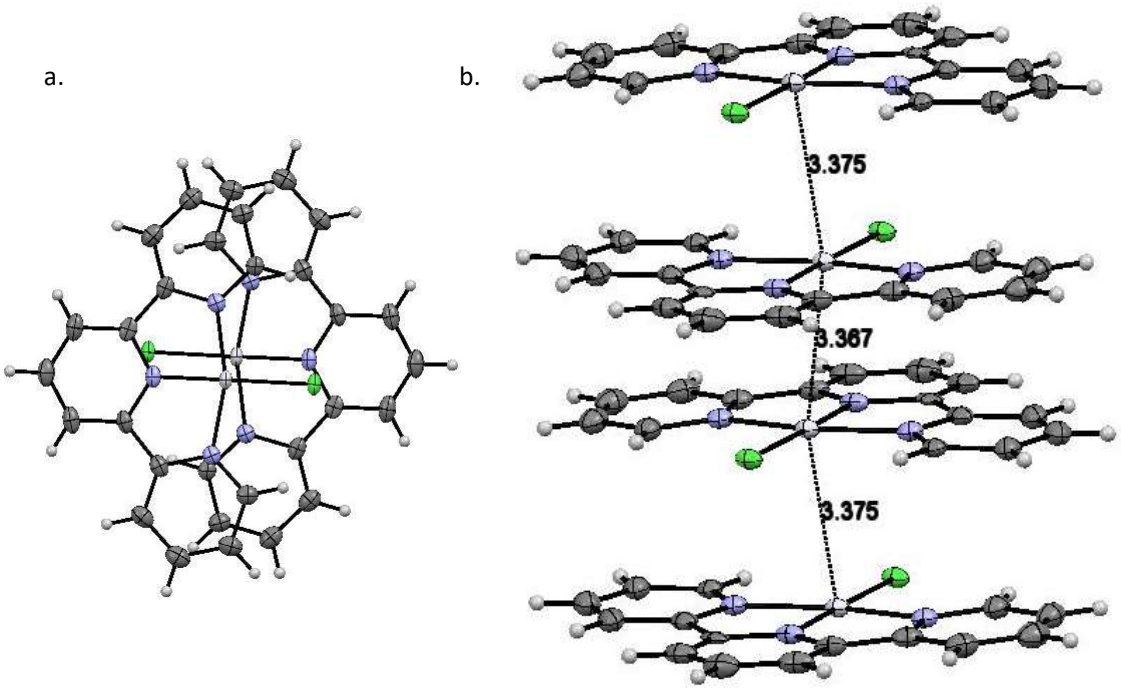

Figure 4.11*: a. Complex **1** viewed along the a axis. b. stacking of complex **1** in the solid state, ellipsoids shown at 50% probability. Counter-ions and solvents removed for clarity.*

The molecules are arranged head to tail in the structure, with channels of solvent and counter-ions separating each stack. Figure 4.11b shows the alternating distances between platinum centres of 3.3751(6) and 3.3665(6) Å, there is however a slight misalignment between the pairs of platinum centres. The distances fall in the range of 3.0-3.5 Å, which is the required distance for

a dz^2 interactions to occur. This accounts for the bright red-orange colour and strong luminescence this complex exhibits in the solid state.

For complex **1** the offset distance between the two centres was calculated as 0.84 Å, with a Pt-Pt-Pt angle of 157°. These measurements indicate that the stacks in complex **1** are not linear, as clearly shown in Figure 411a. In this instance complex **1** still shows strong luminescence in the solid state, so the effect of the loss of linearity in the stacking is minimal.

4.3.4 X –Ray Powder Analysis

Complex **1**, has several different solvates and it is important to determine that the bulk powder is the same the single crystal sample. A powder analysis was carried out on a new sample, Figure 4.12. The top trace (red) in Figure 4.12 is the predicted powder generated from the crystal structure and the bottom trace (black) is the experimental powder.

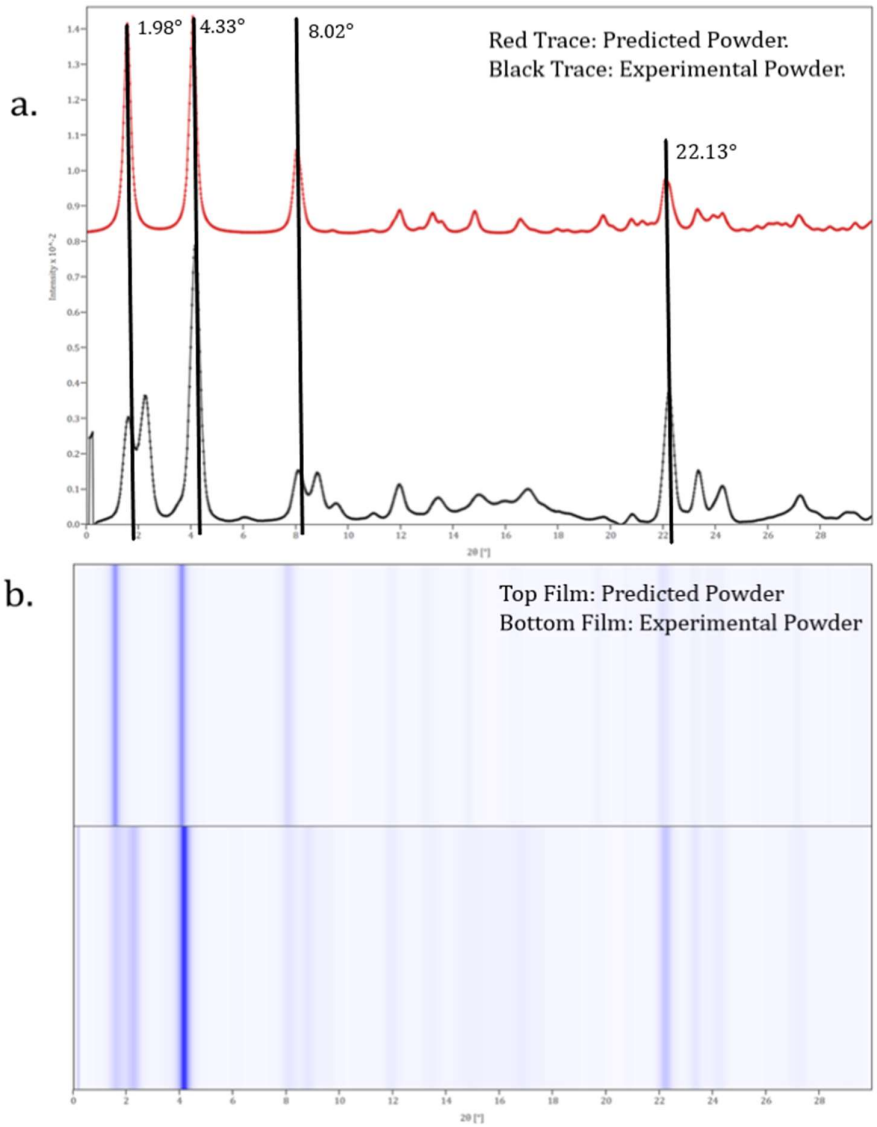

Figure 4.12*: a. Complex **1** powder plot. b. Film representation of powder of Complex **1**. Top trace is the predicted powder generated from crystal structure and bottom trace is the experimental powder.*

The trace for the predicted powder and experimental powder do not match exactly, this is suggestive that in the bulk there is a mixture of solvates present. The acetonitrile that was used during the recrystallization process had not been dried, this means some of the water solvate could have formed in addition to the acetonitrile solvate.

4.3.5 Reflectance Spectroscopy

The solid-state properties of the compounds need to be studied to fully understand there potential applications. Due to equipment restraints solid-state emission spectra could not be obtained for this complex, however the reflectance spectrum could be measured and is shown in Figure 4.13.

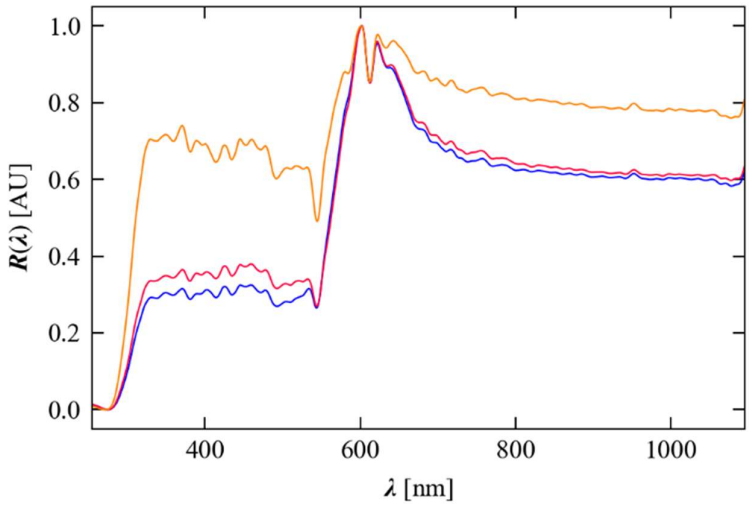

Figure 4.13*: Reflectance spectra of complex **1**.*

Three profiles have been recorded for complex **1** and they show good agreement. The edge of the spectra lies at 600 nm, which is what would be expected for a bright red complex. While the powder trace suggests that the spectroscopy does not match the single crystal data, the colour between the acetonitrile and water solvate is undetectable by eye. The split at approximately 600 nm could be attributed to the difference in solvates.

4.4.0 2,2':6',2''-Terpyridine Platinum Chloride Tetrafluoroborate. (2) Water/Acetone Solvate

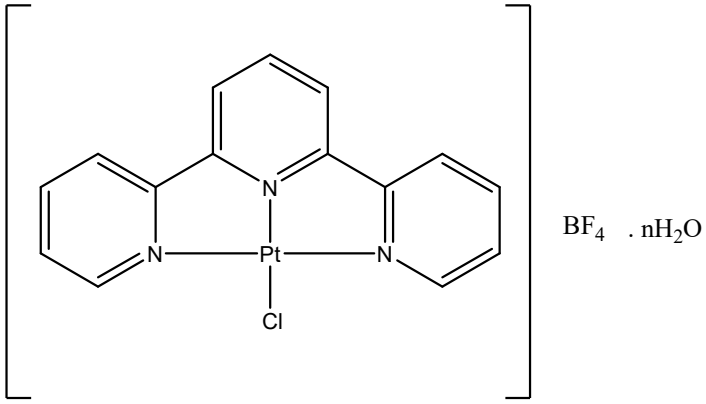

Complex **2** is the water solvate of 2,2':6',2''-terpyridine platinum chloride tetrafluoroborate. In this case the complex has been precipitated from a mixture of water and acetone. Upon recrystallization of the compound, three distinct forms of complex **2** were observed, Figure 4.14.

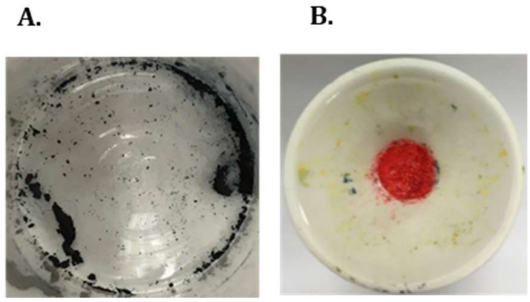

Figure 4.14*: Blue form of complex **2**. a. In the conical flask, b. In the filter with red and yellow form.*

NMR and IR spectroscopic data for this solvate is the same as for complex **1**. This is to be expected as the solvate will not change the solution state spectroscopy. The solution state spectroscopy is consistent with the literature.[43] The three solid-state forms have been characterised using single crystal crystallography.

4.4.1 Solution State Spectroscopy

When the complex is dissolved in a solution of water and acetone, the solution is yellow in colour as observed with complex **1**. The solution state UV-Vis was comparable to that detailed for complex **1** and the literature.[43]

4.4.2 Vapo/Solvachromic Behaviour

The observation of three distinct forms of this complex is suggestive of vapochromic behaviour. A film of the complex was made by depositing a slurry of the complex onto a glass slide, the solvents used were water and acetone in a 1:1 mixture. The solvent was then allowed to evaporate, leaving the thin film. The film deposited on the slide is red in colour and upon exposure to a source of dry argon, turned yellow. This transition is reversible, when the dry argon source is removed the complex returns to its red colour. This transition occurs on the sub-second timescale. The transition is shown in Figure 4.15.

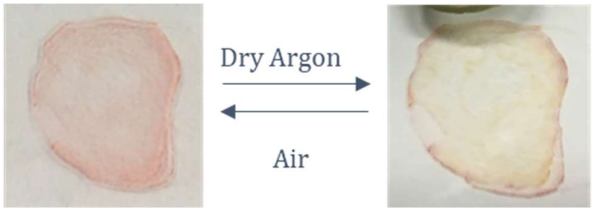

Figure 4.15*: Vapochromic behaviour of complex **2**.*

In addition to inert gas, vapours of various solvents were tested but no further transitions were observed. During testing of the blue form collected from the recrystallization, it turned yellow in the presence of inert gas, but the reverse transition formed the red form of complex **2**. To determine the conditions the blue form of complex **2** forms under, a crystallisation study was initiated, where the ratio of water: acetone was systematically varied and the vials were left to slowly evaporate. Table 4.1 summarises the results from this crystallisation study.

Table 4.1*: The preferred solvent conditions for the growth of the different forms of complex **2**.*

Water: Acetone ratio	**Form**
10:0	Did not dissolve
9:1	Blue
8:2	Blue
7:3	Blue
6:4	Blue
5:5	Blue
4:6	Red
3:7	Red
2:8	Red
1:9	Red
0:10	Yellow

The change in colour of crystals is shown in Figure 4.16.

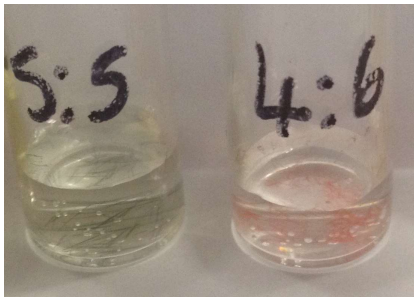

Figure 4.16*: Blue crystals formed in 1:1 mixture of water to acetone and red crystals formed in a 4:6 mixture of water to acetone.*

The blue form of complex **2** only formed under conditions where high water concentrations were present. The requirement for high concentration of water suggests that the red form is the more stable under ambient conditions, which is why a reversible transition between yellow and blue was not observed.

4.4.3 Crystal Structure Analysis

Crystal Structure: Red Form.

Red/ orange crystals of complex **2** was grown from slow evaporation of a water/ acetone mixture. The salt crystallises in the monoclinic space group $P2_1/c$, with one cation and one anion making up complex **2** and one molecule of water in the asymmetric unit. The structure is shown in Figure 4.17 and data provided in Table 4.2.

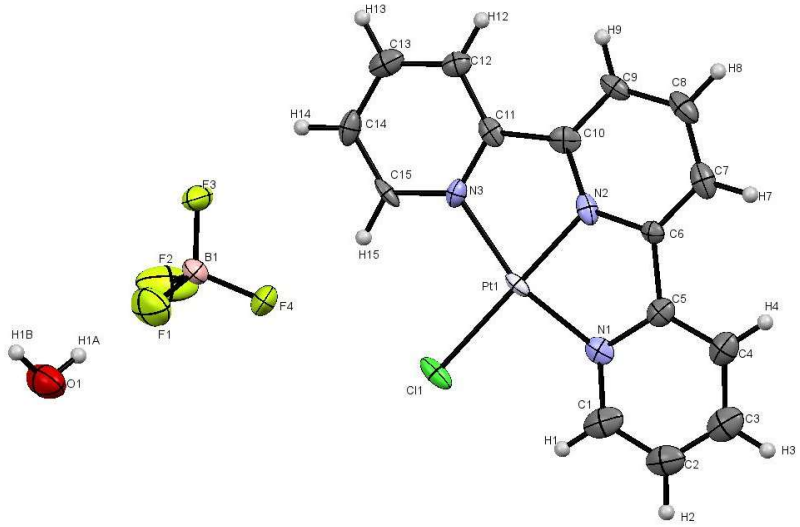

Figure 4.17*: Crystal structure of complex* ***2****, ellipsoids shown at 50% probability.*

Table 4.2: *Crystal data and structure refinement for complex **2***

Identification code	Bath 2509
Empirical formula	$C_{15}H_{15}BN_3OF_4ClPt$
Formula weight	570.65
Temperature/K	100
Crystal system	monoclinic
Space group	$P2_1/c$
a/ Å	6.5614(4)
b/ Å	10.4583(7)
c/ Å	24.4190(17)
α/°	90
β/°	97.026(3)
γ/°	90
Volume/ Å^3	1663.08(19)
Z	4
ρ_{calc}g/cm^3	2.279
μ/mm^{-1}	10.743
F(000)	1080.0
Crystal size/mm^3	0.8 × 0.05 × 0.03
Radiation	Synchrotron (λ = 0.7749 Å)
2Θ range for data collection/°	4.624 to 57.93
Index ranges	-8 ≤ h ≤ 8, -13 ≤ k ≤ 13, -30 ≤ l ≤ 30
Reflections collected	22244
Independent reflections	3390 [R_{int} = 0.0573, R_{sigma} = 0.0318]
Data/restraints/parameters	3390/0/239
Goodness-of-fit on F^2	1.394
Final R indexes [I>=2σ (I)]	R_1 = 0.0433, wR_2 = 0.0841
Final R indexes [all data]	R_1 = 0.0502, wR_2 = 0.0857
Largest diff. peak/hole / e Å^{-3}	2.44/-2.44

In complex **2** the cation has a distorted square planar geometry around the Pt centre with the N1-Pt1-N3 angle measuring 162.3(3)˚. This distortion from the expected angle of 180˚ can be attributed to the bite angle of the pincer and is consistent with similar complexes in the literature.[98] The rest of the bond lengths and angles provided in Table 4.3 are consistent with similar complexes.

The terpyridine ligand used in complex **2** is unsubstituted and because of this the complex in planar in the solid state. The torsion angles in Table 4.3c are close to linearity and the dihedral angle is negligible. Complex **2** is therefore planar in the solid state, this will help to facilitate any interactions between adjacent Pt centres.

Table 4.3: *a. Table of bond lengths for **2**, red form. b. Table of bond angles for **2**, red form. c. Torsion angles for **2**, red form.*

a. Bond Lengths		
Atom	**Atom**	**Length/ Å**
Pt1	Cl1	2.3007(17)
Pt1	N3	2.043(7)
Pt1	N2	1.961(6)
Pt1	N1	1.994(7)
F1	B1	1.377(11)

b. Bond Angles			
Atom	**Atom**	**Atom**	**Angle/°**
N3	Pt1	Cl1	100.34(19)
N2	Pt1	Cl1	179.9(3)
N2	Pt1	N3	79.6(3)
N2	Pt1	N1	82.7(3)
N1	Pt1	Cl1	97.4(2)
N1	Pt1	N3	162.3(3)

c. Torsion Angles				
A	**B**	**C**	**D**	**Angle/°**
Pt1	N3	C11	C10	0.7(8)
Pt1	N3	C11	C12	179.0(6)
Pt1	N3	C15	C14	-179.3(5)
Pt1	N2	C6	C5	-0.4(8)

The planarity of the complex in the solid state means that there is an increased chance for the complex to form π-π interactions and hydrogen bonds. The data for these interactions is provided in Table 4.4. The π-π interactions form between plane 1 and 3, this are the pyridyl rings on adjacent molecules. Figure 4.18a shows that the molecules stack in an alternating fashion, therefore Plane 1 and 3 are closest in the solid-state structure.

In complex **2** hydrogen bonds form between the pyridyl rings and the solvent, this helps stabilise the structure in the solid state, as it is the red form, which is the form that presides in the solid state. In addition, hydrogen bonds form to the chloride group in the 4th co-ordination site of the Pt centre. This interaction forms in the layers not between the different layers. It is possible that this interaction dictates the structure in the individual layers.

Table 4.4: *a. Planes Present in solid state structure, complex **2**, red form. b. π-π Interactions in complex **2**, red form. c. Hydrogen bonds in complex **2**, red form.*

a. Plane Identification	
Plane Number	Atoms in plane
1	N1 C5 C4 C3 C2 C1
2	N2 C6 C7 C8 C9 C10
3	N3 C15 C14 C13 C12 C11

b. π-π Interactions	
Planes	Distance (Å)
1-3[1]	3.673
1-3[2]	3.683

c. Hydrogen bonds			
Atoms	(D…A) Distance (Å)	(H…A) Distance (Å)	D…H…A Angle/°
C1-H1-O1	3.26(2)	2.46	141.9
C8-H8-Cl1	3.532(8)	2.586	174.1

Where [1](1-X,1-Y,1-Z) and [2](2-X,1-Y,1-Z)

Crystal Packing: Stacking and Pt Offset, Red Form.
This vapochromic behaviour is indicative of stacking in the solid state. The unit cells and space groups for complexes **1** and **2** are very similar. The differences between the solvates are subtle and a detailed analysis of the solid-state packing is required to understand why only complex **2** shows vapochromic behaviour.

Figure 4.18b shows the Pt…Pt stacking in the red form of complex **2**. Comparison with complex **1** shows a very similar stacking motif for this complex. The molecules pack head to tail as with complex **1**, with alternating distances between the platinum atoms but in the case of complex **2** the platinum distances are shorter; they are measured at 3.3189(5) and 3.3412(4) Å. Once again as with complex **1**, the platinum atoms are not fully aligned and there are two distinct positions in the crystal structure as shown in Figure 4.18. The offset distance was calculated at 0.47 Å, this is much less than the observed distance for complex **1** and will enhance the dz^2 overlap.

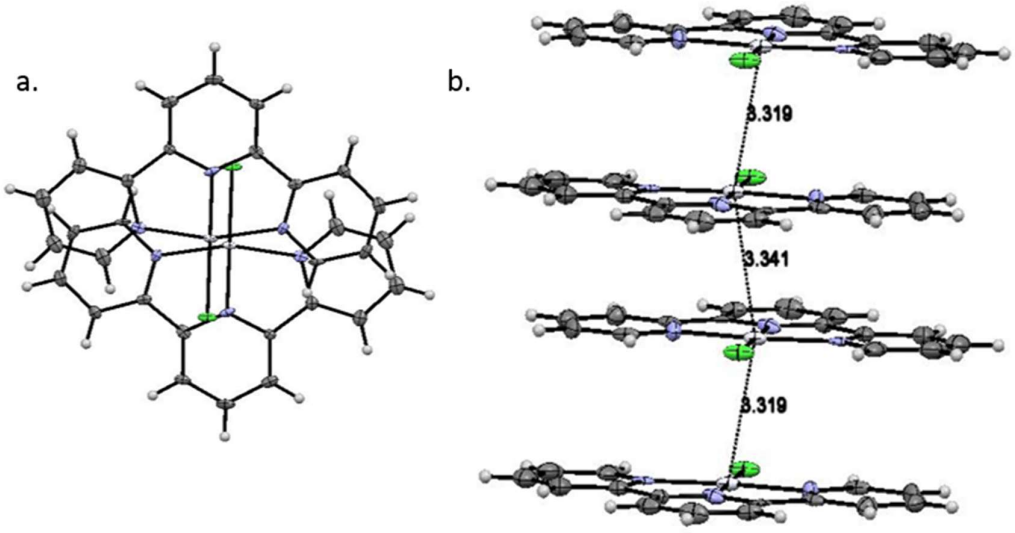

Figure 4.18*: a. View of complex **2**, red form, along the 'a' axis at 100 K. b. Stacking in complex **2**, red form, at 100 K. Ellipsoids shown at 50% probability. The counter-ion and solvent has been removed for clarity.*

The difference in stacking distance can be attributed to the location of solvent in the structure. In the case of complex **1** the acetonitrile sits close to the pincer ligand; this allows the nitrogen of the acetonitrile to form a hydrogen bond to the hydrogen on the pincer ligand. Whereas for complex **2** the water forms a halogen bond to the fluorine on the BF_4^- counter-ion and does not sit close enough to the pincer to form any hydrogen bonds. The removal of solvent from the immediate area of the pincer ligand has allowed the Pt…Pt distances to decrease and complex **2** to form closer stacks.

Crystal Structure: High Temperature Red Form.
Attempts were made to grow crystals of the yellow form, so this could be studied using single crystal X-ray diffraction. Unfortunately, no crystals of this form could be grown and each attempt yielded a yellow powder. In addition, single crystals of the red hydrate form were placed under a dry argon atmosphere to induce the transition but the crystals did not survive the transition and no structure could be obtained.

In 2013 Connick *et al* studied a related complex crystallographically by heating the crystal while mounted on the diffractometer to induce a transition.[63] It was thought that a similar method could be used for complex **2**, because the hypothesis was that the transition from red to yellow was loss of water from the structure. Dehydrating the structure should simulate the transition observed when the complex is placed under an atmosphere of inert gas. The dehydration of complex **2** was studied crystallographically, increasing the temperature from 100 K to 450 K in 50 K increments. The last conclusive structure was obtained from the 350 K data set, after which the crystal degraded and turned yellow, no structure could be extracted from the final data sets. The structure for the high temperature form of complex **2** is provided in Figure 4.19 and Table 4.5.

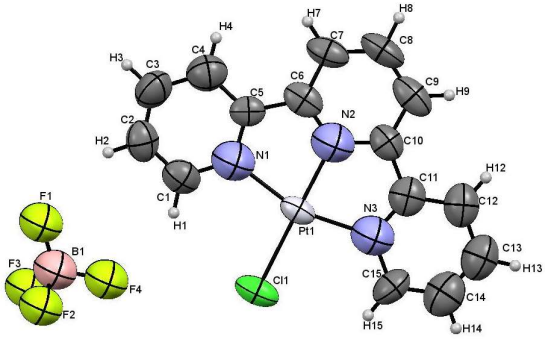

Figure 4.19*: Crystal structure of complex **2** at 350 K, ellipsoids shown at 50% probability.*

Table 4.5: *Crystal data and structure refinement for complex **2** at 350 K.*

Identification code	Bath 2516
Empirical formula	$C_{15}H_{15}BN_3F_4ClPt$
Formula weight	570.65
Temperature/K	350
Crystal system	monoclinic
Space group	$P2_1/c$
a/ Å	6.7473(3)
b/ Å	10.4659(4)
c/ Å	24.3484(12)
α/°	90
β/°	95.996(2)
γ/°	90
Volume/ Å^3	1709.98(15)
Z	4
ρ_{calc}g/cm^3	2.217
μ/mm^{-1}	10.448
F(000)	1080.0
Crystal size/mm^3	0.8 × 0.05 × 0.03
Radiation	Synchrotron (λ = 0.7749 Å)
2Θ range for data collection/°	4.622 to 57.922
Index ranges	$-30 \leq h \leq 30$, $-13 \leq k \leq 13$, $-30 \leq l \leq 30$
Reflections collected	23076
Independent reflections	3494 [R_{int} = 0.0426, R_{sigma} = 0.0283]
Data/restraints/parameters	3494/216/184
Goodness-of-fit on F^2	1.196
Final R indexes [I>=2σ (I)]	R_1 = 0.0701, wR_2 = 0.1812
Final R indexes [all data]	R_1 = 0.0910, wR_2 = 0.1907
Largest diff. peak/hole / e Å^{-3}	2.93/-2.14

The high temperature form of complex **2** has retained its square planar geometry around the Pt centre with same N1-Pt1-N3 angle distortion, which can be attributed to the bite angle of the pincer ligand. The rest of the bond lengths and angles provided in table 4.6a/b were consistent with similar complexes.

A select number of torsion angles have been provided in Table 4.6c to show that the complex retains its planarity at 350 K. The measured dihedral angles for this complex were negligible.

Table 4.6: *a. Table of bond lengths for **2**@350 K. b. Table of bond angles for **2**@350 K. c. Torsion angles for **2**@350 K.*

a. Bond Lengths		
Atom	**Atom**	**Length/ Å**
Pt1	Cl1	2.297(4)
Pt1	N2	1.94(2)
Pt1	N3	2.01(2)
Pt1	N1	2.07(2)
F1	B1	1.28(4)

b. Bond Angles			
Atom	**Atom**	**Atom**	**Angle/°**
N2	Pt1	Cl1	179.4(7)
N2	Pt1	N1	79.8(9)
N3	Pt1	Cl1	98.1(7)
N3	Pt1	N1	161.1(10)
F1	B1	F2	109(3)

c. Torsion Angles				
A	**B**	**C**	**D**	**Angle/°**
Pt1	N2	C6	C7	179.2(13)
Pt1	N2	C10	C11	0(2)

As observed with complex **2** at 150 K, the high temperature form forms π-π interactions between the pyridyl rings in adjacent molecules. However, in the high temperature form the distance between the molecules has increased. This could be attributed to the loss of solvent from the solid-state structure.

This complex has maintained one of the hydrogen bonds that was observed in the structure at 150 K. This is the interaction between the chloride group and the back of the next pincer. However, the hydrogen bond between the water solvent and the complex is no longer found due to the dehydration of the crystal. The angle of the remaining hydrogen bond has shifted slightly from planarity and the distance between the 2 molecules has shifted. This can be attributed to the loss of solvent from the structure and the subsequent changes in the observed solid-state structure.

Table 4.7: *a. Planes Present in solid state structure of **2**, red form @ 350 K. b. π-π Interactions of **2**, red form @ 350 K. c. Hydrogen bonds of **2**, red form @ 350 K.*

a. Plane Identification	
Plane Number	Atoms in plane
1	N1 C5 C4 C3 C2 C1
2	N2 C10 C9 C8 C7 C6
3	N3 C15 C14 C13 C12 C11

b. π-π Interactions	
Planes	Distance (Å)
1-3[1]	3.814
1-3[2]	3.767

c. Hydrogen bonds			
Atoms	(D…A) Distance (Å)	(H…A) Distance (Å)	D…H…A Angle/°
C8-H8-Cl1	3.59(2)	2.669	169

Where [1](-X,1-Y,-1-Z) and [2](1-X,1-Y,-Z)

Crystal Packing: Stacking and Offset, High temperature Red Form.
The stacking and alignment of the red form of complex **2** at 350 K is shown in Figure 4.20.

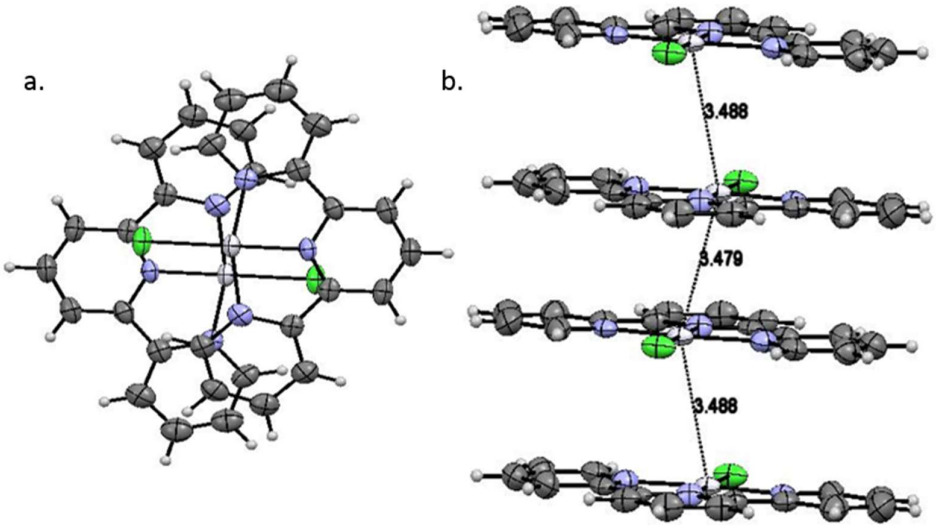

Figure 4.20*: a. View of complex **2** along the 'a' axis at 350 K. b. Stacking in complex **2** at 350 K. Ellipsoids shown at 50% probability. The counter-ion has been removed for clarity.*

In this structure the complex has lost the water present in the red form of the complex and as hypothesised completely dehydrated. As expected, the distances have lengthened and are now at the top end of the required range for Pt overlap, this coupled with an offset distance of 0.90 Å, explains why this complex is yellow when the water is removed from the crystal structure.

Crystal Structure: Blue Form.
Crystals of the blue form were obtained by slow evaporation of a water/acetone mix in the ratio 6:4. This form of complex **2** crystallises in the orthorhombic space group *P*bcm. The Pt(II) pincer cation sits on a crystallographic mirror plane in the structure and is rigorously planar as a result. The BF_4^- anion also lies across a crystallographic mirror plane with B1 and F1 sitting on the mirror plane and F2 and F3 being reflected across it. The water molecules sit in general positions. Thus, the asymmetric unit of the crystal structure contains half a cation, half an anion and one independent water molecule. The crystal structure is shown in Figure 4.21, with crystal and refinement data given in Table 4.8.

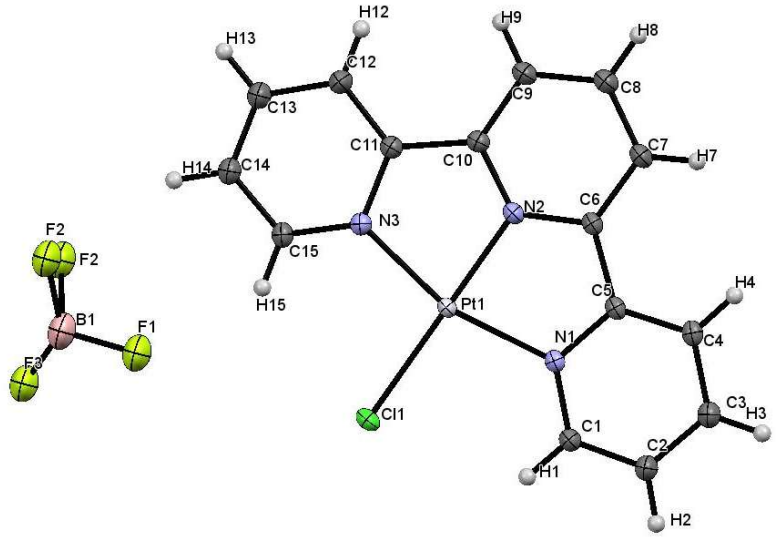

Figure 4.21*: Crystal structure of complex **2**, blue form, ellipsoids shown at 50% probability. Water molecules removed for clarity.*

Table 4.8*: Crystal data and structure refinement for complex **2**, blue form.*

Identification code	Bath 2505
Empirical formula	$C_{15}H_{15}BN_4O_2F_4PtCl$
Formula weight	568.75
Temperature/K	100
Crystal system	orthorhombic
Space group	*P*bcm
a/ Å	14.8682(8)
b/ Å	17.1639(10)
c/ Å	6.5464(4)
α/°	90
β/°	90
γ/°	90
Volume/ Å^3	1670.62(17)
Z	4
ρ_{calc}g/cm^3	2.2611
μ/mm^{-1}	7.588
F(000)	1037.0
Crystal size/mm^3	0.8 × 0.04 × 0.03
Radiation	synchrotron (λ = 1.1271 Å)
2Θ range for data collection/°	4.34 to 88.1
Index ranges	-17 ≤ h ≤ 18, -21 ≤ k ≤ 20, -7 ≤ l ≤ 8
Reflections collected	12800
Independent reflections	1763 [R_{int} = 0.0465, R_{sigma} = 0.0348]
Data/restraints/parameters	1763/0/150
Goodness-of-fit on F^2	1.079
Final R indexes [I>=2σ (I)]	R_1 = 0.0382, wR_2 = 0.0680
Final R indexes [all data]	R_1 = 0.0610, wR_2 = 0.0747
Largest diff. peak/hole / e Å^{-3}	2.04/-1.86

The blue form of complex **2** has retained the square planar geometry around the Pt centre with the same angular distortion observed for the other 2 forms, which can be attributed to the pincer bite angle.[62] The bond lengths and angles are consistent for complexes of this type.[43] The torsion angles in this complex are equal to 0 or 180˚, a selection have been provided in Table 4.9c. Consistent with the other 2 forms of this complex there is no appreciable dihedral angle, this complex is therefore planar in the solid state.

Table 4.9*: a. Table of bond lengths for complex **2**, blue form. b. Table of bond angles for complex **2**, blue form. c. Torsion angles for complex **2**, blue form.*

a. Bond Lengths		
Atom	**Atom**	**Length/ Å**
Cl1	Pt1	2.310(3)
N1	Pt1	2.040(10)
N2	Pt1	1.944(10)
N3	Pt1	2.020(11)
B1	F1	1.41(2)

b. Bond Angles			
Atom	**Atom**	**Atom**	**Angle/˚**
N1	Pt1	Cl1	99.4(3)
N2	Pt1	Cl1	179.7(3)
N2	Pt1	N1	80.9(4)
N3	Pt1	N1	162.1(4)
F1	B1	F2	106.4(13)

c. Torsion Angles				
A	**B**	**C**	**D**	**Angle/˚**
C7	C6	N2	Pt1	180.0
C7	C8	C9	C10	0.0
C8	C9	C10	C11	180.0
C8	C9	C10	N2	0.0

The interactions in the blue form of complex **2** differ from the other two forms previously studied in this thesis. There is only one π-π interaction present in the molecule, this forms between the pyridyl rings, but unlike the red form it is between the same pyridyl rings in the structure. This has occurred because the complex has stacked with full alignment in the solid state, Figure 4.22. In addition, the distance between the planes is shorter than previously observed, this is indicative of the change in observed colour from red to blue suggesting that the molecules are closer in the solid state.

Due to the difficulty in modelling the solvent in the structure, hydrogen bonding from the solvent to the complex could not be analysed. However, there was hydrogen-bonding present between the chloride group and the pincer of the adjacent molecule within the layers but not the stacks in the solid-state structure, data is provided in Table 4.10c.

Table 4.10: *a. Planes Present in solid-state structure of complex **2**, blue form. b. π-π Interactions of complex **2**, blue form. c. Hydrogen bonds of complex **2**, blue form.*

a. Plane Identification	
Plane Number	Atoms in plane
1	N1 C5 C4 C3 C2 C1
2	N2 C10 C9 C8 C7 C6
3	N3 C15 C14 C13 C12 C11

b. π-π Interactions	
Planes	Distance (Å)
3-3[1]	3.614

c. Hydrogen bonds			
Atoms	(D…A) Distance (Å)	(H…A) Distance (Å)	D…H…A Angle/°
C3-H3-C11	3.52	2.931	121.7
C4-H4-Cl1	3.46	2.789	128.4

Where [1](+X, 3/2-Y, 1-Z)

Crystal Packing: Stacking and Pt Offset, Blue Form.

The blue colour of this form would suggest that the distances between the Pt centres in the Pt…Pt stacks are closer together and more linearly aligned in comparison to form I. Figure 4.22 shows the alignment and stacking for this form.

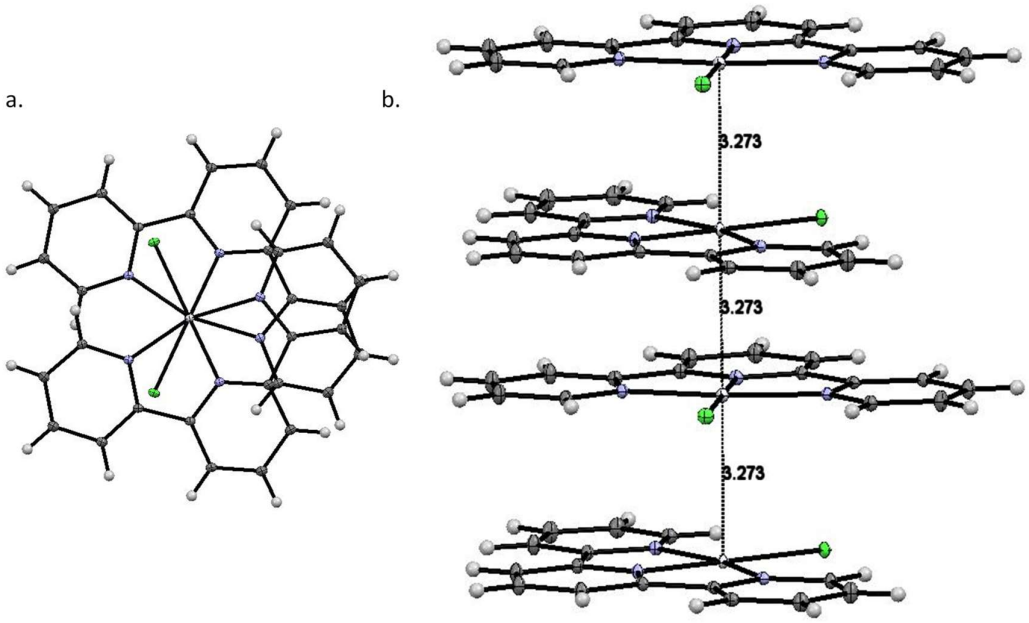

Figure 4.22: *a. View of the blue form of complex **2**, along the c axis. b. Stacking in the blue form of complex **2**. Ellipsoids shown at 50% probability. Solvent removed for clarity.*

The blue form of complex **2** has the shortest Pt…Pt distance of 3.2734(0) Å, in addition the platinum centres are perfectly aligned due to the crystal symmetry of the unit cell. This is shown by the measured value of 0.0 Å for the Pt offset value and the near linear Pt-Pt-Pt angle. This

analysis is in agreement with the literature (Section 1.5.3), which states that better dz^2 overlap and shorter Pt…Pt distance red shifts the absorption. This is why the observed colour for this solvent polymorph is blue.

On comparison of the blue and red form of complex **2**, it is observed that the main difference in the crystal structure of these two complexes is the placement of the solvent. In the red form there is only one molecule of water per complex, but in the blue form this is now two. The increased water content of blue form relative to the red form, explains why the blue form is only formed in solutions with high water content. Analysis of the short contacts in the red and blue form reveal they are similar with the water molecules forming short contacts with two counter-ions and the hydrogen atoms on the pincer ligand. In addition to the amount, the placement of the water in the crystal structure varied slightly between the two forms, this is best shown by analysing the void space left when the water is removed from the crystal structure. Void space diagrams were generated using the program Mercury,[87] with the following parameters, probe radius 1.2 Å and approximate grid spacing 0.1 Å, the results are shown in Figure 4.23.

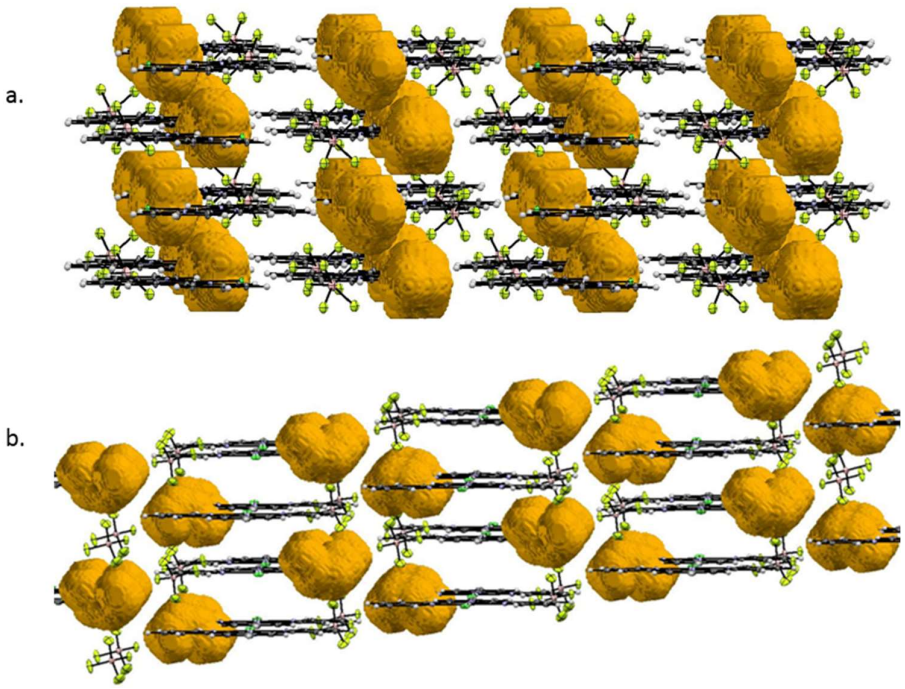

Figure 4.23*: a. Void space in the blue form of complex **2**. b. Void space in the red form of complex **2**. Ellipsoids shown at 50% probability.*

In each instance there are individual pockets of void space, but in Figure 4.21a, the blue form, the void spaces are in closer proximity to each other, therefore almost forming a channel. The void space for the red form, Figure 4.23b, is compact with larger distances between the voids.

It is also interesting to note that the position of the counter-ion relative to the void space changes between the two forms. Figure 4.23a shows that in the blue form the counter-ion sits adjacent to the water molecules, whereas Figure 4.23b shows an arrangement where the void and counter-ion alternates for the red form. This could account for the increased distance observed between the void space. All of these factors have a positive or negative impact on the stacking observed in these complexes. These factors were detailed in the literature review, Section 1.5.4.

4.4.4 X- Ray Powder Analysis

Due to having two solvates that have a very similar crystal habit and appearance but very different spectral properties the bulk powder needs to be investigated. Figure 4.12 showed that a mixture of solvates existed in the acetonitrile grown powder and the water grown powder was investigated in the same manner. The results are shown in Figure 4.24.

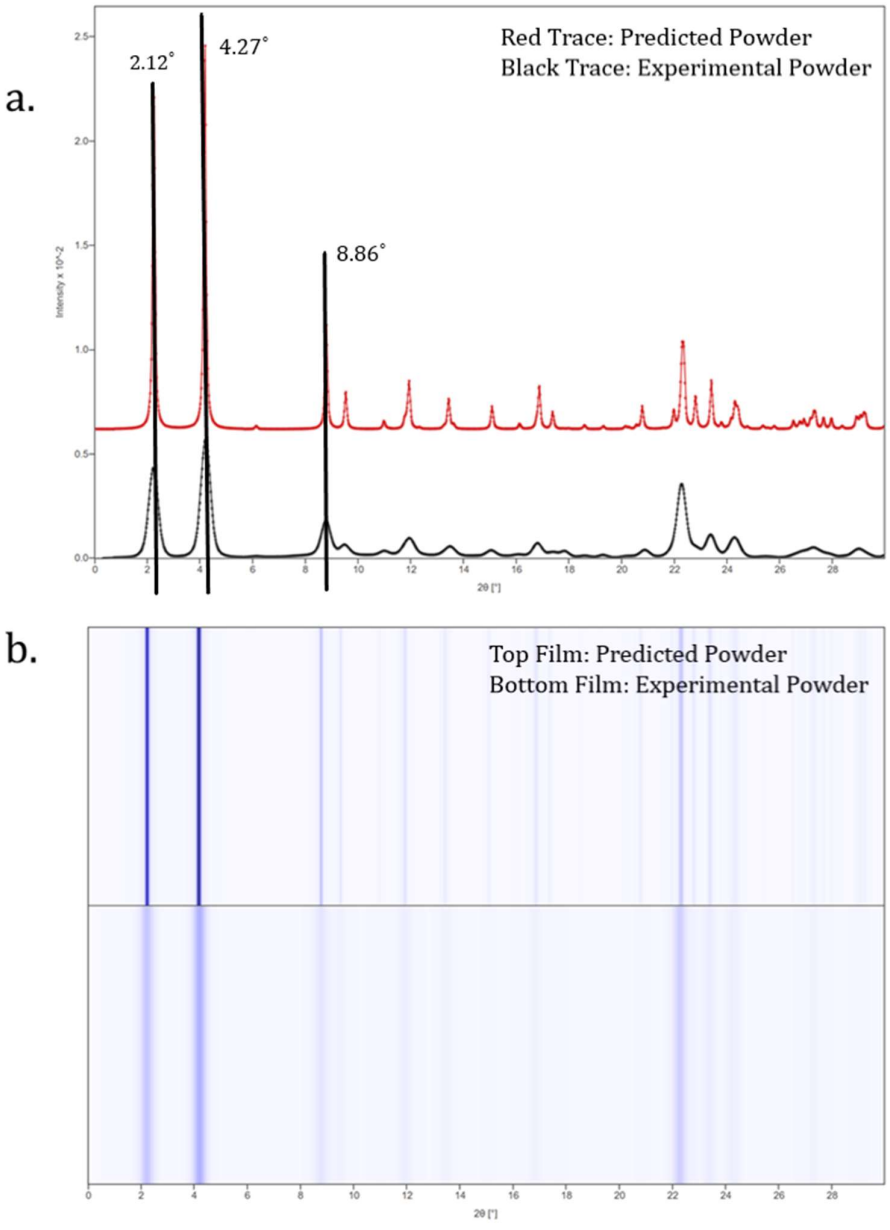

Figure 4.24*: a. Complex* ***2****, red form, powder plot. b. Film representation of powder of Complex* ***2****, red form. Top trace is the predicted powder (red) generated from crystal structure and bottom trace is the experimental powder (black).*

In this instance the experimental and predicted powder are in full agreement for the red form of complex **2**. This confirms that the bulk powder observed in the films is consistent with the observed crystal structure.

4.5.0 4'-phenyl-2,2':6',2''-Terpyridine Platinum Chloride Tetrafluoroborate. (3)

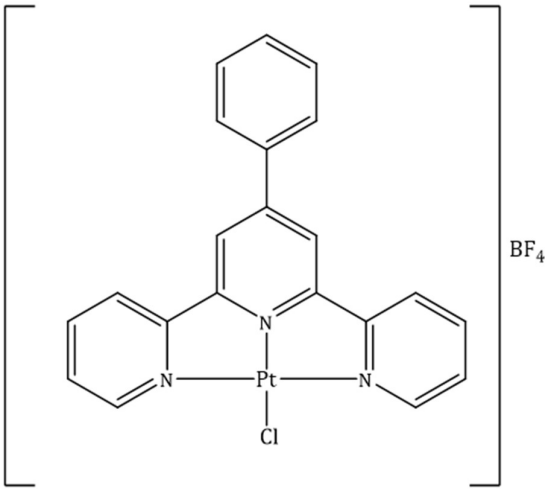

This complex was synthesised according to literature methods[43] with the ligand synthesised using the method described in Scheme 4.2.

Complex **3** has been fully characterised. In the IR spectrum, there was a peak present at 1028 cm^{-1}, which can be assigned to the B-F stretch of the counter-ion. ^{1}H NMR spectroscopy and single crystal X-ray diffraction confirmed the structure of the complex, which was consistent with the literature.[43]

4.5.1 Solution State Spectroscopy

The solution state UV-Vis and emission spectra are given in Figure 4.25.

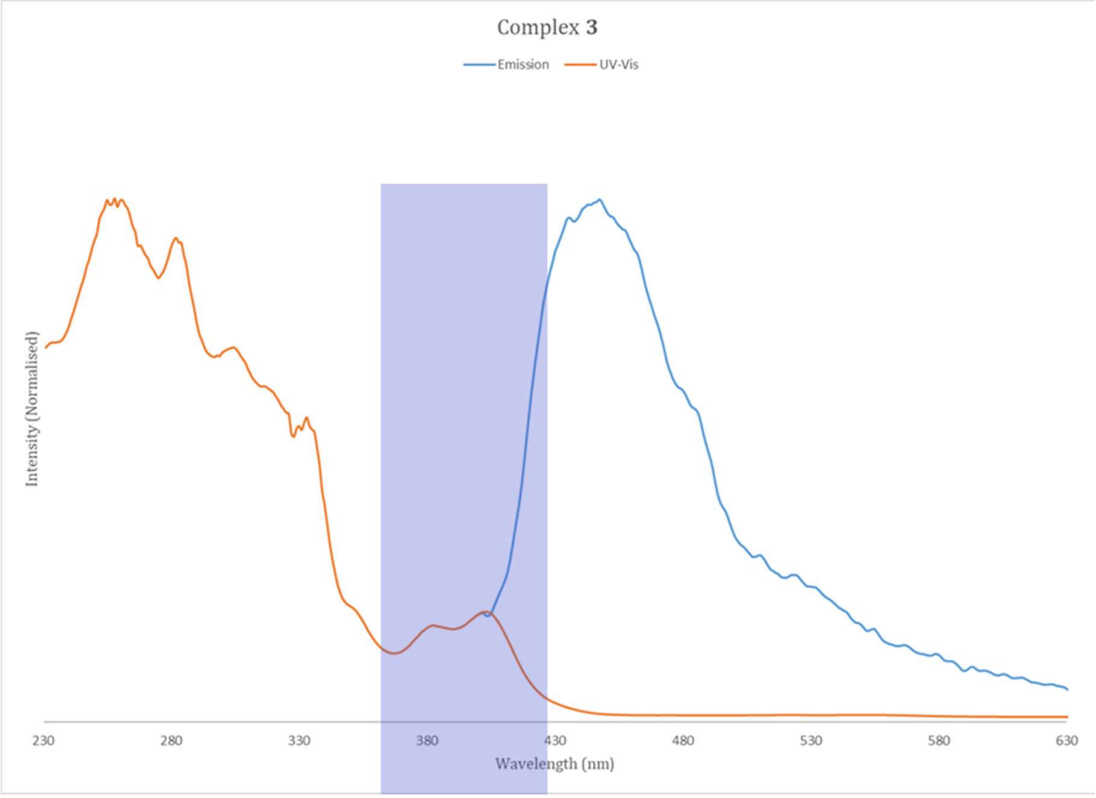

Figure 4.25*: Absorption spectrum of complex **3**, orange line, MLCT highlighted on diagram. Emission spectra for complex **3**, blue line, λ_{ex}= 340 nm. Solution concentration 1×10^{-4} M in acetonitrile.*

The UV-Vis spectrum in Figure 4.25 is not as clearly defined as that observed for complex **1.** The peak at 350 nm is only a shoulder for complex **3**. Even with this lack of definition in the spectra the peaks can be assigned to the same transitions as those for complex **1**, inclusive of the peaks at the wavelengths greater than 350 nm. This set of peaks, in the range 370-420 nm can be assigned as the MLCT state, highlighted on figure 4.25, as the intensity is too high for it to be classified as forbidden triplet states.

The emission for this complex is shifted slightly to a higher wavelength but has a similar profile to that observed for complex **1**. As observed with complex **1** the emission in the solution state was relatively weak.

4.5.2 Vapo/Solvachromic Behaviour

This complex or any of its solvates did not show any spectral changes when exposed to a variety of stimuli. The common laboratory solvents were tested such as chlorinated solvents, acetone, water and alcohols and no vapochromic response was observed. In addition, the complex was crushed under UV-light to test whether a change in emission would be observed with the application of pressure but no mechanochromic response was observed.

One reason for the lack of a vapochromic response can be hypothesised upon analysis of the crystal packing. The solvent in the crystal structure does not sit within channels in the structure,

instead it sits in pockets. This means that the movement of solvent in and out of the structure will either be much slower or will not occur at all.

4.5.3 Crystal Structure Analysis

The structure of complex **3** is shown in Figure 4.26, with structural and refinement data given in Table 4.11. Red crystals of this complex were grown from slow evaporation of acetonitrile. The complex crystallises in the triclinic space group P-1, with two molecules in the asymmetric unit cell, in addition to two molecules of acetonitrile solvent. This structure is in agreement with the literature.[43]

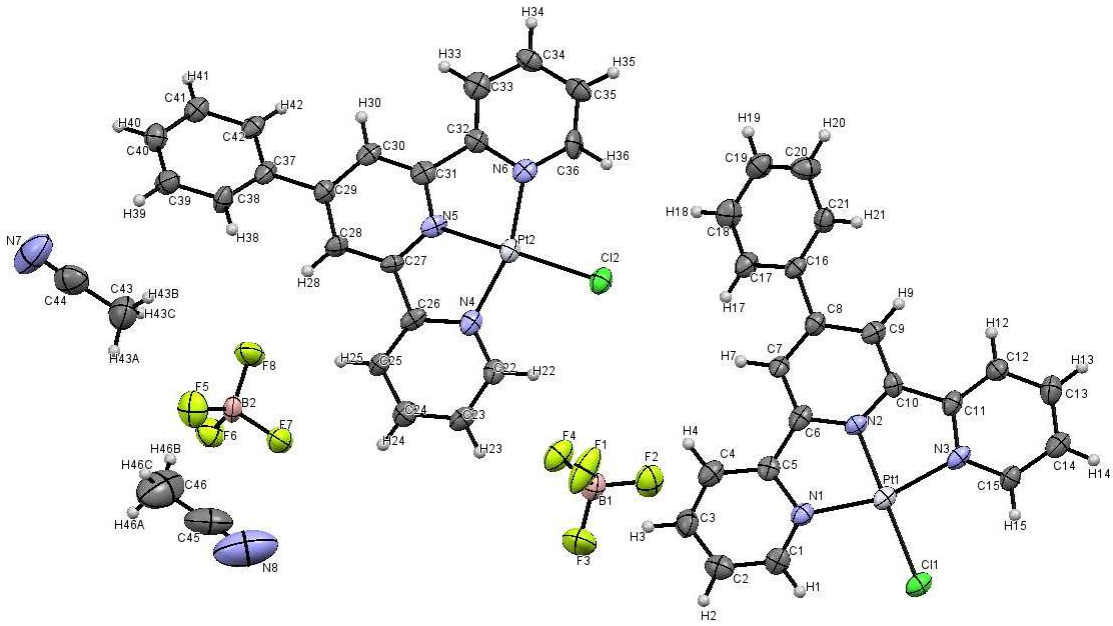

Figure 4.26*: Single crystal X-ray structure for complex **3** grown from slow evaporation of an acetonitrile. Ellipsoids shown at 50% for clarity*

Table 4.11: *Crystal data and structure refinement for Complex **3**.*

Identification code	S16prr17
Empirical formula	$C_{23}BN_4F_4ClPtH_{18}$
Formula weight	667.76
Temperature/K	150
Crystal system	triclinic
Space group	*P*-1
a/ Å	12.6052(6)
b/ Å	13.6738(5)
c/ Å	14.4954(10)
α/°	70.850(5)
β/°	85.170(5)
γ/°	72.188(4)
Volume/ Å^3	2246.7(2)
Z	4
ρ_{calc}mg/mm^3	1.974
μ/mm^{-1}	6.417
F(000)	1280.0
Crystal size/mm^3	0.5 × 0.1 × 0.2
Radiation	MoKα (λ = 0.71073 Å)
2Θ range for data collection	4.33 to 58.792°
Index ranges	-17 ≤ h ≤ 15, -18 ≤ k ≤ 18, -17 ≤ l ≤ 19
Reflections collected	17285
Independent reflections	10208 [R_{int} = 0.0401, R_{sigma} = 0.0811]
Data/restraints/parameters	10208/0/615
Goodness-of-fit on F^2	1.090
Final R indexes [I>=2σ (I)]	R_1 = 0.0519, wR_2 = 0.1108
Final R indexes [all data]	R_1 = 0.0795, wR_2 = 0.1237
Largest diff. peak/hole / e Å^{-3}	3.22/-1.84

For the two independent molecules of the cation in Complex **3** the geometry at the Pt(II) centres is square planar. The angular distortion around the Pt centres is present with angles measured at 162.0(3)˚ and 162.2(3)˚ for molecule 1 and 2 respectively (Table 4.12b). Table 4.12a/b provides the key bond lengths and angles for this complex, these are consistent with similar complexes.

The addition of the phenyl group to the 4th position of the central pyridyl ring has created the potential for loss of planarity in the solid state that was observed for complex **1**and **2**. Table 4.12c lists the key torsion angles for this complex, the majority of which are centred on the substituent, which is not planar in the solid state. The dihedral angle was measured at 34.25˚ this was measured between the plane of the phenyl ring substituent and the square plane of the central Pt centre. This loss of planarity has caused disruption to the solid-state packing and is partially responsible for the lack of *'switching'* behaviour in the solid state.

Table 4.12: *a. Table of bond lengths for **3**. b. Table of bond angles for **3**. c. Torsion angles for **3**.*

a. Bond Lengths		
Atom	**Atom**	**Length/ Å**
Pt1	Cl1	2.3001(19)
Pt1	N2	1.941(6)
Pt1	N3	2.035(8)
Pt1	N1	2.008(7)
F1	B1	1.390(12)
Pt2	Cl2	2.296(2)
Pt2	N4	2.009(7)
Pt2	N5	1.922(7)
Pt2	N6	2.008(7)
F6	B2	1.393(13)

b. Bond Angles			
Atom	**Atom**	**Atom**	**Angle/°**
N2	Pt1	Cl1	179.7(3)
N2	Pt1	N1	81.3(3)
N1	Pt1	Cl1	98.9(2)
N1	Pt1	N3	162.0(3)
F2	B1	F1	109.9(9)
N4	Pt2	Cl2	98.50(19)
N5	Pt2	Cl2	179.2(2)
N5	Pt2	N4	81.2(3)
N6	Pt2	N4	162.2(3)
F5	B2	F6	109.7(8)

c. Torsion Angles				
A	**B**	**C**	**D**	**Angle/°**
C28	C29	C37	C38	22.8(13)
C28	C29	C37	C42	-157.7(8)
C7	C8	C16	C17	-32.5(12)
C7	C8	C16	C21	149.3(9)
C9	C8	C16	C17	145.7(8)
C9	C8	C16	C21	-32.4(12)

There are a number of interactions present in this complex. The π interactions occur between the pyridyl rings of the pincer, which occur between the layers of the complex. The π interactions occur between the two molecules in the asymmetric unit cell and between the same molecule in the extended solid-state structure.

There are also a number of hydrogen bonding interactions in the crystal structure. They predominantly occur between the solvent and the pincer ligand in addition to the chlorine group and the pincer ligand of the adjacent molecule. These interactions act to stabilise the complex in the solid state.

Table 4.13*: a. Planes Present in solid-state structure for **3**. b. π-π Interactions for **3**. c. Hydrogen bonds for **3**.*

a. Plane Identification	
Plane Number	Atoms in plane
1	C37 C42 C41 C40 C39 C38
2	N4 C26 C25 C24 C23 C22
3	N5 C27 C28 C29 C30 C31
4	N6 C36 C35 C34 C33 C32
5	C16 C21 C20 C19 C18 C17
6	N3 C15 C14 C13 C12 C11
7	N2 C6 C7 C8 C9 C10
8	N1 C1 C2 C3 C4 C5

b. π-π Interactions	
Planes	Distance (Å)
2-4[1]	3.703
2-6[2]	3.699
6-8[3]	3.721

c. Hydrogen bonds			
Atoms	(D…A) Distance (Å)	(H…A) Distance (Å)	D…H…A Angle/°
C34-H34-N7	3.46(1)	2.58	158.1
C40-H40-Cl1	3.515(9)	2.814	133.0
C1-H1-N8	3.28(2)	2.63	127.0
C2-H2-N8	3.31(2)	2.74	120.7

Where [1](1-X, 1-Y, 1-Z), [2](2-X,-Y, 1-Z) and [3](3-X,-Y, 1-Z)

Crystal Packing: Stacking, Pt Offset and Torsion Angles.

The packing of complex **3** in the solid state is a little more complex than that observed for complex **1**. Molecules are grouped into stacks of four with no stacking observed between the groups. Within these groups are two pairs of molecules with alternate stacking distances between them. (Figure 4.27)

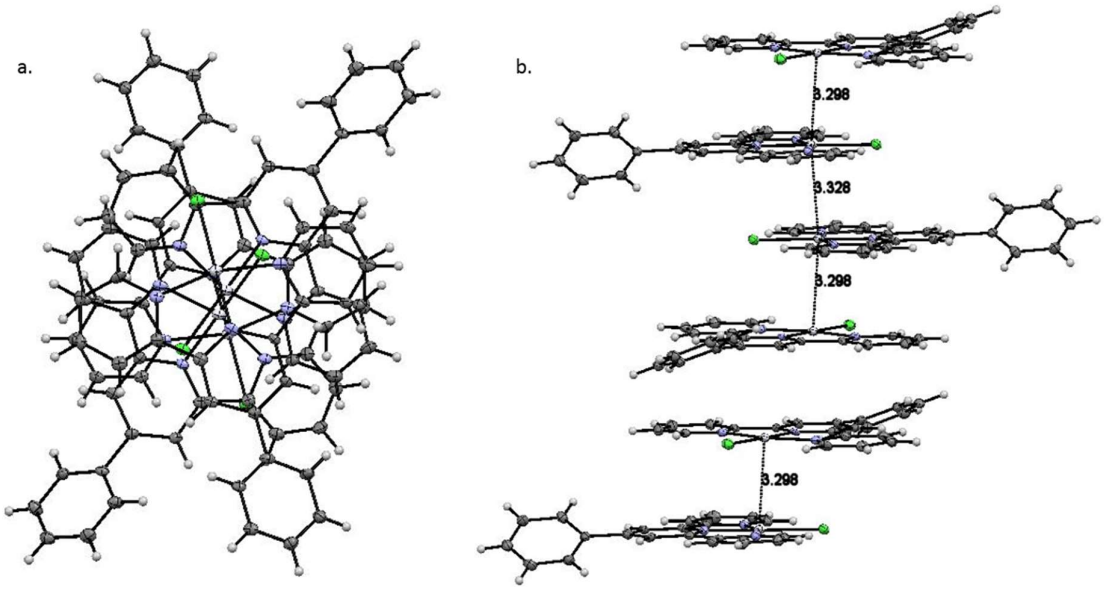

Figure 4.27*: a. Complex **3** viewed along the b axis. b. Stacking in complex **3**. Ellipsoids shown at 50% probability. Counter-ions and solvent removed for clarity.*

The alignment of the platinum atoms in the stacks of four is shown in Figure 4.27a. Due to the steric bulk of the ligand, it is not easy to see the two positions that the platinum centre adopts within each individual quartet, which means they are not perfectly aligned as with the blue form of complex **2**. The Pt offset for the Pt in the quartets is measured at 0.48 Å and between the quartets, the offset is measured at 2.79 Å. The platinum offset measured within the individual quartets is of comparable distance to that observed for the red form of complex **2**. Comparison of the distances between the Pt centres show they alternate between 3.3276(6) and 3.2976(6) Å as shown in Figure 4.27b, these distances are shorter than the distances measured for the red form of complex **2**.

The packing of complex **3** and the red form of complex **2** is similar, but they exhibit different behaviour in the solid state. The first visual indication of this is their colour. Complex **3** is deep red whereas complex **2** is a bright red. One possible reason for these observed differences is that for complex **2** the stacks are infinite, whereas for complex **3** the stacks contain only four molecules, which does not allow for extended dz^2 overlap. This disruption in the Pt stacks has been caused by the phenyl rings substituted on the 4' position of the central pyridine ring. Figure 4.27b shows how the phenyl rings have twisted out the molecule plane to avoid unfavourable steric interactions. The torsion angle between the phenyl ring and the central ring of the pincer ligand were measured at 22.75° and 25.45°, had the phenyl group been co-planar with the ligand a more extended stacking arrangement could have been observed.

4.5.4 X-Ray Powder Analysis

The powder analysis in Figure 4.28 shows that, as with complex **1**, there is a mixture of solvates in the bulk powder of this complex.

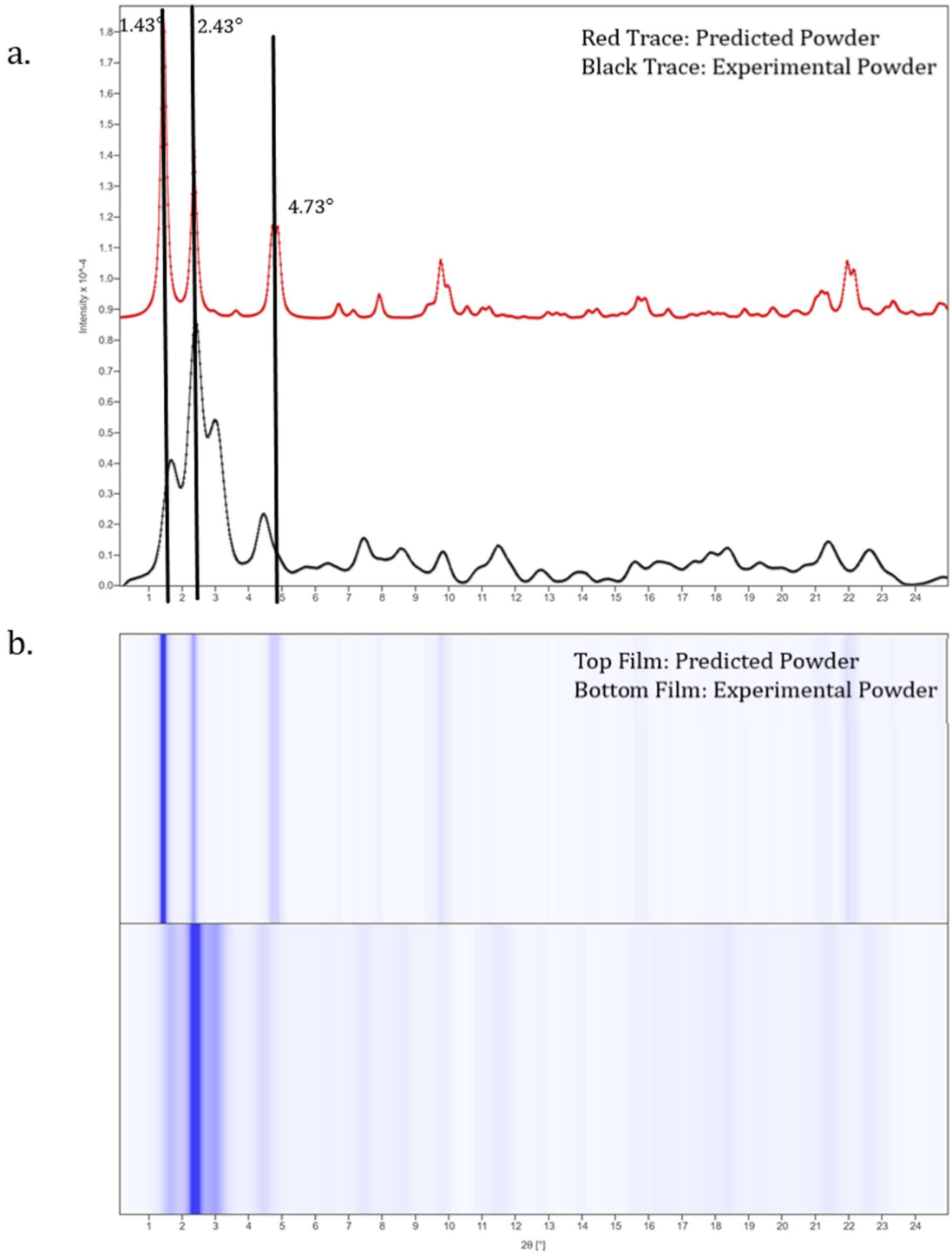

Figure 4.28: *a. Complex **3**, powder plot. b. Film representation of powder of Complex **3**. Top trace is the predicted powder (red) generated from crystal structure and bottom trace is the experimental powder (black).*

The powder had not been crystallised under the same crystallisation conditions as the single crystal and this clear when the experimental and predicted powder are compared. While there are some peaks that overlap there are a series of peaks that have split and lie at slightly different 2θ. This would suggest the presence of a different solvate, in the bulk powder.

4.5.5 Reflectance Spectroscopy

The reflectance spectra of complex **3** was measured and the results shown in Figure 4.29.

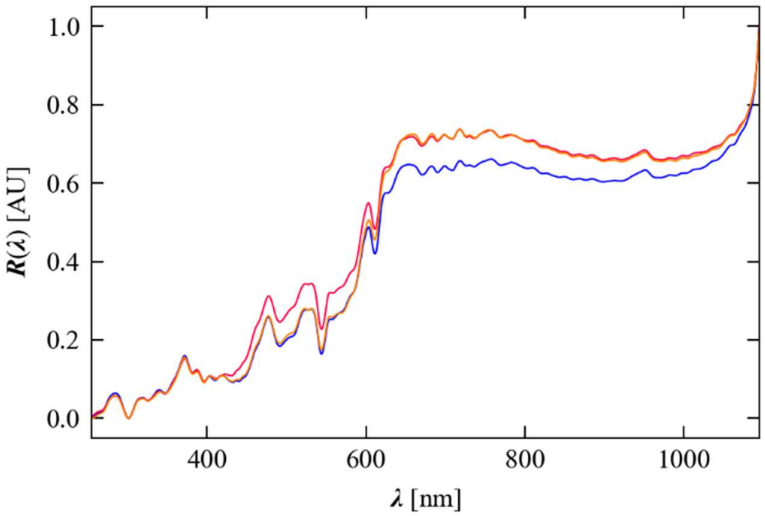

Figure 4.29*: Reflectance spectra of Complex **3**.*

Comparison of the reflectance spectra of Complex **1** and **3** show a very similar profile with an edge at approximately 600 nm. This is consistent with the complexes displaying similar colours in the solid state.

4.6.0. 4'-(p-tolyl)-2,2':6',2''-Terpyridine Platinum Chloride Tetrafluoroborate (4)

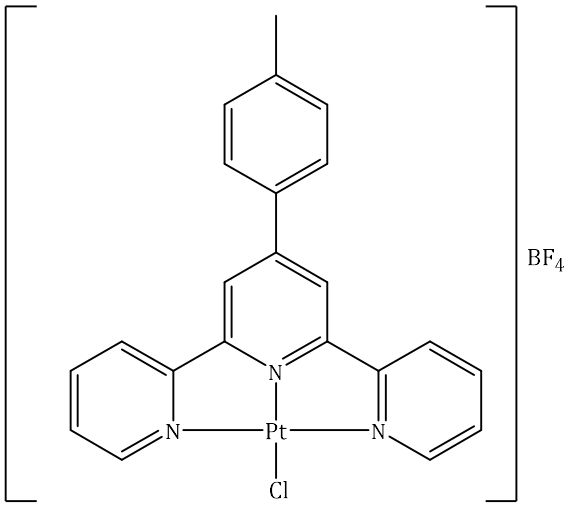

The ligand was used as purchased from Sigma Aldrich and the complex synthesised using the method outlined in Scheme 4.2.

Complex **4** was successfully characterised using IR spectroscopy, where the peak at 1029 cm^{-1} confirmed the presence of the BF_4^- counter-ion. ^1H NMR spectroscopy and single crystal X-ray diffraction confirmed the structure.

4.6.1 Solution State Spectroscopy

The solution state spectroscopy measured for this complex is given in Figure 4.30.

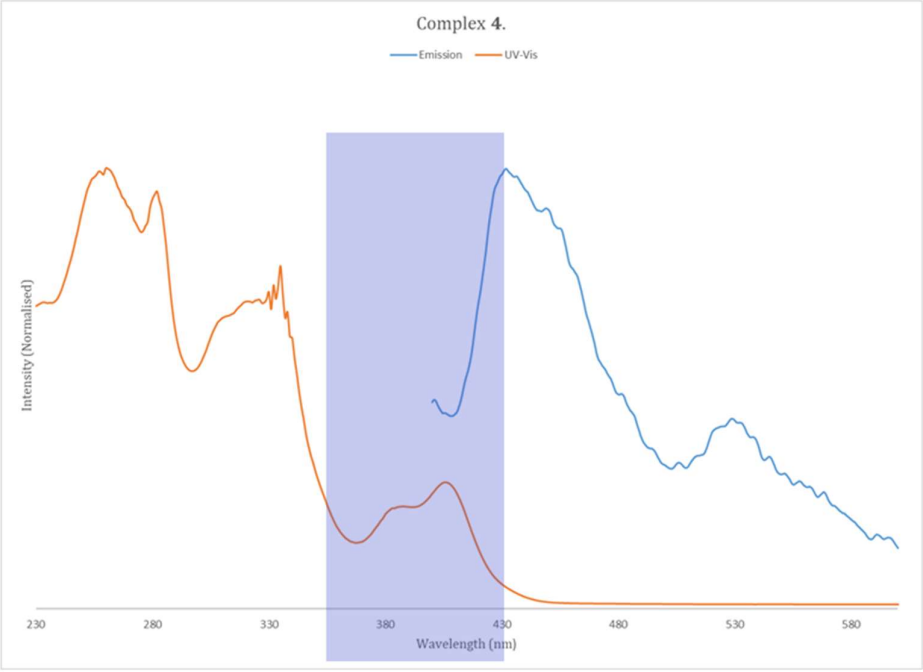

Figure 4.30: *Absorption spectrum of complex **4**, orange line, MLCT highlighted. Emission spectra for complex **4**, blue line, λ_{ex}=340 nm. Solution concentration 1×10^{-4} M in acetonitrile.*

Once again, the UV-Vis spectra have similar profiles to that recorded for complex **1, 2** and **3**. The peak at 350 nm is no longer visible, but the band in the region 290-340 nm represents the π-π* transitions of the co-ordinated terpyridine ligand. With the peak in the range 360-430 nm representing the MLCT band, highlighted on Figure 4.30.

The emission spectra shown by the blue line in Figure 4.30, was of low intensity before normalisation against the UV-Vis spectrum. Unlike complex **1** and **3**, in the case of complex **4** there is a second peak at 530 nm. This could have arisen because this complex is known to π stack and π interactions are known to exist in the solution state, as discussed in Section 1.5.1.

4.6.2 Vapo/Solvachromic Behaviour

The isolated solid of this complex is yellow which is indicative of there being no dz^2 overlap in the solid state, therefore any stacking observed would most likely not be between Pt centres. As with previous complexes, it was tested for changes in spectral properties with a variety of stimuli but no changes were observed. For example, it was tested for vapochromic behaviour with the standard laboratory solvents such as alcohols, acetone, water and chlorinated solvents in addition to solvents such as toluene and DMF, which have precedence in the literature for causing vapochromic changes.[69, 74, 99]

4.6.3 Crystal Structure Analysis

Crystal Structure.

Yellow crystals of complex **4** were crystallised by slow evaporation of acetonitrile. The structure crystallises in the triclinic space group P-1 with one molecule in the asymmetric unit. The structure is given in Figure 4.31, with structural and refinement data available in Table 4.14.

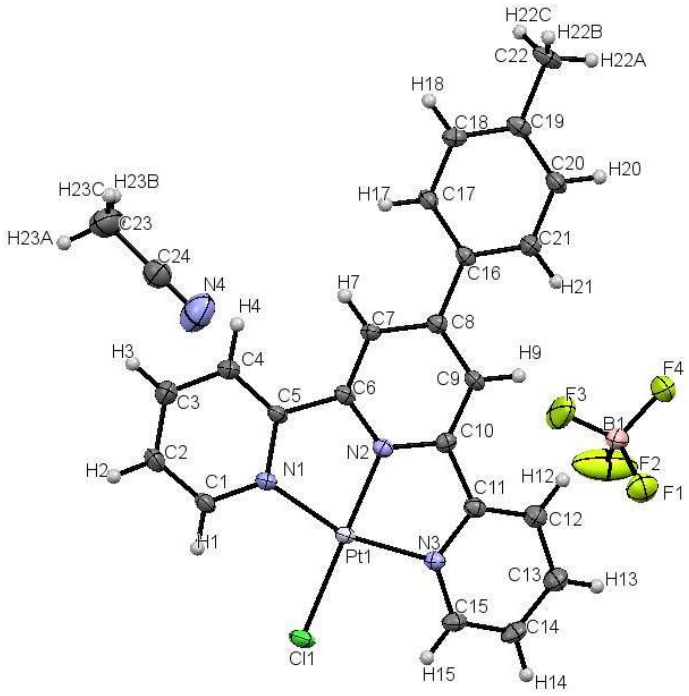

Figure 4.31*: Single crystal X-ray structure for complex* ***4*** *grown by slow evaporation of an acetonitrile. Displacement ellipsoids are shown at 50%*

Table 4.14: *Crystal data and structure refinement for Complex **4**.*

Identification code	s16prr60
Empirical formula	$C_{23}BN_4F_4ClPtH_{20}$
Formula weight	669.78
Temperature/K	150
Crystal system	triclinic
Space group	*P*-1
a/ Å	7.3862(2)
b/ Å	13.0174(5)
c/ Å	13.1508(4)
α/°	70.466(3)
β/°	89.053(3)
γ/°	78.384(3)
Volume/ Å^3	1165.48(7)
Z	2
ρ_{calc}mg/mm^3	1.909
μ/mm^{-1}	6.186
F(000)	644.0
Crystal size/mm^3	0.6 × 0.1 × 0.1
Radiation	MoKα (λ = 0.71073 Å)
2Θ range for data collection	5.47 to 58.484°
Index ranges	-10 ≤ h ≤ 9, -17 ≤ k ≤ 17, -17 ≤ l ≤ 11
Reflections collected	9185
Independent reflections	5293 [R_{int} = 0.0219, R_{sigma} = 0.0366]
Data/restraints/parameters	5293/0/318
Goodness-of-fit on F^2	1.144
Final R indexes [I>=2σ (I)]	R_1 = 0.0236, wR_2 = 0.0665
Final R indexes [all data]	R_1 = 0.0258, wR_2 = 0.0677
Largest diff. peak/hole / e Å^{-3}	0.69/-1.44

Complex **4** is square planar around the Pt centre with an angular distortion see for the N1-Pt1-N3 angle, this is consistent with other complexes in the literature.[110] Select bond lengths and angles have been provided in Table 4.15, these are consistent with similar complexes.

Table 4.15c is a selection of the torsion angles for this complex. The majority of the torsion angles in this complex are close to 0° or 180° confirming planarity of the complex cation. This is unexpected due to the size of the substituent on the 4th position of the central pyridyl ring. The key dihedral angles showing this planarity are:

- Plane 1: N2 Pt1 C5 N1 N3 C6 C10 C11 and Plane 2: C17 C16 C18 C20 C19 C21. Dihedral angle of 0.56˚.
- Plane1: N2 Pt1 C5 N1 N3 C6 C10 C11 and Plane 2: N3 C14 C13 C11 C15 C12. Dihedral angle of 7.50˚.
- Plane1: N2 Pt1 C5 N1 N3 C6 C10 C11 and Plane 2: C5 N1 C1 C3 C2 C4. Dihedral angles of 3.58˚.

These dihedral angles show that the arene substituent is co-planar with the square plane of the Pt centre, however the pyridyl rings are found at a slight upward angle. This could be attributed

to the strain of the bite angle with a tridentate ligand. This is illustrated further with a small number of torsion angles that are not measured at 0/180°.

Table 4.15*: a. Table of bond lengths for **4**. b. Table of bond angles for **4**. c. Torsion angles for **4**.*

a. Bond Lengths		
Atom	**Atom**	**Length/ Å**
Pt1	Cl1	2.2994(9)
Pt1	N2	1.934(3)
Pt1	N1	2.016(3)
Pt1	N3	2.020(3)
F1	B1	1.376(6)

b. Bond Angles			
Atom	**Atom**	**Atom**	**Angle/°**
N2	Pt1	Cl1	177.17(9)
N2	Pt1	N1	81.16(12)
N1	Pt1	Cl1	98.60(9)
N1	Pt1	N3	161.79(12)
F2	B1	F1	108.4(4)

c. Torsion Angles				
A	**B**	**C**	**D**	**Angle/°**
N2	C10	C11	N3	-4.3(5)
N2	C10	C11	C12	172.0(4)
N1	C5	C6	N2	1.5(5)
N1	C5	C6	C7	-178.4(4)
N1	C5	C4	C3	-0.5(6)

Complex **4** has a number of interactions in the solid state and these have been summarised in Table 4.16. There are a couple of π interactions between the pyridyl rings and the substituted arene ring. This could have attributed to the head to toe packing observed in the solid state, Figure 4.32, by providing a stabilising interaction. In addition, there are a number of hydrogen bonds between the solvent and the Pt complex cation.

Table 4.16*: a. Planes Present in solid-state structure of **4**. b. π-π Interactions of **4**. c. Hydrogen bonds of **4**.*

a. Plane Identification	
Plane Number	Atoms in plane
1	C16 C21 C20 C19 C18 C17
2	N2 C10 C9 C8 C7 C6
3	N1 C1 C2 C3 C4 C5
4	N3 C15 C14 C13 C12 C11

b. π-π Interactions	
Planes	Distance (Å)
1-3[1]	3.727
4-4[2]	3.731

c. Hydrogen bonds			
Atoms	(D…A) Distance (Å)	(H…A) Distance (Å)	D…H…A Angle/°
C9-H9-N4	3.624(6)	2.700	172.9
C21-H21-N4	3.382(7)	2.467	127.6(3)
C23-H23B-Cl1	3.570(6)	2.760	142.5

Where [1](2-X, 1-Y, 1-Z) and [2](1-X, 2-Y, 1-Z)

Crystal Packing: Stacking, Pt Offset and Torsion Angles.

In the solid state this complex is yellow, which suggests that the distances between the Pt centres are longer than 3.5 Å or the platinum centres are not aligned. The stacking observed for this complex is shown in Figure 4.32.

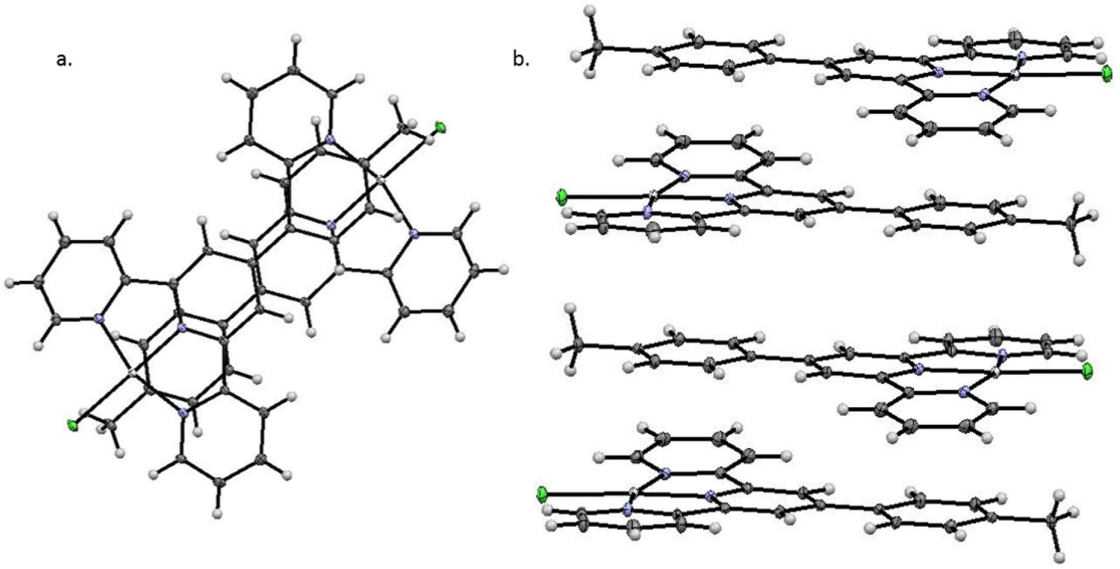

Figure 4.32*: a. Complex **4** viewed along the a axis. b. Stacking in complex **4**. Ellipsoids shown at 50% probability. Counter-ions and solvent have been removed for clarity.*

The packing arrangement of complex **4** in the solid state is shown in Figure 4.32a. The complex has packed in a head to toe manner, therefore the Pt centres are completely misaligned, hence why the complex is yellow in colour. One potential reason why they have packed in this manner is that the torsion angle of the tolyl group on the pincer, is only 1.67°, and is therefore essentially planar (Figure 4.32b). The planarity of the complex can cause steric interactions, to avoid the unfavourable interactions the complex has stacked head to toe as shown in Figure 4.32. In the case of complex **4** stacking head to toe must be the lowest energy conformation. This is because it is able to maximise favourable π-π stacking interactions as the complexes in the stacks are 3.264 Å apart, this is within the required range for π stacking to occur. This type of stacking and π-π interactions agrees with examples in the literature.[106]

4.6.4 X-Ray Powder Analysis

The powder analysis of complex **4** is shown in Figure 4.33. The bulk of the experimental powder is in agreement with that observed for the predicted pattern. This suggests that the crystal structure is representative of the majority of the bulk. However like previously observed with these complexes, there looks to be a solvate effect present with small shoulders present on the main peaks.

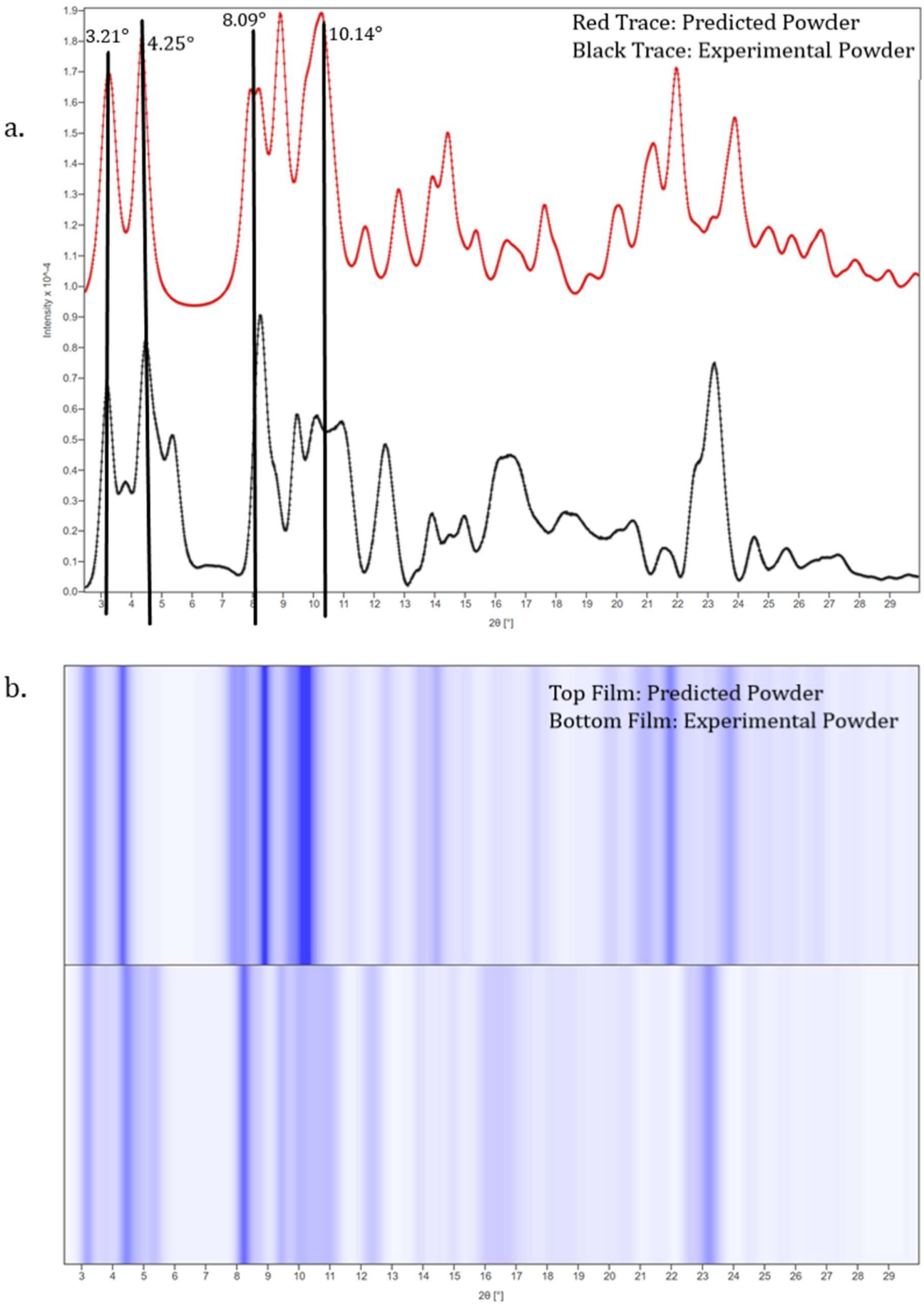

Figure 4.33: *a. Complex **4**, powder plot. b. Film representation of powder of Complex **4**. Top trace is the predicted powder (red) generated from crystal structure and bottom trace is the experimental powder (black).*

4.6.5 Reflectance Spectra

The reflectance spectra for this complex is shown in Figure 4.34. It does not have a clearly defined edge as seen with complex **1** and **2**, instead there is a gradual slope in the range 350-580 nm. This is in agreement with the observed colour of the complex being a yellow/orange.

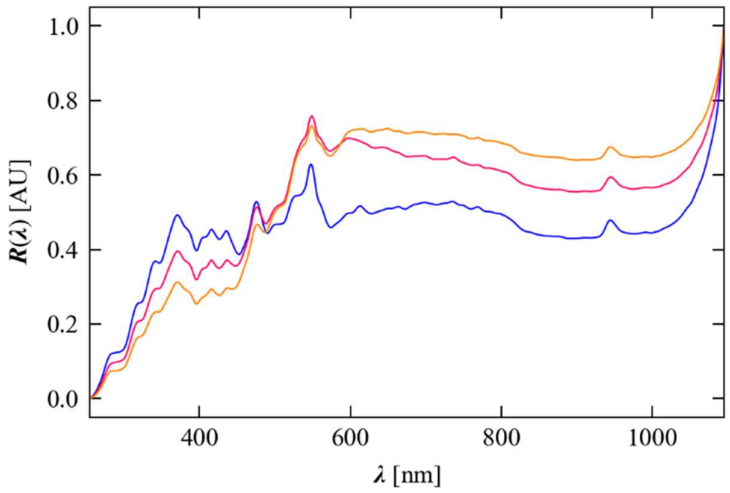

Figure 4.34*: Reflectance spectra of Complex **4**.*

4.7.0 2,2':6',2''-Terpyridine Platinum Chloride Hexafluorophosphate . (5)

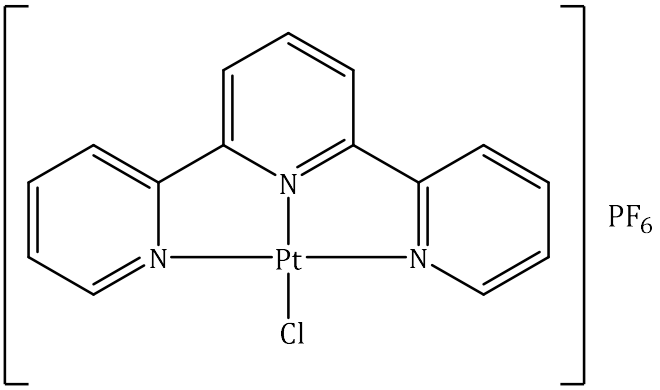

Complex **5** was synthesised by a counter-ion exchange reaction between complex **1** and ammonium hexafluorophosphate, details are shown in Scheme 4.4.

The complex was characterised by IR spectroscopy with a P-F stretch observed at 831 cm^{-1} in the spectrum and phosphorus NMR confirming the presence of the counter-ion. The structure was confirmed using ^{1}H NMR spectroscopy and single crystal X-ray diffraction.

4.7.1 Solution State Spectroscopy

The solution state UV-Vis spectrum for complex **5** is shown in Figure 4.35.

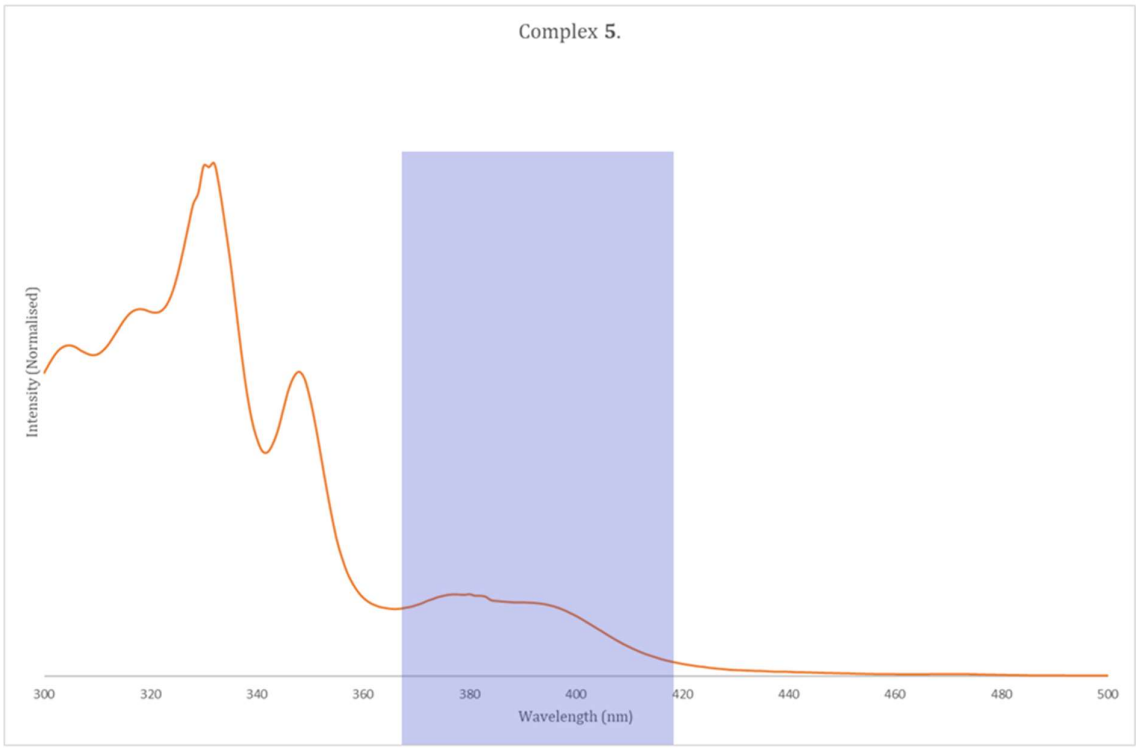

Figure 4.35: *Absorption spectrum of complex **5**. Solution concentration 1×10^{-4} M in acetonitrile. MLCT highlighted.*

When the absorption spectrum of both complex **1** and complex **5** are compared the profile looks similar, there is a well-defined region for the π-π transition and between 360-420 nm a peak for the metal-ligand charge transfer. Changing the counter-ion has had no visible effect on the solution state spectroscopy; this is to be expected because there is no peak on the spectrum assigned to the counter-ion and in solution, the cation and anions will have no direct interaction between them. The counter-ion on the other hand does change the colour of the complex in the solid state. Upon exchange of the BF_4^- to PF_6^- the complex turned from bright red to orange in colour.

4.7.2 Vapo/Solvachromic Behaviour

This complex is well documented in the literature and has been studied by three separate research groups. The first notable paper about this complex was discussed in Section 1.5.4. The paper by Connick *et al* described the colour and luminescence change when the complex was exposed to an aqueous solution of perchlorate and a counter-ion exchange reaction occurred.[62] In addition to the perchlorate ion the compound was exposed to a number of other ions and no other exchange occurred in solution, meaning this counter-ion exchange was selective in this instance. The observed colour change from yellow to red upon exposure to the perchlorate ion is consistent with a shortening of the Pt…Pt distance and was proved spectroscopically. The complex with the perchlorate counter-ion was subsequently found to produce a vapochromic response to water.[63]

The second paper of interest was published in 2010 by the Doerrer group. In this paper, they investigated a series of complexes with Pt…Pt interactions as well as Pt…Au interactions. The series was used to probe whether luminescence could be used to determine whether M-M interactions are present, as opposed to crystallography.[111] In this study they were able grow yellow needles of the complex, which had a pair-wise stacking arrangement and a Pt…Pt distance measured at 3.324(2) Å; no solvent was present in the crystal lattice. The complex did show luminescent behaviour in the solid state, however the Pt…Au dimers provided more unusual spectral properties.

The final paper described a vapochromic effect with the acetonitrile solvate, the same as was synthesised here. The paper published by Cao *et al* in 2014 described a reversible red to yellow transition when the complex was exposed to acetone returning to red upon exposure to acetonitrile.[44] Figure 4.36c shows the colour change in this vapochromic transition and it reversibility with the vapochromic properties of the complex not degrading over a series of cycles.

In addition, the authors were able to obtain crystal structures of both forms of the complex, shown in Figure 4.36a and b. The structures obtained here were different to those published by *Doerrer et al*[111], however they were able to isolate the two vapochromic forms of the complex. Figure 4.36a is the non-solvated form and is a yellow/ orange in colour, as described by Doerrer *et al* the same pair-wise stacking is observed however, the measured difference between the Pt centres is slightly different. On moving to the red form the Pt distances have increased slightly but there is infinite chain of complexes in comparison to the pairs observed for the de-solvated form. This is facilitated by the presence of acetonitrile in the structure and gives rise to the observed deep red colour.

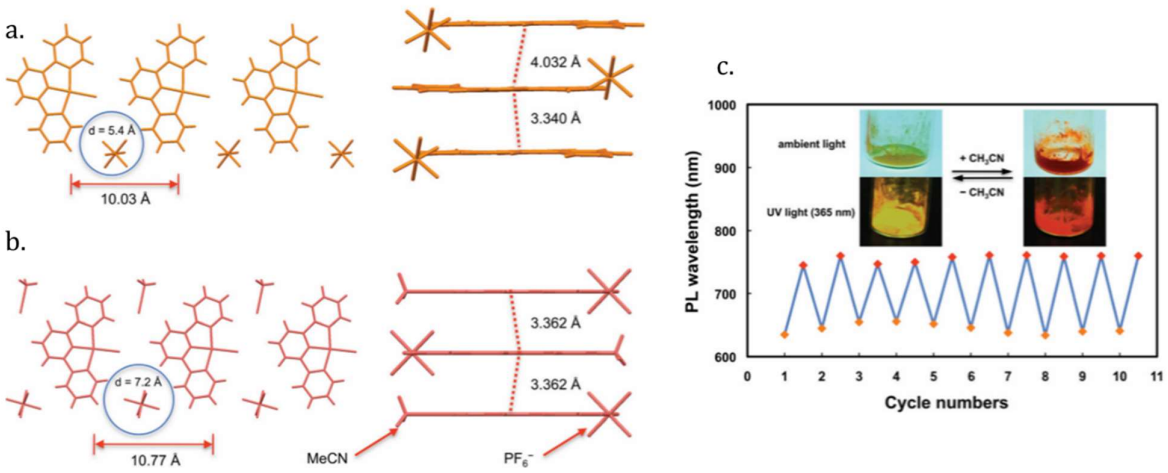

Figure 4.36*: a. Crystal structure of [Pt(Terpy)Cl]PF6, no solvent. b. Crystal structure of [Pt(Terpy)Cl]PF6.MeCN. c. Colour and luminescence change of [Pt(Terpy)Cl]PF6 when exposed to acetonitrile vapour. Images have been taken from the literature.*[44]

Upon investigation of complex **5**, it was found to show analogous vapochromic and counter-ion exchange properties as detailed in this section.

4.7.3 Crystal Structure Analysis

Crystal structure.

The complex was crystallised from the slow evaporation of acetonitrile. The crystals were red/ orange in colour and needle-like in shape. Complex **5** has crystallised in the orthorhombic space group *P*nma, with two molecules in the asymmetric unit cell as well as two molecules of solvent. The structure grown is the same as previously reported in the literature and details are given in Figure 4.36b.[44]

Crystal Packing-Stacking and Pt Offset.

Figure 4.37 shows the alignment of the Pt atoms and the observed Pt distances in the stacks for complex **5**.

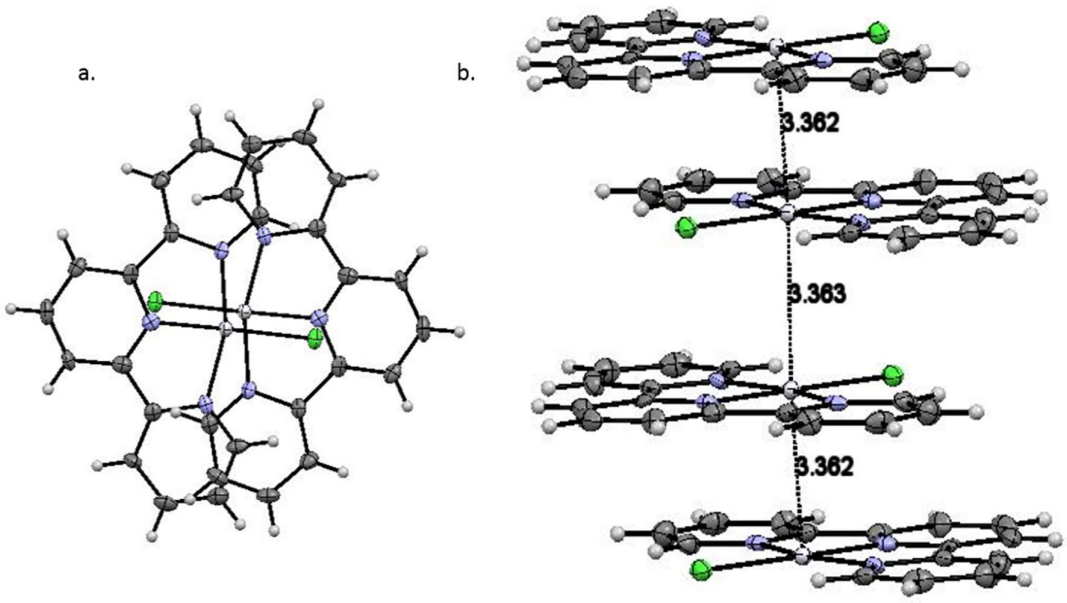

Figure 4.37*: a. Complex **5** viewed along the b axis. b. Stacking in complex **5**. Ellipsoids shown at 50% probability. Counter-ions and solvent have been removed for clarity.*

As shown in Figure 4.37a there are two platinum positions within the stacks of complex. This can be attributed to the head to toe stacking observed in Figure 4.37b. The Pt Offset was calculated as 0.64 Å, while longer than the distance observed for the red form of complex **2**, it is shorter than **1**. The head to toe stacking with two platinum positions in the stacks is a common feature in the crystal packing systems of these terpyridine systems. Analysis of the short contacts in the program Mercury,[87] shows that with the plain terpyridine complexes, there are interactions between the hydrogen atoms on the pincer and the chloride of another complex in the same plane. These short contacts interactions could potentially hold the molecules in this stacking arrangement.

The measured distance between the Pt atoms is 3.362 Å, which is agreement with the distance reported in the literature.[44] This distance falls within the required parameters for dz^2 overlap to occur. Vapochromic behaviour has been reported in the literature and the same behaviour has been observed for this complex.

4.7.4 X-Ray Powder Analysis

Figure 4.38 shows the experimental and predicted powder for the acetonitrile solvate of complex **5**. Both traces are in good agreement which shown that the crystal grown from acetonitrile is representative of the bulk.

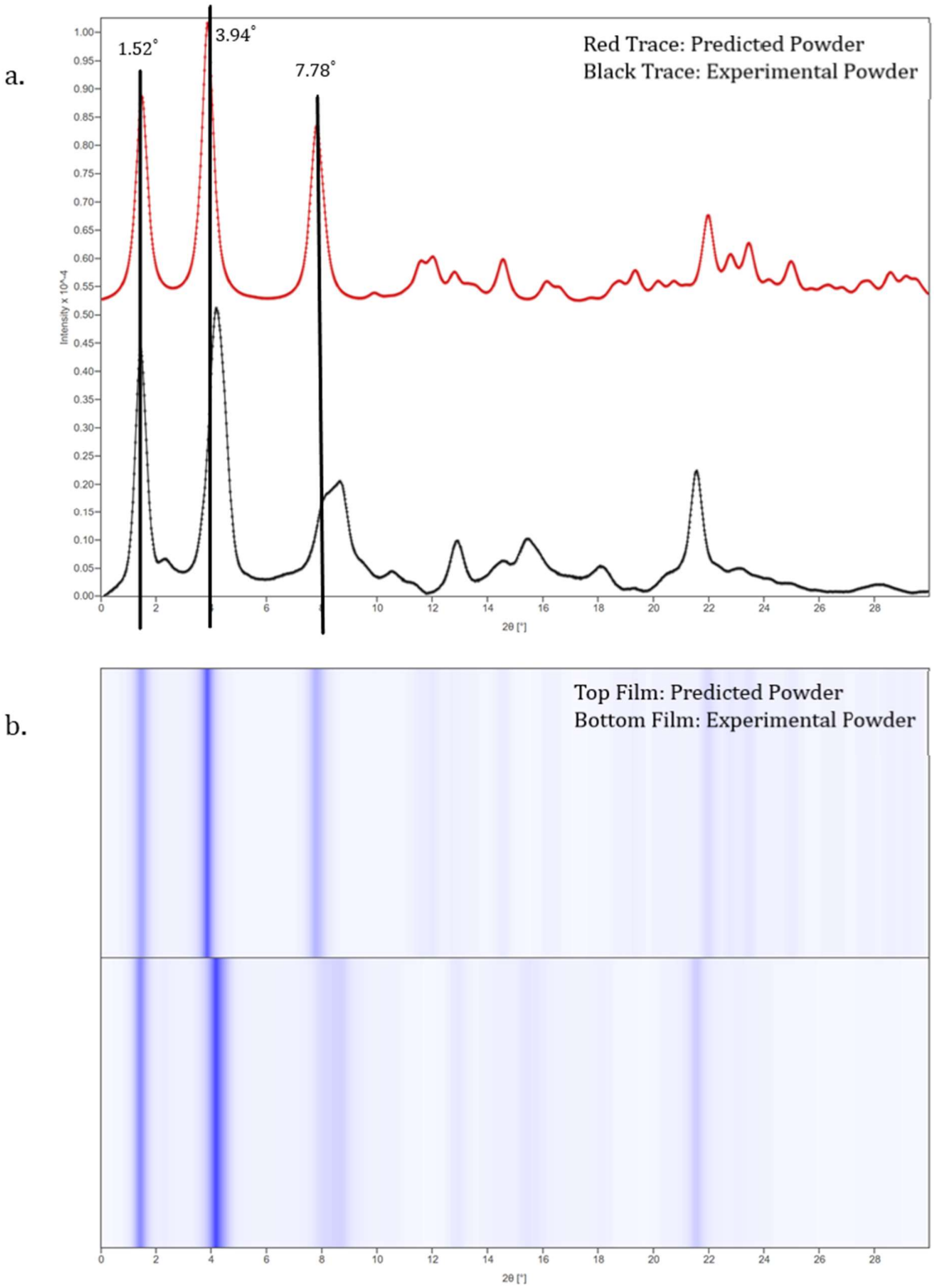

Figure 4.38: *a. Complex **5**, powder plot. b. Film representation of powder of Complex **5**. Top trace is the predicted powder (red) generated from crystal structure and bottom trace is the experimental powder (black).*

4.7.5 Reflectance Spectra

The reflectance trace for the acetonitrile solvate of complex **5** is shown in Figure 4.39, the edge of the spectra is consistent with the observed colour.

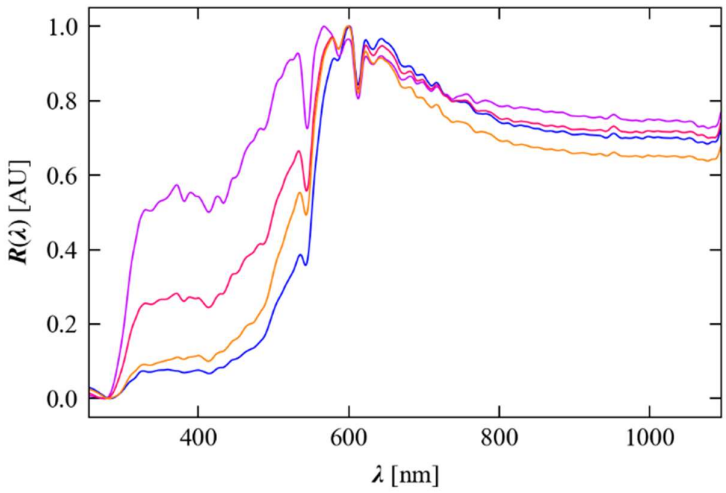

Figure 4.39*: Reflectance spectra of Complex **5**.*

4.8.0 4'-phenyl-2,2':6',2''-Terpyridine Platinum Chloride Hexafluorophosphate. (6)

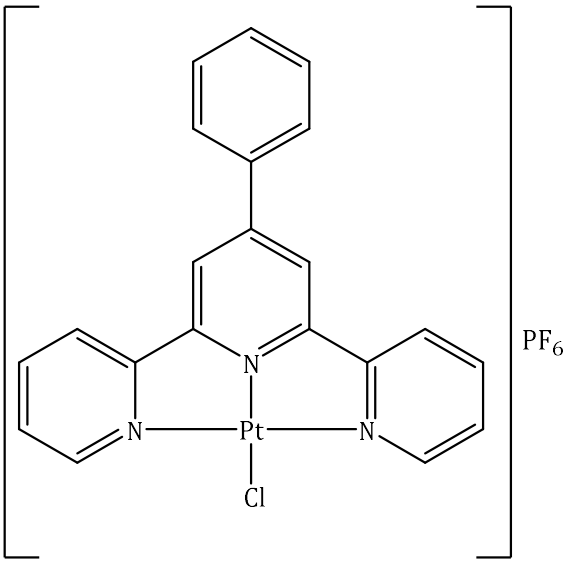

Complex **6** was synthesised using the method of counter-ion exchange, detailed in Scheme 4.4.

The product was confirmed by IR spectroscopy and ^{1}H NMR spectroscopy and the solid-state structure determined by single crystal diffraction. The presence of the counter-ion was confirmed using IR and phosphorus NMR.

4.8.1 Solution State Spectroscopy

The solution state UV-Vis for this complex is shown in Figure 4.40.

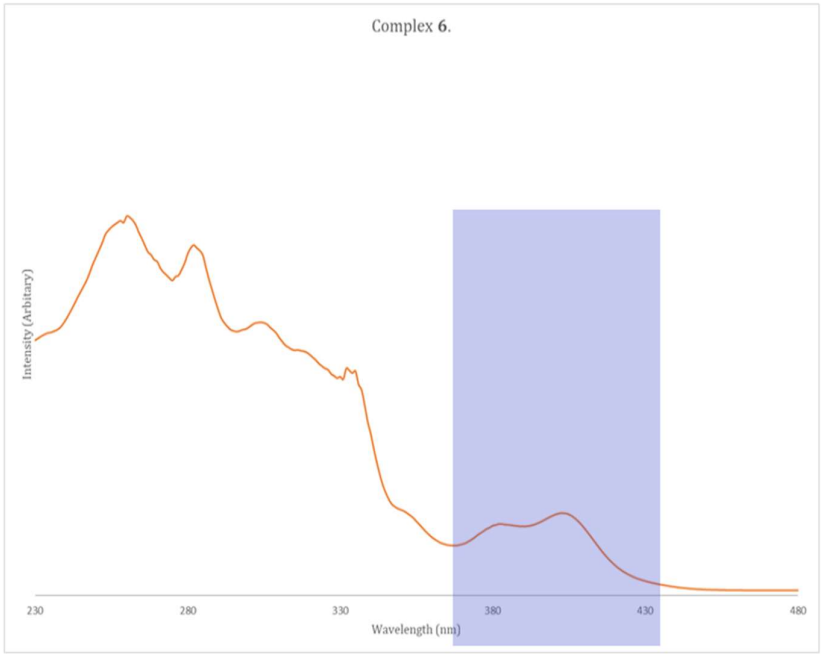

Figure 4.40: *Absorption spectrum of complex **6**. Solution concentration 1×10^{-4} M in acetonitrile. MLCT highlighted.*

The UV-Vis spectrum for complex **6** in Figure 4.40 is assigned as follows. The shoulder at 350 nm and peaks prior to this in the spectrum are π-π transition from the ligand. The set of peaks, in the range 370-420 nm can be assigned as the MLCT band. This spectrum is very similar to the recorded spectra for complex **3**, hence why the same assignments have been made. As expected, as observed with complex **5**, the counter-ion has had no effect on the solution state spectra.

4.8.2 Vapo/Solvachromic Behaviour

The BF_4^- version of this complex is brick red in the solid state, whereas the PF_6^- version was yellow. This change in colour would suggest the disruption of Pt stacks in the complex. The disruption of stacking would make it unlikely that the spectral properties of this complex change, and when tested this was indeed the case. The complex was tested for vapochromic behaviour with a selection of common laboratory solvents and for mechanochromic behaviour by grinding a sample under ambient and UV-light. No spectral changes were observed with this testing.

4.8.3 Crystal Structure Analysis

After several attempts, the only crystals that could be grown for this complex were only of suitable quality to prove the connectivity of this complex and an in-depth structure analysis of this complex could not be achieved. The basic connectivity of complex **6** is shown in Figure 4.41 and crystal structure and refinement data is provided in Table 4.17.

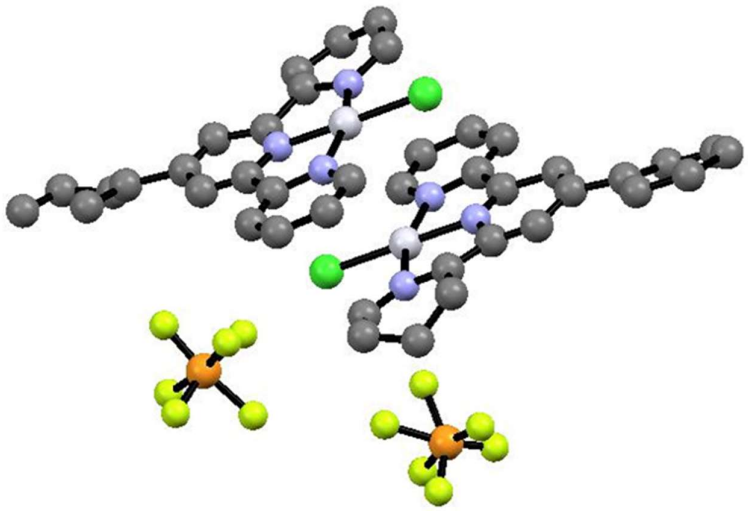

Figure 4.41*: Connectivity of Complex **6** in the solid state.*

Table 4.17: *Crystal data and structure refinement for Complex **6**.*

Identification code	Bath2717
Empirical formula	$C_{20}H_{15}N_3F_6PClPt$
Formula weight	672.86
Temperature/K	150 K
Crystal system	orthorhombic
Space group	$Pna2_1$
a/ Å	25.9832(9)
b/ Å	7.3518(2)
c/ Å	21.5812(8)
α/°	90
β/°	90
γ/°	90
Volume/ Å^3	4122.5(2)
Z	8
ρ_{calc}g/cm^3	2.168
μ/mm^{-1}	8.799
F(000)	2560.0
Radiation	Synchrotron (λ = 0.7749 Å)
2Θ range for data collection/°	5.35 to 61.354
Index ranges	-34 ≤ h ≤ 34, -9 ≤ k ≤ 9, -28 ≤ l ≤ 28
Reflections collected	40312
Independent reflections	9809 [R_{int} = 0.1251, R_{sigma} = 0.1054]
Data/restraints/parameters	9809/1/262
Goodness-of-fit on F^2	1.511
Final R indexes [I>=2σ (I)]	R_1 = 0.1558, wR_2 = 0.3769
Final R indexes [all data]	R_1 = 0.1878, wR_2 = 0.4023
Largest diff. peak/hole / e Å^{-3}	26.35/-8.52
Flack parameter	0.50(4)

This image shows the basic connectivity of complex **6**, unlike predicted this complex seems to have some Pt…Pt interactions present, the Pt…Pt distance is measured at 3.440(3) Å. This is because upon crystallisation a previously unknown red form was obtained, the colour of this new form would be consistent with having extended Pt stacks in the solid state. In addition, the phenyl rings seem to lie in the same plane as the rest of the terpyridine ligand, which could facilitate this Pt interaction.

4.8.4 X-Ray Powder Analysis

A comparison of the experimental and predicted powder from the incomplete crystal data is shown in Figure 4.42.

The preliminary peak at approximately three on the 2θ scale is in good agreement in both the experimental and predicted traces, however while there is agreement in the peaks lower on the 2θ scale the intensity is much lower on the predicted spectra. This would suggest that the bulk was in good agreement with the proposed crystal structure, however there could be a mixture of

solvates/ forms present in the bulk powder or the single crystal structure was not of a high enough resolution to get a detailed powder pattern. This mixture could be one of the reasons why this complex was difficult to crystallise.

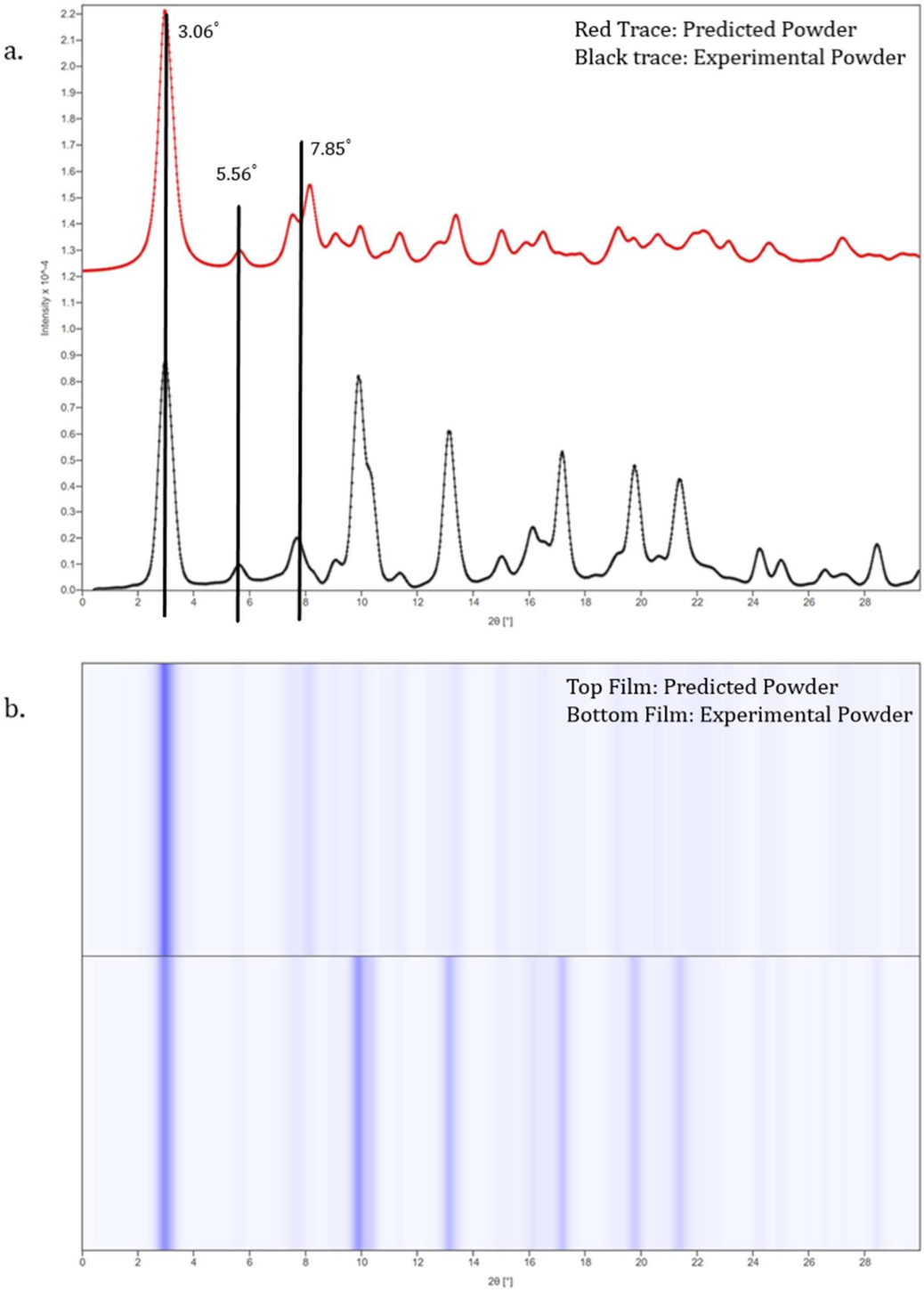

Figure 4.42*: a. Complex* ***6****, powder plot. b. Film representation of powder of Complex* ***6****. Top trace is the predicted powder (red) generated from crystal structure and bottom trace is the experimental powder (black).*

4.8.5 Reflectance Spectra

Figure 4.43 shows the reflectance spectrum for complex **6**, there is reasonable agreement between the traces, however problems with the background, have caused issues with the high wavelength on the blue trace. The edge appears at between 450-600 nm this is consistent with the observed colour.

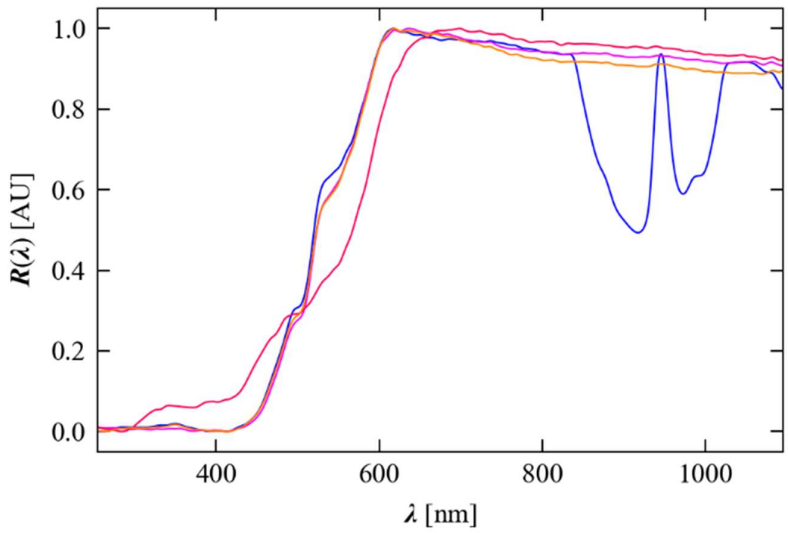

Figure 4.43*: Reflectance spectra of Complex* ***6****.*

4.9.0. 4'-(p-tolyl)-2,2':6',2''-Terpyridine Platinum Chloride Hexafluorophosphate (7)

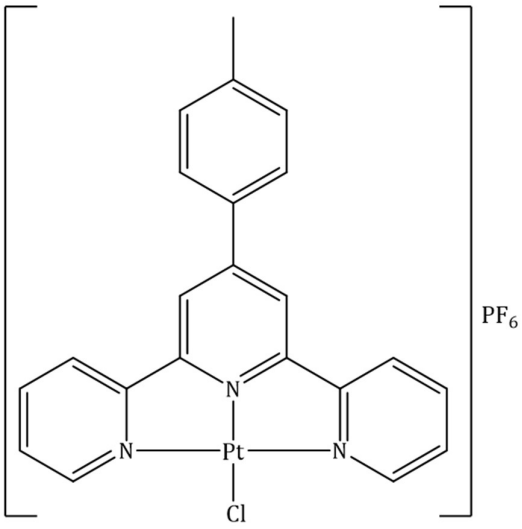

This complex was synthesised by the methodology of counter-ion exchange detailed in Section 4.2.3, Scheme 4.4. Complex **7** is yellow in the solid state.

This complex was characterised by IR spectroscopy, where a peak at 831 cm^{-1} in the spectrum represents the P-F stretch of the counter-ion. ^{1}H NMR spectra and single crystal X-ray diffraction data were also obtained for this complex.

4.9.1 Solution State Spectroscopy

The spectra for the solution state UV-Vis of complex **7** can be found in Figure 4.44.

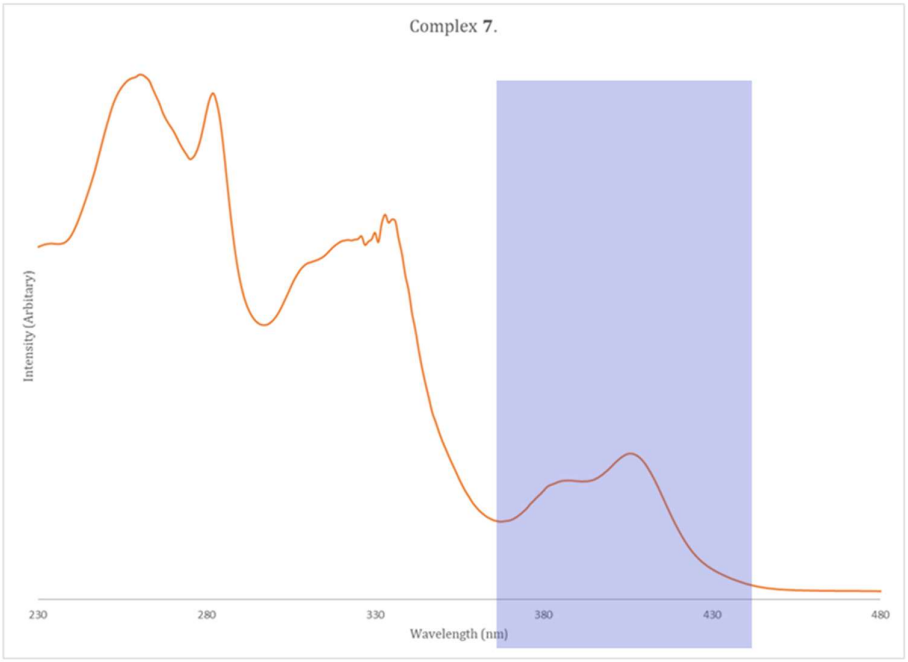

Figure 4.44: *Absorption spectrum of complex **7**. Solution concentration 1×10^{-4} M in acetonitrile. MLCT highlighted*

The same conclusions reached for complexes **5** and **6** can be applied to complex **7**. Comparison of the UV-Vis spectra for complex **4** and **7**, Figure 4.30 and 4.44, respectively, shows that they have a very similar profile and the same assignments can be made in this instance.

4.9.2 Vapo/Solvachromic Behaviour

The isolated complex was yellow, which based on previous results is indicative of no Pt stacking in the solid state. Regardless of this result, the complex was tested for changes in spectral properties, in case it exhibited high level of π… π stacking as observed with complex **4**. A number of common laboratory solvents were used to test the vapochromic behaviour of **7** and no spectral response was observed. In addition, the crystalline material was ground under ambient and UV-light and no change was observed. Therefore, the conclusion is that this complex does not *'switch'* in the solid state.

4.9.3 Crystal Structure Analysis

Crystal structure.

The complex was crystallised from the slow evaporation of acetone. The crystals were yellow and needle shaped. Complex **7** has crystallised in the monoclinic space group $P2_1/c$, with one molecule in the asymmetric unit. The structure is given in Figure 4.45 with structural and refinement data provided in Table 4.18.

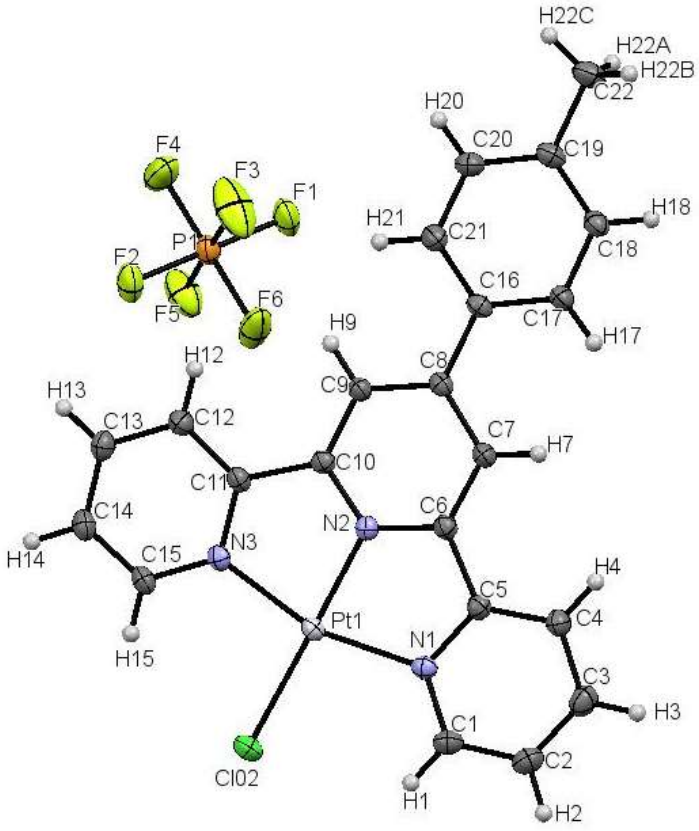

Figure 4.45*: Single crystal X-ray structure for complex* ***7*** *grown from slow evaporation of an acetone. Displacement ellipsoids are shown at 50% probability.*

Table 4.18: *Crystal data and structure refinement for Complex **7**.*

Identification code	Bath2719
Empirical formula	$C_{22}H_{17}ClF_6N_3PPt$
Formula weight	698.90
Temperature/K	273.15
Crystal system	monoclinic
Space group	$P2_1/c$
a/ Å	7.5776(3)
b/ Å	21.7092(10)
c/ Å	12.8910(6)
α/°	90
β/°	94.809(2)
γ/°	90
Volume/ Å^3	2113.15(16)
Z	4
ρ_{calc}g/cm^3	2.197
μ/mm^{-1}	8.589
F(000)	1336.0
Crystal size/mm^3	0.2 × 0.03 × 0.04
Radiation	Synchrotron (λ = 0.7749 Å)
2Θ range for data collection/°	4.092 to 79.062
Index ranges	-12 ≤ h ≤ 12, -35 ≤ k ≤ 35, -20 ≤ l ≤ 21
Reflections collected	37001
Independent reflections	9759 [R_{int} = 0.0529, R_{sigma} = 0.0515]
Data/restraints/parameters	9759/0/308
Goodness-of-fit on F^2	1.080
Final R indexes [I>=2σ (I)]	R_1 = 0.0406, wR_2 = 0.0739
Final R indexes [all data]	R_1 = 0.0598, wR_2 = 0.0789

Complex **7** displays a square planar geometry around the Pt centre with the expected angular distortions, attributed to the bite angle of the pincer ligand. Selected bond angles and lengths have been provided in Table 4.19 and are consistent with similar complexes.[106]

The torsion angles for this complex are close to planarity except for those on the tolyl substituent which unlike complex **4** does not sit co-planar with the plane of the pincer. The dihedral angle was measured between the following two planes:

- Plane 1: Pt1 C5 N3 N1 N2 C11 C10 C6
- Plane 2: C16 C17 C21 C18 C20 C19.

The dihedral angle has a value of 16.83˚, this shows there is a small shift away from planarity for this complex.

Table 4.19: *a. Table of bond lengths for **7**. b. Table of bond angles for **7**. c. Torsion angles for **7**.*

a. Bond Lengths		
Atom	**Atom**	**Length/ Å**
Pt1	Cl02	2.2916(8)
Pt1	N3	2.018(3)
Pt1	N1	2.018(3)
Pt1	N2	1.931(3)
P1	F2	1.598(3)

b. Bond Angles			
Atom	**Atom**	**Atom**	**Angle/°**
N3	Pt1	Cl02	98.55(8)
N3	Pt1	N1	162.33(11)
N1	Pt1	Cl02	99.11(8)
N2	Pt1	Cl02	178.62(9)
N2	Pt1	N1	81.33(11)
F2	P1	F1	179.61(18)
F4	P1	F2	90.23(16)

c. Torsion Angles				
A	**B**	**C**	**D**	**Angle/°**
Pt1	N3	C11	C10	0.7(4)
Pt1	N2	C10	C11	-0.8(4)
C8	C16	C21	C20	-178.7(3)

There are a number of π interactions present in the solid-state structure of **7** and these are listed in Table 4.20b. The interactions fall between the tolyl substituent and the pyridyl ring of the pincer ligand. Further analysis of the crystal structure shows that the complex sits head to toe in the solid state, Figure 4.46. This would explain why the complex is yellow in the solid state and does not show any *'switching'* behaviour. The complex forms one hydrogen bond between the chloride group and the pincer ligand on the adjacent molecule. No solvent is found in this crystal structure so an extended hydrogen-bonding network is not observed.

Table 4.20: *a. Planes Present in solid-state structure of **7**. b. π-π Interactions of **7**. c. Hydrogen bonds of **7**.*

a. Plane Identification	
Plane Number	Atoms in plane
1	C16 C21 C20 C19 C18 C17
2	N1 C5 C4 C3 C2 C1
3	N3 C15 C14 C13 C12 C11
4	N2 C6 C7 C8 C9 C10

b. π-π Interactions	
Planes	Distance (Å)
1-1[1]	3.927
1-3[2]	3.638
2-3[3]	3.720

c. Hydrogen bonds			
Atoms	(D…A) Distance (Å)	(H…A) Distance (Å)	D…H…A Angle/°
C15-H15-Cl02	3.422(4)	2.7118	133.8

Where [1](1-X, 1-Y, 1-Z), [2](1+X, +Y, +Z) and [3](-X, 1-Y, 2-Z)

Crystal Packing-Stacking and Pt Offset.

The crystal packing for complex **7** is shown in Figure 4.46.

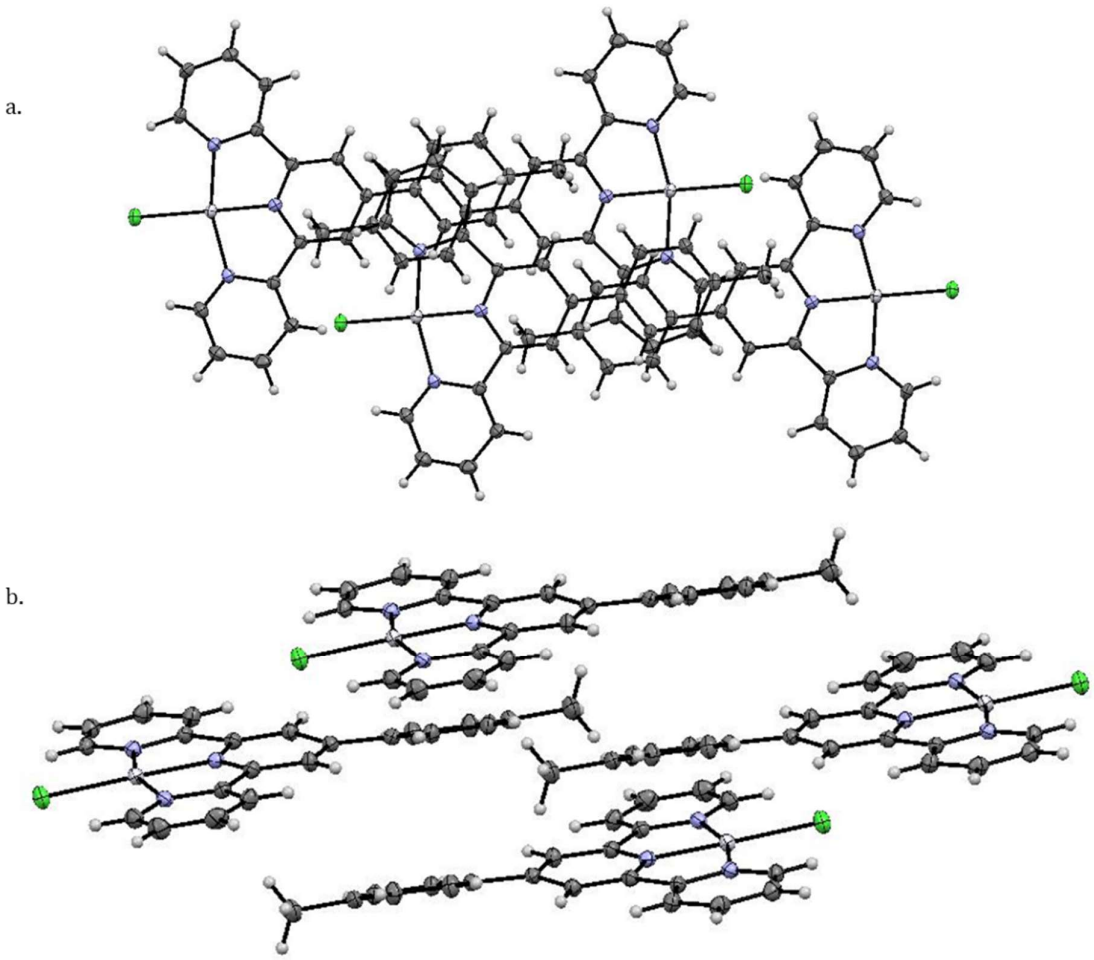

Figure 4.46*: a. Complex **7** viewed along the a axis. b. Stacking in complex **7**, Ellipsoids shown at 50% probability. Counter-ions have been removed for clarity.*

Figure 4.46a clearly shows there is no Pt overlap in the solid-state structure for complex **7**. In addition, the distance between the overlapping phenyl rings is 4.350(5) Å, this distance is too large for any significant π stacking effect to be observed in this complex. An example in the literature discusses how the same ligand can π stack provided the tolyl group is close to co-planar with the plane of the terpyridine ligand.[106] In the case of complex **7** the measured torsion angle between the central ring of the terpyridine ligand and the tolyl group is -16.78˚, which is close to being co-planar, however π stacking is not observed in this example. The complex has no solvent present in the crystal structure and no significant void space is present, suggest that it has close packed and the counter-ion is responsible for the vertical intermolecular interactions.

There are interactions present in this solid-state structure, however they are in a sheet-like arrangement between the terpyridine ligand and counter-ion opposed to a column-like set of interactions.

4.9.4 X-Ray Powder Analysis

The crystal structure presented in Section 4.9.3, had no solvent located in the structure however the powder pattern of a sample grown from similar conditions, does not show good agreement with the crystal structure provided, Figure 4.47.

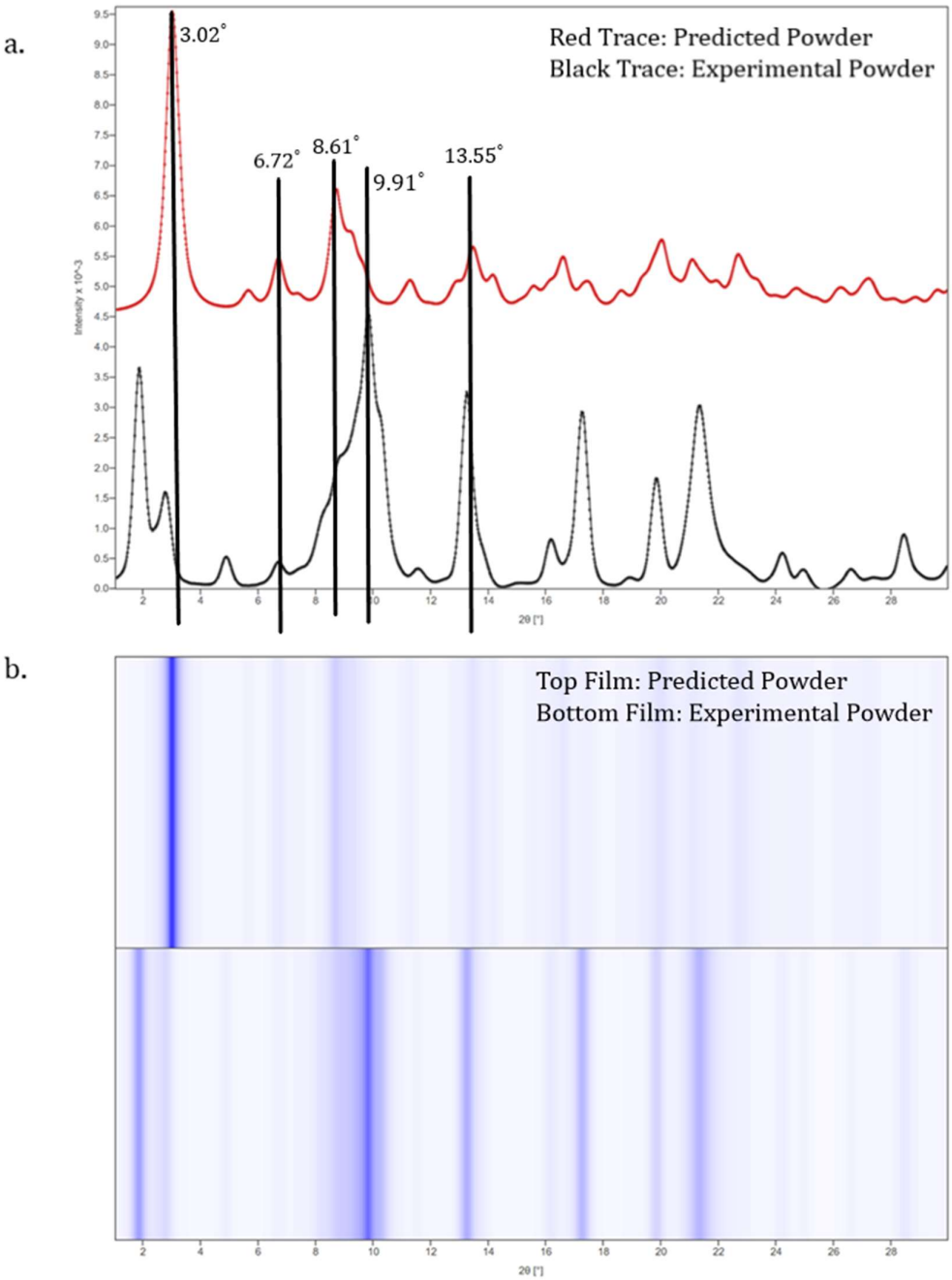

Figure 4.47*: a. Complex* ***7****, powder plot. b. Film representation of powder of Complex* ***7****. Top trace is the predicted powder (red) generated from crystal structure and bottom trace is the experimental powder (black).*

This poor agreement in structure is readily seen in Figure 4.47b, where the powder has a series of peaks that are at much higher intensity and displaced from the predicted peak. This suggests

that the bulk power contains a series of polymorphic/ solvated forms of complex **7** that have not been isolated as a single crystal.

4.9.5 Reflectance Spectra

The edge of the reflectance spectrum sits at approximately 500 nm, this is consistent with the observed colour in the solid state.

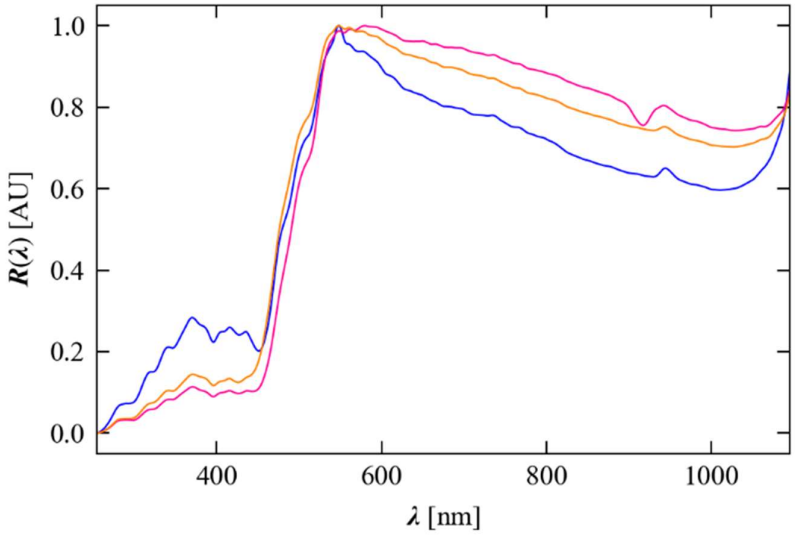

Figure 4.48: *Reflectance Spectra of Complex **7**.*

4.10.0. 2,2':6',2''-Terpyridine Platinum Chloride Tosylate (8)

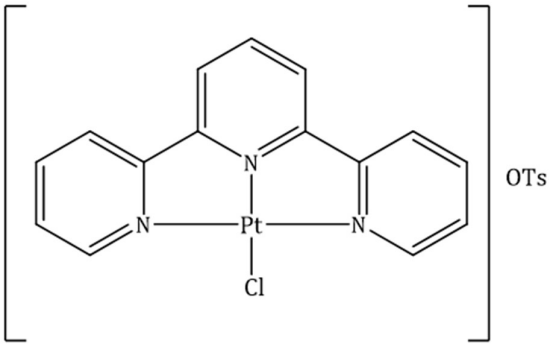

Scheme 4.3 details the synthesis of complex **8**.

Product confirmed by ^{1}H NMR, IR and single crystal diffraction.

4.10.2 Vapo/Solvachromic Behaviour

This complex is a deep red in the solid state, which is suggestive of Pt overlap or a high degree of π overlap that could be manipulated. Unfortunately when exposed to a series of vapours and crystallisation solvents there was no change in the observed spectral properties and the deep red colour was maintained.

4.10.3 Crystal Structure Analysis

Crystal structure.

The complex was crystallised from the vapour diffusion of diethyl-ether into a concentrated methanol solution at -18˚C. The crystals were red, needle shaped and desolvated rapidly when removed from the mother liquor. Complex **8** has crystallised in the monoclinic space group *P*21/c, with one molecule in the asymmetric unit cell. The structure is given in Figure 4.49 with structural and refinement data provided in Table 4.21.

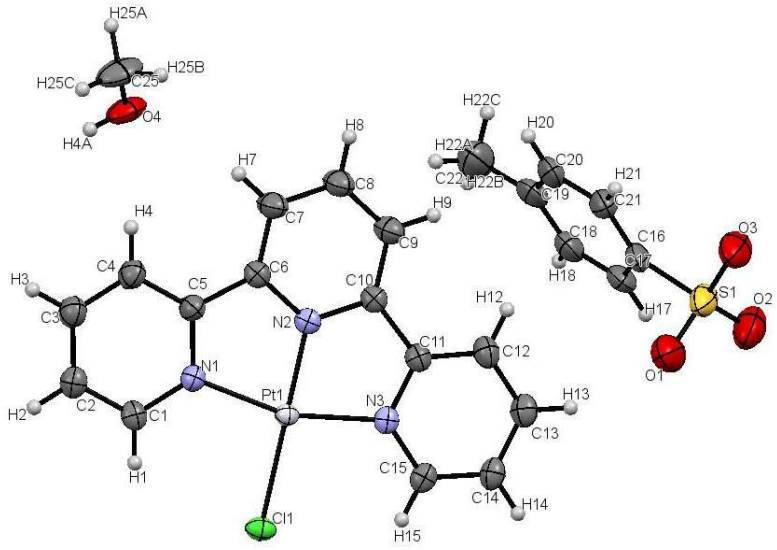

Figure 4.49*: Single crystal X-ray structure for complex **8** grown from vapour diffusion of diethyl-ether into a concentrated methanol solution at -18˚C. Ellipsoids shown at 50%*

Table 4.21: *Crystal data and structure refinement for Complex **8**.*

Identification code	S16prr218
Empirical formula	$C_{23}N_3H_{22}O_3Pt_1Cl_1S_1$
Formula weight	634.99
Temperature/K	150
Crystal system	monoclinic
Space group	$P2_1/c$
a/ Å	6.6681(2)
b/ Å	26.3387(9)
c/ Å	13.4150(4)
α/°	90
β/°	90.082(3)
γ/°	90
Volume/ Å^3	2356.08(14)
Z	4
ρ_{calc}g/cm^3	1.790
μ/mm^{-1}	6.185
F(000)	1224.0
Crystal size/mm^3	0.8 × 0.2 × 0.2
Radiation	MoKα (λ = 0.71073)
2Θ range for data collection/°	4.64 to 52.734
Index ranges	-8 ≤ h ≤ 7, -32 ≤ k ≤ 32, -16 ≤ l ≤ 11
Reflections collected	16564
Independent reflections	4690 [R_{int} = 0.0363, R_{sigma} = 0.0412]
Data/restraints/parameters	4690/270/274
Goodness-of-fit on F^2	1.077
Final R indexes [I>=2σ (I)]	R_1 = 0.0407, wR_2 = 0.1011
Final R indexes [all data]	R_1 = 0.0507, wR_2 = 0.1057
Largest diff. peak/hole / e Å^{-3}	2.23/-0.84

The cation in complex **8** adopts the expected square planar around the Pt centre with an angular distortion on the N3-Pt1-N1 angle attributed to the pincer bite angle. The key bond angles and lengths have been provided in Table 4.22 and are as expected.

The Pt cation is planar in the solid state. Selected torsion angles are provided in Table 4.22c and confirm that the molecule is close to planar. The counter-ion sits close to perpendicular to the plane of the complex, with the angle measured as 72.97°.

Table 4.22: *a. Table of bond lengths for **8**. b. Table of bond angles for **8**. c. Torsion angles for **8**.*

a. Bond Lengths		
Atom	**Atom**	**Length/ Å**
Pt1	Cl1	2.3009(19)
Pt1	N2	1.886(3)
Pt1	N1	2.020(3)
Pt1	N3	2.009(6)

b. Bond Angles			
Atom	**Atom**	**Atom**	**Angle/°**
N2	Pt1	Cl1	179.3(2)
N2	Pt1	N1	81.33(18)
N1	Pt1	Cl1	98.73(14)
N3	Pt1	N1	162.1(2)

c. Torsion Angles				
A	**B**	**C**	**D**	**Angle/°**
Pt1	N3	C11	C10	-0.3(10)
Pt1	N3	C11	C12	-178.9(7)
N2	C6	C7	C8	0.0
N2	C6	C5	N1	0.2(7)

There is limited π interactions in the solid state with the only interaction forming between two pyridyl rings in adjacent molecules, Table 4.23. However, this complex has an extended hydrogen-bonding network, with hydrogen bonds forming between the counter ions, solvent and the pincer. This acts to stabilise the complex, in addition, the hydrogen bonds have short donor-acceptor distances and are close to linear which suggests that they are relatively strong and would require energy to break them if the lattice was to be disrupted by a vapochromic process. Therefore the energy required to overcome the hydrogen bonds in the solid state, could in part explain why the complex is not vapochromic, as it would be unfavourable to remove this solvent and replace it with a different solvent.

Table 4.23: *a. Planes Present in solid-state structure of **8**. b. π-π Interactions of **8**. c. Hydrogen bonds of **8**.*

a. Plane Identification	
Plane Number	Atoms in plane
1	N2 C10 C9 C8 C7 C6
2	N1 C5 C4 C3 C2 C1
3	N3 C11 C12 C13 C14 C15
4	C17 C18 C19 C20 C21 C16

b. π-π Interactions	
Planes	Distance (Å)
2-3[1]	3.611

c. Hydrogen bonds			
Atoms	(D…A) Distance (Å)	(H…A) Distance (Å)	D…H…A Angle/°
O4-H4A-O2	2.98(2)	2.406	128
C4-H4-O4	3.26(2)	2.36	161.4
C7-H7-O4	3.43(2)	2.54	158.7
C8-H8-O2	3.16(1)	2.371	141.9
C20-H20-O2	3.53(1)	2.629	164.0
C13-H13-O1	3.19(1)	2.478	133.9
C18-H18-O1	3.40(2)	2.66	137.8

Where [1](-X, 1-Y, 1-Z)

Crystal Packing-Stacking and Pt Offset.

The colour of this complex suggests that there is Pt interactions present in the solid state and this is clearly shown in Figure 4.50b, where there is alternating Pt distances of 3.490(5) and 3.345(5) Å, which is toward the upper limit for dz^2 interactions to occur. The alternating Pt distances occurs due to the Pt positions in the solid state and the Pt offset is measured at 0.36 Å. This is the smallest Pt offset measured for the plain terpyridine based ligand, except for the blue form of complex **2** and would explain why the complex was deep red in colour.

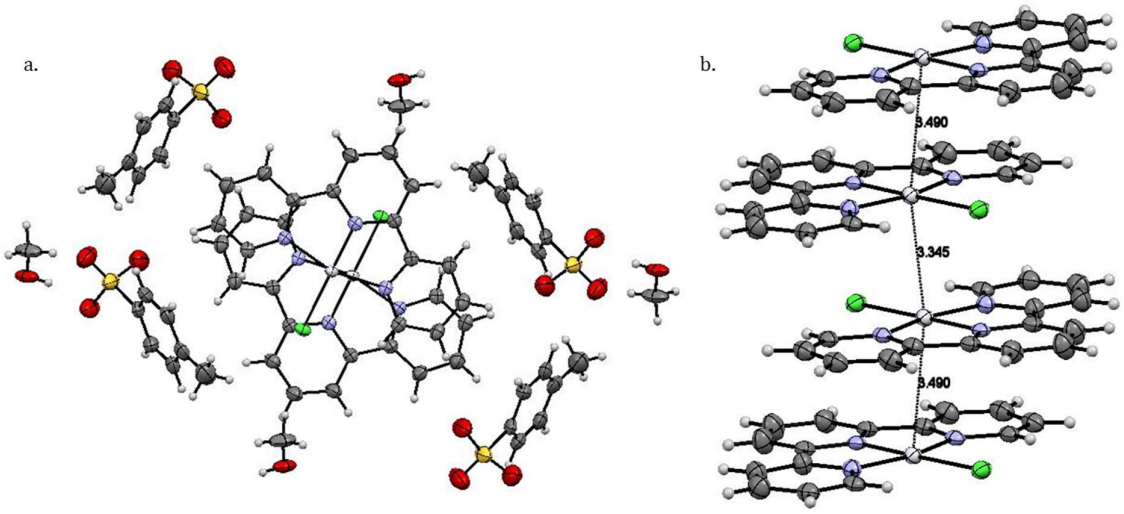

Figure 4.50*: a. Complex **8** viewed along the b axis. b. Stacking in complex **8**, Ellipsoids shown at 50% probability. Counter-ions and solvent have been removed for clarity.*

In Figure 4.50a the counter-ion and solvent molecules have been left in the diagram this is to show how the tosylate counter-ion frames the Pt complex in the solid state. An extensive hydrogen-bonding network forms between the oxygen of the tosylate groups and the hydrogens on the pincer ligand. This could explain why the complex shows no sensing capabilities because the hydrogen-bonding network provides stabilising interactions that holds the individual molecules in place in the solid state.

For each counter-ion there is a methanol molecule, due to the rapid desolvation of the crystal upon mounting to the diffractometer the methanol is only partially present in the crystal structure. However, the methanol molecule provides additional hydrogen bonding opportunities within the solid-state structure and aids the formation of an extensive network.

4.10.4 X-Ray Powder Analysis

The powder grown for this experiment could not be grown under the same conditions due to the tendency of the crystals to desolvate and lose their crystallinity. The powder trace shown in Figure 4.51 (black line) has been measured from a powder grown from the slow evaporation of methanol. While there is some agreement in the major peaks suggesting that the bulk material has a similar structure to the one detailed in Section 4.10.3 the main difference can be attributed to the lack of solvent in the bulk powder.

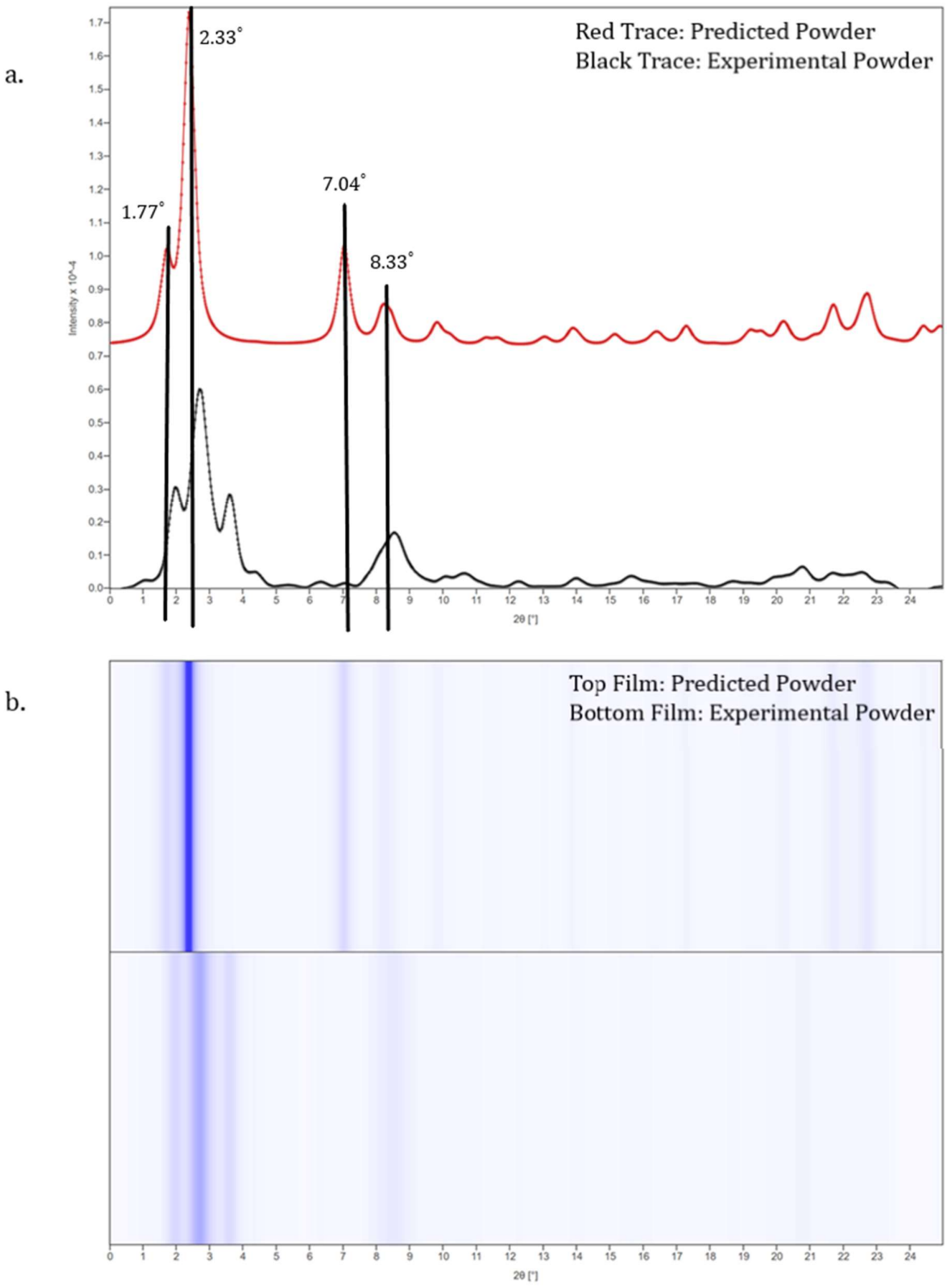

Figure 4.51: *a. Complex **8**, powder plot. b. Film representation of powder of Complex **8**. Top trace is the predicted powder (red) generated from crystal structure and bottom trace is the experimental powder (black).*

4.10.5 Reflectance Spectra

The edge of the reflectance spectrum, Figure 4.52 falls between 580-620 nm. This transition is expected for the observed colour and is in a similar range to that observed for complexes of a similar colour.

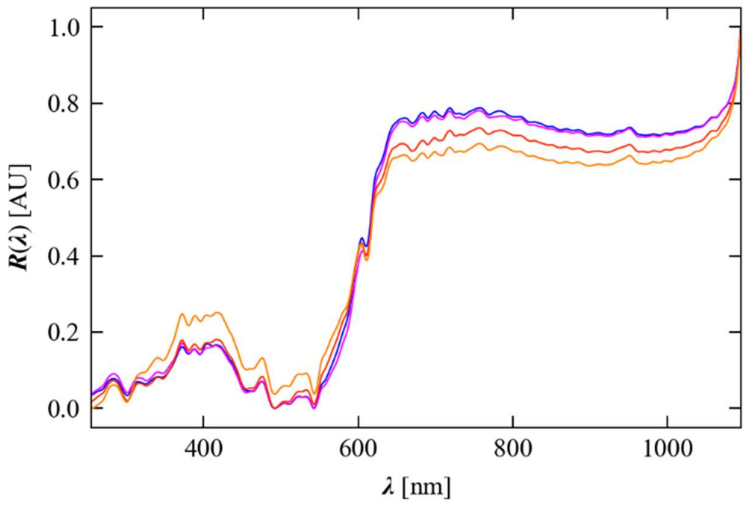

Figure 4.52*: Reflectance spectrum of Complex* ***8.***

4.11.0 4'-phenyl-2,2':6',2''-Terpyridine Platinum Chloride Tosylate. (9)

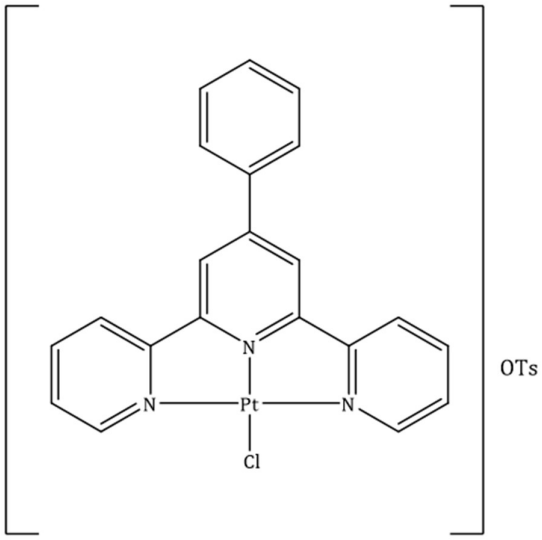

Complex **9** was synthesised using the method described in Scheme 4.3.

The structure was confirmed by ^{1}H NMR and IR spectroscopy and by single crystal X-ray diffraction.

4.11.2 Vapo/Solvachromic Behaviour

Upon filtration of the precipitate from the reaction flask, a yellow solid is obtained which, upon recrystallization from methanol, turns red.

Further investigation of the complex showed that the compound is yellow in the presence of acetonitrile and red in the presence of methanol. The complex is not vapochromic and the different coloured forms can only be accessed by recrystallization in the representative solvent. When fully dissolved in solvent the solution is a pale yellow, suggesting the effect is present in the solid state and could be caused by a Pt…Pt stacking interaction.

4.11.3 Crystal Structure Analysis

Crystal structure, Red Form

The complex was crystallised from the vapour diffusion of diethyl ether into a concentrated methanol and acetonitrile solution at -18°C. The crystals were pink, needle shaped and desolvated rapidly upon removal from the crystallisation vial. Complex **9** has crystallised in the monoclinic space group $P2_1/c$, with two molecules in the asymmetric unit. The structure is given in Figure 4.53 with structural and refinement data provided in Table 4.24.

The solvent in the crystal structure could not be modelled successfully, due to the rapid desolvation of the crystal it is likely that the solvent is not 100% present, for this reason it had been omitted from the diagrams.

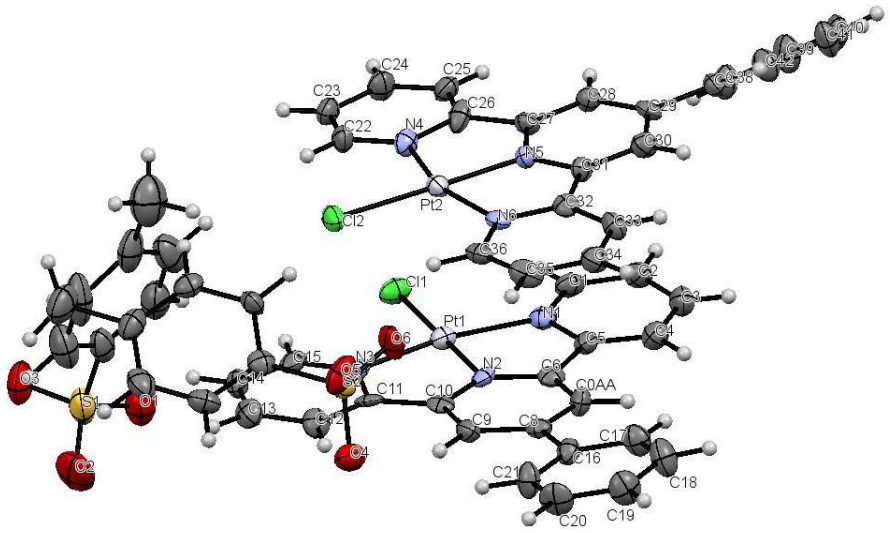

Figure 4.53*: Single crystal X-ray structure for complex* ***9*** *grown from vapour diffusion of diethyl-ether into a concentrated methanol and acetonitrile solution at -18°C. Ellipsoids shown at the 50% probability level. Solvent omitted for clarity.*

Table 4.24: *Crystal data and structure refinement for Complex* ***9***.

Identification code	S16prr216
Empirical formula	$C_{28}H_{22}ClN_3O_3PtS$
Formula weight	725.54
Temperature/K	150.00(10)
Crystal system	monoclinic
Space group	$P2_1/c$
a/ Å	12.9315(5)
b/ Å	30.1493(14)
c/ Å	13.3812(6)
α/°	90
β/°	98.949(4)
γ/°	90
Volume/ Å^3	5153.5(4)
Z	8
ρ_{calc}g/cm^3	1.870
μ/mm^{-1}	5.670
F(000)	2826.0
Crystal size/mm^3	0.7× 0.2 × 0.2
Radiation	MoKα (λ = 0.71073)
2Θ range for data collection/°	4.294 to 56.594
Index ranges	-16 ≤ h ≤ 16, -39 ≤ k ≤ 35, -17 ≤ l ≤ 14
Reflections collected	34115
Independent reflections	11033 [R_{int} = 0.0510, R_{sigma} = 0.0754]
Data/restraints/parameters	11033/0/688
Goodness-of-fit on F^2	1.046
Final R indexes [I>=2σ (I)]	R_1 = 0.0551, wR_2 = 0.0796
Final R indexes [all data]	R_1 = 0.0996, wR_2 = 0.0916
Largest diff. peak/hole / e Å^{-3}	1.91/-2.89

Each of the two independent cations in complex **9** adopt the expected square planar geometry around the Pt centre. There is an angular distortion around the Pt centres which has been caused by the bite angle of the pincer. Select bond lengths and angles have been reported in Table 4.25 and these are consistent with similar complexes.[108, 112]

The torsion angles reported in Table 4.25c, confirm that the complex is planar around the Pt centre. However, the phenyl substituent does not sit planar with respect to the plane of the Pt centres. The dihedral angles for the two molecules in the asymmetric unit are as follows:

- For Molecule 1 a dihedral angle of 10.50˚ was measured between the following planes: C6 C10 C11 Pt1 N1 C5 N3 N2 and C17 C18 C16 C20 C21 C19.
- For Molecule 2 a dihedral angle of 31.32˚ was measured between the following planes: Pt2 C31 N4 C27 C26 C32 N6 N5 and C38 C37 C39 C40 C42 C41.

The dihedral angle is different for the two molecules in the asymmetric unit; this is not unusual and has been previously reported in this thesis. The difference in dihedral angle is thought to arise to maximise packing efficiency in the solid state. The torsion angles associated with the phenyl substituent show it not to be co-planar with the pincer framework.

Table 4.25*: a. Table of bond lengths for **9**. b. Table of bond angles for **9**. c. Torsion angles for **9**.*

a. Bond Lengths		
Atom	**Atom**	**Length/ Å**
Pt1	Cl1	2.310(2)
Pt1	N2	1.945(7)
Pt1	N1	2.032(7)
Pt1	N3	2.028(7)
Pt2	Cl2	2.303(2)
Pt2	N4	2.016(7)
Pt2	N5	1.937(7)
Pt2	N6	2.024(6)

b. Bond Angles			
Atom	**Atom**	**Atom**	**Angle/˚**
N2	Pt1	Cl1	179.5(2)
N2	Pt1	N1	81.0(3)
N1	Pt1	Cl1	99.3(2)
N3	Pt1	N1	162.0(3)
N4	Pt2	Cl2	98.9(2)
N4	Pt2	N6	161.9(3)
N5	Pt2	Cl2	179.08(19)
N5	Pt2	N4	81.2(3)

c. Torsion Angles				
A	**B**	**C**	**D**	**Angle/˚**
Pt2	N4	C26	C27	-1.7(9)
Pt2	N4	C26	C25	176.2(6)
C26	C27	C28	C29	179.3(8)
C26	C27	N5	Pt2	-2.5(9)
C26	C27	N5	C31	-179.3(7)

There are a number of interactions in this complex, even when the solvent molecule in the crystal structure is disregarded. The π interactions occur between the pyridyl rings of adjacent molecules in a similar manner to other complexes in this chapter.

There are a large number of hydrogen bonds in this molecule, a high number of the hydrogen bonds form between the counter-ion and the pincer ligand of the Pt cation. Had the solvent been successfully modelled in this structure then further interactions could have been seen. A large amount of energy would be required to break these intermolecular interactions and form new ones upon removal and reintroduction of solvent which could in part explain why this complex only *'switches'* when it has been recrystallized.

Table 4.26*: a. Planes Present in solid-state structure for* ***9****. b. π-π Interactions for* ***9****. c. Hydrogen bonds for* ***9****.*

a. Plane Identification	
Plane Number	Atoms in plane
1	C37 C38 C39 C40 C41 C42
2	N6 C32 C33 C34 C35 C36
3	N5 C27 C28 C29 C30 C31
4	N4 C26 C25 C24 C23 C22
5	C16 C21 C20 C19 C18 C17
6	N2 C10 C9 C8 C0AA C6
7	N1 C5 C4 C3 C2 C1
8	N3 C15 C14 C13 C12 C11
9	C46 C47 C48 C43 C44 C45
10	C55 C54 C53 C52 C51 C50

b. π-π Interactions	
Planes	Distance (Å)
2-6[1]	3.527
2-8[2]	3.766
3-7[1]	3.600
4-7[2]	3.663

c. Hydrogen bonds			
Atoms	(D…A) Distance (Å)	(H…A) Distance (Å)	D…H…A Angle/°
C30-H30-O1	3.46(1)	2.551	167.3
C33-H33-O1	3.34(1)	2.434	165.4
C33-H33-O2	3.30(1)	2.699	123.3
C4-H4-O7	3.34(1)	2.418	174.9
COAA-HOAA-O7	3.37(1)	2.446	173.0
C17-H17-O7	3.48(1)	2.564	166.5
C19-H19-O2	3.47(1)	2.642	147.9
C23-H23-O3	3.15(1)	2.361	142.2
C49-H49C-O3	3.43(1)	2.603	144.1
C36-H36-O6	2.96(1)	2.324	125.3
C34-H34-O2	3.28(1)	2.676	123.7
C12-H12-O4	3.42(1)	2.536	157.7
C9-H9-O4	3.45(1)	2.568	158.3
C21-H21-O4	3.52(1)	2.658	155.0

Where [1](+X, +Y, +Z), [2](+X, 1/2-Y, 1/2+Z)

Crystal Packing-Stacking and Pt Offset, Red Form

The crystal packing of the red form of complex **9** is shown in Figure 4.54. Interestingly when viewed down the b axis the Pt atoms look aligned, however there are two Pt distances, which is consistent with the presence of two independent Pt centres in the asymmetric unit. When investigated, the Pt offset showed that the Pt centres are aligned, which would suggest that the two Pt distances has been caused by a different effect. Closer investigation of the crystal structure showed that the phenyl ring has twisted by varying degrees. The torsion angles have been measured as 30.82° and 6.24°, the difference in torsion angle could account for the difference in the observed Pt distances of 3.314(5) and 3.385(5) Å because of differences in the local packing

environment. The measured distances also account for the observed red colour, as the Pt centres are close enough for dz^2 orbital overlap to occur.

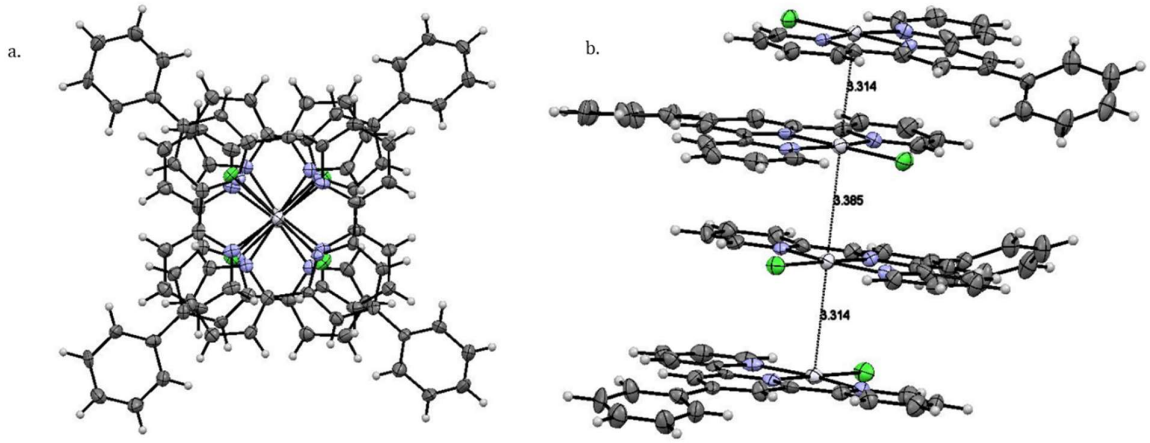

Figure 4.54*: a. Complex **9** viewed along the b axis. b. Stacking in complex **9**, Ellipsoids shown at 50% probability. Counter-ions and solvent have been removed for clarity.*

Unfortunately, a crystal of the yellow form could not be grown that was suitable for single crystal X-ray diffraction analysis.

4.11.4 X-Ray Powder Analysis

The two forms of complex **9** could not be studied using single crystal X-ray diffraction due to the unsuitability of the yellow crystals, however a powder analysis could be achieved with this material. Figure 4.55 shows the results of this analysis. The red powder grown from methanol is in good agreement with the predicted powder generated from the crystal structure, this can be seen from the graph and the film trace.

The yellow powder, the yellow line in Figure 4.55 is similar to the powder trace of the red form however there are some distinct differences for example the intensity of the peak in the 2θ range 0-2.1, have been reversed. The similarity in the trace would suggest that it is the same complex however there are differences present in the solid-state packing of the structure.

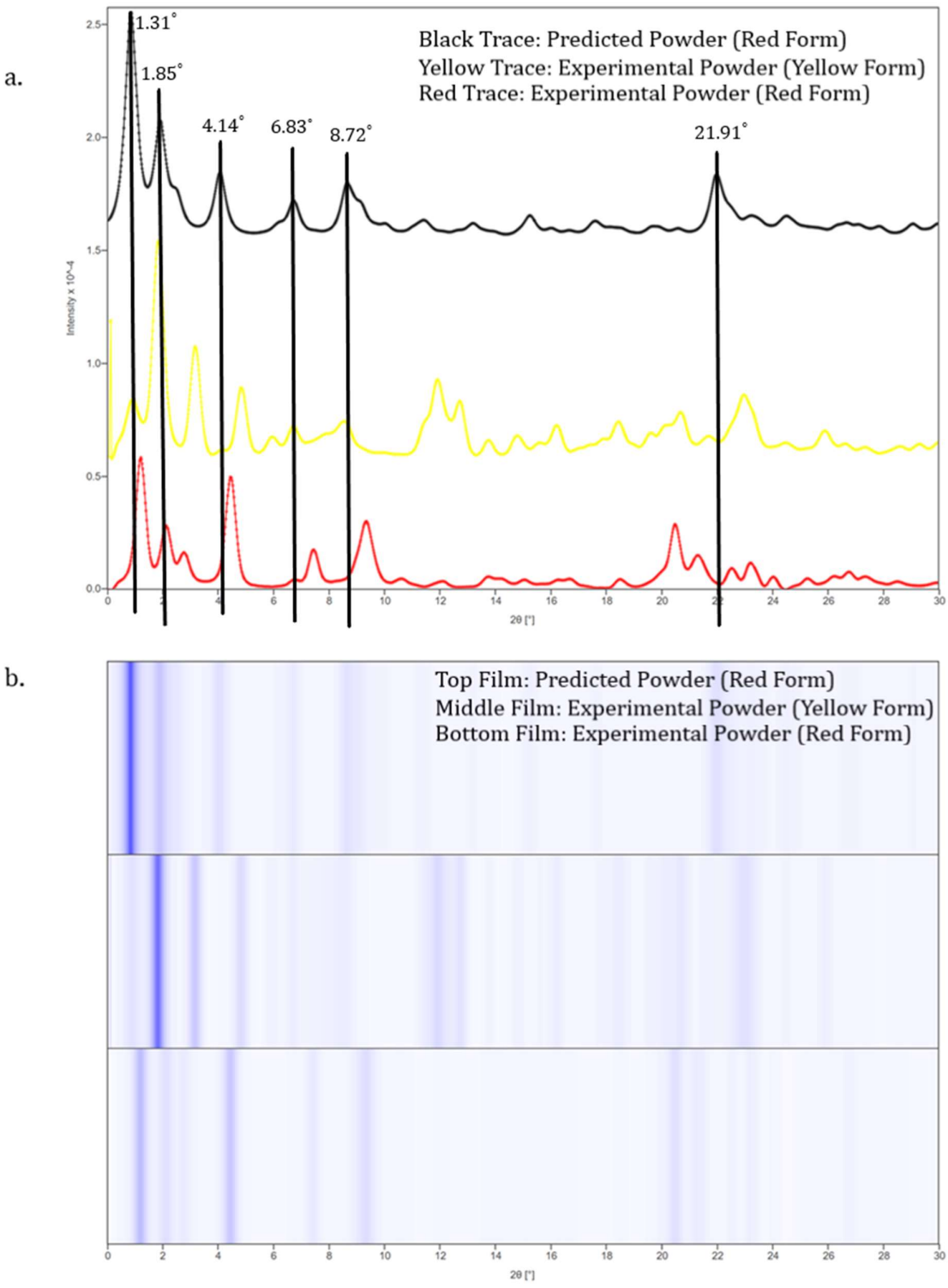

Figure 4.55: *a. Complex* ***9****, powder plot. b. Film representation of powder of Complex* ***9****. Black trace is the predicted Red form from the crystal structure, red line is the red form and the yellow line is the yellow form.*

4.12.0. 4'-(p-tolyl)-2,2':6',2''-Terpyridine Platinum Chloride Tosylate (10)

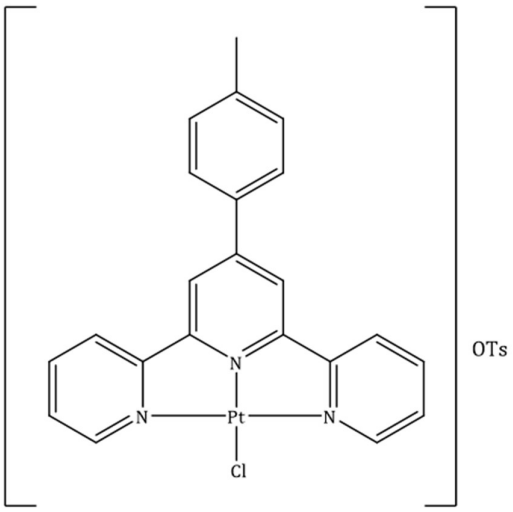

A counter-ion exchange method outlined in Scheme 4.4 was successful in synthesising this complex.

The complex was fully characterised by ^{1}H NMR spectroscopy where the appropriate peaks were present in the NMR spectra for the counter-ion. These were as follows, for the aromatic hydrogens there was a defined doublet 7.11 ppm and a doublet overlapped with terpyridine ligand peaks at 7.47 ppm, with the methyl hydrogens at 2.27 ppm. In addition to the NMR spectroscopy, IR spectroscopy and single crystal X-ray data were collected and used to characterise the compound.

4.12.1 Solution State Spectroscopy

The UV-Vis spectra for complex **10** recorded in the solution state is given in Figure 4.56.

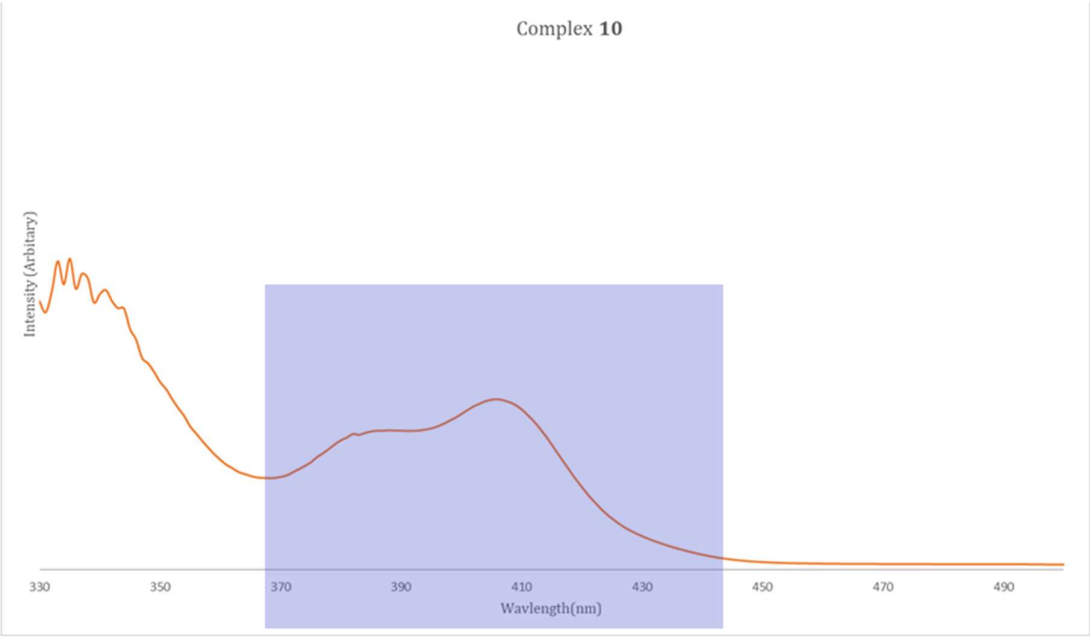

Figure 4.56: *Absorption spectrum of complex 10. Solution concentration 1×10^{-4} M in acetonitrile. MLCT highlighted*

When comparing Figure 4.33 with the UV-Vis spectra for complexes **4** and **7**, Figure 4.30 and 4.56 respectively, the π-π transition does not seem to be defined in this instance. The π-π transitions are centred on the terpyridyl ligand and are found in the range 300-360 nm. The peak for the metal to ligand transition is still well defined in the range 380-420 nm. This transition has been allowed because of the large spin orbit coupling of the Pt centre.

4.12.2 Vapo/Solvachromic Behaviour

As with the other tolyl-substituted complexes synthesised during the process of this report, this complex does not display any changes in spectral properties. The same regime of testing described for other complexes was used to confirm this.

4.12.3 Crystal Structure Analysis

Crystal Structure.

Yellow crystals of complex **10** were grown by the slow evaporation of acetonitrile. It is important to note that the acetonitrile is not dry, which is why in this instance there is a molecule of water in the unit cell. Complex **10** crystallises in the triclinic space group *P*-1, with one molecule in the asymmetric unit. The structure of complex **10** is given in Figure 4.57 with structural and refinement data available in Table 4.27.

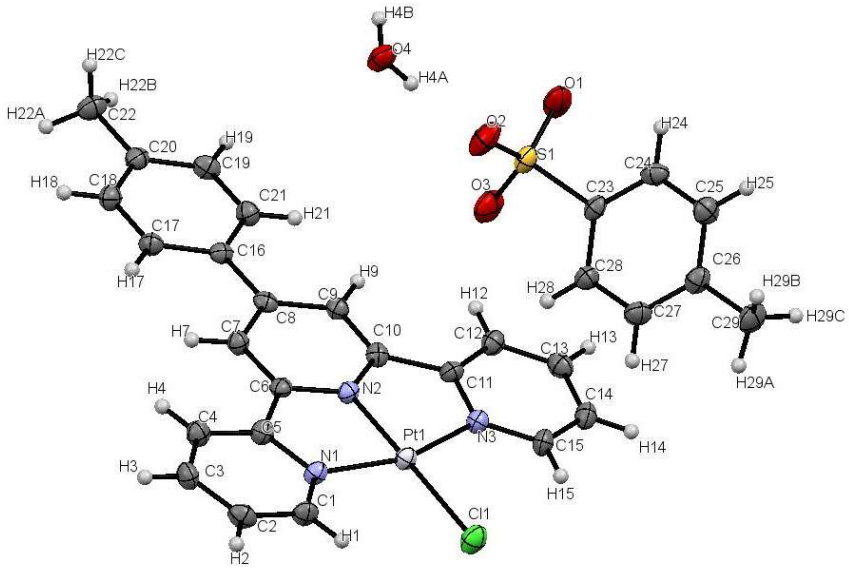

Figure 4.57*: Single crystal X-ray structure for complex **10** grown from slow evaporation of an acetonitrile. Ellipsoids shown at 50% probability level.*

Table 4.27: *Crystal data and structure refinement for complex **10**.*

Identification code	s16prr61
Empirical formula	$C_{29}N_3O_3SClPtH_{26}$
Formula weight	712.92
Temperature/K	150
Crystal system	triclinic
Space group	*P*-1
a/ Å	7.7304(3)
b/ Å	11.5138(3)
c/ Å	15.7685(6)
α/°	82.406(3)
β/°	77.868(3)
γ/°	70.791(3)
Volume/ Å^3	1292.73(8)
Z	2
ρ_{calc}g/cm^3	1.832
μ/mm^{-1}	5.656
F(000)	672.0
Crystal size/mm^3	0.5 × 0.1 × 0.2
Radiation	MoKα (λ = 0.71073 Å)
2Θ range for data collection/°	4.444 to 58.778
Index ranges	-10 ≤ h ≤ 10, -15 ≤ k ≤ 15, -21 ≤ l ≤ 21
Reflections collected	19477
Independent reflections	6194 [R_{int} = 0.0366, R_{sigma} = 0.0430]
Data/restraints/parameters	6194/0/358
Goodness-of-fit on F^2	1.093
Final R indexes [I>=2σ (I)]	R_1 = 0.0272, wR_2 = 0.0646
Final R indexes [all data]	R_1 = 0.0336, wR_2 = 0.0820
Largest diff. peak/hole / e Å^{-3}	0.65/-0.98

As in all the previous salts the Pt centre in complex **10** adopts a square planar geometry with an angle of 161.73(15)˚ for N1-Pt1-N3, this distortion from 180˚ can be attributed to the bite angle of the pincer ligand. A selection of bond lengths and angles have been provided in Table 4.28a/b and are as expected for a complex of this type.

Unlike complex **9**, **10** appears to be planar in the solid state. This is confirmed by the torsion angles that are close to 0° or 180°, Table 4.28c, and the dihedral angle of 0 ° when the plane of the Pt centre is compared to the plane of the substituent on the ligand.

Table 4.28: *a. Table of bond lengths for **10**. b. Table of bond angles for **10**. c. Torsion angles for **10**.*

a. Bond Lengths		
Atom	**Atom**	**Length/ Å**
Pt1	Cl1	2.3155(11)
Pt1	N3	2.024(4)
Pt1	N2	1.941(3)
Pt1	N1	2.017(4)

b. Bond Angles			
Atom	**Atom**	**Atom**	**Angle/°**
N3	Pt1	Cl1	99.01(11)
N2	Pt1	Cl1	178.83(10)
N2	Pt1	N3	80.91(14)
N1	Pt1	N3	161.73(15)

c. Torsion Angles				
A	**B**	**C**	**D**	**Angle/°**
Pt1	N2	C10	C11	0.1(5)
Pt1	N2	C10	C9	179.0(3)
Pt1	N1	C5	C6	1.2(5)
C16	C8	C9	C10	-179.1(4)
C16	C8	C7	C6	-179.2(4)
C16	C17	C18	C20	0.3(7)

In this complex similar π bonding interactions are observed with analogous complexes in this chapter, Table 4.29b. These interactions have occurred due to the head to toe stacking observed in the solid state, Figure 4.58.

Interestingly this complex has an extensive hydrogen-bonding network, with hydrogens bonds forming between the solvent and the pincer in addition to occurring between the solvent and the counter-ion. Distances and angles have been provided in Table 4.29c, however a deeper analysis of the hydrogen bonding in this complex is available in Figure 4.59.

Table 4.29: *a. Planes Present in solid-state structure for **10**. b. π-π Interactions for **10**. c. Hydrogen bonds for **10**.*

a. Plane Identification	
Plane Number	Atoms in plane
1	C16 C21 C19 C20 C18 C17
2	N2 C10 C9 C8 C7 C6
3	N3 C15 C14 C13 C12 C11
4	N1 C1 C2 C3 C4 C5
5	C27 C28 C23 C24 C25 C26

b. π-π Interactions	
Planes	Distance (Å)
1-3[1]	3.639
1-4[2]	3.758
2-2[2]	3.975

c. Hydrogen bonds			
Atoms	(D…A) Distance (Å)	(H…A) Distance (Å)	D…H…A Angle/°
C4-H4-O3	3.348(5)	2.427	171.0
C21-H21-O4	3.310(6)	2.384	173.5
C9-H9-O4	3.321(7)	2.397	171.8
C12-H12-O4	3.461(6)	2.543	169.7
O4-H4B-O1	2.768(5)	1.977	154.2
O4-H4A-O2	2.743(5)	1.902	170.2

Where [1](-X, 1-Y, 1-Z), [2](1-X, 1-Y, 1-Z)

Crystal Packing: Stacking and Pt Offset.

This complex is yellow in the solid state and as expected, there are no significant Pt…Pt interactions present. Figure 4.58 shows the Pt alignment and stacking in the solid state.

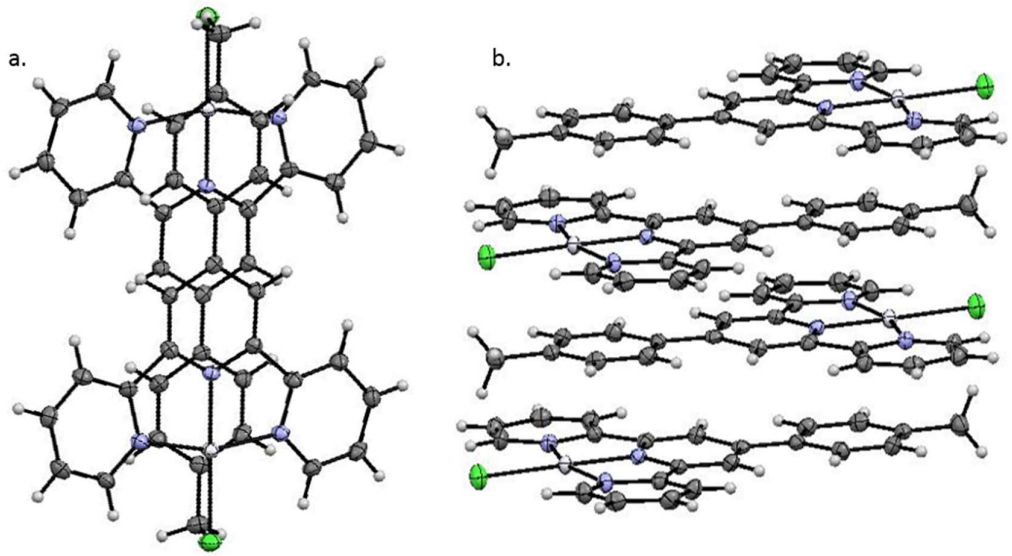

Figure 4.58*: a. Complex **10** viewed along the a axis. b. Stacking in complex **10**. Ellipsoids shown at 50% probability. Counter-ions and solvent have been removed for clarity.*

The packing for complex **10** is analogous to that observed for complex **4**. In each case they have stacked in a head to toe manner, to maximise π overlap as shown in Figure 4.58. The distance between the planes of the molecules is measured at 3.321 Å; this is a comparable distance to that measured for complex **4**. This short distance between the molecules facilitates the π-stacking observed.

The original hypothesis for the inclusion of this counter-ion in this investigation stated that the tosylate anion was thought to sit planar and parallel to the molecules in the solid state. Figure 4.57 shows this is not the case and the tosylate anion actually sits perpendicular to the plane of the molecule. This has enabled it to form a hydrogen bond with the solvent, as shown in Figure 4.59.

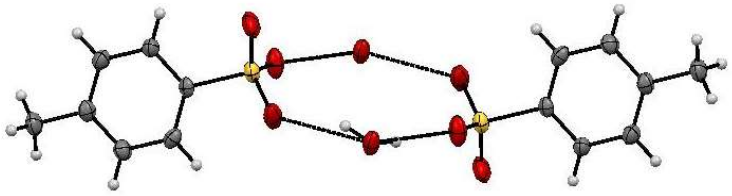

Figure 4.59*: Hydrogen bonding between counter-ion and solvent. Pt molecules have been removed for clarity. Ellipsoids shown at the 50% probability level*

This hydrogen bonding network can be described by graph notation, which utilises Etter's rules.[113] The graph set is: $R\frac{4}{4}(12)$, and the ring sits on an inversion centre in the crystal. The Pt

terpyridine complex does not have good hydrogen bonding acceptors, with the chlorine atom being the only possibility. The most stable configuration is shown in Figure 4.59 and this ring network has formed in the channels either side of the Pt molecules, which is one potential reason why the counter-ion sits perpendicular to the plane of the molecule.

4.12.4 X-Ray Powder Analysis

The powder analysis shows good agreement between the predicted powder trace the experimental trace, this means that in this instance the obtained crystal structure is representative of the bulk.

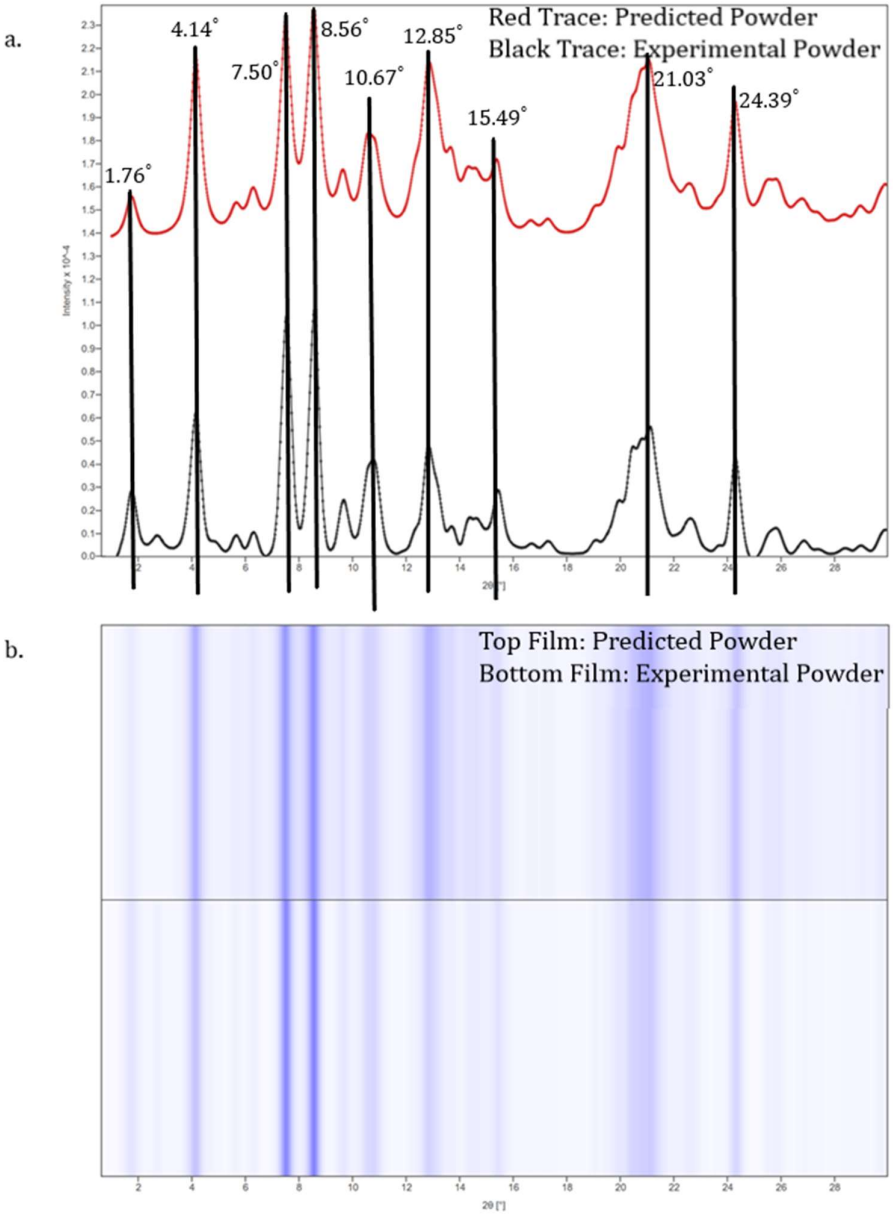

Figure 4.60: *a. Complex **10**, powder plot. b. Film representation of powder of Complex **10**. Red trace the predicted powder trace from the crystal structure. Black trace is the experimental powder*

4.13.0 2,2':6',2''-Terpyridine Platinum Chloride Tetraphenylborate (11)

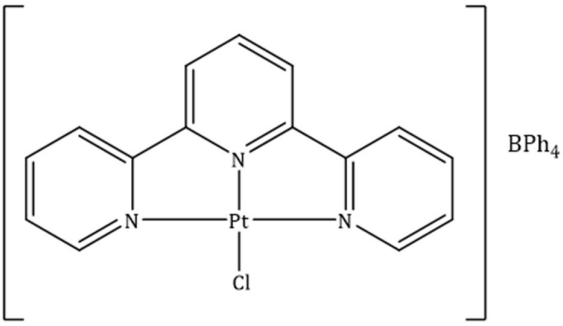

Complex **11** was synthesised using a counter-ion exchange method, described in Scheme 4.4.

The product was fully characterised by ^{1}H NMR spectroscopy: peaks at 7.16 ppm (m, 8H), 6.92 ppm (t,8H) and 6.78 ppm (t,4H) in the spectrum can be assigned to the counter-ion. In addition an IR spectrum was obtained and a crystal structure were used to confirm the identity of the product.

4.13.1 Solution State Spectroscopy

Solution state UV-Vis is shown in Figure 4.61.

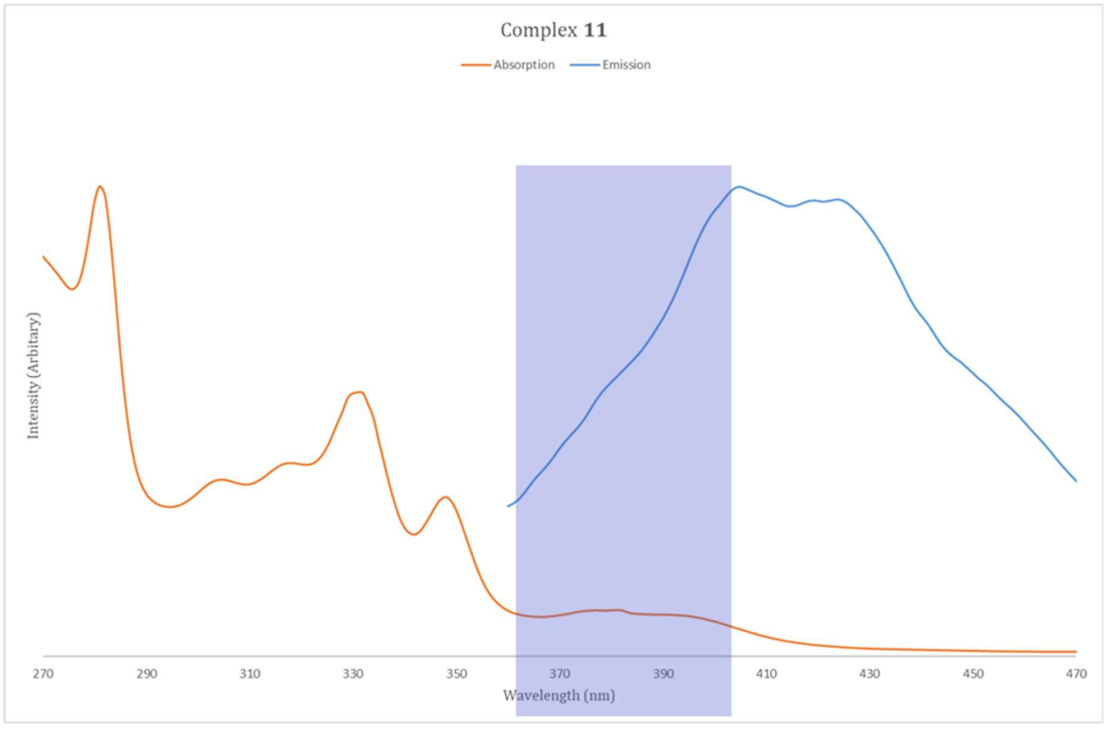

Figure 4.61: *Absorption spectrum of complex **11**, MLCT highlighted. Emission spectrum λ_{ex}:340 nm. Solution concentration 1×10^{-4} M in acetonitrile.*

As observed with complex **5**, the UV-Vis spectrum for complex **11** exhibits the same profile as complex **1**. There is a clear peak between 280-340 nm, which represents π-π transitions that are based on the terpyridine ligand. With a subsequent peak at approximately 350 nm that can be assigned to the MLCT band.

The emission properties of this complex are very weak in solution and the profile is shown in Figure 4.61. The peak lies at 420 nm, this provides a Stokes Shift of 30 nm. The measured peak looks as if it could split into two distinct peaks and provide some fine detail and further information about the excited states of the Pt complex.

4.13.2 Vapo/Solvachromic Behaviour

The BPh_4^- counter-ion was used in this investigation to completely disrupt the stacking present in systems with a smaller counter-ion. The change of colour from bright red for complex **1** to beige would suggest that indeed this is what has occurred. The complex was tested for any sensitivity to VOCs and pressure as well as any changes when recrystallized from varying solvents, but as expected no changes in spectral properties were observed.

4.13.3 Crystal Structure Analysis

Crystal Structure.

Crystals of complex **11** were grown by vapour diffusion of diethyl ether into a concentrated acetonitrile solution at -18°C. The crystals grown were beige in colour and a block in shape.
The structure is given in Figure 4.62, structural and refinement data is available in Table 4.30.

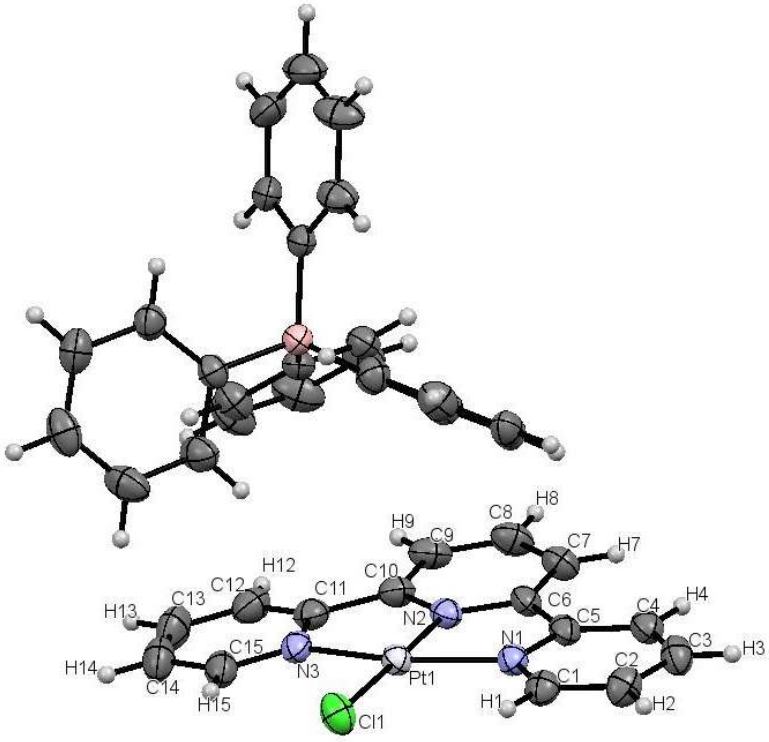

Figure 4.62*: Single crystal X-ray structure for complex **11**. Ellipsoids shown at 50% for clarity.*

Table 4.30: *Crystal data and structure refinement for Complex **11.***

Identification code	p16prr40
Empirical formula	$C_{39}BN_3ClPtH_{31}$
Formula weight	752.02
Temperature/K	150
Crystal system	monoclinic
Space group	$P2_1/c$
a/ Å	15.8712(5)
b/ Å	13.3056(3)
c/ Å	16.1658(4)
α/°	90
β/°	115.500(3)
γ/°	90
Volume/ Å^3	3081.26(16)
Z	4
ρ_{calc}mg/mm^3	1.621
μ/mm^{-1}	4.672
F(000)	1421.0
Crystal size/mm^3	0.6 × 0.4 × 0.5
Radiation	MoKα (λ = 0.71073 Å)
2Θ range for data collection	5.058 to 59.222°
Index ranges	-17 ≤ h ≤ 20, -18 ≤ k ≤ 16, -22 ≤ l ≤ 22
Reflections collected	23669
Independent reflections	7599 [R_{int} = 0.0344, R_{sigma} = 0.0434]
Data/restraints/parameters	7599/0/406
Goodness-of-fit on F^2	1.115
Final R indexes [I>=2σ (I)]	R_1 = 0.0389, wR_2 = 0.0924
Final R indexes [all data]	R_1 = 0.0603, wR_2 = 0.1008
Largest diff. peak/hole / e Å^{-3}	3.90/-2.05

The Pt centre in cation in complex **11** is square planar with the expected N1-Pt1-N3 angular distortion of 162.42(18)˚. The bond lengths and angles in this complex are comparable to similar complexes.

This complex is planar in the solid state with a 0° dihedral angle for the terpy ligand. The angles of the pyridyl rings relative to the plane of the Pt centre was also analysed and the associated dihedral angle was found to be negligible. Table 4.31 contains a sample of the torsion angles in this complex, the majority are close to linear. This further confirms that the complex is planar in the solid state.

Table 4.31: *a. Table of bond lengths for **11**. b. Table of bond angles for **11**. c. Torsion angles for **11**.*

a. Bond Lengths		
Atom	**Atom**	**Length/ Å**
Pt1	Cl1	2.2900(13)
Pt1	N2	1.930(4)
Pt1	N1	2.012(4)
Pt1	N3	2.014(4)

b. Bond Angles			
Atom	**Atom**	**Atom**	**Angle/°**
N2	Pt1	N1	81.05(17)
N1	Pt1	Cl1	99.35(13)
N1	Pt1	N3	162.41(18)
N2	Pt1	Cl1	179.25(13)

c. Torsion Angles				
A	**B**	**C**	**D**	**Angle/°**
C11	C10	C9	C8	-179.5(5)
C11	C12	C13	C14	-1.5(9)
C5	N1	C1	C2	1.0(7)
C5	C4	C3	C2	0.1(8)

There are no π-π interactions in this complex. Further analysis of the crystal structure shows that the counter-ion has disrupted the stacking in the complex so that the discrete dimers that form are too far apart to form any π interactions, Figure 4.63. Hydrogen bonds form in the layers of the crystal structure, the data is provided in Table 4.32.

Table 4.32: *Hydrogen bonds for **11**.*

Hydrogen bonds			
Atoms	(D…A) Distance (Å)	(H…A) Distance (Å)	D…H…A Angle/°
C8-H8-Cl1	3.782(7)	2.938	151.5

Crystal Packing: Stacking and Pt Offset.

Inspection of the packing of this structure shows potential dimer stacking in the solid state as shown in Figure 4.63b. The measured distances between the Pt atoms yields a distance of 4.1383(4) Å, this falls outside of the distance required for dz^2 orbital overlap between adjacent Pt centres.

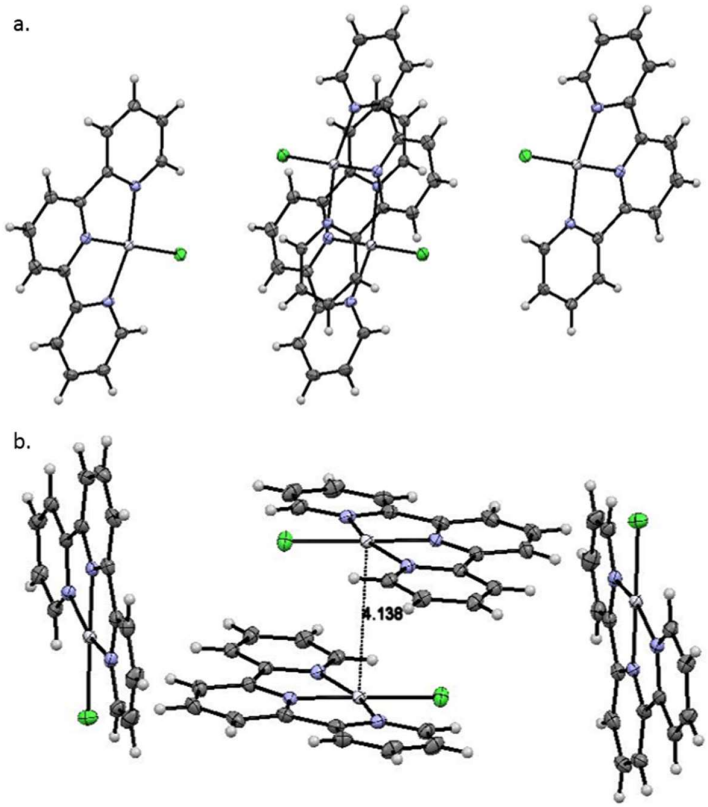

Figure 4.63*: a. Complex **11** viewed along the b axis. b. Dimer stacking present in complex **11**. Ellipsoids shown at 50% probability. Counter-ions removed for clarity.*

In Figure 4.63b the Pt centres in the dimers look aligned, it is not until the molecule is viewed along the *b* axis in Figure 4.63a that it can be seen clearly that this is not the case. This is confirmed by the calculated Pt offset value of 2.46 Å. It is for both of these reasons that this complex is not brightly coloured in the solid state.

The reason for this change in stacking can be attributed to the larger counter-ion, which has completely disrupted the extended dz^2 orbital interactions seen for complex **1** and **4**. The anion now dominates the packing instead of the platinum complex. The counter-ion has arranged in such a way that 4 of the molecules form a cage-like structure in which the two cations sit. This extended network of counter-ions is the most sterically favourable because the phenyl rings have arranged in such a way that they are not in close contact with each other. This is different to the arrangement of counter-ions seen for complex **1**, here the counter ions have arranged in channels running parallel to the cation stacks. This is favourable in this instance because the counter ions are able to halogen bond to the solvent molecules in the structure.

4.14.0 4'-phenyl-2,2':6',2''-Terpyridine Platinum Chloride Tetraphenylborate. (12)

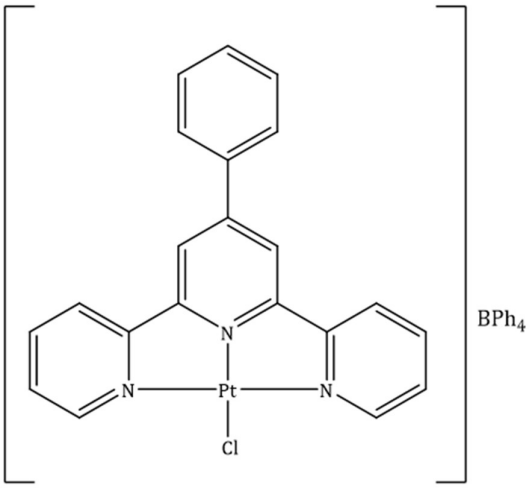

Complex **12** was synthesised using a counter-ion exchange reaction, this method is detailed in Scheme 4.4.

The presence of the BPh_4^- counter-ion was confirmed by ^1H NMR spectroscopy. The peaks representing the counter-ion were present in the spectrum at 7.16 ppm (m, 8H), 6.92 ppm (t, 8H) and 6.78 ppm (t, 4H). An IR spectrum and a crystal structure were also obtained for the complex, which confirmed it was the correct structure.

4.14.1 Solution State Spectroscopy

Figure 4.64 is the solution state UV-Vis for complex **12.** The emission spectrum was also recorded but no emission for this complex in the solution state was observed.

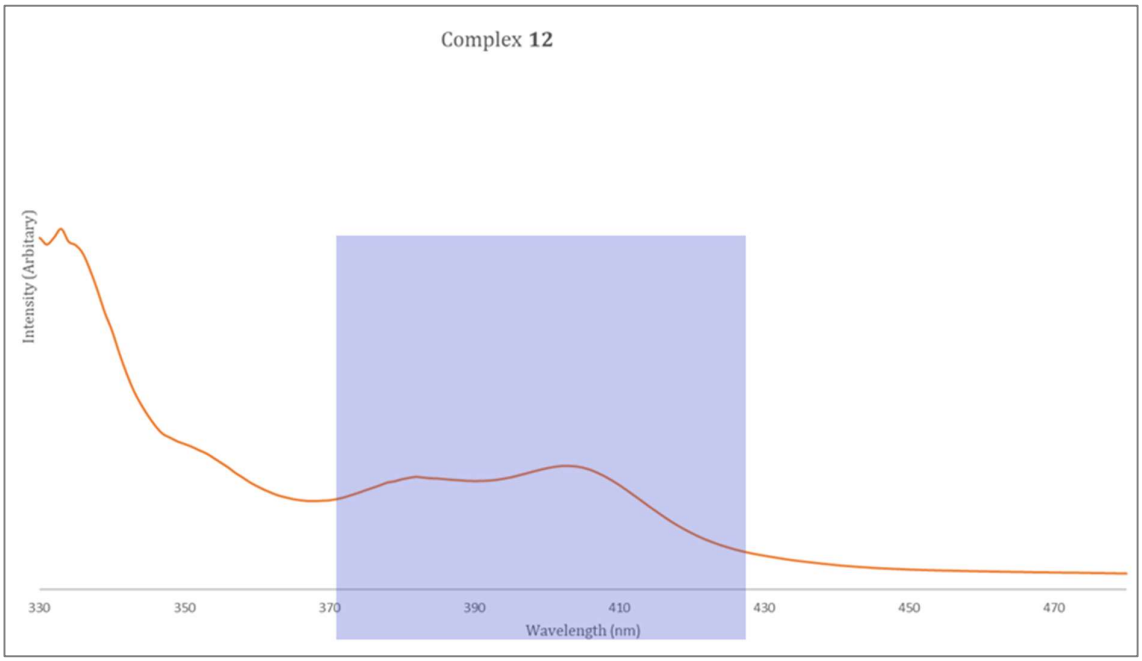

Figure 4.64*: Absorption spectrum of complex* ***12.*** *Solution concentration* 1×10^{-4} *M in acetonitrile. MLCT highlighted.*

As expected the UV-Vis spectra is the same as that observed for complex **3** and **6**; in this instance the same assignments can be made.

4.14.2 Vapo/Solvachromic Behaviour

As with the plain terpyridine complex, there has been a significant colour change during the counter-ion exchange reaction, from brick red to brown. This colour change is indicative that the counter-ion has disrupted the stacking in the complex. No changes in spectral properties were observed for this complex when the compound was investigated for vapochromic and mechanochromic behaviour. The same techniques described earlier in this chapter were used here.

4.14.3 Crystal Structure Analysis

Crystal Structure.

Complex **12** was crystallised by slow evaporation of acetonitrile. It adopts the monoclinic space group *C*2/*c*. The structure is shown in Figure 4.65, structural and refinement data is given in Table 4.33.

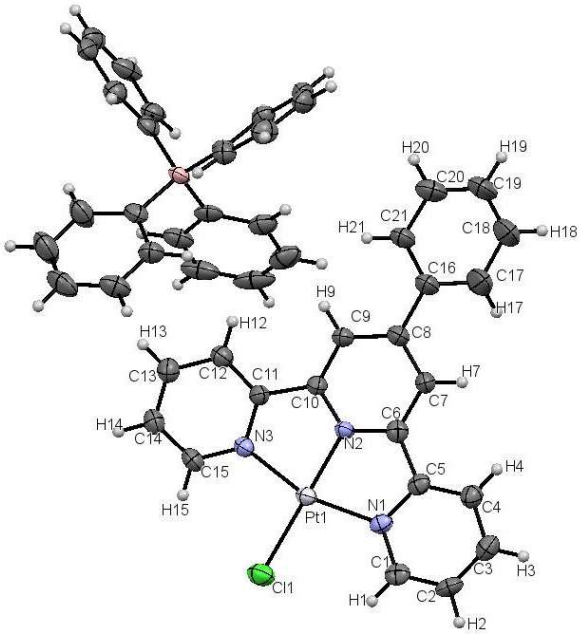

Figure 4.65*: Single crystal X-ray structure for complex* ***12****. Ellipsoids shown at 50% probability for clarity.*

Table 4.33: *Crystal data and structure refinement for Complex **12**.*

Identification code	p16prr53
Empirical formula	$C_{45}BN_3ClPtH_{35}$
Formula weight	823.96
Temperature/K	150
Crystal system	monoclinic
Space group	$C2/c$
a/ Å	28.9947(7)
b/ Å	17.2095(4)
c/ Å	15.8074(4)
α/°	90
β/°	101.452(2)
γ/°	90
Volume/ Å^3	7730.6(3)
Z	8
ρ_{calc}mg/mm^3	1.416
μ/mm^{-1}	3.732
F(000)	3129.0
Crystal size/mm^3	0.5 × 0.6 × 0.6
Radiation	MoKα (λ = 0.71073 Å)
2Θ range for data collection	5.15 to 59.322°
Index ranges	-37 ≤ h ≤ 25, -23 ≤ k ≤ 23, -21 ≤ l ≤ 19
Reflections collected	27315
Independent reflections	9403 [R_{int} = 0.0389, R_{sigma} = 0.0522]
Data/restraints/parameters	9403/0/460
Goodness-of-fit on F^2	1.091
Final R indexes [I>=2σ (I)]	R_1 = 0.0423, wR_2 = 0.1232
Final R indexes [all data]	R_1 = 0.0836, wR_2 = 0.1406
Largest diff. peak/hole / e Å^{-3}	2.36/-0.82

As with all the other complexes in this chapter the Pt centre adopts the expected square planar geometry in the complex salt **12**.The angular distortion around the N1-Pt1-N3 unit is attributed to the bite angle of the pincer.[100, 114] The bond lengths and angles are in agreement with other complexes of this type, Table 4.34a/b.

The cation in complex **12** does not adopt a completely planar configuration in the solid state as with other complexes detailed in this chapter with the same ligand substitution pattern. The dihedral angle was measured as 29.32˚, between the following two planes: C11 N2 N1 N3 C10 Pt1 C6 C5 and C19 C20 C17 C21 C16 C18. While the torsion angles centred on the Pt centre are close to planarity, Table 4.34c, those between the pincer and the arene substituent are not planar. Comparing these measurements to similar complexes in this chapter, this is the smallest measured dihedral angle. However, the measured dihedral angles all fall between the range 29-36˚, this suggests that the arene substituent will only twist a certain amount in the solid state.

Table 4.34: *a. Table of bond lengths for **12**. b. Table of bond angles for **12**. c. Torsion angles for **12**.*

a. Bond Lengths		
Atom	**Atom**	**Length/ Å**
Pt1	N3	2.021(5)
Pt1	N2	1.923(4)
Pt1	N1	2.018(5)
Pt1	Cl1	2.2853(17)

b. Bond Angles			
Atom	**Atom**	**Atom**	**Angle/°**
N2	Pt1	N1	81.0(2)
N2	Pt1	Cl1	179.39(15)
N1	Pt1	N3	161.9(2)
N1	Pt1	Cl1	99.16(15)

c. Torsion Angles				
A	**B**	**C**	**D**	**Angle/°**
Pt1	N3	C15	C14	-178.6(5)
Pt1	N2	C10	C11	0.3(7)
Pt1	N2	C10	C9	179.5(5)
Pt1	N2	C6	C5	0.7(7)

There are a limited number of π interactions in complex **12** they are found between the pyridyl rings of the pincer ligand in adjacent molecules. Figure 4.66 illustrates the extended packing of this complex in the solid state. No hydrogen bonds are found in the crystal structure of this complex.

Table 4.35: *a. Planes Present in solid-state structure of **12**. b. π-π Interactions of **12**.*

a. Plane Identification	
Plane Number	Atoms in plane
1	C16 C17 C18 C19 C20 C21
2	N3 C15 C14 C13 C12 C11
3	N2 C6 C7 C8 C9 C10
4	N1 C5 C4 C3 C2 C1
5	C30 C31 C32 C33 C28 C29
6	C22 C23 C24 C25 C26 C27
7	C40 C41 C42 C43 C44 C45
8	C34 C39 C38 C37 C36 C35

b. π-π Interactions	
Planes	Distance (Å)
2-4[1]	3.584
4-4[2]	3.951

Where [1](1-X, 1-Y, 1-Z), [2](1-X, +Y, 1/2-Z)

Crystal Packing: Stacking and Pt Offset.

Even with the large counter-ion there is localised paired stacking in the structure, the distance between the Pt centres in adjacent molecules is measured at 3.3415(6) Å (Figure 4.64b). This paired interaction is not enough to create a vibrantly coloured solid, as it appears beige in powder and crystal form. The pairs are separated by a diagonal distance of 5.070 Å, this diagonal distance is to long for any type of Pt…Pt interaction and completely disrupts overlap.

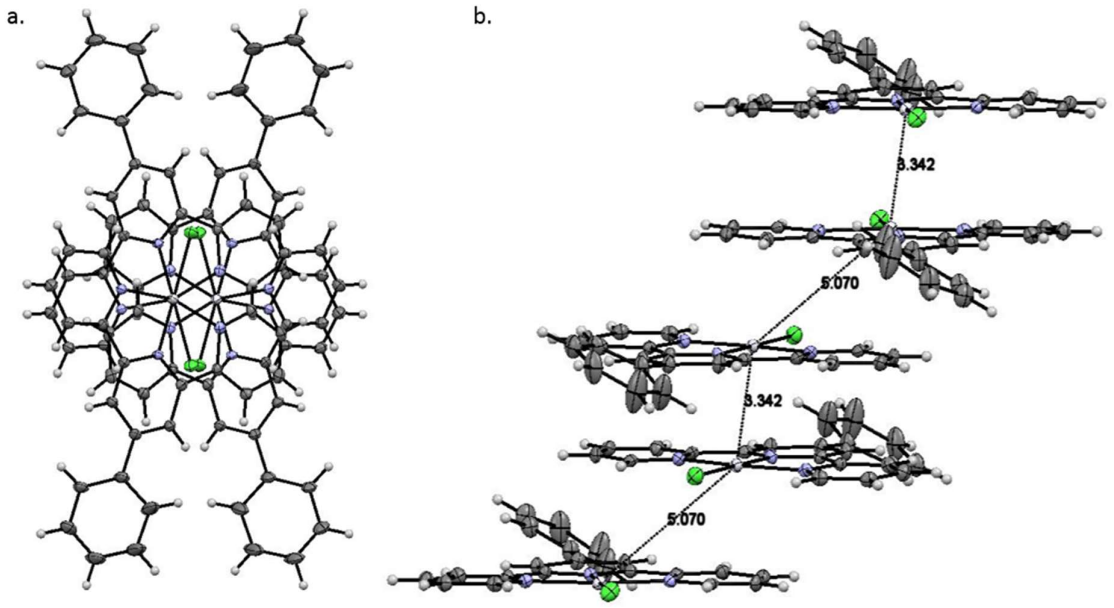

Figure 4.66*: a. Complex **12** viewed along the c axis. b. Stacking between pairs of molecules in complex **12**. Ellipsoids shown at 50% probability. Counter-ions removed for clarity.*

The paired molecules stack head to toe. Figure 4.66a shows that the Pt centres are not aligned with two positions in the structure. The alignment could not be calculated using the method described in Section 4.1.2, because of this the Pt-Pt-Pt angle was measured for this complex. The measured value was 139°, for complexes that are aligned this value would be close to 180°. The first impression of the stacking in this complex was therefore incorrect as the angle is too far away from linearity for dz^2 orbital overlap. This misalignment of the Pt centres seems to have been caused by the twisting of the phenyl group on the terpyridine ligand, not allowing the molecules to sit directly on top of each other. This is confirmed by the increase in torsion angle from 23° to 28°, when compared to complex **3**. The increase in torsion angle could have been caused by the relative rigidity of the BPh_4^- anion in comparison to the phenyl group on the pincer. The BPh_4^- anion is constrained to a tetrahedral geometry, to minimise steric interactions. These phenyl rings cannot twist in the same manner in comparison to the phenyl/ tolyl groups on the back of the pincer ligand, which have the ability to fully rotate. The increase in torsion angle could therefore be attributed to minimisation of steric interactions between the cation and anion.

Unlike complex **11,** the counter-ions sit in channels either side of the platinum molecules. One potential reason for this change in counter-ion arrangement could be attributed to the phenyl ring on the pincer ligand. This additional group has increased the steric bulk of the molecule, it is now of comparable size to the counter-ion because of this it would no longer fit in the caged structure.

4.14.4 X-Ray Powder Analysis

The predicted powder trace from the crystal structure is very simple and the recorded powder trace shares that simplicity. However as can be seen most clearly from Figure 4.67b the peaks of the experimental powder seem to be shifted relative to the predicted. While the crystallised

powder seems to contain the majority of the polymorph discussed in Section 4.14.3 there seems to be at least one more polymorph present in the bulk powder.

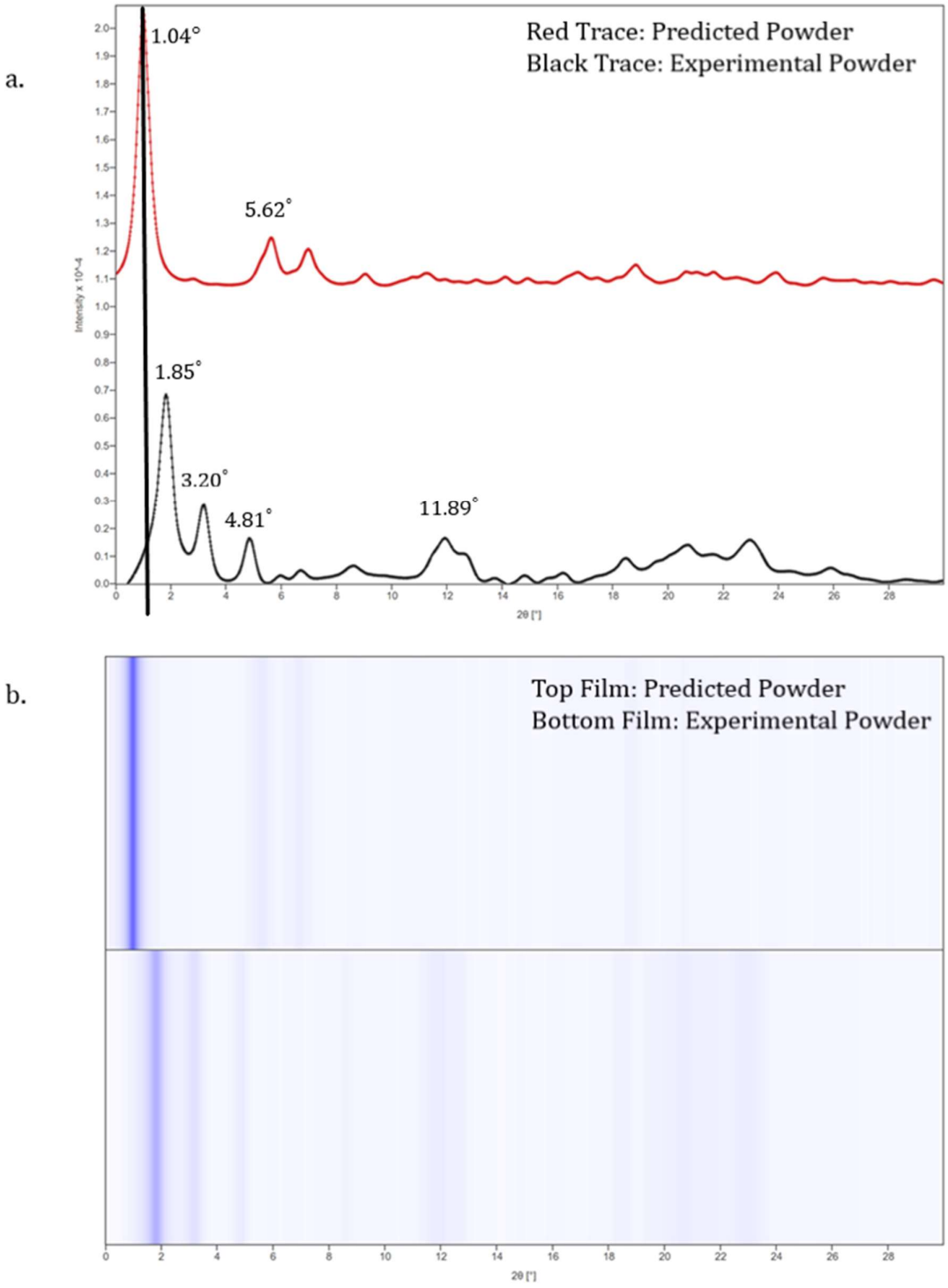

Figure 4.67*: a. Complex **12**, powder plot. b. Film representation of powder of Complex **12**. Red trace the predicted powder trace from the crystal structure. Black trace is the experimental powder*

4.14.5 Reflectance Spectra

The edge of the reflectance spectrum of complex **12** is broad and not well defined. It falls between the range of 400- 600 nm, however this range is consistent with the observed colour of a yellow/ brown solid.

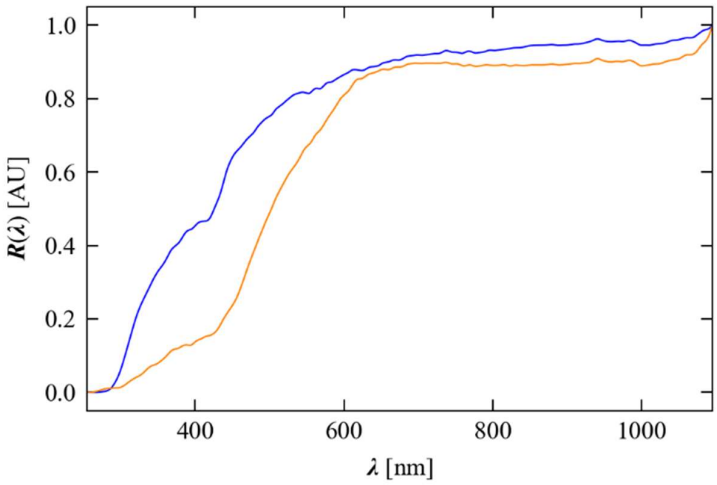

Figure 4.68*: Reflectance Spectra of Complex **12**.*

4.15.0 4'-(p-tolyl)-2,2':6',2''-Terpyridine Platinum Chloride Tetraphenylborate (13)

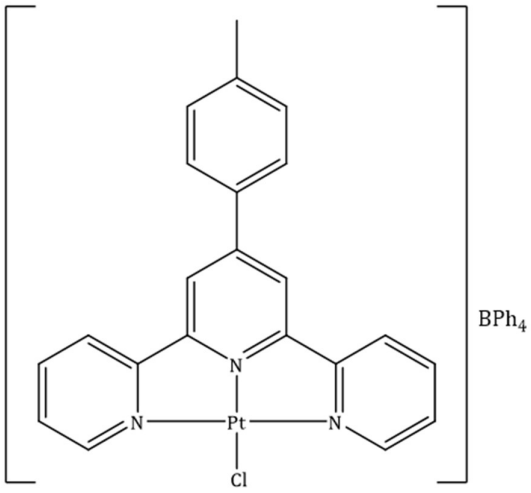

Complex **13** was synthesised using a counter-ion exchange technique, the details of which are given in Scheme 4.4.

The counter-ion was detected by the use of ^{1}H NMR spectroscopy, with the peaks 7.16 ppm (m, 8H), 6.92 ppm (t, 8H) and 6.78 ppm (t, 4H) in the spectrum representing the aromatic hydrogen atoms on the tetraphenylborate. An IR spectrum and an X-ray crystal structure determination were used to establish the structure of complex **13**.

4.14.1 Solution State Spectroscopy

The solution state UV-Vis spectra for complex **13** is given in Figure 4.69, as with complex **12** there was no appreciable emission observed for this complex.

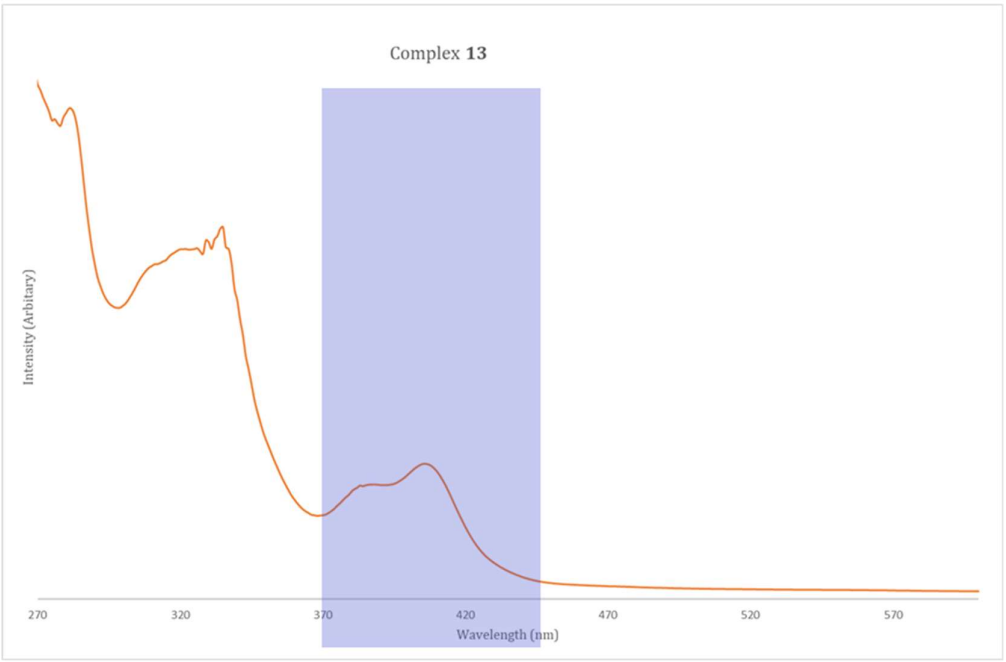

Figure 4.69: *Absorption spectrum of complex **13**. Solution concentration 1×10^{-4} M in acetonitrile. MLCT highlighted.*

The profile of complex **13** is the same as was measured for complex **4, 7** and **10**, therefore the same peak assignments can be made.

4.14.2 Vapo/Solvachromic Behaviour

Complexes using the tolyl group on the pincer ligand have so far been yellow, because the complex stacks in a head to tail manner in the solid-state, which has completely disrupted the stacking. Since complex **13** is also a dark yellow this would suggest there is are no dz^2 orbital interactions between the Pt centres for any 'switching' behaviour to utilise. This is indeed the case and no spectral changes were observed with this complex when it was tested with a variety of stimuli, such as pressure and common laboratory solvents.

4.14.3 Crystal Structure Analysis

Crystal Structure.

Brown crystals of complex **13** were grown by slow evaporation of acetonitrile at room temperature. The complex crystallises in the triclinic *P*-1 space group where there is one molecule of the platinum cation, one molecule of the counter- ion and a molecule of solvent (acetonitrile) in the asymmetric unit. The structure is given in Figure 4.70, structural and refinement data is available in Table 4.36.

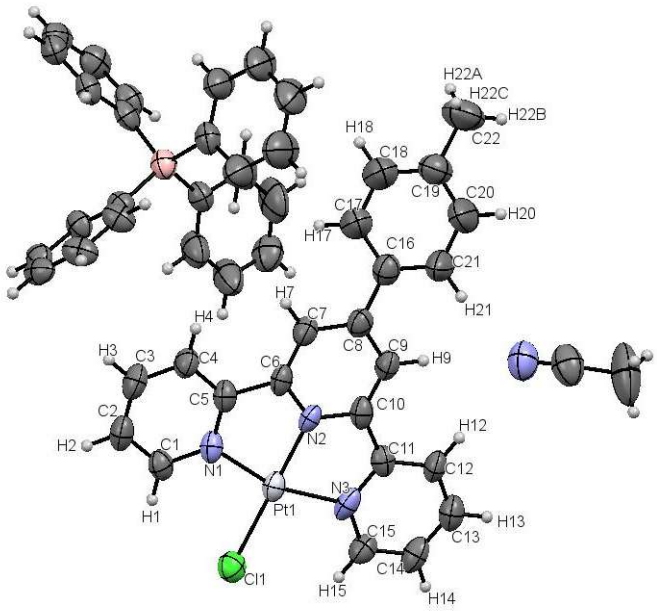

Figure 4.70*: Single crystal X-ray structure for complex **13**. Ellipsoids shown at 50% for clarity*

Table 4.36*: Crystal data and structure refinement for Complex **13**.*

Identification code	p16prr60
Empirical formula	$C_{46}BN_3ClPtH_{37}$
Formula weight	836.34
Temperature/K	150
Crystal system	triclinic
Space group	*P*-1
a/ Å	7.6704(3)
b/ Å	15.7297(4)
c/ Å	16.8191(6)
α/°	77.358(3)
β/°	88.615(3)
γ/°	76.150(3)
Volume/ Å^3	1921.66(12)
Z	2
ρ_{calc}mg/mm^3	1.445
μ/mm^{-1}	3.754
F(000)	795.0
Crystal size/mm^3	0.4 × 0.5 × 0.5
Radiation	MoKα (λ = 0.71073 Å)
2Θ range for data collection	4.966 to 58.384°
Index ranges	-9 ≤ h ≤ 7, -19 ≤ k ≤ 21, -22 ≤ l ≤ 22
Reflections collected	14929
Independent reflections	8837 [R_{int} = 0.0544, R_{sigma} = 0.0893]
Data/restraints/parameters	8837/0/499
Goodness-of-fit on F^2	1.042
Final R indexes [I>=2σ (I)]	R_1 = 0.0576, wR_2 = 0.1202
Final R indexes [all data]	R_1 = 0.0816, wR_2 = 0.1355
Largest diff. peak/hole / e Å^{-3}	2.44/-1.70

The cation in the complex salt **13** displays the expected square planar geometry around the Pt centre with a distorted N2-Pt1-N3 angle of 162.2˚, which can be attributed to the pincer bite angle. The other bond parameters were found to fall with expected values for this type of complex.

The arene functional group that is substituted on the 4th position of the central pyridyl ring of the terpy ligand is twisted; the dihedral angle was measured as 28.30˚ between the plane of the Pt centre (C6 N2 C5 N3 Cl1 C10 N1 Pt1) and the plane of the substituent group (C19 C18 C20 C16 C17 C21). The lack of planarity of the complex in the solid state would have disrupted the packing, this is illustrated in Figure 4.71. A selection of torsion angles are provided in Table 4.37c, overall the pincer ligand is planar with the exception of the arene substituent.

Table 4.37: *a. Table of bond lengths for **13**. b. Table of bond angles for **13**. c. Torsion angles for **13**.*

a. Bond Lengths		
Atom	**Atom**	**Length/ Å**
Pt1	Cl1	2.3067(19)
Pt1	N1	2.018(6)
Pt1	N2	1.951(5)
Pt1	N3	2.023(6)

b. Bond Angles			
Atom	**Atom**	**Atom**	**Angle/°**
N1	Pt1	Cl1	99.46(18)
N1	Pt1	N3	162.1(3)
N2	Pt1	Cl1	178.76(15)
N2	Pt1	N1	81.1(2)

c. Torsion Angles				
A	**B**	**C**	**D**	**Angle/°**
Pt1	N1	C5	C6	0.9(7)
Pt1	N1	C5	C4	179.3(5)
Pt1	N1	C1	C2	-178.4(5)
Pt1	N2	C10	C11	0.2(7)
Pt1	N2	C10	C9	179.0(5)
Pt1	N2	C6	C5	0.2(7)

The π bonding interactions in this complex would suggest that the complex stacks head to toe in the solid state as interactions form between opposite pyridyl rings on adjacent molecules in the solid state, this is further illustrated in figure 4.71. In addition, the solvent forms hydrogen bonds to the pincer ligand. This helps stabilise the solvent in the solid state.

Table 4.38: *a. Planes Present in solid-state structure of **13**. b. π-π Interactions of **13**. c. Hydrogen bonds of **13**.*

a. Plane Identification	
Plane Number	Atoms in plane
1	C16 C21 C20 C19 C18 C17
2	N1 C1 C2 C3 C4 C5
3	N2 C6 C7 C8 C9 C10
4	N3 C15 C14 C13 C12 C11
5	C31 C32 C33 C34 C29 C30
6	C35 C36 C37 C38 C39 C40
7	C41 C42 C43 C44 C45 C46
8	C23 C24 C25 C26 C27 C28

b. π-π Interactions	
Planes	Distance (Å)
2-4[1]	3.990

c. Hydrogen bonds			
Atoms	(D…A) Distance (Å)	(H…A) Distance (Å)	D…H…A Angle/°
C9-H9-N4	3.482(9)	2.557	173.2
C12-H12-N4	3.45(1)	2.528	174.3

Where [1](1-X, 1-Y, 1-Z)

Crystal Packing: Stacking and Pt Offset.

This complex packs in a head to tail arrangement, which differs due to the packing observed for complex **12**, however, this is the same arrangement seen for this ligand in complexes **4** and **10.**

There are alternating Pt…Pt distances of 3.4352(4) Å and 4.4507(4) Å in the stacks of complexes (Figure 4.71b). It is clear when looking at the packing along the *c* axis that the closest pairs of complexes are not perfectly aligned, instead it is every other molecule in the structure, which is aligned along this direction, Figure 4.71a shows the two positions of the platinum centres, related by symmetry, in the molecule. The lack of dz^2 orbital interactions in the complex is the reason that it is dark yellow in colour. Figure 4.71 shows the packing arrangement in the crystal structure.

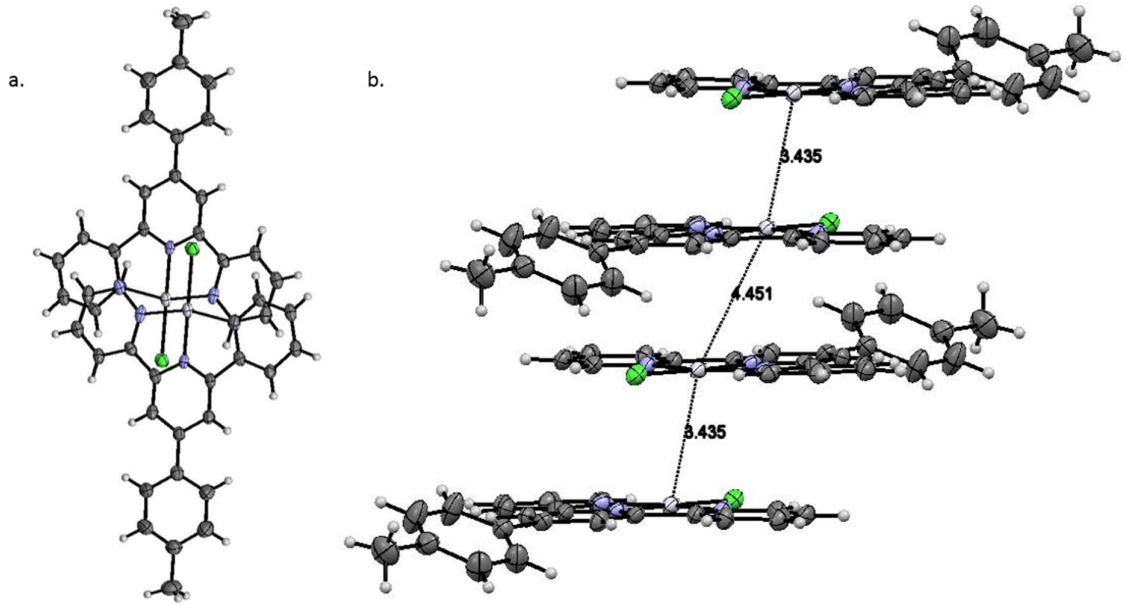

Figure 4.71*: a. Complex **13** viewed along the a axis. b. Stacking of molecules in complex **13**. Counter-ion and solvent molecules removed for clarity. Ellipsoids shown at 50%*

The head to toe stacking arrangement seems to have occurred because of the steric constraints of the ligand substituent, on the other hand it has allowed favourable π-stacking of the ligand to occur. Each molecule in complex 4 is approximately 3.3 Å apart, which is within the range for occurrence of π-stacking.[106]

4.14.4 X-Ray Powder Analysis

The peaks at a 2θ range on the experimental and predicted pattern are in good agreement, which confirms that the crystal structure obtained for this compound is representative of the bulk.

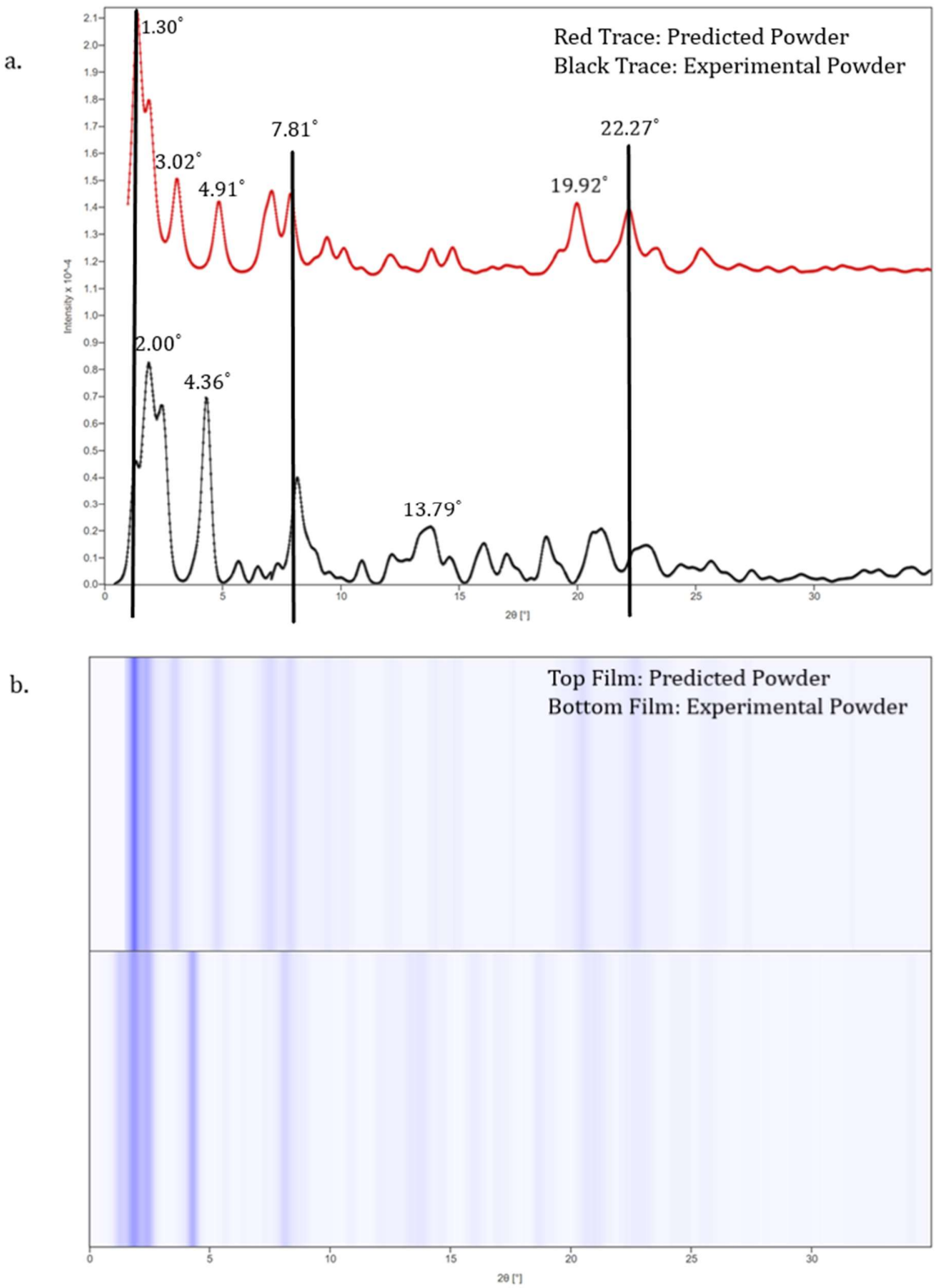

Figure 4.72: *a. Complex **13**, powder plot. b. Film representation of powder of Complex **13**. Red trace the predicted powder trace from the crystal structure. Black trace is the experimental powder*

4.14.5 Reflectance Spectra

The reflectance spectrum for complex **13** is more defined than seen for the other tetraphenylborate salts synthesized in this chapter. The edge falls between 430-590 nm and this is consistent with the colour of the complex observed in the solid state.

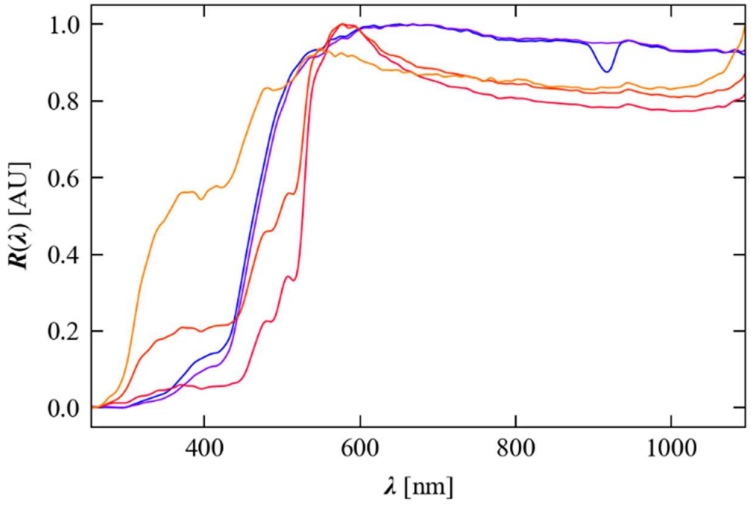

Figure 4.73*: Reflectance Spectra of Complex* ***13.***

4.15.0 2,2':6',2''-Terpyridine Platinum Cyanide Tetrafluoroborate. (14)

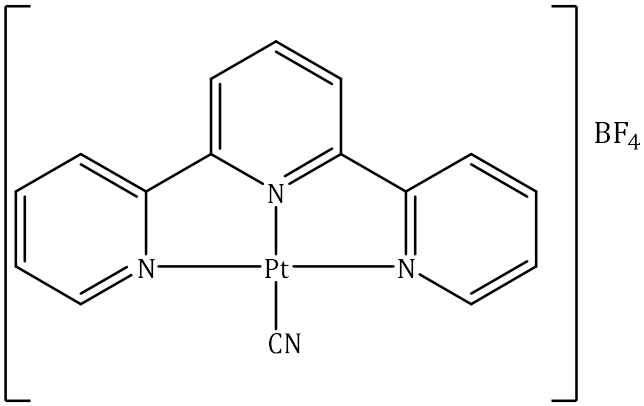

Complex **14** was characterised by ^{1}H NMR spectroscopy where the peaks had shifted to higher ppm when compared to the chloride analogue (Complex 1), which suggested the cyanide had bound to the metal centre. This was subsequently confirmed by the IR spectrum where a C=N stretching frequency was observed at 2150 cm^{-1}. This value is consistent to that observed in the literature, for transition metal complexes.[115, 116] Single crystals of suitable quality were grown from the vapour diffusion of diethyl ether into a concentration acetonitrile solution as well as by the slow evaporation of acetonitrile.

4.15.1 Synthetic Strategy

Complex **14** was synthesised in a one-step reaction using complex **1** as starting material. The ligand exchange mechanism used is detailed in Scheme 4.5 and has been adapted from a literature procedure.[117] A more detailed synthetic procedure is available in the experimental section.

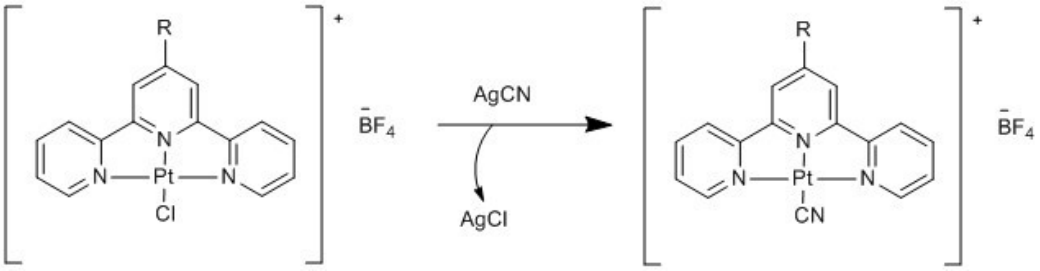

Scheme 4.5*: Conversion of chloride species into the cyanide species via a ligand exchange reaction*

Silver cyanide has been chosen as the cyanide source in these reactions instead of cheaper salts such as KCN, because it is thought that the KCN reacts too quickly and the chloride is not abstracted before the CN attacks. This leads to the formation of a negatively charged complex with K^{+} as the counter-ion. The AgCN reacts more slowly and the expected product is isolated in higher yield. In addition, the AgCN is of lower toxicity when compared to KCN.

4.15.2 Vapo/Solvachromic Behaviour

Complex **14** exhibits colour changing behaviour in the solid state, changing colour from orange to yellow as it is dried under vacuum, in addition solvatochromic behaviour was observed upon

addition of diethyl ether to an acetonitrile solution. Figure 4.74 shows the colour change as diethyl ether is added to an acetonitrile solution of complex **14.**

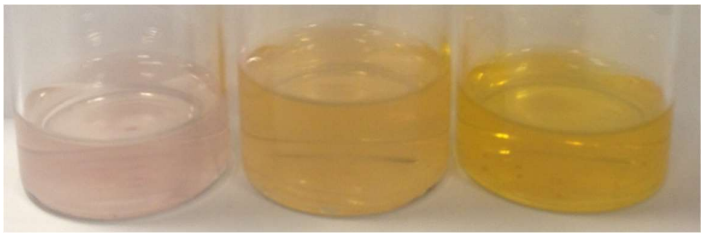

Figure 4.74*: Complex **14** displays solvatochromic behaviour with diethyl ether. On the left, red solution of complex **14** in acetonitrile, C= 1×10^{-3}M. Centre vial, acetonitrile solution and diethyl ether, ratio, 2:8. Right hand vial acetonitrile solution and diethyl ether, ratio, 0.5:5*

As shown in Figure 4.74 the solution of complex **14** in acetonitrile is red, upon increased concentration of diethyl ether the solution turns progressively yellow. Aggregation of solid was observed in the vial on the right after approximately 30 minutes. This behaviour is analogous to that described in the literature review in Section 1.5.4.

4.15.3 Solution State Spectroscopy.

The most effective way of studying the solvatochromic behaviour is solution state UV-Vis. Figure 4.75 shows how the UV-Vis spectra changed on the addition of diethyl ether to the acetonitrile solution.

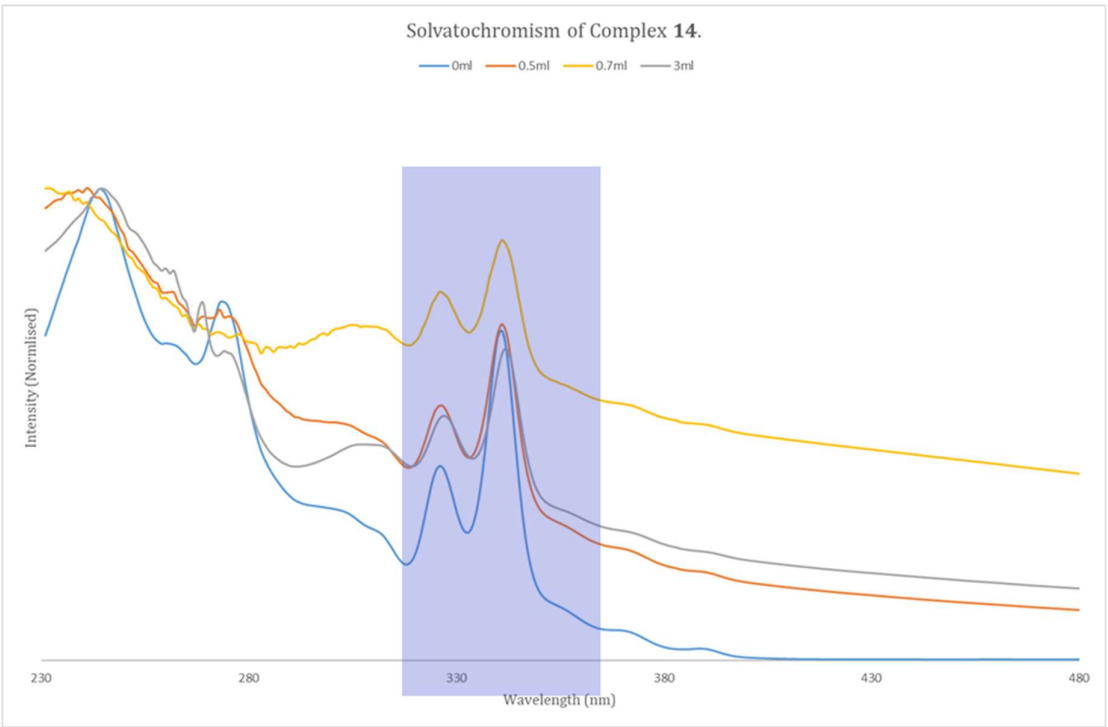

Figure 4.75*: UV-Vis spectra showing how the UV-Vis changes upon addition of diethyl ether to a solution of complex **14.** Initial solution concentration: 1×10^{-4} M in acetonitrile. Diethyl ether added to stock solution via syringe, measured against an acetonitrile reference. Spectra have been normalised, to the peak at 240 nm. Spectra were recorded at 5 minute intervals.*

The ground state spectra, shown by the blue line in Figure 4.75, has a very distinct profile, with which similarities can be drawn with complex **1**. The region between the wavelengths 230-320 nm is identical to that observed for complex **1** and can be assigned to π-π transitions in the terpyridine ligand. Differences start to arise in the spectra between 330-380 nm where a sharp doublet is observed for complex **14**, but for complex **1** these intensities are reversed, again these peaks can be assigned to ligand transitions.[109] For complex **1** there is a clear peak at 380 nm that can be assigned to MLCT band, for complex **14** they are present but as a shoulder to the main observed peak at 340 nm (highlighted area).

Figure 4.75 depicts what happens as diethyl ether is added to the stock solution of complex **14.** For the solution up to where 0.7 ml of diethyl ether was added, the detail in spectrum profile is lost between 230-280 nm, from 280-380 nm the profile of the spectrum is similar to that observed for the acetonitrile solution, just at a higher intensity. Once the solution had been saturated with diethyl ether the intensity of the spectrum started to decrease and the detail at lower wavelengths returned (Figure 4.75, Grey line). A change was also seen in the stock solution, at lower concentration percentages of diethyl ether the solution was opaque, whereas when it became saturated the solution became clear, but tinged with pink.

Another important feature of these complexes is their luminescence, Figure 4.76 shows the absorption and emission spectra in the solution state for complex **14** when dissolved in just acetonitrile. Whereas Figure 4.77 is the absorption and emission spectra when the solution has been saturated with diethyl ether.

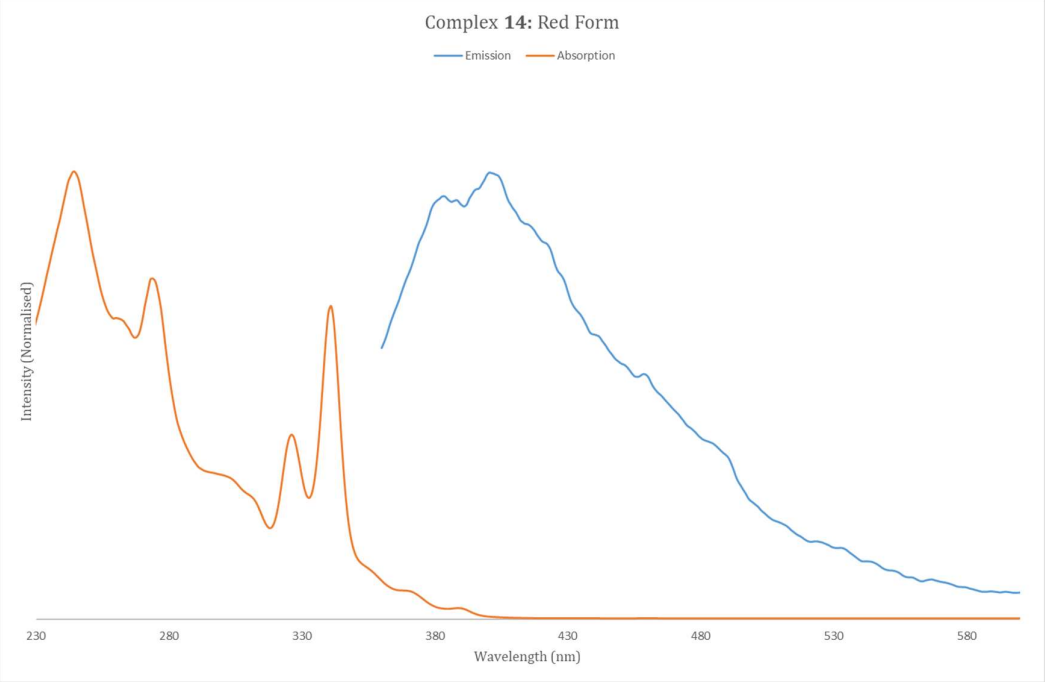

Figure 4.76*: Absorption and emission spectrum of complex **14**. Solution concentration 1×10^{-4} M in acetonitrile. Excitation wavelength for emission spectrum is 340 nm.*

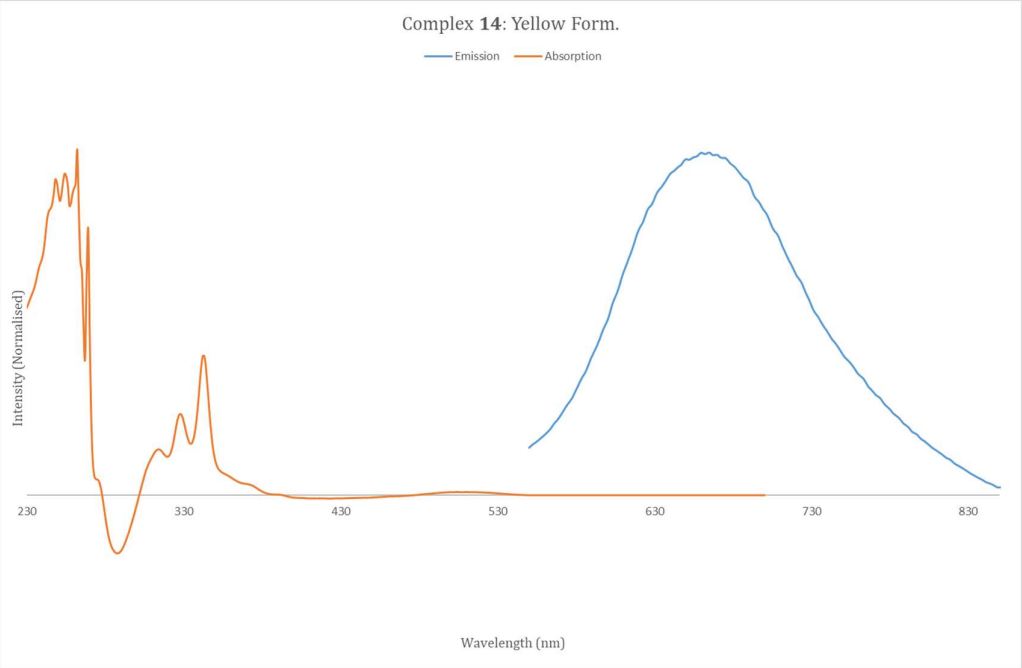

Figure 4.77*: Absorption and emission spectrum of complex **14**. Solution concentration 1×10^{-4} M in acetonitrile, which has been saturated with diethyl ether. Excitation wavelength used in emission spectrum is 500 nm.*

It is immediately clear on comparison of Figure 4.76 and 4.77 that the emission profile and therefore the luminescence of complex **14** has changed upon addition of the diethyl ether with little structural change. In Figure 4.76, it can be seen that the emission profile almost overlaps the absorption profile, the Stokes shift would be very small and therefore phosphorescent emission may not be occurring. However when the solution has been saturated the emission profile changes dramatically. Excitation of the solution at 340 nm, shows a weak emission peak at 400 nm but it was clear that there was emission at a longer wavelength. The excitation wavelength was therefore changed to 500 nm and strong emission at 650 nm is observed.

An enhancement of the solution state emission properties were also reported for an analogous system described in the literature (Figure 1.24, Section 1.5.4).[61] Yam *et al* reported that upon addition of diethyl ether an emission peak was observed at 785 nm, which was dependant on the concentration of diethyl ether in the solution. The new emission band was seen in conjunction with a new low energy absorption band in the UV-Vis spectrum of the complex arising at 615 nm, this band is again dependent on the concentration of the diethyl ether in solution. The authors attributed this effect to the formation of aggregates in the solution, which increases the number of Pt…Pt and π-π interactions. This would be an appropriate assumption because they observe a colour change from red to green, which occurs because of shortening of the Pt-Pt distances and is consistent with the crystallographic data. The data recorded for complex **14** would suggest a similar effect occurring but the colour transition observed in a concentrated solution is from red to yellow, which is suggestive of longer Pt…Pt interactions. On the other hand the Pt…Pt interactions may have decreased but π-π interactions in the solution state may have increased. More detailed UV-Vis and emission studies would have to be performed before final conclusions on the mechanism of the solvatochromic effect could be drawn.

4.15.4 Crystal Structure Analysis

Crystal Structure: Red Form

Red/Orange crystals of complex **14** were grown by vapour diffusion of diethyl ether into a concentrated acetonitrile and methanol solution at -18°C. Complex **14** crystallises in the orthorhombic space group $P2_12_12_1$. The structure of complex **14** is shown in Figure 4.78, with extended refinement data found in Table 4.39.

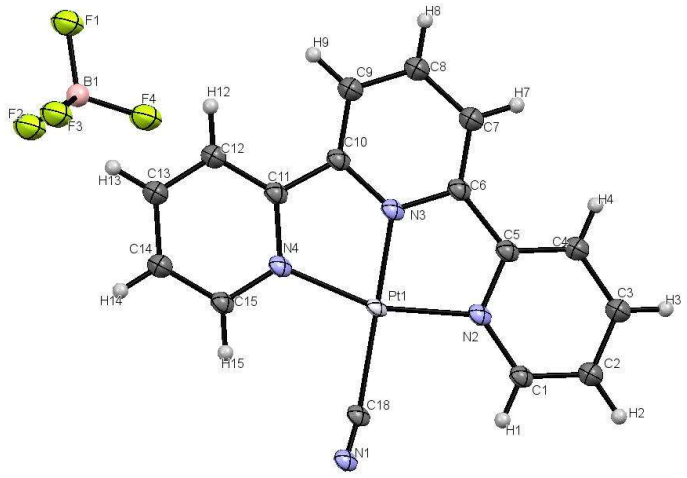

Figure 4.78: *Crystal structure of complex **14**, red/orange form. Disordered solvent molecule removed for clarity. Ellipsoids shown at 50%.*

Table 4.39: *Crystal data and structure refinement for complex **14***

Identification code	Bath2557
Empirical formula	$C_{15}H_{15}BN_4OF_4Pt$
Formula weight	569.20
Temperature/K	100
Crystal system	orthorhombic
Space group	$P2_12_12_1$
a/ Å	6.5804(4)
b/ Å	10.6855(6)
c/ Å	24.9074(14)
α/°	90
β/°	90
γ/°	90
Volume/ Å^3	1751.36(18)
Z	4
ρ_{calc}g/cm^3	2.1585
μ/mm^{-1}	6.645
F(000)	1040.8
Crystal size/mm^3	0.4 × 0.1 × 0.02
Radiation	synchrotron (λ = 1.1271 Å)
2Θ range for data collection/°	5.18 to 88.28
Index ranges	-8 ≤ h ≤ 8, -13 ≤ k ≤ 12, -30 ≤ l ≤ 30
Reflections collected	13924
Independent reflections	3351 [R_{int} = 0.0511, R_{sigma} = 0.0537]
Data/restraints/parameters	3351/0/111
Goodness-of-fit on F^2	1.205
Final R indexes [I>=2σ (I)]	R_1 = 0.0735, wR_2 = 0.1439
Final R indexes [all data]	R_1 = 0.0933, wR_2 = 0.1527
Largest diff. peak/hole / e Å^{-3}	4.49/-2.31
Flack parameter	0.40(16)

The red form of the complex cation in **14** adopts the square planar geometry around the Pt centre with the expected angular distortion of 161.0(4)˚ for N4-Pt1-N2; this can be attributed to the bite angle of the pincer ligand. Bond parameters for this complex fall within the expected values.[93, 107] The complex is essentially planar with a dihedral angle of 0° and torsion angles being close to 0° or 180°.

Table 4.40: *a. Table of bond lengths for **14**. b. Table of bond angles for **14**. c. Torsion angles for **14**.*

a. Bond Lengths		
Atom	**Atom**	**Length/ Å**
C18	N1	0.98(2)
C18	Pt1	2.131(16)
N2	Pt1	2.019(7)
N3	Pt1	1.920(7)
N4	Pt1	2.015(7)

b. Bond Angles			
Atom	**Atom**	**Atom**	**Angle/°**
N1	C18	Pt1	167(2)
C1	N2	Pt1	126.2(5)
N3	Pt1	N2	80.6(4)
N4	Pt1	N2	161.0(4)
N4	Pt1	C18	98.9(6)

c. Torsion Angles				
A	**B**	**C**	**D**	**Angle/°**
N2	C5	C6	C7	178.6(13)
C1	N2	C5	C4	0.0
C1	N2	C5	C6	-179(2)
C1	C2	C3	C4	0.0
C2	C3	C4	C5	0.0
C3	C4	C5	N2	0.0
C3	C4	C5	C6	179(2)
Pt1	N3	C6	C7	179.4(14)

The solvent in the red form of the cyanide complex could not be fully modelled, this was attributed to the mixture of solvents that had to be used in the crystallisation process being present in the solid state. Therefore, the hydrogen bonding in this complex could not be fully analysed. However, there was hydrogen-bonding present between the cyanide group and the terpyridine ligand. This is within the layer and does not seem to have any effect on the distance of the Pt centres in the solid state.

In addition to hydrogen bonding interactions there are π interactions between the pyridyl rings in the stacks. Details are provided in Table 4.41b. The π interactions that form are similar to those seen in the chloride complexes in this chapter.

Table 4.41: *a. Planes Present in solid-state structure of **14**. b. π-π Interactions of **14**. c. Hydrogen bonds of **14**.*

a. Plane Identification	
Plane Number	Atoms in plane
1	N2 C5 C4 C3 C2 C1
2	N3 C10 C9 C8 C7 C6
3	N4 C15 C14 C13 C12 C11

b. π-π Interactions	
Planes	Distance (Å)
1-3[1]	3.701
1-3[2]	3.676

c. Hydrogen bonds			
Atoms	(D…A) Distance (Å)	(H…A) Distance (Å)	D…H…A Angle/°
C8-H8-N1	3.28(2)	2.52	137

Where [1](-1/2+X, 1/2-Y, 1-Z), [2](1/2+X, 1/2-Y, 1-Z)

Crystal structure: Yellow Form

Yellow crystals of complex **14** were grown from the slow evaporation of an acetonitrile solution. It adopts the monoclinic space group $P2_1/n$, with two molecules and counter-ions in the asymmetric unit. Figure 4.79 with structural and refinement data available in Table 4.42.

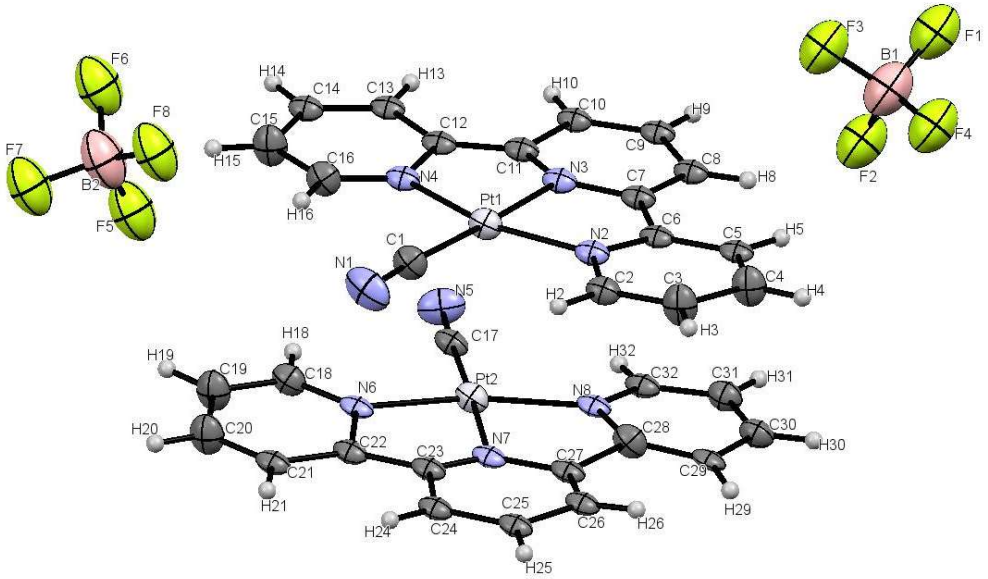

Figure 4.79*: Crystal structure of complex **14**, yellow form. Ellipsoids shown at the 50% probability level.*

Table 4.42: *Crystal data and structure refinement for complex **14**- yellow form.*

Identification code	Bath 2563
Empirical formula	$C_{20}H_{15}BN_4F_4Pt$
Formula weight	593.26
Temperature/K	100
Crystal system	monoclinic
Space group	$P2_1/n$
a/ Å	7.0401(10)
b/ Å	17.556(2)
c/ Å	26.670(4)
α/°	90
β/°	105.260(9)
γ/°	90
Volume/ Å^3	3180.2(8)
Z	6
ρ_{calc}g/cm^3	1.859
μ/mm^{-1}	8.273
F(000)	1692.0
Crystal size/mm^3	0.4 × 0.1 × 0.05
Radiation	synchrotron (λ = 1.1271 Å)
2Θ range for data collection/°	4.28 to 58.214
Index ranges	-8 ≤ h ≤ 8, -21 ≤ k ≤ 22, -33 ≤ l ≤ 33
Reflections collected	37997
Independent reflections	6541 [R_{int} = 0.2315, R_{sigma} = 0.1602]
Data/restraints/parameters	6541/444/379
Goodness-of-fit on F^2	*1.085*
Final R indexes [I>=2σ (I)]	R_1 = 0.1127, wR_2 = 0.2362
Final R indexes [all data]	R_1 = 0.1936, wR_2 = 0.2738
Largest diff. peak/hole / e Å^{-3}	5.12/-4.36

The yellow form of the complex salt **14** maintains its square planar geometry around the Pt centre with the same angular distortion seen in both molecules in the asymmetric unit, Table 4.43b. The other parameters are as expected for this complex.[67, 107] The complex is planar in the solid state with a dihedral angle of 0° for this form of complex **14**.

Table 4.43: *a. Table of bond lengths for **14** yellow form. b. Table of bond angles for **14** yellow form. c. Torsion angles for **14** yellow form.*

a. Bond Lengths		
Atom	**Atom**	**Length/ Å**
C1	N1	1.09(4)
C1	Pt1	2.03(3)
N2	Pt1	2.01(2)
N3	Pt1	2.01(2)
N4	Pt1	2.01(2)
C17	N5	1.07(4)
C17	Pt2	2.02(3)
N6	Pt2	1.99(2)
N7	Pt2	2.03(2)
N8	Pt2	2.02(2)

b. Bond Angles			
Atom	**Atom**	**Atom**	**Angle/°**
N1	C1	Pt1	174(3)
N2	Pt1	C1	99.3(11)
N2	Pt1	N3	81.1(9)
N2	Pt1	N4	161.5(9)
N3	Pt1	C1	177.6(10)
N5	C17	Pt2	173(3)
C17	Pt2	N7	177.8(10)
N6	Pt2	C17	97.2(10)
N6	Pt2	N7	81.4(9)
N6	Pt2	N8	163.0(9)

c. Torsion Angles				
A	**B**	**C**	**D**	**Angle/°**
C2	C3	C4	C5	1(5)
C3	C2	N2	C6	5(4)
C3	C2	N2	Pt1	-179(2)
C3	C4	C5	C6	-1(4)
C4	C5	C6	C7	179(3)

The yellow form of complex **14** has a large number of interactions in the solid state. These interactions are analogous to those seen in the red form of this complex. The π interactions form between the pyridyl rings and the hydrogen bonding interactions occur between the cyanide group and the terpyridine pincer ligand in adjacent molecules.

Table 4.44: *a. Planes Present in solid-state structure for **14** yellow form. b. π-π Interactions for **14** yellow form. c. Hydrogen bonds for **14** yellow form.*

a. Plane Identification	
Plane Number	Atoms in plane
1	N2 C6 C5 C4 C3 C2
2	N3 C11 C10 C9 C8 C7
3	N4 C16 C15 C14 C13 C12
4	N6 C22 C21 C20 C19 C18
5	N8 C32 C31 C30 C29 C28
6	N7 C27 C26 C25 C24 C23

b. π-π Interactions	
Planes	Distance (Å)
1-5[1]	3.717
1-6[2]	3.845
2-5[2]	3.835
3-4[2]	3.701

c. Hydrogen bonds			
Atoms	(D…A) Distance (Å)	(H…A) Distance (Å)	D…H…A Angle/°
C10-H10-N5	3.36(4)	2.42	172
C13-H13-N5	3.39(4)	2.44	174
C24-H24-N1	3.37(4)	2.39	170
C21-H21-N1	3.37(4)	2.42	173

Where [1](1+X, +Y, +Z), [2](+X, +Y, +Z)

Crystal Packing: Stacking and Pt-Offset for Red and Yellow Form.

Structures for the two forms are different, with solvent found in the red form but the yellow form being completely dehydrated. A similar example given in the literature review, Section 1.5.4, saw different stacking motifs for the different solvates of the complex. Further crystallographic analysis saw a similar trend for this complex. Figure 4.80 showing the differences in packing arrangements of the complexes.

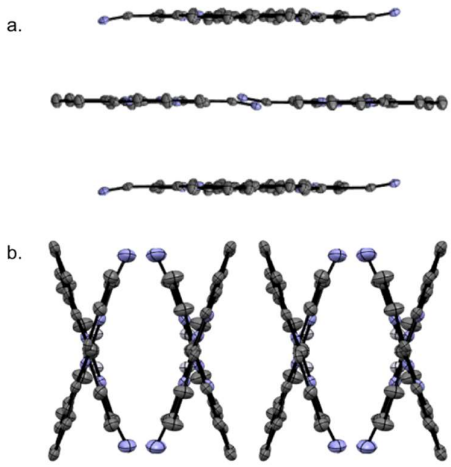

Figure 4.80: *Packing diagram of complex **14**. a. red form, b. yellow form. Counter-ions, hydrogens and solvent removed for clarity. Ellipsoids shown at the 50% probability level*

Similarly to the paper published by Yam *et al*[61] the two forms of this complex show different packing arrangements based on the colour. The red form, a series of stacks is observed whereas for the yellow form a zig-zag arrangement has formed. The stacking parameters for these two forms are shown in Figure 4.81.

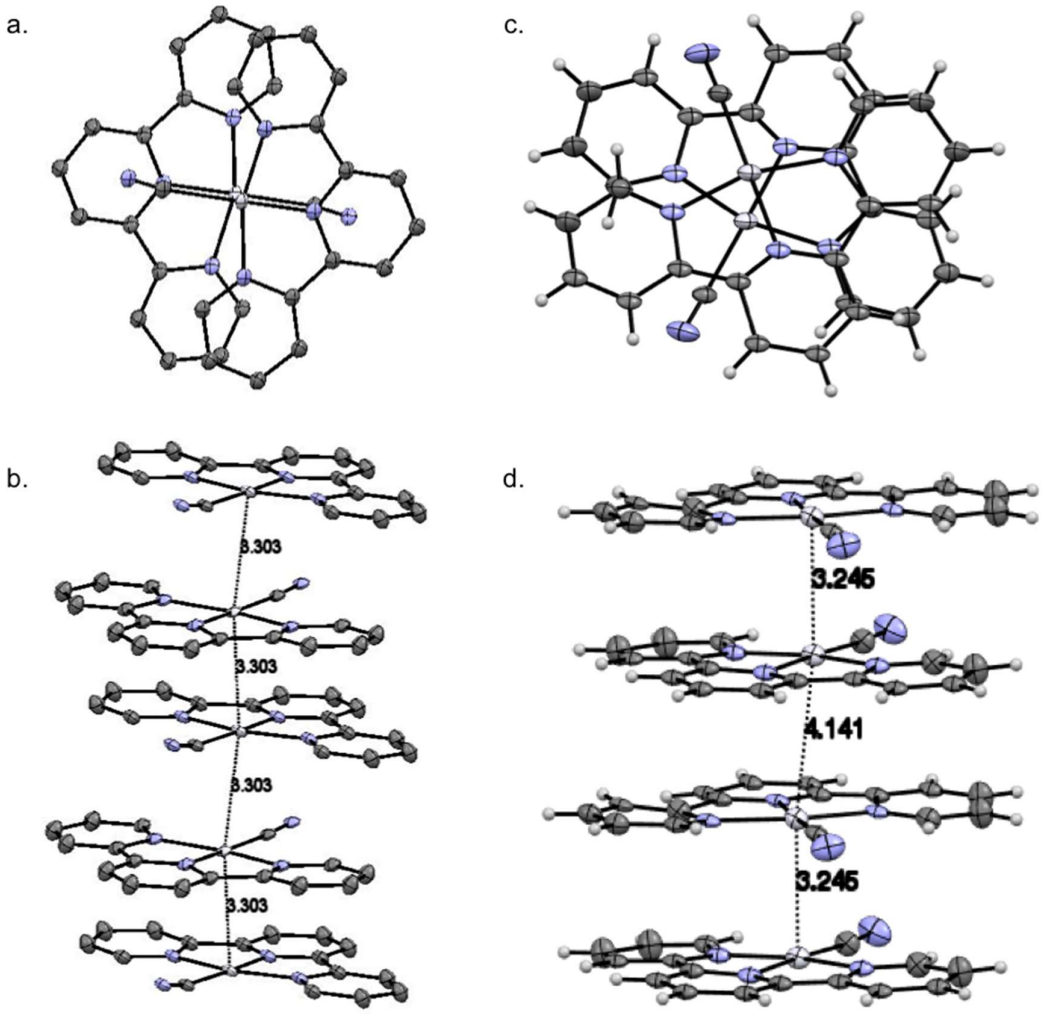

Figure 4.81:*a. Red form of Complex **14** viewed along the a axis. b. Stacking in the red form of complex **14** between the molecules in the solid state. Solvent, counter-ion and hydrogens removed for clarity. Ellipsoids shown at 50% probability. c. yellow form of complex **14** viewed along the a axis. d. stacking between the molecules in the yellow form of complex **14**. Counter-ions removed for clarity, ellipsoids shown at 50%*

The red form of complex **14** stacks along the *a* axis, with a distance of 3.303(1) Å between the platinum centres. This distance falls within the range required for dz^2 orbital overlap to occur, as shown in Figure 4.81b. This distance falls between those observed for the red and blue form of complex **2**. Figure 4.81b shows the stacking arrangement in this complex with the complexes stacking in a head to toe manner. The platinum atoms occupy two different positions that are related by symmetry, as shown in Figure 4.81a. The offsets of the platinum atoms were calculated as discussed in Section 4.1.2, the distance was calculated as 0.27 Å and the Pt-Pt-Pt angle as 170°.

The stacks are close to full alignment as observed for the blue form of complex **2**, it is these minor differences that means this complex is orange in colour as opposed to blue.

The stacking for the yellow form differs to that of the orange/red form, which is to be expected. The Pt-Pt-Pt angle is measured at 144.52° and Pt offset as 6.74 Å, this move from linearity can be explained by the removal of solvent, which created space in the crystal structure, allowing movement of the molecules in the structure. This movement in structure could be attributed to loss of close contacts or hydrogen bonds with the removal of solvent, which potentially hold the stacks in place. Due to the heavy disorder associated the solvent molecule in the red form of complex **14,** this effect could not be studied. The distances between the Pt atoms in the yellow form alternate. This is a common trend for the terpyridine complexes and was widely seen with the chloride complexes discussed previously. The distances alternate at 3.247(2) and 4.1410(2) Å, while the shorter distance fall within the range for dz^2 orbital overlap the larger does not, this form is yellow because of the lack of long range Pt…Pt interactions as seen with complexes **11, 12** and **13**.

4.16.0 Conclusion

In this chapter the crystal structures of a series of Pt(II) terpyridyl salt complexes with a variety of substituents on the terpy ligand, a variety of negatively charged ligands in the fourth coordination site on the square planar Pt(II) centre, and a range of anions having different steric requirements have been determined. The molecular and crystal packing parameters have been established, and these have been correlated with the luminescent properties of the complex salts in the solid state and in solution. Of particular relevance to the luminescent properties is the Pt…Pt distance between the cations in solution and in the solid state. There is a clear correlation between the structural parameters, the luminescence observed, and whether or not the salts will undergo visible colour changes upon the addition of VOCs. The Pt…Pt distance cannot alone be used to determine spectral properties of the complexes. This is because in a number of the complexes the Pt centres were not perfectly aligned. Instead there were two Pt positions in the solid state. In the cases where this occurred the Pt offset was calculated, Figure 4.7, this in conjunction with the Pt…Pt distance gave a more accurate picture. These parameters are summarised in Table 4.45.

Table 4.45*: Summary of crystallographic parameters.*

Substituent	Counter-Ion	Pt Offset (Å)	Pt…Pt Distance (Å)
H	BF_4	Form(I): 0.47 Form(II): 0.90 Form(III): 0.0	Form(I): 3.3189(5)/3.32412(4) Form(II): 3.488(4)/3.479(3) Form(III): 3.2734(0)
H	PF_6	0.64	3.3633(3)
H	OTs	0.36	3.3457(5)/3.4899(5)
H	BPh_4	2.46	4.1383(4)
Ph	BF_4	0.48/2.79	3.3276(6)/3.2976(6)
Ph	PF_6	-	3.4401(3)
Ph	OTs	-	3.3142(5)/3.3853(5)
Ph	BPh_4	-	3.3415(6)
***P*-Tolyl**	BF_4	Packed head to toe to maximise π interactions	
***P*-Tolyl**	PF_6	Not Stacked	
***P*-Tolyl**	OTs	Packed head to toe to maximise π interactions	
***P*-Tolyl**	BPh_4	-	3.4353(4)/4.4507(4)

It can be seen that on moving from a non-substituted terpyridine ligand to a phenyl substituent to a tolyl group that significant changes in the solid state structure occurred which effected the observed spectral properties for a complex. In the case for the *p*-tolyl substituent there is no Pt overlap for the complexes as they have packed in a head to toe manner to maximise stabilising π interactions, as discussed in the literature.[106]

It should also be noted that a larger Pt offset generally indicated a longer Pt…Pt distance. This is not surprising because the angle of the Pt centres would incur a larger difference. In addition these complexes rarely show any type of spectral properties that can be manipulated.

Based on this investigation π interactions cannot be manipulated by changing the solvent conditions or by exposing the complexes to vapour. Where the complex did exhibit dz^2 orbital interactions changes in spectral properties were not always observed, but the powder diffraction data suggested that there were a number of solvates present in the bulk powder. This is difficult to control particularly when a complex has been recrystallized a number of times.

This complete investigation of terpyridine chloride complexes did provide evidence that the counter-ion has a significant effect on the solid-state packing of the complexes and therefore their spectral properties. However, it is clear that it is not just the size and steric bulk of the counter-ion that effects the solid-state properties of these complexes and ligand substituents as well as solvates need to be carefully considered during the design of future 'smart' materials.

In addition, the effect of the π donating/ accepting effect of the 4th ligand in the co-ordination sphere was investigated. Substituting the chloride ligand for a cyanide changed the sensing properties of the complexes. In addition, the cyanide complex had superior solution state emission properties. The emission properties of complex **14** are summarised in Figure 4.82.

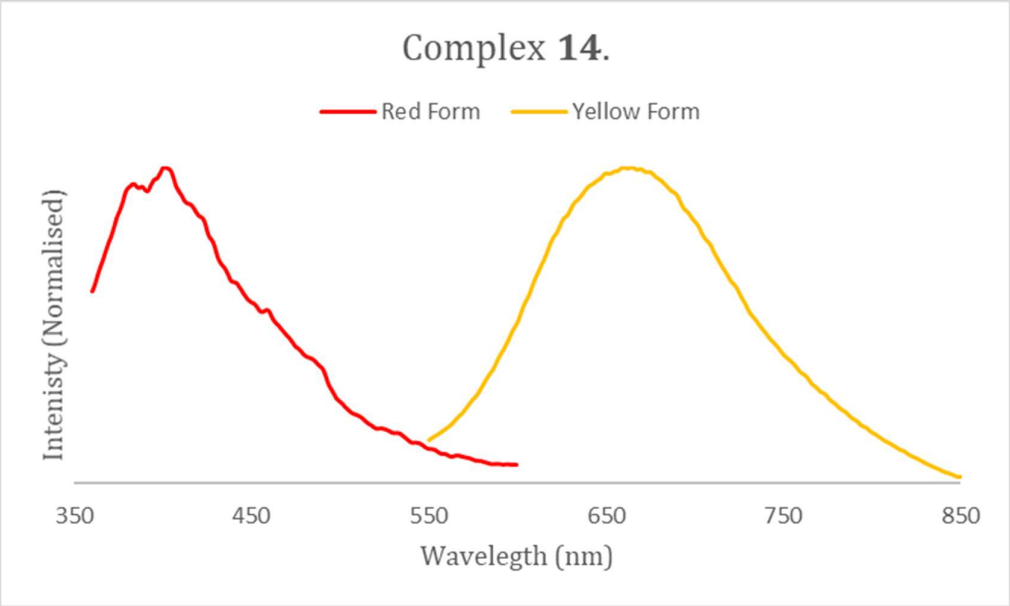

Figure 4.82*: Emission properties of complex **14***

To conclude this chapter provides an extensive insight into how solid-state properties can be tuned via synthetic modifications. A couple of the complexes had been reported previously in the literature[43, 110] however, this chapter provides an alternative insight into the properties of the complexes. In addition, the literature research was developed further and a complete series of compounds was synthesised. This allowed for a thorough analysis of the solid-state structures and the effects of counter-ions and intermolecular interactions on vapochromic properties.

CHAPTER 5

Ligand Manipulation

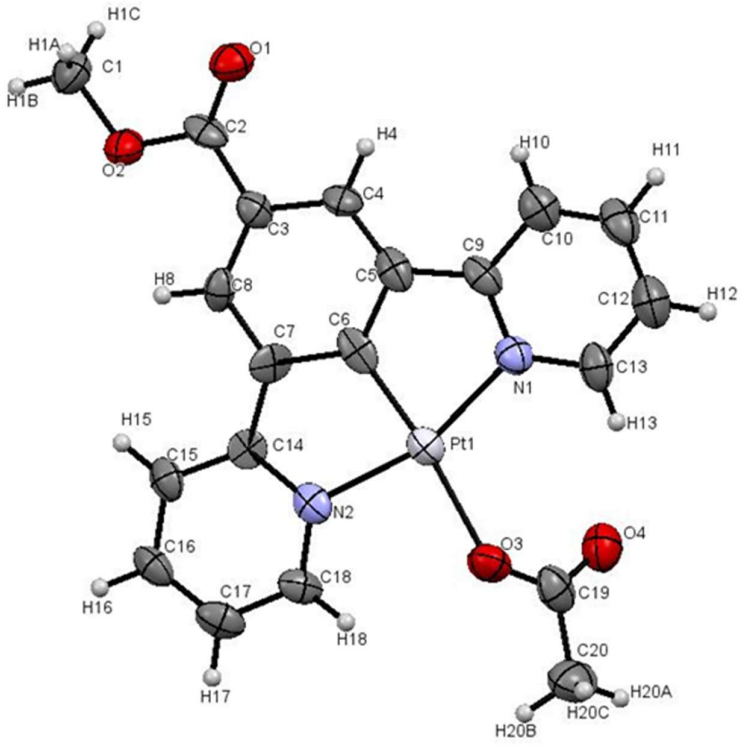

5.1.0 Introduction

The spectral properties of the terpyridine based Pt(II) complexes were studied in Chapter 4. However as discussed in Section 1.4.5, complexes containing the N^C^N ligand has superior luminescent properties due to electronic effect of the M-C bond. The tridentate ligand can be functionalised in two main ways. The first is to functionalise the 4'-position of the central arene ring, and this method has been used extensively in the literature.[18, 26, 118] The second method is to change the identity of the ligand in the 4th co-ordination site of the platinum square-planar coordination plane[51, 93]. In this chapter the focus will be on developing and exploiting method 2, changing the ligand in the 4th position of the platinum co-ordination plane. The overall aim is to produce a versatile chemical sensor that could be used in industrial, healthcare or environmental fields.

5.1.1 'Smart' Materials

The Raithby group has previously published a complex that acts as a rapidly responding, vapochromic chemical sensor.[93] The structure of the complex is shown in Figure 5.1. This complex utilises the N^C^N ligand configuration with a methyl ester substituent on the 4'-position of the phenyl ring. In the 4th co-ordination site there is a cyanide ligand. This is a strong field ligand that is high in the spectrochemical series.

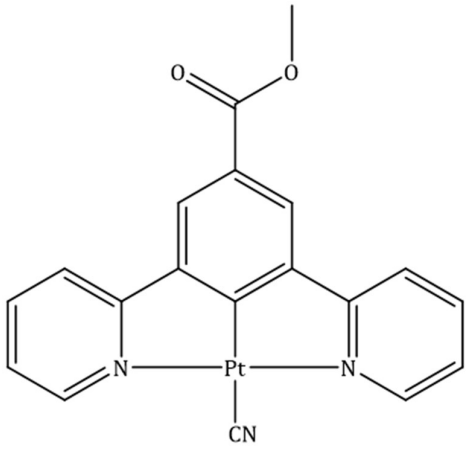

Figure 5.1*: Vapochromic Platinum Complex.*

The use of the cyanide ligand provided a means to fine-tune the electronic properties of the complex and raises the energy of the d_{z^2} orbital, so it lies closer to the frontier orbitals (Section 1.5.0). This change in energy of the d_{z^2} orbital allows the tuning of the vapochromic response. In the case of this complex, it shows a rapid and selective vapochromic response as illustrated in Figure 5.2a. The image shows there are three distinct forms of this complex. The ambient form, Form-I, is red and its solid-state emission has a main peak at approximately 720 nm (Figure 5.2c), this is consistent with the colour observed in the solid state when irradiated with 360 nm light.

This red form can be transformed into a yellow, Form-II, and a blue, Form-III, by the action of N_2 gas and methanol vapour, respectively. Each of the different forms has a unique absorption and emission profile, this means that in addition to following the transition by eye, it can be observed using spectroscopic techniques.

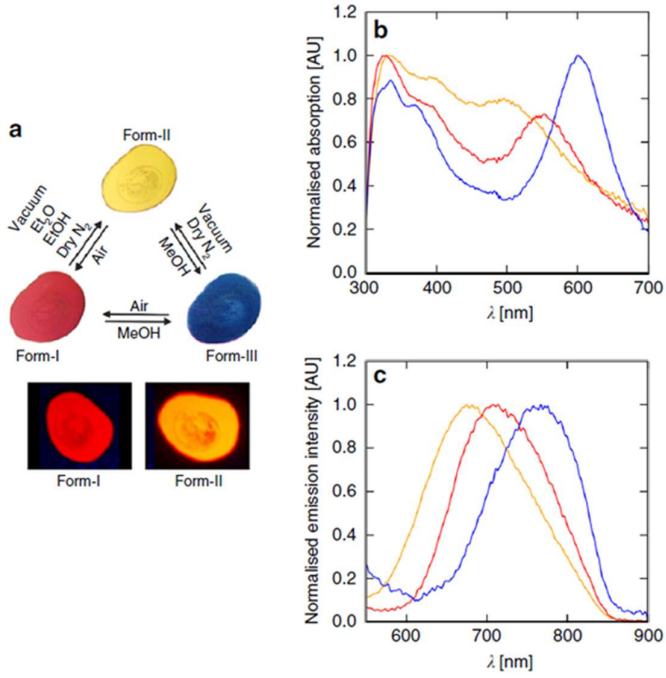

Figure 5.2: *Vapochromic platinum complex. a. Vapochromic response in the solid state. b. Solid state absorption spectra. c. solid-state emission spectra.* [93]

The transition between the three colours can be rationalised by the observed distance between the platinum centres, in adjacent molecules, in the solid state. The authors of this paper used X-ray crystallographic techniques to study this phenomenon in the solid state. The crystal structures are presented in Figure 5.3.

Figure 5.3a, shows the intermolecular interactions and the Pt…Pt distances present in the three different forms are:

- Form-I: 3.45(3) Å,
- Form-II: 3.66(1) Å,
- Form-III: 3.38(1) Å.

The differences in the Pt…Pt distances provide a rational explanation for the rapid vapochromic response, Form-III has the shortest distance whereas Form-II has the longest distance. This change in Pt distance causes a change in the ^{3}MMLCT profile, concomitant with a change in colour.

Figure 5.3a also depicts the various intermolecular interactions that are present between the forms in the solid state. Form-II has no intermolecular interactions with solvent molecules in the solid state, which is as expected since there is no solvent of crystallisation in this form. However, in the case of Form-I and Form-III the hydrogen bonding interaction between the cyanide and solvent water and methanol molecules are vital for orienting the Pt-Pt stacks. Figure 5.3b is a representation the Pt orbital overlap (4.0.0) observed in each of the three forms. This diagram shows that in addition to holding the stacks together the solvent can be used to orientate adjacent molecules to enhance the Pt overlap in the solid state.

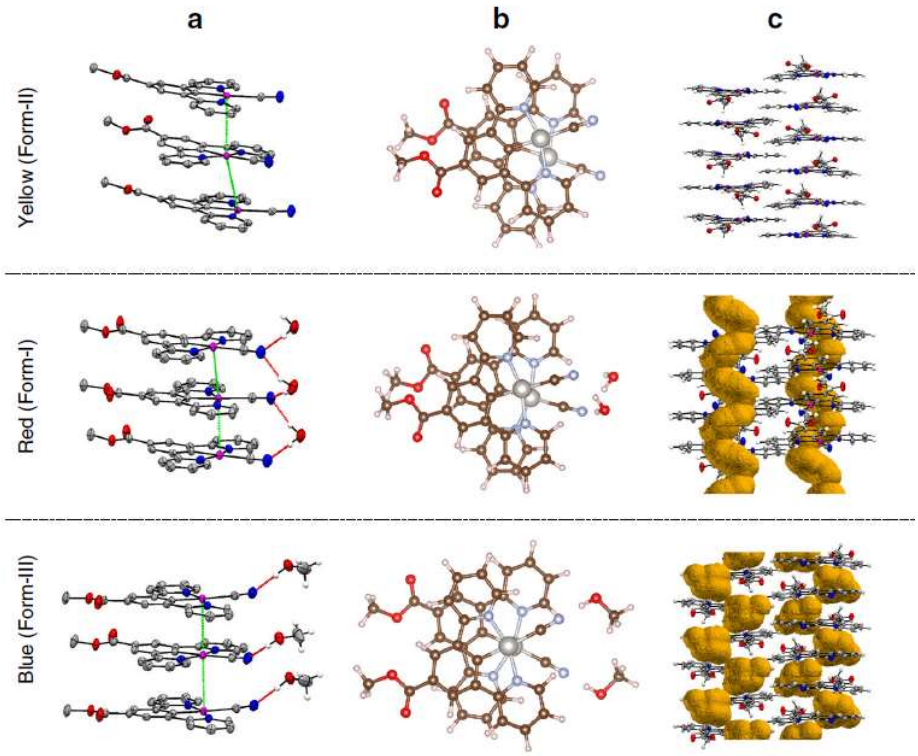

Figure 5.3: *Vapochromic platinum complex. a. crystal structure, showing intermolecular interactions. b. Pt…Pt Overlap. c. Void space and packing diagram.* [93]

The rapid nature of the vapochromic response was explained by the void analysis of the solid-state structure shown in Figure 5.3c. Form-I has a channelled void space, which the solvent occupies. The channel structure allows the solvent to move in and out of the crystal rapidly, as opposed to a more pocketed structure.

This type of vapochromic complex could be used in chemical sensing and when incorporated into a porous polymer could be applied to a variety of surfaces to act as a vapochromic coating.[80]

Vapochromism is not the only property that this family of platinum pincer complexes exhibit that may be of interest, as 'smart' materials. These Pt(II) complexes can also show mechanochromic behaviour, an example of a complex which undergoes this type of transition is shown in Figure 5.4.

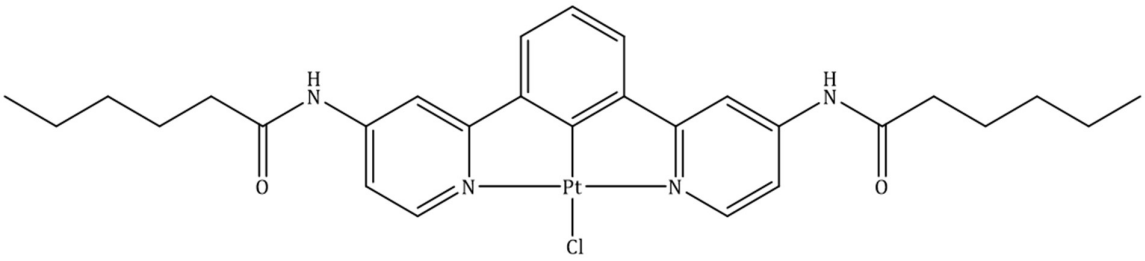

Figure 5.4: *Mechanochromic Pt(II) complex, bearing amide moieties.*[69]

The authors initially thought that this complex was mechanochromic, with a transition from green to red seen upon grinding or heating the sample. The reverse process could only be achieved upon recrystallization from DMF, Figure 5.5. However further investigation of the complex revealed a 3rd vapochromic form, which was achieved upon exposure of either the red or green form to methanol. The three forms of the complex and how they are interconverted are shown in Figure 5.5.

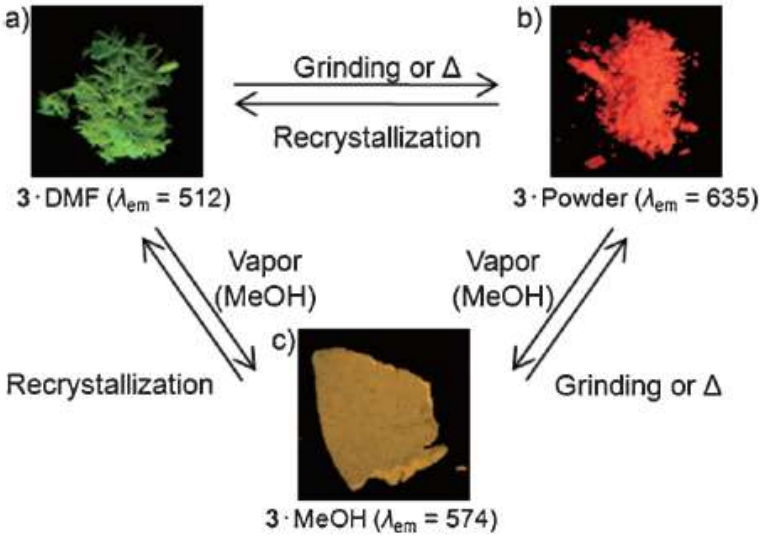

Figure 5.5*: Spectral properties of a Pt(II) complex bearing amide moieties.*[69]

Figure 5.5 shows the three forms of this complex. The green form is obtained by recrystallization form DMF and this can be converted into an orange form by grinding and a yellow form by exposure to MeOH vapour. The process is reversible, however, in most instances it requires recrystallization from DMF or high temperatures to reverse the process. The structures of the green and yellow forms were obtained by single crystal X-ray diffraction. The data suggested that the hydrogen bonding network that formed between the solvent molecules and the amide groups facilitated the Pt…Pt interactions by holding the complex in the correct orientation. This is a similar observation to the previous example. A crystal of the orange form could not be grown, however the transition from the green to orange form was studied using powder diffraction. Upon grinding of the sample, crystallinity was lost and no diffraction data could be collected, the authors could not conclude whether the mechanochromic effect was caused by a change in the Pt…Pt stacking parameters.

Research conducted by Moreno *et al* investigated the vapoluminescence of a Pt/Pb cluster. The structure of which is given in Figure 5.6.[66] The authors discovered that upon exposure to acetone vapour the luminescence changed from orange to yellow over several minutes. Further studies showed that the same process occurred with other donor solvents such as THF. However, the same vapoluminescence effect was not observed with non- donor solvents such as hexane. The vapoluminescence effect was attributed to the stereoactivity of the lone pair on the Pb centre, which causes a distortion of the geometry around this centre when it has been photo-excited.

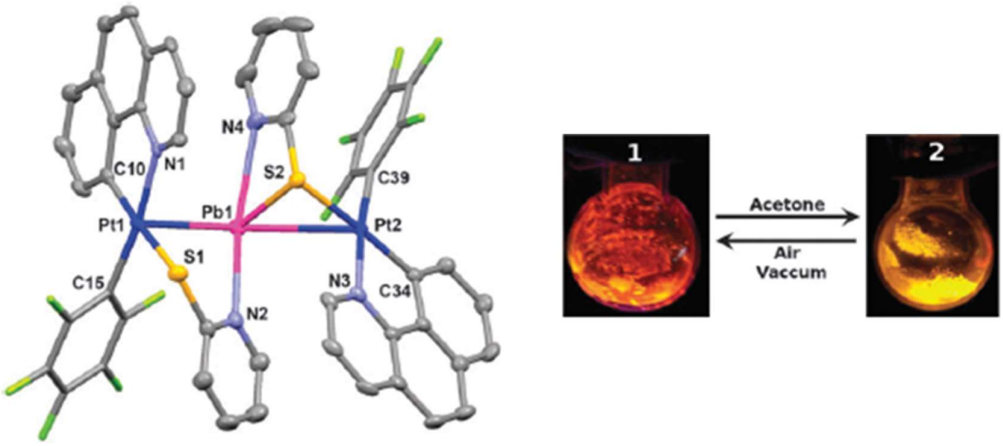

Figure 5.6*: Structure and Vapoluminescence of Pt/Pb Clusters upon contact with acetone.* [66]

5.1.2 Spectrochemical Series

The examples given in Section 5.1.1 show that by manipulation of the ligands and by changing the substituent positions on the ligand or complex a variety of modifications to the spectral properties can be achieved. The research in this chapter will investigate the effect of changing the ligand in the 4th position of the Pt co-ordination sphere.

The spectrochemical series will form the basis of this investigation. The spectrochemical series is a tool used to identify the energy gaps within the d-orbital energy manifold of transition metal complexes. The strength of the resultant ligand field can influence the coordination number and geometry adopted by the complex and whether the complex will exist in a high or low spin state. The ligand spectrochemical series is shown in Scheme 5.1.

$$I^- < Br^- < \boldsymbol{S}CN^- < Cl^- < F^- < NCO^- < OH^- < \boldsymbol{N}CS^- < NH_3 < en < bipy < phen < \boldsymbol{N}O_2^- < PPh_3 < CN^- < CO$$

Scheme 5.1*: Ligand spectrochemical series, placed in order of increasing field strength.*

The weak field ligands such as the halides produce a smaller ligand field splitting than the strong field ligands such as cyanide. This results in Δ_0 for octahedral complexes being larger for the strong field ligand (Figure 5.7). Pt(II) adopts a square planar geometry and the relationship between Δ_o and square planar geometry is shown in Figure 5.7.

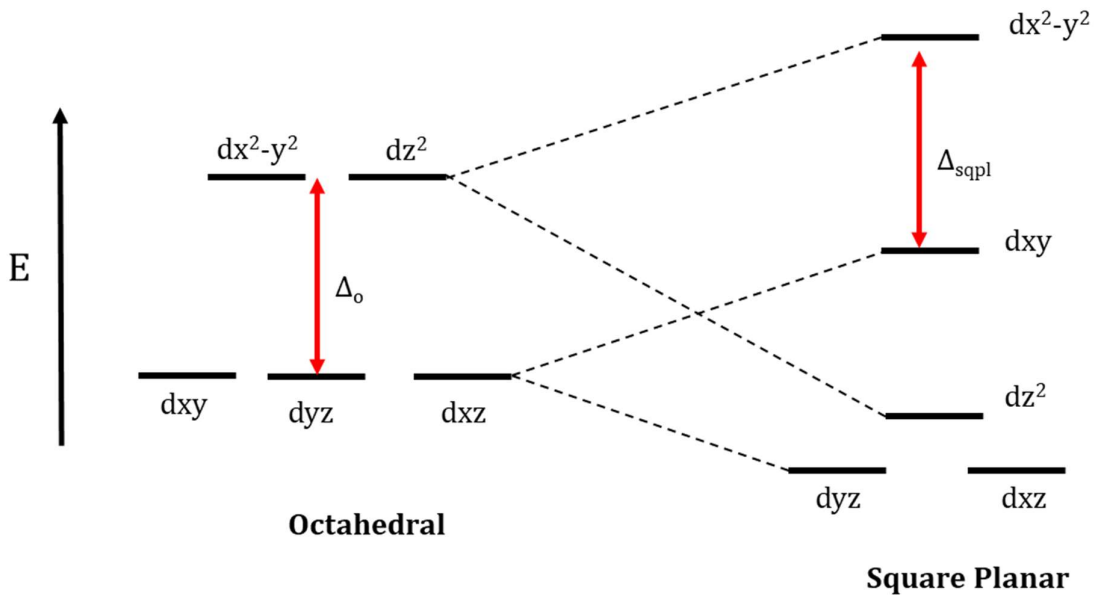

Figure 5.7*: Octahedral vs square planar splitting diagram and the role of Δ_o and Δ_{sqpl}.*

Figure 5.7 illustrates that when Δ_o is increased by the use of a strong field ligand such as cyanide the d_{xy} orbital is pushed toward the frontier orbital and away from the antibonding orbital, which itself is raised in energy. This should substantially alter the spectral properties of the complexes under investigation, because the anti-bonding orbital is unlikely to become occupied when the complexes are photo-excited and therefore luminescence efficiency is increased (Section 1.4.1).

In addition to a spectrochemical series of ligands, there is an analogous series for metal centres. The strength of the field of the metal is dependent on the position of the metal in the d-block and on its oxidation state; the higher oxidation states give larger splitting, and the splitting increases in the order 1st row < 2nd row < 3rd row. This will not be discussed here as the same metal in the same oxidation state will be used throughout this study.

5.1.3 Methyl 3,5-di(pyridin-2-yl)benzoate Platinum Chloride (15)

During this investigation the same N^C^N pincer will be used. The complex depicted in Figure 5.8 will be used as starting material and via a ligand exchange metathesis the chloride ligand will be substituted for a variety of different ligands.

This complex is a known literature complex and has been studied in detail by the Williams group, however its simple synthesis and reasonable solubility makes this a sensible starting material.[47] In addition this pincer backbone has been previously used in the Raithby group to synthesise a rapid vapochromic sensor, detailed in Section 5.1.1. Use of this precursor will therefore allow for the new complexes to be compared to previously reported materials.

The solution state spectroscopy and powder diffraction data has been obtained for this complex under the same conditions as the subsequent complexes detailed in this chapter. This will allow for a more accurate comparison of data.

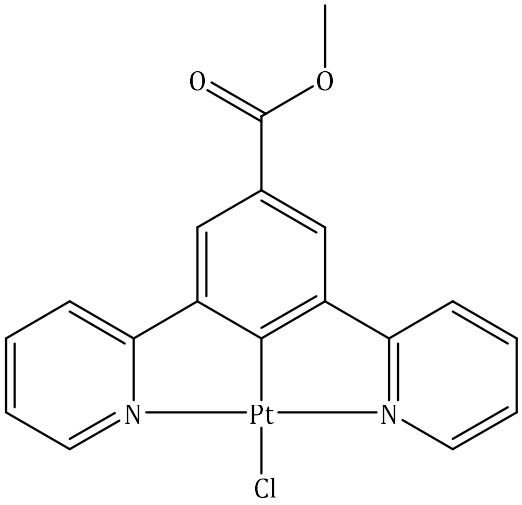

Figure 5.8: *Structure of complex **15*** [47]

The solution state spectroscopy of complex **15** is shown in Figure 5.9 and is in agreement with the literature.[119]

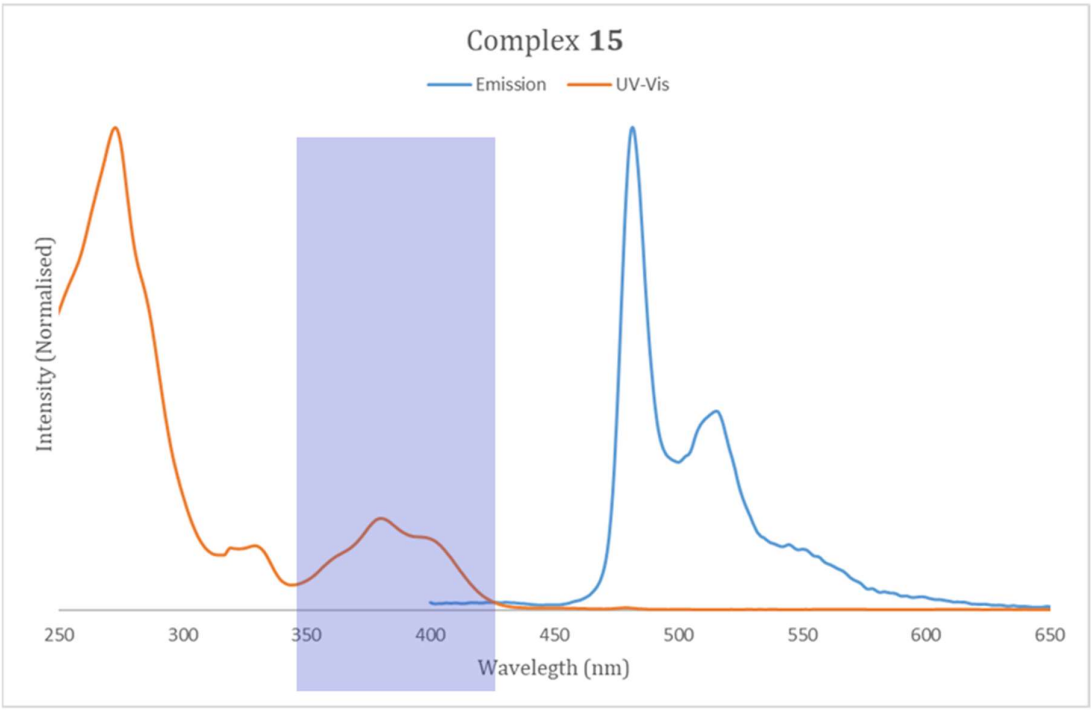

Figure 5.9: *Solution state spectroscopy of Complex **15**, Orange line: UV-Vis absorption solution concentration 1×10^{-4} M in DCM, $^{3}\pi$-π^* transition highlighted, Blue line: Emission solution concentration 1×10^{-7}M in DCM, λ_{ex}380 nm.*

The peaks below 300 nm can be attributed to a $^{1}\pi$-π^* transition, the broad peak between 350-440 nm has been caused by overlapping peaks. There is some $^{1}\pi$-π^* character but the dominant transition is $^{3}\pi$-π^*, which has been facilitated by the high spin coupling constant of the platinum.

In the solution state emission spectrum the blue line in Figure 5.9 is characteristic of a $^3\pi$-π^* due to the pronounced vibrational structure. The small Stokes shift associated with this complex is not compatible with a CT excited state. An excitation wavelength of 380nm was chosen based on the wavelength of the $^3\pi$-π^* transition, which is highlighted in Figure 5.9. The single crystal data collected is consistent with the literature.[47]

5.2.0 Synthetic Strategy

The synthesis of these complexes requires three individual steps, they are as follows:

1. Ligand Synthesis,
2. Cyclometallation Reaction,
3. Ligand Exchange Reaction.

The three steps will be discussed in detail in the following sections.

5.2.1 Ligand Synthesis

The literature method[119] of synthesising Methyl 3,5-di(pyridin-2-yl)benzoate is shown in the top line of Scheme 5.2. The Stille reaction is reliable and yields vary between 50-60%, however the use of organic tin makes this reaction toxic and expensive.

Other potential methods of synthesising this ligand were investigated and the most promising reaction was the Negishi reaction, detailed on the bottom arrow of Scheme 5.2.[120] This method uses milder conditions and has a faster reaction time. In addition, the average yield was 68%, which is consistently higher than that achieved for the Stille reaction. This method was subsequently used for the synthesis of Methyl 3,5-di(pyridin-2-yl)benzoate, however in later chapters this method could not be used with more highly substituted dibromo species.

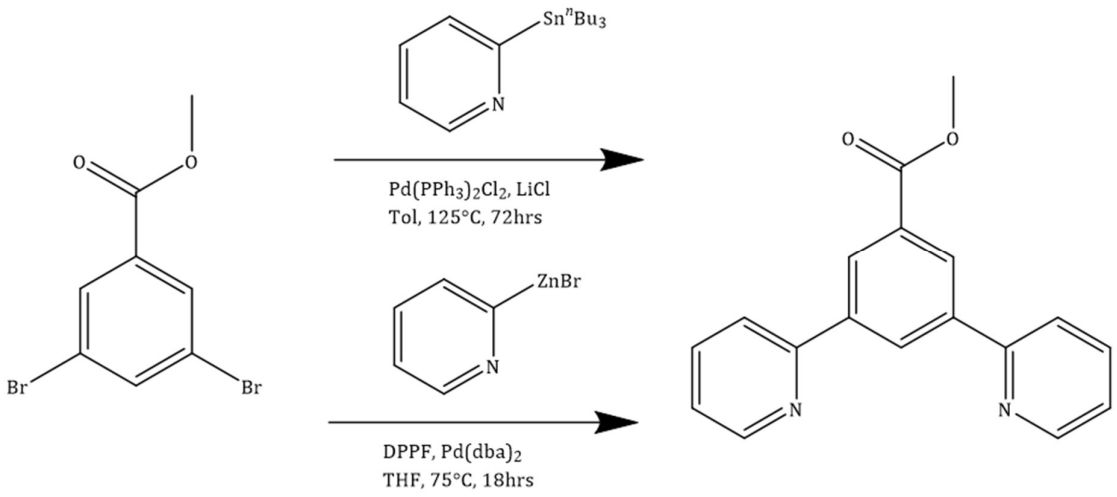

Scheme 5.2: *Synthesis of Methyl 3,5-di(pyridin-2-yl)benzoate using the Stille Reaction (Top) or Negishi Reaction (Bottom).*

5.2.2 Chloride Starting Material (15)

This complex **15** was synthesised by a cyclometallation reaction as published in the literature[119] and a yield of 98% was consistently recovered. The reaction conditions are shown in Scheme 5.3.

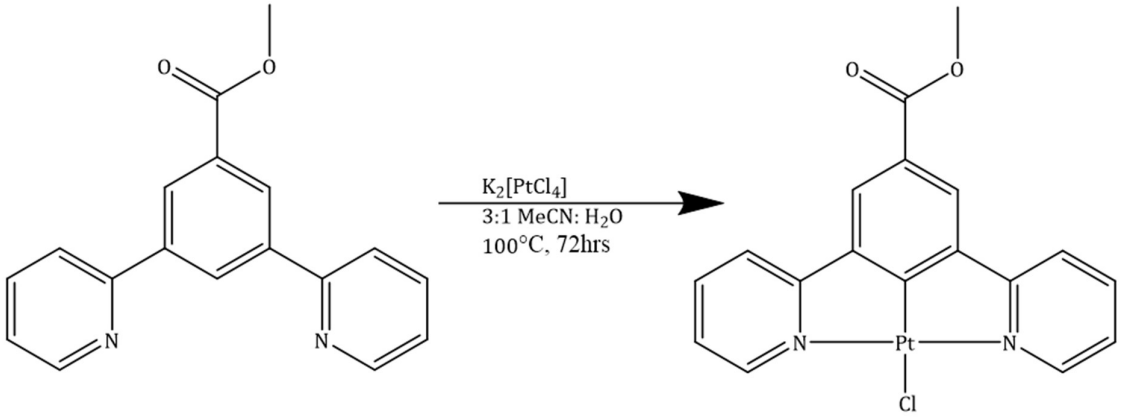

Scheme 5.3*: Synthesis of Methyl 3,5-di(pyridin-2-yl)benzoate platinum chloride.*

5.2.3 Ligand Exchange

To synthesise the complexes of interest a simple ligand exchange reaction was carried out, which is detailed in Scheme 5.4.

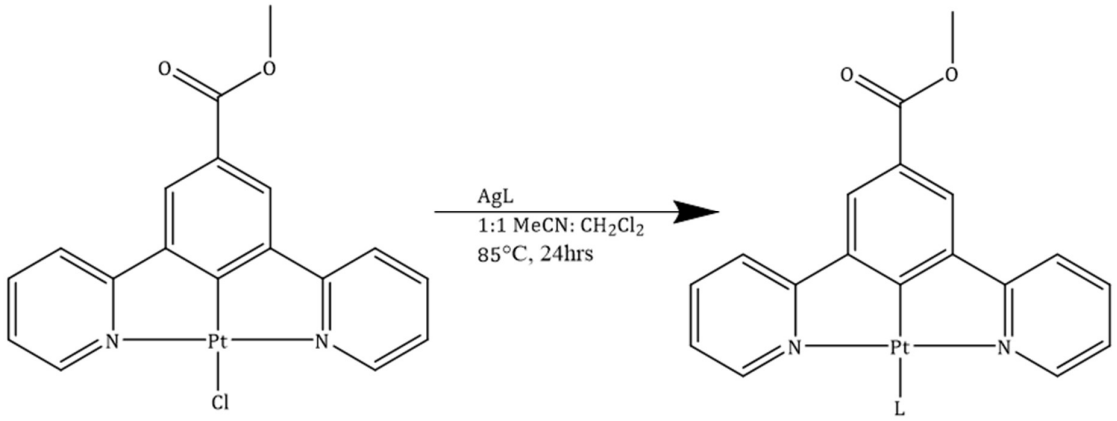

Scheme 5.4*: Ligand exchange reaction.*

A silver salt has been used in this reaction as opposed to a sodium or potassium salt to ensure the right product is isolated. It was observed that when using the sodium/ potassium salts the chloride would not always be abstracted fully before the new ligand co-ordinated. This meant that one of the pyridines on the ligand is displaced. The use of a silver salt ensures the chlorine is fully abstracted before the new ligand then attacks, due to the formation of silver chloride as a by-product.

5.3.0 Methyl 3,5-di(pyridin-2-yl)benzoate Platinum Cyanate (16)

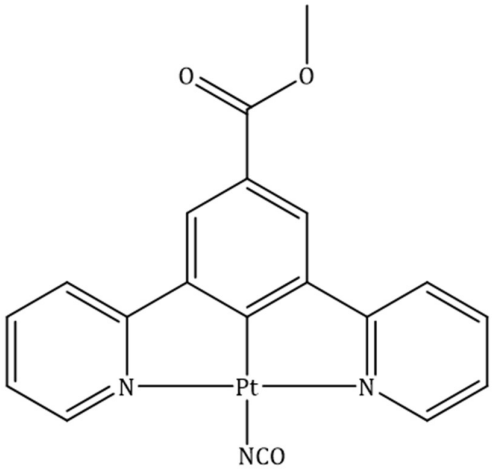

Complex **16** was synthesised from complex **15** using a ligand exchange reaction, detailed in Scheme 5.4. A bright yellow solid was isolated in a good yield. ^{1}H NMR spectroscopy, IR, powder diffraction and single crystal X-ray analysis confirmed the structure of the complex.

5.3.1 Solution State Spectroscopy

Solution state UV-Vis absorption and emission spectroscopy was carried out for this complex. Figure 5.10 and 5.11 shows the measured spectra.

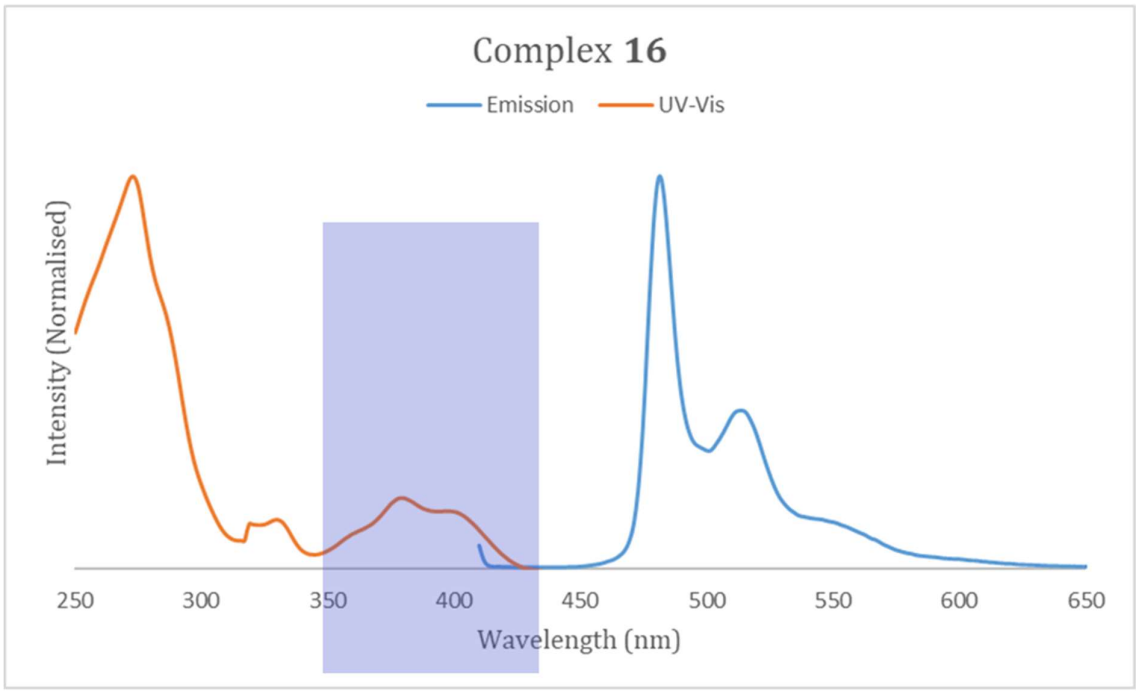

Figure 5.10*: Solution state spectroscopy of Complex **16**, Orange line: UV-Vis solution concentration 1×10^{-5} M in DCM, $^{3}\pi$-π^* transition highlighted, Blue line: Emission solution concentration 1×10^{-6}M in DCM, λ_{ex}400 nm.*

The UV-Vis absorption and emission profile for complex **16** is very similar to the profiles measured for complex **15** and can be assigned in the same way. However, Figure 5.11 shows the emission spectra of complex **16** at a higher concentration. In this instance the pronounced vibrational structure of the $^{3}\pi$-π^* transition remains, but there is an addition broad peak between 600-750 nm. This broad band is indicative of excimer formation,[119] which can occur when at high concentrations of Pt are present due to a self- quenching effect or aggregation of the molecules.

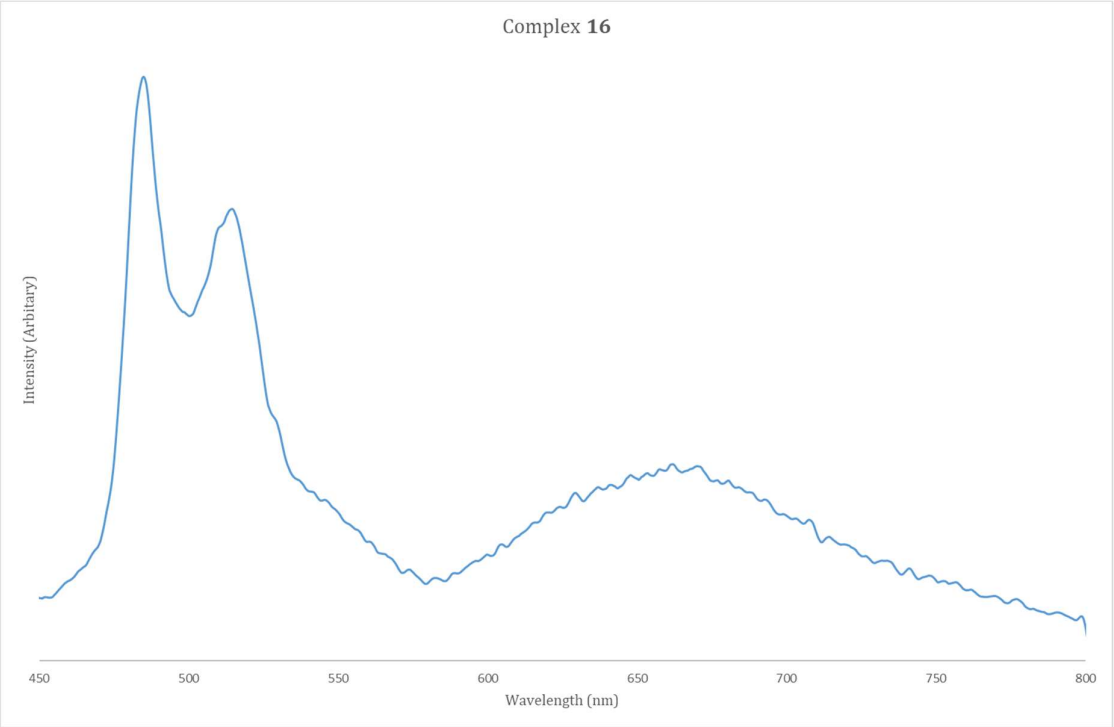

Figure 5.11*: Solution state spectroscopy of Complex **16**, Blue line: Emission solution concentration 1×10^{-3} M in DCM, λ_{ex}400 nm*

5.3.2 Vapo/Solvatochromic Behaviour

Complex **16** is a yellow solid, which based on the research presented in Chapter 4 would suggest that no vapo/solvatochromic behaviour would be observed in this complex. The complex was tested in the solution state by dissolving in a variety of solvents and in the solid state by exposure to a series of vapours. No spectral changes were observed when the complex was tested, the reason for this is evident from the solid-state structure of the complex.

5.3.3 Crystal Structure Analysis

Crystal Structure

Crystals of complex **16** were grown from the slow evaporation of a mixture of solvents. The complex crystallises in the triclinic space group P-1, with one molecule in the asymmetric unit. The structure is given in Figure 5.12 and crystal and structural refinement data can be found in Table 5.1.

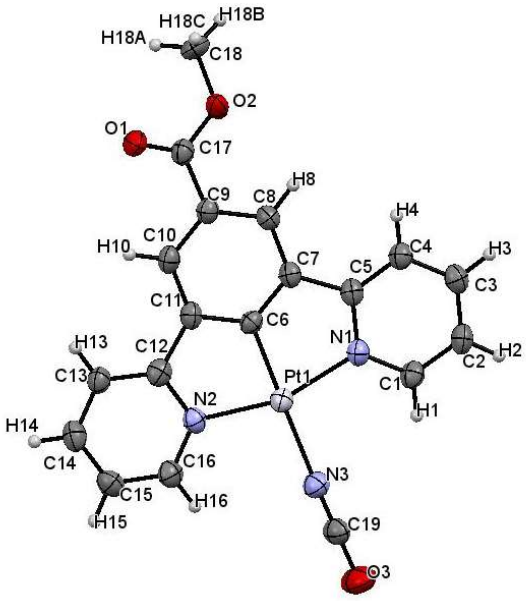

Figure 5.12*: Single crystal X-ray structure for complex* ***16*** *grown from slow evaporation of a mixture of solvents. Ellipsoids shown at the 50% probability level.*

Table 5.1*: Crystal data and structure refinement for Complex* ***16***

Identification code	P17prr74
Empirical formula	$C_{19}H_{13}N_3O_3Pt$
Formula weight	526.41
Temperature/K	150(8)
Crystal system	triclinic
Space group	P-1
a/ Å	7.2737(4)
b/ Å	10.8511(5)
c/ Å	11.9475(7)
α/°	64.988(5)
β/°	88.479(4)
γ/°	72.764(4)
Volume/ Å^3	810.85(8)
Z	2
ρ_{calc}g/cm^3	2.156
μ/mm^{-1}	8.678
F(000)	500.0
Radiation	MoKα (λ = 0.71073)
2Θ range for data collection/°	6.908 to 52.736
Index ranges	-9 ≤ h ≤ 8, -13 ≤ k ≤ 13, -14 ≤ l ≤ 14
Reflections collected	12218
Independent reflections	3297 [R_{int} = 0.0499, R_{sigma} = 0.0396]
Data/restraints/parameters	3297/0/236
Goodness-of-fit on F^2	1.026
Final R indexes [I>=2σ (I)]	R_1 = 0.0272, wR_2 = 0.0628
Final R indexes [all data]	R_1 = 0.0306, wR_2 = 0.0649
Largest diff. peak/hole / e Å^{-3}	1.65/-0.67

16 has the expected square planar geometry around the Pt centre. There is a slight distortion with the N1-Pt1-N2 angle which has been measured at 161.15(17)˚, this is attributed to the bite of the pincer ligand.[93] The multiple bonds in the NCO group are shorter than the rest of the measured bond lengths, which is expected, Table 5.2a. The NCO group is close to linear with the angles provided in Table 5.2b.

The dihedral angles for the complex were negligible and the torsion angles were close to 0° or 180°. The methyl ester group sits parallel to the plane of the pincer ligand. Analysis of the bond angles and torsion angles of the NCO group showed that the group deviates slightly from linearity in the solid state.

Table 5.2*: a. Table of bond lengths for **16**. b. Table of bond angles for **16**. c. Torsion angles for **16**.*

a. Bond Lengths		
Atom	**Atom**	**Length/ Å**
Pt1	N1	2.033(4)
Pt1	N2	2.033(4)
Pt1	N3	2.091(4)
Pt1	C6	1.908(5)
N3	C19	1.154(6)
O3	C19	1.207(7)

b. Bond Angles			
Atom	**Atom**	**Atom**	**Angle/˚**
N1	Pt1	N2	161.15(17)
N1	Pt1	N3	98.76(17)
N2	Pt1	N3	100.10(16)
C6	Pt1	N1	80.57(18)
C19	N3	Pt1	177.1(4)
C6	Pt1	N3	178.78(15)
N3	C19	O3	178.9(6)

c. Torsion Angles				
A	**B**	**C**	**D**	**Angle/˚**
N3	Pt1	N2	C16	-3.6(5)
N3	Pt1	N1	C1	-0.7(5)
Pt1	N1	C5	C7	-0.2(5)
Pt1	N2	C12	C11	1.2(6)
Pt1	C6	C7	C5	-0.8(6)
Pt1	C6	C11	C12	-2.2(6)
C6	Pt1	N3	C19	9(16)
Pt1	N3	C19	O3	-111(34)

There are two sets of π-π interactions in this complex, based on the planes in which these π interactions act between, they are present between the pyridyl rings in adjacent layers. This is clearly shown in Figure 5.13b. In addition to the π interactions there are a number of hydrogen bonding interactions present in the solid state. These interactions occur between the NCO ligand and the oxygen of the methyl ester group. This suggests that the complex packs head to tail as shown in Figure 5.13a.

Table 5.3: *a. Planes Present in solid-state structure for **16**. b. π-π Interactions for **16**. c. Hydrogen bonds for **16**.*

a. Plane Identification	
Plane Number	Atoms in plane
1	C10 C9 C8 C7 C6 C11
2	N2 C16 C15 C14 C13 C12
3	N1 C1 C2 C3 C4 C5

b. π-π Interactions	
Planes	Distance (Å)
1-3	3.677
2-3	3.883

c. Hydrogen bonds			
Atoms	(D…A) Distance (Å)	(H…A) Distance (Å)	D…H…A Angle/°
C16-H16-O3	3.184(8)	2.603	121.1
C15-H15-O3	3.123(9)	2.492	125.4
C13-H13-O1	3.193(6)	2.417	140.9

Crystal Packing: Stacking and Pt Offset

Complex **16** showed no vapo/solvatochromic behaviour and the reason for this is that the complex packs head to tail in the solid state, shown in Figure 5.13. Further analysis of the void space in the complex was completed using the program Mercury.[87] There was no appreciable void space found in the crystal structure of **16**. This implies that there is not the available space for solvent to move in and out of the crystal structure in the solid state, providing further evidence for the lack of vapo/solvatochromic behaviour.

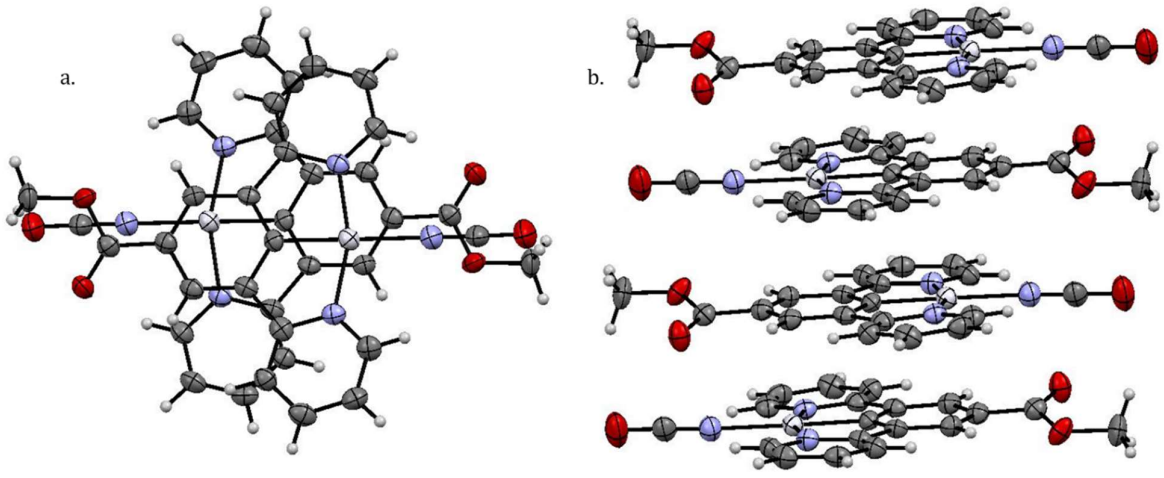

Figure 5.13: *a. Complex **16** viewed along the a axis. b. stacking of complex **16** in the solid state. Ellipsoids shown at 50% probability.*

Figure 5.13a shows two different Pt positions in the solid state, these are related by a centre of symmetry due to only one molecule in the asymmetric unit. There are no Pt…Pt interactions in the solid state to manipulate and the lack of solvent in the structure accounts for no hydrogen-

bonding network, which may have drawn the Pt centres into alignment, as seen with examples discussed in Section 5.1.2.

The NCO ligand sits only a couple of positions higher than the chloride ligand in the spectrochemical series (Scheme 5.1) and is a weak field ligand, so the lack of strong Pt interactions was predicted.

5.3.4 X-Ray Powder Analysis

Figure 5.14 depicts the experimental and predicted powder trace for Complex **16**. It can be seen they are in full agreement. This means that the single crystal data discussed in Section 5.3.3 is representative of the bulk powder.

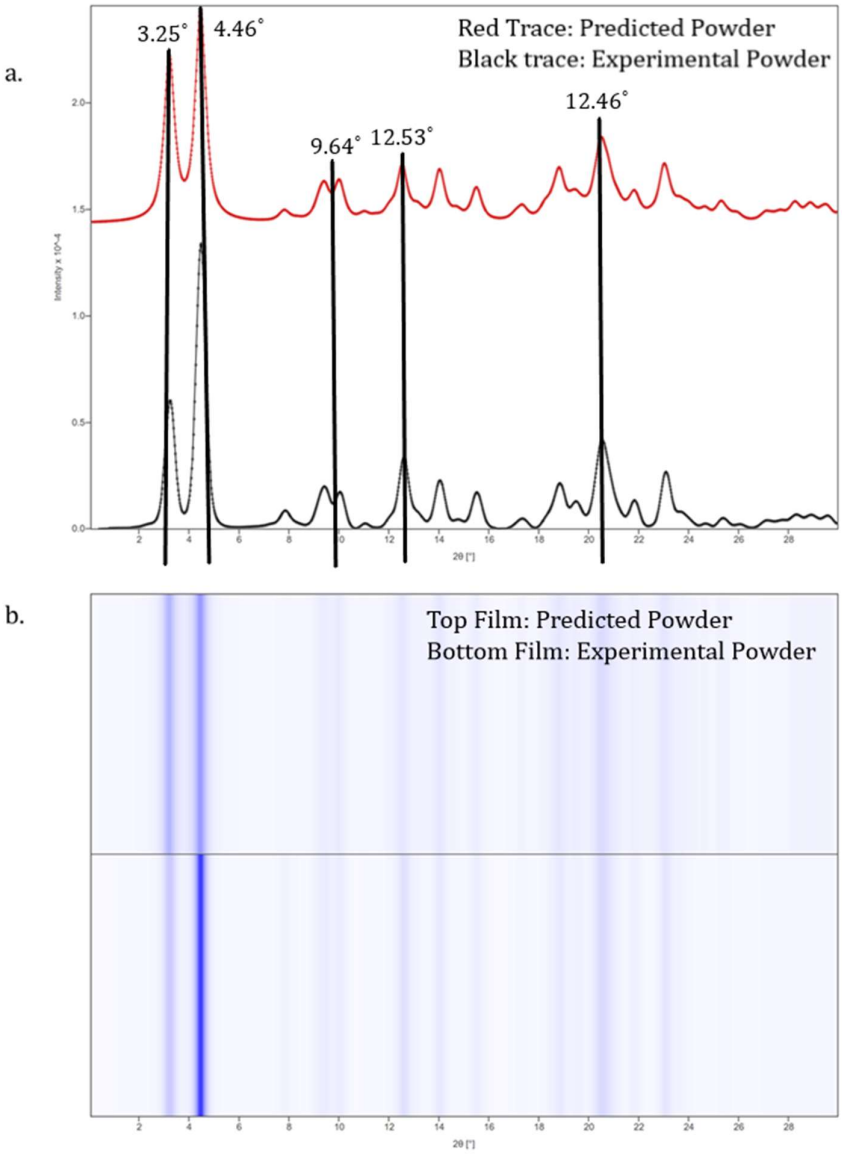

Figure 5.14*: a. Complex **16** powder plot. b. Film representation of powder of Complex **16**. Top trace is the predicted powder generated from crystal structure (red) and bottom trace is the experimental powder (black).*

5.4.0 Methyl 3,5-di(pyridin-2-yl)benzoate Platinum Thiocyanate (17)

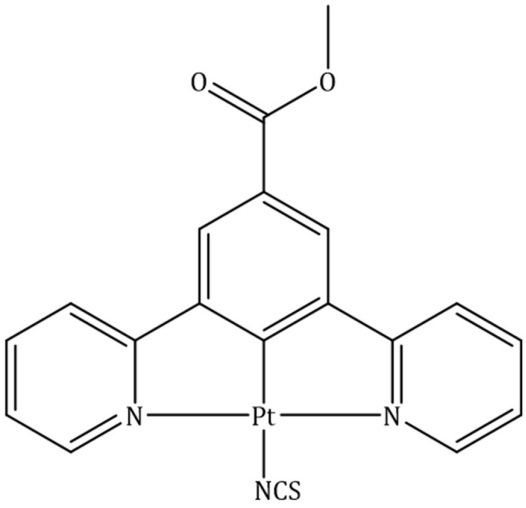

Complex **17** was isolated in good yield as a yellow solid. The structure was confirmed by IR, ^{1}H NMR spectroscopies and by X-ray diffraction techniques.

5.4.1 Solution State Spectroscopy

The solution state UV-vis absorption and emission spectroscopy for Complex **17** are shown in Figure 5.15 and 5.16.

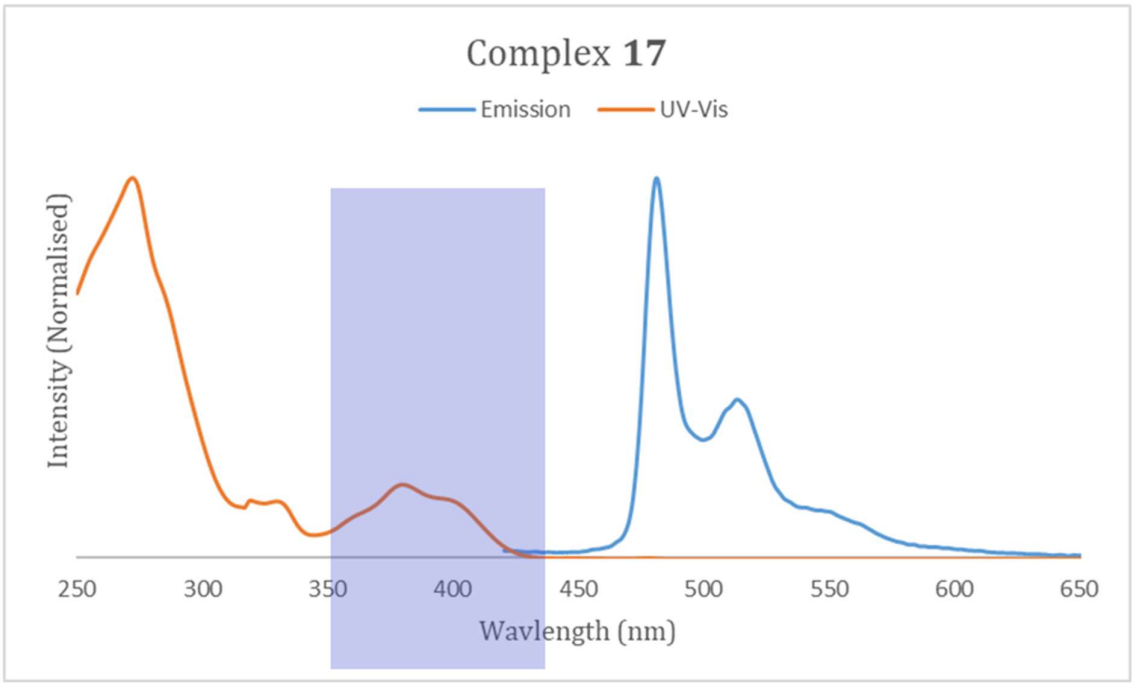

Figure 5.15*: Solution state spectroscopy of Complex **17**, Orange line: UV-Vis solution concentration 1×10^{-4} M in DCM, $^{3}\pi$-π^* transition highlighted, Blue line: Emission solution concentration 1×10^{-6} M in DCM, λ_{ex}400 nm.*

The profile of the solution state spectroscopy for Complex **17** is similar to that measured for complex **15**. The UV-Vis absorption and emission peaks are the same shape and the major peaks

appear at the same wavelength. This suggests that the change to a mid-field ligand does not have any effect on the solution state spectral properties of the complex.

Figure 5.16 shows the change in emission profile with change in concentration of the solution. As observed with Complex **16**, there is excimer formation at high Pt concentrations. However, the excimer is not as pronounced with the NCS ligand.

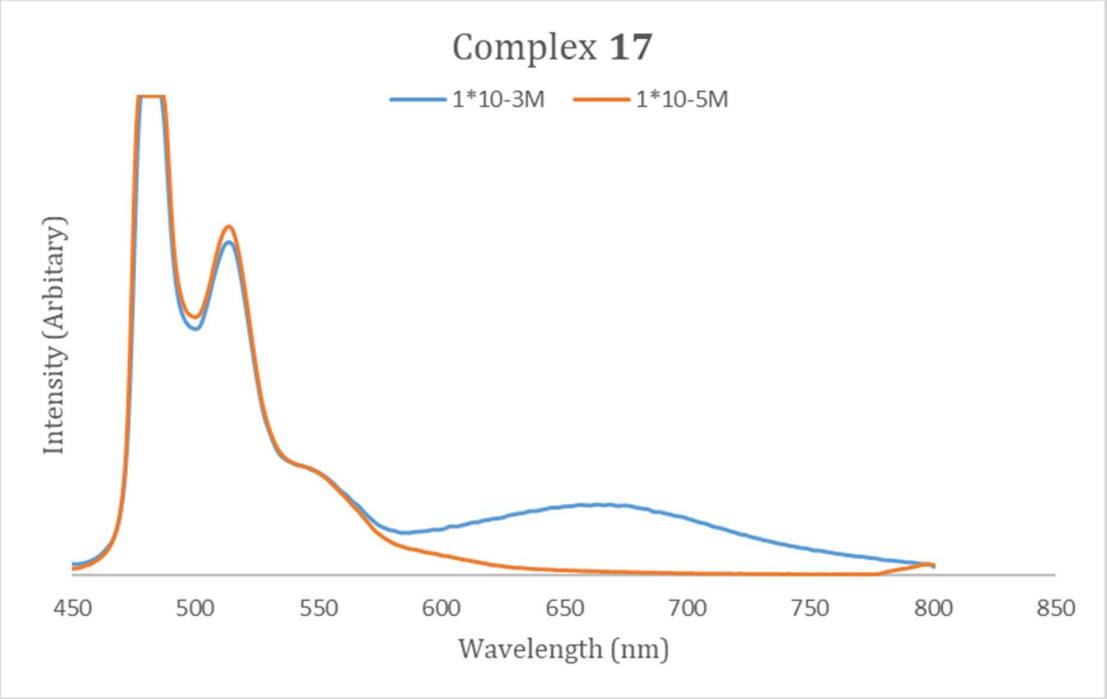

Figure 5.16*: Solution state spectroscopy of Complex **17**, Blue line: Emission solution concentration 1×10^{-3} M in DCM, orange line 1×10^{-5} M. λ_{ex}400 nm*

5.4.2 Vapo/Solvatochromic Behaviour

This complex is a deep yellow/pale orange in colour, which initially suggested that some Pt…Pt overlap existed that could be manipulated. However, upon further investigation of the complex no spectral changes were observed.

5.4.3 Crystal Structure Analysis

Crystal Structure

Crystals of complex **17** were grown from the slow diffusion of diethyl ether into a concentrated acetonitrile solution at -18°C. It crystallises in the monoclinic space group $P2_1/c$, with one molecule in the asymmetric with no solvent present.

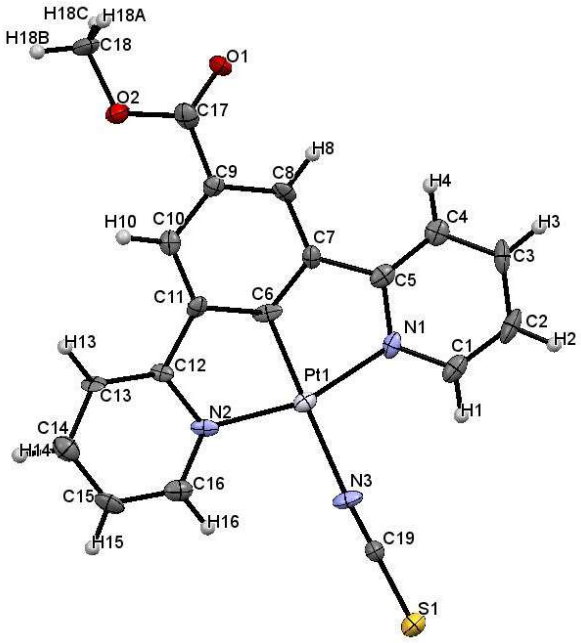

Figure 5.17*: Single crystal X-ray structure for complex **17** grown from a vapour diffusion of diethyl ether into a concentrated acetonitrile solution. Ellipsoids are shown at the 50% probability level.*

Table 5.4*: Crystal data and structure refinement for Complex **17***

Identification code	s17prr181
Empirical formula	$C_{19}H_{13}N_3O_2PtS$
Formula weight	542.47
Temperature/K	150.00(10)
Crystal system	monoclinic
Space group	$P2_1/c$
a/ Å	7.7842(8)
b/ Å	22.6186(9)
c/ Å	13.3599(14)
α/°	90
β/°	136.167(19)
γ/°	90
Volume/ Å^3	1629.1(5)
Z	4
ρ_{calc}g/cm^3	2.212
μ/mm^{-1}	8.761
F(000)	1032.0
Radiation	MoKα (λ = 0.71073)
2Θ range for data collection/°	5.688 to 52.736
Index ranges	-7 ≤ h ≤ 9, -27 ≤ k ≤ 18, -16 ≤ l ≤ 16
Reflections collected	5570
Independent reflections	3155 [R_{int} = 0.0390, R_{sigma} = 0.0789]
Data/restraints/parameters	3155/0/236
Goodness-of-fit on F^2	0.996
Final R indexes [I>=2σ (I)]	R_1 = 0.0406, wR_2 = 0.0661
Final R indexes [all data]	R_1 = 0.0601, wR_2 = 0.0744
Largest diff. peak/hole / e Å^{-3}	1.12/-1.61

17 adopts the square planar geometry around the Pt centre with a slight distortion in the N1-Pt1-N2 angle caused by the pincer bite angle, Table 5.5b. The measured angles and distances are in line with those previously reported in the literature. The SCN group is bound via the nitrogen group as is expected with Pt complexes. It is close to linearity with the Pt centre with only a 5° deviation measured.

The torsion angles are close to zero, except those detailed in table 5.5c. This shows that the ligand is planar with the deviation from linearity seen with a slight twist of the NCS group. The dihedral angles between the Pt centre and the plane of the pincer ligand and the NCS group is negligible. This suggests that overall the complex adopts a planar geometry in the solid state.

17 adopts a very similar solid-state structure and geometry to **16**, this is not surprising due to the presence of a three-atom ligand in the 4th co-ordination site.

Table 5.5*: a. Table of bond lengths for **17**. b. Table of bond angles for **17**. c. Torsion angles for **17**.*

a. Bond Lengths		
Atom	**Atom**	**Length/ Å**
Pt1	C6	1.909(7)
Pt1	N2	2.036(6)
Pt1	N1	2.034(6)
Pt1	N3	2.097(6)
S1	C19	1.637(7)
C19	N3	1.139(8)

b. Bond Angles			
Atom	**Atom**	**Atom**	**Angle/°**
N1	Pt1	N2	161.0(2)
N1	Pt1	N3	99.0(2)
C6	Pt1	N1	80.3(3)
C6	Pt1	N3	178.0(3)
C19	N3	Pt1	175.8(7)
N3	C19	S1	179.5(7)

c. Torsion Angles				
A	**B**	**C**	**D**	**Angle/°**
N2	Pt1	N3	C19	-157(11)
N1	Pt1	N3	C19	21(11)

There are two major π-π interactions in this complex, as observed with **16** the complex forms intermolecular π interactions between the pyridyl rings and the central phenyl ring of the pincer ligand in adjacent layers. Figure 5.18 shows that as with **16** the complex stack head to tail.

There are a number of hydrogen bonds that form in this structure, Table 5.6c. These form between the methyl ester group, the pyridyl rings, and the hydrogen atoms on the pyridyl ring and the sulphur atom on the NCS group.

Table 5.6: *a. Planes Present in solid-state structure for **17**. b. π-π Interactions for **17**. c. Hydrogen bonds for **17**.*

a. Plane Identification	
Plane Number	Atoms in plane
1	C8 C9 C10 C11 C6 C7
2	N1 C1 C2 C3 C4 C5
3	N2 C12 C13 C14 C15 C16

b. π-π Interactions	
Planes	Distance (Å)
1-3[1]	3.913(2)
2-3[2]	3.659(1)

c. Hydrogen bonds			
Atoms	(D…A) Distance (Å)	(H…A) Distance (Å)	D…H…A Angle/°
C3-H3-S1	3.77(1)	2.990	142.8
C14-H14-O2	3.49(2)	2.640	152.2
C15-H15-O1	3.32(1)	2.615	133.3

Where [1] (1-X, 1-Y, 1-Z), [2] (2-X, 1-Y, 1-Z).

Crystal Packing: Stacking and Pt Offset

Due to the lack of vapo/solvatochromic behaviour in this complex, it would be predicted that the complex would not stack in the solid state. Figure 5.18 confirms this prediction. In addition a void space calculation was performed in Mercury;[87] this showed that the complex had no void space for a solvent to diffuse in and out. This lack of void space or solvent channels in the crystal structure further confirms that vapochromic behaviour in this complex would not be observed.

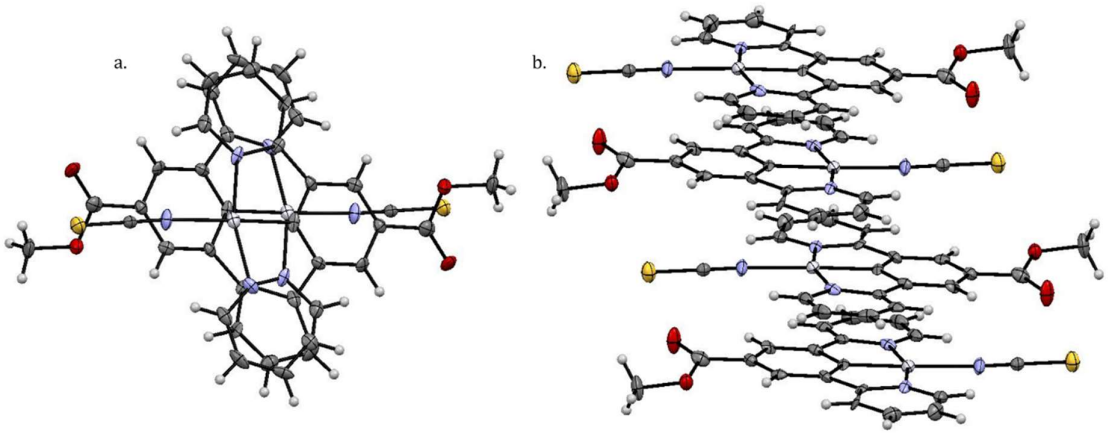

Figure 5.18: *a. Complex **17** viewed along the a axis. b. stacking of complex **17** in the solid state. Ellipsoids shown at 50% probability.*

Complex **17** has adopted the same solid state packing as observed for complex **16**. There are two Pt positions in the structure that are related by a centre of symmetry. In the stacks the molecules have stacked head to tail minimising steric interactions of the methyl ester pincer.

The SC**N** ligand sits higher than both the Cl and NCO ligands in the spectrochemical series, Scheme 5.1. Even with it being classified as a mid-strength ligand the SC**N** ligand is not of a high enough field strength to alter the solid and solution state properties of the complex, as was observed with the cyanide example provided in Section 5.1.2.

5.4.4. X-Ray Powder Analysis

Figure 5.19 is a comparison of the single crystal isolated in Section 5.4.3 and the bulk powder. Unfortunately, the powder patterns are not in full agreement, suggesting that the single crystal data is not consistent with the bulk powder. The reason for this could be due to presence of other solvates or polymorphs present in the power. The crystal studied in Section 5.4.3 was not the only crystalline material grown, however the other samples were not suitable for analysis by single crystal diffraction. It could therefore be these other crystalline forms that are present in the bulk powder. Due to the single crystal structure not being representative of the bulk power, the solid-state structure and solution state spectroscopy studies cannot be compared.

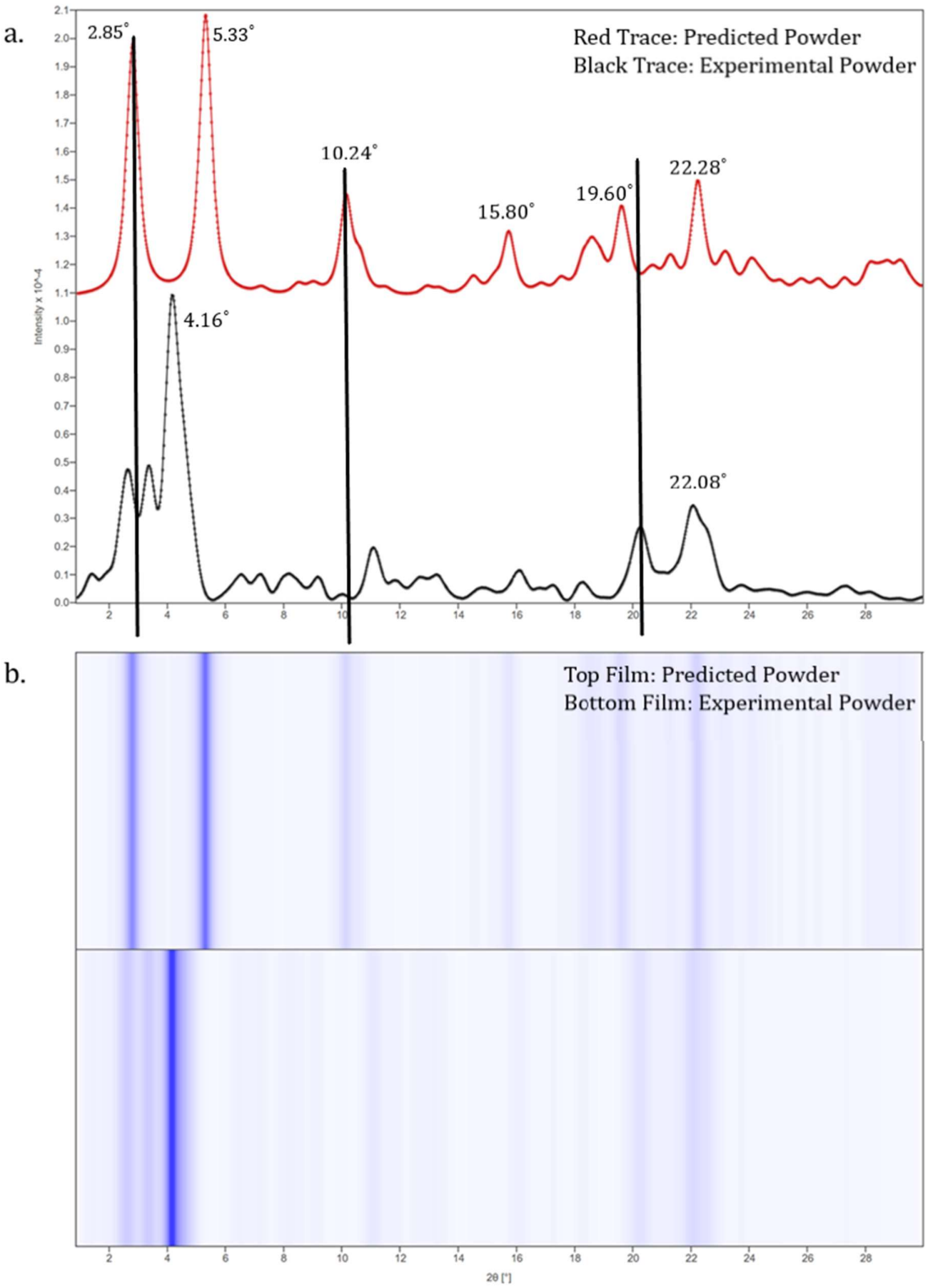

Figure 5.19: *a. Complex **17** powder plot. b. Film representation of powder of Complex **17**. Top trace is the predicted powder generated from crystal structure (red) and bottom trace is the experimental powder (black).*

5.5.0 Methyl 3,5-di(pyridin-2-yl)benzoate Platinum Acetate (18)

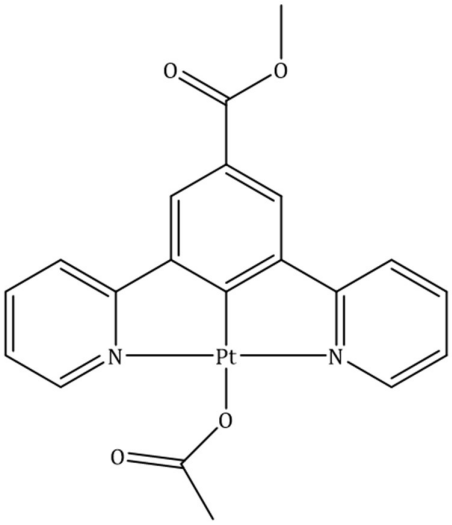

This complex was isolated as a beige powder in good yield. The structure was confirmed by IR and ^{1}H NMR spectroscopies in addition to X-ray diffraction techniques.

5.5.1 Solution State Spectroscopy

Complex **18** was initially studied in the solution state, and as for complexes **16** and **17**, the profile of the UV-vis absorption and emission solution state spectroscopy matches complex **15**.

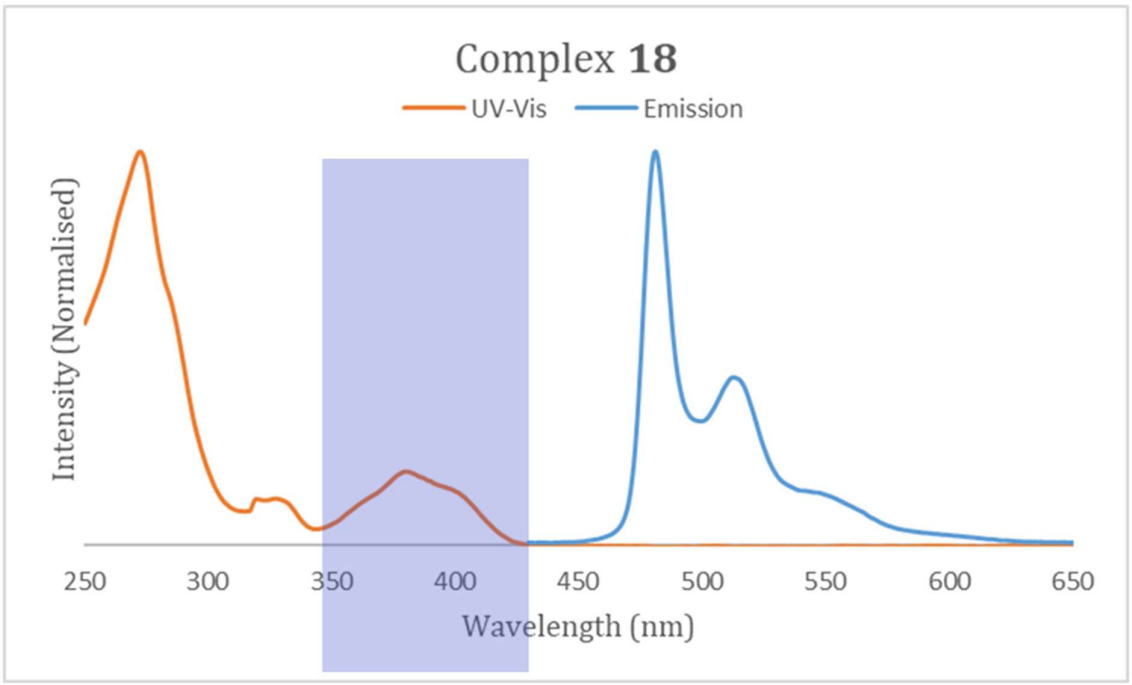

Figure 5.20: *Solution state spectroscopy of Complex **18**, Orange line: UV-Vis solution concentration 1×10^{-4} M in DCM, $^{3}\pi$-π^* transition highlighted, Blue line: Emission solution concentration 1×10^{-6} M in DCM, λ_{ex}400 nm.*

The reason for the same profile could be attributed to the fact that the majority of the transitions present in the solution state occur from the pincer ligand and not the ligand in the 4th co-ordination site. By substituting the chloride for another ligand, the profile of the solution state spectra would then not be expected to change.

5.5.2 Vapo/Solvatochromic Behaviour

This complex is isolated as a beige solid but upon recrystallization from DCM there was a slight change in colour from the orange/beige colour to a lighter yellow. Upon further testing with methanol it was found that is turned a green/blue colour. The three different forms are shown in Figure 5.21 where thin films of the aqueous material have been deposited on glass slides and either dried or treated with methanol.

Figure 5.21*: The three forms of complex* ***18.***

The forms shown in Figure 5.21 were isolated using vapochromic techniques. The orange form exists under standard conditions and the yellow form is accessed by the use of DCM vapour or by passing a stream of dry N_2 over the film. Finally, the blue form is created by the use of methanol vapour.

Solid-state UV-vis absorption spectra showed three distinct profiles for the different forms of this complex, as shown in Figure 5.22. In this instance the peaks define the colour of the complex, this enables monitoring of the colour change using spectroscopy as well as by eye.

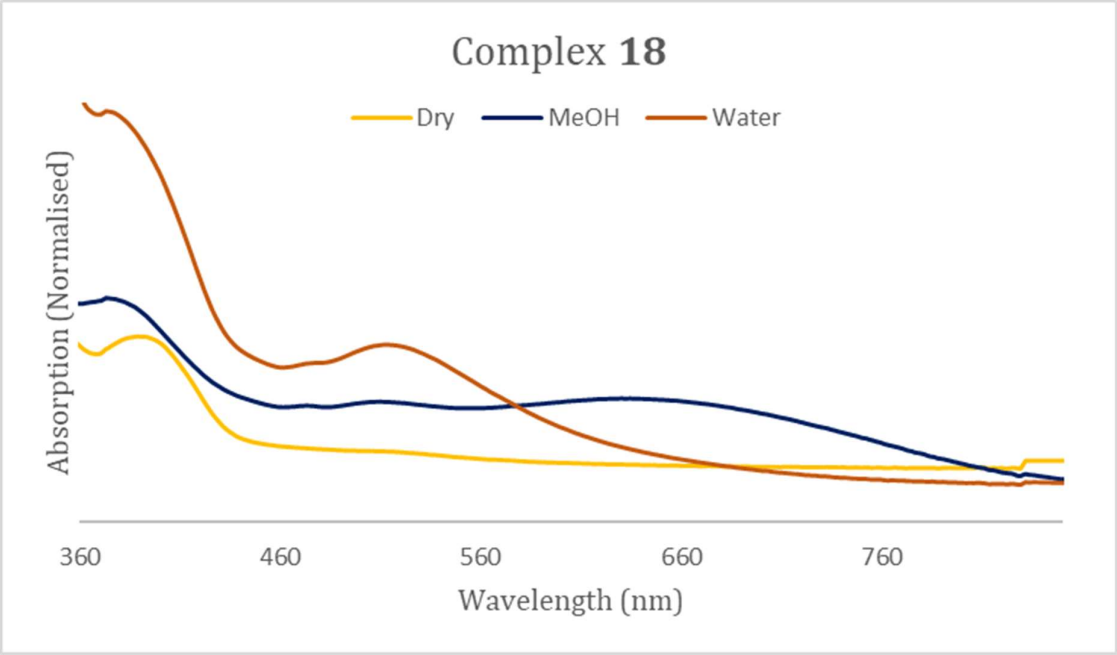

Figure 5.22*: Solid State UV-Vis Absorption of Complex* ***18.***

The potential solvatochromic capabilities of the complex were studied using solution state spectroscopy. In Section 5.5.1, it was shown that the identity of the ligand in the 4th co-ordination site does not change the solution state UV-Vis spectra. However, addition of methanol to a solution may cause aggregation of the Pt molecules and a shift in colour from yellow to a blue/green. The results of this study are shown in Figure 5.23.

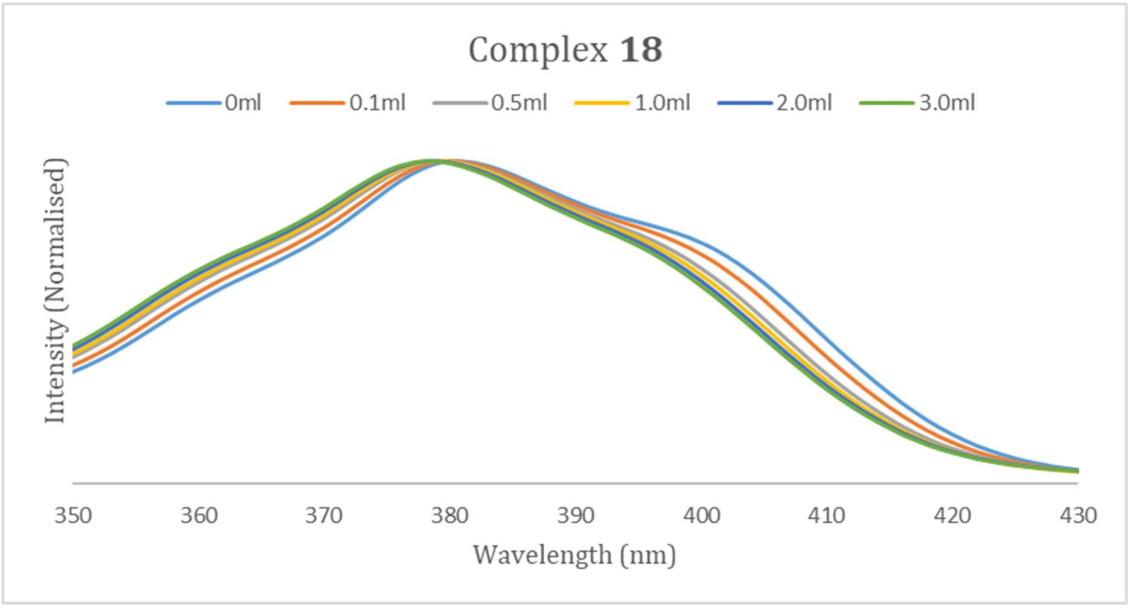

Figure 5.23*: UV-Vis study of Complex* ***18****, 1×10-4 M Solution of Complex* ***18*** *in DCM, MeOH Added.*

Figure 5.23 shows there is a slight shift in profile upon the addition of the MeOH to the solution. The UV-Vis spectra are shown between 350-430 nm due the transitions that occur in this region,

this peak can be attributed to the $^{1}\pi$-π^* and $^{3}\pi$-π^* transitions of the complex. While these transitions occur on the pincer ligand it is the high spin orbit coupling associated with the Pt centre that allows this intersystem crossing, so any changes centre the Pt environment may be communicated via this peak.

Figure 5.23 shows a slight shift in the peak maxima upon addition of the MeOH, however this change is not significant. There was also no visual changes in the vial and the complex did not look like it was aggregating. The emission spectra were also collected under the same conditions and no changes were observed upon the addition of the MeOH. Based on this evidence complex **18** can be classified as vapochromic but shows no solvatochromic properties.

5.5.3 Crystal Structure Analysis

Crystal Structure: Water Form

Single crystals of a hydrated from of complex **18** were isolated from the slow evaporation of a water and acetone mix. There is one molecule in the asymmetric unit and thus two symmetry related molecules in the unit cell, along with four molecules of water, since the complex crystallises in the triclinic space group, P-1. The structure is given in Figure 5.24 and crystal and structural refinement data can be found in Table 5.7.

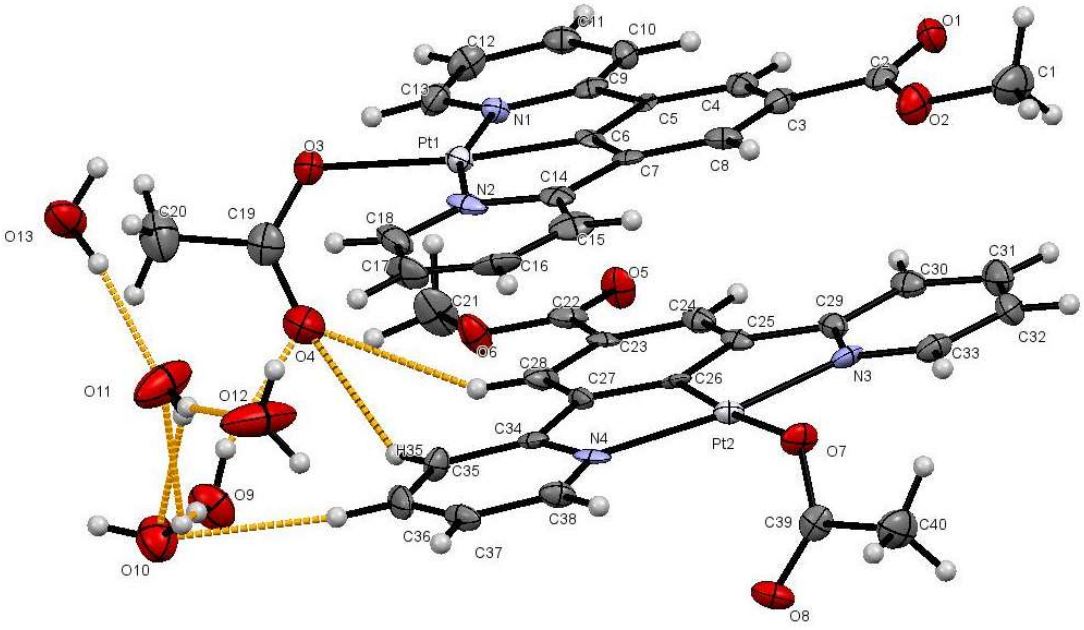

Figure 5.24*: Single crystal X-ray structure for complex* ***18*** *grown from a slow evaporation of a water and acetone solvent mixture. Hydrogen bonds depicted in orange. Ellipsoids are shown at the 50% probability level.*

Table 5.7: *Crystal data and structure refinement for Complex **18**, hydrated form.*

Identification code	s15prr141
Empirical formula	$C_{40}H_{42}N_4O_{13}Pt_2$
Formula weight	1176.95
Temperature/K	150(2)
Crystal system	triclinic
Space group	P-1
a/ Å	7.08014(16)
b/ Å	15.7289(7)
c/ Å	18.5245(7)
α/°	73.209(4)
β/°	84.553(3)
γ/°	80.933(3)
Volume/ Å^3	1947.65(13)
Z	2
ρ_{calc}g/cm^3	2.007
μ/mm^{-1}	7.248
F(000)	1140.0
Radiation	MoKα (λ = 0.71073)
2Θ range for data collection/°	6.678 to 58.672
Index ranges	-9 ≤ h ≤ 8, -20 ≤ k ≤ 20, -24 ≤ l ≤ 24
Reflections collected	16807
Independent reflections	8945 [R_{int} = 0.0451, R_{sigma} = 0.0845]
Data/restraints/parameters	8945/0/569
Goodness-of-fit on F^2	1.036
Final R indexes [I>=2σ (I)]	R_1 = 0.0471, wR_2 = 0.0706
Final R indexes [all data]	R_1 = 0.0689, wR_2 = 0.0775
Largest diff. peak/hole / e Å^{-3}	2.69/-1.26

18, water form has the expected square planar geometry around the Pt centre with the same N1-Pt1-N2 angular distortion seen for other Pt complexes in this chapter. This distortion is caused by the bite angle of the pincer and is present for both molecules in the asymmetric unit. The other bond lengths and angles reported in table 5.8 are in agreement with Pt pincer complexes in the literature.

The majority of the torsion angles in this complex are close to 0 or 180˚, suggesting that the majority of the complex is planar. However, there is deviation from planarity in the ligand that occupies the 4th co-ordination site. Figure 5.24 seem to show the acetyl group perpendicular to the plane of the ligand. Closer investigation of the crystal structure shows that this is not the case. The dihedral angles between the plane of the pincer and the plane of the acetyl ligand were measured for both of the molecules in the asymmetric unit, the results were as follows:

1. **Molecule 1**:
- Plane 1: N2 Pt1 C14 C9 N1 C5 C6 C7
- Plane 2: O3 C19 O4 C20
- Dihedral Angle: 75.7(8)˚
2. **Molecule 2**:
- Plane 1: C25 C34 C29 C26 N3 N4 Pt2
- Plane 2: C40 C39 O8 O7
- Dihedral Angle: 57.4(6)˚

It can be seen from the dihedral angles and the torsion angles in Table 5.8c that the acetyl groups are not fully perpendicular to the plane of the ligand, in addition, the twist of the ligand is different for molecule 1 and 2. This change in orientation of the 4th ligand is different to that seen for other complexes in this chapter in which the ligand was parallel to the plane of the pincer. This could have been caused by the type of ligand and may be related to hydrogen bonding network in which the acetyl ligand is involved in this form of the complex.

Table 5.8*: a. Table of bond lengths for **18** water form. b. Table of bond angles for **18** water form. c. Torsion angles for **18** water form.*

a. Bond Lengths		
Atom	**Atom**	**Length/ Å**
C6	Pt1	1.894(6)
C26	Pt2	1.909(6)
N1	Pt1	2.033(5)
N3	Pt2	2.021(6)
O3	Pt1	2.139(5)
O7	Pt2	2.154(4)
C19	O4	1.254(8)
C2	O1	1.215(8)
C22	O5	1.212(8)
C39	O8	1.233(8)

b. Bond Angles			
Atom	**Atom**	**Atom**	**Angle/°**
N2	Pt1	N1	162.3(2)
C6	Pt1	N1	81.6(2)
C6	Pt1	O3	174.0(2)
C19	O3	Pt1	123.0(5)
N3	Pt2	N4	162.0(2)
C26	Pt2	N3	81.5(2)
C26	Pt2	O7	174.8(2)
C39	O7	Pt2	123.2(4)

c. Torsion Angles				
A	**B**	**C**	**D**	**Angle/°**
Pt2	O7	C39	O8	-22(1)
Pt1	O3	C19	O4	-3(1)

Analysis of this structure in OLEX2,[121] shows there are a couple of π-π interactions in the solid state. These occur between the central phenyl rings of the two molecules in the asymmetric unit and the pyridyl rings between the two molecules. The π-π interactions are comparable to those seen with other complexes in this chapter. The aromaticity of the arene rings may account for the ease at which π interactions form between the pincer ligands.

There is an extensive hydrogen-bonding network in the water form of **18,** this is depicted in Figure 5.24, due to the large number of hydrogen bonds a select number have been provided in Table 5.9c. The presence of this hydrogen-bonding network stabilises the complex in the solid state, which could explain why the water form of the powder is the one found under ambient conditions.

Table 5.9*: a. Planes Present in solid-state structure for **18** water form. b. π-π Interactions for **18** water form. c. Hydrogen bonds for **18** water form.*

a. Plane Identification	
Plane Number	Atoms in plane
1	C3 C8 C7 C6 C5 C4
2	N1 C13 C12 C11 C10 C9
3	N2 C18 C17 C16 C15 C14
4	C23 C28 C27 C26 C25 C24
5	N3 C33 C32 C31 C30 C29
6	N4 C38 C37 C36 C35 C34

b. π-π Interactions	
Planes	Distance (Å)
1-4[1]	3.774
3-6[2]	3.585

c. Hydrogen bonds			
Atoms	(D…A) Distance (Å)	(H…A) Distance (Å)	D…H…A Angle/°
C35-H35-O4	3.307(9)	2.526	141.8
C28-H28-O4	3.47(1)	2.702	140.1
C36-H36-O10	3.49(1)	2.580	165.1
C12-H12-O13	3.451(9)	2.575	157.4
C8-H8-O8	3.294(9)	2.481	145.9
C14-H15-O8	3.46(1)	2.671	143.5
O9-H9A-O4	2.866(9)	2.15(8)	164(8)
O11-H11B-O12	2.73(1)	1.94(8)	161(7)

Where [1] (-1+X, +Y, +Z) [2] (+X, +Y, +Z).

Crystal Structure: Anhydrous Form

A crystal of an alternative form of complex **18**, was grown from the vapour diffusion of di-ethyl ether into a concentrated DCM solution at -18˚C. There is one molecule in the asymmetric unit, with no solvent, making this the dehydrated form of complex **18**. It crystallises in the orthorhombic space group P*bca*. The structure is shown in Figure 5.25 and crystal and structural refinement data can be found in Table 5.10.

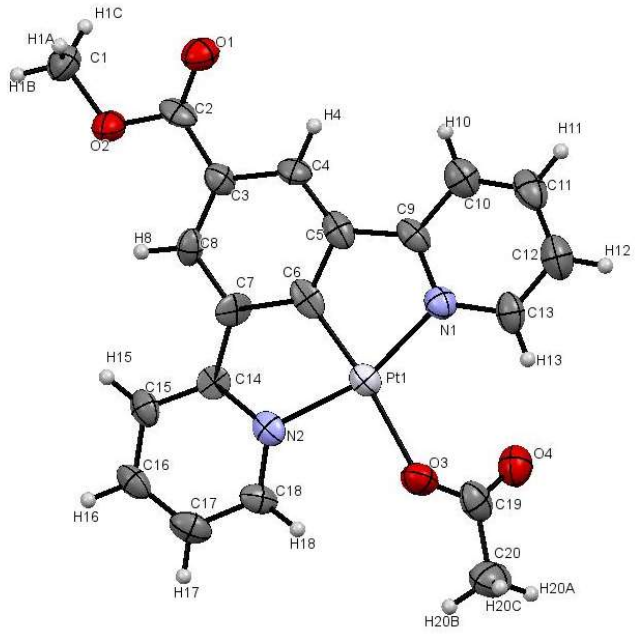

Figure 5.25*: Single crystal X-ray structure for complex* ***18*** *grown from vapour diffusion of diethyl-ether into a concentrated DCM solution at -18˚C. Ellipsoids shown at the 50% probability level.*

Table 5.10*: Crystal data and structure refinement for Complex* ***18****, dehydrated form.*

Identification code	S15prr143
Empirical formula	$C_{20}N_2O_4PtH_8$
Formula weight	535.37
Temperature/K	150(2)
Crystal system	orthorhombic
Space group	Pbca
a/ Å	6.9591(3)
b/ Å	21.0481(10)
c/ Å	23.5102(13)
α/°	90
β/°	90
γ/°	90
Volume/ Å^3	3443.7(3)
Z	8
ρ_{calc}g/cm^3	2.065
μ/mm^{-1}	15.510
F(000)	2016.0
Radiation	CuKα (λ = 1.54184)
2Θ range for data collection/°	8.402 to 143.784
Index ranges	-7 ≤ h ≤ 8, -15 ≤ k ≤ 25, -28 ≤ l ≤ 28
Reflections collected	13637
Independent reflections	3339 [R_{int} = 0.0976, R_{sigma} = 0.0765]
Data/restraints/parameters	3339/0/246
Goodness-of-fit on F^2	1.091
Final R indexes [I>=2σ (I)]	R_1 = 0.0864, wR_2 = 0.2170
Final R indexes [all data]	R_1 = 0.1067, wR_2 = 0.2333
Largest diff. peak/hole / e Å^{-3}	8.99/-1.69

The anhydrous form of complex **18** has the same square planar geometry around the Pt centre with an N1-Pt1-N2 angular distortion as seen with related complexes in this thesis. This distortion is attributed to the bite angle of the N^C^N ligand. The bond lengths and angles are in agreement with similar complexes.

Figure 5.25 provided an illusion that the acetyl group is parallel to the plane of the ligand. However, the acetyl is twisted with respect to the plane of the pincer. The dihedral angle was measured at 42.90° between the following two planes; Plane 1: C5 C6 C7 N1 Pt1 N2 C9 C14 and Plane 2: O3 C19 O4 C20. The acetyl group is not twisted to the same degree as that observed with the water form of complex **18**. The rest of the molecule is planar with respect to the Pt centre, which is evidenced by torsion angles.

Table 5.11*: a. Table of bond lengths for **18** dry form. b. Table of bond angles for **18** dry form. c. Torsion angles for **18** dry form.*

a. Bond Lengths		
Atom	**Atom**	**Length/ Å**
C6	Pt1	1.878(18)
N1	Pt1	2.038(13)
O3	Pt1	2.143(12)
C19	O3	1.28(2)

b. Bond Angles			
Atom	**Atom**	**Atom**	**Angle/°**
N1	Pt1	N2	161.0(6)
C6	Pt1	N2	80.7(6)
C6	Pt1	O3	172.4(5)
C19	O3	Pt1	127.8(12)

c. Torsion Angles				
A	**B**	**C**	**D**	**Angle/°**
C20	C19	O3	Pt1	-168.0(12)

The anhydrous form of **18** has fewer π-π interactions and hydrogen bonds in the structure. The π bonds form between the pyridyl rings in adjacent structures as seen in Figure 5.27a. This is consistent with other complexes in this thesis. There are a number of hydrogen bonds that form in the structure, they form between the acetate group and the ester group in addition to the pincer and the acetate group. Similar hydrogen bonding was observed with the water form of this complex as discussed earlier.

Table 5.12: *a. Planes Present in solid-state structure for **18** dry form. b. π-π Interactions for **18** dry form. c. Hydrogen bonds for **18** dry form.*

a. Plane Identification

Plane Number	Atoms in plane
1	C3 C8 C7 C6 C5 C4
2	N1 C13 C12 C11 C10 C9
3	N2 C18 C17 C16 C15 C14

b. π-π Interactions

Planes	Distance (Å)
3-3[1]	3.929

c. Hydrogen bonds

Atoms	(D…A) Distance (Å)	(H…A) Distance (Å)	D…H…A Angle/°
C16-H16-O1	3.30(2)	2.58	134
C15-H15-O4	3.22(2)	2.59	125
C1-H1B-O2	3.52(2)	2.70	143
C12-H12-O4	3.18(3)	2.36	147
C13-H13-O4	3.21(2)	2.49	134
C20-H20B-O1	3.54(3)	2.58	174

Where [1] (-1/2+X, +Y, 1/2-Z).

Crystal Packing: Stacking and Pt Offset

Unlike the example presented in Section 5.1.2, the distance between Pt atoms in adjacent molecules in the hydrated form is too long for there to be Pt…Pt orbital overlap. Instead **18** (hydrated) adopts a similar stacking motif to complex **16** and **17**, where there are two symmetry related Pt positions in the stacks, Figure 5.26a. Analysis of the solid-state packing suggests that the complexes have packed in a manner to minimise steric interactions and to maximise the intermolecular contacts between the functional groups and water solvent.

An in-depth analysis of the intermolecular interactions of complex **18**, shows that for the hydrated form there is an extensive hydrogen-bonding network between the water molecules, not shown in Figure 5.26 for clarity. In addition, short contacts form between the acetate groups on the back and front of the complex. The data for the core hydrogen bonds is available in Table 5.9. Unlike the cyanide example this does not hold the molecules in a stack in which the Pt centres are aligned.

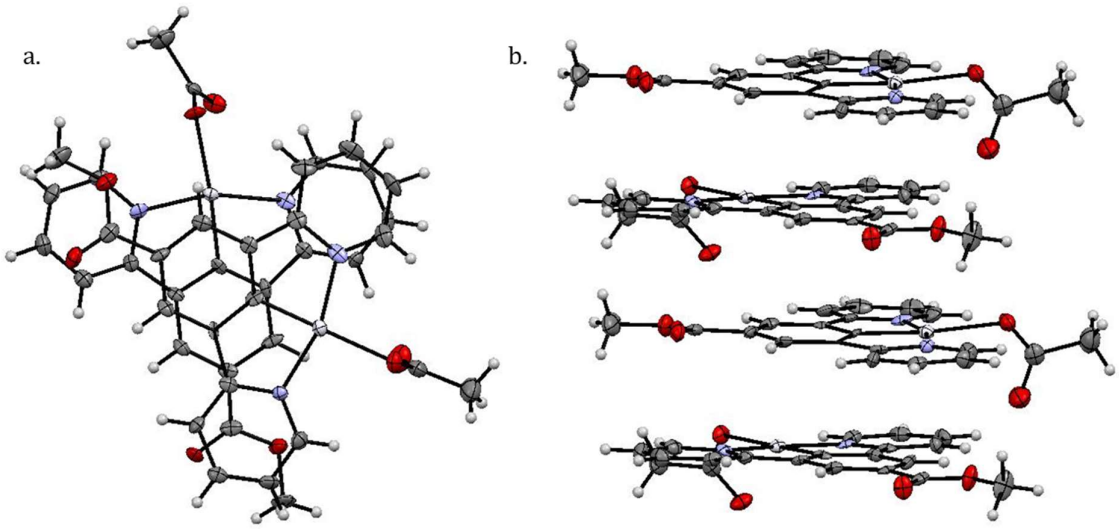

Figure 5.26*: a. Hydrated form of Complex **18** viewed along the a axis. b. stacking of the hydrated form of complex **18** in the solid state. Ellipsoids shown at 50% probability. Solvent has been removed for clarity.*

Figure 5.27 shows the stacking of the anhydrous form of complex **18**, as with the hydrated form there are two symmetry related Pt positions, which are situated at right angles to each other, so, again, there is no possibility of Pt…Pt overlap in the solid state. There are fewer intermolecular interactions in this form, data available in Table 5.12. One reason for this is the distance between the molecules in the stacks is longer, which discourages the formation of the short contacts.

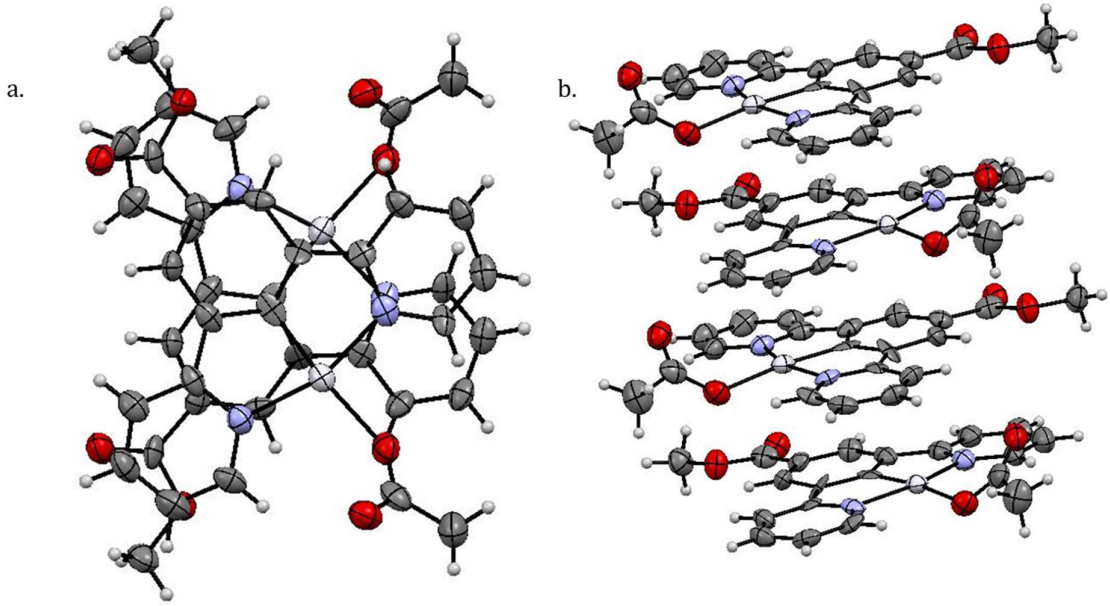

Figure 5.27*: a. Dry form of Complex **18** viewed along the a axis. b. stacking of the dry form of complex **18** in the solid state. Ellipsoids shown at 50% probability.*

The solid-state structures of complex **18** are not as predicted. Based on the literature[76, 77, 93, 118, 122] it would be expected that the Pt centres in the solid state would be aligned and the change in distance between them would produce the observed spectral changes discussed in Section 5.5.2.

Instead, the molecules are at near right angles to each other in the both forms and are held together by π-π stacking. It is important to note that Pt complexes are known to grow a number of different polymorphs and the forms that have been grown here do not interconvert but have to be crystallised separately, evidenced by the different crystal systems and space groups they adopt. The single crystal will be compared to the bulk power to confirm that the single crystal structures that have been determined are not vapochromic forms.

5.5.4 X-Ray Powder Analysis

X-ray powder diffraction was used to analyse the bulk powder so the diffraction could be compared to the data collected for the single crystals. Figure 5.27 and 5.28 provides a comparison for the hydrated and dry form respectively. It can be seen that there is a large difference between the bulk powder and single crystal analysis. This confirms that the solid-state structure isolated in the single crystal is not representative of the vapochromic powder.

It is likely that the vapochromic powder would be stacked, with Pt alignment, consistent with the literature. Due to the stacked nature of the complex, the crystal morphology is likely to be a needle. Fine fibrous crystalline material was grown however, it was not suitable for single crystal analysis.

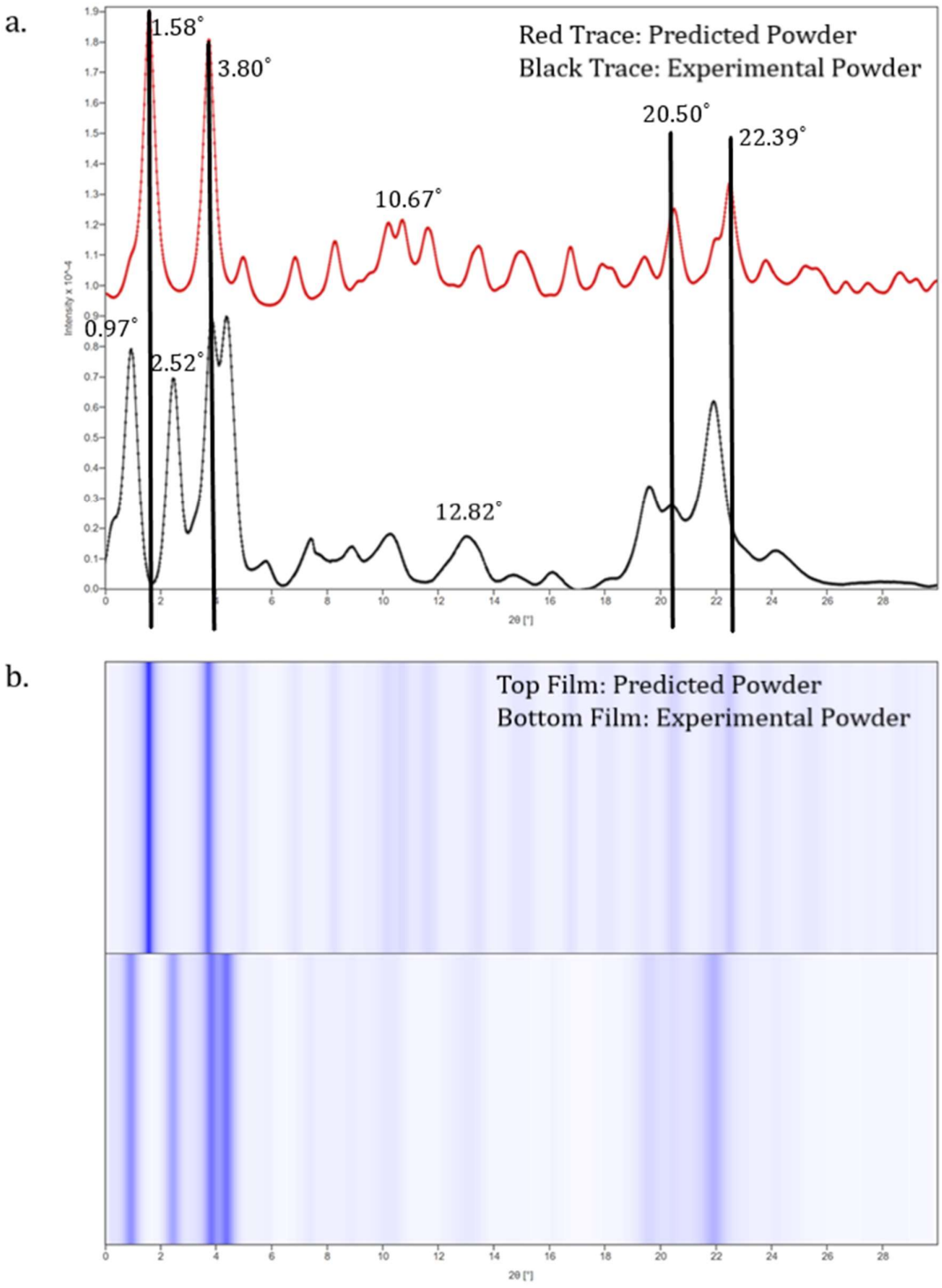

Figure 5.28*: a. Complex **18**, hydrated form powder plot. b. Film representation of powder of Complex **18**, hydrated form. Top trace is the predicted powder generated from crystal structure (red) and bottom trace is the experimental powder (black).*

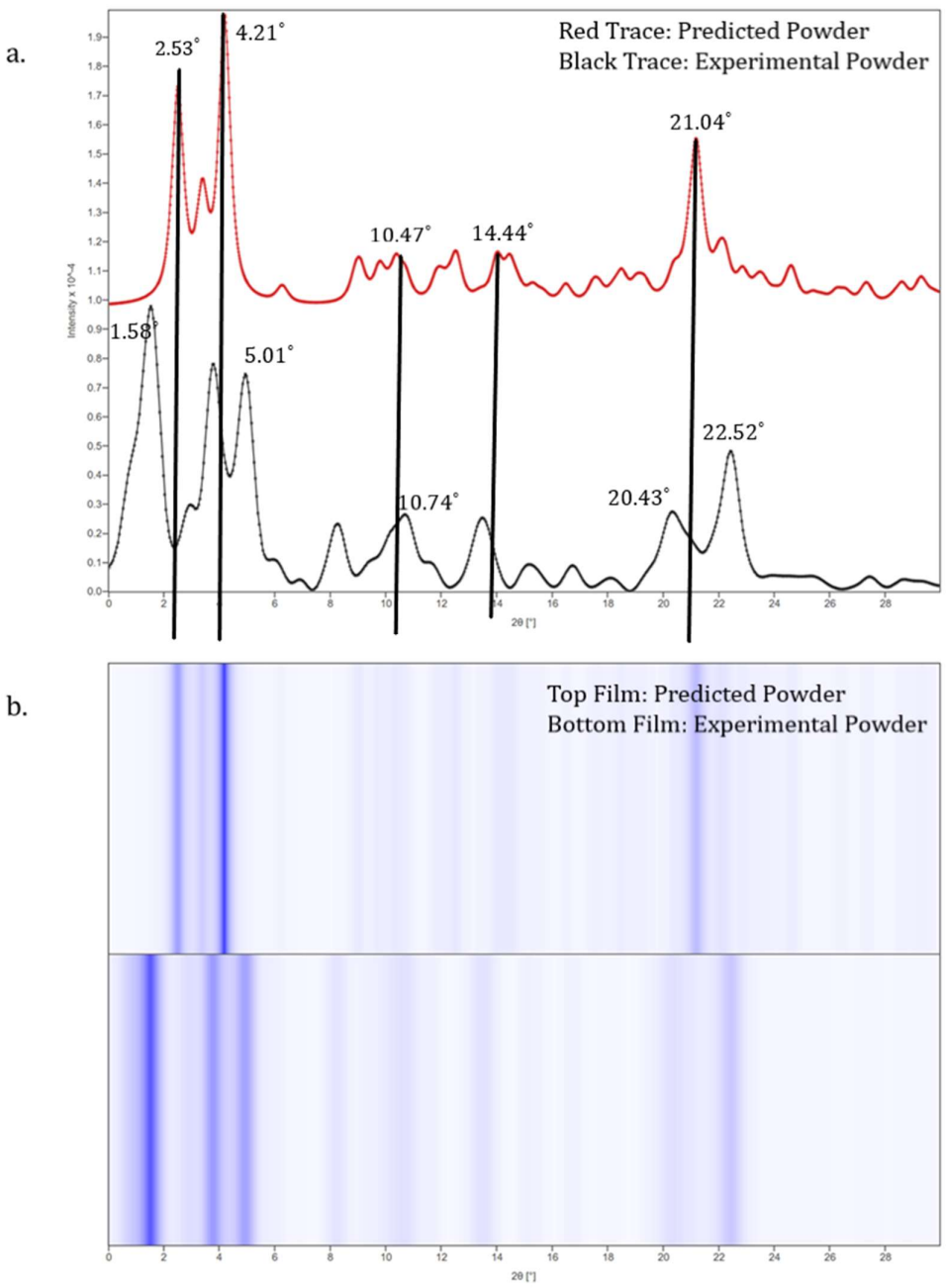

Figure 5.29*: a. Complex **18**, anhydrous form powder plot. b. Film representation of powder of Complex **18**, anhydrous form. Top trace is the predicted powder generated from crystal structure (red) and bottom trace is the experimental powder (black).*

Figure 5.30 is a comparison of the vapochromic powder of the three different forms. The dry form was isolated by loading the capillary and placing it under a vacuum, this has the same effect as using dry N_2. The methanol form was isolated by placed a small piece of methanol soaked cotton wool in the bottom of the capillary and then filling with the complex. As the methanol vapour diffused though the capillary the methanol form of complex **18** was isolated.

The powder diffraction pattern contains the same peaks between the values of 10-25 for 2θ, the differences arise between the values 0-8 for 2θ. The major peaks are shifted by a few units, while the weaker peaks fall at the same values. Preferred orientation effects could have caused this.

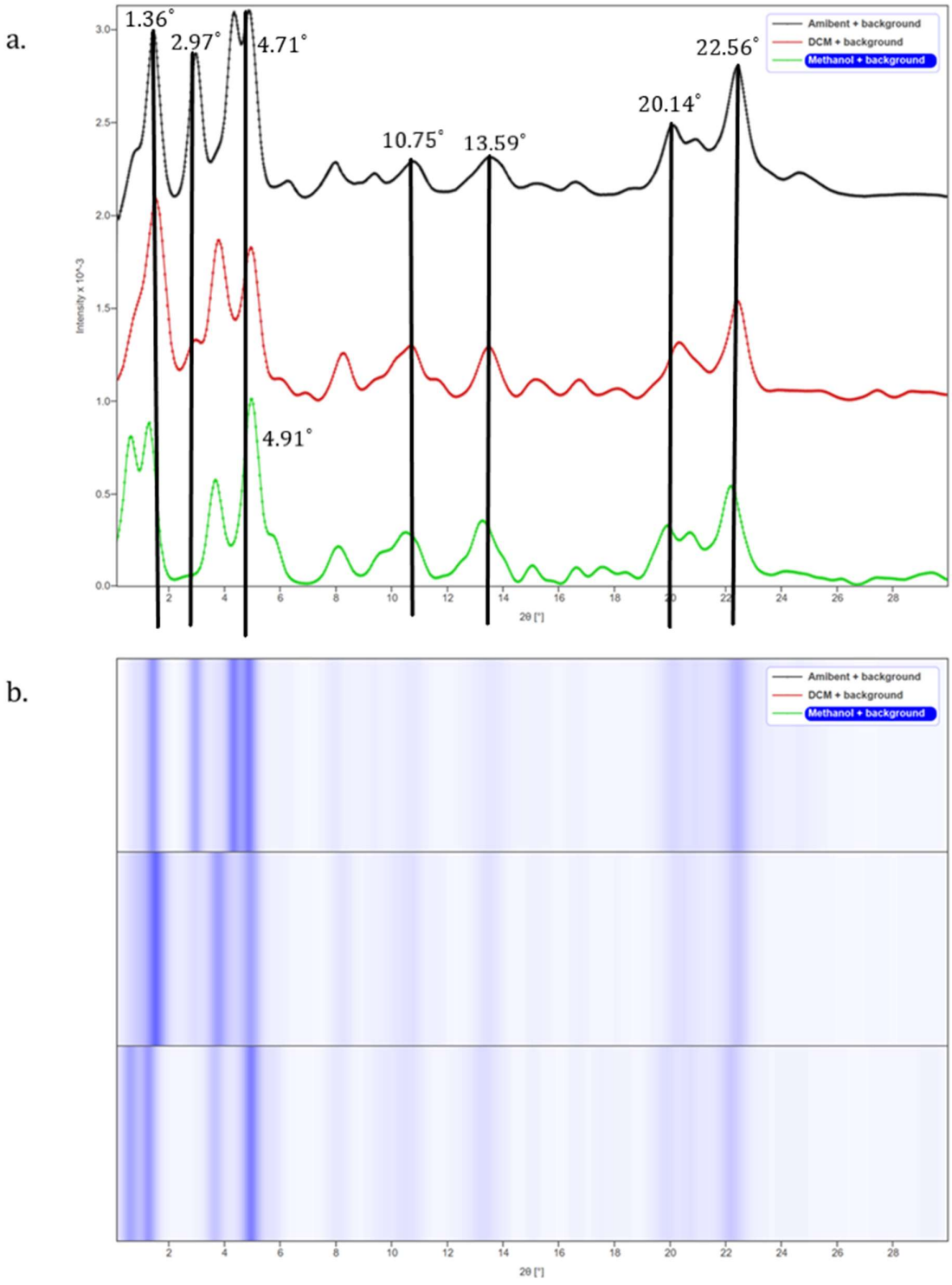

Figure 5.30*: a. Complex **18** powder plot. b. Film representation of powder of Complex **18**. Black trace is the hydrated form, red trace is the dry form and the green trace is the methanol form.*

5.6.0 Methyl 3,5-di(pyridin-2-yl)benzoate Platinum Trifluoroacetate (19)

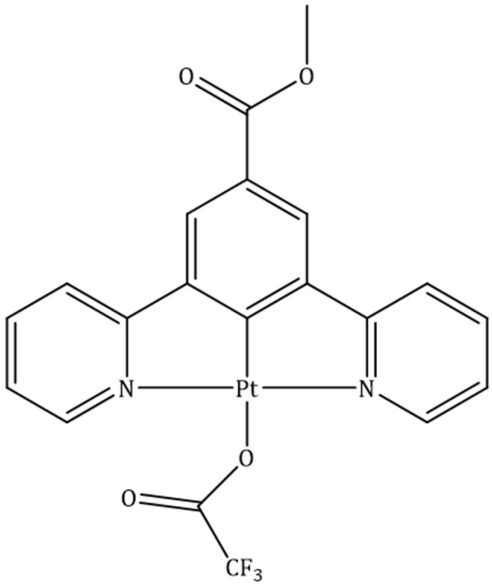

The discovery of a vapochromic complex with the acetate group in the 4th co-ordination site prompted further investigation of related complexes.

The first synthetic modification attempted was to substitute the methyl group for a CF_3 group, this modification is regularly used in organic chemistry to alter the solubility of the complex. It would therefore be predicted that the isolated complex might show solvatochromic capabilities.

The bright yellow solid was isolated in good yield and the structure confirmed by ^{1}H NMR and IR spectroscopies and by X-ray powder diffraction analysis. IR and fluorine NMR were used to confirm the presence of the CF_3 functional group.

5.6.1 Solution State Spectroscopy

Complex **19** is highly soluble in both DCM and MeCN and the solution state spectroscopy has been measured in both solvents for completeness. The profile of the UV-Vis spectra is similar to that observed for complex **15**, and the peaks can be assigned as follows. The peaks below 300 nm can be attributed to $^1\pi$-π^* transition, the broad peak between 350-440 nm has the result of the dominant transition $^3\pi$-π^*. However, the $^3\pi$-π^* has been blue shifted in the MeCN solution. This will be discussed in the next section of this chapter.

Figure 5.31 and 5.32 show two UV-vis emission profiles, one at a lower concentration and the other at a higher concentration. The peak situated between 450-550 nm is characteristic of the $^3\pi$-π^* transition due to the pronounced vibrational structure, however at the higher concentration a broad peak is observed at a higher wavelength. As seen with previous complexes, this peak is caused by excimer formation due to the high concentration of complex **19** in the solution.

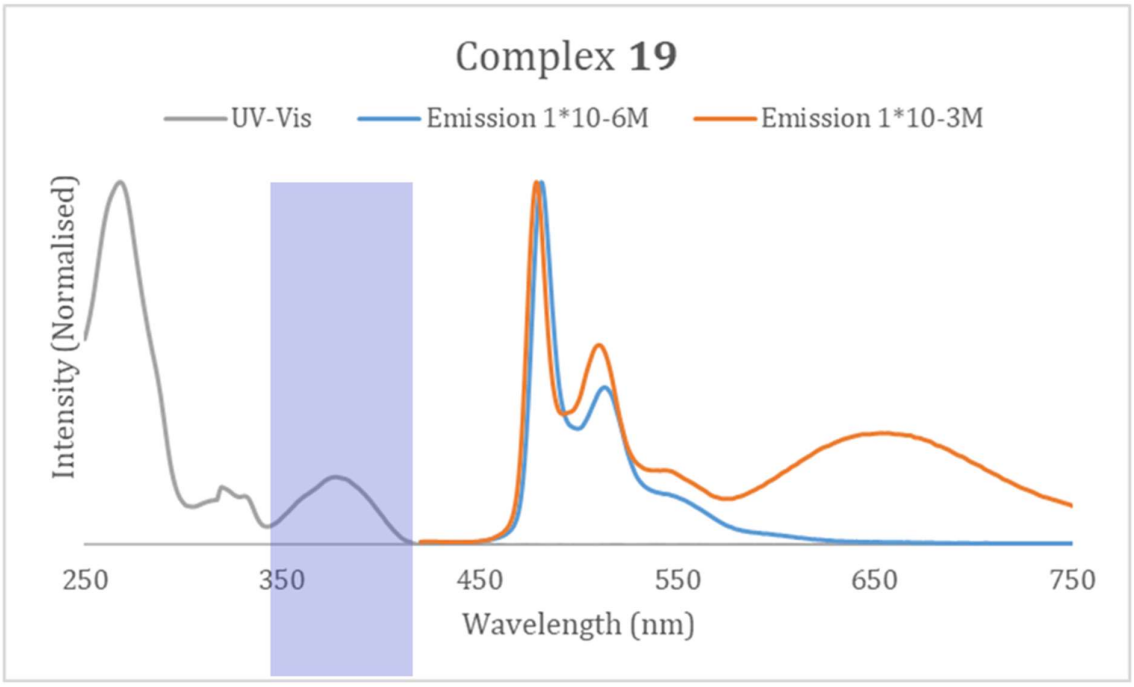

Figure 5.31: *Solution state spectroscopy of Complex **19**, Grey line: UV-Vis solution concentration 1×10^{-5} M in DCM, $^{3}\pi$-π^* transition highlighted, Blue line: Emission solution concentration 1×10^{-6} M in DCM, λ_{ex}400 nm, Orange line: Emission solution concentration 1×10^{-3} M in DCM, λ_{ex}400 nm.*

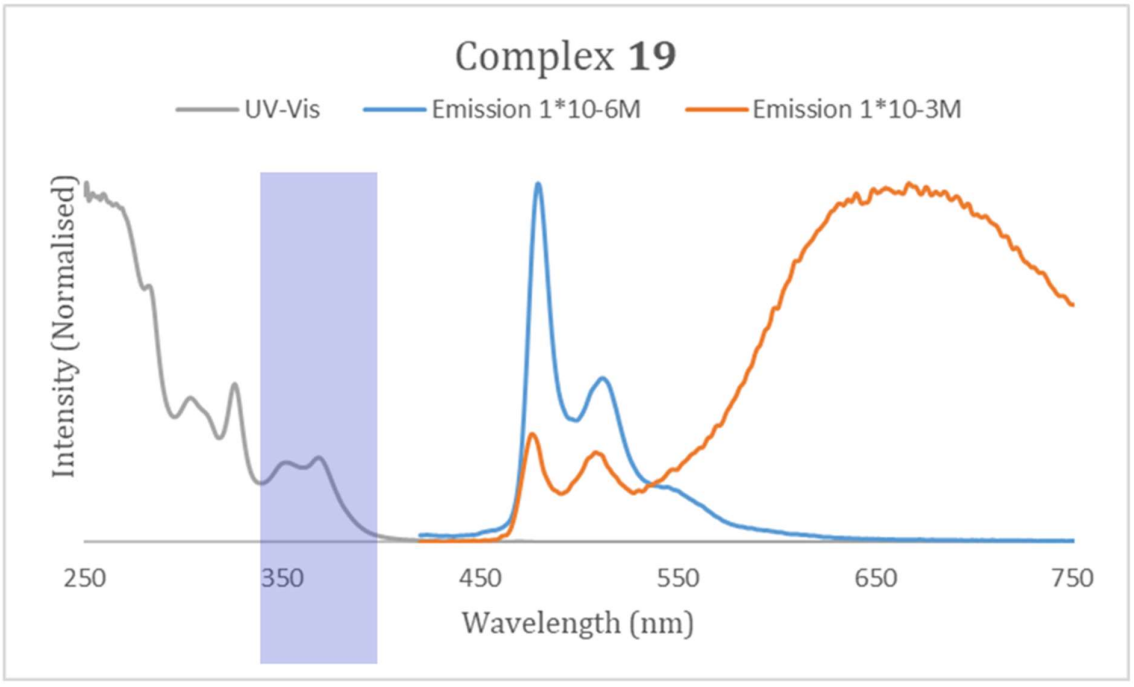

Figure 5.32: *Solution state spectroscopy of Complex **19**, Grey line: UV-Vis solution concentration 1×10^{-4} M in MeCN, $^{3}\pi$-π^* transition highlighted, Blue line: Emission solution concentration 1×10^{-6} M in MeCN, λ_{ex}400 nm, Orange line: Emission solution concentration 1×10^{-3} M in MeCN, λ_{ex}400 nm.*

5.6.2 Vapo/Solvatochromic Behaviour

In Section 5.6.0, it was predicted that the modification of the methyl to a CF_3 group, would cause a change in solubility in the complex and therefore induce solvatochromic behaviour. The complex was initially isolated as a bright yellow solid, which is indicative of no Pt…Pt stacking in the solid state and usually a complex that does not show any spectral changes when exposed to external stimuli. However, with complex **19**, this was not the case, upon recrystallization from acetonitrile, the solid changed from yellow to orange, figure 5.33.

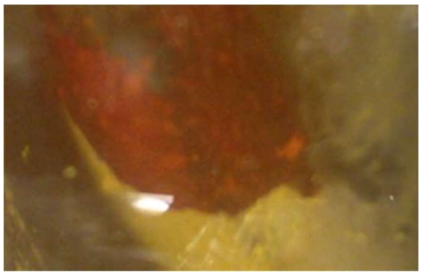

Figure 5.33*: Two different solvates of complex **19**, Yellow is the DCM solvate and orange is upon exposure to acetonitrile.*

Complex **19** rapidly changes colour to orange upon exposure to the MeCN vapour and solvent, however due to its high solubility it dissolves rapidly in the solvent to form a bright orange solution. The yellow form is not recovered by the removal of the acetonitrile solvent, instead a deep red colour is observed in the solid state, Figure 5.34c. The yellow solid is only recovered upon recrystallization from DCM.

Figure 5.34 shows the transition of the orange, MeCN form of complex **19** to the deep red of the desolvated form. In Figure 5.34b, the crystalline material has started to dissolve into the remaining acetonitrile, before the acetonitrile evaporates leaving a deep red residue.

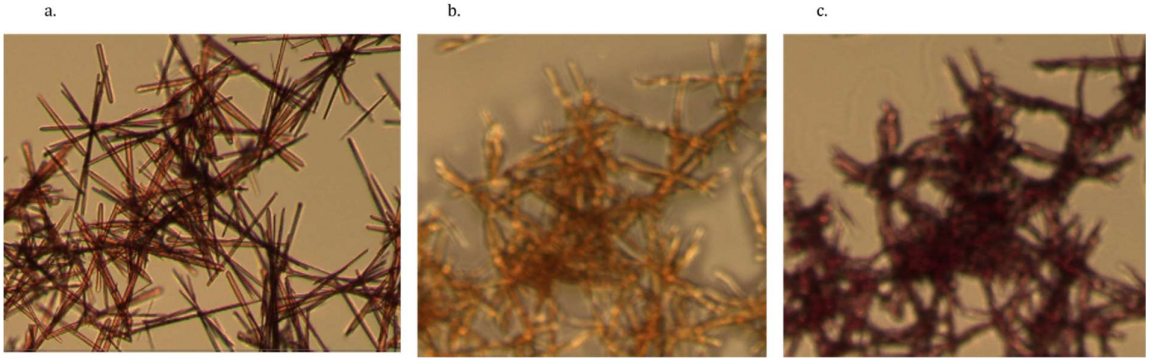

Figure 5.34*: Monitoring the loss of MeCN from a crystalline sample of complex **19**. a. orange crystals grown from an MeCN/di-ethyl ether vapour diffusion. b. upon evaporation of the di-ethyl ether the remaining MeCN starts to dissolve the crystals, however they maintain their orange colour. C. upon evaporation of the solvation a deep red powder remains.*

The solvatochromic behaviour of complex **19** was studied using solution state spectroscopy. This property of the complex was alluded to in section 5.6.1. A full comparison of the UV-Vis spectrum of **19** is shown in figure 5.35.

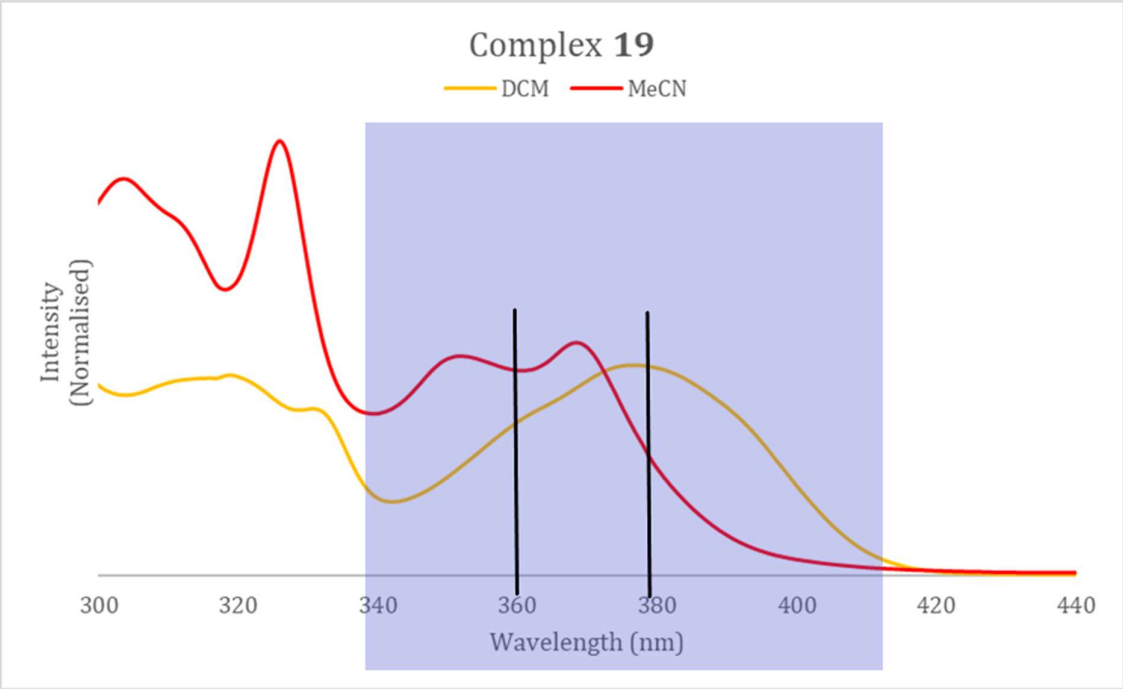

Figure 5.35*: Comparison of the different solvatochromic forms of complex **19**, solution concentration 1×10^{-4} M. $^{3}\pi$-π^* transition highlighted.*

It can be seen clearly from the results presented in Figure 5.35 that the different solvatochromic forms differ in the region 340-420 nm. This peak is dominated by the $^{3}\pi$-π^* transition and the change in solvent has affected at which wavelength it appears. The blue shift of the peak complements the colour of the solution as it changes from a pale yellow to a deep orange.

The solution state emission was also measured, however the peak that resides between 450-550nm does not change in the different solvents. At higher concentrations, the broad peak caused by excimer formation does shift slightly in the different solvents. This suggests that the solid-state emission would vary for the yellow and deep red form of the complex. Unfortunately, due to equipment restraints this could not be confirmed.

5.6.3 X-Ray Powder Analysis

Due to the high solubility and tendency of the crystals to desolvate, single crystals of **19** suitable for single crystal diffraction could not be isolated. However, the bulk powder could be studied using powder diffraction.

The yellow powder was recrystallized from DCM. The orange form was more challenging to isolate because the red form isolated by evaporation of acetonitrile was not crystalline. The orange form was therefore isolated by trapping a small amount of acetonitrile in a capillary and allowing the MeCN vapour to diffuse through the capillary. Due to the sensitivity of **19** to MeCN, the vapour was enough to convert from the yellow to the orange form.

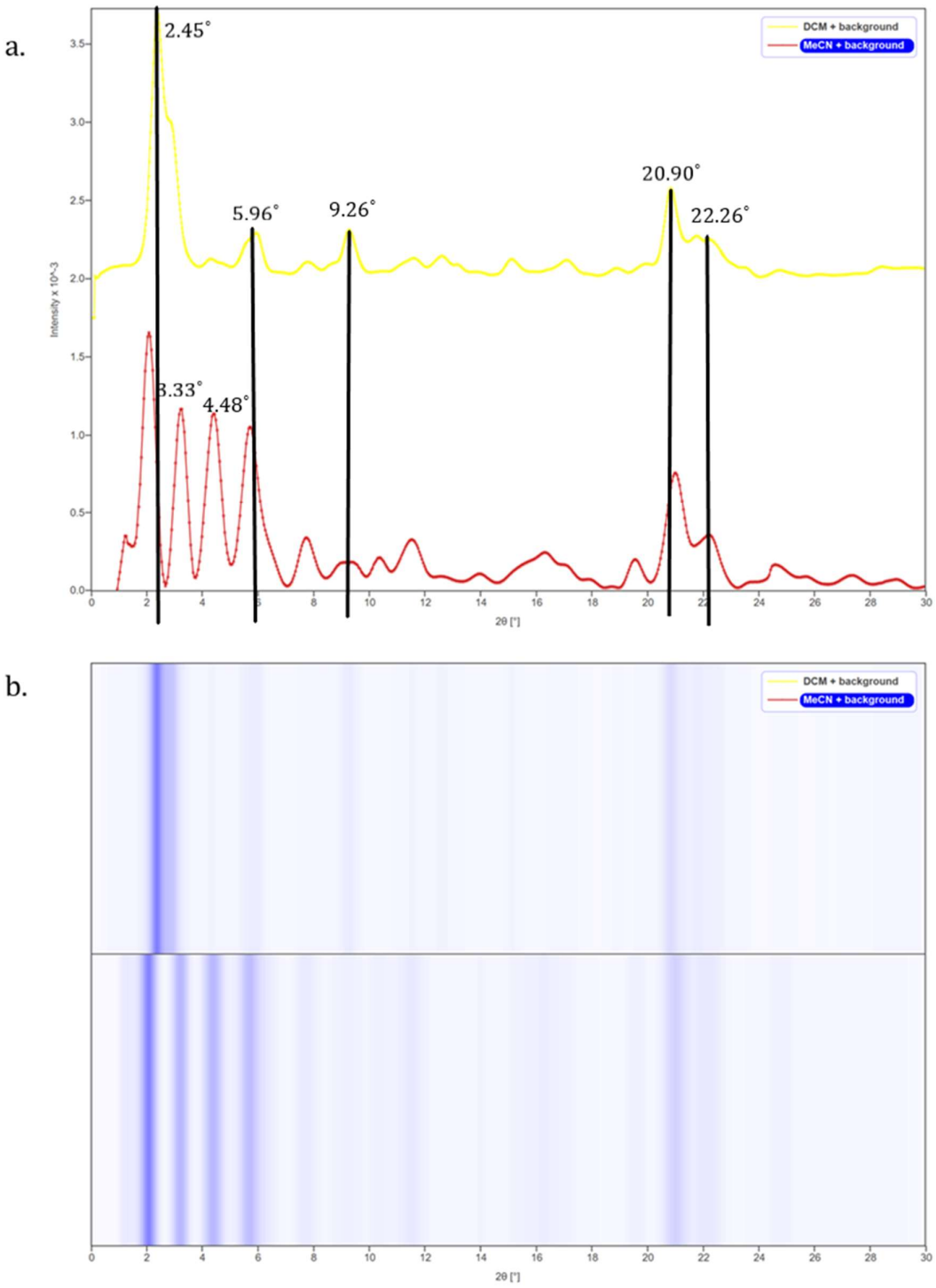

Figure 5.36: *a. Complex **19** powder plot. b. Film representation of powder of Complex **19**. Yellow trace is the DCM form; red trace is the MeCN form.*

The powder trace shown in Figure 5.36, show similarities at a high 2θ value but at low 2θ value there are major differences between the traces. This shows that the two forms are structurally related but there are substantial differences in their solid-state arrangement.

5.7.0 Methyl 3,5-di(pyridin-2-yl)benzoate Platinum Triflate (20)

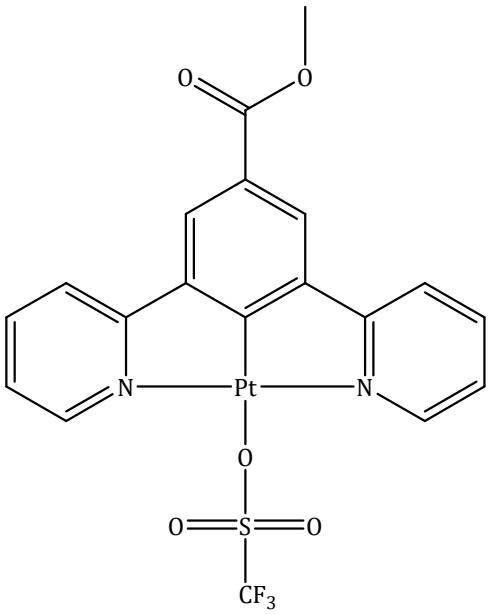

By systematically manipulating the ligand in the 4th co-ordination site, we have discovered a vapochromic and solvatochromic material. In this section, the CF_3 group will be maintained but instead of an acetate group a triflate group will be used. The aim is to synthesise a new solvatochromic material with different spectral properties.

Complex **20** was isolated in good yield as a yellow solid. The structure was confirmed using ^1H NMR and IR spectroscopies, CHN analysis and X-ray power diffraction. IR and fluorine NMR confirmed the presence of the CF_3 functional group.

5.7.1 Solution State Spectroscopy

The solution state spectroscopy of this complex in DCM is given in Figure 5.37. The UV-Vis emission spectrum was measured at a series of concentrations from 1×10^{-7} M to 1×10^{-3} M, two concentrations are given in Figure 5.37 to show how the emission varies with concentration.

The profile of the UV-Vis absorption and emission spectra are analogous to the spectra measured in DCM for all of the previous complexes in this chapter.

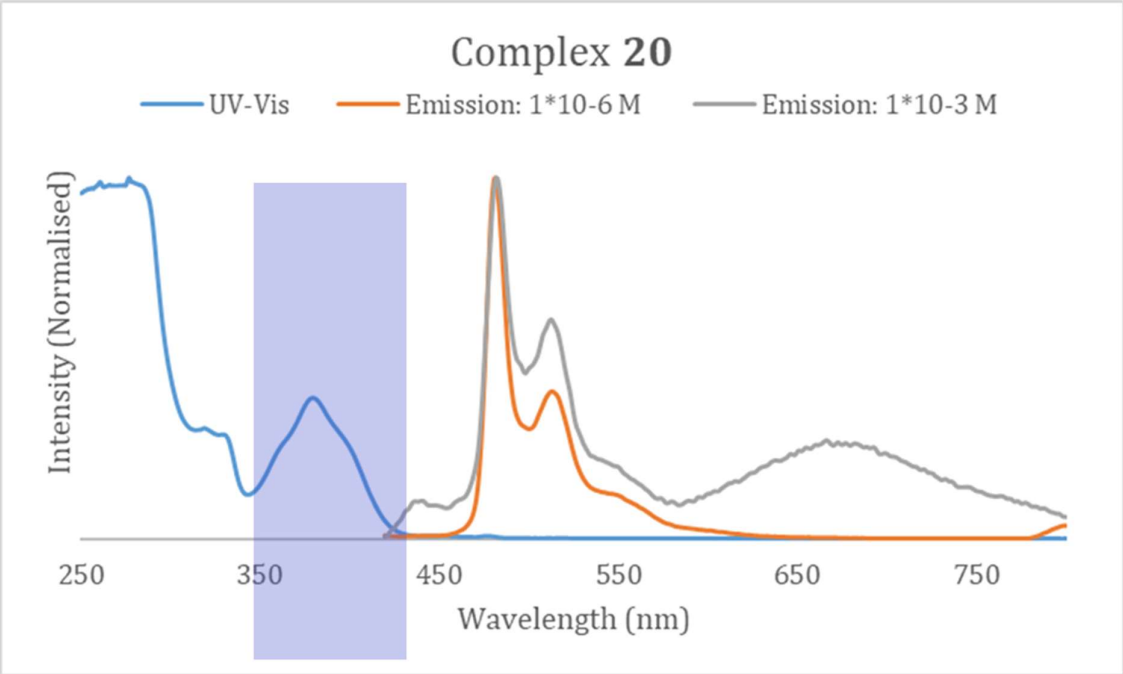

Figure 5.37*: Solution state spectroscopy of Complex **20**, Blue line: UV-Vis solution concentration 1×10^{-4} M in DCM, $^{3}\pi$-π^* transition highlighted. Orange line: Emission solution concentration 1×10^{-6} M in DCM, λ_{ex}400 nm, Grey line: Emission solution concentration 1×10^{-3} M in DCM, λ_{ex}400 nm.*

5.7.2 Vapo/Solvatochromic Behaviour

Complex **20** display solvatochromic behaviour as anticipated, however it shows the same solvatochromic properties as complex **19**. This suggests that perhaps it is the CF_3 functional group that is the driving force behind this property. The solvachromic capabilities of **20** are shown in Figure 5.38.

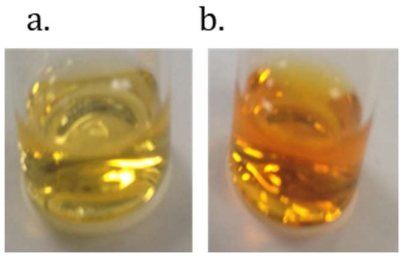

Figure 5.38*: Two different solvates of complex **20**, a. yellow form is in DCM. b. orange form in MeCN.*

As observed with complex **19**, a yellow solution is formed with DCM and an orange film with acetonitrile. However, with this complex when the acetonitrile form is deposited onto a slide and the MeCN allowed to evaporate an orange powder was recovered opposed to the deep red residue in the case of complex **19.** The two forms could only be accessed by recrystallization from solvent and not using vapochromic techniques.

The solvent dependency of **20** was also studied using solution state spectroscopy the results are presented in figure 5.39.

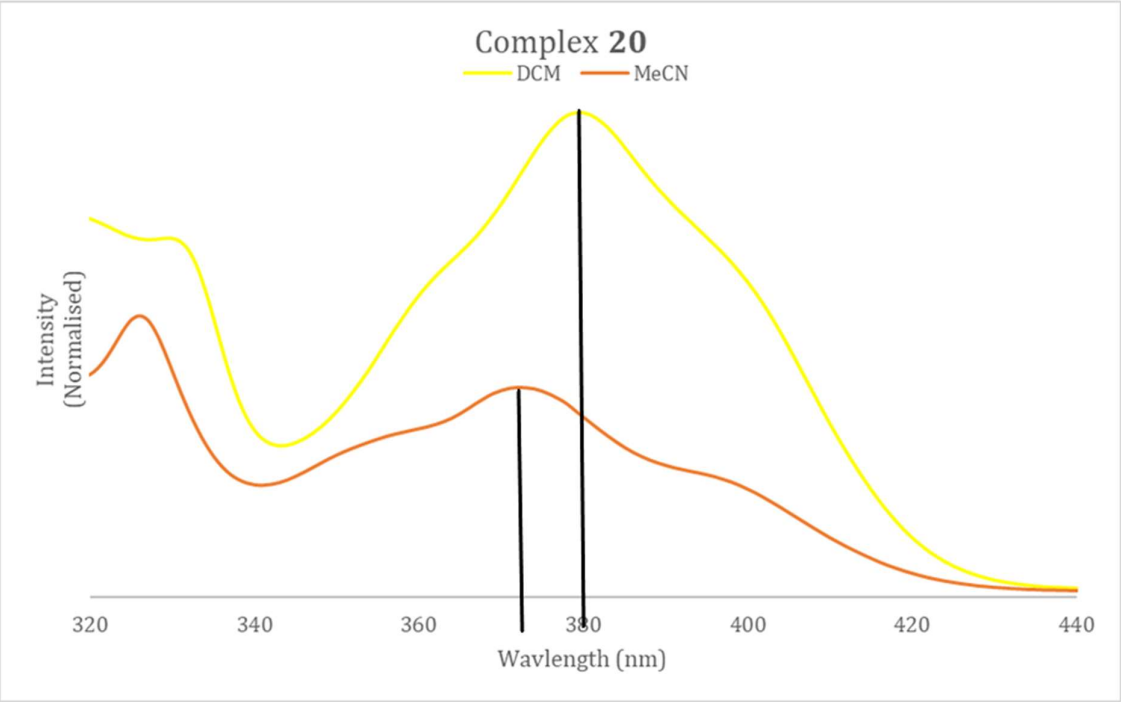

Figure 5.39*: Comparison of the different solvatochromic forms of complex **20**, solution concentration 1×10^{-4} M.*

There is a small shift observed in the peak maxima between the two different solvates of complex **20**. This shift is not as large as that observed for complex **19**. The blue shift of 10 nm observed for the MeCN form is consistent with the change in colour from yellow to a pale orange.

The emission profiles for both forms were measured and in this case were the same, with no change in excimer energy measured.

Unfortunately, this complex could not be studied in the solid state using single crystal techniques, as no crystals of suitable quality could be grown.

5.7.3 X-Ray Powder Analysis

Due to the lack of suitable single crystal analysis, powder diffraction studies were carried out, the results are shown in figure 5.40. The powder was grown from recrystallizing from the solvents DCM and MeCN.

Comparison of the yellow and orange forms showed identical traces, this is more readily observed in the film representation, Figure 5.40b. This suggests that the solid-state structure of both solvates is very similar. The fact that the solvatochromic transition is slower than that observed for the acetate analogue of this complex suggest the SO_3-R group has an effect in the properties of the complex.

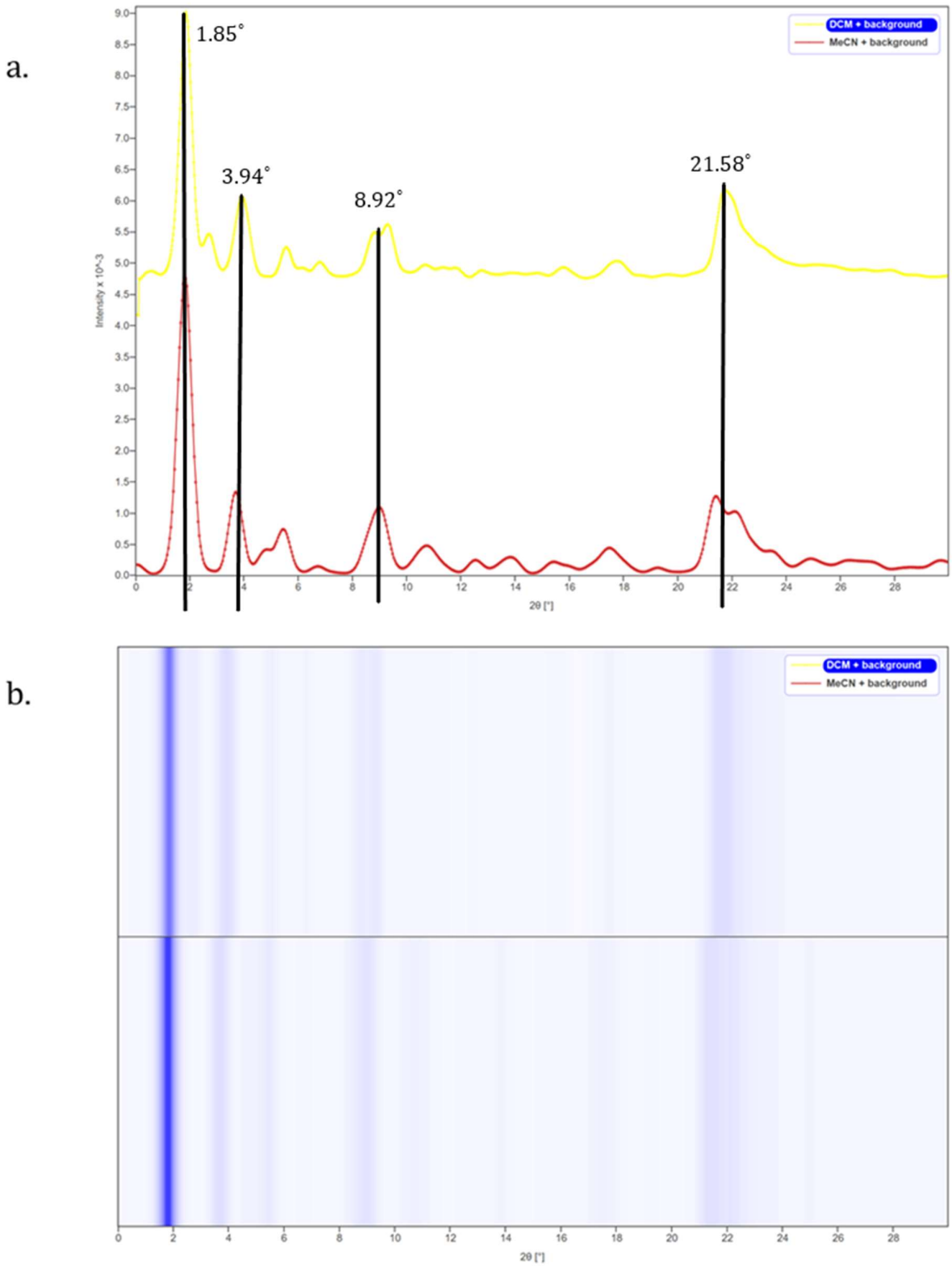

Figure 5.40: *a. Complex **20** powder plot. b. Film representation of powder of Complex **20**. Yellow trace is the DCM form; red trace is the MeCN form.*

5.8.0 Methyl 3,5-di(pyridin-2-yl)benzoate Platinum Tosylate (21)

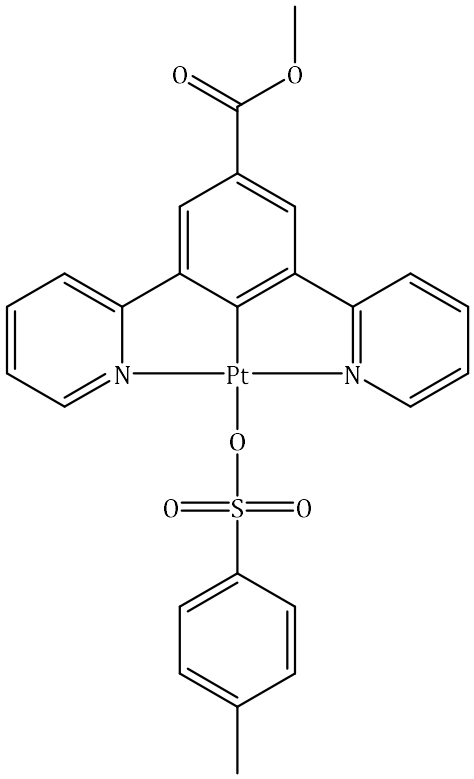

The final complex discussed in this chapter is with a tosylate functional group substituent. This complex was synthesised to investigate the effect of using a large aromatic group in the 4th co-ordination site.

The complex was synthesised using the ligand exchange method described in Scheme 5.4. The purple solid was isolated in good yield. The structure was confirmed using ^{1}H NMR and IR spectroscopies, by CHN microanalysis, and by X-ray powder diffraction.

5.8.1 Solution State Spectroscopy

The solution state UV-vis spectroscopy of this complex was measured and the results shown in figure 5.41. **21** was isolated as a dark purple solid, upon dissolving into DCM to make the spectroscopy solutions; it changed into a pale-yellow solution. This is indicative of solid-state Pt…Pt interactions being broken when the complex is in the solution state.

The spectra shown in Figure 5.41 adopt the same profile seen for this group of complexes, with the transition described in detail in section 5.1.3.

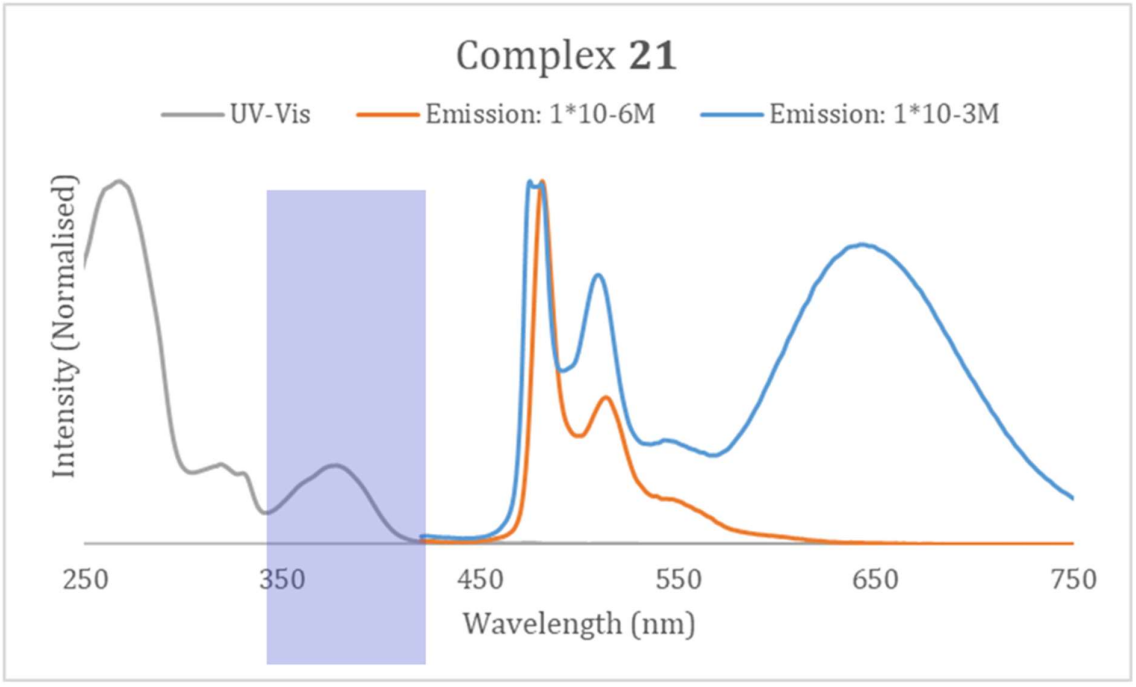

Figure 5.41: *Solution state spectroscopy of Complex **21**, Grey line: UV-Vis solution concentration 1×10^{-4} M in DCM, $^{3}\pi$-π^* transition highlighted. Blue line: Emission solution concentration 1×10^{-3} M in DCM, λ_{ex}400 nm, Orange line: Emission solution concentration 1×10^{-6} M in DCM, λ_{ex}400 nm.*

5.8.2 Vapo/Solvatochromic Behaviour

Complex **21** displayed both vapo and solvatochromic behaviour. This is illustrated in Figure 5.42, where a purple to yellow transition is observed with methanol, this can be reversed with MeCN.

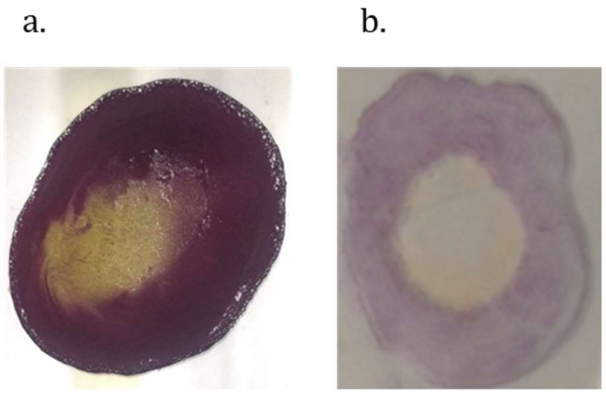

Figure 5.42: *a. Vapochromic behaviour of complex **21**, when exposed to methanol vapour. b. Solvatochromic behaviour of complex **21** when exposed to methanol.*

Unlike previous examples, where there was an ambient form, which would reversibly switch under standard conditions, complex **21** has a reversible transition between MeCN and MeOH, this was confirmed by the use of a bubbler to create MeCN and MeOH vapour. It is important to know that both forms are stable under standard room conditions.

The solvatochromic behaviour of this complex has been studied using spectroscopic techniques. The complex turns yellow in DCM as well as in MeOH so for comparative purposes the solution state spectroscopy has been carried out in MeCN and DCM. Figure 5.43 shows the difference in UV-Vis spectra in the different solvents.

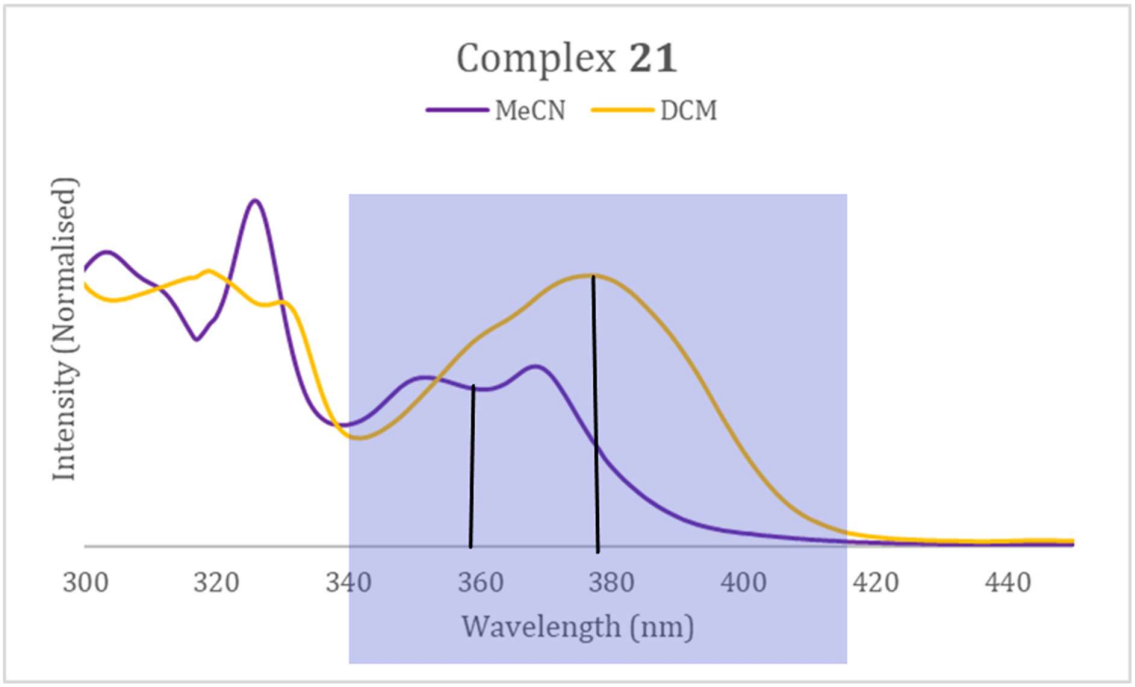

Figure 5.43*: Comparison of the different solvatochromic forms of complex **21**, solution concentration 1×10^{-4} M. $^{3}\pi$-π^* transition highlighted.*

The peaks between 300-350 nm can be attributed to the $^{1}\pi$-π^* transitions and the dominant transition between 340-420 nm is $^{3}\pi$-π^*, with some $^{1}\pi$-π^* character. The yellow line for the DCM solution follows the typical profile, observed for all of the other complexes in this chapter. The MeCN has been blue shifted with respect to the DCM, which is unexpected based on its solid- state colour. As observed when the complex is dissolved in DCM, the purple colour is lost but in acetonitrile **21** adopts a deep orange colour.

In addition to investigating the solvatochromic effect in pure solvents, solution state spectroscopy was carried out on solvent mixtures, to see how this affected the spectra. The results of this study are shown in Figure 5.44. The results are interesting because when the solution strength is 10% MeCN, the profile of the spectra converts from the shape of the DCM spectra to that observed for the complex when it is measured in pure MeCN. This change in profile has not been observed for any of the other solvatochromic complexes, discussed in this chapter. One potential reason for this is that the complex is more stable in MeCN due to solvent- molecule interactions.

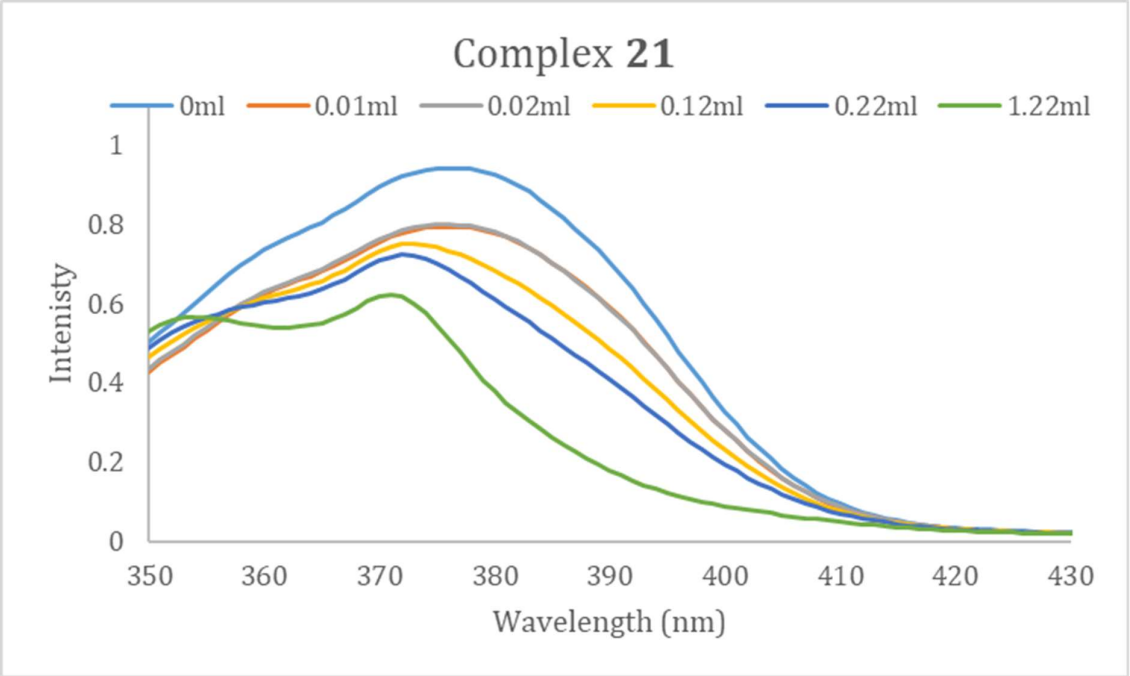

Figure 5.44*: UV-Vis study of Complex **21**, 1×10^{-4} M Solution of Complex **21** in DCM, MeCN Added.*

In addition to monitoring how the UV-Vis spectrum was affected by the change in solvent, the emission in different solvents was also measured. The results are shown in Figure 5.45 and 5.46. Comparing the emission profiles of the complex in two different solvents, show there is no change in the low wavelength emission, between 450-550 nm which is characteristic of $^{3}\pi$-π^*. On the other hand, the excimer emission is blue shifted when moving from DCM to MeCN as a solvent. This suggests that the solid-state emission would have differing peak maxima. This would be useful when considering potential applications such as OLEDs.[29, 48, 50, 118, 123]

Figure 5.46 are the emission results for the same study detailed in Figure 5.44. The results focus on the excimer excitation peak and it can be seen that at 5% MeCN the excimer emission peak has started to shift. However, when this was increased to 30% the change is minimal, the emission profile does not change as readily for complex **21.**

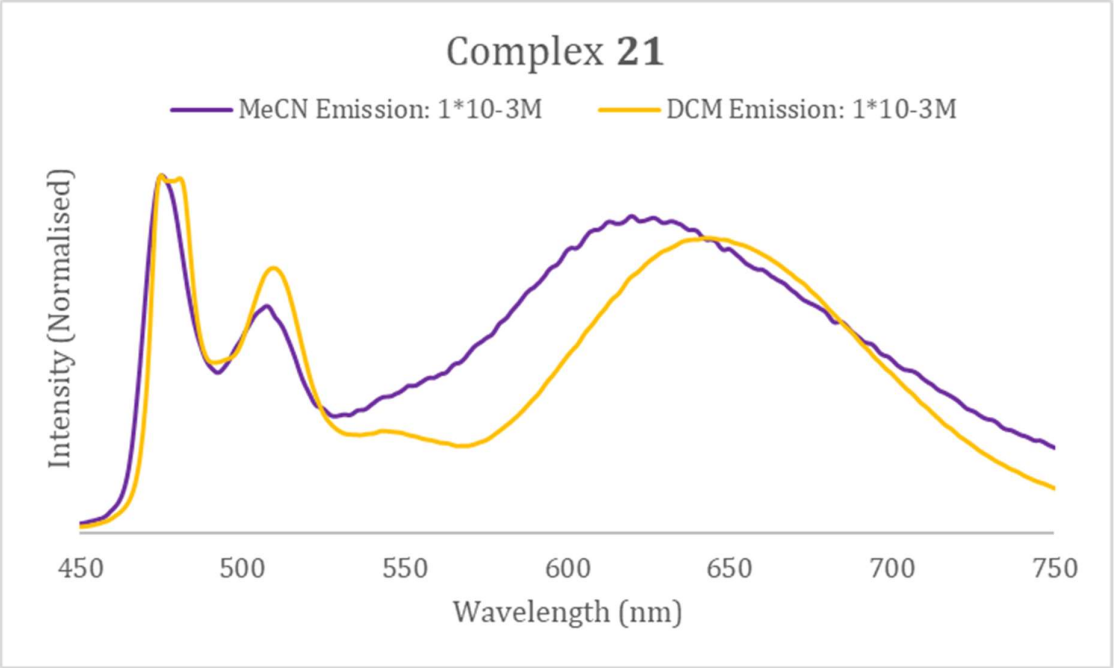

Figure 5.45: *Solution state emission spectroscopy of Complex **21**, Purple line: 1×10^{-3} M in MeCN, λ_{ex}400 nm, Yellow line: 1×10^{-3} M in DCM, λ_{ex}400 nm.*

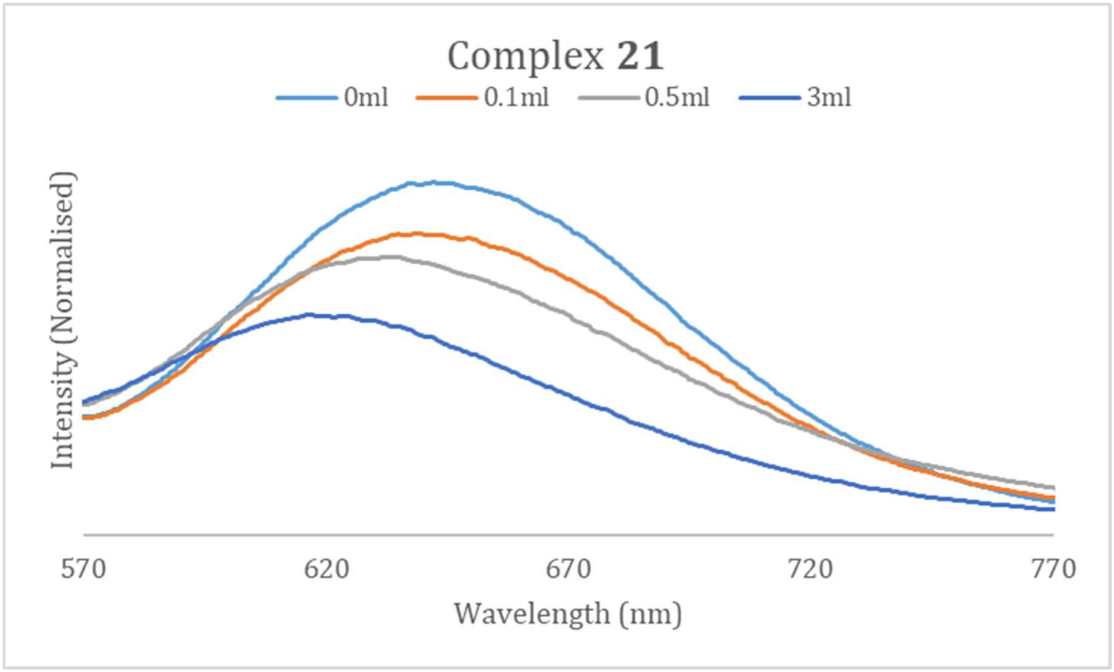

Figure 5.46: *Emission study of Complex **21**, 1×10^{-3} M Solution of Complex **21** in DCM, MeCN Added*

5.8.3 X-Ray Powder Analysis

Single crystals of complex **21** suitable for single crystal analysis could not be grown. However, clean purple and yellow powders of complex **21** was isolated. The yellow powder is the vapochromic MeOH form. This form was obtained by trapping a small amount of MeOH in the end

of a capillary with cotton wool and allowing the vapour to diffuse through the capillary, turning the purple complex yellow.

The results presented in Figure 5.47 show that the two different forms have different powder patterns. This is to be expected, as the purple colour is indicative of a high level of Pt…Pt overlap, however the yellow would suggest complete disruption of the stacks in the solid state.

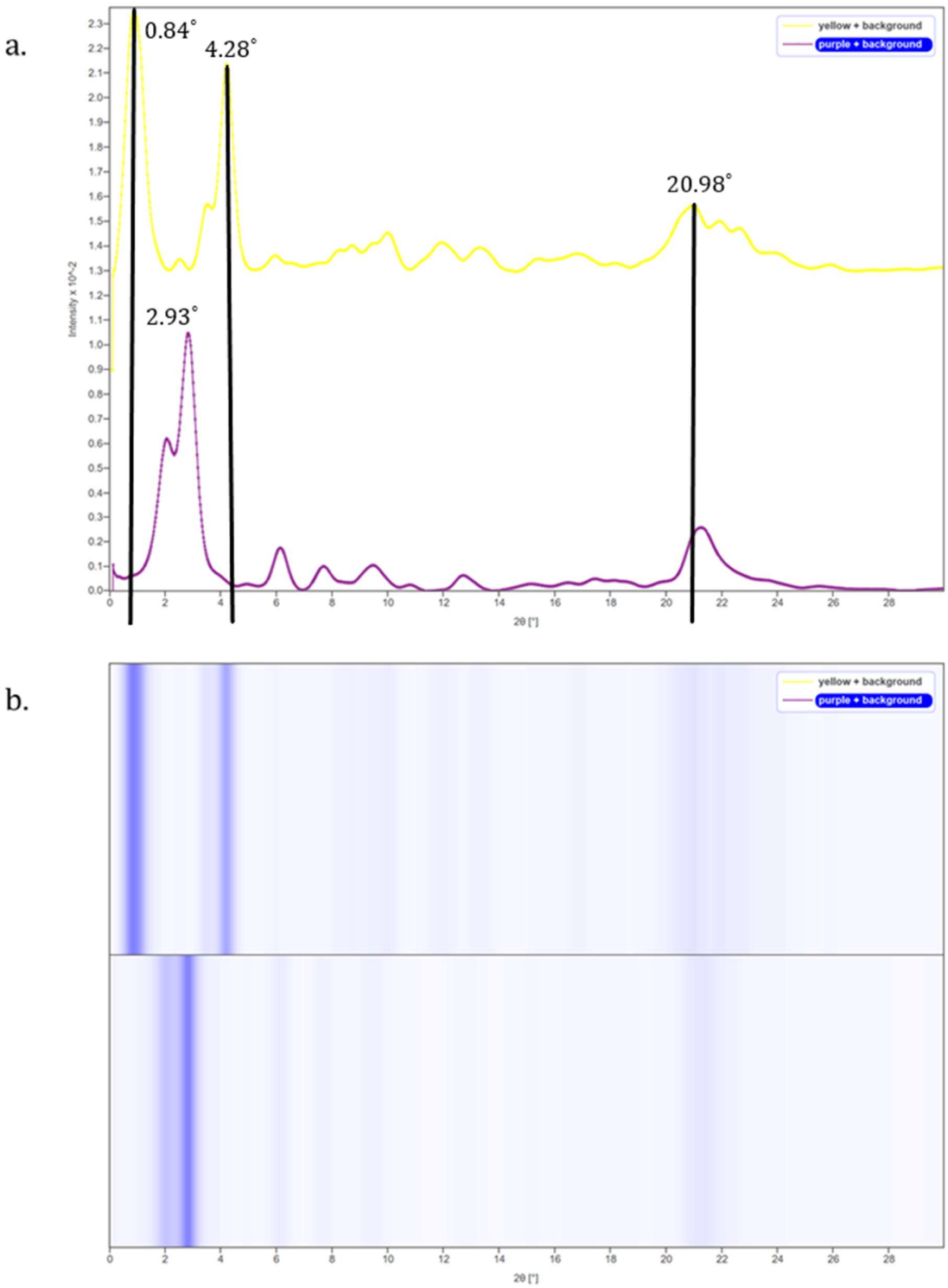

Figure 5.47*: a. Complex **21** powder plot. b. Film representation of powder of Complex **21**. Yellow trace is the MeOH form, purple trace is the MeCN form.*

5.9.0 Conclusion

The focus of this chapter was to develop the initial research carried out in the Raithby group on Pt(II) Pincer complexes. To achieve this aim seven complexes have been studied in depth to ascertain whether the identity of the ligand in the 4th co-ordination site has any influence on the spectral properties of the complex. Investigation of a number of mid-field ligands such as SCN and NCO, in the spectrochemical series supported the theory that a strong field ligand was required for a complex to exhibit changing spectral properties. The complexes that utilised the mid-field ligands were yellow in colour and contained predominantly π interactions in the solid state structure.

The study was subsequently expanded to include ligands that could form hydrogen-bonding networks with the solvent in an analogous manner observed with the cyanide complex described in section 5.1.2.[93] The acetate group was chosen for this role due to its potential to hydrogen bond through the carbonyl. This complex showed rapid vapochromic response to MeOH, dry N2, and could be applied to glass as a smart coating. The solid-state structures of the vapochromic form were not successfully isolated and therefore a comparison to the literature standard could not be made. However the powder diffraction showed that the 3 different forms of the acetate complex do differ in their solid state structure, which would suggest a change in the solid state packing upon diffusion of the solvent in and out of the structure.

Following on from the success of introducing a more complex ligand into the co-ordination sphere of the Pt centre, further functional groups were investigated. Unlike the initial research conducted in this chapter the rest of the ligands contained more than 2 or 3 atoms. This led to the discovery of a number of interesting complexes that displayed solvatochromic and vapochromic behaviour. The introduction of these groups also affected the physical properties of the complexes, in particular the solubility. The Pt complexes previously synthesised had all had limited solubility, however the introduction of CF_3 and tosylate groups increased there solubility in solvents and altered which solvents they would dissolve into. This was attributed to the effect of the functional group in the 4th position of the co-ordination sphere. While improved solubility is advantageous when investigated solution state properties of these complexes, it made crystallising them more challenging. Unfortunately single crystals of these complexes could not be isolated after trialling a number of different crystallisation conditions in a number a different solvents. Crystallisation methods included, low temp vapour diffusion, slow cooling and evaporative techniques at a number of temperatures.

Complexes **19** and **20** showed similar vapochromic properties, this was attributed to both ligands in the 4th co-ordination site containing a CF_3 group. These complexes had a distinctive solvatochromic transition between yellow and orange in response to solvents. As previously explained the solid state structure could not be isolated for these complexes, therefore structural analysis of the solid state interactions could not take place. However it is thought that their behaviour could be attributed to halogen interactions between the complex and the solution as opposed to Pt…Pt interactions. This is because in solution it is unlikely that the complexes would stack in columns with Pt centres overlapping. Alternatively it would be possible that in solution for the complex to aggregate into smaller discrete stacks, held together with halogen and π interactions. Further studies would have to be undertaken to confirm this theory.

The final complex discussed in this chapter was complex **21**, which showed the most versatile and complex spectral changes. The main consistent transition observed for this complex was a reversible colour change from purple to yellow when the methanol solvate was exposed to acetonitrile. If the complex had been recrystallized from an alternative solvent then the observed transition was slower and not seen throughout the whole of the deposited film. This complex was sensitive to the solvate and the solvent used. This could be attributed to subtle differences in the solid state structure, unfortunately a solid state structure was not obtained for this complex. However the vapochromic behaviour of this complex could be attributed to a change in Pt…Pt distance.

Further development of a known complex, has led to the discovery of a number solvatochromic and vapochromic complexes. It is clear that the origin of the spectral behaviour can't be attributed to a single factor, this is shown clearly by complex **21** in which a particular solvate is required to observe a specific transition. Further solid state and computational studies are required before we are able to predict the behaviour of a complex from its connectivity.

CHAPTER 6

Light Sensitive N^C^N Complexes

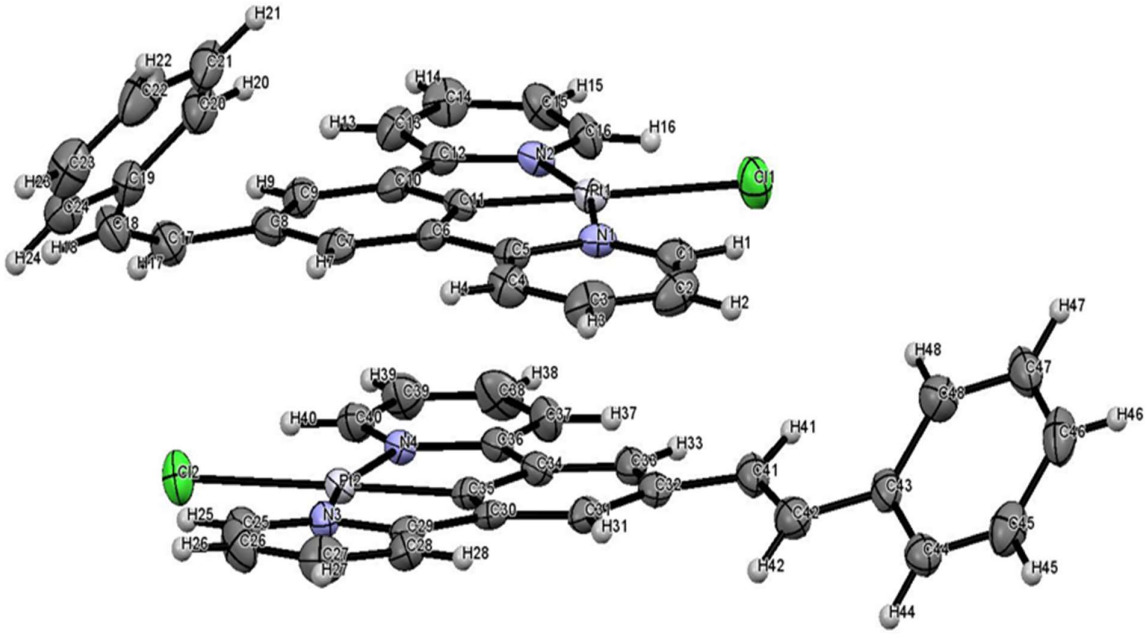

6.1.0 Introduction

Complexes with light switching moieties are of interest because of potential applications in the optoelectronics industry, for example optical memory, photo-optical switches and displays.[124-128] The majority of this research has focussed on the solution state switching of azobenzenes and stilbenes; the isomerism of the functional groups is easier to achieve in solution than in the solid state. However, an article published in 2015 investigated the solid-state switching properties of an azobenzene tetramer.[129] The researchers discovered that the reversible photo-isomerism provided an on/off switch for optical properties. This compound was organic and contained no metals.

In this chapter, I will investigate the inclusion of light switching functional groups in a Pt Pincer complex with the aim of synthesising a complex that will undergo photo isomerisation in the solid state.

6.1.1 Azobenzenes and stilbenes

For this research, the azobenzene and stilbene functional groups (Figure 6.1) have been chosen to act as benchmark compounds. The photochemical reactions of both groups has been well documented in the literature,[125, 130-132] and the *cis*- *trans* photoisomerisation reactions have been widely studied, primarily in solution. The large change in size, shape and polarity of the molecules means they have been used extensively in the design of 'smart' materials. [126]

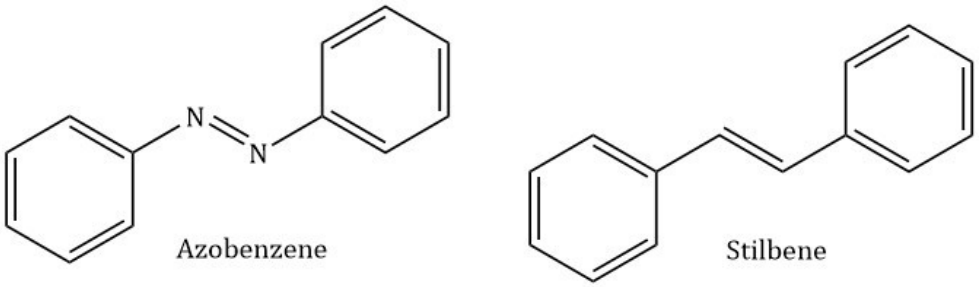

Figure 6.1*: Structure of the azobenzene and stilbene functional groups.*

Azobenzenes are found in the stable *trans* form because the *cis* isomer is normally too unstable to be isolated because of the unfavourable intramolecular interactions generated. However it can be studied using spectroscopic methods due to *cis* azobenzenes absorbing at a lower wavelength in the UV range in comparison to the *trans* form, 280 nm and 314 nm respectively.[133] The *cis* form is usually stable at low temperature and in the dark because exposing it to light will favour the *trans* form, Figure 6.2.

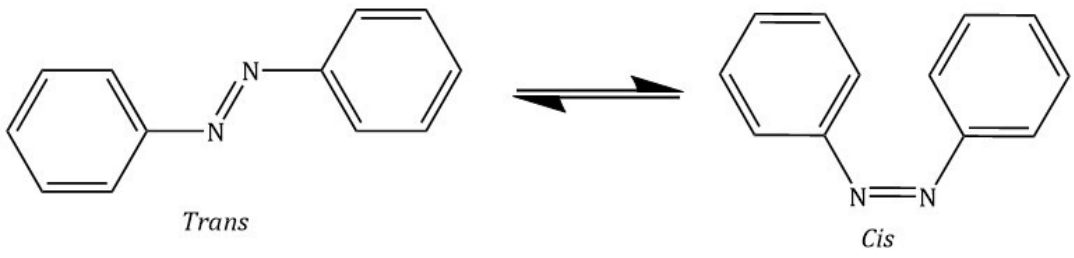

Figure 6.2*: Photoisomerisation of the azobenzene group*

The mechanism of photoisomerisation is still widely debated with several pathways being postulated. A paper published in 2004 used computational methods to investigate the decay and photoisomerisation of the S_1 to S_0 state.[134] This study discovered three possible routes by which this state could decay, they are as follows:

1. Change in torsion angle around the N=N bond,
2. Change in torsion around the N=N bond combined with inversion,
3. Inversion about the mid-point of the N=N bond.

The first mechanism was favoured, as it was the lowest energy process, but it is important to note that this transition is symmetry forbidden so the N=N bond needs to be distorted for the first mechanism to occur.

The all carbon analogue of an azobenzene is a stilbene, Figure 6.1. As observed with the azobenzene molecule stilbenes undergo a *cis- trans* isomerisation however the mechanism by which this transition occurs differs to the mechanism postulated for azobenzene. It is thought that the mechanism proceeds via a triplet state, but this is still under debate.

The extent of photo-isomerisation that occurs for both azobenzene and stilbene is dependent on the solution concentration, solvent, substituents and temperature.[135, 136]

6.1.2 'Smart' materials

Photo-responsive groups have been incorporated into a several different compounds for a variety of applications. Azobenzenes and stilbenes have been used extensively in this research area and in this section a few examples highlighting their use is presented.

One application is for the biological sensing of ions in solution, Shinkai and collaborators developed a series of azo-bridged crown ethers. This research took advantage of the *trans-cis* isomerisation observed in azobenzene groups in solution. The study found that in solution the compound would adopt a *trans* configuration and when K^+, Na^+ or Rb^+ was added the molecule configuration changed to *cis* and the ion became encapsulated (Figure 6.3). This process was found to be reversible and the ion would be released upon the solution being irradiated with visible light.[137]

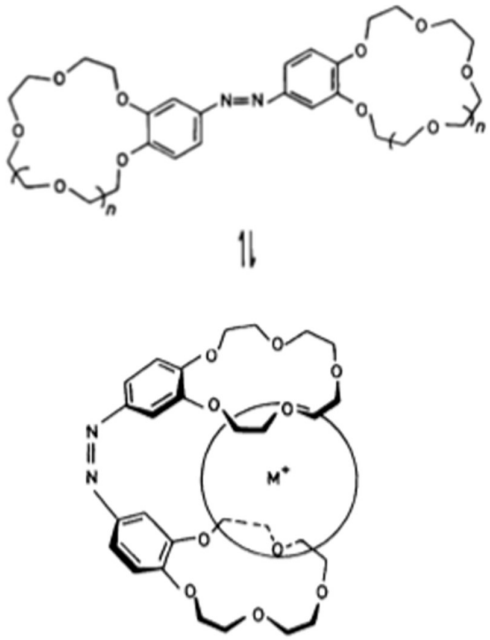

Figure 6.3*: Isomerisation of a molecules in the presence of a metal ion.*[137]

Pipoosananakaton published a second supramolecular example used in biological sensing. In this research a calix[4]arene derivative was capped with azo groups, unusually the *cis* form was found to be the most stable isomer in solution, this was attributed to substitution effects. However, when irradiated with visible light the *trans* isomer could be accessed. When the complexes ion-binding ability was tested, they found that the *trans* isomer preferentially bound K^+ and the *cis* isomer bound Na^+.[138]

An example that is more relevant to the research presented in this chapter is the azobenzene functionalised complex shown in Figure 6.4.

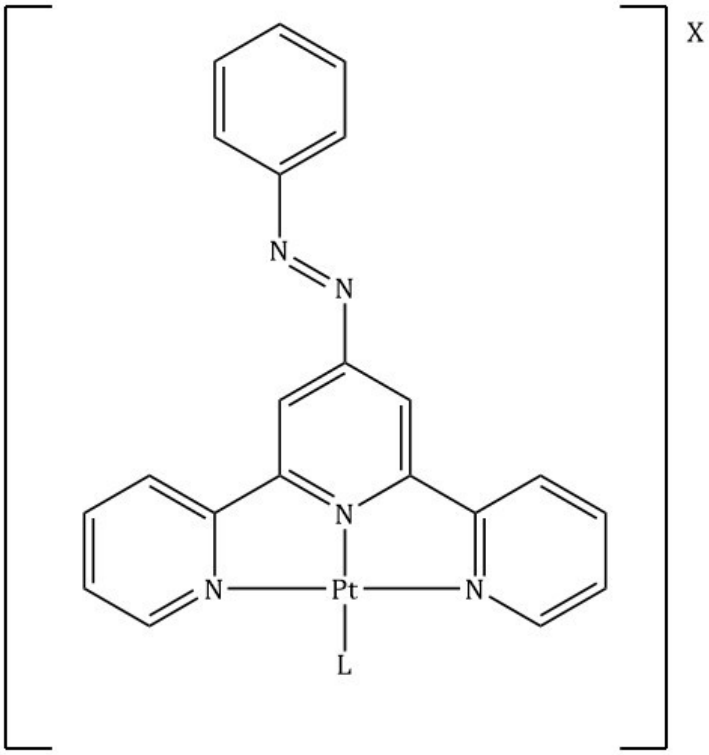

Figure 6.4*: Terpyridine complex, with light switching capabilities. Where L=py or Cl and X=PF_6^-.*

This is a square planar Pt^{2+} complex with a functionalised azobenzene pincer, synthesised by Yutaka et al. When a 4.2×10^{-5} M solution of this complex in DMF was irradiated with 366 nm light the UV-Visible spectrum showed a decrease in the azo π- π* absorption band and an increase in the azo n-π* absorption band. This was indicative of a *trans-cis* isomerisation occurring. In addition, when L=py the *cis* form had an intensive band at 450 nm and when L=Cl the *cis* form had an intensive band at 470 nm, which showed how the absorption spectrum profile differed dependent on the group occupying the 4th co-ordination site. The isomerisation was not solvent dependent and the same isomerisation was seen in various solvents. However, when the isomerisation was reversed, it was found that the solution contained a 50:50 ratio of *cis* to *trans* this was attributed to the following two factors, the photo-stationary state had been reached and there was some degradation of the sample.[139]

The majority of the materials research that uses a stilbene functional group has been used in developing complexes for the photonics industry.[140-142] However, uses in biological sensing have not been as widely developed for stilbene motifs as they have been for azobenzenes. One reason behind this is because the *cis* isomer is prone to irreversible oxidation and cyclisation reactions which are unfavourable for these applications.[143]

One complex in the literature that is of particular interest is shown in Figure 6.5.

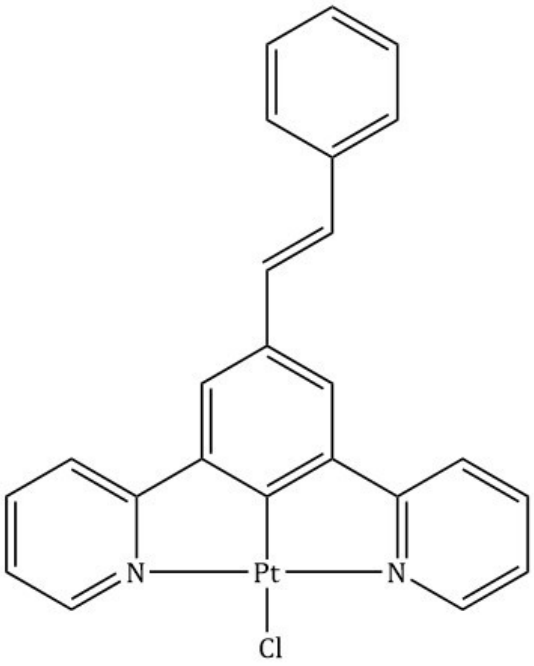

Figure 6.5*: Pt chloride complex with an N^C^N Stilbene functionalised ligand.*

This complex has been studied as part of the research presented in this chapter (Complex 27), however, it was also synthesised by Baggi *et al* and its second-order non-linear optical (NLO) response measured.[144] For a NLO response to occur the molecule needs to be capable of a intramolecular charge transfer from the Pt centre to the cyclometallated ligand and have a donor/acceptor push-pull system. This research concluded that using an organometallic complex offered more flexibility in the NLO response as the complexes were more tuneable through changing the co-ordination sphere of the metal and its oxidation state in comparison to an organic alternative.

6.1.3 Substitution Patterns and Orbitals

As discussed in Section 1.5.0, 'Introducing a Switch', there are two main requirements for inducing a switching process in solid-state d^8 metal complexes. The first is *via* dz^2 stacking in the solid-state structure and the second is *via* changing the electronic π-influence on the metal. To explore these two methods the compounds shown in Figure 6.6 will be synthesised.

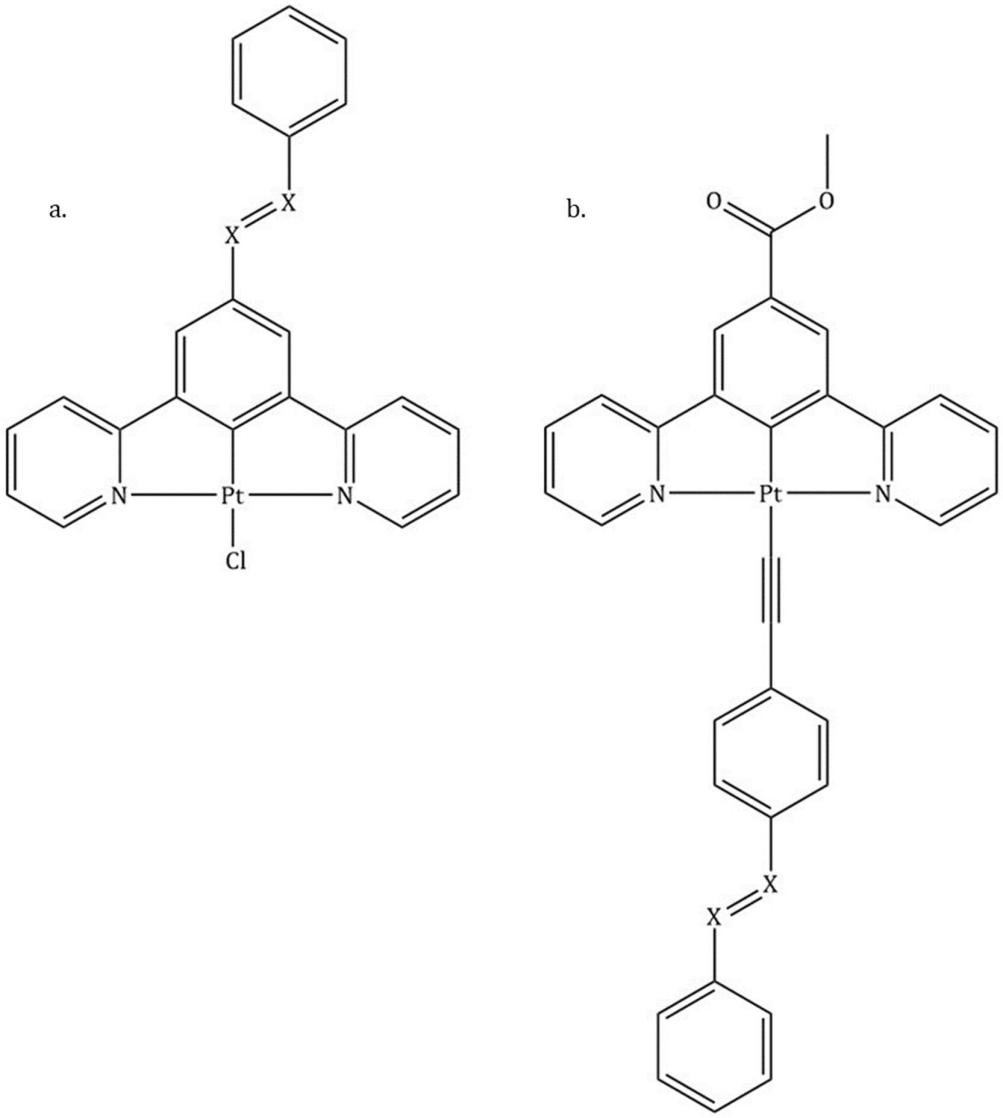

Figure 6.6*: When X=N, a. Complex* ***24*** *b. Complex* ***22****. When X=C a. Complex* ***27.*** *b. Complex* ***25***

In Figure 6.6, the complex in *a*, utilises the method of facilitating dz^2 interactions by substituting the pincer ligand on the 4'-position of the central arene ring so that the planarity around the Pt(II) centre is retained. However, the size of the substituent on the pincer ligand may interrupt this interaction in the solid state. In the case of complex b, in Figure 6.6, the acetylide ligand is being used to facilitate the π-influence on the Pt(II) centre.

In addition to the potential intermolecular interactions in the solid state, the character of the HOMO and LUMO will be vital in determining the switching properties of the complexes. For a photo- isomerisation to occur the LUMO will need to be of π-character and centred on the photo-switch fragment. The different substitution patterns should give rise to different orbital contributions in the HOMO and LUMO in each case and different properties may be observed. To analyse the character of the orbitals DFT calculations have been used to simulate the orbitals of interest.

DFT calculations were carried out in the gas phase using B3LYP in the NW Chem package.[145] The basis function 6-31+g* was used for atoms: C, N, O and H and the basis set lanl2dz for the Pt atom. The HOMO-2, HOMO-1, HOMO, LUMO, LUMO+1 and LUMO+2 were calculated and diagrams have been created using the visualisation program VESTA.

DFT calculations were carried out to ascertain the identity of the frontier orbitals involved in absorptions and the *cis-trans* isomerisation. The calculated HOMO and LUMO of complex **22** and **24** are given in Figure 6.7.

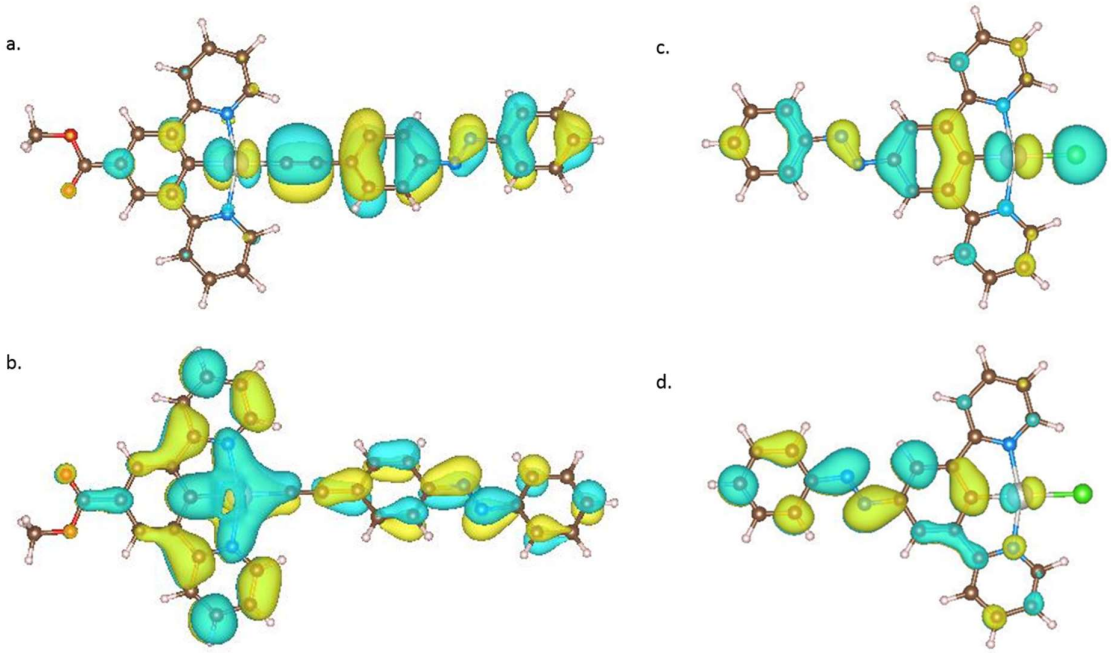

Figure 6.7*: a. Calculated HOMO for complex **22**. b. Calculated LUMO for complex **22**. c. Calculated HOMO for Complex **24**. d. Calculated LUMO for complex **24**.*

The calculated HOMO for **22** is shown in Figure 6.7a. It appears by the shape of the orbital on the Pt centre that this is a π* arrangement of the Pt d_{xz} orbital with the surrounding ligands. The majority of the orbital character is based on the Pt centre and the azobenzene fragment, with minor character based on the central arene ring and the ester group. The LUMO, Figure 6.7b, has orbital character based on the azobenzene ligand, but most of the electron density is based on the pincer ligand, in particular the pyridine rings.

For a photochemical reaction to occur the orbital character of the excited state has to be considered. The LUMO for a pure azobenzene is usually a π-type orbital that is fully conjugated and delocalised. In the case of complex **22** that is not the case, instead the HOMO is the π- type orbital and has the most orbital contribution from the azobenzene ligand. For the *trans-cis* isomerisation reaction to occur the LUMO has to be based on the azobenzene fragment. One method of facilitating this reaction would be to move the azobenzene fragment to the pincer. The HOMO and the LUMO for this configuration is shown in Figure 6.7 c and d, respectively. The HOMO for the complex with the azobenzene fragment on the pincer ligand is similar to that observed for complex **22**, with the majority of the electron density centred on the Pt centre and the chloride

ligand. The LUMO on the other hand has the majority of the electron density centred on the azobenzene fragment, with only a small amount of electron density located on the pyridine rings. The character of the orbitals for this complex look like they might be a more viable option to observe *cis-trans* isomerisation, due to the delocalised nature of the orbitals on the pincer.

6.2.0 Methyl 3,5-di(pyridine-2-yl)benzoate Platinum (E)-((4-(phenyldiazenyl)phenyl)ethynyl) (22)

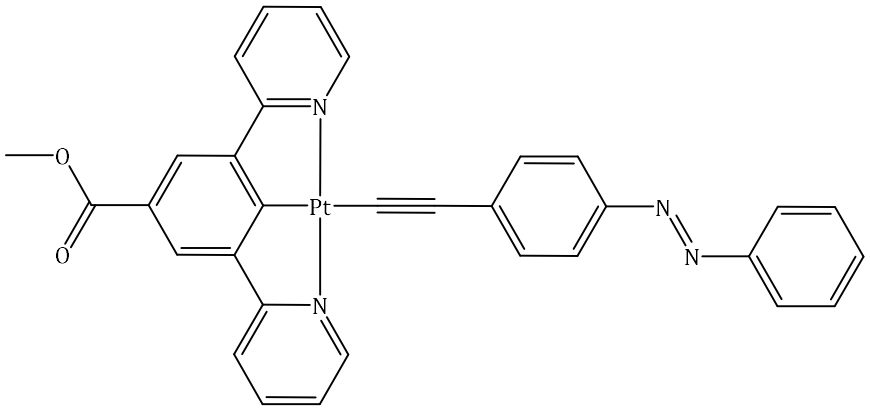

6.2.1 Synthesis

The synthesis of complex **22** is shown in Scheme 6.1. The first step is to synthesis the acetylide ligand. The first reaction performed is the Mills reaction that has been adapted from the literature,[146] this converts an NH_2 group to the respective azobenzene group. Before this can be co-ordinated to the platinum centre, the acetylide has to be deprotected, this is achieved simply by stirring the ligand with base under an inert atmosphere. Complex **15** is then added to the deprotected ligand with 5 cm^3 of DCM to aid dissolution. The mixture is then heated to 55˚C and left for 48 h under an inert atmosphere.

The reaction is then cooled and the solvent removed in *vacuo*, the residue was re-dissolved in DCM and filtered, the product was isolated by recrystallization.

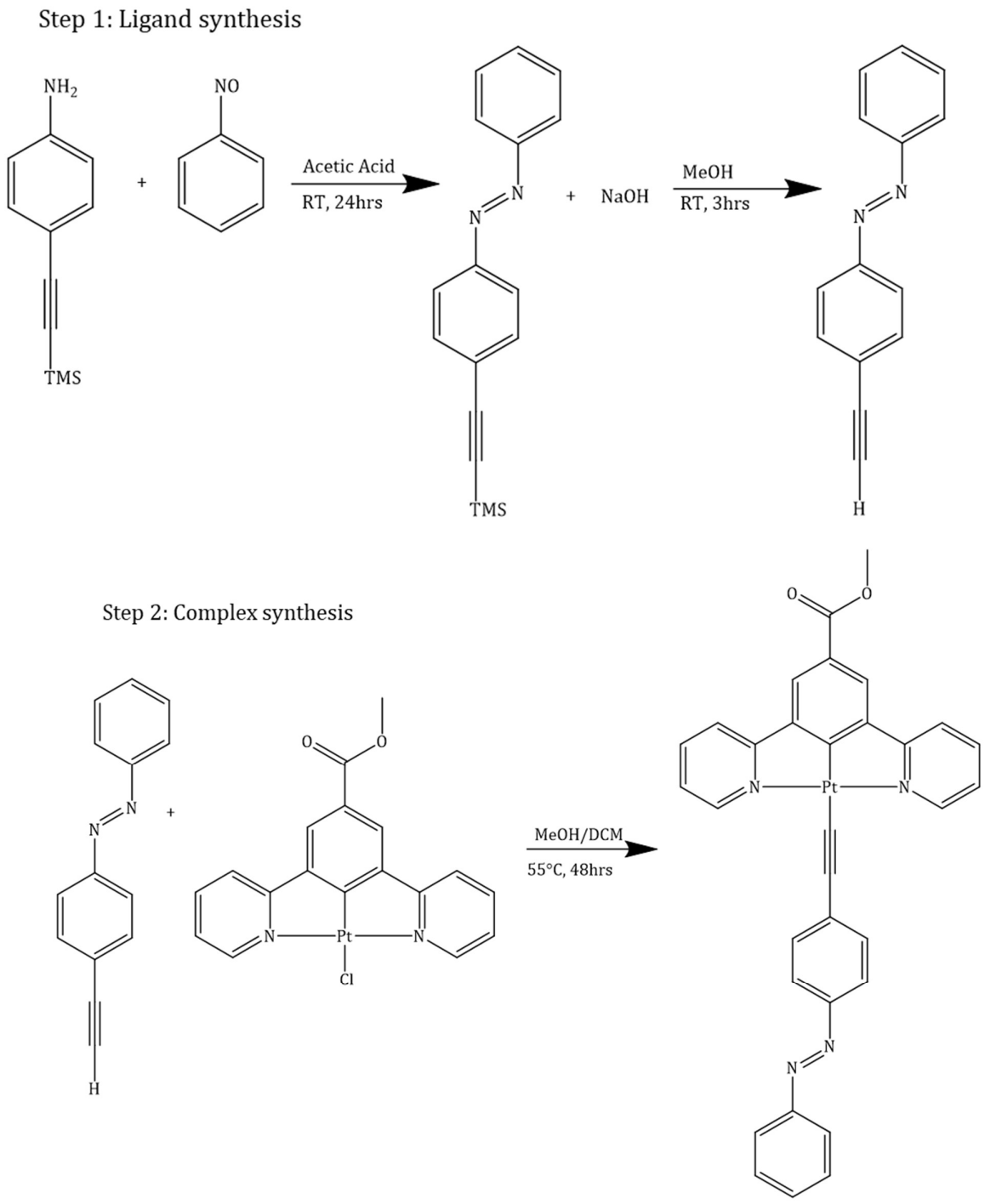

Scheme 6.1*: Synthesis of complex* ***22.***

6.2.2 Isomerisation behaviour

The DFT calculations discussed in Section 6.1.3, suggested that this complex would not undergo *cis-trans* isomerisation because the nature of the HOMO and LUMO was in contrast to the orbital contributions required for the isomerisation to occur.

Solution state spectroscopy was used to analyse the isomerisation behaviour of complex **22**. A solution was irradiated with 365 nm light and the UV-Visible absorption spectrum was measured at 1, 2 and 5 minutes and then every 5 minutes until 30 minutes. An irradiation wavelength of 365 nm was chosen, because literature precedence suggested that the *trans-cis* isomerisation occurred when irradiated with light of 340 nm wavelength,[124] in this instance the closest wavelength that could be achieved was 365 nm. The results of this study are shown in Figure 6.8.

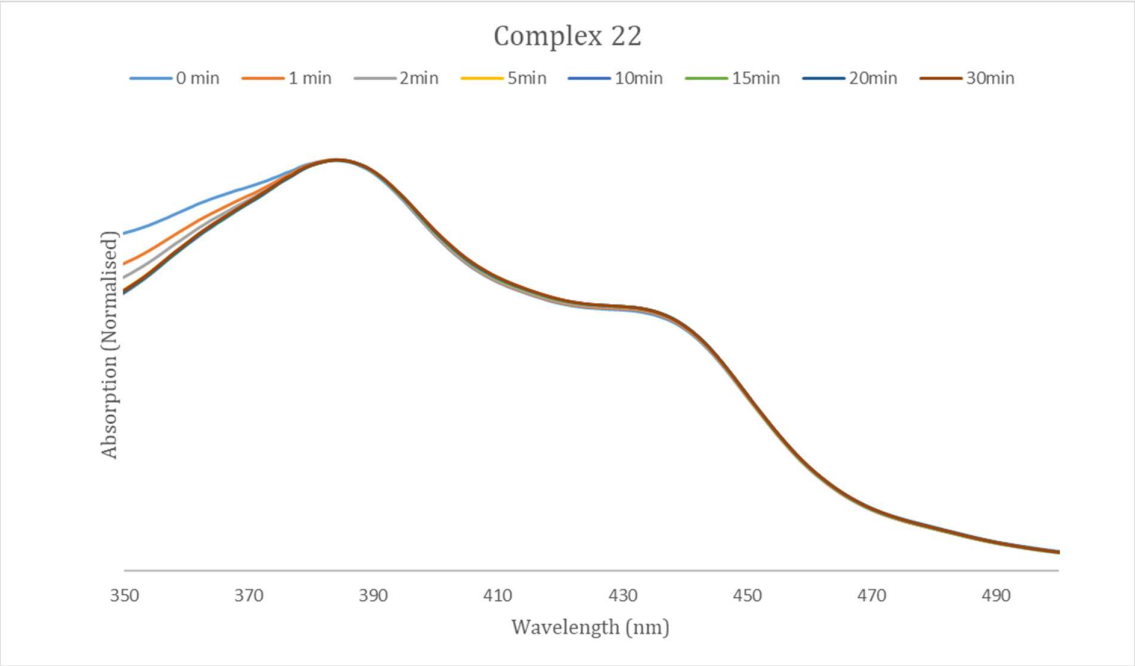

Figure 6.8: *UV-Visible spectrum of Complex **22**, after it had been irradiated at specified times using 365 nm light. The absorption has been normalised to the peak at 385 nm. Solution was 1×10^{-4} M in DCM.*

The spectrum in Figure 6.8 shows that the absorption profile did not change after it had been irradiated with light, this is indicative of no *trans-cis* isomerisation occurring. In addition to the UV-Visible spectrum being recorded the solution state emission spectra was collected at the same time. The emission spectra shown in Figure 6.9, has been normalised but as with the UV-Vis spectra shows no considerable change in peak profile after irradiation for 30 minutes.

These results are in agreement with the theoretical prediction that the orbital configurations are not appropriate for the isomerisation to occur in this complex.

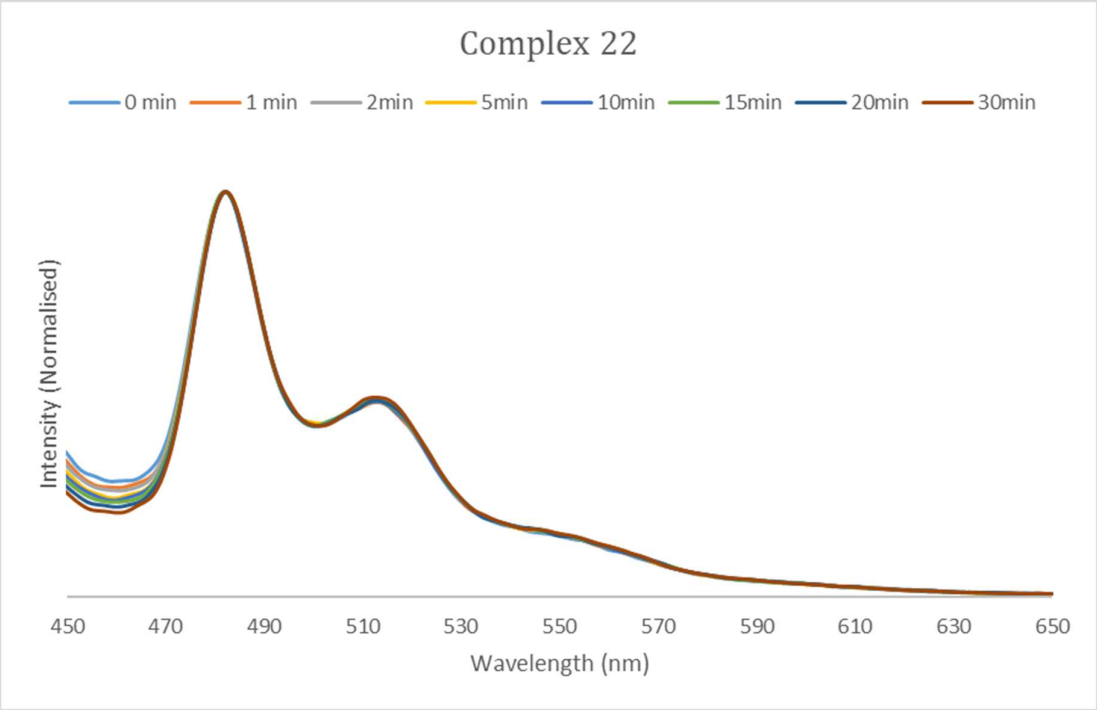

Figure 6.9: *Emission spectrum of Complex **22**, after it had been irradiated at specified times using 365 nm light. The absorption has been normalised to the peak at 480 nm. Solution was 1×10^{-7} M in DCM.*

6.2.3 Crystal Structure Analysis

Crystal Structure:

The crystal structure of this complex is shown in Figure 6.10. It crystallises in the monoclinic space group $P2_1/n$, with one molecule in the asymmetric unit. Bright orange crystals were grown from the slow evaporation of DCM, there are no molecules of solvent in the unit cell. Extended crystal and refinement data are presented in Table 6.1.

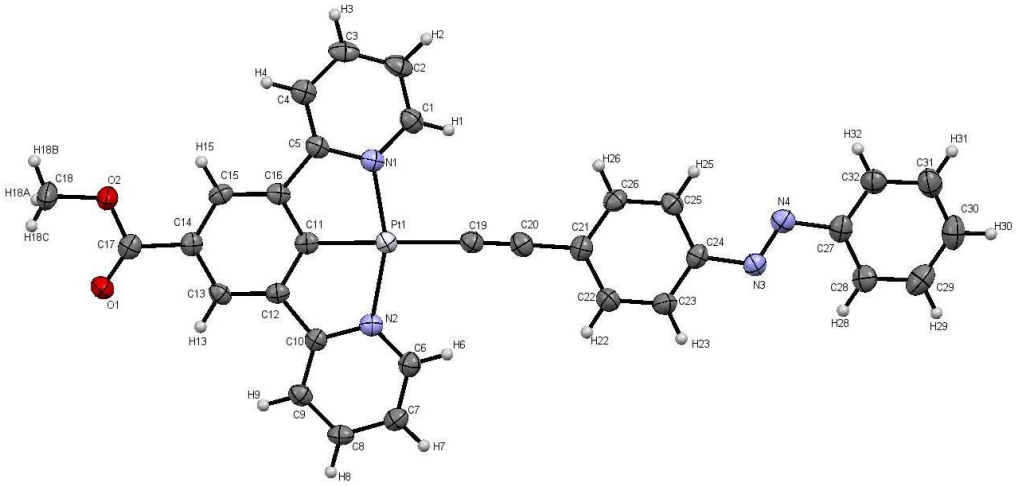

Figure 6.10: *Crystal structure of Complex **22**. Ellipsoids shown at 50%.*

Table 6.1: *Crystal data and structure refinement for Complex* ***22.***

Identification code	e15prr87
Empirical formula	$C_{34}H_{22}N_4O_2Pt$
Formula weight	685.62
Temperature/K	150
Crystal system	monoclinic
Space group	$P2_1/n$
a/ Å	12.0909(3)
b/ Å	10.2540(2)
c/ Å	20.5181(5)
α/°	90
β/°	91.593(2)
γ/°	90
Volume/ Å^3	2542.86(10)
Z	4
ρ_{calc}g/cm^3	1.791
μ/mm^{-1}	5.554
F(000)	1336.0
Crystal size/mm^3	0.5 × 0.4 × 0.5
Radiation	MoKα (λ = 0.71073 Å)
2Θ range for data collection/°	6.496 to 58.564
Index ranges	-15 ≤ h ≤ 16, -14 ≤ k ≤ 14, -26 ≤ l ≤ 28
Reflections collected	42854
Independent reflections	6433 [R_{int} = 0.0541, R_{sigma} = 0.0445]
Data/restraints/parameters	6433/0/353
Goodness-of-fit on F^2	1.038
Final R indexes [I>=2σ (I)]	R_1 = 0.0377, wR_2 = 0.0723
Final R indexes [all data]	R_1 = 0.0591, wR_2 = 0.0787
Largest diff. peak/hole / e Å^{-3}	1.19/-0.59

The molecular structure of complex **22** is square planar around the Pt centre, with a slight distortion of the angle N1-Pt1-N2, 160.13(13)˚ attributed to the pincer bite angle. The other bond parameters listed in table 6.2 fall within the expected parameters. The bond length measured for the C≡C triple bond, C19-C20 is 1.201(6) Å and this is consistent with values previously reported in the literature.[147, 148]

The azobenzene group in complex **22**, adopts the *trans* conformation, this is of lowest energy and takes up the smallest amount of space in the crystal structure. The majority of torsion angles are close to 0˚, 180˚ or -180˚ as would be expected for a planar complex. However, there were two that deviated from this value, these are localised to the azobenzene group, table 6.2c. This is consistent with a slight shift from planarity observed in the crystal structure. Using the program Mercury[87] the dihedral angle between the plane of the pincer molecule, mean plane: Pt1-C12-N1-C11-C5-C10-C16-N2, and the arene rings of the azobenzene group, mean plane: C31-C28-C32-C30-C29 could be measured. The dihedral angle was measured at 7.63(11)˚. This further illustrates the slight twist of the functional group when compared to the plane of the molecule.

Table 6.2: *a. Table of bond lengths for **22**. b. Table of bond angles for **22**. c. Torsion angles for **22**.*

a. Bond Lengths		
Atom	**Atom**	**Length/ Å**
Pt1	C19	2.057(4)
Pt1	N2	2.044(3)
Pt1	N1	2.035(3)
Pt1	C11	1.919(4)
C19	C20	1.201(6)

b. Bond Angles			
Atom	**Atom**	**Atom**	**Angle/°**
N1	Pt1	N2	160.13(13)
C20	C19	Pt1	176.2(4)
C19	C20	C21	178.9(5)

c. Torsion Angles				
A	**B**	**C**	**D**	**Angle/°**
N3	N4	C27	C32	-171.7(4)
N3	N4	C27	C28	9.0(6)

Analysis of the structure in OLEX 2[121] shows there are three sets of π-π interactions present in the molecule. OLEX assigned five planes to complex **22**, as described in table 6.3a, and π-π interactions were found to exist between planes 2-4, 4-5 and 5-5, table 6.3b. The strong π-π interactions form between the pyridyl rings as well as the pyridyl rings and the azobenzene substituent on adjacent molecules. The presence of these interactions would decrease the probability of an isomerisation reaction occurring in the solid state had the orbitals been ordered correctly. This is because these interactions would have a stabilising effect on the solid-state structure and additional energy would have been required to overcome them.

In addition to these π interactions, there is the presence of hydrogen bonding between the O1 atom and the adjacent molecule as well as between N1 and N2 and the adjacent molecule. Distances are given in table 6.3c. As with the π interactions, these weak bonds would have to be broken upon isomerisation, which could destabilise the solid-state structure.

Table 6.3: *a. Planes Present in solid-state structure for **22**. b. π-π Interactions for **22**. c. Hydrogen bonds for **22**.*

a. Plane Identification	
Plane Number	Atoms in plane
1	C11 C16 C15 C14 C13 C12
2	C21 C22 C23 C24 C25 C26
3	C27 C28 C29 C30 C31 C32
4	N2 C10 C9 C8 C7 C6
5	N1 C1 C2 C3 C4 C5

b. π-π Interactions	
Planes	Distance (Å)
2-4[1]	3.65(5)
4-5[2]	3.83(7)
5-5[3]	3.84(2)

c. Hydrogen bonds			
Atoms	(D…A) Distance (Å)	(H…A) Distance (Å)	D…H…A Angle/°
C8-H8-N3	3.437(5)	2.555(5)	158.5(4)
C3-H3-N4	3.379(6)	2.565(6)	146.9(5)
C26-H26-O1	3.586(5)	2.672(5)	167.7(4)

Where [1] (1-X, 1-Y, 1-Z), [2] (-X, 1-Y, 1-Z), [3] (-X, 2-Y, 1-Z)

Crystal Packing.

The crystal packing of this complex is shown in Figure 6.11, the lack of solvent inclusion in the structure would suggest that the molecules have been able to pack in a manner so that there is no void space in the structure. This has been confirmed using the program Mercury, the following parameters were used to carry out this calculation: Probe radius: 1.2 Å and grid spacing of 0.1 Å.

Adjacent molecules have packed in a head to toe manner with molecules running perpendicular to the length. The lack of available space or void space in the crystal structure means that even if the orbitals had been in the correct orientation the isomerism most likely would not occur in the single crystal. This is because the lattice strain caused by the azobenzene group isomerising would mean the crystal would lose its crystallinity. However had the orbitals had the correct positioning the isomerisation could have occurred in a powder form, where the lattice strain is not such an important factor.

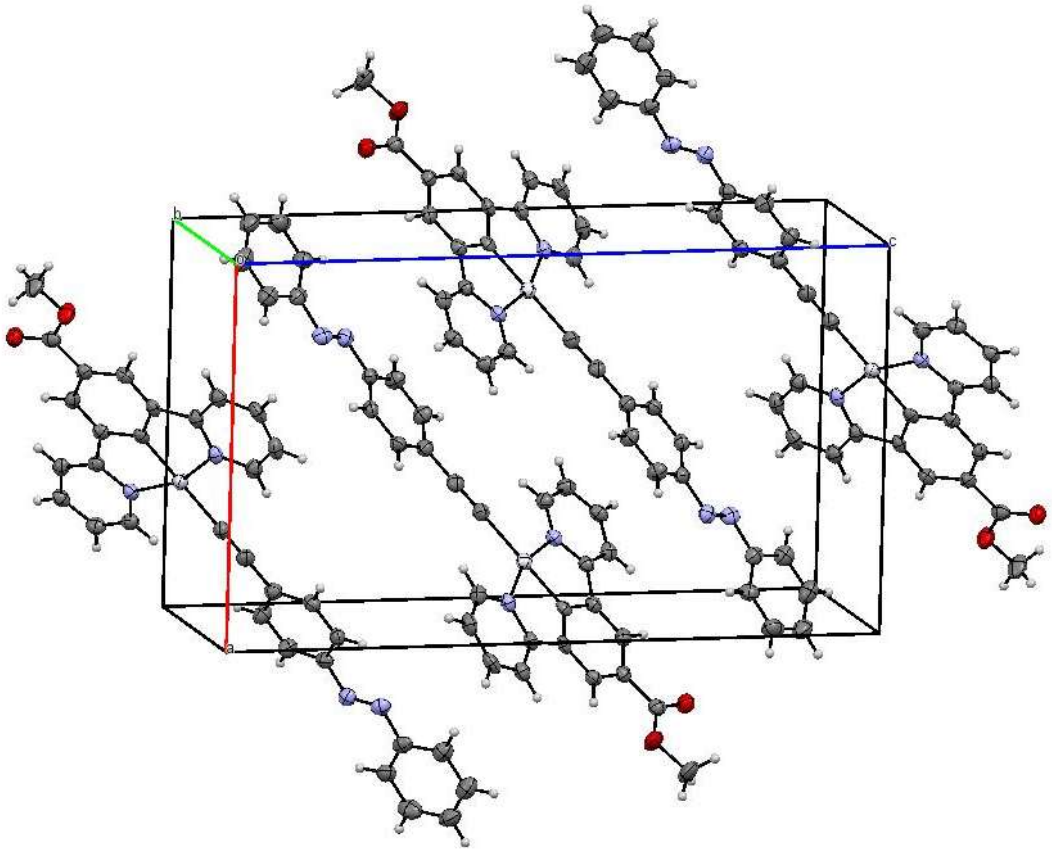

Figure 6.11*: Crystal packing of Complex* ***22****. Ellipsoids shown at 50%.*

6.2.4 Solution State Spectroscopy

The solution state UV-Vis and emission spectroscopy was recorded for **22** and the results are shown in Figure 6.12. The peak that resides between 250-350 nm can be assigned to the π-π transitions of the N^C^N pincer ligand. The peak between 350-450 nm can be attributed to a ^{3}π-π* transition.

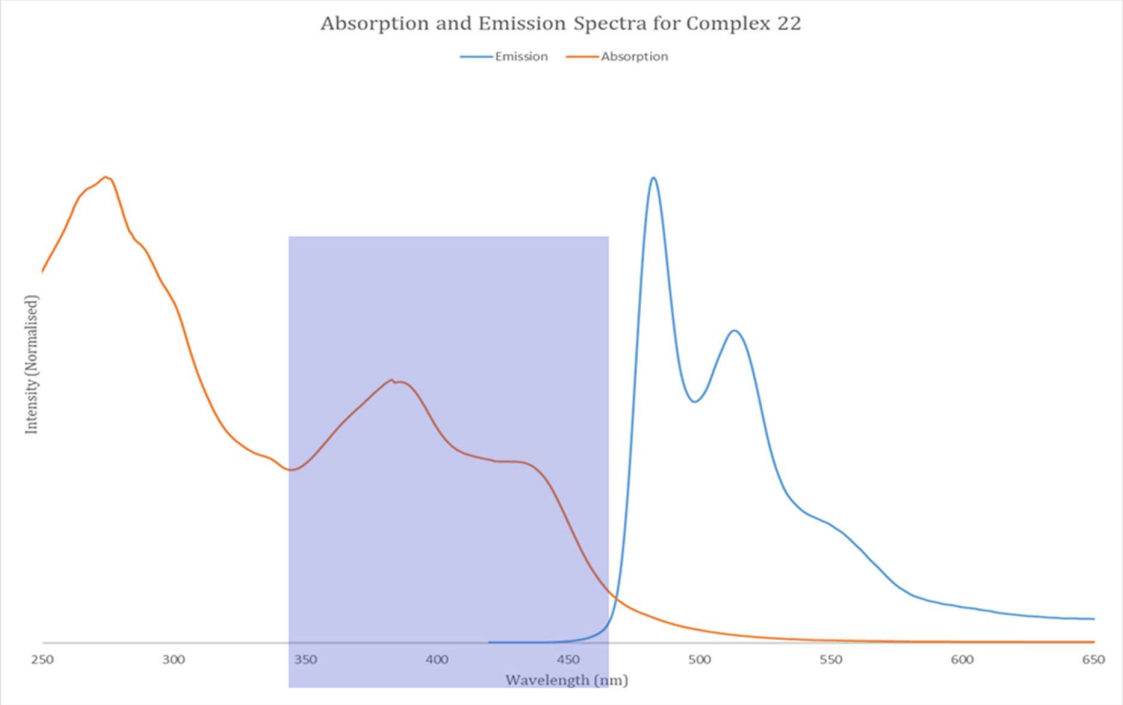

Figure 6.12: *Absorption (^{3}π-π* transition highlighted) and emission spectrum of complex **22**. Solution concentration 1×10^{-4} M in DCM. λ_{ex}=400 nm.*

The complex was excited at a wavelength of 400 nm and a defined doublet is observed in the spectrum. The Stokes shift for this complex is calculated at 130 nm, which is suggestive of phosphorescent emission.

6.3.0 (*E*)-2,2'-(5-(phenyldiazenyl)-1,3-phenylene)dipyridine (23)

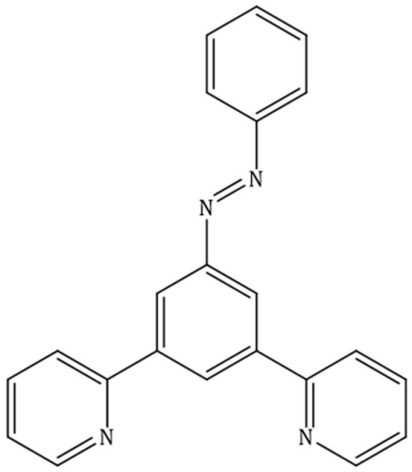

6.3.1 Synthesis

Complex **23,** is a new compound so it will be reported as a precursor to the formation of the Pt complex. **23** was synthesised *via* two different routes to assess which gave the highest yield. The first route is detailed in Scheme 6.2 and the second route is detailed in Scheme 6.3.

The first route is to make the aniline pincer using a Stille coupling and then using the Mills reaction[146] to convert the NH_2 to the azo functional group. This was the first method attempted and the product was isolated in a good yield. However, it took 7 days to get this percentage yield. It was thought that the pyridines rings were responsible for the slow rate of reaction, due to their electron-withdrawing capabilities resulting in slow kinetics.

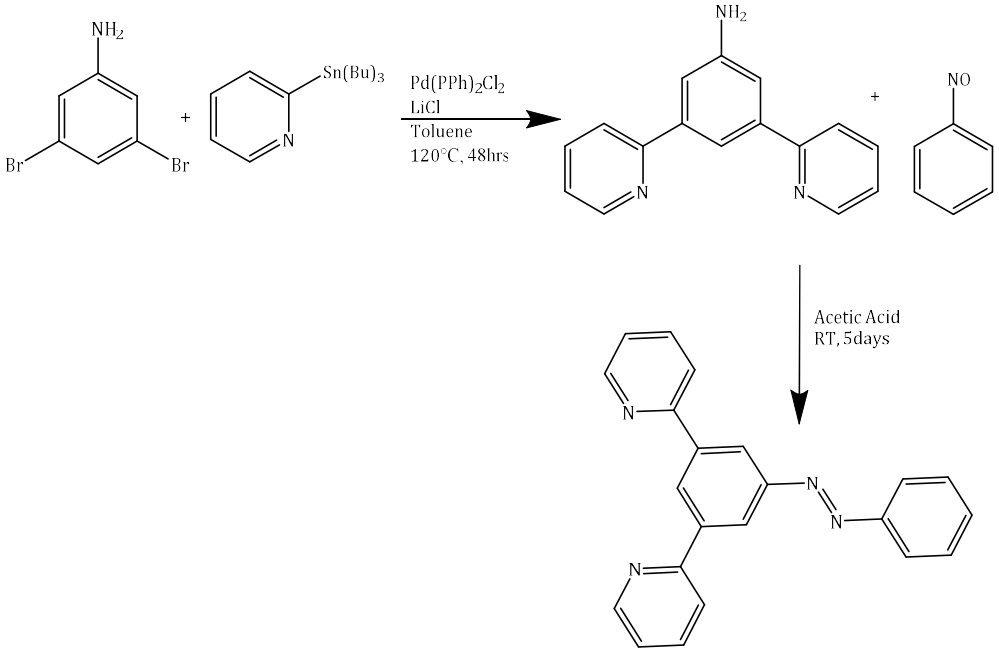

Scheme 6.2*: Synthesis of compound **23**, by the first route.*

In the second method, the aniline group was converted to the azo before the subsequent coupling reaction, shown in Scheme 6.3. This method was far more effective and **23** was isolated in good yield after only 72 h.

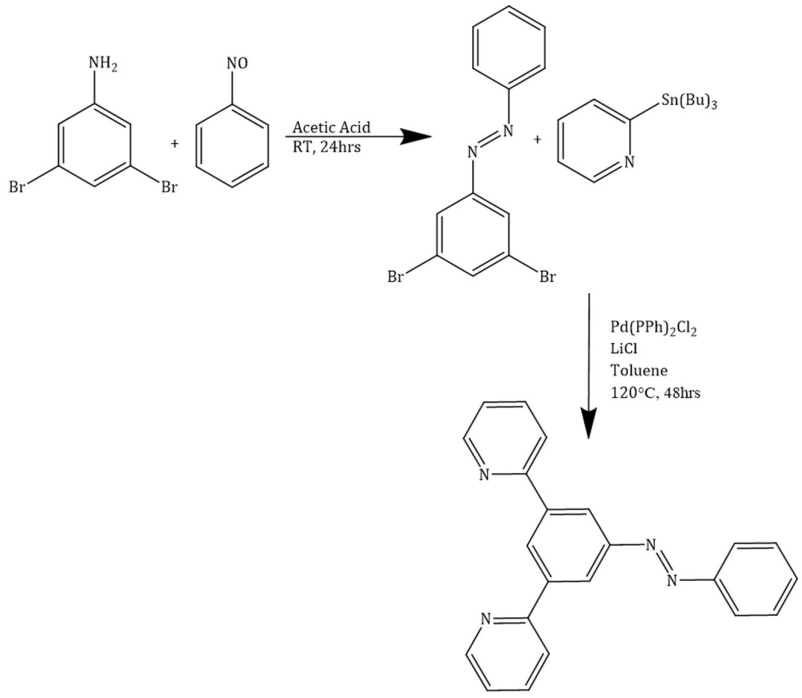

Scheme 6.3*: Synthesis of **23**, by the second route*

6.3.2 Isomerisation behaviour

The computational results suggested that the orbital ordering on the azobenzene when incorporated into a pincer ligand would facilitate a *trans-cis* isomerisation (Section 6.1.3). As with complex **22**, the *trans*-cis isomerisation process was studied using solution state spectroscopy, the absorption and emission results are detailed in Figure 6.13 and 6.15, respectively.

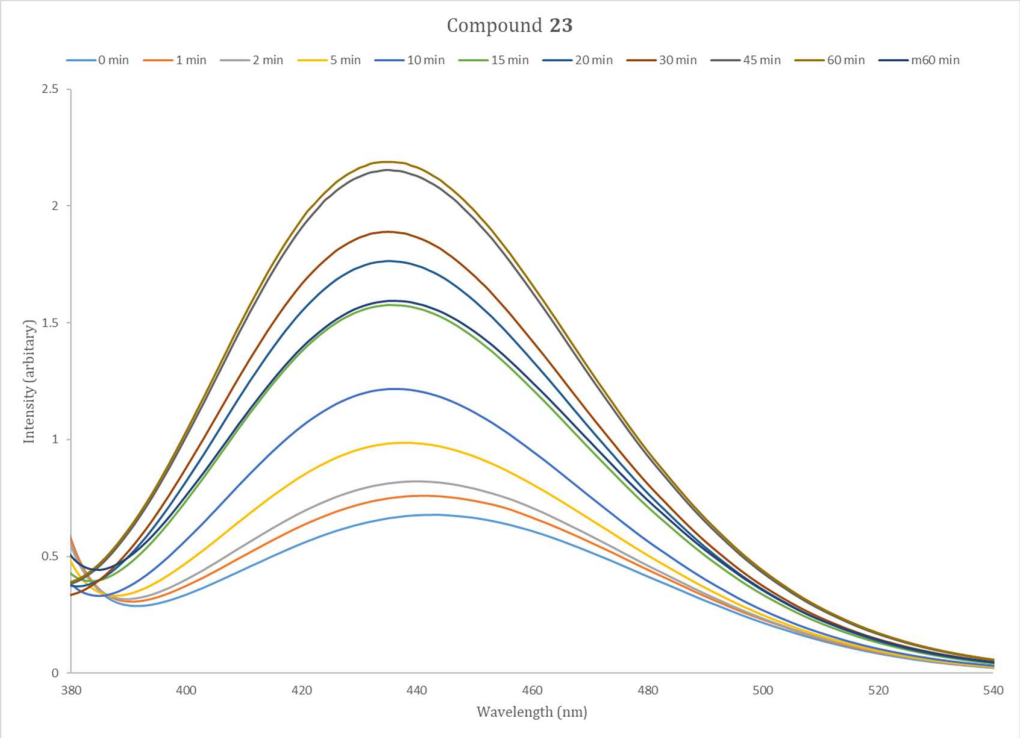

Figure 6.13: *UV-Visible spectrum of Compound **23**, after it had been irradiated at specified times using 365 nm light. Solution was 1×10^{-3} M in DCM.*

Figure 6.13 shows that as the solution is irradiated with 365 nm light, there is a slight blue shift in wavelength and a large increase in intensity. The change in peak wavelength is very subtle and has been measured at 9 nm. The change in intensity is a better indication that an isomerisation process is occurring. In addition to the experiment detailed above, DFT measurements of the complex were carried out and gas phase UV-Vis spectra were simulated for compound **23**. The results are depicted in Figure 6.14.

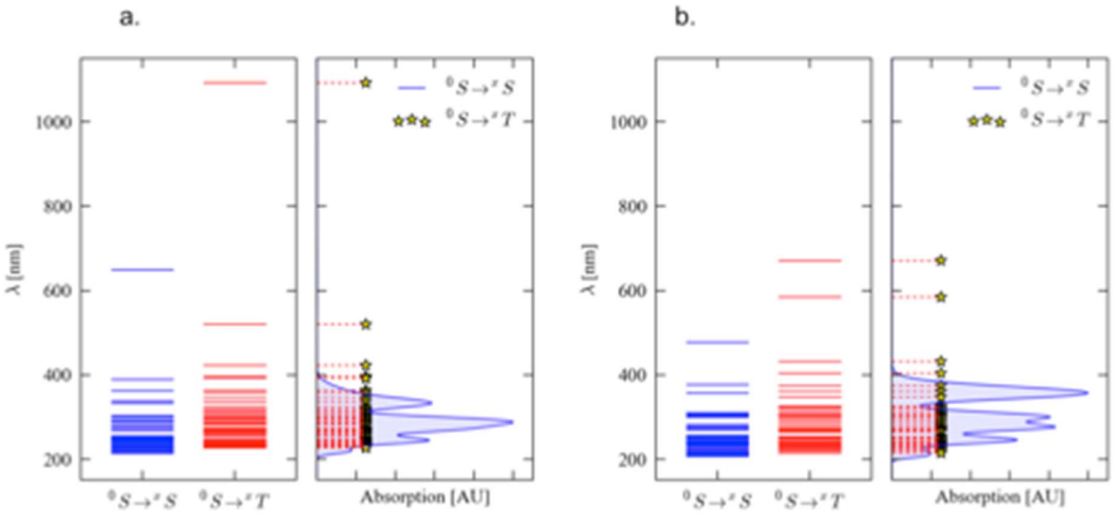

Figure 6.14: *Simulated UV-Vis for compound **23** in the gas phase. a. Cis form, b. Trans form.*

Remembering that the DFT calculations have been completed in the gas phase, so that the peaks have been blue shifted with respect to the peaks observed experimentally, as the experimental data was collected in the solution state. Other than this artefact of the calculation, the theoretical data is in good agreement with the observed data. The peak observed at 380 nm in Figure 6.14b is the peak that correlates to the data presented in Figure 6.13. When this peak is compared to the corresponding peak in Figure 6.14a, the *cis* form, it is clear that there has been a slight blue shift, which is comparable to the experimental data and confirms that **23** undergoes a *trans-cis* isomerisation.

After irradiation, the solution was left in ambient light for an hour, to see if the *cis-trans*-isomerisation took place. As can be seen in Figure 6.13 the intensity of the peak has decreased and the wavelength shifted slightly, suggesting that the reverse process is occurring, however, it is expected that the photo-stationary state has been achieved which is why further *cis-trans* isomerisation has not taken place.

Figure 6.15 depicts the corresponding emission spectra. It can be seen that as the *trans-cis* isomerisation occurs the intensity of the emission increases and the emission wavelength is blue shifted by 10 nm. After an hour of the solution being in ambient light the emission intensity falls but the peak is still shifted by 3nm, due to reaching the photo-stationary state.

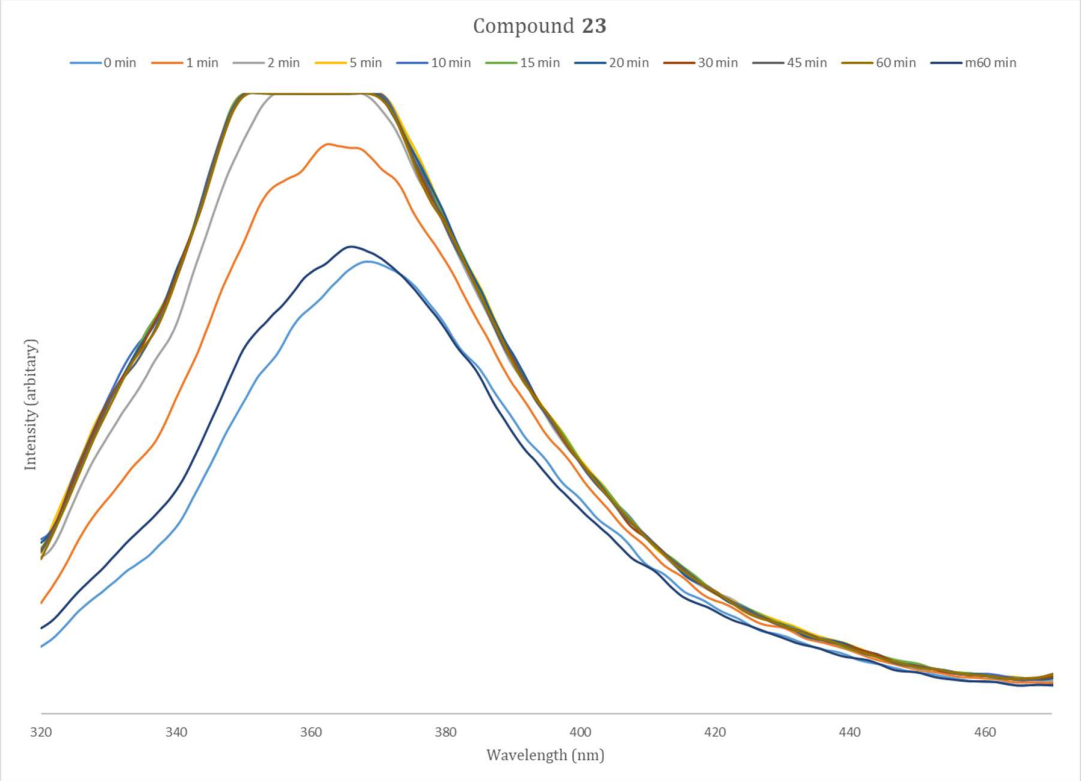

Figure 6.15*: Emission spectrum of* ***23,*** *after it had been irradiated at specified times using 365 nm light. Solution was 1×10^{-7} M in DCM. Excitation wavelength: 300 nm.*

6.3.3 Crystal Structure Analysis

Crystal Structure.

Thin orange needle crystals of **23** were successfully grown from the slow evaporation of DCM. The compound crystallises in the monoclinic space group $P2_1/c$, with one molecule in the asymmetric unit. The structure of **23** is shown in Figure 6.16, with extended crystal and structural refinement data found in Table 6.4.

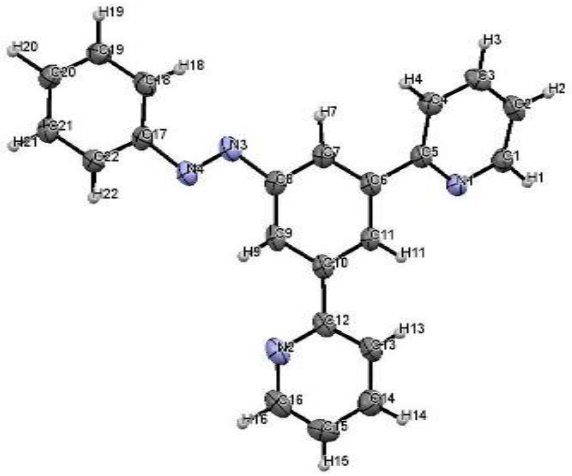

Figure 6.16*: Crystal structure of* ***23****. Ellipsoids shown at 50%.*

Table 6.4: *Crystal data and structure refinement for* ***23.***

Identification code	s15prr202
Empirical formula	$C_{22}H_{17}N_4$
Formula weight	337.39
Temperature/K	150
Crystal system	monoclinic
Space group	$P2_1/c$
a/ Å	11.5192(4)
b/ Å	20.4411(8)
c/ Å	7.4363(3)
α/°	90
β/°	108.354(4)
γ/°	90
Volume/ Å^3	1661.91(12)
Z	4
ρ_{calc}g/cm^3	1.348
μ/mm^{-1}	0.645
F(000)	708.0
Crystal size/mm^3	0.3 × 0.1 × 0.1
Radiation	CuKα (λ = 1.54184 Å)
2Θ range for data collection/°	8.086 to 143.48
Index ranges	-14 ≤ h ≤ 13, -24 ≤ k ≤ 24, -8 ≤ l ≤ 5
Reflections collected	6163
Independent reflections	2967 [R_{int} = 0.1025, R_{sigma} = 0.1089]
Data/restraints/parameters	2967/0/299
Goodness-of-fit on F^2	1.048
Final R indexes [I>=2σ (I)]	R_1 = 0.0474, wR_2 = 0.1229
Final R indexes [all data]	R_1 = 0.0634, wR_2 = 0.1347
Largest diff. peak/hole / e Å^{-3}	0.26/-0.20

Compound **23** does not adopt a planar structure unlike when tridentate ligands are cyclometallated to a Pt centre. This is exemplified by the key torsion angles showing significant deviations from 0 or 180°, table 6.5. The torsion angles listed in table 6.5 are those between the N=N bond and phenyl ring and the central phenyl ring to the pyridyl ring. These angles show there has been a significant deviation from planarity with this complex.

Using the program Mercury[87] the dihedral angles in the complex can be calculated. They are as follows:

- The dihedral angle of the mean plane C6-C7-C8-C9-C10-C11 and C17-C18-C19-C20-C21-C22 is 26.00˚
- The dihedral angle of the mean plane C6-C7-C8-C9-C10-C11 and N1-C1-C2-C3-C4-C5 is 30.99˚.

This confirms that the structure is not planar. The bond angles and bond lengths are consistent with similar compounds.

Table 6.5: *Torsion angles in* ***23***

Torsion Angles				
A	**B**	**C**	**D**	**Angle/°**
N3	N4	C17	C18	-20.6(3)
C11	C6	C5	N1	29.4(2)
C9	C10	C12	N2	18.7(3)

Analysis of the complex using OLEX2[121] shows there are no π-π interactions in this complex. Further analysis using the program Mercury[87] shows there are two types of interactions in this complex, hydrogen bonding and short contacts, table 6.6. These interactions explain why no π stacking interactions are observed with this complex. Three out of four of the short contacts exist between carbon and hydrogen atoms. The single short contact between two carbon atoms, has the longest measured distance and inspection of the overlap in Mercury, shows that it is just single carbon atoms that overlap not the plane of the ring.

Table 6.6: *Short Contacts and hydrogen bonds in* ***23***

a. Short Contacts	
Atoms	Distance (Å)
C2-H21	2.88(3)
C7-H4	2.80(3)
C19-H1	2.87(3)
C9-C22	3.362(3)

b. Hydrogen bonds			
Atoms	(D…A) Distance (Å)	(H…A) Distance (Å)	D…H…A Angle/°
C19-H19-N1	3.520(3)	2.65(3)	146(2)

Crystal Packing.

The azobenzene group in compound **23**, adopts a *trans* configuration, as expected as this is the lowest energy conformation. There are no molecules of solvent in the structure, which suggests the molecules have packed efficiently so there is no void space in the structure; a void space calculation in the program Mercury confirms this. The lack of void space in the structure suggests that the ligand may not be able to undergo the analogous isomerisation reaction in the solid state. Figure 6.17 depicts the packing within a unit cell of complex **23**, illustrated with the space-fill style.

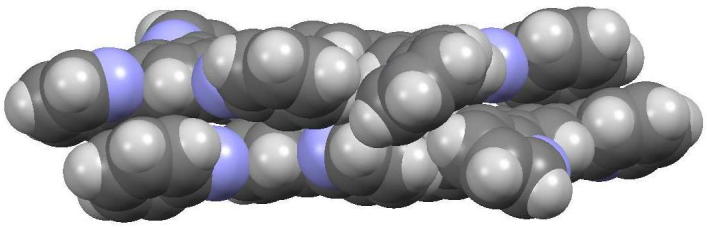

Figure 6.17*: Packing of Complex **23** in a unit cell. Shown in the space-fill style.*

This diagram clearly shows that there is no space within the unit cell for the isomerisation reaction to occur. For potential isomerisation of the azobenzene group, it is thought that by cyclometallating the ligand to the platinum, there will be a disruption in the packing so an isomerisation reaction could occur.

6.3.4 Solution State Spectroscopy

Solution state UV-Vis and emission spectroscopy were carried out for **23**, the spectra are shown in Figure 6.18.

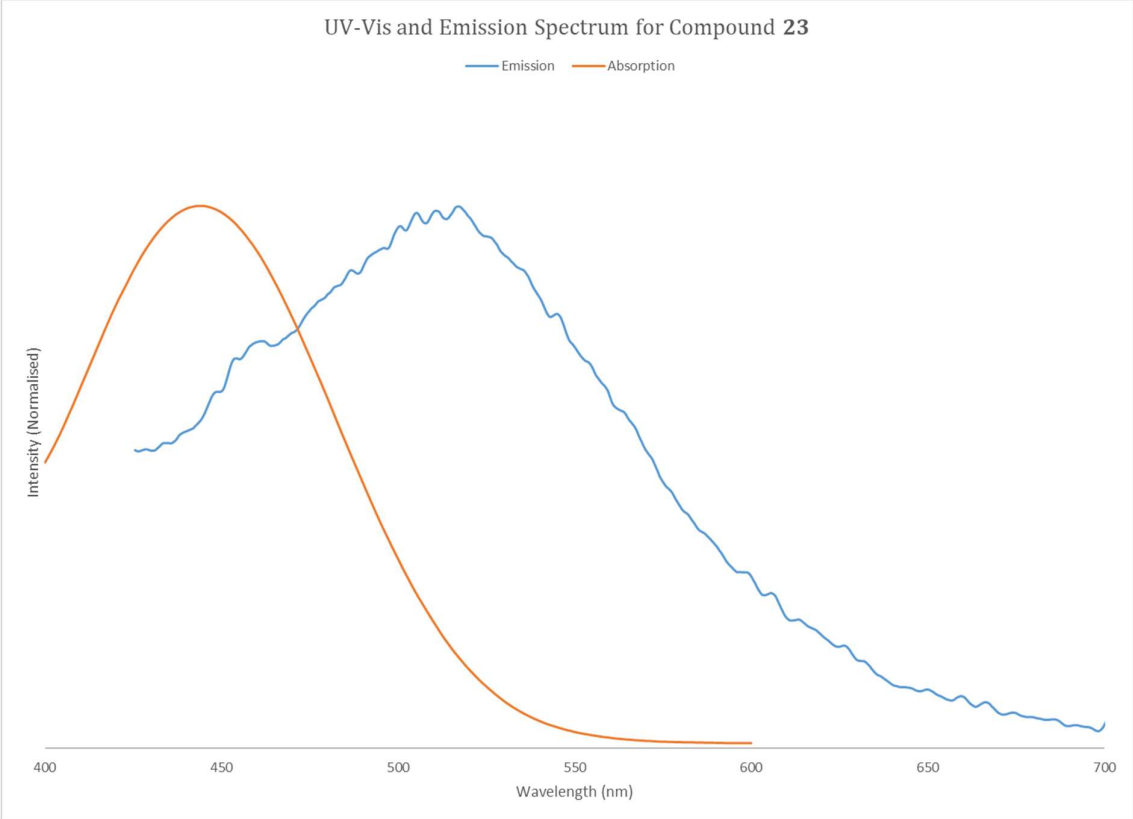

Figure 6.18*: Absorption and emission spectrum of **23**. Solution concentration 1×10^{-3} M in DCM. λ_{ex}=400 nm.*

There is one clean peak in the UV-Vis spectrum for compound **23**, which can be attributed to the π-π transitions for the pincer ligand. The emission is slightly red shifted in comparison to the UV-Vis spectrum, which is consistent with the Franck-Condon principle.

6.3.5 Solid State Spectroscopy

This compound was also studied in the solid-state using reflectance spectroscopy. The compound was drop-cast from a DCM solution onto a glass slide, leaving an orange film of the complex. The blue line in Figure 6.20 shows the reflectance spectrum of **23**, without irradiation. The absorption edge of the spectrum is consist with what would be expected for an orange compound and falls in the range 520-580 nm.

The solid-state isomerisation behaviour was also investigated, using the set-up in Figure 6.19. This figure illustrates how a 520 nm LED was used to irradiate the slide, while the reflectance spectra was being collected. The orange line in Figure 6.29 shows how the profile of the spectrum has not changed with irradiation of **23**. This suggests that the *trans-cis* isomerisation does not take place in the solid state. This is not an unexpected result, if the crystal packing of the system is considered the compound is closely packed suggesting the azobenzene group does not have the required space to move.

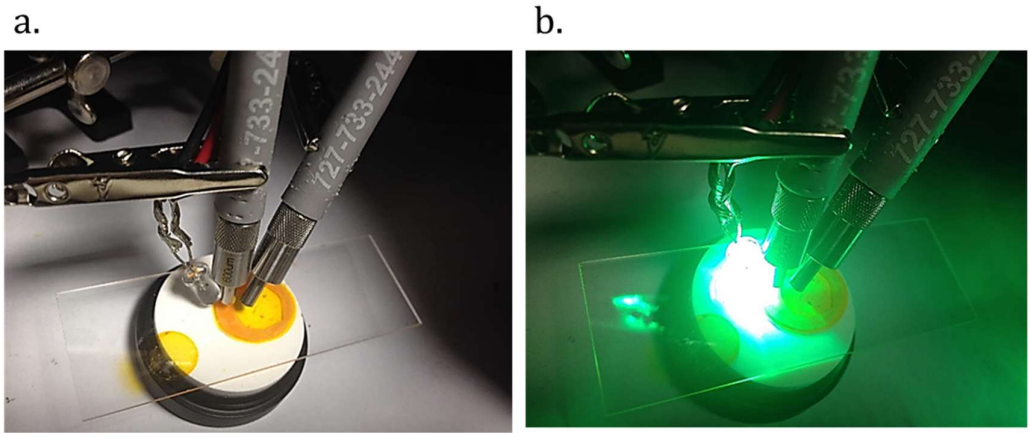

Figure 6.19*: Irradiation of **23** while collecting the reflectance spectrum.*

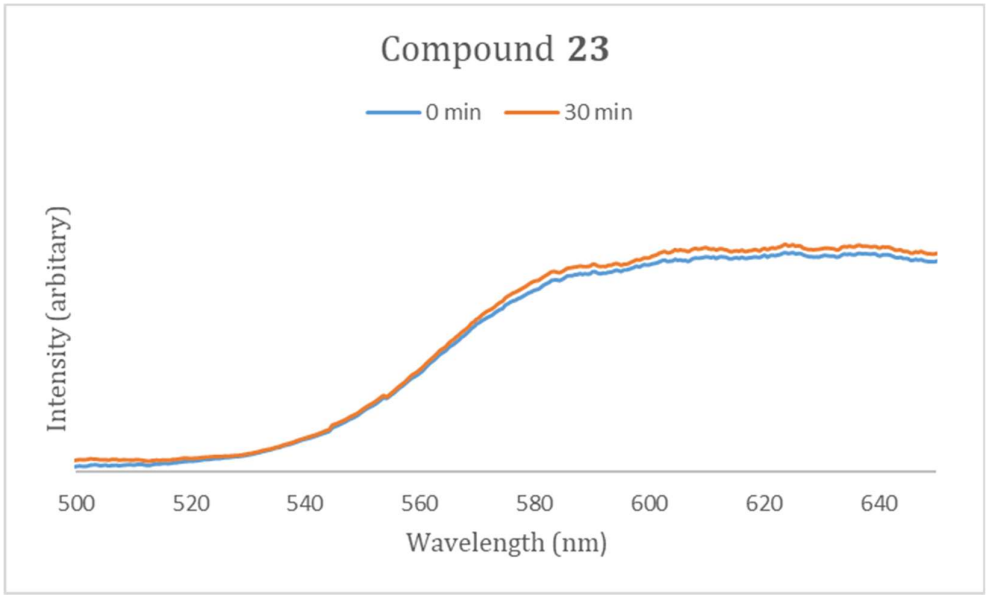

Figure 6.20*: Reflectance spectrum of **23** before and after irradiation of 520 nm light.*

6.4.0 (*E*)-2,2'-(5-(phenyldiazenyl)-1,3-phenylene)dipyridine Platinum Chloride (24)

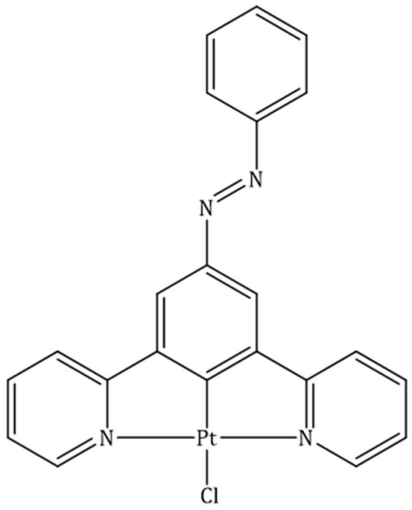

Complex **24**, obtained from the reaction of **23** with $[PtCl_4]^{2-}$, is yet to be isolated as a pure complex. A series of different reaction conditions have been attempted with different solvents and Pt salts but unfortunately the complex has not been successfully synthesised.

6.5.0 Methyl 3,5-di(pyridine-2-yl)benzoate Platinum (E)-1-ethynyl-4-styrylbenzene (25)

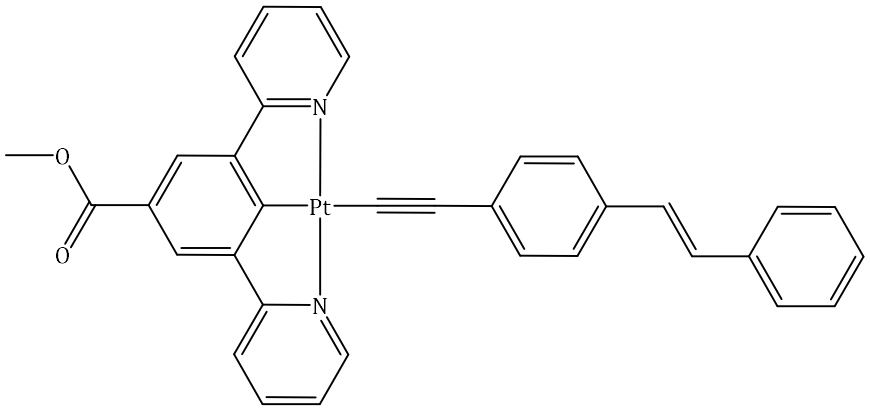

6.5.1 Synthesis

The synthesis of complex **25** is shown in Scheme 6.4. The first step to synthesise the ethyl styryl benzene (not shown in Scheme 6.4), using a Sonagashira coupling reaction. The product is then deprotected using a base and then stirred with complex 15 for 48 h. The product is isolated by filtration.

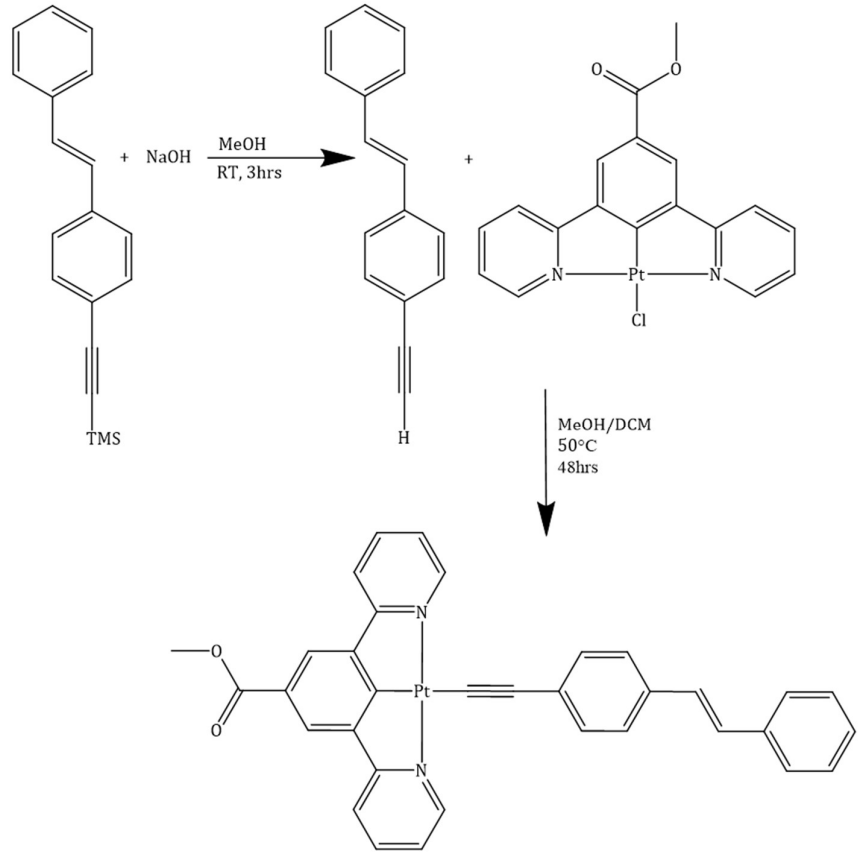

Scheme 6.4: *Synthesis of complex **25**.*

6.5.2 Isomerisation behaviour

For comparison, the stilbene equivalents of the azobenzene groups have been studied. Using the same orbital argument discussed in Section 6.1.3, complex **25** should not undergo an isomerisation reaction. This was confirmed using solution state spectroscopy. The UV-Visible spectrum and emission spectra are shown in Figure 6.21 and 6.22, respectively. There is no significant change in the profile of the spectra after 30 minutes of irradiation, this would suggest that no *trans-cis* isomerisation is taking place for complex **25**.

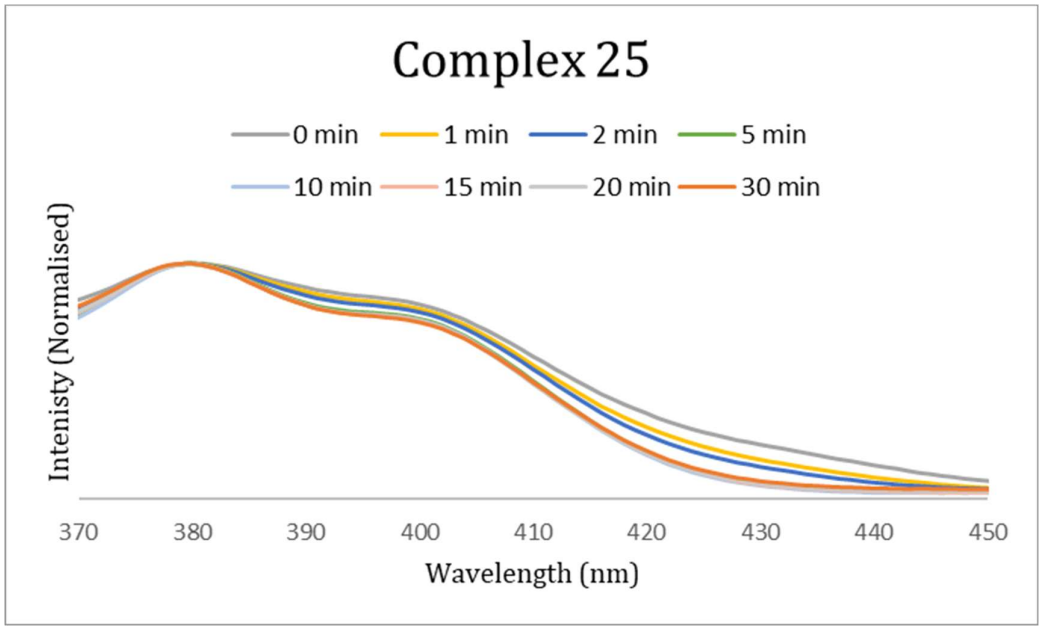

Figure 6.21: *UV-Visible spectrum of Complex **25**, after it had been irradiated at specified times using 365 nm light. Solution was 1×10^{-5} M in DCM.*

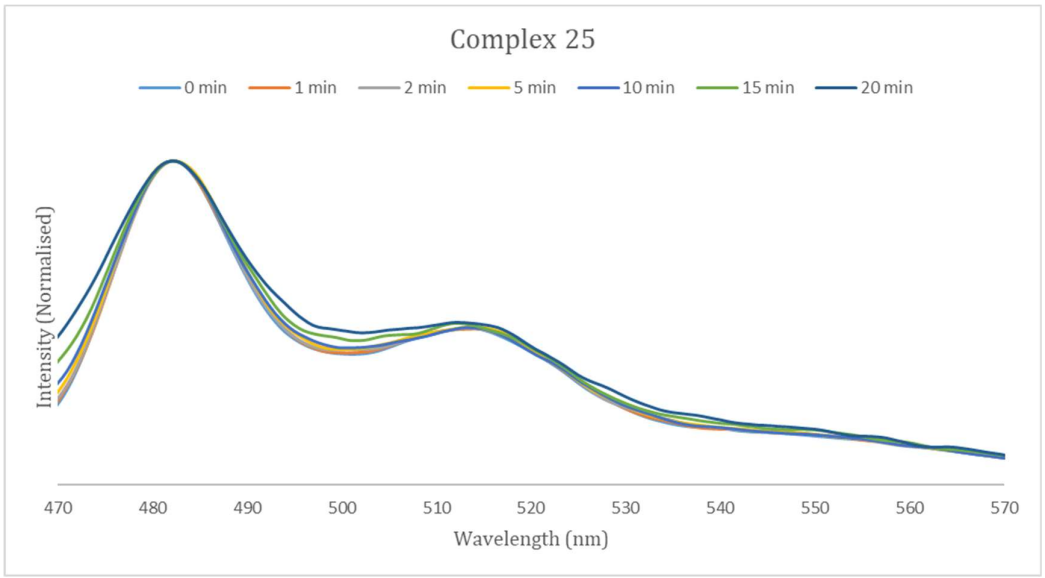

Figure 6.22: *Emission spectrum of Complex **25**, after it had been irradiated at specified times using 365 nm light. Solution was 1×10^{-7} M in DCM. Excitation wavelength: 380 nm.*

6.6.0 (*E*)-2,2'-(5-styryl-1,3-phenylene)dipyridine (26)

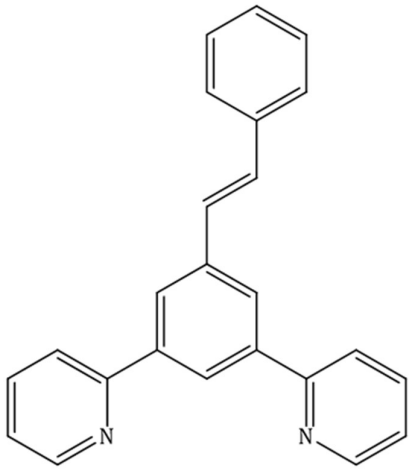

6.6.1 Synthesis

Compound **26** was prepared using literature methods,[144] the synthetic route is shown in Scheme 6.5. The Horner-Wadworth Emmons reactions was utilised to synthesise the dibromostilbene, followed by a Stille coupling to form the final pincer ligand **26**.

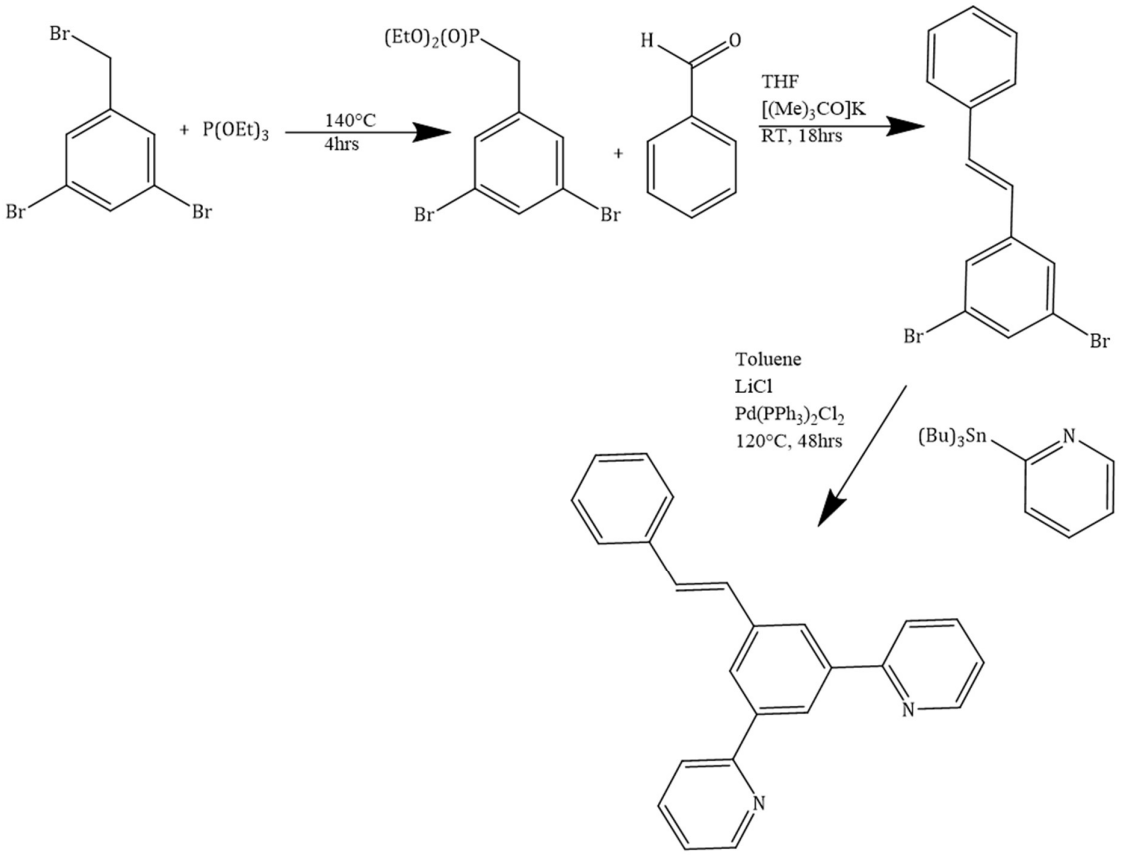

Scheme 6.5*: Synthesis of* ***26.***

6.6.2 Isomerisation behaviour

The isomerisation behaviour of **26** in the solution state was studied in a similar manner to the previous complexes detailed in this chapter. The complex was irradiated with 254 nm light and the UV-Vis and emission spectrum collected at 1, 2 and 5 minutes and then at 5 minute intervals, Figure 6.23 and 6.25, respectively.

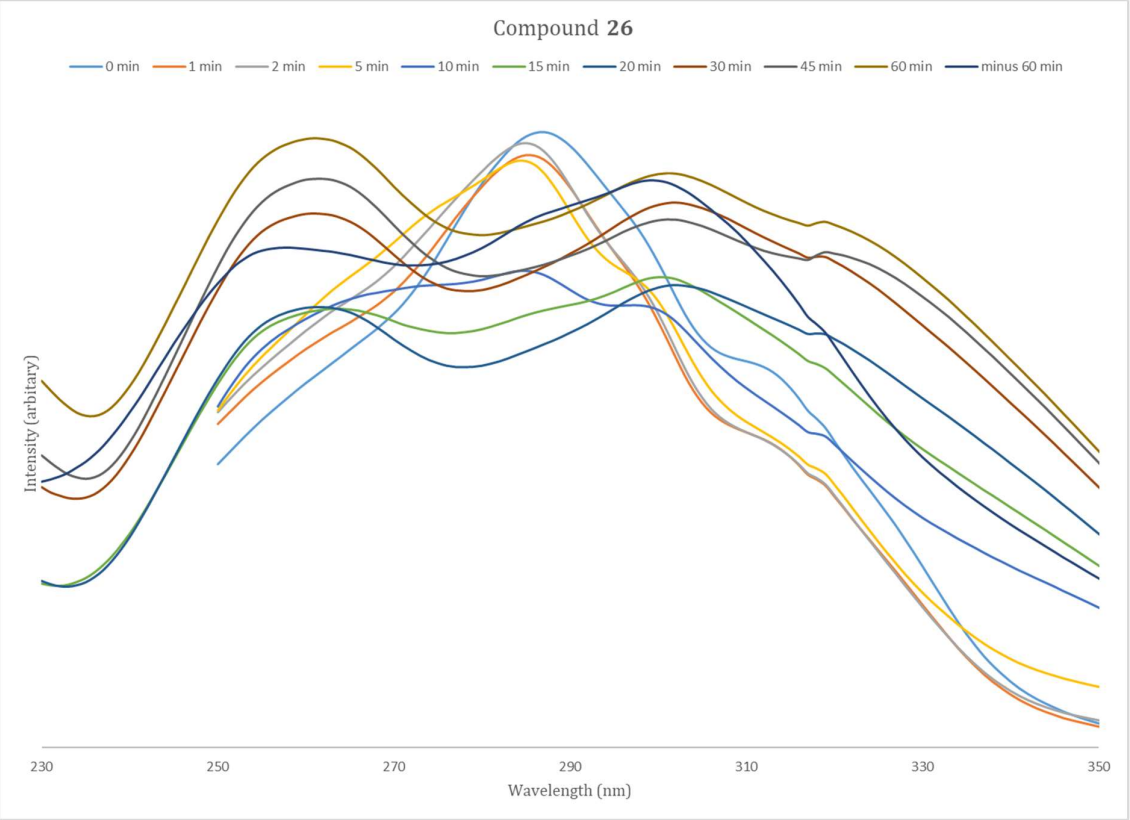

Figure 6.23*: UV-Visible spectrum of **26**, after it had been irradiated at specified times using 254 nm light. Solution was 1×10^{-5} M in DCM.*

Figure 6.23 shows the UV-Vis spectrum measured over the course of 1 h. The distinct peak at 287 nm is lost after 5 minutes of irradiation with 254 nm light. The peak then splits into a double peak, with the maxima measured at 260 nm and 306 nm. This suggests that a change in the geometry is occurring. However, as was discussed in the introduction, Section 6.1.2 that the stilbene functional group is prone to cyclisation as well as isomerisation. Therefore, the theoretical UV-Vis was calculated for comparison with the experiment. Figure 6.24 shows the results of the DFT calculations.

This plot shows that the peak of interest does blue shift as observed experimentally and the *cis* form does have a split in the major peak, however it is less pronounced than that seen experimentally. This suggests that a *trans-cis* isomerisation has occurred.

As with **23** the reverse isomerisation was studied. After 60 minutes in ambient light, the UV-Vis spectrum was still predominantly the *cis* form, suggesting that either the photo-stationary state has been reached or a different wavelength of light is required to initiate the *cis-trans* isomerisation process.

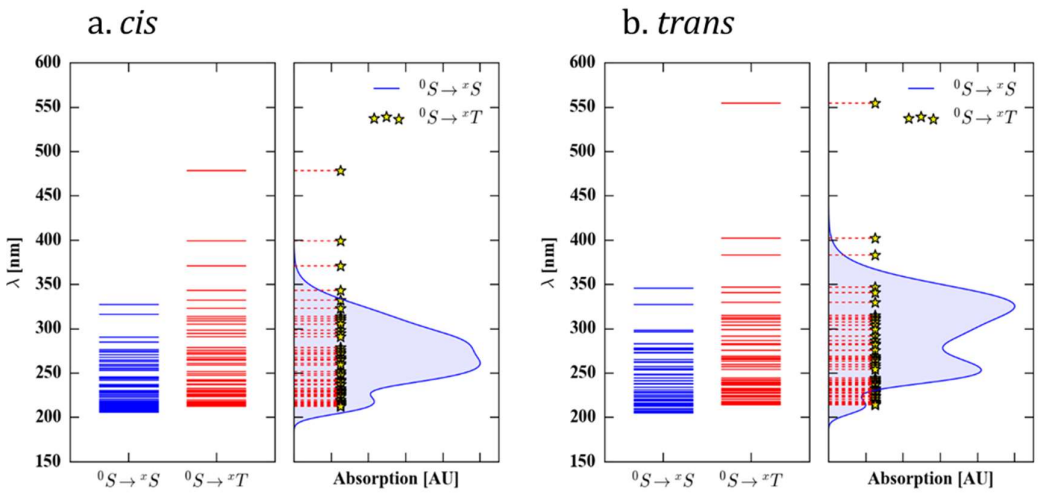

Figure 6.24: *Theoretical UV-Visible spectrum of Compound **26** in the gas phase, a. cis form, b. trans form.*

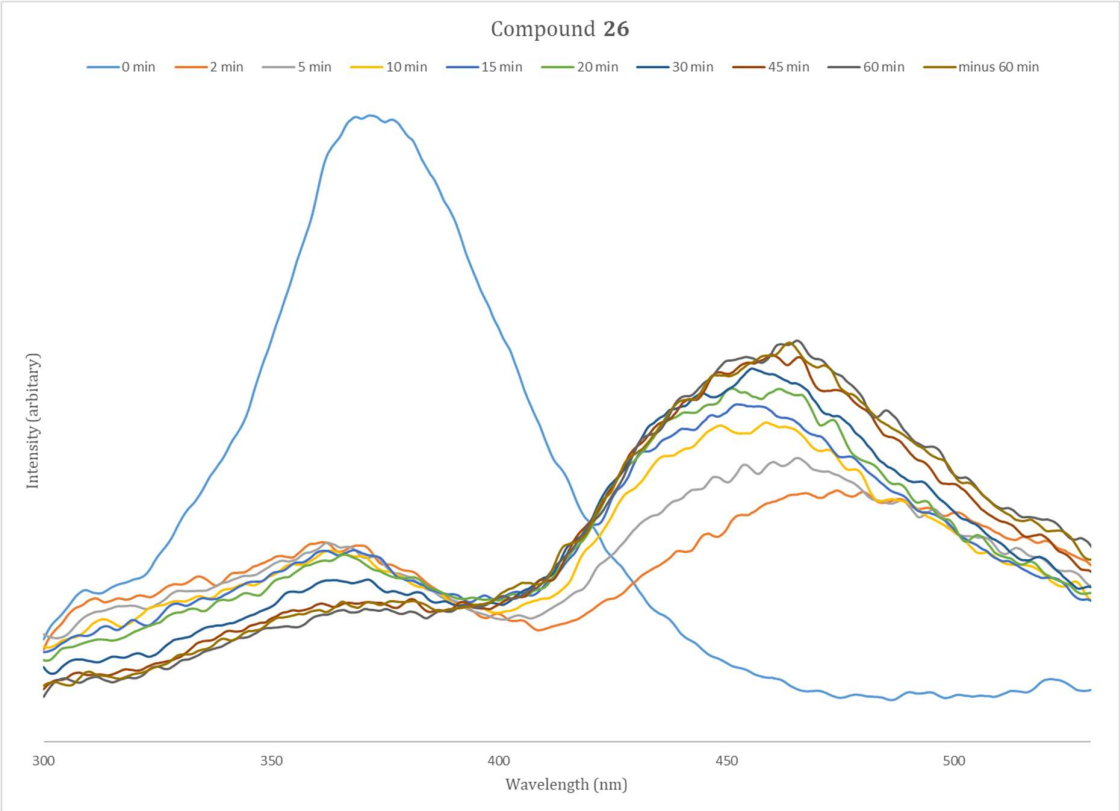

Figure 6.25: *Emission spectrum of **26**, after it had been irradiated at specified times using 254 nm light. Solution was 1×10^{-10} M in DCM. Excitation wavelength: 280 nm.*

The corresponding emission spectra were also collected, Figure 6.25. It can be clearly seen that peak at 360 nm is greatly reduced after 2 minutes and a new peak forms at 475 nm, before shifting to 460 nm, this means that the formation of the *cis* form can be studied by the change in its emission profile.

6.6.3 Crystal Structure Analysis

Crystal Structure.

Single crystals of compound **26** were grown from the slow evaporation of THF. This molecule crystallises the orthorhombic space group $P2_12_12_1$. There is one molecule in the asymmetric unit, and no inclusion of solvent in the structure. The structure is shown in Figure 6.26 and extended crystal and refinement data can be found in Table 6.7.

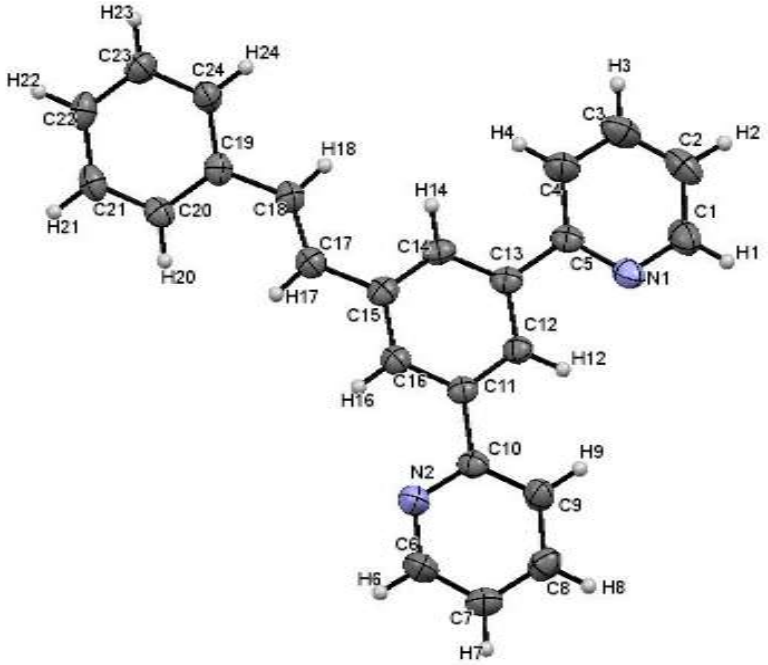

Figure 6.26*: Crystal structure of* ***26****. Ellipsoids shown at 50%.*

Table 6.7: *Crystal data and structure refinement for* ***26.***

Identification code	p16prr133
Empirical formula	$C_{24}N_2H_{18}$
Formula weight	316.51
Temperature/K	150
Crystal system	orthorhombic
Space group	$P2_12_12_1$
a/ Å	5.7568(2)
b/ Å	15.6464(4)
c/ Å	19.3701(5)
α/°	90
β/°	90
γ/°	90
Volume/ Å^3	1744.73(9)
Z	4
ρ_{calc}g/cm^3	1.205
μ/mm^{-1}	0.072
F(000)	633.0
Crystal size/mm^3	0.4 × 0.5 × 0.5
Radiation	MoKα (λ = 0.71073 Å)
2Θ range for data collection/°	4.946 to 59.32
Index ranges	-7 ≤ h ≤ 7, -21 ≤ k ≤ 21, -26 ≤ l ≤ 26
Reflections collected	30291
Independent reflections	4541 [R_{int} = 0.0316, R_{sigma} = 0.0222]
Data/restraints/parameters	4541/0/235
Goodness-of-fit on F^2	1.046
Final R indexes [I>=2σ (I)]	R_1 = 0.0417, wR_2 = 0.0966
Final R indexes [all data]	R_1 = 0.0537, wR_2 = 0.1030
Largest diff. peak/hole / e Å^{-3}	0.16/-0.19

Compound **26** is close to planar however, investigation of the torsion angles show there are values that deviate from 0 or 180˚ when the stilbene functional group is considered, table 6.8. The dihedral angles provide additional evidence for this loss of planarity. They have been measured and are as follows:

- The dihedral angle between the two mean average planes: C11-C12-C13-C14-C15-C16 and N2-C6-C7-C8-C9-C10 is 5.83˚,
- The dihedral angle between the two mean average planes: C11-C12-C13-C14-C15-C16 and C19-C20-C21-C22-C23-C24 is 14.75˚.

This shows there is a significant loss in planarity due to the stilbene functional group, however the measured angles are smaller than those observed for compound **23.**

Table 6.8: *Torsion angles in* ***26***

Torsion Angles				
A	**B**	**C**	**D**	**Angle/˚**
C20	C19	C18	C17	-10.0(3)
C24	C19	C18	C17	169.9(2)

Analysis of the intermolecular interactions using OLEX[121] shows there are no π-π interactions in this complex. However inspection of the close contacts using Mercury[87] show there is one possible interaction that could be attributed to π transitions between C18 and C21. This is the overlap of one of the carbons on the C=C double bond and the stilbene arene ring, Figure 6.27b. The other interactions present in the complex are listed in table 6.9.

Table 6.9*: Short contacts and hydrogen bonds in **26***

a. Short Contacts	
Atoms	Distance (Å)
H23-H1	2.38(7)
H6-C24	2.82(5)
C22-H21	2.90(1)
C18-C21	3.36(1)

b. Hydrogen bonds			
Atoms	(D…A) Distance (Å)	(H…A) Distance (Å)	D…H…A Angle/°
C7-H7-N1	3.527(3)	2.714	146.5

Crystal Packing.

Complex **26** has packed in the solid state to minimise void space in the structure. The packing of 26 in the unit cell is shown in Figure 6.27a. There are four molecules in the unit cell, when illustrated with the space-fill style in the program Mercury it can be seen that the molecules have packed efficiently and there is no room for an isomerisation reaction to occur.

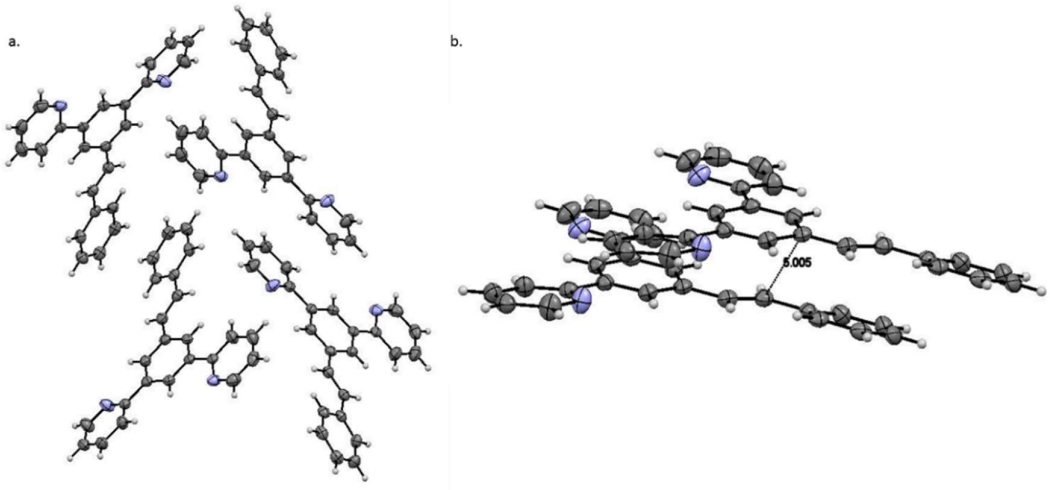

Figure 6.27*: a. Crystal Packing in the unit cell of **26**. b. Distance between two stacked molecules of **26** in the unit cell. Ellipsoids shown at 50%.*

Further analysis of the packing of **26** in the solid state showed that there is presence of stacking between dimers in the structure. If these dimers were stacked in close proximity, there is an

opportunity for inducing a [2+2] cycloaddition reaction. For a cycloaddition to occur in the solid state the bonds have to co-planar and less than 4.2 Å apart.[149]

Although the molecule shows *trans-cis* isomerisation in the solution state, the restraints of packing in the solid state ensures the same behaviour cannot be observed.

6.6.4 Solution State Spectroscopy

The solution state UV-Vis and emission is given in Figure 6.28

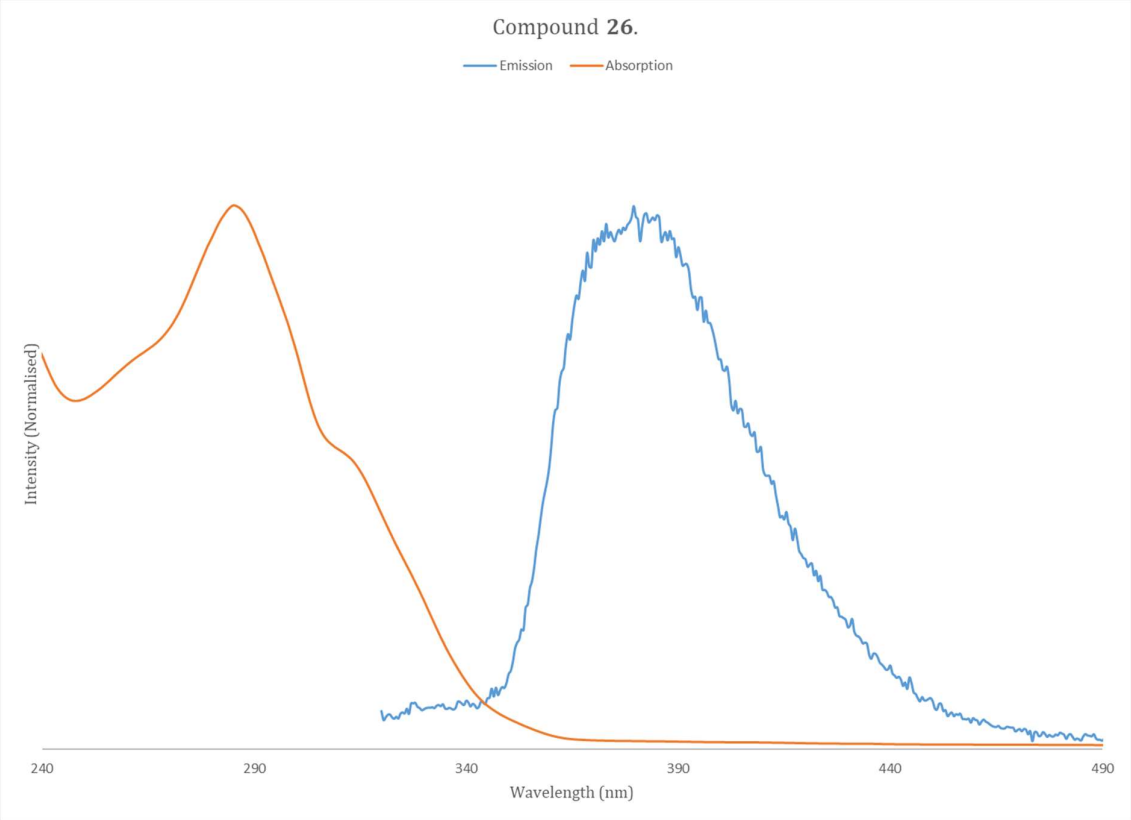

Figure 6.28*: Absorption and emission spectrum of* ***26.*** *Solution concentration 1×10^{-8} M in DCM. λ_{ex}=300 nm.*

As expected, the solution state UV-Vis profile is at much lower wavelength than that observed for the azobenzene analogue, due to its observed pale yellow colour. There is a clear peak in the region 250-320 nm that can be attributed to the intramolecular π-π transitions of the ligand.

The emission spectrum for **26** is shown in Figure 6.28, there is a strong peak at 390 nm that matches the profile of the spectrum observed for the UV-Vis. The stilbene emission is much stronger than that observed for the azobenzene; Figure 6.29 shows a comparison between **23** and **26**.

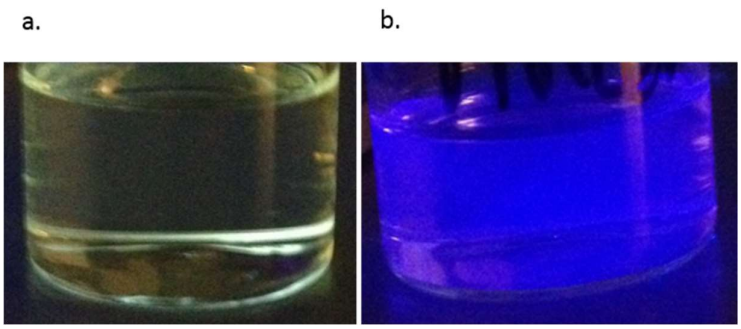

Figure 6.29*: a. Emission spectrum of* ***23****. Solution concentration 1×10^{-3} M in DCM. b. Emission of* ***26****. Solution concentration 1×10^{-8} M in DCM. λ_{ex}=364 nm.*

Figure 6.29 shows clearly the difference in emission between the azobenzene and the stilbene. It is thought that the enhanced emission could have arisen due to the C=C double bond *vs* the N=N double bond in the structure.

6.7.0 (*E*)-2,2'-(5-styryl-1,3-phenylene)dipyridine Platinum chloride (27)

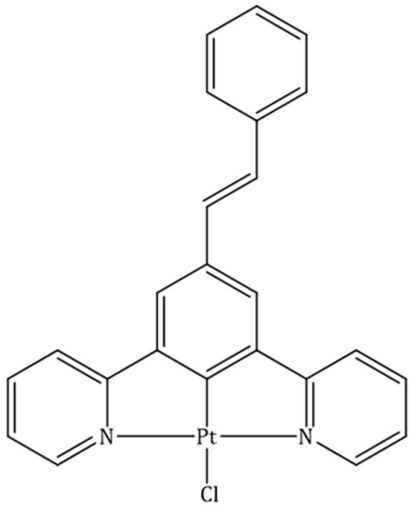

6.3.1 Synthesis

The synthesis of complex **27** is shown in Scheme 6.6. This synthesis has been adapted from a literature procedure,[144] in this instance a mixture of acetic acid and water has been used to synthesise complex **27**. The product was isolated by filtration.

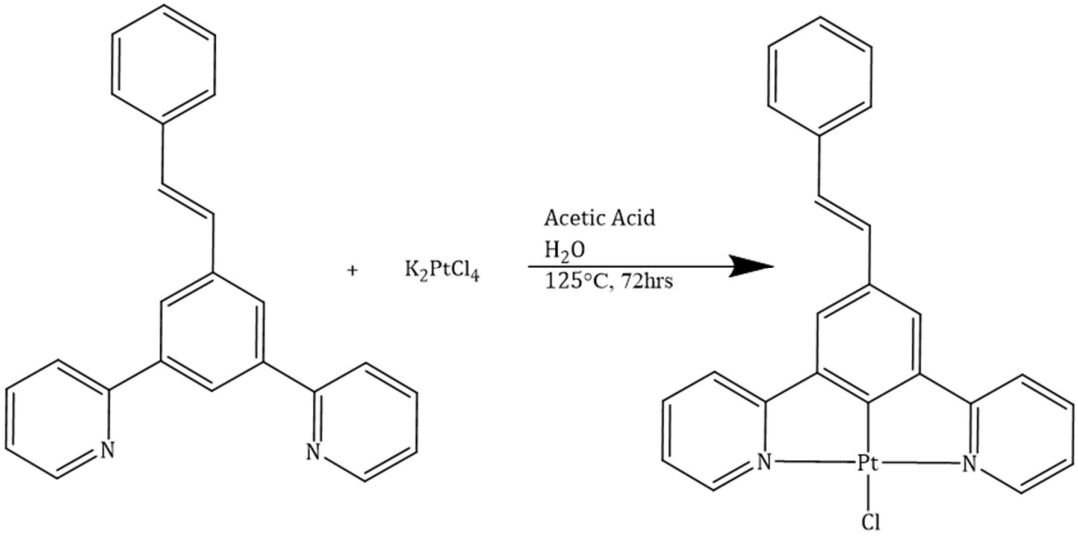

Scheme 6.6*: Synthesis of complex* ***27.***

6.7.2 Isomerisation Behaviour

The UV-Vis and emission spectra were recorded 1, 2, and 5 minutes and then every 5 minutes until a total time of 30 minutes. Complex **27** was irradiated with 265 nm light, and the results are shown in Figure 6.30 and 6.31, respectively. Only the peak profile between 350 and 490 nm has been shown as this peak represents the MLCT from the Pt centre to the ligand. It is expected that as the complex isomerises that the absorption profile of the MLCT would change.

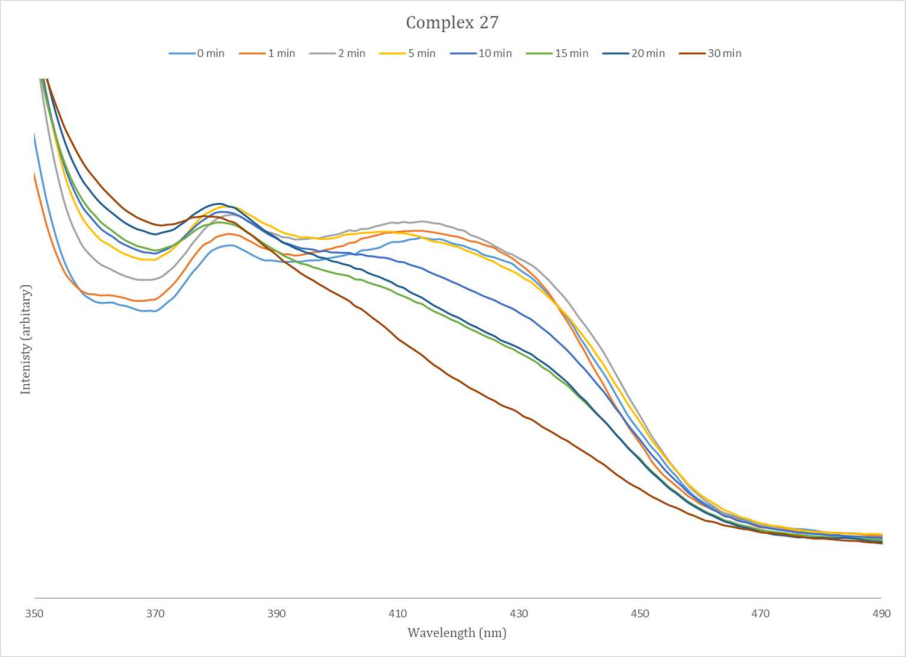

Figure 6.30: *UV-Visible spectrum of Complex **27**, after it had been irradiated using 254 nm light. Solution was 1×10^{-5} M in DCM.*

Figure 6.30 clearly shows how the MLCT band changes upon irradiation. After 30 minutes, the profile of the peak at 325 nm has been lost and the second peak at 380 nm has been blue shifted. This would suggest that the *trans-cis* isomerisation has taken place.

Further investigation of the emission profile, Figure 6.31 shows how the emission is blue shifted and the fine detail is lost after 30 minutes of irradiation, confirming the conversion to the *cis* form.

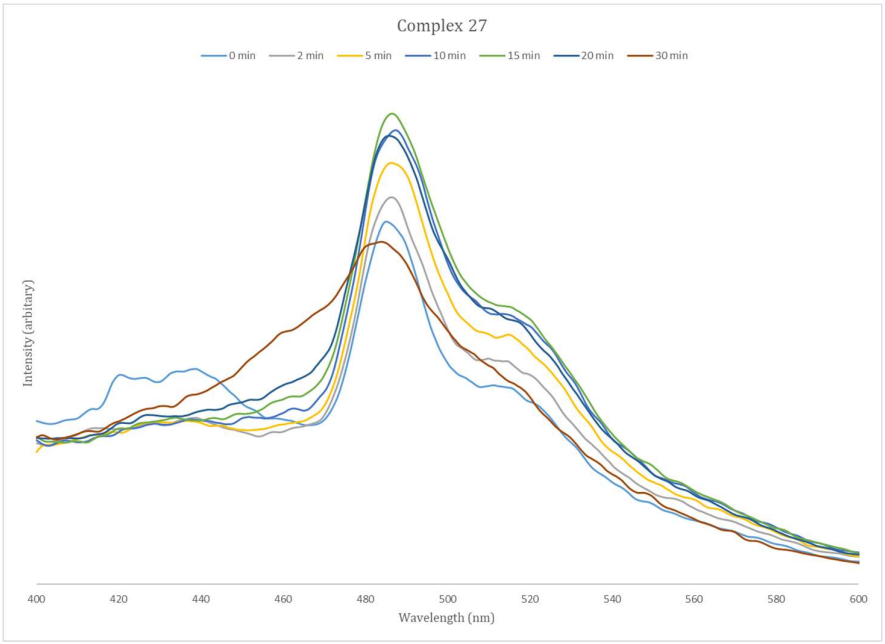

Figure 6.31: *Emission spectrum of Complex **27**, after it had been irradiated using 254 nm light. Solution was 1×10^{-5} M in DCM. Excitation wavelength: 380 nm.*

6.7.3 Crystal Structure Analysis

Crystal Structure.

Block-shaped single crystals that were suitable for single crystal X-ray diffraction, were grown from the slow evaporation of the following mixture of solvents: DCM, THF, acetone, diethyl ether and hexane at room temperature. Complex **27** crystallises in the monoclinic space group $P2_1/c$, with no solvent present in the crystal structure. There are two independent molecules in the asymmetric unit.

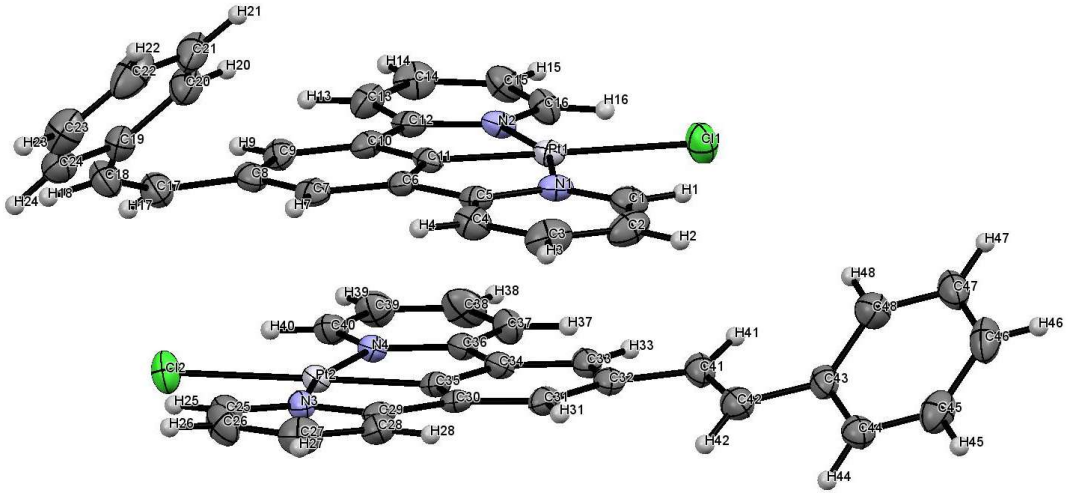

Figure 6.32*: Crystal structure of complex **27**. Ellipsoids shown at 50% probability level.*

Table 6.10: *Crystal data and structure refinement for Complex **27**.*

Identification code	s17prr179
Empirical formula	$C_{24}H_{17}Cl_1N_2Pt_1$
Formula weight	1127.87
Temperature/K	150
Crystal system	monoclinic
Space group	$P2_1/c$
a/ Å	10.2934(2)
b/ Å	20.1138(5)
c/ Å	18.0889(4)
α/°	90
β/°	93.873(2)
γ/°	90
Volume/ Å^3	3736.56(14)
Z	4
ρ_{calc}g/cm^3	2.005
μ/mm^{-1}	7.666
F(000)	2160.0
Crystal size/mm^3	0.3 × 0.3 × 0.4
Radiation	MoKα (λ = 0.71073)
2Θ range for data collection/°	6.002 to 52.732
Index ranges	-12 ≤ h ≤ 12, -23 ≤ k ≤ 25, -22 ≤ l ≤ 21
Reflections collected	27349
Independent reflections	7432 [R_{int} = 0.0445, R_{sigma} = 0.0440]
Data/restraints/parameters	7432/0/505
Goodness-of-fit on F^2	1.026
Final R indexes [I>=2σ (I)]	R_1 = 0.0301, wR_2 = 0.0648
Final R indexes [all data]	R_1 = 0.0410, wR_2 = 0.0699
Largest diff. peak/hole / e Å^{-3}	2.57/-1.24

Figure 6.32, shows that once **26** had been cyclometallated to a Pt centre that the overall complex no longer remains planar. This is illustrated by the torsion angle data provided in table 6.11c. the torsion on the *cis* form is 23.49(1)˚ and the *trans* form is 12.6(9)˚ compare this to the torsion around the Pt centre close to zero for both molecules in the unit cell. Therefore it is planar around the Pt centre, but not on the substituted ligand. The measured dihedral angles in both molecules of the unit cell further reinforce this. They have been measured as follows:

- Mean average planes: N2-C11-C5-C10-N1-Pt1-C6-C12 and C22-C19-C20-C23-C24-C21. Dihedral angle= 47.07˚
- Mean average planes: C35-N3-C36-C29-C30-Pt2-N4-C34 and C47-C46-C44-C45-C48. Dihedral angle= 43.36˚.

The bond angles, table 6.11b, show the angles expected of a Pt centre in a square planar geometry, with a slight distortion due to the bite of the ligand. The bond lengths and bond angles are consistent with the literature for similar complexes.

Table 6.11*: a. Table of bond lengths for* ***27.*** *b. Table of bond angles for* ***27****.c. Torsion angles for* ***27.***

a. Bond Lengths		
Atom	**Atom**	**Length/ Å**
Pt1	Cl1	2.4039(14)
Pt1	N1	2.033(4)
Pt1	N2	2.041(4)
Pt1	C11	1.907(5)
Pt2	Cl2	2.4059(13)
Pt2	N3	2.030(4)
Pt2	N4	2.028(4)
Pt2	C35	1.906(5)

b. Bond Angles			
Atom	**Atom**	**Atom**	**Angle/˚**
N1	Pt1	N2	160.67(17)
C11	Pt1	Cl1	179.22(15)
N4	Pt2	N3	161.17(16)
C35	Pt2	Cl2	179.39(15)

c. Torsion Angles				
A	**B**	**C**	**D**	**Angle/˚**
C20	C19	C18	C17	23.49(1)
C48	C43	C42	C41	12.6(9)
Pt1	N2	C12	C10	-0.4(6)
Pt1	N1	C5	C6	0.2(6)

Analysis of this complex with OLEX2[121] has shown there are a series of π-π interactions present, table 6.12b. The extended π stacking infrastructure has been facilitated by the presence of both a *cis* and *trans* form in the crystal structure. Further investigation of the complex in Mercury showed that all of the short contacts could be attributed to π interactions. There is also hydrogen-bonding present between hydrogens on the pyridyl ring and the chlorine on the adjacent molecule, table 6.12c.

Table 6.12: *a. Planes Present in solid-state structure for **27**. b. π-π Interactions for **27**. c. Hydrogen bonds for **27**.*

a. Plane Identification

Plane Number	Atoms in plane
1	C11 C10 C9 C8 C7 C6
2	C19 C24 C23 C22 C21 C20
3	N1 C1 C2 C3 C4 C5
4	N2 C16 C15 C14 C13 C12
5	C30 C31 C32 C33 C34 C35
6	C43 C48 C47 C46 C45 C44
7	N3 C25 C26 C27 C28 C29
8	N4 C40 C39 C38 C37 C36

b. π-π Interactions

Planes	Distance (Å)
3-8[1]	3.819
4-8[2]	3.557
5-7[3]	3.589

c. Hydrogen bonds

Atoms	(D…A) Distance (Å)	(H…A) Distance (Å)	D…H…A Angle/°
C15-H15-Cl1	3.644(6)	2.787	153.5
C44-H44-Cl2	3.745(6)	2.866	157.9

Where [1](1+X, +Y, +Z), [2](+X, +Y, +Z), [3](2-X, 1-Y, 1-Z)

Crystal packing

Figure 6.32 shows that there are two molecules in the asymmetric unit, on closer investigation it can be seen that one of these molecules adopts the *cis* conformation and the other adopts the *trans* conformation. The presence of the *cis* conformation in the asymmetric unit cell is unusual because it is the *trans* form that is usually of lowest energy. However, looking at the packing of the complex in the solid state may provide reasoning as to why both geometrical isomers are seen in this instance.

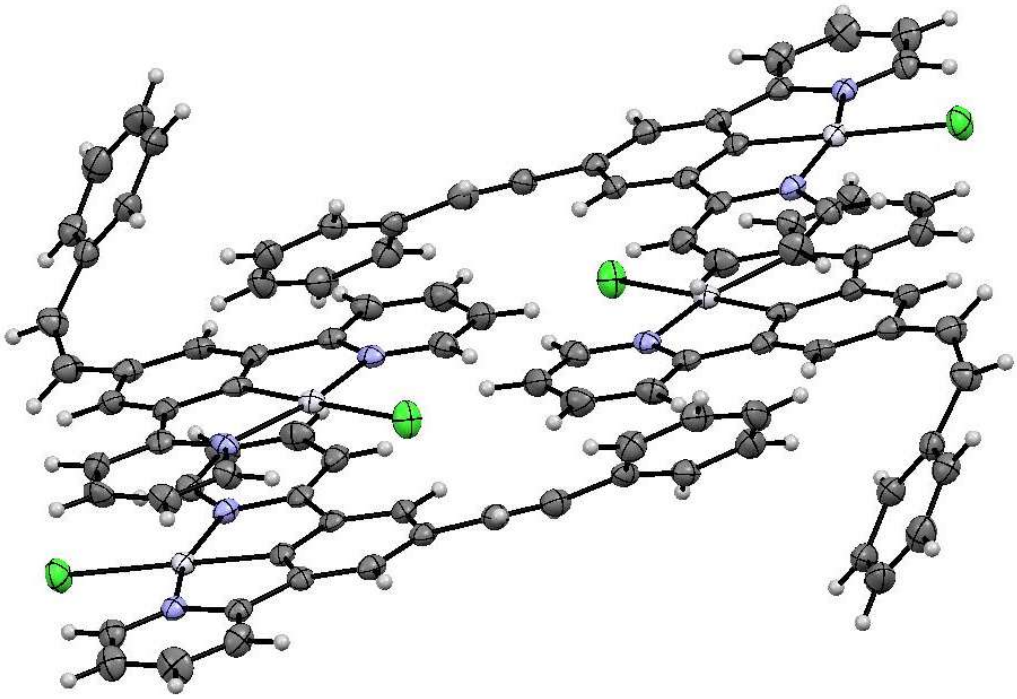

Figure 6.33*: Packing of complex* ***27****. Ellipsoids shown at 50% probability level.*

Figure 6.33 shows the packing of the structure in more detail. There is no solvent contained within the crystals suggesting that there are no significant pockets that solvent could sit inside. The space-fill diagram in Figure 6.34 confirms this. Instead, when the phenyl ring sits *cis* it hooks around the phenyl ring that sits *trans*. This in turn creates a close packed structure, in which no movement of the phenyl rings can occur. This suggests that a *trans-cis* isomerisation process in the solid state could not occur in the solid state due to the large size of the phenyl rings.

Investigation of the solid-state structure shows there is no Pt…Pt stacking present in this complex as was hypothesised, however table 6.12b shows there is an extensive π interactions network. The π interactions act to stabilise the complex in the solid state, which is advantageous. Unfortunately, on the other hand, if this complex were to isomerise in the solid state then these favourable π interactions would have to be broken. This could limit the capabilities of this complex as a photo-switch.

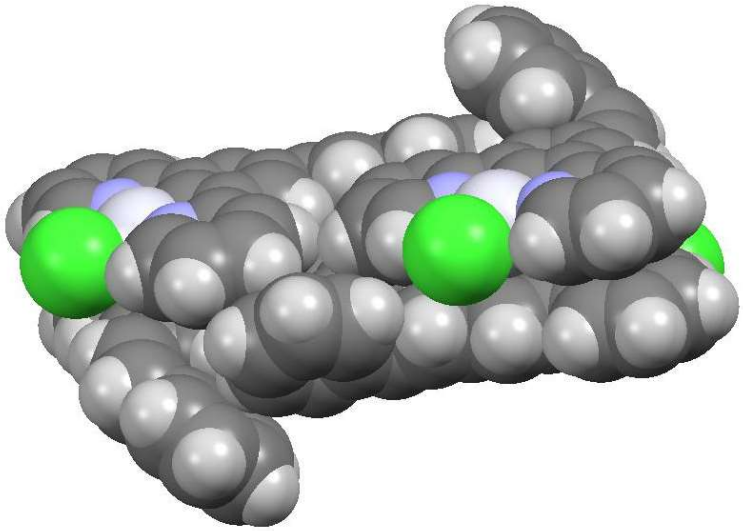

Figure 6.34*: Space-fill representation of complex **27.***

Single crystals of **27** were also grown from a vapour diffusion of diethyl ether into a concentrated chloroform solution. The crystals isolated from this crystallisation vial were of different morphology to those represented in the previous data. Only a preliminary data set could be collected from the yellow plate crystals before they decomposed in the synchrotron X-ray beam. The preliminary data is only of good enough quality to suggest possible connectivity in complex **27**, however it can be seen that the complex fully adopts the *cis* conformation. (Figure 6.35)

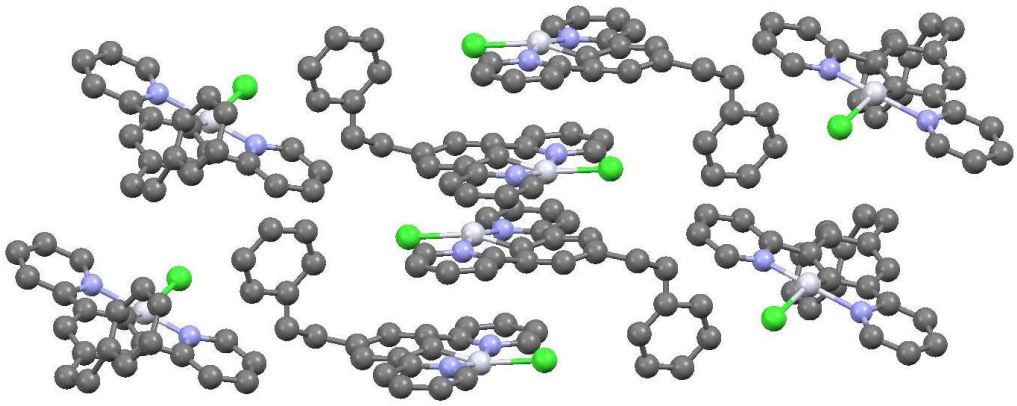

Figure 6.35*: Second solvate of **27,** disordered chloroform solvent removed for clarity.*

The presence of this second polymorph however shows that different solid-state packing motifs could be accessed; however, these crystals were not stable enough for a detailed crystallographic analysis.

6.7.4 Solution State Spectroscopy

Figure 6.36 shows the solution state UV-Vis and emission spectra recorded for **27**.

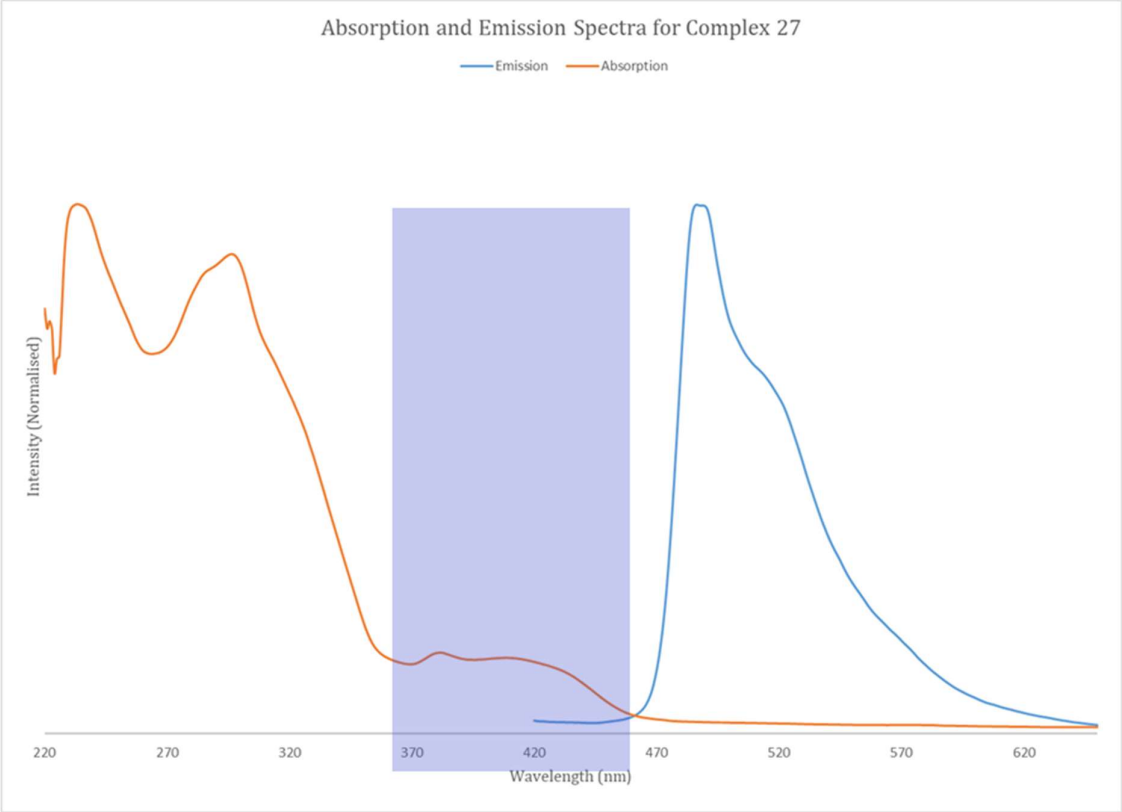

Figure 6.36: *Absorption ($^3\pi$-π^* transition highlighted) and emission spectrum of complex **27**. Solution concentration 1×10^{-5} M in DCM. λ_{ex}=400 nm.*

The profile of the absorption spectrum is similar to that observed for complex **22**, but it has been blue shifted slightly. The peaks between 270-330 nm can be attributed to intramolecular π-π transitions of the pincer ligand, with the peak at 370-450 nm representing the MLCT from the Pt centre to the ligand.

The solution state emission spectrum was recorded after excitation at 400 nm, the peak maxima is recorded at 500 nm, which has an undefined shoulder. The Stokes shift for this complex is approximately 200 nm, which is a good indication that phosphorescent emission is occurring.

This complex is highly luminescent in solution at RT, due to the N^C^N configuration of the ligand. The emission maximum has also been red shifted when compared to the emission spectra for complex **26**. This is more clearly shown in Figure 6.37, where the luminescence has changed from blue to green, upon cyclometallation of complex 26 to Pt.

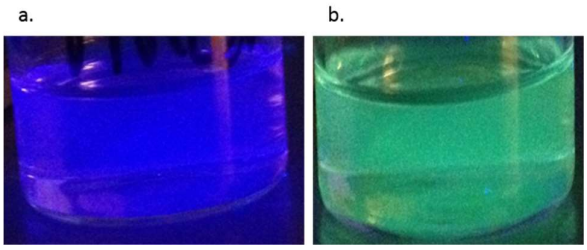

Figure 6.37*: a. Emission spectrum of complex **26**. Solution concentration 1×10^{-8} M in DCM. b. Emission spectrum of complex **27**. Solution concentration 1×10^{-5} M in DCM λ_{ex}=364 nm.*

6.7.5 Solid State Spectroscopy

The data presented in Section 6.7.3 suggested that due to the packing of the non-solvated form of complex **27** in the solid state that an isomerisation process would not be possible. However, using the set-up described in Section 6.3.5 the reflectance of the non- solvated form of complex **27** in the solid state was studied during irradiation. The results are shown in Figure 6.38.

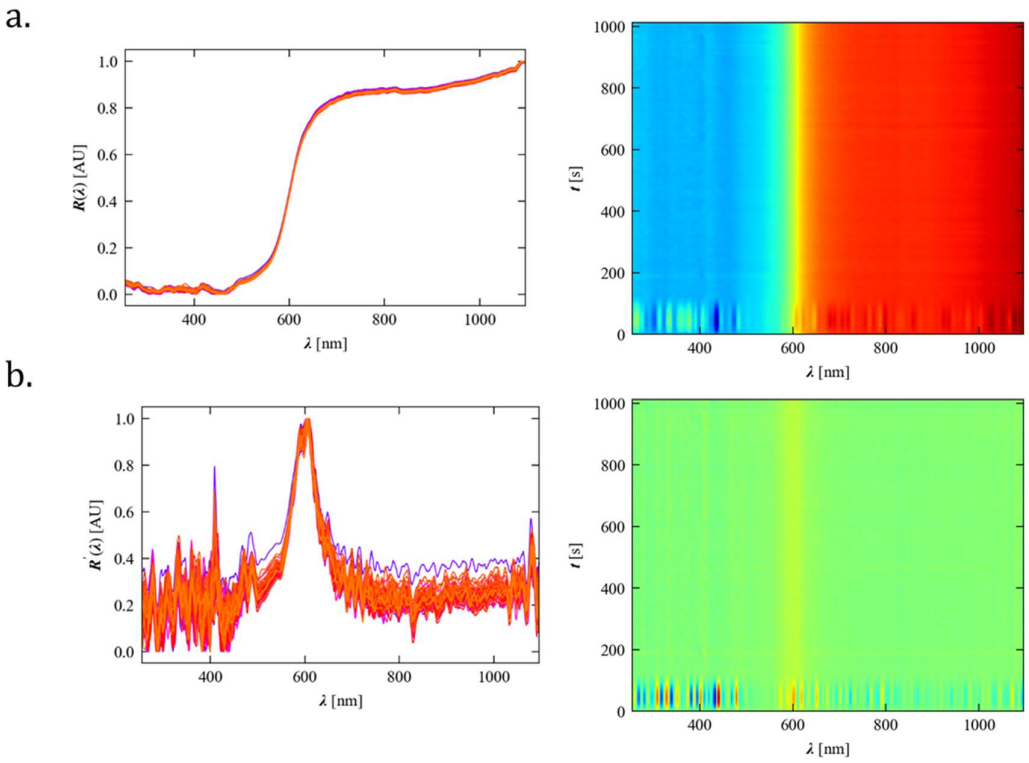

Figure 6.38*: a. Reflectance spectra of complex **27**, during irradiation with 250 nm light. Depicted as a function of intensity (left) and as a function of time (right). b. 1st derivative of the reflectance spectra of complex **27**, during irradiation with 250 nm light. Depicted as a function of intensity (left) and as a function of time (right).*

As expected, the results clearly show that no *cis-trans* isomerisation occurs in the solid state of the non-solvated form of complex **27**. The graphs on the right-hand side of Figure 6.38 show the results as a function of time and over the duration of the experiment you can see there is no deviation of the complex from its ground state colour.

6.8.0 Conclusion

In this chapter, five novel compounds have been synthesised and studied for their potential use as optical switches. Unlike previous chapters computational techniques were first used to predict the behaviour of the complexes before they were synthesised.
The complexes of this chapter were chosen because the behaviour of the optical switches are well documented in the literature and can be attributed to the ordering of the orbitals. Two different substitution patterns were tested as part of this research and preliminary computational results suggested that substituting the pincer ligand as opposed to a functional acetylide ligand would provide an optical switch as the switching fragment was in the correct orbital. The results of this computational study were investigated using a variety of analytical techniques such as UV-Vis, emission and reflectance spectroscopy as well as single crystal analysis, to fully assess the potential isomerisation in solution and in the solid state.

The experimental results agreed with the computational results and *trans-cis* isomerisation were observed for **23**, **26** and **27** in solution. However, these *cis-trans* isomerisation's were not observed in the solid state. This is not unexpected as the arene rings are required to twist for the isomerisation to take place. This requires a large structural rearrangement that would be unfavourable in the solid state due to the size of the arene rings and substantial steric strain would need to be overcome to achieve this.

In addition to investigating the Pt containing complexes the organic ligands were also investigated for optical switching. As observed with their Pt containing counterparts these complexes also underwent *trans-cis* isomerisation. In this instance an organic based compounds might be more flexible for this function. However by incorporating a metal centre into the complex this could allow for additional functionality when investigating alternative optical switching fragments.

Using azobenzene and stilbene groups has provided a good benchmark for further studies of platinum (II) complexes that could switch in the solid state. As a result of this research, a design methodology can be used in the development of further complexes in this area. In this methodology, the following would need to be considered:

- The size of the functional group, in future studies smaller groups would be investigated so less strain would be placed on the crystal lattice.
- The ability of the groups to π stack or hydrogen bond to adjacent molecules. The aromatic nature of the N^C^N ligand means, it would be challenging to remove all π interactions from the solid state. However to promote an isomerisation process they would have to be limited.
- Introduction of void space into the crystal structure. The solid-state structures investigated in this chapter have packed efficiently with no appreciable void space. This means the group is less likely to isomerise in the solid state and the crystal would lose its crystallinity during this process.

The results presented in this chapter illustrated that computational techniques are a powerful tool that can be effectively used to predict the behaviour of some Pt complexes that have been designed with a specific function. This could significantly speed up the discovery and

investigation of functional complexes. The use of this technique is vital when developing this area further by investigation of a broader range of functional groups. Future research would need to consider the use of smaller optical switches if the use of a metal centre is to be fully justified.

CHAPTER 7

pH Sensitive Complexes

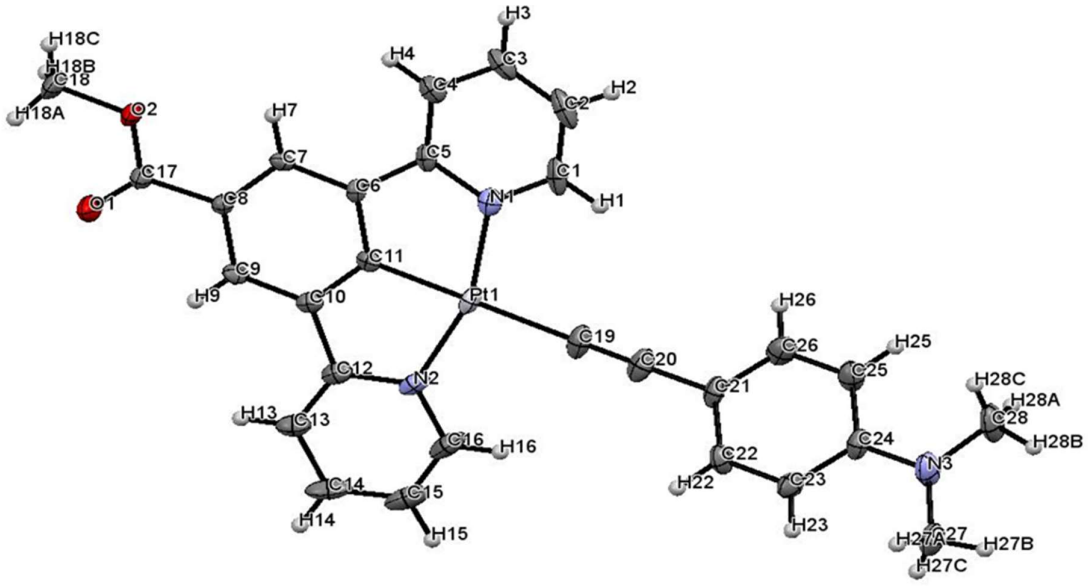

7.1.0 Introduction

The luminescent properties of Pt(II) complexes are versatile and of great interest for use as sensors and for applications in the photonics industry.[26, 78, 93, 150] In this section, the potential uses of these platinum(II) pincer complexes for acid and base sensing will be investigated. This chapter will further develop the findings from Chapter 6 and investigate how the placement of the functional groups in the complexes and their orbital contributions affect the 'switching' behaviour of the complexes.

7.1.1 'Smart' Materials

A search of the literature provided a series of known Pt(II) complexes that exhibited 'switching' properties upon exposure to acid in solution or to acidic vapours. The first example to be discussed was published by Li *et al* in 2011.[151] The authors used a N^C^N ligand to promote the luminescence of the complex. Their initial aim was to substitute the chloride in the 4th co-ordination site with a carbene group and investigate its response to acidic media. However, upon reacting the chloride form with a carbene, one of the N-Pt dative covalent bonds became displaced and two carbene groups bound to the Pt centre. Figure 7.1a shows the structure of the complex of interest.

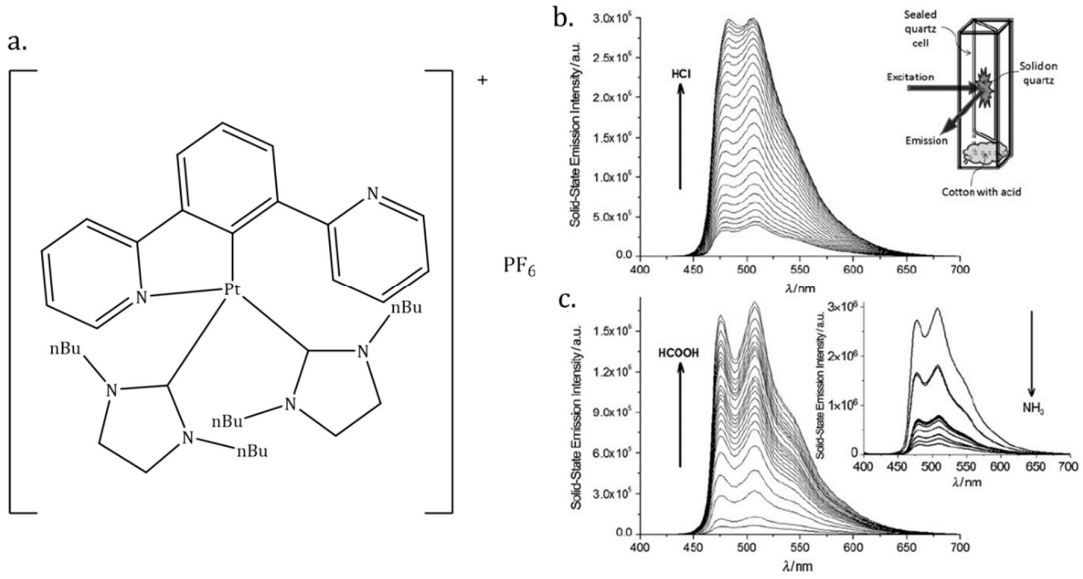

Figure 7.1*: a. complex synthesised by Li et al. b. Solid-state emission of complex upon exposure to HCl vapour, inset image is the experimental set-up. c. Solid state emission of complex upon exposure to formic acid vapour, inset image is the deprotonation of the complex with ammonia. Image taken directly from the paper.* [151]

The complex only showed very weak luminescence with this ligand substitution pattern. The authors reasoned that the lone pair of electrons on the nitrogen atom of the un-bound pyridyl ring was interacting with the Pt centre and quenching the luminescence in the solid state. The electronic excited states of these Pt complexes are known to be sensitive to the local environment, which is why they have been heavily investigated for their use in the sensing industry. It would, therefore, be sensible to conclude that the quenching of emission in caused by the lone pair of electrons on the nitrogen of the pyridyl ring. Upon subsequent protonation of this pyridyl group the emission of the complex increased.

In subsequent investigations of this complex, the authors manipulated the differences in observed emission between the protonated and deprotonated forms of the complex. The results in Figure 7.1b show that upon exposure to the acidic vapour the solid-state emission intensity rapidly increased, however the wavelength at which the emission occurred did not alter. The transition occurred at 521 nm, which is consistent with other values for similar complexes found in the literature.[47, 147] The deprotonation could only be achieved by the use of ammonia vapour.

The next example, uses an N^C^N ligand, but instead of using the 4th co-ordination site of Pt centre to induce acid-sensing capabilities, the N^C^N ligand has been functionalised directly with an acid sensitive NH_2 group. The complex is shown in Figure 7.2.

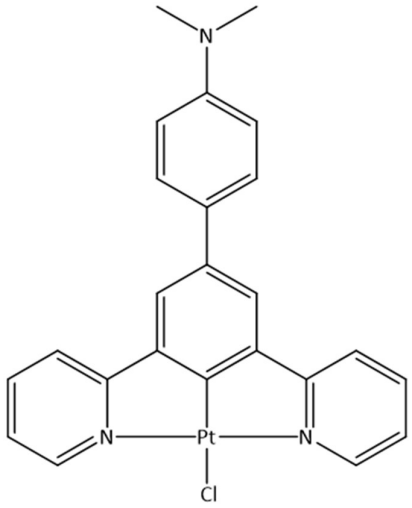

Figure 7.2*: Complex synthesised by Farley et al.*[119]

The solution state emission of this complex was broad and unstructured (Figure 7.3, red line). In addition the emission profile was significantly red shifted relative to complexes without the $C_6H_4NMe_2$ substituent. This evidence, along with the observed solvachromic shift of the emission peak in different solvents suggests the excited state is of a different character to that observed for similar complexes. The authors determined from the data that the emission is caused by a ILCT as opposed to a transition with ^{3}LC character.

When this complex is exposed to a solution of trifluoroacetic acid the emission profile of the complex changes, Figure 7.3 blue line. The peak has been blue shifted by 3700 cm^{-1} and the profile of the peak is now structured and the complex is displaying excimer formation. The protonation of the complex has switched the character of the excited state from a ILCT to a transition with ^{3}LC character. The reverse switch is achieved by neutralising the solution with a base.

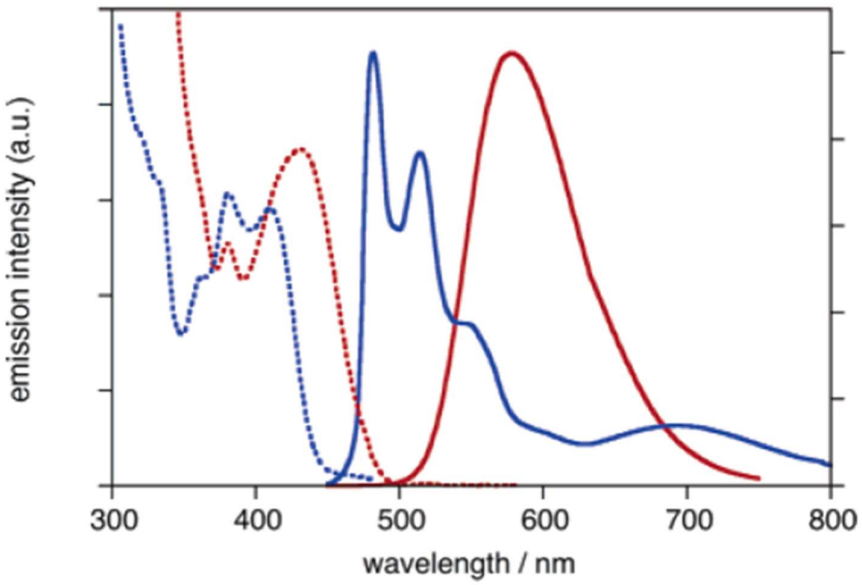

Figure 7.3: *Red Line, solution state emission spectra of complex in DCM solution. Blue line is the solution state emission spectra after protonation. Image taken directly from the paper*. [119]

The example shown in Figure 7.3 differs to other examples in the literature, as there is a change in energy observed when the protonation occurs, not just a change in intensity, which has been seen with other complexes in the literature. The next example of a *'smart'* material utilises a terpyridine ligand with a functionalised acetylide ligand in the 4th co-ordination site. The functional group used is NMe_2, with BF_4^- as the counter-ion.

The structure of this complex is shown in Figure 7.4. Unlike the previous two examples, the pincer ligand used in this instance is a terpyridine ligand analogous to that used in chapter 4 of this thesis. In addition, it is the ligand in the 4th co-ordination site of the complex that has been functionalised with the pH sensitive group.

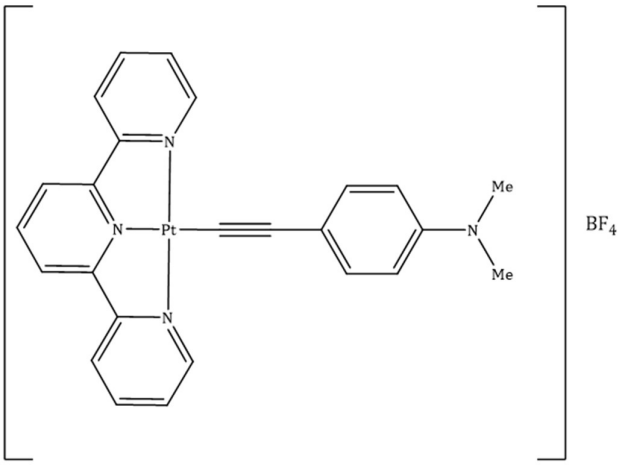

Figure 7.4: *Complex synthesised by Zheng et al.*[152]

In acetonitrile solution, this complex is deep purple in colour, turning yellow upon addition of acid. Figure 7.5 illustrates the spectroscopic studies the authors carried out when analysing this behaviour. Figure 7.5a shows the solution state UV-Vis spectrum upon addition of acid illustrating the change in colour from deep purple to yellow.

The authors found that as the concentration of the acid varied the peaks in the UV-Vis spectrum varied in intensity. They attributed this to the change in energy of the frontier orbitals. When the NMe_2 group is protonated, its electron donating ability is decreased and this in turn lowers the energy of the HOMO of the acetylide. The result of this is that the MLCT becomes the lowest energy transition and a change in colour results.

The effect of protonation on the emission spectra is shown in figure 7.5b. When the complex is deprotonated, it is non-emissive. This is normal for terpyridine complexes as they tend to decay non-radiatively. Once the functional group is protonated, a broad emission peak is observed due to the MLCT transition, which forms upon re-ordering of the orbitals. This process can be reversed using base.

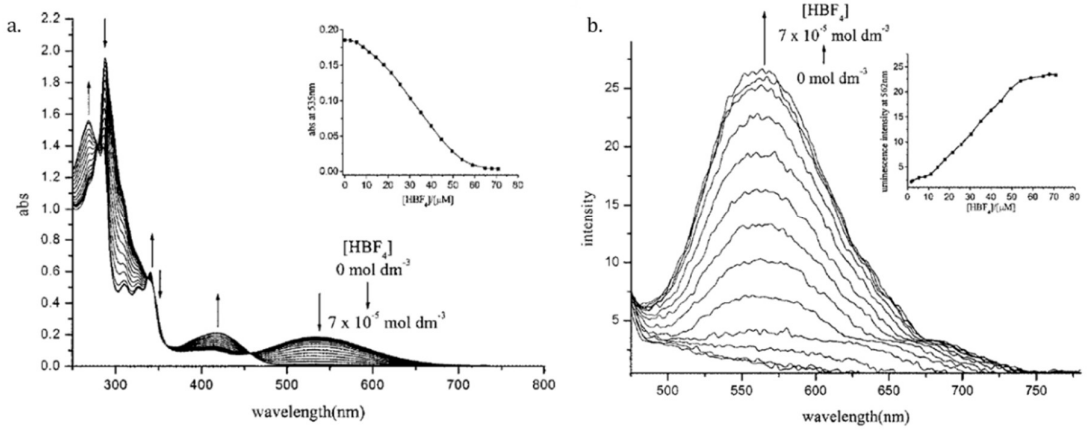

Figure 7.5*: a. UV-Vis of solution upon the addition of acid. b. Solution state emission of complex upon addition of acid. Image taken directly from the paper*. [152]

The final example of a *'smart'* material is shown in Figure 7.6. This complex once again contains a terpyridine ligand, but in this case, the central terpyridine arene ring is functionalised with a carboxylate group as opposed to an amine group. This complex undergoes a transition from yellow to blue in the solid-state upon deprotonation and the reverse protonation is achieved using HCl vapour. Both processes take in excess of 24 h to occur, so further tuning is required before this could be used as an effective solid-state sensor.

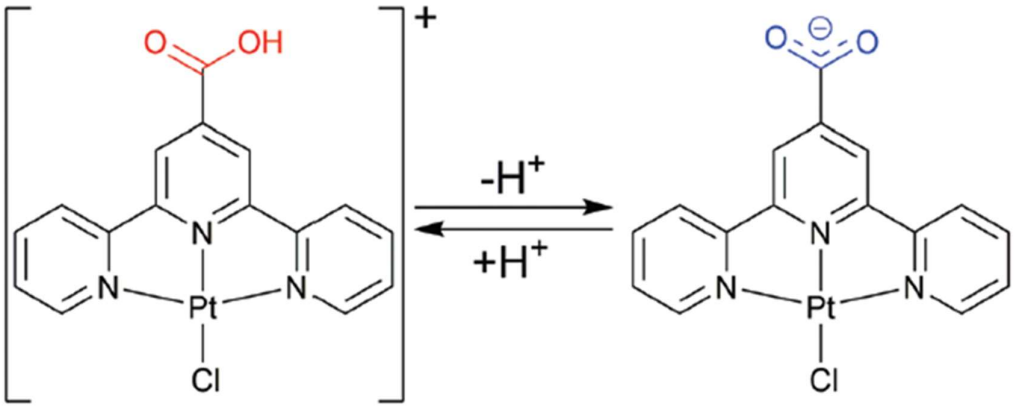

Figure 7.6: *Complex synthesised by Kobayashi et al. Image taken from paper.* [94]

7.1.2 pH Sensitive Functional Groups

The literature provided several examples of different functional groups being used in the field of pH sensing, section 7.1.1. However, analysis of the literature suggested that the use of an amine functionality provided faster sensing response times than the examples when carboxylate groups are used. The carboxylate group took at least 24 h for a switch to occur in the solid state, whereas the NMe_2 group was substantially faster. Based on previous literature precedence the amine functional groups will be investigated in this chapter.

7.1.3 Orbital Discussion

In Chapter 6 the effect of different substituent patterns were investigated on the switching capabilities of classic photo-switching functional groups. It was found that the azobenzene/ stilbene group had to be in a specific place in the molecule for the switching to occur. In the case of the pH functional groups a '*switch*' may not be determined by the ligand substitution patterns, however the difference in the frontier orbitals may induce different types of '*switching*' behaviour.

Examples of this have been given in section 7.1.1. Farley *et al* used a functionalised pincer when researching pH sensitive compounds. This gave rise to a compound that had emission profiles of different energies dependent on whether the amine group was protonated.[119] On the other hand Yang *et al* used a functionalised acetylide to communication changes in π effects to the metal centre. This gave rise to a complex that showed changes in emission intensity when the amine group was protonated.[152]

This chapter will combine the research from Chapter 6 and the current literature on pH sensitive complexes, to synthesise a series of complexes that bear an amine functionality in different substitution positions around the Pt pincer complexes.

Figure 7.7 shows the frontier orbitals for the complexes discussed in this chapter. It can be clearly seen that the make-up of these orbitals varies dependent on where the complex in functionalised. In the case of complex **30** where the amine group is substituted directly onto the N^C^N pincer the HOMO is made up of contributions from the metal centre and the arene ring, whereas in the LUMO the pyridyl rings are the major contributor. In contrast, complex **28** has the majority of the

orbital contributions for the HOMO based on the acetylide, which in this case incorporates the amine group again. The LUMO is once again made up of contributions from the pyridyl rings.

Unlike the photo-switching groups in Chapter 6 and the examples in the literature, the functional groups can contribute to the HOMO of both configurations. This would suggest that the complexes would show similar spectral behaviour.

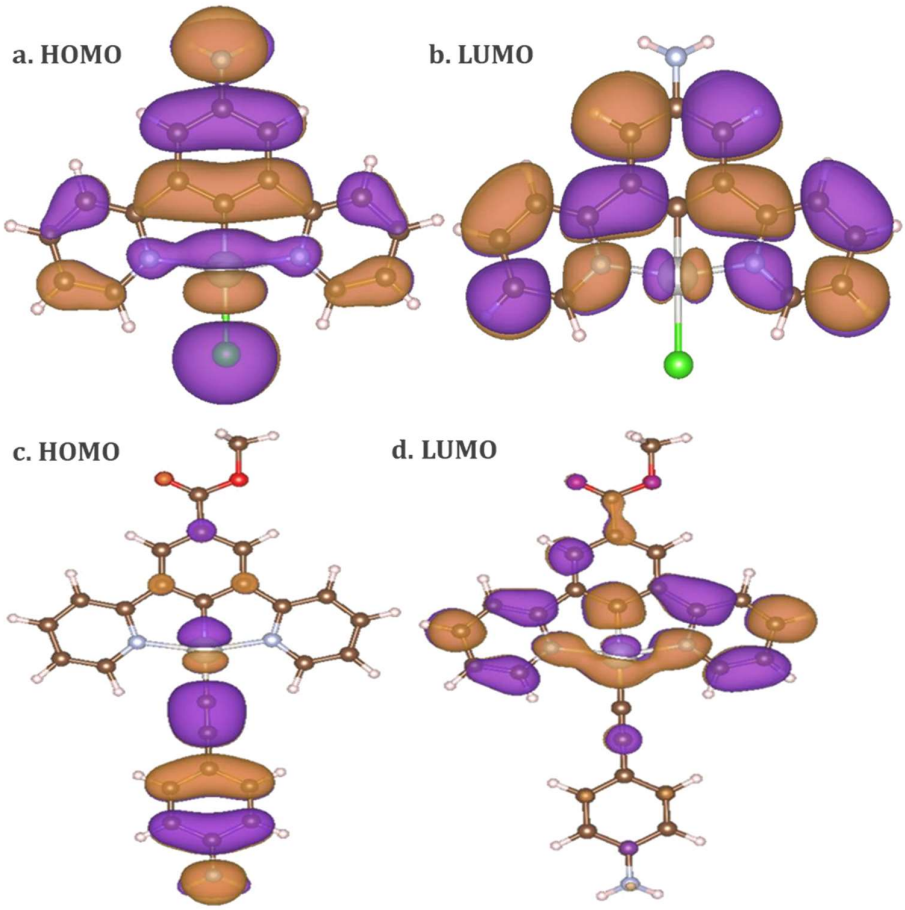

Figure 7.7: *Frontier orbitals of complexes investigated in this chapter. a. HOMO complex **30**. b. LUMO of complex **30**. c. HOMO of complex **28**. d. LUMO of complex **28**.*

7.2.0 4-ethynyl-N,N-dimethylaniline-Methyl3,5-di(pyridin-2-yl)benzoate Platinum (28)

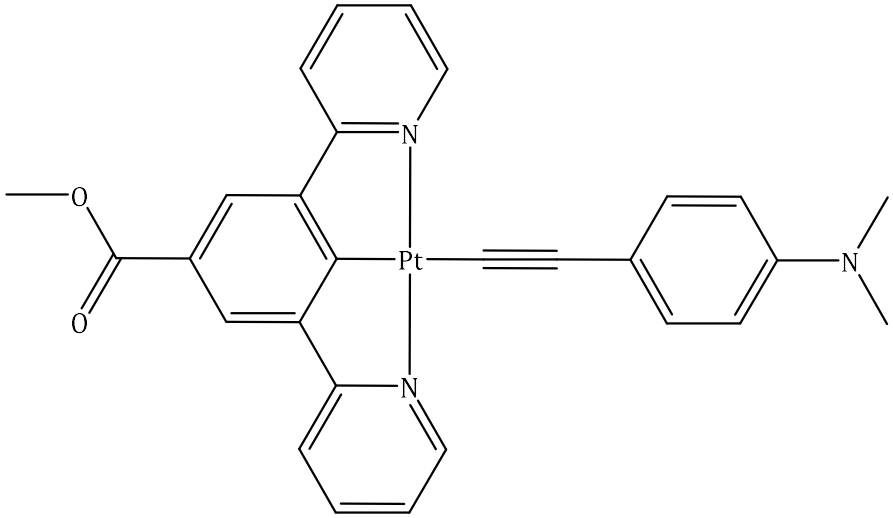

Complex **28** was synthesised in good yield and powder was isolated, which contained both red and yellow plates. ^{1}H NMR and IR spectroscopy and CHN analysis confirmed the product was pure and none of the starting material remained. The two different colours are therefore suggestive of different polymorphs of this complex.

7.2.1 Synthetic Strategy

The synthesis of complex **28** is detailed in Scheme 7.1. The first stage is to synthesise the acetylide ligand. This is achieved using a Sonagashira coupling reaction adapted from the literature;[153] the difference being an increased reaction temperature to ensure the reaction reached completion, with a 90% yield.

The next step is to react this ligand with the Pt precursor. As was seen in Chapters 5 and 6, complex **15** has been used as starting material for the reaction with the various ligand systems. This ligand exchange was achieved by deprotecting the TMS group using base and then stirring with complex **15** at 40˚C overnight. The product was isolated by filtration.

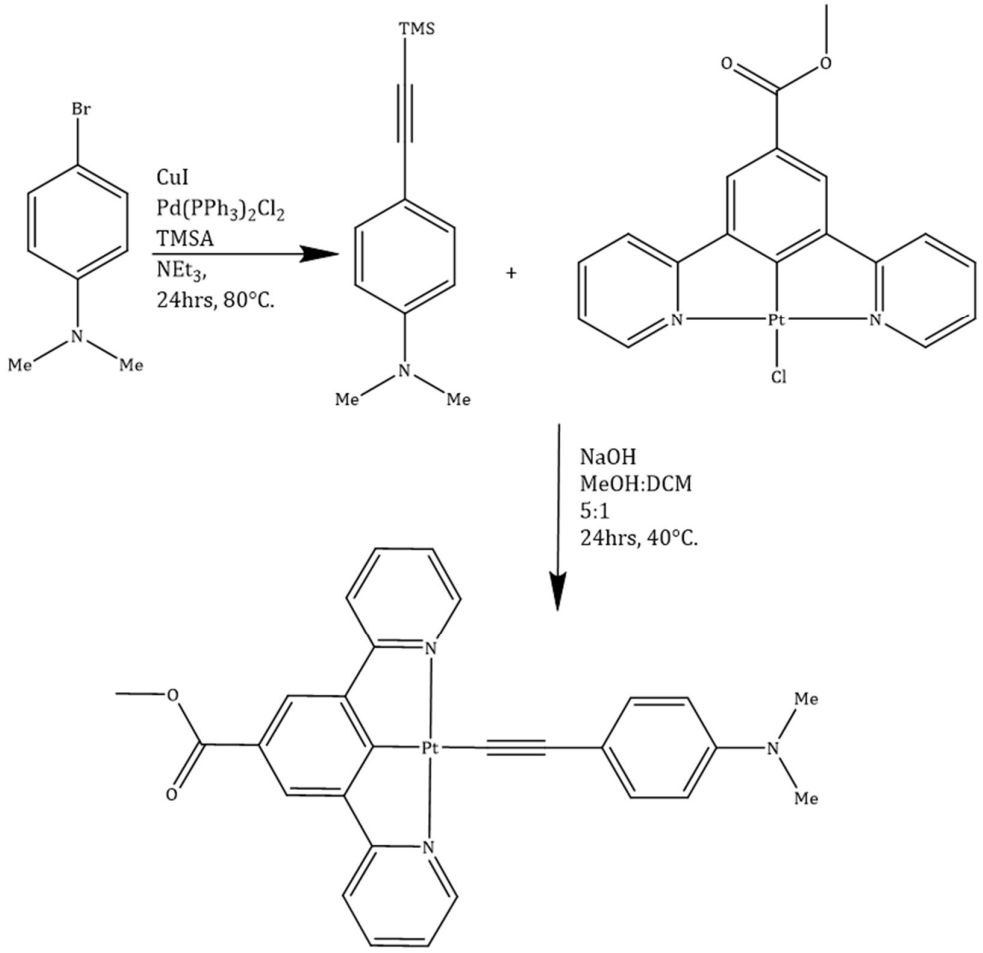

Scheme 7.1*: Synthetic route to isolate Complex **28**.*

7.2.2 Solution State Spectroscopy

Once complex **28** had been dissolved into DCM the two distinct colours formed an orange solution, suggesting the colour differences has been caused by different solid-state interactions. The solution state UV-Vis absorption and emission spectra are shown in Figure 7.8.

The UV-Vis absorption and emission spectra have similar profiles to those observed for analogous N^C^N Pt complexes in this thesis. Figure 5.9 showed the spectra for the chloride starting material; there is one clear difference which is the peak attributed to the $^3\pi$-π^* transition. For complex **28** this appears at a higher wavelength, 400-550 nm opposed to 350-420 nm for the complex **15**.

However, the emission profile is in the same wavelength region and has the same characteristic twin peak. This pronounced vibrational structure can be attributed to the $^3\pi$-π^* transition. Due to the change in energy of the UV-Vis spectrum, the absorption and emission spectra now overlap significantly, with no appreciable Stokes shift. It is important to note that the spectrum here has been normalised to allow for comparison of wavelength. When the emission spectra is compared to other Pt complexes detailed in Chapter 5 and 6, the emission is of very low intensity. This could be caused by the amine group on the acetylide donating its pair of electrons to the Pt centre, creating a pathway that can decay non-radiatively.

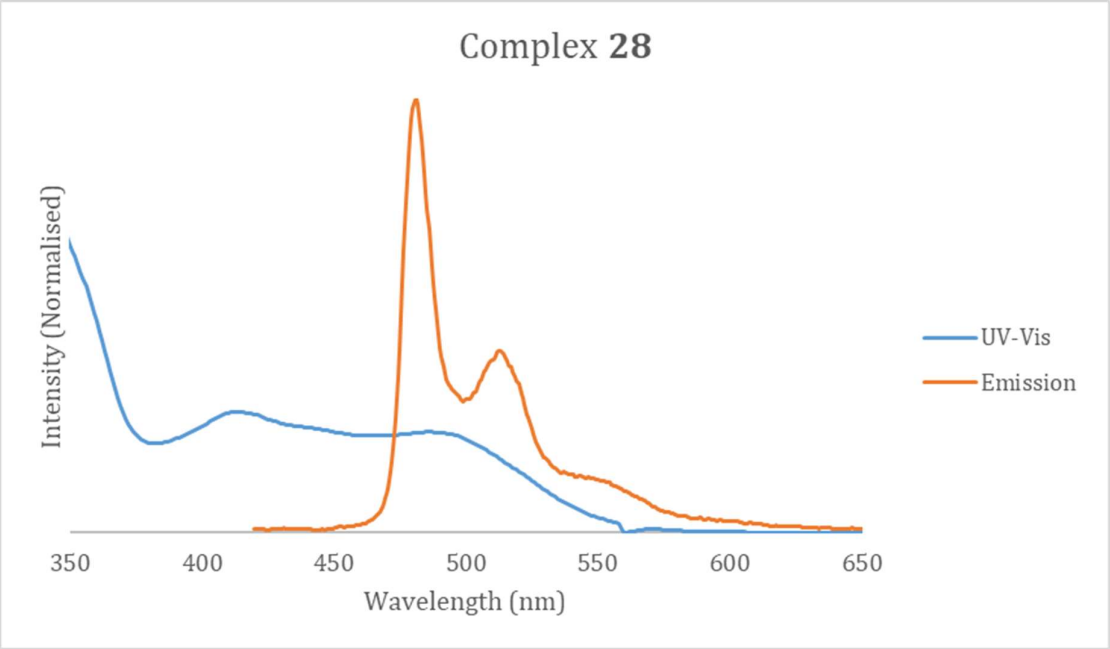

Figure 7.8: *Solution state spectroscopy of Complex **28**, in DCM. Blue line: UV-Vis, solution concentration 1×10^{-4} M. Orange line: Emission, solution concentration 1×10^{-6} M, λ_{ex} 400 nm.*

7.2.3 pH Sensing Capabilities

The pH sensing capabilities of these complexes were initially tested in the solution state using UV-Vis absorption and emission spectroscopy. This is in-line with similar studies carried out in the literature.[94, 119, 152] In this instance the acid used was ρ-tolylsulphonic acid and the UV-Vis spectrum was measured at varying concentrations of acid; the results are shown in Figure 7.9.

The UV-Vis spectra in Figure 7.9 show the change in energy of the $^3\pi$-π^* transition as acid is added. In addition, upon protonation of complex **28**, the peak between 300-400 nm becomes more defined and it is clear that the majority of the contribution is due to the $^3\pi$-π^* transition, however, there is still some contribution from the $^1\pi$-π^* transition. This change in peak energy coincides with a visible change in colour of the solution. The solution turns colourless from a deep orange.

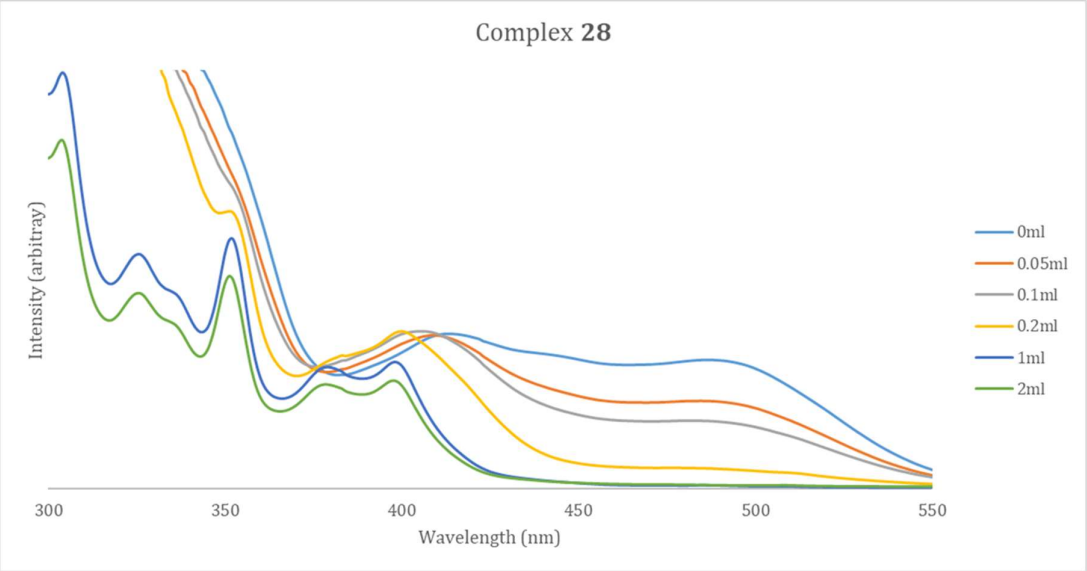

Figure 7.9: *Solution state spectroscopy of Complex **28**, solution concentration 1×10^{-4} M in DCM. Acid used: ρ-tolylsulphonic acid, concentration, 1×10^{-3} M in DCM.*

Figure 7.10 shows how the emission of complex **28** varies with the addition of acid. The initial emission profile of this complex is very weak. As acid is added the intensity of the emission increases until 1ml of acid of 1×10^{-3} M concentration has been added to 10 ml of complex **28** in solution. Concentration studies have shown there is little effect on the emission profile with concentration, so the change in emission can be attributed to protonation of the NMe_2 group. The emission then starts to decrease, this could be for a variety of factors such as quenching by the presence of oxygen.

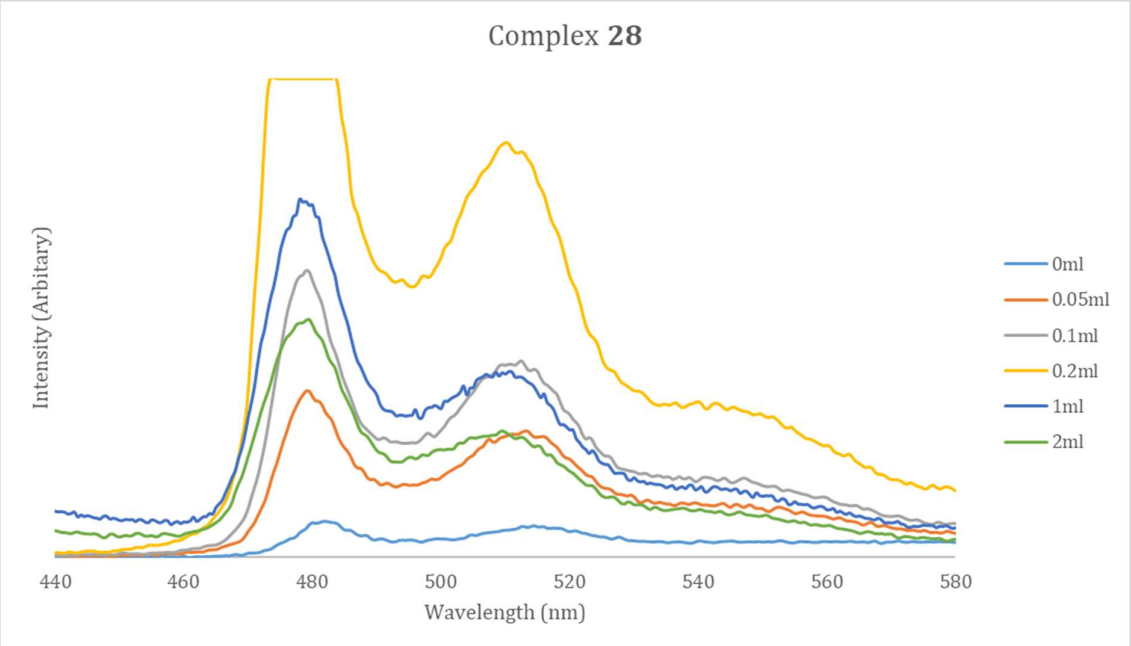

Figure 7.10: *Solution state spectroscopy of Complex **28**, solution concentration 1×10^{-4} M in DCM. Acid used: ρ-tolylsulphonic acid, concentration, 1×10^{-3} M in DCM. λ_{ex} 400 nm.*

It was expected that this complex would behave in a similar manner to the complex reported by Yang *et al* in 2004, which used the terpyridine ligand as opposed to the N^C^N. This has indeed been the case, where a distinct colour change has been observed upon the addition of acid and a change in the emission intensity upon the protonation of the amine group. This colour change happened immediately by eye. Unlike that literature example, this protonation is not reversible upon the addition of triethyl amine. Different bases would have to be tried before concluding whether this is an irreversible protonation.

Complex **28** has two groups, which could potentially be affected by changes in pH, the amine group and the ester functionality on the pincer backbone. Solution IR and ^{1}H NMR confirmed that it is the protonation of the amine group that gives rise to these spectral effects and not the hydrolysis of the ester functionality.

7.2.4 Crystal Structure Analysis

This complex has two distinct polymorphs in the solid state, a yellow form and a red form. Single crystals of both forms have been successfully grown and their crystal and molecular structures will be discussed in this section.

Crystal Structure: Yellow

The crystal structure of complex **28 yellow** is shown in Figure 7.11. It crystallises in the monoclinic space group $P2_1/c$, with one molecule in the asymmetric unit. Bright yellow crystals were grown from vapour diffusion of diethyl ether into a concentrated chloroform solution at -18°C. There are no molecules of solvent in the unit cell. Extended crystal and refinement data are found in Table 7.1.

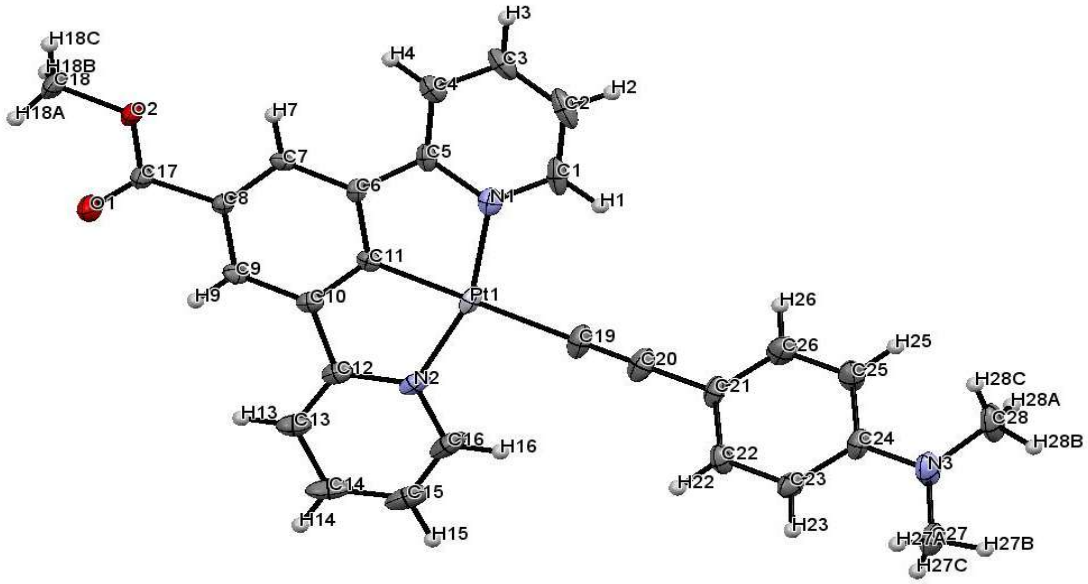

Figure 7.11*: Crystal structure of Complex **28**, yellow form. Ellipsoids shown at 50%.*

Table 7.1: *Crystal data and structure refinement for Complex **28**, yellow form.*

Identification code	Bath2800
Empirical formula	$C_{28}H_{22}N_3O_2Pt_1$
Formula weight	627
Temperature/K	150
Crystal system	monoclinic
Space group	$P2_1/c$
a/ Å	15.7525(6)
b/ Å	7.4617(3)
c/ Å	19.6110(8)
α/°	90
β/°	99.791(2)
γ/°	90
Volume/ Å^3	2271.51(16)
Z	4
ρ_{calc}g/cm^3	1.838
μ/mm^{-1}	6.209
F(000)	1224.0
Crystal size/mm^3	0.4 × 0.2 × 0.05
Radiation	Synchrotron (λ = 0.7749 Å)
2Θ range for data collection/°	2.624 to 56.794
Reflections collected	5672
Data/restraints/parameters	5672/0/310
Goodness-of-fit on F^2	1.118
Final R indexes [I>=2σ (I)]	R_1 = 0.0282, wR_2 = 0.0671
Final R indexes [all data]	R_1 = 0.0413, wR_2 = 0.0794
Largest diff. peak/hole / e Å^{-3}	0.93/-1.12

In the molecular structure of complex **28** the central Pt(II) atom adopts the expected square planar geometry. The bond angle, N1-Pt1-N2 has been measured at 160.08(14)˚, this slight distortion from true square planar geometry has been attributed to the bite angle of the pincer ligand. The other bond parameters listed in Table 7.2 fall within the expected parameters. The bond length measured for the C≡C triple bond, C19-C20 is 1.202(6) Å and this is consistent with values previously reported in the literature.[147, 148]

Figure 7.11 provides an impression that the molecule is planar in the solid state. Analysis of the torsion angles show that the pincer ligand and the methyl ester substituent is co-planar with respect to the pincer ligand, however the functionalised acetylide is twisted out of the Pt-pincer plane. This is shown by the torsion angles provided in Table 7.2. In addition, the dihedral angle between the following planes was measured at 33.83˚.

- Plane 1: C23 C22 C24 C21 C25 C26
- Plane 2: C6 N1 Pt1 C11 N2 C12 C5 C10

The bond angles in the –NMe_2 group are 119.2(4) and 120.2(4)˚, Table 7.2. These fall with the expected parameters. The torsion angles and a plane analysis using the program Mercury[87] shows that the group is co-planar with the arene ring on the functionalised acetylide.

Table 7.2: *a. Table of bond lengths for **28** yellow form. b. Table of bond angles for **28** yellow form. c. Torsion angles for **28** yellow form.*

a. Bond Lengths		
Atom	**Atom**	**Length/ Å**
Pt1	N1	2.023(4)
Pt1	C11	1.919(4)
Pt1	N2	2.031(4)
Pt1	C19	2.058(4)
C19	C20	1.202(6)

b. Bond Angles			
Atom	**Atom**	**Atom**	**Angle/°**
N1	Pt1	N2	160.08(14)
N1	Pt1	C19	98.97(17)
C11	Pt1	N1	80.62(15)
C11	Pt1	C19	178.55(16)
C20	C19	Pt1	173.6(4)
C28	N3	C27	119.2(4)
C24	N3	C28	120.2(4)

c. Torsion Angles				
A	**B**	**C**	**D**	**Angle/°**
C26	C21	C20	C19	-89(12)
N1	Pt1	C19	C20	64(4)

Analysis of the π-π interactions in OLEX2[121] show there is one set of π interactions in the solid state structure of complex **28** at a measured distance of 3.57(7) Å. This set of π interactions is localised between the pyridyl rings of the pincer ligand on adjacent molecules. There are no significant hydrogen bonds present between the amine group and the adjacent molecule. However, hydrogen bonds do form between the methyl ester group and the pyridine ring of the adjacent molecule.

Crystal Packing: Yellow

Figure 7.12 shows the crystal packing of the yellow form of complex **28** along the b and c axis. Figure 7.12a shows that the complex forms a herringbone motif, which disrupts the possibility for Pt…Pt stacking. The closest Pt…Pt interaction is measured at 7.462(5) Å, this means the difference in colour between the two polymorphs cannot be attributed to Pt-Pt stacking.

Closer inspection of the solid-state packing reveals that the closest contact between adjacent molecules is between the pyridyl rings of the N^C^N pincer, giving rise to π-π interactions, which may be responsible for the colour in the solid state.

Figure 7.12b show that the amine group lies adjacent to each other in the solid-state structure, this is to maximise packing efficiency, in addition to forming short contacts. This packing motif has no solvent in the crystal structure, and void analysis shows there is no significant space left in the structure for the solvent to occupy.

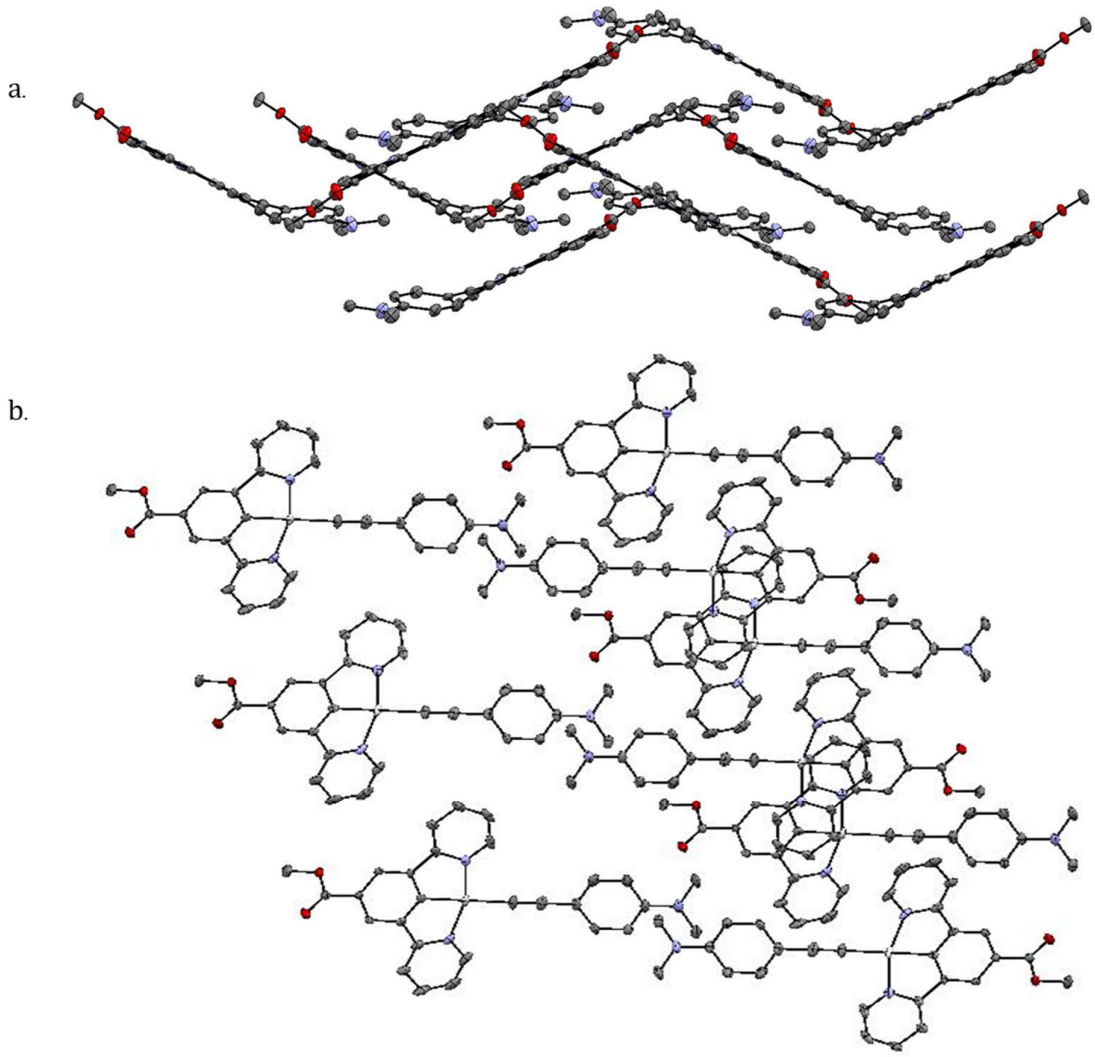

Figure 7.12: *a. View of complex **28** along the 'a' axis at 150 K. b. View of complex **28** along the 'c' axis at 150 K. Hydrogen has been removed for clarity. Ellipsoids shown at 50% probability.*

Crystal Structure: Red

The crystal structure of complex **28 red** is shown in Figure 7.13. It crystallises in the triclinic space group *P*-1, with one molecule in the asymmetric unit. Red, plate crystals were grown from the same vapour diffusion of diethyl ether into a concentrated chloroform solution at -18˚C. There are no molecules of solvent in the unit cell. Extended crystal and refinement data is found in Table 7.3.

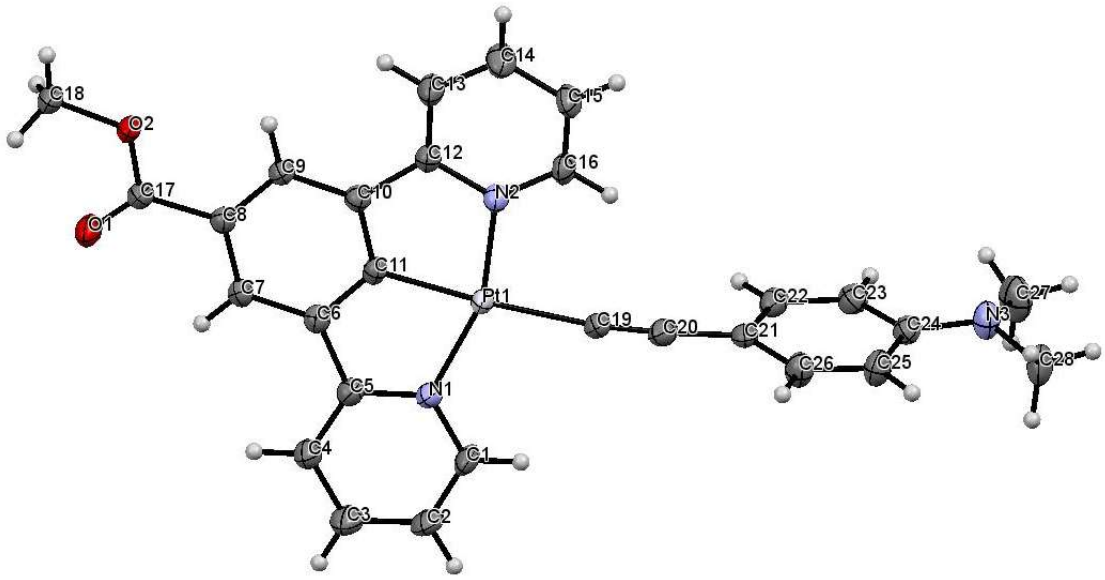

Figure 7.13*: Crystal structure of Complex **28**, red form. Ellipsoids shown at 50%.*

Table 7.3*: Crystal data and structure refinement for Complex **28**, red form.*

Identification code	Bath 2871
Empirical formula	$C_{28}H_{22}N_3O_2Pt_1$
Formula weight	627
Temperature/K	150
Crystal system	triclinic
Space group	P-1
a/ Å	7.5409(4)
b/ Å	8.6125(4)
c/ Å	18.1550(9)
α/°	79.296(2)
β/°	78.074(2)
γ/°	76.792(2)
Volume/ Å^3	1111.19(10)
Z	2
ρ_{calc}g/cm^3	1.972
μ/mm^{-1}	7.881
F(000)	650.0
Crystal size/mm3	0.2 × 0.3 × 0.03
Radiation	Synchrotron (λ = 0.7749 Å)
2Θ range for data collection/°	2.526 to 57.932
Reflections collected	4529
Data/restraints/parameters	4529/0/310
Goodness-of-fit on F^2	1.084
Final R indexes [I>=2σ (I)]	R_1 = 0.0206, wR_2 = 0.0504
Final R indexes [all data]	R_1 = 0.0226, wR_2 = 0.0510
Largest diff. peak/hole / e Å^{-3}	1.74/-0.93

The red form of complex **28** has a slightly distorted square planar geometry around the Pt centre. The bond angle N1-Pt1-N2 has been measured at 159.71(11)˚, this distortion from linearity is common in Pt pincer molecules and has been attributed to the pincer bite angle.[93] The other parameters listed in Table 7.4 and are within the expected ranges. The acetylide bond between C19 and C20 was measured at 1.194(5) Å, which is consistent with the literature.[147, 148]

Figure 7.13 shows that the difference between the red and yellow polymorphs is the orientation of the $-C_6H_4(NMe_2)$ group in space. Figure 7.13 shows the $-C_6H_4(NMe_2)$ group is perpendicular to the plane of the pincer molecule. The dihedral angle between the following two planes was measured at 87.68˚.

- Plane 1: C22 C23 C21 C24 C25 C26
- Plane 2: C5 C6 N1 C10 C12 Pt1 C11 N2.

The torsion angles provided in Table 7.4c provide additional evidence for the twist of the functionalised acetylide in relation to the plane of the pincer molecule.

Table 7.4*: a. Table of bond lengths for **28** red form. b. Table of bond angles for **28** red form. c. Torsion angles for **28** red form.*

a. Bond Lengths		
Atom	**Atom**	**Length/ Å**
Pt1	N1	2.023(3)
Pt1	N2	2.029(3)
Pt1	C11	1.932(3)
Pt1	C19	2.058(3)
C19	C20	1.194(5)

b. Bond Angles			
Atom	**Atom**	**Atom**	**Angle/˚**
N1	Pt1	N2	159.71(11)
N1	Pt1	C19	100.36(11)
C11	Pt1	N1	80.16(12)
C11	Pt1	C19	172.69(12)
C20	C19	Pt1	172.3(3)
C27	N3	C28	114.6(3)
C24	N3	C28	119.2(3)

c. Torsion Angles				
A	**B**	**C**	**D**	**Angle/˚**
C16	N2	Pt1	C19	-12.5(3)
C22	C21	C20	C19	-101(4)
Pt1	C19	C20	C21	79(5)
C23	C24	N3	C27	-18.6(5)

OLEX 2[121] has been used to analyse the π-π interactions in the red form of complex **28**. There are two distinctive π-π interactions in this complex between adjacent molecules, details of which have been provided in Table 7.5. The first interaction is between Plane 2 and Plane 2, this plane is the functionalised arene ring bonded to the acetylide group. The extended crystal packing of this structure shows that this group stacks in the solid state as opposed to the Pt-Pt stacking that was anticipated, Figure 7.14.

The other π-π stacking interaction is located between the pyridyl rings of the pincer molecule. This type of π interactions has been frequently seen throughout this thesis.

Table 7.5: *a. Planes Present in solid-state structure **28** red form. b. π-π Interactions **28** red form. c. Hydrogen bonds **28** red form.*

a. Plane Identification

Plane Number	Atoms in plane
1	C21 C22 C23 C24 C25 C26
2	N1 C5 C4 C3 C2 C1
3	N2 C16 C15 C14 C13 C12

b. π-π Interactions

Planes	Distance (Å)
2-2[1]	3.81(2)
3-4[2]	3.65(1)

c. Hydrogen bonds

Atoms	(D…A) Distance (Å)	(H…A) Distance (Å)	D…H…A Angle/°
C14-H14-O2	3.568(4)	2.687	158.5
C7-H7-O1	3.498(3)	2.584	167.6
C4-H4-O1	3.343(4)	2.427	168.0

Where [1] (1-X, 2-Y, 2-Z), [2] (1+X, +Y, +Z).

The hydrogen bonds, Table 7.5c, originate from the oxygen atoms of the methyl ester group, on the 4th position of the central phenyl ring. They are intermolecular hydrogen bonds as they connect to a hydrogen a neighbouring molecule, this is general a hydrogen atom on the pincer ligand.

Crystal Packing: Red

It is immediately clear from Figure 7.13 that the main difference between the yellow and red form of complex **28** is the orientation of the $-C_6H_4(NMe_2)$ group in space. In the yellow form, figure 7.11 the arene ring is twisted by 33.83° from the plane of the N^C^N pincer. However, in the red form the arene ring sits perpendicular to the plane of the N^C^N pincer. This difference in orientation has induced significant difference in the solid-state packing of the complex.

Figure 7.14 shows the packing of the red form of complex **28**. This diagram clearly shows that there is no Pt…Pt overlap, however as observed with the yellow form there is significant π-π overlap. The orientation of the arene rings provides additional π overlap as the rings sit parallel to each other in the solid state. It is these subtle differences in π overlap and change in close contacts that has given rise to the different colour.

As with the yellow form, this polymorph packs efficiently in the solid state with no void space present. Therefore, no solvent is found in the structure.

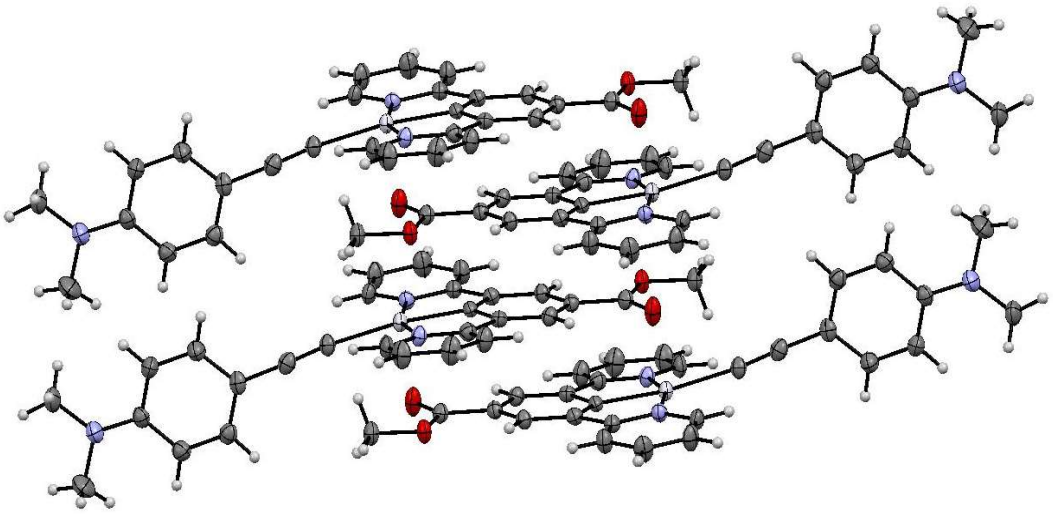

Figure 7.14*: View of complex **28** along the 'a' axis at 150 K. Ellipsoids shown at 50% probability.*

7.2.5 Reflectance Spectroscopy

Reflectance spectra for the two forms of complex **28** are shown in Figure 7.15. The change in energy of the shoulder, confirms the two different colours observed in the solid-state.

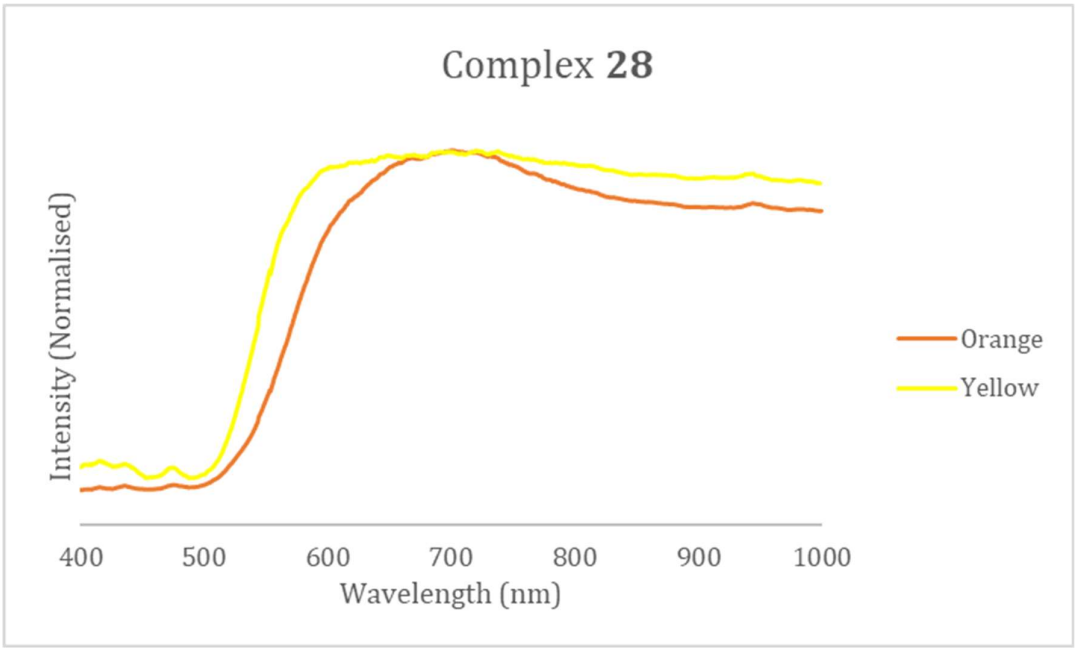

Figure 7.15*: Reflectance spectra of the red and yellow polymorph of complex **28**.*

Upon addition of acid to a thin film of complex **28,** no appreciable difference in the reflectance spectra was observed.

7.3.0 N,N-dimethyl-3,5-di(pyridin-2-yl)aniline (29)

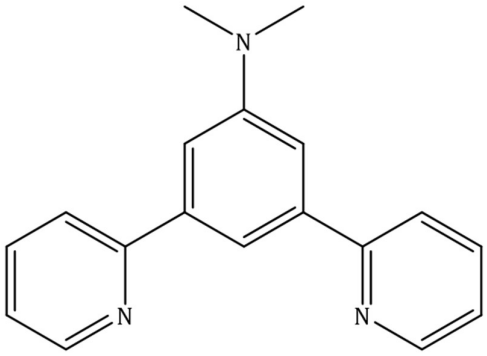

Compound **29** is a white crystalline solid and was isolated in a 52% yield. Its structure was confirmed by IR, ^{1}H NMR, ^{13}C NMR spectroscopies and by single crystal X-ray analysis.

7.3.1 Synthetic Strategy

Compound **29** was synthesised in a two-step process, illustrated in Scheme 7.2. Initially the aniline was converted to the dimethyl-dibromo species using a simple methylation reaction. The second step was a Stille reaction, adapted from the literature.[47] The ligand was isolated in 52% yield after purification by flash column chromatography.

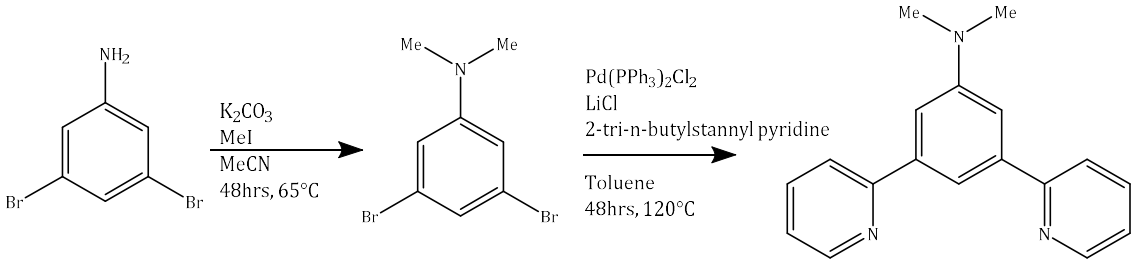

Scheme 7.2*: Synthetic route to isolate **29**.*

7.3.2 Solution State Spectroscopy

The solution state UV-Vis absorption and emission spectra were measured for compound **29** and the results are presented in Figure 7.16.

In the solution state UV-Vis absorption spectrum there is a clear peak between 300-400 nm, this is high in energy for an organic ligand, however a similar spectral profile was observed for compound **23**. This transition can be attributed to the π-π transitions in the ligand.

The compound also displays strong luminescence properties. Most complexes that contain an N^C^N ligand will are strongly luminescent because of effect of the central arene ring. However, for **29**, being a ligand precursor, strong luminescence was not expected because of the presence of the amine group, which is known to have detrimental effects on luminescence. Figure 7.16 shows two emission spectra for **29**. The orange line, being of low concentration and the grey line being of high concentration. As the concentration of the compound is increased the emission peak is red shifted, this change is not significant enough for a change in the observed spectral properties of the complex.

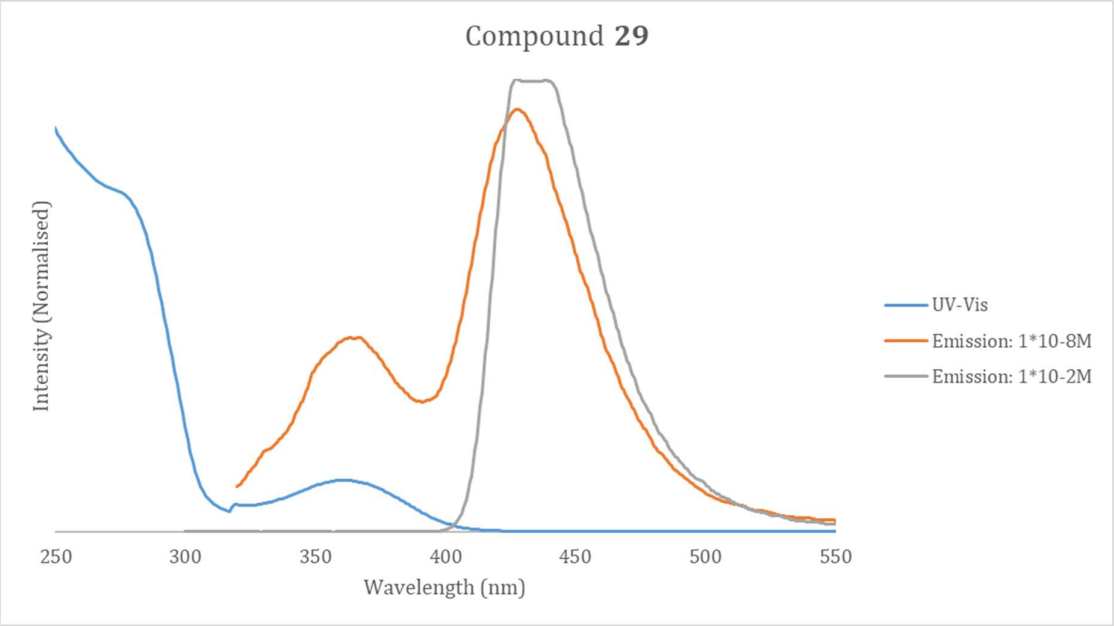

Figure 7.16: *Solution state spectroscopy of Compound **29**, in DCM. Blue line: UV-Vis, solution concentration 1×10^{-5} M. Orange line: Emission, solution concentration 1×10^{-8} M. Grey Line: Emission, solution concentration 1×10^{-2} M. λ_{ex} 300 nm.*

7.3.3 pH Sensing Capabilities

The pH sensing capabilities of this compound have been tested for comparison when the ligand is cyclometallated with Pt in complex **30**. Initially the pH response was tested in the solution state, Figure 7.17 is a photograph of before and after ρ-tolylsulphonic acid is added to a DCM solution of the compound **29**. There is a clear colour change from colourless to yellow on the addition of acid; this has been investigated further using solution state spectroscopy.

Figure 7.17: *Photograph of a solution of Compound **29** before (clear) and after (yellow) acid addition.*

The results of the UV-Vis spectroscopic pH investigation are shown in Figure 7.18. There is a clear shift in the energy of the peak attributed to π-π* transition and this is seen in conjunction with a change in colour of the solution from colourless to yellow. This change in colour can be attributed to the protonation of the amine group.

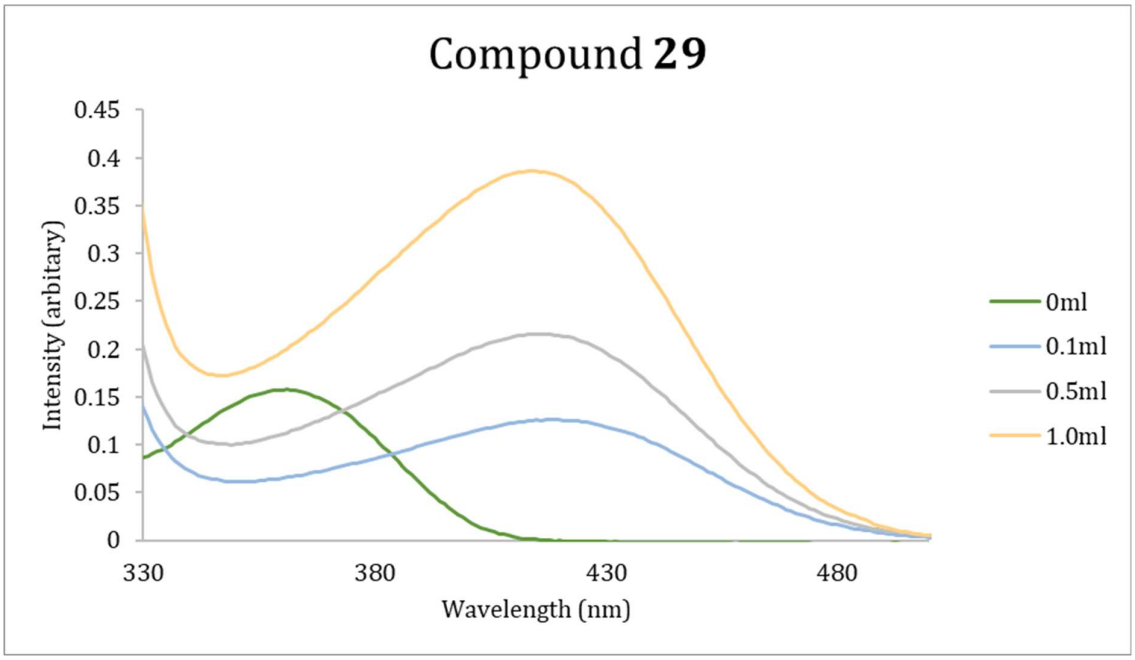

Figure 7.18: *Solution state spectroscopy of **29**, solution concentration 1×10^{-5} M in DCM. Acid used: ρ-tolylsulphonic acid, concentration, 1×10^{-3} M in DCM.*

Figure 7.19 illustrates the change in emission profile, as the amine group on the pincer is protonated. There is a slight shift in emission energy; however, the protonation of the amine group leads to a large decrease in emission intensity, to the point where it can no longer be measured. Protonation of the amine group acts as a switch to turn off the emissive properties of **29.** The reverse process has not yet been achieved.

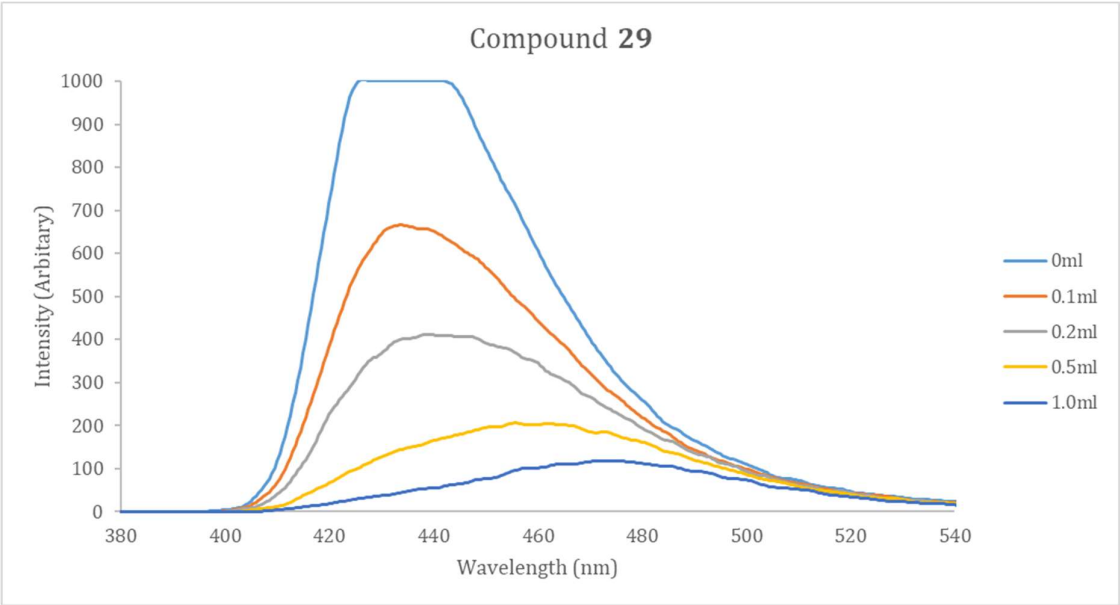

Figure 7.19: *Solution state spectroscopy of **29**, solution concentration 1×10^{-2} M in DCM. Acid used: ρ-tolylsulphonic acid, concentration, 1×10^{-3} M in DCM. λ_{ex} 300 nm.*

Compound **29** has also been tested for potential pH sensing capabilities in the solid-state. However, no visible spectral changes has been observed. It can be concluded that the sensor does not operate in the solid state or the protonation would be very slow in the solid state and the change cannot be seen by eye, which was one of the criterion that we used to establish whether the compound was an effective solid-state sensor.

7.3.4 Crystal Structure Analysis

Crystal Structure

The crystal structure of compound **29** is shown in Figure 7.20. It crystallises in the orthorhombic space group *Pbcn*. Clear, block-shaped crystals were grown from the slow evaporation of DCM. There are no molecules of solvent in the unit cell. Extended crystal and refinement data are found in Table 7.6.

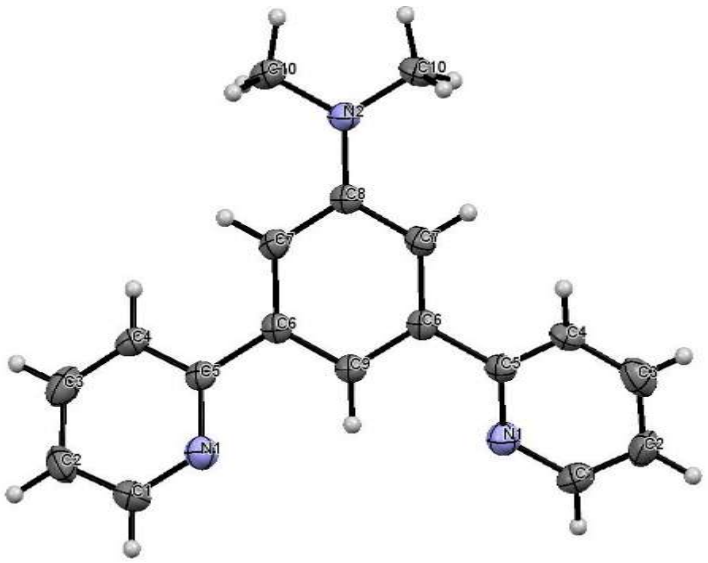

Figure 7.20*: Crystal structure of compound **29.** Ellipsoids shown at 50% probability level.*

Table 7.6: *Crystal data and structure refinement for Compound **29**.*

Identification code	p17prr320
Empirical formula	$C_{18}H_{17}N_3$
Formula weight	275
Temperature/K	150
Crystal system	orthorhombic
Space group	Pbcn
a/ Å	16.8825(7)
b/ Å	10.0466(4)
c/ Å	8.2416(3)
α/°	90
β/°	90
γ/°	90
Volume/ Å^3	1397.87(10)
Z	4
ρ_{calc}g/cm^3	1.323
μ/mm^{-1}	0.080
F(000)	596.0
Crystal size/mm^3	0.5 × 0.3 × 0.2
Radiation	MoKα (λ = 0.71073)
2Θ range for data collection/°	6.834 to 52.736
Index ranges	-21 ≤ h ≤ 17, -12 ≤ k ≤ 12, -10 ≤ l ≤ 9
Reflections collected	8790
Independent reflections	1436 [R_{int} = 0.0320, R_{sigma} = 0.0201]
Data/restraints/parameters	1436/0/98
Goodness-of-fit on F^2	1.160
Final R indexes [I>=2σ (I)]	R_1 = 0.0507, wR_2 = 0.1488
Final R indexes [all data]	R_1 = 0.0612, wR_2 = 0.1595
Largest diff. peak/hole / e Å^{-3}	0.30/-0.41

Compound **29** lies on a crystallographic mirror plane, this bisects the compound perpendicular to the plane of the compound at N2, C8 and C9 as illustrated in Figure 7.20. The parameters for compound **29** are provided in Table 7.7a and are consistent with values for similar complexes. The angles are provided in Table 7.7b, the majority lie close to 120˚, which is the expected value.

Table 7.7c shows the torsion angles for **29**, it the methyl group lies close to planar with the central phenyl ring, which is the same as the other complexes in this chapter. However closer inspection of the torsion angles for **29** shows that the pyridyl ring is not planar with respect to the central arene ring. The torsion angle has been measured at 27.1˚, this is in close agreement with the measured dihedral angle of 28.18˚ between the following two planes:

- Plane 1: C6 C8 C7 C9 C7' C6'
- Plane 2: C3 C4 C1 C2 C1 C5.

Table 7.7: *a. Table of bond lengths for **29**. b. Table of bond angles for **29**. c. Torsion angles for **29**.*

a. Bond Lengths		
Atom	**Atom**	**Length/ Å**
N2	C10	1.444(2)
N1	C5	1.364(2)
N1	C1	1.361(3)
C4	C5	1.363(3)
C4	C3	1.359(3)

b. Bond Angles			
Atom	**Atom**	**Atom**	**Angle/°**
C8	N2	C10	120.22(11)
C10[1]	N2	C10	119.6(2)
N1	C5	C6	118.45(16)
C9	C6	C5	119.13(17)
N2	C8	C7	121.07(12)
C4	C3	C2	121.4(2)

[1]1-X,+Y,1/2-Z

c. Torsion Angles				
A	**B**	**C**	**D**	**Angle/°**
C9	C6	C5	N1	27.1
C7	C8	N2	C10	-3.3

There are no π-π interactions or hydrogen bonds in this structure.

Crystal Packing

Figure 7.21a shows the solid-state packing of **29** along the b axis, as with complex **28** it forms a herringbone motif. The space-fill representation in Figure7.21b shows the lack of void space in the crystal structure which has meant that there is no solvent present in the crystal structure. This lack of space in the crystal structure could also explain why **29** displays no solid-state sensing behaviour. If there were channels present in the solid state this would allow the acidic vapour to move more readily in and out of the channels and a response may be observed,

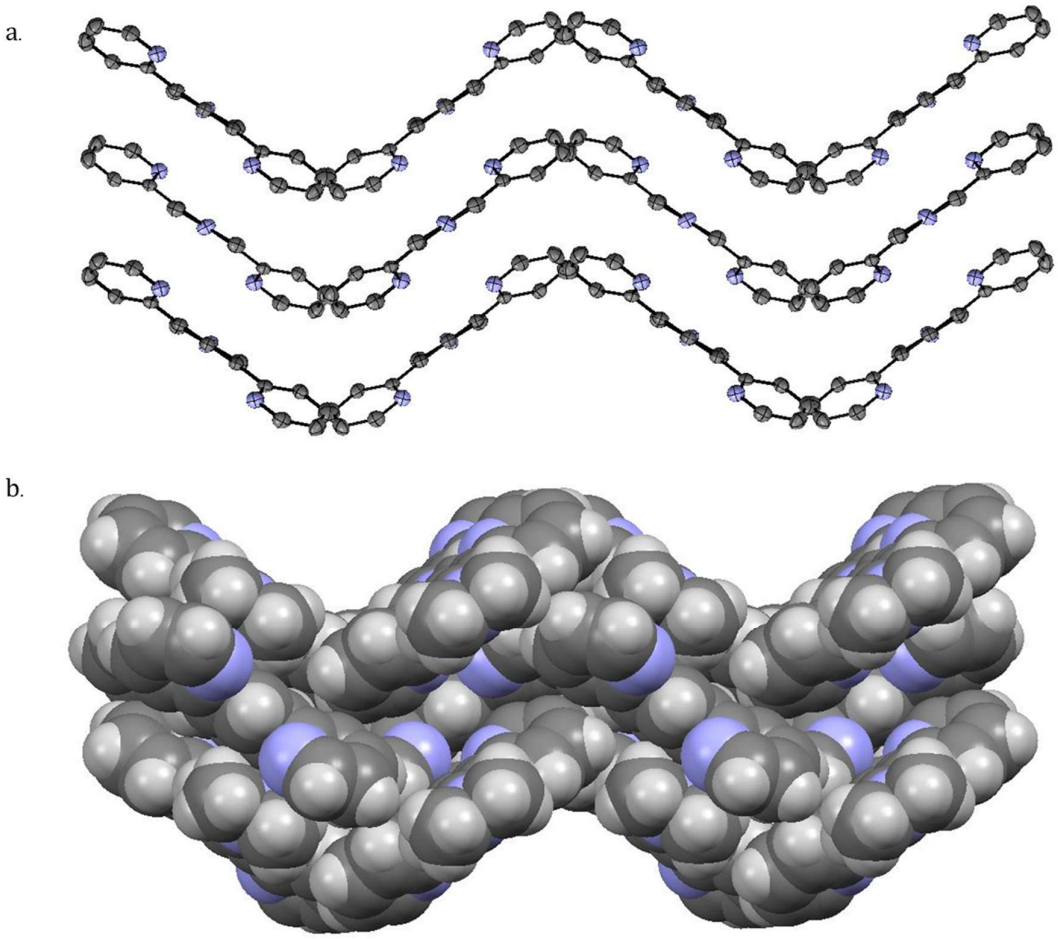

Figure 7.21*: a. View of* ***29*** *along the 'b' axis at 150 K. Ellipsoids shown at 50% probability. Hydrogen has been removed for clarity. b. Space-fill representation of* ***29****.*

7.4.0 N,N-dimethyl-3,5-di(pyridin-2-yl)aniline Platinum Chloride (30)

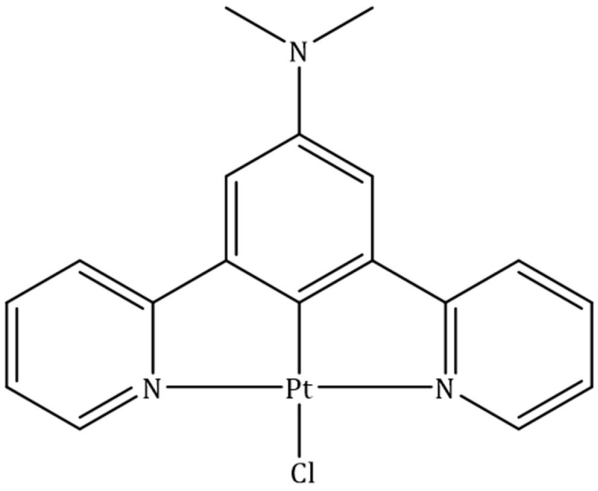

This complex was isolated as a yellow solid in 82% yield. The product was confirmed by IR, ^{1}H NMR spectroscopy and by single crystal diffraction X-ray analysis.

7.4.1 Synthetic Strategy

This complex was synthesised by a cyclometallation reaction, Scheme 7.3. The ligand was heated under reflux in a mixture of acetonitrile and water with the $[PtCl_4]^{2-}$ salt. Upon cooling, a yellow powder precipitated from the solution.

The product is not soluble in chlorinated solvents was therefore purified by re-crystallisation from methanol.

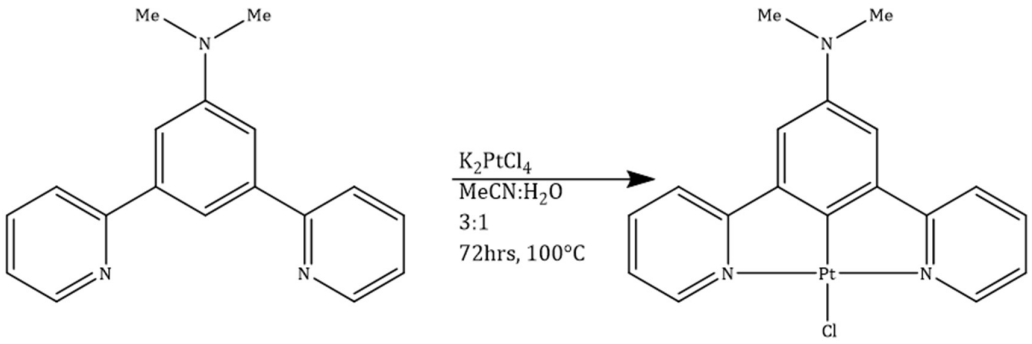

Scheme 7.3*: Synthetic route to isolate Complex* ***30****.*

7.4.2 Solution State Spectroscopy

Due to the different solubility of complex **30**, the solution state spectroscopy for this complex could not be conducted using DCM; instead, the solvent used for the measurements is MeOH. The UV-Vis absorption and emission profile for this complex is shown in Figure 7.22.

The UV-Vis spectrum has a similar profile observed for other platinum chloride complexes studied in this thesis. However, the peak at 420-520 nm attributed to the $^{3}\pi$-π^* transition is high in energy, similar to that observed for complex **28**.

The emission spectra in Figure 7.22 has been normalised for an effective comparison with the UV-Vis absorption spectrum because it is very weak. The emission follows a similar profile to the UV-Vis for the neutral complex and no Stokes shift is observed. In addition, a visual check of the solution does not show significant luminescence. One potential reason for this lack of emission could be the solvent used for the solutions. Chlorinated solvents are generally used in solution state spectroscopy because they simulate solid-state emission. This is because they are a non-coordinating solvent with a low dielectric constant.[106] However, due to the solubility profile of complex **30** methanol had to be used instead. This polar, co-ordinating solvent is known to quench luminescence.[106] In addition the amine group could quench luminescence due to its electron-donating power, this has been discussed in section 7.1.1 and in the literature.[119]

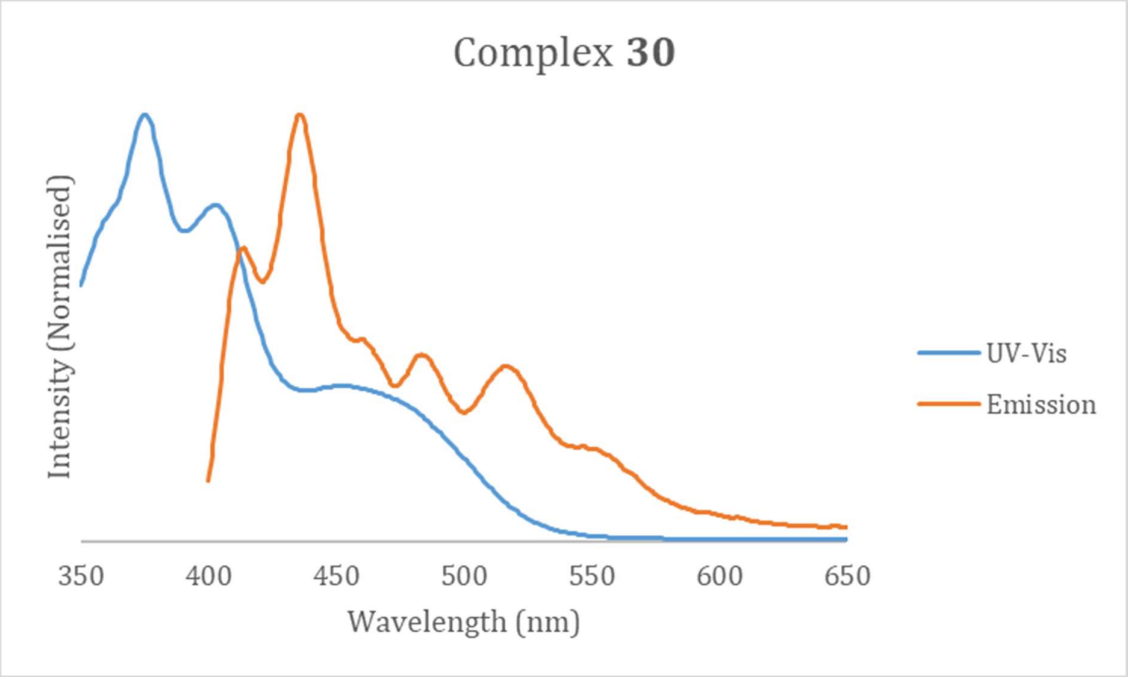

Figure 7.22*: Solution state spectroscopy of Complex **30**, in MeOH. Blue line: UV-Vis, solution concentration 1×10^{-4} M. Orange line: Emission, solution concentration 1×10^{-4} M. λ_{ex} 380 nm.*

7.4.3 pH Sensing Capabilities

Consistent with the other complexes discussed in this chapter the pH sensing capabilities of this complex were assessed in the solution state. The results of the initial investigation are shown in Figure 7.23. When the acid is added to the neutral solution turns yellow. This is observed in the presence of a variety of acids and in the case of trifluoroacetic acid, the complex precipitates. Subsequently when base is added to the neutral complex, not the acidified solution, the colour turns a deeper orange, turning green when the base is in excess. This is the first instance that the complexes synthesised in this chapter has displayed any sensing capabilities with base. However, the reverse colour change was not observed when the solutions were neutralised.

Figure 7.23*: pH-sensing capabilities of complex **30**, all solution in methanol. From right to left: Vial 1 with 2 drops of tolyl-sulphonic acid, Vial 2 with two drops of HCl, Vial 3 with 2 drops of trifluoroacetic acid, Vial 4 Neutral complex, Vial 5 with 2 drops of tri ethyl amine.*

The initial investigation provided evidence that spectral changes are seen in response to acidic solutions. Therefore, the same solution state spectroscopy experiment was used for complex **30**, in which the UV-Vis absorption and emission of the sample was measured as acid was added to the solution.

Figure 7.24 shows the spectra collected as part of this pH sensing investigation. Analysis of the results suggests that complex **30** is more sensitive to acidified solution as the change in spectral properties is observed more rapidly than for the other complexes discussed in this chapter. The time for the transition to occur has not been recorded precisely but happens on the second timescale. This is exemplified by the change in UV-Vis spectral profile after the addition of 0.1ml of acid, this profile does not subsequently change on the addition of any further acid. The reduction of the peak attributed to the $^{3}\pi$-π^* transition has been observed upon protonation of other complexes in this chapter.

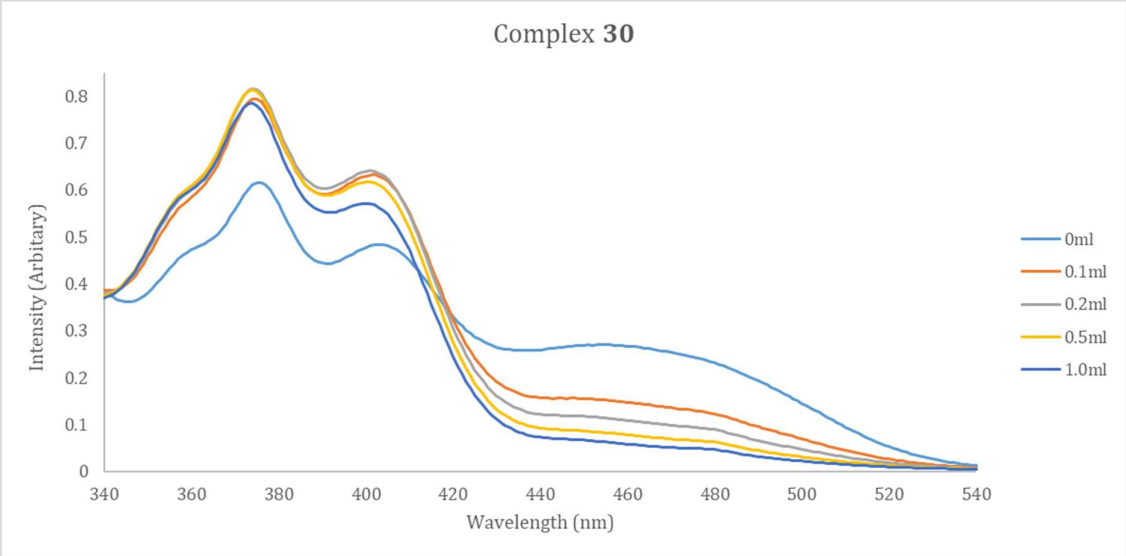

Figure 7.24*: Solution state spectroscopy of Complex **30**, solution concentration 1×10^{-4}M in MeOH. Acid used: ρ-tolylsulphonic acid, concentration, 1×10^{-3} M in MeCN.*

The solution state emission spectrum was measured in tandem with that of the UV-Vis spectra and the results are shown in Figure 7.25. Unfortunately, no change in emission profile was observed upon protonating complex **30**. Further investigations of the luminescence of this complex are required before final conclusions can be drawn.

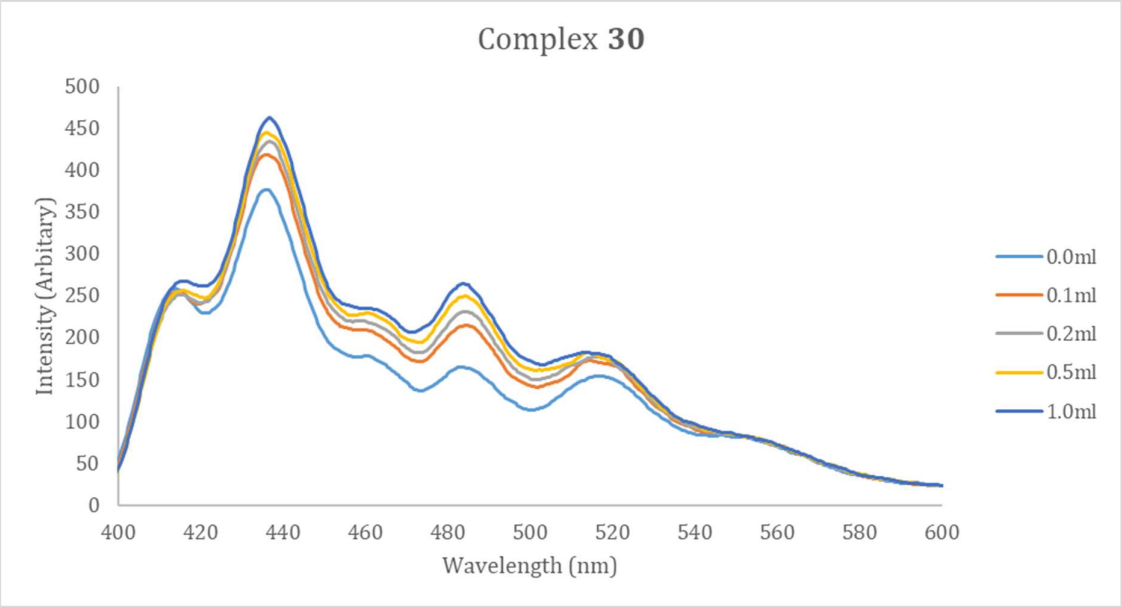

Figure 7.25*: Solution state spectroscopy of Complex **30**, solution concentration 1×10^{-4} M in MeOH. Acid used: ρ-tolylsulphonic acid, concentration, 1×10^{-3} M in MeCN. λ_{ex} 380 nm.*

In addition to investigating the solution state properties of this complex, initial studies were carried out in the solid state. The results are illustrated in Figure 7.26.

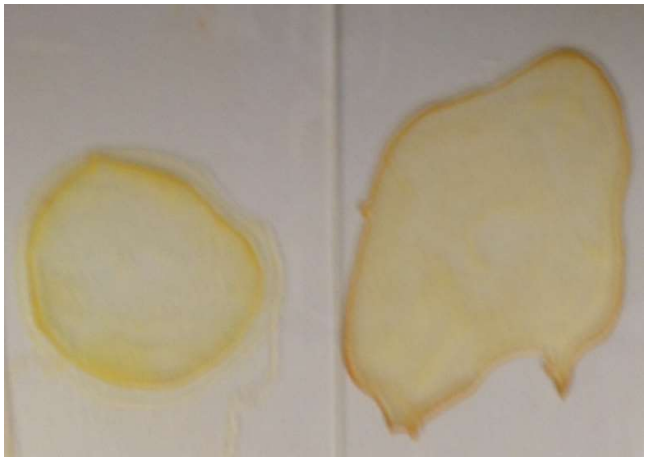

Figure 7.26*: LHS: Thin film of Complex **30**, deposited from a concentrated MeOH solution. RHS: Thin film of complex **30** after exposure to acidic vapour.*

The colour change in solid-state takes approximately a minute to take effect and the colour is very similar to the initial thin film. Due to equipment restraints, quantitative studies could not be conducted. However, the applications for this complex would be limited in the solid-state due to its slow response in comparison to similar literature vapochromic compounds.[93] In addition only a slight colour change has been observed in the solid state, which will make it more challenging to follow the process.

7.4.4 Crystal Structure Analysis

Crystal Structure

Repeated attempts were made to grow yellow crystals of complex **30**, however each attempt produced either powder or non-crystalline material. However, a red polymorph, grown from a vapour diffusion of hexane into a concentrated methanol solution at -18°C, of complex **30** was found suitable for single crystal diffraction. The results will be discussed here to ascertain whether the change in colour is caused by Pt…Pt stacking or π interactions in the solid state.

The crystal structure of complex **30** is shown in Figure 7.27. It crystallises in the orthorhombic space group *Pbcn*. Red block crystals were grown from a vapour diffusion of hexane into a concentrated methanol solution at -18°C. Methanol and hexane are not miscible; however, the crystal grew at the interface between the two solvents at this low temperature. There are no molecules of solvent in the unit cell. Extended crystal and refinement data is found in Table 7.8.

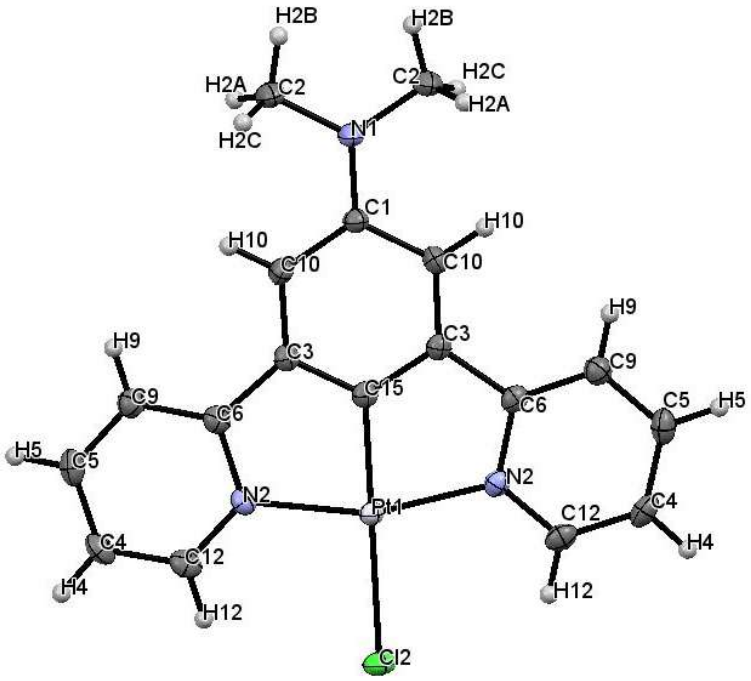

Figure 7.27*: Crystal structure of Complex **30**, red form. Ellipsoids shown at 50%.*

Table 7.8: *Crystal data and structure refinement for Complex **30***

Identification code	P17prr465
Empirical formula	$C_{18}H_{16}ClN_3Pt$
Formula weight	504.88
Temperature/K	150
Crystal system	orthorhombic
Space group	Pbcn
a/ Å	13.2733(4)
b/ Å	12.7623(3)
c/ Å	9.3713(3)
α/°	90
β/°	90
γ/°	90
Volume/ Å^3	1587.48(8)
Z	4
ρ_{calc}g/cm^3	2.112
μ/mm^{-1}	9.009
F(000)	960.0
Crystal size/mm^3	0.4 × 0.5 × 0.2
Radiation	MoKα (λ = 0.71073)
2Θ range for data collection/°	6.138 to 52.744
Index ranges	-16 ≤ h ≤ 16, -15 ≤ k ≤ 15, -11 ≤ l ≤ 11
Reflections collected	24354
Independent reflections	1623 [R_{int} = 0.0314, R_{sigma} = 0.0118]
Data/restraints/parameters	1623/0/108
Goodness-of-fit on F^2	1.049
Final R indexes [I>=2σ (I)]	R_1 = 0.0124, wR_2 = 0.0243
Final R indexes [all data]	R_1 = 0.0207, wR_2 = 0.0268
Largest diff. peak/hole / e Å^{-3}	0.39/-0.39

In the crystal, molecules of **30** sit on a crystallographic mirror plane passing through N1, C1, C15, Pt1 and Cl2, so that the asymmetric unit contains half a molecule. The Pt(II) centre adopts the expected square planar geometry with a distortion in the N2-Pt1-N2' bond angle, which is attributed to the bite angle of the pincer ligand.[93] All other bond lengths and angles fall within expected ranges.

The torsion angles provided in Table 7.9c show that the molecule is planar by crystallographic symmetry. The dihedral angle between the following two planes was measured at 0.47°:

- Plane 1: N2 C3 C6 Pt1
- Plane 2: C5 C9 C4 C6 C12 N2.

This planarity in the solid state is a good indication that the complex could contain Pt-Pt stacks. The crystal packing of **30** will be discussed later.

Table 7.9: *a. Table of bond lengths for **30**. b. Table of bond angles for **30**. c. Torsion angles for **30**.*

a. Bond Lengths		
Atom	**Atom**	**Length/ Å**
Pt1	Cl2	2.4089(8)
Pt1	N2	2.037(2)
Pt1	C15	1.910(3)
N1	C2	1.449(3)

b. Bond Angles			
Atom	**Atom**	**Atom**	**Angle/°**
N2	Pt1	Cl2	99.62(6)
N2	Pt1	N2[1]	160.77(11)
C15	Pt1	Cl2	180.0
C1	N1	C2	120.47(14)

[1]1-X,+Y,1/2-Z

c. Torsion Angles				
A	**B**	**C**	**D**	**Angle/°**
C2	N1	C1	C10	0.2
C12	Pt1	N2	C12	0.3
Pt1	C15	C3	C6	-0.7
C15	C3	C10	C1	0.4

OLEX 2[121] was used to investigate the potential π-π interactions in **30**. Two planes were found between which stacking interactions occurred. Data is provided in Table 7.10.

Table 7.10: *a. Planes Present in solid-state structure for **30**. b. π-π Interactions for **30**. c. Hydrogen bonds for **30**.*

a. Plane Identification	
Plane Number	Atoms in plane
1	C3 C15 C1 C10
2	N2 C12 C4 C5 C9 C6

b. π-π Interactions	
Planes	Distance (Å)
1-2	3.528

c. Hydrogen bonds			
Atoms	(D…A) Distance (Å)	(H…A) Distance (Å)	D…H…A Angle/°
C2-H2B-Cl2	3.756	2.8117	167.8
C5-H5-Cl2	3.580	2.7613	147.4

The π-π interactions occur between the segments of the pincer ligand that overlap in the solid-state structure as shown in figure 7.28. However, unlike other complexes in this thesis the Pt centres do not stack in the solid state.

In addition to the π-π interactions there are also intermolecular hydrogen bonds present between the chloride and the -NMe_2 as well as the chloride and the adjacent pincer molecule. This helps hold the complex in a herringbone structure as shown in Figure 7.28.

Crystal Packing

Figure 7.28 illustrates the crystal packing of complex **30** in different orientations. This complex displays the herringbone pattern in the solid state (Figure 7.28a) observed with **28** and **29.** Closer analysis of the packing reveals the complex has stacked head to tail, Figure 7.28c. Therefore, Pt

stacking has no effect on the colour of this complex. However, the two molecules are close enough in the solid state for π interactions, which may have induced the deep red colour.

The amine group in this complex sits parallel to the rest of the N^C^N pincer. In the yellow form there may be a torsion angle associated with the amine group which could give rise to different packing and close contacts in that non-crystalline polymorph.

The results of the void space analysis showed there was no void space in the structure for solvent to occupy consistent with the other complexes in this chapter. Should the yellow form have the same lack of void space this could explain the slow response time to acidic vapour in the solid state. Chapter 5 discussed how rapid vapochromic responses are observed when there are channels of void space in the solid-state structure for the solvent to move in and out of. The same solid-state phenomenon would be required for a rapid response to acidic vapour in the solid state.

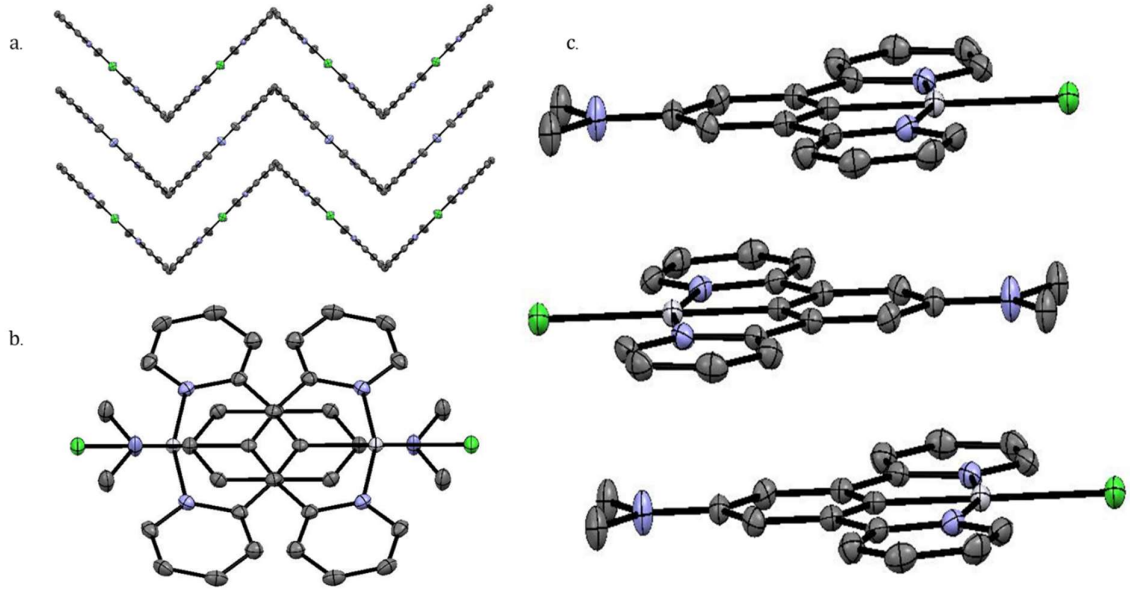

Figure 7.28: *a. View of complex **30** along the 'b' axis at 150 K. b. View of complex **30** along the 'c' axis at 150 K. c. Stacking motif of complex **30**. Ellipsoids shown at 50% probability. Hydrogens have been removed for clarity.*

7.5.0 Conclusion

In this chapter the use of computational techniques used initially in chapter 6 was further developed. In this instance computational techniques were used to predict the pH sensing behaviour of 3 novel complexes. Each of the complexes synthesised in this chapter showed pH sensing behaviour in the solution state with complex **30** showing '*switching'* behaviour in the solid state.

Complex **28**, displayed consistent behaviour in response to acidified solution both in the UV-Vis absorption and emission spectra, however, initial studies suggested this could not be reversed with base. The advantage with the pH sensing behaviour of **29** was that it did not require a heavy metal and would therefore be a significantly cheaper option; however, it has limitations in regards its potential for use as a solid-state sensor. While this example may not have the required characteristics for solid-state sensing there are a number of organic amides in the literature which have been designed for acid-base sensing.[154, 155] These examples in the literature use the hydrogen bonding networks that occur in supramolecular frameworks to illicit anion recognition through fluorescence. In addition to acid-base sensing, they can be readily adapted to sense for small anions such as fluoride and cyanide.

Finally, complex **30** showed the most interesting behaviour; however, it would need to be further developed, as the spectral changes observed are not significant enough for this application. One way to develop this complex would be to try and introduce void space into the crystal structure to further facilitate the potential for solid state sensing. This could be achieved by changing the ligand in the 4th co-ordination site, as investigated for vapochromic complexes in Chapter 5.

CHAPTER 8

Conclusion and Future Work

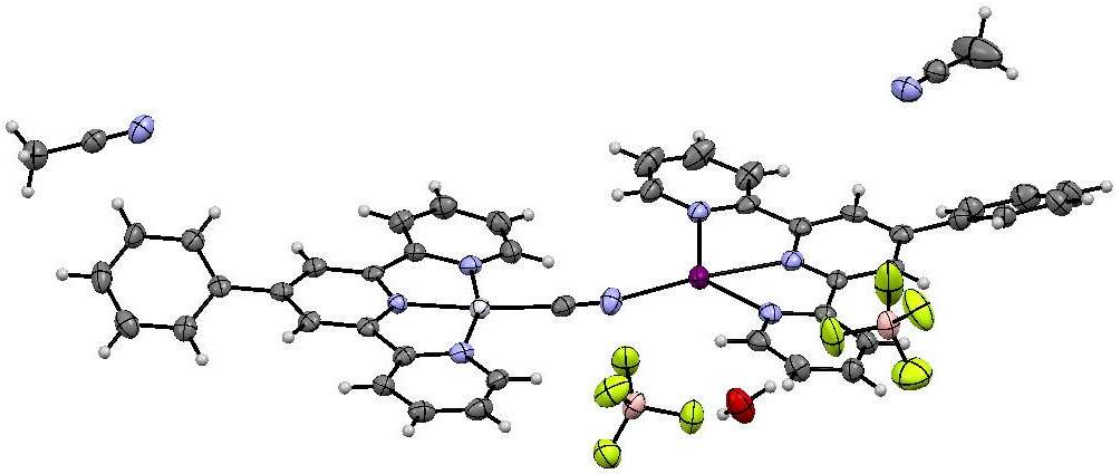

8.1.0 Conclusion

The overall goal of this thesis was to develop a series of novel Pt(II) pincer complexes to further our understanding of why these complexes undergo spectral changes in the solid state. This thesis started by investigating the field of Pt(II) terpyridine complexes. A couple of the complexes detailed in chapter 4 were already known in the literature,[43, 44, 110, 117] however new spectral properties were observed in some of these known complexes. Complex **2** was of particular interest as it underwent a distinct transition in the solid state upon the removal or addition of water without recrystallizing the complex. The complex was red in the presence of water and upon dehydration, it changed from red to yellow. A further blue form could be accessed by recrystallization from water/acetone solvent mixtures.

This systematic study of the terpyridine complexes revealed that a series of factors affect the observed spectral properties including the nature of solvates, counter-ion and void space in the crystal structure. The complexes with the largest of the counter-ions did not show any changes in spectral properties as originally hypothesised primarily because of the lack of Pt…Pt stacking interactions in the solid state. In contrast, the complexes that used the tosylate counter-ion, which is a large counter-ion, displayed interesting physical, chemical and spectral properties. For example, complex **9**, upon recrystallization from methanol the complex turned from yellow to red. Pt(II) complexes tend to have limited solubility in polar solvents; however, the introduction of the tosylate group seemed to enhance the solubility of the complex. This could be attributed to the extended hydrogen-bonding network observed with the complex, which is facilitated by the functional groups on the tosylate counter-ion.

The research focus then evolved to investigate Pt(II) complexes with an N^C^N pincer ligand. Research in the field has found that the presence of the arene ring increases the emission intensity of the complex.[18] The presence of increased emission intensity also provides an alternative spectral change, by the switching on and off of emission.[66, 151] In chapter 5 the functionalisation of Pt(II) N^C^N complexes was investigated. The aim of the research presented in this chapter was to further build on the research previously conducted in the Raithby group,[93] and to investigate the emission profile of these complexes. The spectrochemical series was used to build a series of complexes that the ligand field strength increased between the chloride[47] (weak field) and the cyanide[93] (strong field) ligand. The ligands NCS^- and NCO^- were used to achieve this. Unfortunately, neither of these complexes showed any spectral changes, this was attributed to the length of the ligand, which was now three atoms. This seemed to disrupt the solid state packing so the Pt centres were too far apart for any Pt…Pt orbital overlap to occur.

However, further investigation on varying the ligands in the 4th coordination site of the square planar Pt(II) complexes revealed several new materials that *'switch'* in the solid and solution state. The first of these was complex **18**, which utilised an acetate group. This complex had three distinct forms, unfortunately these were not fully characterised by single crystal crystallography due to the difficulty in growing crystals that corresponded to the powder form of the complex. Subsequent complexes incorporated tosylate and a CF_3 functional group in their structure, complexes **19-21.** These complexes displayed complex behaviour in both the solution and solid state, with solvatochromic and vapochromic behaviour observed. The incorporation of the tosylate group had the same effect that was observed with the terpyridine complex and changed the solubility of the compound. These Pt(II) complexes are usually only sparingly soluble in chlorinated solvents, however upon manipulation of the ligand the complexes would dissolve in

a number of polar solvents such as methanol. The solvatochromic effect meant that changes were observed in both the UV-Vis and emission spectra. The emission of the complex in the solution state was never *'switched'* off but was often shifted in energy and the presence of excimers was affected. While the introduction of these functional groups stimulated fascinating spectral changes, unfortunately the complexes could not be studied in the solid state. This is because crystals suitable for single crystal diffraction could not be grown due to the solubility of the complex.

The change in physical property observed for complexes **19-21** caused by the functional group led the way for the research presented in chapters 6 and 7. In these chapters, the complexes were functionalised for a specific purpose, photo-switching and pH sensing, respectively. In these chapters, the research focussed on the effect on varying the position of the functional group and using computational studies to predict the behaviour of the complex.

Azobenzene and stilbene groups were chosen as the focus of study for the photo-switching groups due to the expansive literature available on the switching properties of complexes containing these groups.[124, 129, 136, 142, 156, 157] Initially computational studies were conducted to determine the best substitution pattern that would facilitate the *'switch'* of the azobenzene/ stilbene group. It was discovered that the photo-switching group needed to be located on the pincer for the *'switch'* to occur due to orbital arrangement. This was subsequently proven correct experimentally, as complex **22** which had been functionalised via an acetylide did not switch when irradiated with UV light. However, the functionalised pincer, **23**, did switch in the solution state when exposed to UV-light and this isomerisation could be revered with visible light. Investigation of the isomerisation in the solid-state using reflectance spectrometry showed that the complex does not isomerise in the solid state. It is thought that the azobenzene group is too large to isomerise in the solid state causing too much distortion to the solid state packing. The functionalised pincer could not then be cyclometallated with a pincer ligand to investigate the effect of the Pt centre on the isomerisation process.

The stilbene functional group was investigated in the same way with both a functionalised pincer, **27**, and functionalised acetylide, **25**, being synthesised. In this instance the stilbene functionalised pincer was an already known complex,[144] however it was being investigated for a different property in this thesis. As with the azobenzene group the stilbene functional group, when located on the N^C^N pincer ligand, underwent a *cis-trans* isomerisation when irradiated with UV-light in the solution state, however the same transition did not occur in the solid state, Figure 6.38. The main difference between when the pincer is free in solution or cyclometallated to the Pt centre is the energy of the emission profile. The emission went from blue to green, which has been seen with a number of complexes in this thesis.

The final results chapter in this thesis explored the synthesis of pH sensitive Pt(II) complexes. There are a limited number of pH sensitive Pt(II) complexes in the literature which use the N^C^N pincer configuration, hence the focus for this chapter.[47, 151] Initially the functional group NH_2 was chosen, however due to synthetic difficulties the NH_2 group needed protecting to stop it reacting with the Pt centre or solvent during the cyclometallation process. A methyl group was chosen as the protecting group; however, it was found that the complexes with the methyl group had interesting spectral properties and therefore these complexes became the focus of this chapter.

The complex was functionalised in two different places as with the photo-switching complexes in chapter 6, however in this case both of the complexes were sensitive to acid/basic solutions in the solution and solid state. However, the responses to the vapours were different between the two complexes. In addition it was found that the solution state emission of complex **28** was switched on upon protonation, a similar phenomenon had been seen in the literature.[151] These complexes where novel and showed promise as pH sensing materials.

During the course of this thesis, a series of novel Pt(II) pincer complexes have been developed that showed interesting spectral properties in addition to re-investigating some terpyridine complexes that had been reported previously from a different perspective. Patterns have been discovered in reactivity and solubility that have allowed the development of a more detailed methodology for the synthesis of smart materials. The ligand in the fourth coordination site on the square planar Pt(II) complexes has been shown to be key in the manipulation of the luminescence and switching properties of these new materials from both the electronic and steric viewpoints.

8.2.0 Future Work

This thesis has thoroughly investigated the reasons behind various spectral properties of Pt(II) complexes. The work developing vapochromic and solvatochromic materials has shown that the properties of these complexes are often difficult to predict and complex to analyse. Therefore the use of computational models to predict this behaviour is not yet fully reliable, however it is useful when analysing the observed behaviour of these complexes. Therefore, in future it would be productive to focus research on results obtained in the last two results chapters, which incorporated specific functionalities into the complexes.

An example would be to investigate the use of smaller photo-switching moieties that could *'switch'* in the solid state because the azobenzene and stilbene groups were too large for this to occur. The first step in this research would be to consider the orbital configurations of the complexes, before synthesising the complexes, as this proved to be a valuable tool in chapters 6 and 7. Potential groups would be NO_2 and SO_2 groups due to their potential for linkage isomerism,[158-161] however, for this process to occur the groups would need to be attached to the metal centre as opposed to the pincer ligand. It is therefore vital that the orbitals of the ground and excited states are carefully considered.

While there are not rules that can yet be followed to guarantee a complex that will undergo specific spectral changes. It is clear that there are a number of factors that need to be controlled when designing these complexes. One of the most important factors is controlling the sterics and planarity of the complex as this allows closer packing in the solid state.

While continuing the themes of this thesis is important in future research to consider other lines of enquiry is a necessity. One area worthy of further investigation is the use of other d^8 metals in neutral square planar complexes to determine whether similar metal-metal interactions could be manipulated. Metals of interest would be palladium, silver and gold. Square planar complexes of these metals are widely known in the literature for catalysis and nanoparticle applications,[162-165] however their use as chemical sensors is not widely reported. One potential issue with this area of research is the cyclometallation of the metals into the correct pincer configuration, for Pd and N^C^N pincer can be used but for Ag and Au a C^N^C pincer will have to be used to maintain neutrality. There are a few examples of gold C^N^C complexes in the literature,[166, 167] the synthesis of these complexes requires an additional transmetallation step to cyclometallate the Au(III). Preliminary studies conducted used the literature method of Hg(II) for the transmetallation step. This was successful in preparing the compound detailed in the literature, however when the pincer was functionalised the yield for the reaction fell and a number of unwanted side products were formed. In future studies would have to be conducted to determine the most effective synthetic pathway before these complexes could be analysed for their spectral properties.

Another area for future development would be the synthesis of bridged mixed metal complexes, figure 8.1. This would be an interesting area of future study because of the mixed metal-metal interactions that could form between hetero-metal complexes and the resultant manipulation of their observable spectral properties.

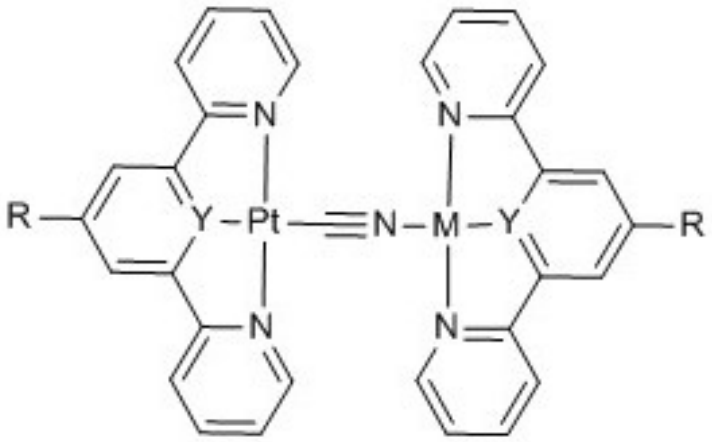

Figure 8.1: Potential structure for a mixed metal bridged complex, where R= Functional group, Y= C/N and M=Ag/Au/Pt/Pd

Finally the overall aim of developing these materials would be to incorporate them into a device. Preliminary work has been focused on incorporating the material into a matrix that could be subsequently coated onto a surface. This has yielded some promising results however the matrix used will vary dependant on the final purpose of the device.

CHAPTER 9

Experimental

9.1.0 General notes.

9.1.1 Instrumentation.

NMR.

The ^{1}H and ^{13}C NMR spectra were measured on a Bruker Avance 300 MHz, 400 MHz or a Agilent 500 MHz spectrometer. The chemical shifts are expressed in parts per million (ppm) and are referenced to either d^{6}-DMSO, $CDCl_3$ or CD_3CN.

The program MNOVA was used to analyse the NMR spectra.

Infrared Spectroscopy

Solid State: IR spectra were collected on the Perkin Elmer, Spectrum 100 FT-IR Spectrometer as neat solids.

UV-Visible Spectroscopy.

UV-Vis spectra were collected on a PerkinElmer Lamda25 spectrometer. The wavelength range was between 230-800 nm. The standard run parameters have been used to collect each of the spectra.

Light excitation UV-Vis was carried out by using a light box fitted with two UV lamps, with the wavelengths 245 nm and 365 nm available, the wavelength used is specified in the report.

Data was exported in the ASCII format and manipulated in Microsoft Excel.

Photoluminescence Spectroscopy.

Photoluminescnce spectroscopy was performed using a PerkinElmer LS55 spectrometer. The excitation wavelengths have been quoted in the results.

Data was exported in the ASCII format and manipulated in Microsoft Excel.

Reflectance Data.

Measured on an Ocean Optics Maya Spectrometer

Data was exported in ASCII format and manipulated in Microsoft excel.

Crystallography.

Single crystal experiments were carried out using the following instruments:

- University Of Bath: Agilent technologies SuperNova diffractometer.
- University Of Bath: Agilent technologies Excalibur diffractometer.
- University of Bath: Agilent technologies Gemini A Ultra diffractometer, fitted with an Atlas CCD detector.
- Advanced Light Source, Lawrence Berkeley National Laboratory, USA: Bruker APEX II CCD diffractometer.

Each diffractometer was equipped with an Oxford Systems Cryostream.

The program OLEX 2[121] was used to solve and refine structures In conjunction with the SHELX suite of programs[168]. Structures were solved using direct methods with SHELXS[169] or SHELXT[170] and refined using SHELXL[171].

9.1.2 Synthesis.

For complexes synthesised in the absence of air and moisture standard Schlenk techniques were employed, under an atmosphere of dry argon. All solvents used in the air sensitive procedures were taken from the dry solvent still and stored over molecular sieves. Glassware was prepared using flame drying techniques. Reaction mixtures were degassed using freeze pump thaw techniques.

All chemicals were purchased from a commercial source and used as received unless otherwise stated.

9.1.3 Crystallisations

The crystallisation of Pt(II) complexes poses a challenge due to there preference for forming crystals with a plate morphology. The common solvents detailed in the thesis were used as these were the most successful. However alternative solvents such as DMF, nitromethane, di-isopropyl ether, toluene and benzonitrile were also used. It was noted that no spectral changes occurred with the use of these solvents suggested the complexes synthesised in this thesis were not sensitive to these solvents.

9.1.4 NMR

^{1}H was used throughout this thesis to confirm the structure of the synthesised complexes. In addition to this techniques, ^{13}C and ^{195}Pt NMR were also investigated. However due to the poor solubility of these complexes the solutions were of too low a concentration to get meaningful spectra.

9.2.0 Terpyridine Complexes.

9.2.1 2,2':6',2''-terpyridine Platinum Chloride Tetrafluoroborate. (**1**)

$[PtCl_2(PhCN)_2]$ (0.10 g, 0.21 mmol) was charged to a round-bottomed flask equipped with a stirrer bar and dissolved in 15 ml of acetonitrile. $AgBF_4$ (0.041 g, 0.21 mmol) was added to the yellow solution. The reaction mixture was heated at reflux for 18h. The reaction mixture was subsequently cooled and the white precipitate (AgCl) was filtered off. The solution was retained and charged to a round bottomed flask (RBF) to this 2,2':6',2''-terpyridine (0.041 g, 0.21 mmol) was added. The reaction mixture was heated at reflux for a further 18h. The reaction mixture was cooled and a vibrant red/ orange precipitate formed. This was then filtered and washed with 10ml of di-ethyl ether to give the product. Single crystals were grown from the slow evaporation of acetonitrile.

Yield: 0.066 g/ 57%

FTIR-ν_{max}(cm^{-1}): 3085 (w, br), 1603 (sh), 1030 (sh, br).
^{1}H NMR (300 MHz, DMSO-d^6): δ 8.71 (dd, $^3J_{H-H}$ = 5.7, 1.4 Hz, 2H), 8.61 – 8.53 (m, 5H), 8.47 (td, $^3J_{H-H}$ = 7.9, 1.5 Hz, 2H), 7.88 (ddd, $^3J_{H-H}$ = 7.5, 5.6, 1.5 Hz, 2H).
Theoretical CHN(%): C 32.72, H 2.01, N 7.62
Experimental CHN(%): C 32.53, H 2.03, N 7.79

CIF file available in supplementary information.

9.2.2 2,2':6',2''-terpyridine Platinum Chloride Tetrafluoroborate. (**2**)

Complex **1** was re-crystallised from a mixture of water and acetone in varying ratios.
CIF file available in supplementary information.

9.2.3 4'-phenyl-2,2':6',2''-terpyridine

A 1.5M NaOH solution was added to a solution of benzaldehyde (0.36 ml, 0.35 mmol) and 2-acetylpyridine (0.80 ml, 0.70 mmol) in 15 ml of ethanol. The solution was stirred at room temperature for 18h. The white precipitate was collected *via* filtration and washed with ethanol. The solid was subsequently suspended in 10 ml of ethanol and added in small portions to an excess of ammonium acetate in ethanol and heated to 86°C. The yellow solution was stirred for 18 h at 86°C. The solution was cooled and the yellow precipitate was collected *via* filtration and washed with ethanol. The final product was yellow and single crystals were grown from the slow evaporation of THF.

Yield: 0.48 g/ 44%

FTIR-ν_{max}(cm^{-1}): 1582 (sh), 1548 (sh), 1466 (sh), 1390 (sh).
^{1}H NMR (400 MHz, Chloroform-d): δ 8.78 – 8.64 (m, 6H), 7.95 – 7.81 (m, 4H), 7.56 – 7.41 (m, 3H), 7.36 (ddd, $^3J_{H-H}$ = 8.2, 5.2, 1.5 Hz, 2H).

CIF file available in supplementary information.
Data consistent with literature.[108]

9.2.4 4'-phenyl-2,2':6',2''-terpyridine Platinum Chloride Tetrafluoroborate. (**3**)

$[PtCl_2(PhCN)_2]$ (0.10 g, 0.21 mmol) was charged to a round-bottomed flask equipped with a stirrer bar and dissolved in 10ml of acetonitrile. $AgBF_4$ (0.041 g, 0.21 mmol) was added to the yellow solution. The reaction mixture was heated at reflux for 18 h. The reaction mixture was subsequently cooled and the white precipitate (AgCl) was filtered off. The solution was retained and charged to a RBF to this 4'-phenyl-2,2':6',2''-terpyridine (0.066 g, 0.21 mmol) was added. The reaction mixture was heated at reflux for a further 18h. The reaction mixture was cooled and the solvent removed in *vacuo* until a precipitate formed. This was then filtered and washed with 10 ml of di-ethyl ether to give the product as a brick red solid. Single crystals were grown from the slow evaporation of acetonitrile.

Yield: 0.11 g/ 90%

FTIR-ν_{max}(cm^{-1}): 3091 (w, br), 2983 (w, br), 1610 (sh), 1028 (s).
^{1}H NMR (300 MHz, DMSO-d_6): δ 8.89 (s, 2H), 8.80 – 8.67 (m, 4H), 8.45 (td, $^3J_{H-H}$ = 7.9, 1.5 Hz, 2H), 8.19 – 8.09 (m, 2H), 7.84 (ddd, $^3J_{H-H}$ = 7.4, 5.6, 1.4 Hz, 2H), 7.73 – 7.64 (m, 3H)
Theoretical CHN(%): C 40.25, H 2.41, N 6.71
Experimental CHN(%): C 40.11, H 2.36, N 6.85

CIF file available in supplementary information.
Data consistent with literature.[43]

9.2.5. 4'-(p-tolyl)-2,2':6',2''-terpyridine Platinum Chloride Tetrafluoroborate (**4**)

$[PtCl_2(PhCN)_2]$ (0.10 g, 0.21 mmol) was charged to a round-bottomed flask equipped with a stirrer bar and dissolved in 10 ml of acetonitrile. $AgBF_4$ (0.041 g, 0.21 mmol) was added to the yellow solution. The reaction mixture was heated at reflux for 18 h. The reaction mixture was subsequently cooled and the white precipitate (AgCl) was filtered off. The solution was retained and charged to a RBF to this 4'-(p-tolyl)-2,2':6',2''-terpyridine (0.068 g, 0.21 mmol) was added. The reaction mixture was heated at reflux for a further 18 h. The reaction mixture was cooled and the solvent removed in *vacuo* until a precipitate formed. This was then filtered and washed with 10 ml of di-ethyl ether to give the product as a yellow solid. Single crystals were grown from the slow evaporation of acetonitrile.

Yield: 0.094 g/ 70%

FTIR-ν_{max}(cm^{-1}): 1602 (w, sh), 1029 (s)
^{1}H NMR (300 MHz, DMSO-d_6): δ 8.85 (s, 2H), 8.80 – 8.62 (m, 4H), 8.45 (td, $^3J_{H-H}$ = 7.9, 1.6 Hz, 2H), 8.07 (d, $^3J_{H-H}$ = 8.2 Hz, 2H), 7.85 (ddd, $^3J_{H-H}$ = 7.4, 5.7, 1.4 Hz, 2H), 7.46 (d, $^3J_{H-H}$ = 8.0 Hz, 2H), 2.44 (s, 3H).
Theoretical CHN(%): C 41.24, H 2.67, N 6.56
Experimental CHN(%): C 39.81, H 2.47, N 6.56

CIF file available in supplementary information.

9.2.6 2,2':6',2''-terpyridine Platinum Chloride hexafluorophosphate . (**5**)

Complex **1** (0.045 g, 0.082 mmol) was dissolved in a 3:1 mixture of acetonitrile to water. NH_4PF_6 (0.0013 g, 0.082 mmol) was added and the product precipitated as an orange solid. The solid was

isolated by filtration and washed with di-ethyl ether. Single crystals were grown from the slow evaporation of acetonitrile.

Yield: 0.027 g/ 54%

FTIR-ν(cm^{-1}): 3101 (w, br), 1606 (w, sh), 831 (s).
^{1}H NMR (300 MHz, DMSO-d): δ 8.76 (dd, $^{3}J_{H-H}$ = 5.6, 1.4 Hz, 2H), 8.65 – 8.55 (m, 5H), 8.48 (td, $^{3}J_{H-H}$ = 7.9, 1.5 Hz, 2H), 7.90 (ddd, $^{3}J_{H-H}$ = 7.4, 5.7, 1.4 Hz, 2H).
^{31}P NMR (300 MHz, DMSO-d): δ -131.62- -155.03 (m)
Theoretical CHN(%): C 29.59, H 1.82, N 6.90
Experimental CHN(%): C 29.82, H 1.86, N 6.74

Data consistent with the literature.[44]

9.2.7 4'-phenyl-2,2':6',2''-terpyridine Platinum Chloride Hexafluorophosphate. (**6**)

Complex **2** (0.030 g, 0.048 mmol) was dissolved in a 2:3 mixture of acetonitrile to water. NH_4PF_6 (0.0088 g, 0.054 mmol) was added and the product precipitated as a yellow solid. The solid was isolated by filtration and washed with di-ethyl ether.

Yield: 0.032 g/ 97%

FTIR-ν_{max}(cm^{-1}): 3053 (w, br), 2983 (w, br), 787 (sh), 764 (sh), 735 (sh), 706 (sh).
^{1}H NMR(300 MHz, DMSO-d_6): δ 8.94 (s, 2H), 8.85 – 8.74 (m, 4H), 8.49 (td, $^{3}J_{H-H}$ = 7.9, 1.5 Hz, 2H), 8.17 (dd, $^{3}J_{H-H}$ = 6.7, 3.0 Hz, 2H), 7.89 (ddd, $^{3}J_{H-H}$ = 7.4, 5.6, 1.3 Hz, 2H), 7.75 – 7.65 (m, 3H).
^{31}P NMR(300 MHz, DMSO-d): δ -131.62- -155.03 (m)
Theoretical CHN(%): C 36.83, H 2.21, N 6.14
Experimental CHN(%): C 36.89, H 2.12, N 6.27

CIF file available in Supplementary information.

9.2.8 4'-(p-tolyl)-2,2':6',2''-terpyridineplatinumChloride Hexafluorophosphate (**7**)

Complex **3** (0.033 g, 0.050 mmol) was dissolved in a 3:2 mixture of acetonitrile to water. NH_4PF_6 (0.0080 g, 0.050 mmol) was added and the product precipitated as a dark yellow solid. The product was collected by filtration and washed with di-ethyl ether.

Yield: 0.018 g/ 52%

FTIR-ν_{max}(cm^{-1}): 1603 (w, sh), 831 (s).
^{1}H NMR (300 MHz, DMSO-d_6): δ 8.89 (s, 2H), 8.84 – 8.74 (m, 4H), 8.48 (td, $^{3}J_{H-H}$ = 7.8, 1.5 Hz, 2H), 8.09 (d, $^{3}J_{H-H}$ = 8.1 Hz, 2H), 7.94 – 7.82 (m, 2H), 7.47 (d, $^{3}J_{H-H}$ = 8.1 Hz, 2H), 2.44 (s, 3H).
^{31}P NMR(300 MHz, DMSO-d): δ -131.62- -155.03 (m)
Theoretical CHN(%): C 37.81, H 2.45, N 6.01
Experimental CHN(%): C 37.54, H 2.08, N 5.85

CIF file available in Supplementary information.

9.2.9. 2,2':6',2''-terpyridine Platinum Chloride Tosylate (**8**)

$[PtCl_2(PhCN)_2]$ (0.10 g, 0.21 mmol) was charged to a round-bottomed flask equipped with a stirrer bar and dissolved in 15ml of acetonitrile. AgOTs (0.060 g, 0.22 mmol) was added to the yellow solution. The reaction mixture was heated at reflux for 18h. The reaction mixture was subsequently cooled and the grey precipitate (AgCl) was filtered off. The solution was retained and charged to a round bottomed flask (RBF) to this 2,2':6',2''-terpyridine (0.041 g, 0.21 mmol) was added. The reaction mixture was heated at reflux for a further 18 h. The reaction mixture was cooled and the solution reduced in *vacuo* to yield a red solid. This was then subsequently washed with ethanol and diethyl ether. Single crystals were grown from a vapour diffusion of diethyl ether into a saturated methanol solution at -18˚C.

Yield: 0.11 g/ 85%

FTIR-$\nu_{max}(cm^{-1})$: 3072(w,Br), 1603 (s), 1399 (s), 815(s)
^{1}H NMR(300 MHz, DMSO-d): δ 8.89 (2 H, dd, *J* 5.9, 1.5), 8.70 – 8.58 (6 H, m), 8.51 (2 H, td, $^3J_{H-H}$ = 7.9, 1.5), 7.95 (2 H, ddd, *J* 7.5, 5.7, 1.5), 7.46 (2 H, d, *J* 8.1), 7.15 – 7.06 (2 H, m), 2.28 (4 H, s).
Theoretical CHN(%): C 41.61, H 2.86, N 6.62
Experimental CHN(%): C 41.40, H 2.58, N 6.57

CIF file available in the supplementary

9.2.10 4'-phenyl-2,2':6',2''-terpyridine Platinum Chloride Tosylate. (**9**)

$[PtCl_2(PhCN)_2]$ (0.10 g, 0.21 mmol) was charged to a round-bottomed flask equipped with a stirrer bar and dissolved in 10ml of acetonitrile. AgOTs (0.060 g, 0.22 mmol) was added to the yellow solution. The reaction mixture was heated at reflux for 18 h. The reaction mixture was subsequently cooled and the white precipitate (AgCl) was filtered off. The solution was retained and charged to a RBF to this 4'-phenyl-2,2':6',2''-terpyridine (0.066 g, 0.21 mmol) was added. The reaction mixture was heated at reflux for a further 18 h. The reaction mixture was cooled and the solvent removed in *vacuo* until a precipitate formed. This was then filtered and washed with 10 ml of di-ethyl ether to give the product as a brick red solid. Single crystals were grown from the vapour diffusion of diethyl ether into a saturated methanol and acetonitrile solution at -18˚C.

Yield: 0.12 g/ 80%

FTIR-$\nu_{max}(cm^{-1})$: 3512 (m), 3042 (w, Br), 1606 (s), 1414(s), 811(s)
^{1}H NMR(300 MHz, DMSO-d): δ 9.00 (2H, s), 8.96 – 8.82 (4H, m), 8.55 (2 H, td, $^3J_{H-H}$ = 7.9, 1.5 Hz), 8.20 (2H, dd, $^3J_{H-H}$ = 6.8, 2.9 Hz), 7.95 (2H, ddd, $^3J_{H-H}$ = 7.2, 1.4 Hz), 7.70 (3 H, dd, $^3J_{H-H}$ = 5.1, 1.8 Hz), 7.51 – 7.41 (2 H, m), 7.10 (2 H, d, $^3J_{H-H}$ = 7.6), 2.28 (4 H, s).
Theoretical CHN(%): C 47.29, H 3.12, N 5.91
Experimental CHN(%): C 43.99, H 3.07, N 6.41

CIF file available in the supplementary information.

9.2.11. 4'-(p-tolyl)-2,2':6',2''-terpyridine Platinum Chloride Tosylate (**10**)

Complex 3 (0.045 g, 0.070 mmol) was dissolved in a 1:1 mixture of acetonitrile to water. NaOTs (0.016 g, 0.084 mmol) was added. Yellow solid precipitated immediately. The product was isolated by filtration and washed with di-ethyl ether. Single crystals were grown from the slow evaporation of acetonitrile.

Yield: 0.040 g/ 79%

FTIR-ν_{max}(cm^{-1}) = 3488 (w, br), 3423 (w, br), 3060 (w, br), 1604 (sh), 1481 (sh), 1404 (sh), 1199 (m).
^{1}H NMR (300 MHz, DMSO-d_6) δ 8.95 (s, 2H), 8.92 – 8.79 (m, 4H), 8.52 (t, $^3J_{H-H}$ = 7.8 Hz, 2H), 8.12 (d, $^3J_{H-H}$ = 8.0 Hz, 2H), 7.93 (t, $^3J_{H-H}$ = 6.8 Hz, 2H), 7.48 (t, $^3J_{H-H}$ = 7.8 Hz, 4H), 7.15 – 7.06 (m, 2H), 2.44 (s, 3H), 2.28 (s, 3H).
Theoretical CHN(%): C 48.04, H 3.34, N 5.80
Experimental CHN(%): C 47.90, H 3.20, N 5.90

CIF file available in the supplementary information.

9.2.12. 2,2':6',2''-terpyridine Platinum Chloride Tetraphenylborate (**11**)

Complex **1** (0.030 g, 0.054 mmol) was dissolved in 1:3 acetone to water mixture. $NaBPh_4$ (0.019 g, 0.054 mmol) was added and product precipitated immediately. Brown solid was collected by filtration and single crystals were grown from the vapour diffusion of di-ethyl ether into a concentrated acetonitrile solution.

Yield: 0.023 g/ 54%.

FTIR-ν_{max}(cm^{-1}): 3054 (w, br), 1607 (w, sh), 1455 (m, sh).
^{1}H NMR (300 MHz, DMSO-d_6) δ 8.86 (dd, $^3J_{H-H}$ =5.7, 1.4 Hz, 2H), 8.66 – 8.59 (m, 5H), 8.50 (td, $^3J_{H-H}$ = 7.9, 1.5 Hz, 2H), 7.93 (ddd, $^3J_{H-H}$ = 7.4, 5.6, 1.4 Hz, 2H), 7.23 – 7.11 (m, 8H), 6.92 (t, $^3J_{H-H}$ = 7.3 Hz, 8H), 6.84 – 6.69 (m, 4H).
Theoretical CHN(%): C 59.82, H 3.99, N 5.37
Experimental CHN(%): C 59.32, H 3.73, N 5.34

CIF file available in supplementary information.

9.2.13 4'-phenyl-2,2':6',2''-terpyridine Platinum Chloride Tetraphenylborate. (**12**)

Complex **2** (0.045 g, 0.072 mmol) was dissolved in 3:2 acetonitrile to water mixture. $NaBPh_4$ (0.025 g, 0.072 mmol) was added and product precipitated immediately. Brown solid was collected by filtration and single crystals were grown from the slow evaporation of an acetonitrile solution.

Yield: 0.042 g/ 68%

FTIR-ν_{max}(cm^{-1}): 3052 (br), 2982 (br), 1607 (s), 1477 (s), 1416 (s).

^{1}H NMR (300 MHz, DMSO-d_6) δ 8.91 (s, 2H), 8.82 – 8.69 (m, 4H), 8.46 (td, $^{3}J_{H-H}$ = 7.9, 1.6 Hz, 2H), 8.16 (dd, $^{3}J_{H-H}$ = 6.6, 3.0 Hz, 2H), 7.85 (td, $^{3}J_{H-H}$ = 6.2, 5.6, 3.2 Hz, 2H), 7.73 – 7.61 (m, 3H), 7.23 – 7.11 (m, 8H), 6.92 (t, $^{3}J_{H-H}$ = 7.3 Hz, 8H), 6.78 (t, $^{3}J_{H-H}$ = 7.2 Hz, 4H).
Theoretical CHN(%): C 62.91, H 4.11, N 4.89
Experimental CHN(%): C 61.08, H 3.89, N 5.26

CIF file available in supplementary information.

9.2.14 4'-(p-tolyl)-2,2':6',2''-terpyridinePlatinumChloride Tetraphenylborate (**13**)

Complex **3** (0.040 g, 0.062 mmol) was dissolved in 1:1 acetonitrile to water mixture. $NaBPh_4$ (0.021 g, 0.062 mmol) was added and product precipitated immediately. Brown solid was collected by filtration and single crystals were grown from the slow evaporation of an acetonitrile solution.

Yield: 0.034 g/ 63%

FTIR-ν(cm^{-1}): 3052 (w, br), 1602 (m, sh), 1476 (m, sh), 1403 (m, sh).
^{1}H NMR (300 MHz, DMSO-d_6): δ 8.87 (s, 2H), 8.82 – 8.70 (m, 4H), 8.46 (td, $^{3}J_{H-H}$ = 7.8, 1.6 Hz, 2H), 8.08 (d, $^{3}J_{H-H}$ = 8.0 Hz, 2H), 7.86 (ddd, $^{3}J_{H-H}$ = 7.3, 5.6, 1.3 Hz, 2H), 7.47 (dd, $^{3}J_{H-H}$ = 7.8, 5.0 Hz, 2H),7.24 – 7.11 (m, 8H), 6.92 (t, $^{3}J_{H-H}$ = 7.3 Hz, 8H), 6.83 – 6.74 (m, 4H), 2.45 (s, 3H).
Theoretical CHN(%): C 63.28, H 4.27, N 4.81
Experimental CHN(%): C 63.81, H 4.13, N 5.44

CIF file available in supplementary information.

9.2.15 2,2':6',2''-terpyridine Platinum Cyanide Tetrafluoroborate. (**14**)

Complex **1** (0.050 g, 0.090 mmol) was charged to a round bottomed flask and 20ml of acetontrile was added. AgCN (0.012 g, 0.090 mmol)was added to this suspension. The reaction mixture was refluxed for 24 h under an argon atmosphere. The reaction was allowed to cool and an orange solid precipitated. The solution was filtered, and the product was dissolved into hot acetonitrile and filtered, while hot to remove the silver chloride. Upon cooling the product precipitated out of the solution and was isolated by filtration. Crystals suitable for single crystal diffraction grown from vapour diffusion of di-ethyl ether into a concentrated acetonitrile solution.

Yield: 0.030 g/60%

FTIR-ν(cm^{-1}): 3042 (w, br), 2148 (s,sh), 1609 (sh), 1032 (s, br).
^{1}H NMR (300 MHz, DMSO-d_6) δ 9.00 – 8.91 (m, 2H), 8.74 – 8.62 (m, 5H), 8.56 (td, $^{3}J_{H-H}$ =7.9, 1.5 Hz, 2H), 7.94 (ddd, $^{3}J_{H-H}$ =7.5, 1.4 Hz, 2H).

CIF file available in supplementary information.

9.3.0 Ligand Manipulation

9.3.1 Methyl 3,5-di(pyridin-2-yl)benzoate platinum chloride (**15**)

a. Methyl 3,5-di(pyridin-2-yl)benzoate

Methyl-5,5-dibromobenzoate (2.00 g, 6.90 mmol), 2-tri-n-butylstannylpyridine (tech. 80%) (6.00 ml), bis(triphenylphosphine)palladium dichloride (300 mg, 0.43 mmol) and LiCl (2.8 g) were added to dry degassed toluene (30 ml) and the mixture was freeze-pump-thaw degassed for three cycles. The mixture was then heated at reflux (125°C) for 72 h under inert atmosphere.

The reaction was allowed to cool to room temperature before a saturated aqueous solution of KF was added to quench the reaction. The resulting slurry was filtered over diatomaceous earth, washed with toluene (10 ml) and the eluent retained and dried under vacuum. To the resulting residue, DCM (150 ml) was added, and the solution purified two times in a separating funnel with 100 ml of 5% aqueous $NaHCO_3$ solution, retaining the DCM solution each time. The solution was then dried with anhydrous $MgSO_4$, filtered, and the solvent removed under reduced pressure.

Flash column chromatography was used to purify the solid. Product obtained 1:3 hexane: diethyl ethyl.

Yield: 0.92 g/46%

^{1}H NMR (300 MHz, chloroform-*d*): δ 8.92 (1 H, t, $^3J_{H-H}$ = 1.8), 8.85 – 8.67 (4 H, m), 7.91 (2 H, dt, $^3J_{H-H}$ = 8.0, 1.1 Hz), 7.81 (2 H, ddd, $^3J_{H-H}$ = 8.0, 1.8 Hz), 7.30 (3 H, ddd, $^3J_{H-H}$ = 7.4, 1.2 Hz), 3.99 (3 H, s), 1.45 – 1.26 (1 H, m), 0.93 (1 H, t, $^3J_{H-H}$ = 7.3).

Data consistent with literature.[47, 93]

b. Methyl 3,5-di(pyridin-2-yl)benzoate platinum chloride

Methyl 3,5-di(pyridin-2-yl)benzoate (0.10 g, 0.30 mmol), K_2PtCl_4 (0.14 g, 0.30 mmol) was charged to a round bottomed flask equipped with a stirrer bar. Acetonitrile (16 ml) and water (4 ml) were added and the mixture refluxed for 72 h. Reaction mixture cooled and filtered. Crystals grown from vapour diffusion of hexane into a concentrated chloroform solution at -18°C.

Yield: 0.98 g/ 98%

Data consistent with the literature.[47, 93]

9.3.2 Methyl 3,5-di(pyridin-2-yl)benzoate platinum Cyanate (**16**)

Methyl 3,5-di(pyridin-2-yl)benzoate platinum chloride (0.10 g, 0.19 mmols) and silver cyanate (0.040 g, 0.19 mmols) were charged to a RBF and suspended 30 ml of a 1:1 solvent mix of MeCN:DCM. Mixture was refluxed at 85°C for 48 h under an inert atmosphere.

Solution was cooled and the solvent removed. 50 ml of DCM was added to the residue and then filtered to remove the AgCl. The DCM was then removed leaving behind a yellow solid. Crystals were grown from the slow evaporation of a mixture of solvents.

Yield: 0.084 g/ 83%

FTIR-ν(cm^{-1}): 2222 (s, Br), 1698 (s), 1592 (s), 1458 (s), 1325 (s), 871 (m)

^{1}H NMR (500 MHz, Chloroform-*d*): δ 9.04 – 8.83 (2 H, m), 8.12 – 7.97 (4 H, m), 7.81 (2 H, ddd, $^{3}J_{H-H}$ = 8.1, 0.8 Hz), 7.37 (2 H, ddd, $^{3}J_{H-H}$ = 7.3, 1.4 Hz), 3.96 (3 H, s)
Theoretical CHN(%): C 43.35, H 2.49, N 7.98
Experimental CHN(%): C 43.19, H 2.76, N 6.89

CIF available in the supplementary information

9.3.3 Methyl 3,5-di(pyridin-2-yl)benzoate platinum Thiocyanate (**17**)

Methyl 3,5-di(pyridin-2-yl)benzoate platinum chloride (0.10 g, 0.19 mmols) and silver thiocyanate (0.030 g, 0.19 mmols) were charged to a RBF and suspended 30 ml of a 1:1 solvent mix of MeCN:DCM. Mixture was refluxed at 85˚C for 48 h under an inert atmosphere. Solution was cooled and the solvent removed. 50 ml of DCM was added to the residue and then filtered to remove the AgCl. The DCM was then removed leaving behind a yellow solid.

Yield: 0.092 g/ 92%

FTIR-ν(cm^{-1}): 2921 (s), 2861 (s), 2080 (s), 1698 (s), 1476 (s), 1236 (s).
^{1}H NMR (500 MHz, Chloroform-*d*): δ 9.10 (s, 2H), 7.96 – 7.81 (m, 4H), 7.69 – 7.41 (m, 2H), 7.29 – 7.05 (m, 2H), 3.92 – 3.71 (m, 3H)
Theoretical CHN(%): C 42.07, C 2.42, N 7.75
Experimental CHN(%): C 41.96, H 2.18, N 7.49

CIF available in the supplementary information

9.3.4 Methyl 3,5-di(pyridin-2-yl)benzoate platinum Acetate (**18**)

Methyl 3,5-di(pyridin-2-yl)benzoate platinum chloride (0.10 g) and silver acetate (0.032 g) were charged to a RBF and suspended 30 ml of a 1:1 solvent mix of MeCN:DCM. Mixture was refluxed at 85˚C for 24 h. Solution was cooled and the solvent removed. 50 ml of DCM was added to the residue and then filtered to remove the AgCl. The DCM was then removed. Crystals grown from the vapour diffusion of di-ethyl ether into a DCM solution at -18˚C and from the slow evaporation of a water and acetone mix.

Yield: 0.052 g/ 52%

FTIR-ν(cm^{-1}): 3448 (w,br), 2166 (m), 2033 (m), 1693 (s), 1605 (s), 1587 (s), 1239 (s).
^{1}H NMR (500 MHz, Chloroform-*d*): δ 9.41 – 9.26 (m, 2H), 8.09 (s, 2H), 7.99 (td, $^{3}J_{H-H}$ = 7.8, 1.6 Hz, 2H), 7.78 (ddd, $^{3}J_{H-H}$ = 7.9, 0.7 Hz, 2H), 7.34 (ddd, $^{3}J_{H-H}$ = 7.3, 1.4 Hz, 2H), 3.95 (s, 3H), 2.02 (d, $^{3}J_{H-H}$ = 1.0 Hz, 3H).
Theoretical CHN(%): C 44.20, H 2.97, N 5.15
Experimental CHN(%): C 39.24, H 3.11, N 4.68

CIF available in the supplementary information

9.3.5 Methyl 3,5-di(pyridin-2-yl)benzoate platinum Trifluoroacetate (**19**)

Methyl 3,5-di(pyridin-2-yl)benzoate platinum chloride (0.10 g, 0.19 mmols) and silver trifluoroacetate (0.020 g, 0.19 mmols) were charged to a RBF and suspended 30 ml of a 1:1 solvent mix of MeCN:DCM. Mixture was refluxed at 85˚C for 48 h under an inert atmosphere.
Solution was cooled and the solvent removed. 50 ml of DCM was added to the residue and then filtered to remove the AgCl. The DCM was then removed leaving behind an orange solid.

Yield: 0.062 g/ 62%

FTIR-ν(cm^{-1}): 1714 (s), 1687 (s), 1416 (s), 1182 (s), 1115 (s), 839 (s).
^{1}H NMR (500 MHz, Chloroform-*d*): δ 8.71 (dt, $^{3}J_{H-H}$ = 5.7, 1.0 Hz, 2H), 8.04 – 7.89 (m, 4H), 7.72 (ddd, $^{3}J_{H-H}$ = 7.9, 1.4, 0.8 Hz, 2H), 7.30 (ddd, $^{3}J_{H-H}$ = 7.3, 1.5 Hz, 2H), 4.27 (s, 3H).
^{19}F NMR (470 MHz, Chloroform-*d*): δ -74.58, -74.74 – -75.20 (m).
Theoretical CHN(%): C 40.21, H 2.19, N 4.69
Experimental CHN(%): C 39.52, H 2.53, N 4.02

9.3.6 Methyl 3,5-di(pyridin-2-yl)benzoate platinum triflate (**20**)

Methyl 3,5-di(pyridin-2-yl)benzoate platinum chloride (0.10 g, 0.19 mmols) and silver triflate (0.020 g, 0.19 mmols) were charged to a RBF and suspended 30 ml of a 1:1 solvent mix of MeCN:DCM. Mixture was refluxed at 85˚C for 48h under an inert atmosphere. Solution was cooled and the solvent removed. 50 ml of DCM was added to the residue and then filtered to remove the AgCl. The DCM was then removed leaving behind an orange solid.

Yield: 0.039 g/ 39%

FTIR-ν(cm^{-1}): 3453(m, br), 1720 (s), 1610 (s), 1239 (s), 1023 (s)
^{1}H NMR (500 MHz, Acetonitrile-d_3): δ 8.15 (d, $^{3}J_{H-H}$ = 5.5 Hz, 2H), 7.94 (dd, $^{3}J_{H-H}$ = 8.6, 7.0 Hz, 2H), 7.62 – 7.54 (m, 4H), 7.25 – 7.19 (m, 2H), 3.89 (s, 3H)
^{19}F NMR (470 MHz, Acetonitrile-d_3) δ -79.33.
Theoretical CHN(%): C 36.03, H 2.07, N 4.42
Experimental CHN(%): C 36.12, H 2.21, N 4.62

9.3.7 Methyl 3,5-di(pyridin-2-yl)benzoate platinum tosylate (**21**)

Methyl 3,5-di(pyridin-2-yl)benzoate platinum chloride (0.10 g, 0.19 mmols) and silver tosylate (0.020 g, 0.19 mmols) were charged to a RBF and suspended 30 ml of a 1:1 solvent mix of MeCN:DCM. Mixture was refluxed at 85˚C for 48 h under an inert atmosphere.
Solution was cooled and the solvent removed. 50 ml of DCM was added to the residue and then filtered to remove the AgCl. The DCM was then removed leaving behind a purple solid.

Yield: 0.032 g/ 32%

FTIR-ν(cm^{-1}): 1705 (s), 1607 (s), 1346 (s), 1248 (s), 1114(s)
^{1}H NMR (300 MHz, Chloroform-*d*): δ 9.45 – 9.33 (m, 2H), 8.18 – 8.07 (m, 3H), 8.01 (td, $^{3}J_{H-H}$ = 7.8, 1.6 Hz, 2H), 7.81 (t, $^{3}J_{H-H}$ = 7.6 Hz, 3H), 7.44 – 7.33 (m, 3H), 7.12 (d, $^{3}J_{H-H}$ = 7.8 Hz, 1H), 3.98 (d, $^{3}J_{H-H}$ = 8.5 Hz, 3H), 3.64 (d, $^{3}J_{H-H}$ = 4.9 Hz, 3H).
Theoretical CHN(%): C 45.80, H 3.08, N 4.27
Experimental CHN(%): C 45.01, H 3.73, N 4.42

9.4.0 Light Sensitive N^C^N Complexes.

9.4.1 Methyl 3,5-di(pyridine-2-yl)benzoate Platinum (E)-((4-(phenyldiazenyl) phenyl) ethynyl) (**22**)

a. (E)-1-phenyl-2-(4-((trimethylsilyl)ethynyl)phenyl)diazene. Procedure adapted from the literature.[146]

4-((trimethylsilyl)ethynyl)aniline (0.15 g, 0.79 mmol) and nitrosobenzene (0.085 g, 0.79 mmol) were dissolved in acetic acid (40 ml) and degassed. The reaction was stirred overnight at RT. The precipitate that formed was filtered and the solid recrystallized from ethanol.

^{1}H NMR (500 MHz, Chloroform-*d*) δ 7.94 – 7.90 (m, 2H), 7.90 – 7.85 (m, 2H), 7.62 – 7.59 (m, 2H), 7.54 – 7.49 (m, 3H), 0.28 (s, 9H).
^{13}C NMR (126 MHz, Chloroform-*d*): δ 132.69, 129.51, 128.61, 125.65, 122.84, 104.53, 96.93.

b. methyl 3,5-di(pyridin-2-yl)benzoate platinum (E)-((4-(phenyldiazenyl)phenyl)ethynyl)

Methyl 3,5-di(pyridin-2-yl)benzoate platinum chloride (0.10 g, 0.19 mmol) and (E)-1-phenyl-2-(4-((trimethylsilyl)ethynyl)phenyl)diazene (0.053 g, 0.19 mmol) were charged to a Schlenk and dissolved in the minimum amount of acetonitrile. The solution was refluxed for 48 h. The orange precipitate was collected by filtration.

Yield: 0.097 g/ 75%

FTIR-ν(cm^{-1}): 2079(s), 1704 (s, sh), 1584 (s), 1584 (s, br), 1473 (m), 1243 (s, br)
^{1}H NMR (300 MHz, Chloroform-*d*) δ = 9.53 (s, 2H), 8.16 (s, 3H), 8.04 – 7.87 (m, 6H), 7.85 – 7.75 (m, 2H), 7.72 – 7.66 (m, 2H), 7.60 – 7.44 (m, 4H), 3.95 (s, 3H).
Theoretical CHN(%): C 55.73, H 3.22, N 8.12
Experimental CHN(%): C 55.48, H 3.58, N 8.19

CIF file available in the supplementary information.

9.4.2. (*E*)-2,2'-(5-(phenyldiazenyl)-1,3-phenylene)dipyridine (**23**)

a. (*E*)-1-(3,5-dibromophenyl)-2-phenyldiazene. Procedure adapted from the literature.[146]

DiBromoaniline (1.00 g, 2.95 mmol) was dissolved in the minimum amount of acetic acid, an excess of nitrosobenzene was added. The solution was stirred at room temperature for 24 h. The orange precipitate was filtered and dried under a high vaccumm for 1hr. Product recrystallised from ethyl acetate.

Yield: 0.56 g/ 72%

FTIR-ν(cm^{-1}): 2108 (s, sh), 1723 (s, sh), 1557 (m, sh), 1201 (s, sh)
^{1}H NMR (300 MHz, Chloroform-*d*) δ = 8.01 (d, $^{3}J_{H-H}$ =1.8, 2H), 7.97 – 7.87 (m, 2H), 7.76 (t, $^{3}J_{H-H}$ =1.8, 1H), 7.60 – 7.48 (m, 3H).
^{13}C NMR (126 MHz, Chloroform-*d*) δ 153.81, 151.99, 135.61, 131.93, 129.13, 124.77, 123.21.

Data consistent with the literature.[172]

b. (*E*)-2,2'-(5-(phenyldiazenyl)-1,3-phenylene)dipyridine. Procedure adapted from the literature.[120]

A 100ml round bottomed flask is charged with a stirrer bar and flame dried. **(***E*)-1-(3,5-dibromophenyl)-2-phenyldiazene (0.64 g, 1.88 mmol), dppf (0.020 g, 0.038 mmol), $Pd(dba)_2$ (0.020 g, 0.038 mmol) were charged to the round bottomed flask. Dry THF (8 ml), 0.5 M pyridylzinc bromide (7.5 ml, 3.75 mmol) were syringed into the flask. The dark brown solution was refluxed for 12 h under a nitrogen atmosphere. The solution was cooled and THF removed in *vacuo*. The remaining solid was purified *via* flash chromatography using a dry load, Pet ether: Ethyl acetate 70:30. Crystals grown from the slow evaporation of DCM.

Yield: 0.45 g/ 70%

FTIR-ν(cm^{-1}): 1583 (s, sh), 1475 (m, sh).
^{1}H NMR (300 MHz, Chloroform-*d*) δ = 8.84 (t, $^3J_{H-H}$ =1.7, 1H), 8.77 (ddd, $^3J_{H-H}$ =4.8, 1.8, 0.9, 2H), 8.62 (d, $^3J_{H-H}$ =1.7, 2H), 8.03 – 7.93 (m, 4H), 7.83 (td, $^3J_{H-H}$ =7.7, 1.8, 2H), 7.64 – 7.45 (m, 3H), 7.31 (ddd, $^3J_{H-H}$ =7.5, 4.8, 1.1, 2H).
^{13}C NMR (126 MHz, Chloroform-*d*): δ 156.43, 153.49, 152.57, 149.69, 140.85, 136.76, 131.05, 129.02, 127.67, 122.90, 122.53, 121.64, 120.77.

CIF file available in supplementary information.

9.4.3. (*E*)-2,2'-(5-(phenyldiazenyl)-1,3-phenylene)dipyridine Platinum Chloride (**24**)

Several different synthetic methods have been tried but unfortunately this complex has not yet been successfully synthesised.

9.4.4 Methyl3,5-di(pyridine-2-yl)benzoate Platinum (E)-1-ethynyl-4-styrylbenzene (**25**)

a. (E)-trimethyl((4-styrylphenyl)ethynyl)silane

6-Bromostilbene (0.50 g), $Pd(PPh_3)Cl_2$ (0.076 g), CuI (0.037 g) and Et_3N (20 ml) was charged to a Schlenk and degassed for 1 h. TMSA (0.90 ml) was added and the mixture was refluxed at 90˚C for 72 h. The solvent was removed and the residue was extracted into hexane and filtered. Flash column chromatography was carried out and the product recovered at 80:20 Hex: ethyl acetate.

^{1}H NMR (500 MHz, Chloroform-*d*): δ 7.53 – 7.49 (m, 2H), 7.45 (s, 4H), 7.36 (dd, $^3J_{H-H}$ = 8.4, 6.9 Hz, 2H), 7.29 – 7.27 (m, 1H), 7.15 – 7.04 (m, 2H), 0.26 (s, 9H).
^{13}C NMR (126 MHz, Chloroform-*d*): δ 132.19, 128.62, 127.81,126.49, 126.15.

b. Methyl3,5-di(pyridine-2-yl)benzoate Platinum (E)-1-ethynyl-4-styrylbenzene

Methyl 3,5-di(pyridin-2-yl)benzoate platinum chloride (0.10 g, 0.19 mmol) and (E)-trimethyl((4-styrylphenyl)ethynyl)silane (0.053 g, 0.19 mmol) were charged to a Schlenk and dissolved in the minimum amount of methanol and DCM. The solution was refluxed for 48 h under an inert atmosphere. The yellow precipitate was collected by filtration.

Yield: 0.11 g/ 80%

FTIR-ν(cm^{-1}): 2959 (s), 2153 (s), 1251 (s), 833 (s)
^{1}H NMR (500 MHz, Chloroform-*d*): δ 9.40 – 9.28 (m, 2H), 8.18 (d, $^{3}J_{H-H}$ = 3.8 Hz, 1H), 8.10 (s, 1H), 7.99 (tdd, $^{3}J_{H-H}$ = 7.8, 3.9, 1.6 Hz, 3H), 7.82 – 7.76 (m, 3H), 7.59 – 7.44 (m, 5H), 7.40 – 7.30 (m, 4H), 7.13 – 7.06 (m, 2H), 3.95 (s, 3H).
Theoretical CHN(%): C 59.39, H 3.52, N 4.07
Experimental CHN(%): C 57.45, H 4.05, N 3.58

9.4.5. (*E*)-2,2'-(5-styryl-1,3-phenylene)dipyridine (**26**)

a. (*E*)-1,3-dibromo-5-styrylbenzene. Procedure adapted from the literature.[173]
1,3-Dibromo-5-(bromomethyl)benzene (1.00 g, 3.06 mmol) and an excess of triethylphosphite were placed in a round bottom flask and heated at 140°C for 4 h. The reaction mixture was cooled, THF (40 ml) and benzaldehyde (0.080 ml, 3.06 mmol) was added. The clear solution was cooled to 0°C in an ice bath and potassium tert butoxide (0.34 g, 3.06 mmol) was added portion wise. The reaction mixture was allowed to reach room temperature and stirred for 18 h under a nitrogen atmosphere.
The cloudy solution was then hydrolyzed with water and stirred for 30 minutes. Ethyl acetate (30 ml) was added and the organic layer was separated, retained and subsequently was with water (30 ml). The organic layer was then dried with $MgSO_4$ and concentrated in *vacuo*. The oil was purified using flash chromatography, hexane: DCM 9:1. White solid was isolated in good yield.

Yield: 0.64 g/ 62%

FTIR-ν(cm^{-1}): 1576 (s), 1547 (s), 1411 (m, sh), 1101 (sh), 966 (s)
^{1}H NMR (300 MHz, Chloroform-*d*) δ = 7.57 (d, $^{3}J_{H-H}$ =1.7, 2H), 7.55 – 7.47 (m, 3H), 7.42 – 7.34 (m, 2H), 7.34 – 7.28 (m, 1H), 7.15 – 6.89 (dd, 2H).
^{13}C NMR (126 MHz, Chloroform-*d*): δ 140.91, 136.18, 132.52, 131.46, 128.71, 128.35, 127.97, 126.69, 125.54, 123.11, 77.11.

b. (*E*)-2,2'-(5-styryl-1,3-phenylene)dipyridine. Procedure adapted from the literature.[120]
A 100ml round bottomed flask is charged with a stirrer bar and flame dried. (*E*)-1,3-dibromo-5-styrylbenzene (0.64 g, 1.87 mmol), dppf (0.020 g, 0.038 mmol), $Pd(dba)_2$ (0.030 g, 0.056 mmol) were charged to the round bottomed flask. Dry THF (10ml), 0.5 M pyridylzinc bromide (15ml, 7.50 mmol) were syringed into the flask. The dark brown solution was refluxed for 12 h under a nitrogen atmosphere. The solution was cooled and THF removed in *vacuo*. The remaining solid was purified *via* flash chromatography using a dry load, Pet ether: Ethyl acetate 80:20. Crystals grown from the slow evaporation of THF.

Yield: 0.37 g/ 59%

FTIR-ν(cm^{-1}): 1582 (s, sh), 1473 (m, sh), 958 (s)
^{1}H NMR (300 MHz, Chloroform-*d*) δ = 8.70 (ddd, $^{3}J_{H-H}$ =4.8, 1.9, 1.0, 2H), 8.42 (t, $^{3}J_{H-H}$ =1.7, 1H), 8.19 (d, $^{3}J_{H-H}$ =1.6, 2H), 7.85 (dt, $^{3}J_{H-H}$ =8.0, 1.1, 2H), 7.76 (td, $^{3}J_{H-H}$ =7.7, 1.8, 2H), 7.57 – 7.47 (m, 2H), 7.40 – 7.27 (m, 3H), 7.27 – 7.17 (m, 4H).

^{13}C NMR (126 MHz, Chloroform-*d*): δ 157.23, 149.82, 140.43, 138.58, 137.39, 136.94, 129.73, 128.85, 128.46, 127.88, 126.74, 125.75, 124.85, 122.53, 120.96.

CIF file available in the supplementary information.

Data is consistent with literature[144]

9.4.6. (*E*)-2,2'-(5-styryl-1,3-phenylene)dipyridine Platinum chloride (**27**)

Complex 19 (0.10 g, 0.30 mmol), K_2PtCl_4 (0.12 g, 0.30 mmol) was charged to a round bottomed flask equipped with a stirrer bar. Acetic acid (16 ml) and water (4 ml) were added and the mixture refluxed for 72 h under an argon atmosphere. Reaction mixture cooled and filtered. The solid residue was stirred in acetonitrile (20 ml) and filtered. A bright yellow solution was obtained, solvent removed in *vacuo* and yellow solid isolated. Crystals grown from vapour diffusion of hexane into a concentrated chloroform solution at -18°C.

Yield: 0.050 g/ 30%

FTIR-ν(cm^{-1}): 2919 (s), 1605 (s), 1467 (m)
^{1}H NMR (500 MHz, Chloroform-*d*) δ = 9.02 (d, 2H), 7.74 (td, $^3J_{H-H}$ =7.8, 1.7, 2H), 7.52 (d, $^3J_{H-H}$ =7.8, 2H), 7.44 – 7.36 (m, 2H), 7.32 (t, $^3J_{H-H}$ =7.2, 2H), 7.23 (d, $^3J_{H-H}$ =8.8, 3H), 7.02 (ddd, $^3J_{H-H}$ =7.3, 5.7, 1.4, 2H), 6.96 – 6.61 (dd, 2H).
Theoretical CHN(%): C 51.12, H 3.04, N 4.97
Experimental CHN(%): C 51.75, H 2.80, N 4.38

CIF file available in the supplementary information.

Data is consistent with literature.[144]

9.5.0 pH Sensitive Complexes

9.5.1 4-ethynyl-N,N-dimethylaniline-Methyl3,5-di(pyridin-2-yl)benzoate Platinum (**28**)

a. N,N-dimethyl-4-((trimethylsilyl)ethynyl)aniline

4-Bromo-N,N-dimethylaniline (2.00 g, 10 mmol), $Pd(PPh_3)Cl_2$ (0.42 g), CuI (0.19 g, 0.10 mmol) and Et_3N (20 ml). the mixture was degassed for 1 h. TMSA was added (4 ml, 30 mmol). The mixture was stirred at 80˚C, under an inert atmosphere for 24 h. The reaction was cooled and the solvent removed. The residue was extracted into hexane and filtered. Flash column chromatography was conducted and the product was isolated at 10% DCM: 90% Hexane.

Yield: 2.14 g

^{1}H NMR (500 MHz, Chloroform-*d*): δ 7.36 – 7.32 (m, 2H), 6.61 – 6.57 (m, 2H), 2.97 (s, 6H), 0.24 (s, 9H).
^{13}C NMR (126 MHz, Chloroform-*d*): δ 133.00, 111.48, 40.06.

b. 4-Ethynyl-N,N-dimethylaniline-Methyl3,5-di(pyridin-2-yl)benzoate Platinum

Methyl 3,5-di(pyridin-2-yl)benzoate platinum chloride (0.10 g, 0.19 mmol) and N,N-dimethyl-4-((trimethylsilyl)ethynyl)aniline (0.062 g, 0.19 mmol) were charged to a Schlenk and dissolved in the minimum amount of methanol and DCM. The solution was stirred at 40˚C for 24 h under an inert atmosphere. The red precipitate was collected by filtration.

Yield: 0.10 g/ 82%

FTIR-ν(cm^{-1}): 1698 (s), 1588 (s), 1235 (s)
^{1}H NMR (500 MHz, Chloroform-*d*): δ 9.38 – 9.22 (m, 2H), 8.16 (s, 1H), 8.04 (s, 2H), 7.97 (dtd, $^3J_{H-H}$ = 10.7, 7.7, 1.7 Hz, 3H), 7.81 – 7.72 (m, 3H), 7.51 – 7.46 (m, 1H), 7.31 (ddd, $^3J_{H-H}$ = 7.4, 5.7, 1.5 Hz, 1H), 6.73 – 6.67 (m, 1H), 3.94 (d, $^3J_{H-H}$ = 4.5 Hz, 6H), 2.96 (s, 3H).
Theoretical CHN(%): C 53.50, H 3.69, N 6.68
Experimental CHN(%): C 52.32, H 3.69, N 6.03

CIF Files available in the supplementary information.

9.5.2 N,N-dimethyl-3,5-di(pyridin-2-yl)aniline (**29**)

a. 3,5-dibromo-N,N-dimethylaniline

3,5-Dibromoaniline (2.00 g) in MeCN (40 ml) was charged to a Schlenk and degassed for 30 minutes. K_2CO_3 (2.00 g) and MeI (0.80 ml) was added and solution stirred at RT for 48 h. Solvent was removed and residue was purified by column chromatography, 16:1 Hexane: Ethyl acetate.

Yield: 1.50 g

FTIR-ν(cm^{-1}): 3093 (s), 2902 (m, br), 1582 (s), 1430(s)
^{1}H NMR (500 MHz, Chloroform-*d*) δ 6.95 (t, $^3J_{H-H}$ = 1.6 Hz, 1H), 6.72 (d, $^3J_{H-H}$ = 1.6 Hz, 2H), 2.94 (s, 6H).

^{13}C NMR (126 MHz, Chloroform-*d*) δ 151.93, 123.34, 121.05, 113.53, 77.11, 40.10.

b. N,N-dimethyl-3,5-di(pyridin-2-yl)aniline

3,5-Dibromo-N,N-dimethylaniline (1.40 g, 5 mmol), 2-tri-n-butylstannylpyridine (tech. 80%) (4.50 ml), bis(triphenylphosphine)palladium dichloride (225 mg, 0.43 mmol) and LiCl (2.80 g) were added to dry degassed toluene (30 ml) and the mixture was freeze-pump-thaw degassed for three cycles. The mixture was then heated at reflux (125°C) for 72 h under inert atmosphere.

The reaction was allowed to cool to room temperature before a saturated aqueous solution of KF was added to quench the reaction. The resulting slurry was filtered over diatomaceous earth, washed with toluene(10 ml) and the eluent retained and dried under vacuum. To the resulting residue, DCM (150 ml) was added, and the solution purified two times in a separating funnel with 100 ml of 5% aqueous $NaHCO_3$ solution, retaining the DCM solution each time. The solution was then dried with anhydrous $MgSO_4$, filtered, and the solvent removed under reduced pressure.

Flash column chromatography was used to purify the solid. Product obtained 4:6 hexane: ethyl acetate.

Yield: 0.50 g/ 36%

FTIR-ν(cm^{-1}): 3046 (m), 2889 (m, br), 1563 (s), 1414 (s), 1234 (s)

^{1}H NMR (500 MHz, Chloroform-*d*) δ 8.71 (ddd, $^3J_{H-H}$ = 4.8, 1.8, 0.9 Hz, 2H), 7.86 – 7.81 (m, 3H), 7.75 (ddd, $^3J_{H-H}$ = 7.9, 7.4, 1.8 Hz, 2H), 7.49 (d, $^3J_{H-H}$ = 1.4 Hz, 2H), 7.23 (ddd, $^3J_{H-H}$ = 7.4, 4.8, 1.2 Hz, 2H), 3.12 (s, 6H).

^{13}C NMR (126 MHz, Chloroform-*d*) δ 158.04, 151.39, 149.38, 140.57, 136.48, 121.94, 120.87, 114.22, 111.75, 40.80.

CIF file available in the supplementary information.

9.5.3 N,N-dimethyl-3,5-di(pyridin-2-yl)aniline Platinum Chloride (**30**)

N,N-Dimethyl-3,5-di(pyridin-2-yl)aniline (0.10 g, 0.30 mmol), K_2PtCl_4 (0.15 g, 0.30 mmol) was charged to a round bottomed flask equipped with a stirrer bar. Acetonitrile (16 ml) and water (4 ml) were added and the mixture refluxed for 72 h. Reaction mixture cooled and filtered and solvent removed. Crystals grown from vapour diffusion of hexane into concentrated methanol solution at -18˚C.

Yield: 0.096 g/ 98%

FTIR-ν(cm^{-1}): 3003 (m), 2217 (s, br), 1808 (s), 1465 (s), 1289 (s)

^{1}H NMR (500 MHz, Methanol-d_4) δ 9.08 – 8.96 (m, 2H), 8.06 (td, $^3J_{H-H}$ = 7.8, 1.6 Hz, 2H), 7.91 (dt, $^3J_{H-H}$ = 7.9, 1.1 Hz, 2H), 7.75 – 7.70 (m, 2H), 7.43 (ddd, $^3J_{H-H}$ = 7.4, 5.7, 1.4 Hz, 2H), 1.31 (s, 6H).

Theoretical CHN(%): C 42.82, H 3.19, N 8.32

Experimental CHN(%): C 42.29, H 3.10, N 8.86

CIF file available in the supplementary information

CHAPTER 10

References

1. R. W. Cattrall, I. D. McKelvie, S. D. Kolev, Y. Zhang, R. W. Cattrall, I. D. McKelvie and S. D. Kolev, Gold Bulletin, 2011, **43**
2. N. F. Golʹdshleger, V. V. Es'kova, A. E. Shilov and A. Shteinman, *A. Zh. Fiz. Khim.*, 1972, **46**, 1353-1354.
3. M. S. Khan, A. Haque, M. K. Al-Suti and P. R. Raithby, *Journal of Organometallic Chemistry*, 2015, **793**, 114-133.
4. R. A. Al-Alawi, K. Laxman, S. Dastgir and J. Dutta, *Applied Surface Science*, 2016, **377**, 200-206.
5. T. Y. Chen and V. O. Rodionov, *Acs Catalysis*, 2016, **6**, 4025-4033.
6. W. Liu and H. L. Wang, *Surface Science*, 2016, **648**, 120-125.
7. P. Du, K. Knowles and R. Eisenberg, *Journal of the American Chemical Society*, 2008, **130**, 12576.
8. E. Wiltshaw, S. Subramarian, C. Alexopoulos and G. H. Barker, *Cancer Treatment Reports*, 1979, **63**, 1545-1548.
9. S. Dilruba and G. V. Kalayda, *Cancer Chemother. Pharmacol.*, 2016, **77**, 1103-1124.
10. M. Atoji, J. W. Richardson and R. E. Rundle, *Journal of the American Chemical Society*, 1957, **79**, 3017-3020.
11. C.-L. Ho and W.-Y. Wong, *Coordination Chemistry Reviews*, 2011, **255**, 2469-2502.
12. W.-Y. Wong, *Dalton Transactions*, 2007, 4495-4510.
13. J. S. Wilson, A. Köhler, R. H. Friend, M. K. Al-Suti, M. R. A. Al-Mandhary, M. S. Khan and P. R. Raithby, *The Journal of Chemical Physics*, 2000, **113**, 7627-7634.
14. W. Y. Wong, *Coordination Chemistry Reviews*, 2005, **249**, 971-997.
15. W.-Y. Wong and C.-L. Ho, *Coordination Chemistry Reviews*, 2006, **250**, 2627-2690.
16. A. Diez, E. Lalinde and M. Teresa Moreno, *Coordination Chemistry Reviews*, 2011, **255**, 2426-2447.
17. V. W. W. Yam, *Nature Chemistry*, 2010, **2**, 790.
18. J. A. G. Williams, *Photochemistry and Photophysics of Coordination Compounds: Platinum*, Springer-Verlag Berlin Heidelberg, 2007.
19. J. Schneider, P. W. Du, P. Jarosz, T. Lazarides, X. Y. Wang, W. W. Brennessel and R. Eisenberg, *Inorganic Chemistry*, 2009, **48**, 4306-4316.
20. P. Shao, Y. J. Li, A. Azenkeng, M. R. Hoffmann and W. F. Sun, *Inorganic Chemistry*, 2009, **48**, 2407-2419.
21. G. Wulfsberg, *Inorganic Chemistry*, University Science Books: Sausalito- CA., 2000.
22. D. P. J. Atkins P, *Elements of Physical Chemistry*, Oxford University Press, 4th edn., 2005.
23. J. R. Lakowicz, *Principles of Fluorescence Spectroscopy*, Springer, 3rd edn., 2006.
24. D. P. J. Atkins P, in *Atkins' Physical Chemistry*, OUP Oxford, 8th edn., 2006, ch. 14, pp. 492-495.
25. P. p. Mertens R, OLED-Info, (accessed 24/06/2016).
26. J. A. G. Williams, S. Develay, D. L. Rochester and L. Murphy, *Coordination Chemistry Reviews*, 2008, **252**, 2596-2611.
27. P.-T. Chou, Y. Chi, M.-W. Chung and C.-C. Lin, *Coordination Chemistry Reviews*, 2011, **255**, 2653-2665.
28. F. Puntoriero, in *Photochemistry, Vol 39*, ed. A. Albini, 2011, vol. 39, pp. 65-87.

29. X. Yang, C. Yao and G. Zhou, *Platinum Metals Review*, 2013, **57**, 2-16.

30. Price comparison of Platinum, Palladium and Nickel, (accessed 27/06/16).

31. R. J. Atkins P, *Inorganic Chemistry*, Oxford University Press, 4th edn., 2006.

32. R. R. deHaas, R. P. M. vanGijlswijk, E. B. vanderTol, H. Zijlmans, T. BakkerSchut, J. Bonnet, N. P. Verwoerd and H. J. Tanke, *Journal of Histochemistry & Cytochemistry*, 1997, **45**, 1279-1292.

33. D. M. E. Freeman, A. Minotto, W. Duffy, K. J. Fallon, I. McCulloch, F. Cacialli and H. Bronstein, *Polymer Chemistry*, 2016, **7**, 722-730.

34. J. R. Sommer, A. H. Shelton, A. Parthasarathy, I. Ghiviriga, J. R. Reynolds and K. S. Schanze, *Chemistry of Materials*, 2011, **23**, 5296-5304.

35. K. R. Graham, Y. X. Yang, J. R. Sommer, A. H. Shelton, K. S. Schanze, J. G. Xue and J. R. Reynolds, *Chemistry of Materials*, 2011, **23**, 5305-5312.

36. R. C. Evans, P. Douglas and C. J. Winscom, *Coordination Chemistry Reviews*, 2006, **250**, 2093-2126.

37. P.-K. Chow, G. Cheng, G. S. M. Tong, W.-P. To, W.-L. Kwong, K.-H. Low, C.-C. Kwok, C. Ma and C.-M. Che, *Angewandte Chemie-International Edition*, 2015, **54**, 2084-2089.

38. W. Lu, B. X. Mi, M. C. W. Chan, Z. Hui, C. M. Che, N. Y. Zhu and S. T. Lee, *Journal of the American Chemical Society*, 2004, **126**, 4958-4971.

39. S. Fuertes, S. K. Brayshaw, P. R. Raithby, S. Schiffers and M. R. Warren, *Organometallics*, 2012, **31**, 105-119.

40. G. W. V. Cave, F. P. Fanizzi, R. J. Deeth, W. Errington and J. P. Rourke, *Organometallics*, 2000, **19**, 1355-1364.

41. W. Lu, M. C. W. Chan, K. K. Cheung and C. M. Che, *Organometallics*, 2001, **20**, 2477-2486.

42. G. Morgan and F. Burstall, *Journal of Chemical Society*, 1934, 1498-1500.

43. R. Buchner, C. T. Cunningham, J. S. Field, R. J. Haines, D. R. McMillin and G. C. Summerton, *Journal of the Chemical Society-Dalton Transactions*, 1999, 711-717.

44. R. Zhang, Z. Liang, A. Han, H. Wu, P. Du, W. Lai and R. Cao, *Crystengcomm*, 2014, **16**, 5531-5542.

45. L. M. Hight, M. C. McGuire, Y. Zhang, M. A. Bork, P. E. Fanwick, A. Wasserman and D. R. McMillin, *Inorganic Chemistry*, 2013, **52**, 8476-8482.

46. D. J. Cardenas, A. M. Echavarren and M. C. R. de Arellano, *Organometallics*, 1999, **18**, 3337-3341.

47. J. A. G. Williams, A. Beeby, E. S. Davies, J. A. Weinstein and C. Wilson, *Inorganic. Chemistry.*, 2003, **42**, 8609-8611.

48. E. Rossi, A. Colombo, C. Dragonetti, D. Roberto, F. Demartin, M. Cocchi, P. Brulatti, V. Fattori and J. A. G. Williams, *Chemical Communications*, 2012, **48**, 3182-3184.

49. E. Rossi, L. Murphy, P. L. Brothwood, A. Colombo, C. Dragonetti, D. Roberto, R. Ugo, M. Cocchi and J. A. G. Williams, *Journal of Materials Chemistry*, 2011, **21**, 15501-15510.

50. Y.-L. Rao, D. Schoenmakers, Y.-L. Chang, J.-S. Lu, Z.-H. Lu, Y. Kang and S. Wang, *Chemistry-a European Journal*, 2012, **18**, 11306-11316.

51. W. A. Tarran, G. R. Freeman, L. Murphy, A. M. Benham, R. Kataky and J. A. G. Williams, *Inorganic Chemistry*, 2014, **53**, 5738-5749.

52. L. Murphy, P. Brulatti, V. Fattori, M. Cocchi and J. A. G. Williams, *Chemical Communications*, 2012, **48**, 5817-5819.

53. W. Sotoyama, T. Satoh, H. Sato, A. Matsuura and N. Sawatari, *Journal of Physical Chemistry A*, 2005, **109**, 9760-9766.

54. D. Beljonne, H. F. Wittmann, A. Kohler, S. Graham, M. Younus, J. Lewis, P. R. Raithby, M. S. Khan, R. H. Friend and J. L. Bredas, *Journal Of Chemical Physics*, 1996, **105**, 3868-3877.

55. M. J. Bryant, University of Bath, 2015.

56. S. L. James, M. Younus, P. R. Raithby and J. Lewis, *Journal of Organometallic Chemistry*, 1997, **543**, 233-235.

57. M. Jura, P. R. Raithby and P. J. Wilson, in *Molecular Design and Applications of Photofunctional Polymers and Materials*, eds. W. Y. Wong and A. S. AbdElAziz, 2012, pp. 56-84.

58. C. Po, C. H. Tao, K. F. Li, C. K. M. Chan, H. L. K. Fu, K. W. Cheah and V. W. W. Yam, *Inorganica Chimica Acta*, 2019, **488**, 214-218.

59. C. K. M. Chan, C. H. Tao, K. F. Li, K. M. C. Wong, N. Y. Zhu, K. W. Cheah and V. W. W. Yam, *Dalton Transactions*, 2011, **40**, 10670-10685.

60. V. W. W. Yam, *Comptes Rendus Chimie*, 2005, **8**, 1194-1203.

61. V. W. W. Yam, K. M. C. Wong and N. Y. Zhu, *Journal of the American Chemical Society*, 2002, **124**, 6506-6507.

62. S. D. Taylor, W. Howard, N. Kaval, R. Hart, J. A. Krause and W. B. Connick, *Chemical Communications*, 2010, **46**, 1070-1072.

63. S. D. Taylor, A. E. Norton, R. T. Hart, Jr., M. K. Abdolmaleki, J. A. Krause and W. B. Connick, *Chemical Communications*, 2013, **49**, 9161-9163.

64. O. S. Wenger, *Chemical Reviews*, 2013, **113**, 3686-3733.

65. D. E. Janzen and K. R. Mann, *Dalton Transactions*, 2015, **44**, 4223-4237.

66. J. R. Berenguer, E. Lalinde, A. Martin, M. T. Moreno, S. Ruiz, S. Sanchez and H. R. Shahsavari, *Chemical Communications*, 2013, **49**, 5067-5069.

67. P. Du, *Inorganica Chimica Acta*, 2010, **363**, 1355-1358.

68. T. J. Wadas, Q. M. Wang, Y. J. Kim, C. Flaschenreim, T. N. Blanton and R. Eisenberg, *Journal of the American Chemical Society*, 2004, **126**, 16841-16849.

69. S. J. Choi, J. Kuwabara, Y. Nishimura, T. Arai and T. Kanbara, *Chemistry Letters*, 2012, **41**, 65-67.

70. X. Zhang, Z. Chi, Y. Zhang, S. Liu and J. Xu, *Journal of Materials Chemistry C*, 2013, **1**, 3376-3390.

71. Y. Sagara and T. Kato, *Nature Chemistry*, 2009, **1**, 605-610.

72. T. Abe, T. Itakura, N. Ikeda and K. Shinozaki, *Dalton Transactions*, 2009, 711-715.

73. M. Cocchi, D. Virgili, V. Fattori, D. L. Rochester and J. A. G. Williams, *Advanced Functional Materials*, 2007, **17**, 285-289.

74. A. Han, P. Du, Z. Sun, H. Wu, H. Jia, R. Zhang, Z. Liang, R. Cao and R. Eisenberg, *Inorganic Chemistry*, 2014, **53**, 3338-3344.

75. M. Kato, *Bulletin of the Chemical Society of Japan*, 2007, **80**, 287-294.

76. A. Dorazco-Gonzalez, *Organometallics*, 2014, **33**, 868-875.

77. M. Albrecht and G. van Koten, *Angewandte Chemie-International Edition*, 2001, **40**, 3750-3781.

78. G. R. Freeman and J. A. G. Williams, in *Organometallic Pincer Chemistry*, eds. G. VanKoten and D. Milstein, Springer-Verlag Berlin, Berlin, 2013, vol. 40, pp. 89-129.

79. J. R. Kumpfer, S. D. Taylor, W. B. Connick and S. J. Rowan, *Journal of Materials Chemistry*, 2012, **22**, 14196-14204.

80. C. M. Sangan, O. J. Pountney, J. A. Scobie, B. Cochrane, C. Stubbs and P. R. Raithby, *International Journal of Heat and Mass Transfer*, 2018, **127**, 437-446.

81. W. Clegg, *Crystal Structure determination*, Oxford University Press, 2011.

82. Unit cell, http://xray0.princeton.edu/~phil/Facility/Guides/XrayDataCollection.html, (accessed 05/06/16).

83. A. E. Goeta and J. A. K. Howard, *Chemical Society Reviews*, 2004, **33**, 490-500.

84. A. L. Patterson, *Physical Review*, 1934, **46**.

85. P. Naumov, in *Advanced X-Ray Crystallography*, ed. K. Rissanen, 2012, vol. 315, pp. 111-131.

86. F. H. Allen, J. C. Cole and J. A. K. Howard, *Acta Crystallographica Section A*, 1995, **51**, 112-121.

87. C. F. Macrae, P. R. Edgington, P. McCabe, E. Pidcock, G. P. Shields, R. Taylor, M. Towler and J. van De Streek, *Journal of Applied Crystallography*, 2006, **39**, 453-457.

88. I. J. Bruno, J. C. Cole, P. R. Edgington, M. Kessler, C. F. Macrae, P. McCabe, J. Pearson and R. Taylor, *Acta Crystallographica Section B-Structural Science*, 2002, **58**, 389-397.

89. R. K. Sabirov, *Fizika Nizkikh Temperatur*, 1992, **18**, 1125-1127.

90. M. Florescu, *Revue Roumaine De Chimie*, 1993, **38**, 905-912.

91. N. Rankin, D. Preiss, P. Welsh, K. Burgess, S. Nelson, D. A. Lawlor and N. Sattar, , 2014.

92. D. E. Oreilly, *Journal of Chemical Physics.*, 1962, **36**, 855-&.

93. M. J. Bryant, J. M. Skelton, L. E. Hatcher, C. Stubbs, E. Madrid, A. R. Pallipurath, L. H. Thomas, C. H. Woodall, J. Christensen, S. Fuertes, T. P. Robinson, C. M. Beavers, S. J. Teat, M. R. Warren, F. Pradaux-Caggiano, A. Walsh, F. Marken, D. R. Carbery, S. C. Parker, N. B. McKeown, R. Malpass-Evans, M. Carta and P. R. Raithby, *Nature Communications*, 2017, **8**, 9.

94. A. Kobayashi, S. Oizumi, Y. Shigeta, M. Yoshida and M. Kato, *Dalton Transactions*, 2016, **45**, 17485-17494.

95. Z. D. Bugarcic, F. W. Heinemann and R. v. Eldik, *Dalton Transactions*, 2004, , 279-286.

96. V. C.-H. Wong, C. Po, S. Y.-L. Leung, A. K.-W. Chan, S. Yang, B. Zhu, X. Cui and V. W.-W. Yam, *Journal of the American Chemical Society*, 2018, **140**, 657-666.

97. L. J. Grove, J. M. Rennekamp, H. Jude and W. B. Connick, *Journal of the American Chemical Society*, 2004, **126**, 1594-1595.

98. L. J. Grove, A. G. Oliver, J. A. Krause and W. B. Connick, *Inorganic Chemistry*, 2008, **47**, 1408-1410.

99. M. L. Muro, C. A. Daws and F. N. Castellano, *Chemical Communications*, 2008, , 6134-6136.

100. J. S. Field, O. Q. Munro and B. P. Waldron, *Dalton Transactions*, 2012, **41**, 5486-5496.

101. A. Maron, A. Szlapa, K. Czerwinska, J. G. Malecki, S. Krompiec and B. Machura, *CrystEngComm*, 2016, **18**, 5528-5536.

102. V. W.-W. Yam, R. P.-L. Tang, K. M.-C. Wong, C.-C. Ko and K.-K. Cheung, *Inorganic Chemistry*, 2001, **40**, 571-574.

103. Q. Z. Yang, Q. X. Tong, L. Z. Wu, Z. X. Wu, L. P. Zhang and C. H. Tung, *European Journal of Inorganic Chemistry*, 2004, 1948-1954.

104. Z.-H. Zhang, J. Liu, L.-Q. Wan, F.-R. Jiang, C.-K. Lam, B.-H. Ye, Z. Qiao and H.-Y. Chao, *Dalton Transactions*, 2015, **44**, 7785-7796.

105. R. P.-L. Tang, K. M.-C. Wong, N. Zhu and V. W.-W. Yam, *Dalton Transactions*, 2009, 3911-3922.

106. J. S. Field, C. R. Wilson and O. Q. Munro, *Inorganica Chimica Acta*, 2011, **374**, 197-204.

107. W. P. Griffith, *Quarterly Reviews*, 1962, **16**, 188-207.

108. E. C. Constable, J. Lewis, M. C. Liptrot and P. R. Raithby, *Inorganica Chimica Acta*, 1990, **178**, 47-54.

109. T. K. Aldridge, E. M. Stacy and D. R. McMillin, *Inorganic Chemistry*, 1994, **33**, 722-727.

110. C. S. Angle, A. G. DiPasquale, A. L. Rheingold and L. H. Doerrer, *Acta Crystallographica Section C*, 2006, **62**, m340-m342.

111. V. Phillips, F. G. Baddour, T. Lasanta, J. M. Lopez-de-Luzuriaga, J. W. Bacon, J. A. Golen, A. L. Rheingold and L. H. Doerrer, *Inorganica Chimica Acta*, 2010, **364**, 195-204.

112. M. Akerman, K. Akerman, D. Jaganyi and D. Reddy, *Acta Crystallographica Section E*, 2011, **67**, m1075-m1076.

113. M. C. Etter, J. C. Macdonald and J. Bernstein, *Acta Crystallographica Section B-Structural Science*, 1990, **46**, 256-262.

114. Y. Fan, Y.-M. Zhu, F.-R. Dai, L.-Y. Zhang and Z.-N. Chen, *Dalton Transactions*, 2007, 3885-3892.

115. T. Kayano, S. Takayasu, K. Sato and K. Shinozaki, *Chemistry-a European Journal*, 2014, **20**, 16583-16589.

116. A. A. Lemus-Santana, J. Rodriguez-Hernandez, L. F. del Castillo, M. Basterrechea and E. Reguera, *Journal of Solid State Chemistry*, 2009, **182**, 757-766.

117. J. S. Field, R. J. Haines, L. P. Ledwaba, R. McGuire, Jr., O. Q. Munro, M. R. Low and D. R. McMillin, *Dalton Transactions*, 2007, 192-199.

118. L. Murphy and J. A. G. Williams, in *Molecular Organometallic Materials for Optics*, eds. H. LeBozec and V. Guerchais, 2010, vol. 28, pp. 75-111.

119. S. J. Farley, D. L. Rochester, A. L. Thompson, J. A. K. Howard and J. A. G. Williams, *Inorganic Chemistry*, 2005, **44**, 9690-9703.

120. T. Bunlaksananusorn, K. Polborn and P. Knochel, *Angewandte Chemie-International Edition*, 2003, **42**, 3941-3943.

121. O. V. Dolomanov, L. J. Bourhis, R. J. Gildea, J. A. K. Howard and H. Puschmann, *Journal of Applied Crystallography*, 2009, **42**, 339-341.

122. W.-P. To, K. T. Chan, G. S. M. Tong, C. Ma, W.-M. Kwok, X. Guan, K.-H. Low and C.-M. Che, *Angewandte Chemie- International Edition*, 2013, **52**, 6648-6652.

123. T.-B. Lim, K. H. Cho, Y.-H. Kim and Y.-C. Jeong, *Optics express*, 2016, **24**, 17950-17959.

124. P.-O. Åstrand, P. S. Ramanujam, S. Hvilsted, K. L. Bak and S. P. A. Sauer, *Journal of the American Chemical Society*, 2000, **122**, 3482-3487.

125. K. Goda, M. Omori and K. Takatoh, *Liquid Crystals*, 2018, **45**, 485-490.

126. R. D. Mukhopadhyay, V. K. Praveen and A. Ajayaghosh, *Materials Horizons*, 2014, **1**, 572-576.

127. J. Zeng, K.-Q. Chen, X. Deng and M. Long, *Journal of Physics D: Applied Physics*, 2016, **49**, 415104.

128. I. V. Lijanova, I. Moggio, E. Arias, T. Klimova and M. Martinez-Garcia, *Tetrahedron*, 2008, **64**, 10258-10266.

129. M. Baroncini, S. d'Agostino, G. Bergamini, P. Ceroni, A. Comotti, P. Sozzani, I. Bassanetti, F. Grepioni, T. M. Hernandez, S. Silvi, M. Venturi and A. Credi, *Nature Chemistry*, 2015, **7**, 634-640.

130. S. Chen, W. Wang and W. Xu, *Materials Letters*, 2016, **180**, 196-199.

131. J. Perez-Miqueo, A. Altube, E. Garcia-Lecina, A. Tron, N. D. McClenaghan and Z. Freixa, *Dalton transactions (Cambridge, England : 2003)*, 2016, **45**, 13726-13741.

132. Y. Amatatsu, *Chemical Physics Letters*, 2015, **631**, 47-53.

133. J. Griffiths, *Chemical Society Reviews*, 1972, **1**, 481-493.

134. A. Cembran, F. Bernardi, M. Garavelli, L. Gagliardi and G. Orlandi, *Journal of the American Chemical Society*, 2004, **126**, 3234-3243.

135. N. Siampiringue, G. Guyot, S. Monti and P. Bortolus, *Journal of Photochemistry*, 1987, **37**, 185-188.

136. P. Bortolus and S. Monti, *The Journal of Physical Chemistry*, 1979, **83**, 648-652.

137. S. Shinkai, K. Shigematsu, M. Sato and O. Manabe, *Journal of the Chemical Society, Perkin Transactions 1*, 1982, 2735-2739.

138. B. Pipoosananakaton, M. Sukwattanasinitt, N. Jaiboon, N. Chaichit and T. Tuntulani, *Tetrahedron Letters*, 2000, **41**, 9095-9100.

139. T. Yutaka, I. Mori, M. Kurihara, J. Mizutani, N. Tamai, T. Kawai, M. Irie and H. Nishihara, *Inorganic Chemistry*, 2002, **41**, 7143-7150.

140. S.-S. Sun and A. J. Lees, *Organometallics*, 2002, **21**, 39-49.

141. S. G. Hahm, S. W. Lee, T. J. Lee, S. A. Cho, B. Chae, Y. M. Jung, S. B. Kim and M. Ree, *The Journal of Physical Chemistry B*, 2008, **112**, 4900-4912.

142. L. A. Faustino, A. E. Hora Machado and A. O. T. Patrocinio, *Inorganic Chemistry*, 2018, **57**, 2933-2941.

143. D. Cameron and S. Eisler, *Journal of physical organic chemistry.*, 2018.

144. N. Baggi, E. Garoni, A. Colombo, C. Dragonetti, S. Righetto, D. Roberto, J. Boixel, V. Guerchais and S. Fantacci, *Polyhedron*, 2018, **140**, 74-77.

145. M. Valiev, E. J. Bylaska, N. Govind, K. Kowalski, T. P. Straatsma, H. J. J. Van Dam, D. Wang, J. Nieplocha, E. Apra, T. L. Windus and W. de Jong, *Computer Physics Communications*, 2010, **181**, 1477-1489.

146. E. Merino, *Chemical Society Reviews*, 2011, **40**, 3835-3853.

147. Y. Chen, K. Li, W. Lu, S. S.-Y. Chui, C.-W. Ma and C.-M. Che, *Angewandte Chemie International Edition*, 2009, **48**, 9909-9913.

148. M. Jura, O. F. Koentjoro, P. R. Raithby, E. L. Sharp and P. J. Wilson, *MRS Proceedings*, 2011, **846**, DD3.7.

149. A. G. Jarvis, H. A. Sparkes, S. E. Tallentire, L. E. Hatcher, M. R. Warren, P. R. Raithby, D. R. Allan, A. C. Whitwood, M. C. R. Cockett, S. B. Duckett, J. L. Clark and I. J. S. Fairlamb, *Crystengcomm*, 2012, **14**, 5564-5571.

150. K. J. Fallon, N. Wijeyasinghe, N. Yaacobi-Gross, R. S. Ashraf, D. M. E. Freeman, R. G. Palgrave, M. Al-Hashimi, T. J. Marks, I. McCulloch, T. D. Anthopoulos and H. Bronstein, *Macromolecules*, 2015, **48**, 5148-5154.

151. K. Li, Y. Chen, W. Lu, N. Zhu and C.-M. Che, *Chemistry-a European Journal*, 2011, **17**, 4109-4112.

152. Y. Qing-Zheng, T. Qing-Xiao, W. Li-Zhu, W. Zi-Xin, Z. Li-Ping and T. Chen-Ho, *European Journal of Inorganic Chemistry*, 2004, **2004**, 1948-1954.

153. E. Najahi, A. Valentin, P.-L. Fabre, K. Reybier and F. Nepveu, *European Journal of Medicinal Chemistry*, 2014, **78**, 269-274.

154. T. Gunnlaugsson, M. Glynn, G. M. Tocci, P. E. Kruger and F. M. Pfeffer, *Coordination Chemistry Reviews*, 2006, **250**, 3094-3117.

155. E. B. Veale and T. Gunnlaugsson, *Annual Reports Section "B" (Organic Chemistry)*, 2010, **106**, 376-406.

156. J. Cabrera-Gonzalez, C. Vinas, M. Haukka, S. Bhattacharyya, J. Gierschner and R. Nunez, *Chemistry (Weinheim an der Bergstrasse, Germany)*, 2016, **22**, 13588-13598.

157. L. Gutierrez-Arzaluz, T. Rocha-Rinza and F. Cortes-Guzman, *Computational and Theoretical Chemistry*, 2015, **1053**, 214-219.

158. S. K. Brayshaw, T. L. Easun, M. W. George, A. M. E. Griffin, A. L. Johnson, P. R. Raithby, T. L. Savarese, S. Schiffers, J. E. Warren, M. R. Warren and S. J. Teat, *Dalton Transactions*, 2012, **41**, 90-97.

159. L. E. Hatcher, J. M. Skelton, M. R. Warren, C. Stubbs, E. L. da Silva and P. R. Raithby, *Physical Chemistry Chemical Physics*, 2018, **20**, 5874-5886.

160. P. R. Raithby, *Iucrj*, 2015, **2**, 5-6.

161. M. R. Warren, S. K. Brayshaw, L. E. Hatcher, A. L. Johnson, S. Schiffers, A. J. Warren, S. J. Teat, J. E. Warren, C. H. Woodall and P. R. Raithby, *Dalton Transactions*, 2012, **41**, 13173-13179.

162. A. Bej, K. Ghosh, A. Sarkar and D. W. Knight, *Rsc Advances*, 2016, **6**, 11446-11453.

163. J. Vaughan, D. J. Carter, A. L. Rohl, M. I. Ogden, B. W. Skelton, P. V. Simpson and D. H. Brown, *Dalton Transactions*, 2015

164. J. Muzart, *European Journal of Organic Chemistry*, 2015, 5693-5707.

165. M. C. Gimeno, J. M. Lopez-de-Luzuriaga, E. Manso, M. Monge, M. E. Olmos, M. Rodriguez-Castillo, M.-T. Tena, D. P. Day, E. J. Lawrence and G. G. Wildgoose, *Inorganic Chemistry*, 2015, **54**, 10667-10677.

166. J. Fernandez-Cestau, B. Bertrand, M. Blaya, G. A. Jones, T. J. Penfold and M. Bochmann, *Chemical Communications (Cambridge, U. K.)*, 2015, **51**, 16629-16632.

167. D. A. Smith, D.-A. Rosca and M. Bochmann, *Organometallics*, 2012, **31**, 5998-6000.

168. G. M. Sheldrick, *Acta Crystallographica Section A*, 2008, **64**, 112-122.

169. G. M. Sheldrick, in *Direct Methods for Solving Macromolecular Structures*, ed. S. Fortier, 1998, vol. 507, pp. 401-411.

170. G. M. Sheldrick, *Acta Crystallographica a-Foundation and Advances*, 2015, **71**, 3-8.

171. G. M. Sheldrick, *Acta Crystallographica Section C-Structural Chemistry*, 2015, **71**, 3-8.

172. N. Anwar, T. Willms, B. Grimme and A. J. C. Kuehne, *Acs Macro Letters*, 2013, **2**, 766-769.

173. S. M. Johnson, S. Connelly, I. A. Wilson and J. W. Kelly, *Journal of Medicinal Chemistry*, 2008, **51**, 6348-6358.